



**HAL**  
open science

# Single-cell RNA Sequencing Analysis of Human Airway Regeneration and Remodeling in Asthma

Elisa Redman

► **To cite this version:**

Elisa Redman. Single-cell RNA Sequencing Analysis of Human Airway Regeneration and Remodeling in Asthma. Cellular Biology. Université Côte d'Azur, 2024. English. NNT: 2024COAZ6017. tel-04850948

**HAL Id: tel-04850948**

**<https://theses.hal.science/tel-04850948v1>**

Submitted on 20 Dec 2024

**HAL** is a multi-disciplinary open access archive for the deposit and dissemination of scientific research documents, whether they are published or not. The documents may come from teaching and research institutions in France or abroad, or from public or private research centers.

L'archive ouverte pluridisciplinaire **HAL**, est destinée au dépôt et à la diffusion de documents scientifiques de niveau recherche, publiés ou non, émanant des établissements d'enseignement et de recherche français ou étrangers, des laboratoires publics ou privés.

# THÈSE DE DOCTORAT

Découverte des mécanismes responsables des défauts de régénération épithéliale dans l'asthme, par approche transcriptomique sur cellules uniques

**Elisa REDMAN**

Institut de Pharmacologie Moléculaire et Cellulaire (IPMC) – UMR 7275 – U1323

**Présentée en vue de l'obtention**  
**du grade de docteur en** Sciences de la Vie et de la Santé option Interactions moléculaires et cellulaires d'Université Côte d'Azur

**Dirigée par** : Dr. Laure-Emmanuelle Zaragosi / Dr. Pascal Barbry

**Soutenue le** : 19 Septembre 2024

Devant le jury, composé de :

Pr. Camille Taillé, PUPH, UPC

Dr. Valérian Dormoy, MC, URCA, P3Cell

Pr. Martijn Nawijn, PR, University of Groningen

Pr. Pascal Chanez, PUPH, AMU, C2VN

Dr. Laure-Emmanuelle Zaragosi, CR, UniCA, IPMC

Dr. Pascal Barbry, DR, UniCA, IPMC





# Découverte des mécanismes responsables des défauts de régénération épithéliale dans l'asthme, par approche transcriptomique sur cellules uniques

## **Jury :**

### **Président du jury**

**Pr. Pascal Chanez**, PUPH, Assistance Publique - Hôpitaux de Marseille, Aix-Marseille Université, Centre de recherche en CardioVasculaire et Nutrition, INSERM 1263 - INRAE 1260

### **Rapporteurs**

**Pr. Camille Taillé**, PUPH, Assistance Publique-Hôpitaux de Paris, Université Paris Cité (Université Paris Diderot), Inserm UMR 1152

**Dr. Valérian Dormoy**, MC, Université de Reims Champagne Ardenne, P3Cell, UMR-S 1250

### **Examineurs**

**Pr. Martijn Nawijn**, PR, University of Groningen, UMCG

**Dr. Laure-Emmanuelle Zaragosi**, CRHC-Inserm, Université Côte d'Azur, IPMC, UMR7275, U1323

**Dr. Pascal Barbry**, DRCE-CNRS, Université Côte d'Azur, IPMC, UMR7275, U1323



# Remerciements

Je tiens tout d'abord à remercier le **Dr. Pascal Barbry** de m'avoir accueillie au sein de son équipe et d'avoir co-encadré ma thèse pendant ces quatre années. Ce fut un honneur pour moi d'intégrer un des laboratoires pionniers du séquençage d'ARN sur cellule unique en France et une chance de me retrouver dans une équipe aussi accueillante et bienveillante.

Merci au **Dr. Laure-Emmanuelle Zaragosi** pour avoir été la meilleure co-encadrante de thèse que j'aurais pu avoir. Merci pour ta gentillesse et ta bienveillance, merci de m'avoir formée à l'art du scRNA-seq et de m'avoir transmis ta passion pour l'épithélium des voies respiratoires. Et merci pour tous tes précieux conseils et retours qui ont toujours été constructifs et pertinents. J'espère aussi un jour avoir la moitié de ton énergie !

Je souhaite remercier mes deux rapporteurs, le **Pr. Camille Taillé** et le **Dr. Valérian Dormoy**, pour avoir évalué mon travail. Merci également à mes examinateurs, **Pr. Martijn Nawijn**, **Pascal** et **Laure-Emmanuelle**. Thank you **Martijn** for having made the trip from the Netherlands. Enfin, merci au **Pr. Pascal Chanez** pour avoir présidé le jury.

Merci au **Pr. Aleksander Edelman** et au **Dr. Bernard Mari** pour avoir constitué mon comité de suivi de thèse et m'avoir suivie tout au long de mon projet.

Je tiens à remercier le **Pr. Charles-Hugo Marquette** et le **Pr. Sylvie Leroy** du Centre Hospitalier Universitaire de Nice, pour m'avoir fourni les biopsies saines.

Un grand merci au **Pr. Pascal Chanez**, au **Dr. Delphine Gras** et au **Dr. Kim Valette** de l'équipe Chanez à Marseille pour m'avoir fourni les biopsies asthmatiques, pour avoir réalisé les manip rhinovirus et pour cette belle collaboration.

Merci à la plateforme wet-lab pour la préparation des librairies 10X et les séquençages, merci à **Marie-Jeanne Arguel**, **Valentine Freschi**, **Marie Couralet** et **Virginie Magnone**. En particulier merci **Marie** pour ta minutie, pour les prières devant le chromium pendant ce fameux été mais aussi pour tous nos moments en 210 et ton soutien pendant les coups durs. Merci **Virginie** pour m'avoir expliqué la construction des librairies, ainsi que pour ta gentillesse.

Merci aussi à mes expertes bio-infos **Morgane Fierville** pour la première partie de thèse, puis **Paola Porracciolo** pour la fin. Merci pour m'avoir transmis une petite partie de votre expertise en R et python et bonne continuation pour vos thèses respectives, je sais avec la plus grande des certitudes que vous avez un bel avenir devant vous (malgré le fait que vous m'avez lâchée !). Merci **Morgane** pour avoir mis en forme mes jeux de données, pour ton attention aux détails et ton excellent contrôle qualité, merci pour les 5000 tours de typage et de scANVI, mais aussi merci pour nos sorties, soirées, concerts et séances de grimpe. Merci **Paola** pour ton travail sur la partie épigénétique et les trajectoires et merci pour ton amitié, ta complicité, ton coaching pour les oraux, nos délires neurodivergents... bref tu sais que je ne pourrais pas décrire en quelques mots ces dernières années dans le même bureau que toi.

Merci **Valentine** et **Pauline** pour nos pauses café et nos discussions sans fins sur les ongles.

Merci au reste de la **team PB** pour avoir été de super collègues et d'avoir créé le meilleur environnement pour passer ma thèse. Merci **Gilles** pour nous avoir honoré de ta prestance et de ta prose, le labo n'est plus pareil sans toi. Merci **Christophe** et **Kévin** pour m'avoir initiée au pipeline single-cell. Thank you **Eamon** for your work on the medium comparison paper. Merci **Brice** pour toute ton aide et pour m'avoir permis de participer au projet multiciliogenesis. **Robin** merci pour m'avoir offert Milo, le plus beau des cadeaux. Merci **Alizé** pour m'avoir aidée sur les manip et pour nos sorties. Merci **Juejun** pour tes gâteaux. Merci aussi à **Pierre**, **Géraldine**, **Reiner**, **Antoine**, **Yvon**, **Magali**.

Merci aux petits et grands stagiaires que j'ai croisé pendant ces quatre années. Merci **Margot** pour m'avoir accompagnée dans mes premières cultures ALI. Merci **Estelle** pour avoir été ma première stagiaire « à 100% », merci pour ton travail et je te souhaite d'aller aussi loin que tu veux dans tes études. Un grand merci et bravo à **Thimotey-Lou** pour tout ton travail sur le projet CRISPR.

Merci à **Sophie** et **Frédéric** de la plateforme imagerie pour m'avoir formée aux microscopes et pour leurs conseils.

Merci à **l'équipe BM** pour toutes nos belles discussions.

**Célia** merci d'avoir été ma partenaire de répétitions pour ma thèse en 180s. Imaginez un champ de roses...

Merci **Noura, Hyame** et **Eirini** pour nos mini pauses au coin d'un couloir ou dans le bus.

Merci à tous mes amis anciens et nouveaux d'avoir embelli ma vie de sudiste. **Nelly**, merci pour ton énergie et merci de m'avoir accueillie à bras ouverts après mon cambriolage. **Arnaud** et les anciens de l'AJC, pour toutes nos sorties et nos karaokés. Coco tu as été une de mes plus belles rencontres ici. **Mélody**, mon meilleur date tinder, pour nos cafés-ragots, on se retrouve vite au Colorado ! **Mathieu** merci pour toutes nos sorties terrasses et tapas, j'espère qu'on se reverra vite aux US aussi ! Merci à **Anna** et **Stéphane** pour nos soirées DND et le co-parentage de chats, en particulier merci infiniment pour avoir gardé et pris soin de Milo à chaque fois que j'ai dû m'absenter. **Léa**, ma copine on sera à jamais unies par le trauma du lycée et je chéris toujours nos retrouvailles car même si elles sont rares elles sont précieuses. **Nathalie**, on s'est tragiquement rencontré à la fin de nos thèses seulement but I am so glad we did meet anyway !

**Vadym**, my favorite ginger, thank you for being my best friend for more than a decade, to ten more years.

Merci **Marine**, la femme de ma vie, ma princesse des îles, d'être mon plus grand soutien depuis toutes ces années. Merci d'être toujours là pour moi, tu es et seras toujours mon amitié la plus précieuse.

Merci à toute ma famille, **Maman, Grand-Mère, Grand-Père, Fanny, Eric**, pour votre soutien et vos encouragements tout au long de ma thèse. Merci de m'avoir transmis vos meilleurs gènes dont j'essaye de faire le meilleur usage pour vous rendre fiers. **Grand-père** merci infiniment de m'avoir aidée à être indépendante pendant toute la durée de mes études, sans toi je n'aurais pas pu y arriver.

Enfin merci à **Milo**, Minouche, mon amour de chat, pour son affection et pour me rappeler que faire des pauses pour jouer c'est bien aussi.

# Résumé

L'épithélium des voies respiratoires est un écosystème complexe composé de cellules basales, de cellules à gobelet et de cellules multiciliées (MCC), ainsi que d'autres types cellulaires plus rares. Les cils motiles des MCC permettent d'éliminer le mucus piègeur d'agents pathogènes produit par les cellules à gobelet. Dans l'asthme, l'épithélium subit une inflammation chronique et un remodelage, menant à une diminution du nombre de MCC et à une hyperplasie des cellules à gobelet, ce qui altère la clairance mucociliaire et aggrave les symptômes. L'interleukine 13 (IL-13), produite par les lymphocytes T helper de type 2 (Th2), les mastocytes, les basophiles et les cellules innées lymphoïdes de type 2, est un médiateur clé de l'asthme de type 2. L'IL-13 cause l'hyperplasie des cellules à gobelet, tandis que les rhinovirus, principales causes d'exacerbation de l'asthme, augmentent la production de mucus et réduisent la fonction ciliaire. Outre l'implication déjà caractérisée du système immunitaire dans l'asthme, la contribution des mécanismes propres à l'épithélium restait à élucider.

Pour étudier les événements moléculaires contrôlant l'équilibre des cellules épithéliales et leur dérèglement dans l'asthme, des biopsies bronchiques de donneurs sains et d'asthmatiques sévères ont été reconstruites in vitro grâce à un modèle d'interface air-liquide (ALI), traitées avec l'IL-13 ou le rhinovirus A16 (RVA16), et analysées par séquençage d'ARN sur cellule unique (scRNA-seq). Plus de 260 000 cellules de 9 donneurs sains et 11 asthmatiques sévères ont été étudiées. Les épithéliums asthmatiques ont présenté une hyperplasie des cellules basales et une signature inflammatoire même en condition contrôle. L'IL-13 a provoqué un remodelage épithélial après 8 jours et a induit le facteur de transcription des cellules à gobelet SPDEF dans une sous-population de MCC que nous avons nommées "cellules mucociliées". L'infection par RVA16 a déclenché une réponse interféron et chimiokine 4,7 fois plus importante dans les épithéliums sains que dans les asthmatiques, selon le nombre de gènes différentiellement exprimés. Deux semaines après retrait de l'IL-13 ou du RVA16, les épithéliums ont retrouvé leur expression génique et/ou composition cellulaire initiales, indiquant des capacités de récupération similaires entre donneurs sains et asthmatiques sévères. Des gènes potentiellement régulateurs de l'asthme et du remodelage épithélial ont été identifiés. Leur rôle est exploré par invalidation via CRISPR-Cas9 et analyse scRNA-seq.

Le modèle ALI joue un rôle central dans toutes les études in vitro et repose sur différents milieux commerciaux ou « maison » dont l'impact sur la différenciation épithéliale au niveau de la cellule unique n'a jamais été étudié. J'ai utilisé le scRNA-seq pour comparer 4 milieux différents et découvert des variations dans la composition cellulaire, dans l'expression des gènes avec notamment une expression différentielle du facteur d'entrée du SARS-CoV-2 ACE2, ainsi que dans les transcrits du sécrétome. La prolifération en PneumaCult-Ex Plus a favorisé un profil sécrétoire, soulignant l'influence clé des milieux de prolifération sur les caractéristiques de différenciation épithéliale. Mes données fournissent un répertoire détaillé pour évaluer les effets des conditions de culture sur la différenciation épithéliale des voies respiratoires.

Enfin, j'ai participé à la caractérisation de la différenciation des cellules multiciliées en étudiant le locus génomique MIR34B/C, hôte des gènes BTG4, LAYN et HOATZ. Les microARN miR-34b/c sont étroitement liés à la famille miR-449 connus comme régulateurs de la multiciliogenèse. En utilisant le scRNA-seq et la microscopie à super-résolution, nous avons démontré que le locus MIR34B/C, comme son homologue MIR449, est un locus multiciliaire englobant des gènes qui sont des régulateurs potentiels de la multiciliogenèse.

**Mots clés :** Single-cell RNA seq, Asthme, Voies respiratoires, Humain, Epithélial, Régénération



# Summary

The airway surface epithelium is a complex cellular ecosystem that includes basal, goblet, multiciliated cells, as well as other rarer cell types. Motile cilia on multiciliated cells clear the pathogen-trapping mucus secreted by goblet cells. In asthma, the epithelium undergoes chronic inflammation and remodeling, which results in a decreased number of multiciliated cells and a goblet cell hyperplasia that impairs mucociliary clearance and worsen symptoms. Interleukin 13 (IL-13), produced by type-2 lymphocyte T helper (Th2) cells, mast cells, basophils, and type-2 innate lymphoid cells, is a major mediator of type 2 high asthma, the most common asthma endotype. IL-13 directly causes goblet cell hyperplasia, while rhinovirus infections, the leading causes of asthma exacerbation, increase mucus production and reduce ciliary function. Apart from the already well-characterized implication of the immune system in asthma, the underlying contribution of epithelium-specific mechanisms remained so far unresolved.

To investigate the molecular events controlling airway epithelial cells balance and their dysregulation in asthma, bronchial biopsies from healthy and severe asthma donors were reconstructed in vitro using an Air-Liquid Interface (ALI) model. They were treated with IL-13 or rhinovirus A16 (RVA16) and analyzed by single-cell RNA sequencing (scRNA-seq). Over 260,000 cells from 9 healthy and 11 severe asthma donors were analyzed. Severe asthma epithelia showed basal cell hyperplasia and an inflammatory signature, even under control conditions. IL-13 treatment caused significant epithelial remodeling after 8 days in both healthy and severe asthma epithelia and induced expression of the goblet-specific transcription factor SPDEF in a multiciliated cell subpopulation that we labeled "mucous-ciliated cells." RVA16 infection triggered an interferon and chemokine response 4.7 times greater in healthy epithelia than in asthmatic ones, assessed by the number of differentially expressed genes. Two weeks after IL-13 or RVA16 removal, epithelia recovered their initial cell composition and/or gene expression, indicating similar recovery capacities between severe asthmatic and healthy donors. A set of genes was identified as potential regulators of the asthmatic phenotype and airway epithelial remodeling. Their putative role in remodeling is currently investigated by CRISPR-Cas9 invalidation and scRNA-seq analysis.

The ALI model plays a central role in all in vitro studies and its careful characterization is essential. It relies on different commercial and home-made media, but their impact on epithelial cell differentiation at the single-cell level had never been evaluated. I used scRNA-seq to quantify cell type distribution and gene expression variations across 4 distinct media. I found variations in cell composition, gene expression, and secretome transcripts that I illustrated more precisely with the differential expression of the SARS-CoV-2 entry factor ACE2. Proliferation in PneumaCult-Ex Plus favored secretory cell fate, highlighting the key influence of proliferation media on epithelial differentiation. My data provide a comprehensive repertoire for evaluating culture condition influence on airway epithelial differentiation.

Lastly, I participated in the characterization of multiciliated cell differentiation by investigating the MIR34B/C genomic locus, host to the genes BTG4, LAYN, and HOATZ. The miR-34b/c microRNAs are closely related to the miR-449 family known as multiciliogenesis regulators. Using scRNA-seq and super-resolution microscopy, we demonstrated that the MIR34B/C locus, like its homolog MIR449, is a multiciliary locus encompassing genes that are potential regulators of multiciliogenesis.

**Keywords:** Single-cell RNA seq, Asthma, Airway, Human, Epithelial, Regeneration

# Table of contents

Remerciements .....	3
Résumé.....	5
Summary .....	6
List of figures .....	iv
Chapter I. Introduction.....	1
A. Airway epithelium .....	1
1. Composition.....	4
Cell types.....	4
Structures.....	16
Cellular junctions .....	18
2. Functions of the airway epithelium .....	20
Physical barrier.....	20
Mucociliary clearance .....	20
Immune defense .....	27
3. Development of the lung and the respiratory airways .....	28
Embryonic origin of the upper airway epithelium .....	28
Embryonic origin of the lower airway epithelium.....	29
4. Homeostasis and regeneration .....	30
Multiciliogenesis .....	30
Regeneration and remodeling.....	33
Signaling pathways and molecular mechanisms controlling development and regeneration .....	34
Cellular trajectories.....	43
5. Models for studying the airway epithelium regeneration.....	44
Animal models .....	44
In vitro cultures .....	45
B. Asthma .....	47
1. Definition and clinical features .....	47
2. Classification .....	47
Type 2-high .....	48
Type 2-low.....	48
Severe asthma.....	49
3. Pathophysiology.....	49
Inflammation.....	49
Remodeling in asthma .....	50
4. Interleukin-13 .....	53
Signaling pathway .....	53
IL-13 in vitro .....	54
Effect of IL-13 on goblet cells .....	54

Effect of IL-13 on multiciliated cells .....	55
5. Rhinovirus .....	55
6. Treatments of asthma .....	56
Biologics .....	57
7. Murine models of asthma .....	58
C. Cellular memory .....	58
1. Trained immunity .....	58
2. Epigenetics .....	60
Chapter II. Results .....	62
A. Single-cell Analysis of Human Airway Regeneration and Remodeling in Asthma .....	62
Introduction .....	62
Building of an asthma-centric perturbation atlas .....	65
IL-13 induces remodeling in healthy and severe asthma epithelia. ....	65
Single-cell RNA-sequencing dataset .....	66
Differences of composition and transcriptomic profiles between <i>in vitro</i> severe asthma and healthy cells .....	70
Asthma epithelium maintains a phenotype of disease <i>in vitro</i> .....	70
Characterization of cell types and states induced during remodeling and regeneration events .....	78
Characterization of cell types and states induced by IL-13 in healthy epithelium .....	78
Characterization of cell types and states induced by IL-13 in severe asthma epithelium .....	85
Comparison of the differences in response to IL-13 between asthmatic and healthy epithelia .....	93
Cell trajectories inference .....	98
Characterization of cell types and states induced by rhinovirus A16 in healthy and severe asthma epithelia .....	106
Discussion and opening .....	110
Context .....	110
Reconstituted epithelia from severe asthmatics have a different cellular and molecular composition .....	110
Memory of disease .....	111
Severe asthma epithelia have a different cellular and molecular response to IL-13 than healthy epithelia .....	113
A mucous-ciliated cell population is increased after IL-13 treatment .....	115
Cell trajectory inferences show that multiciliated cells can transdifferentiate into goblet cells .....	116
Characterization of cell types and states induced by rhinovirus A16 in healthy and severe asthma epithelia .....	117
Organ-specific differences in the asthmatic response .....	118
Dosage of secreted mucus .....	118
miRNA .....	119
Functional analysis of human airway regeneration and remodeling in asthma by CRISPR-Cas9 .....	119
B. Functional analysis of human airway regeneration and remodeling in asthma by CRISPR-Cas9 .....	120
Introduction and objectives .....	120
Results .....	124
Characterization of IL-13-induced epithelial remodeling in BCI cell cultures .....	124
Invalidation of <i>EHF</i> and <i>GATA3</i> genes by CRISPR-Cas9 RNP .....	126
Characterization of the effect of target gene inactivation on epithelial remodeling .....	131
Single-cell RNA sequencing analysis of invalidated epithelia .....	134

Discussion .....	138
C. Cell culture differentiation and proliferation conditions influence the in vitro regeneration of the human airway epithelium .....	141
D. The MIR34B/C genomic region contains multiple potential regulators of multiciliogenesis .....	144
Chapter III: Materials and methods .....	146
Cell culture .....	146
IL-13 treatment .....	147
Rhinovirus infection .....	147
Virus replication quantification .....	148
Cytokine quantification with LEGENDplex™ .....	148
MUC5AC and MUC5B quantification with ELISA .....	148
Immunofluorescence microscopy .....	149
CRISPR Cas9 RNP .....	149
Quality control .....	150
Quantitative RT-PCR .....	150
Western blot .....	151
Dot Blot .....	152
Single-cell RNA-sequencing of primary cells .....	152
IL-13 experiment sequencing approach .....	152
RVA experiment sequencing approach .....	153
Preprocessing, integration, normalization and clustering .....	154
Sequencing, alignment, demultiplexing and count table generation .....	157
Library preparation and sample multiplexing of IL-13 experiments .....	157
Quality control and cell filtering .....	159
Integration / Annotation .....	161
Differential expression analysis .....	165
Analysis of cell type proportions .....	165
Enrichment analysis .....	165
Cell trajectory inference pipeline .....	165
A. Verifying and subsetting data .....	166
B. Velocityto for RNA velocity calculation .....	166
C. scVelo .....	167
D. CellRank kernels .....	169
E. CellRank estimators .....	171
Flex single-cell RNA sequencing (BCi cells) .....	173
CUT&Tag chromatin analysis .....	173
Sample preparation .....	174
Sequencing .....	175
Analysis .....	175
References .....	177

# List of figures

<b>Figure 1:</b> Frontal section of nasal and paranasal cavities.....	1
<b>Figure 2:</b> Organization of the human lung.....	2
<b>Figure 3:</b> Anatomical comparison between mouse and human airways. ....	3
<b>Figure 4:</b> Overview of the different lung cell types featured in CellCards.....	4
<b>Figure 5:</b> Cell composition of the surface airway epithelium.....	5
<b>Figure 6:</b> Basal cells. ....	6
<b>Figure 7:</b> Basal cells maintain the stem cell niche.....	7
<b>Figure 8:</b> Mucus secretion. ....	11
<b>Figure 9:</b> Multiciliated cells structure and components.....	12
<b>Figure 10:</b> Mucous-ciliated cells.....	15
<b>Figure 11:</b> Goblet cells are precursors of multiciliated cells.....	15
<b>Figure 12:</b> Schematic representation of a submucosal gland. ....	16
<b>Figure 13:</b> Markers and cre lines of the main epithelial cell types.....	17
<b>Figure 14:</b> Hillocks. ....	18
<b>Figure 15:</b> Schematic representation of the different epithelial junctions. ....	20
<b>Figure 16:</b> Characteristic of mucins. ....	21
<b>Figure 17:</b> Representative glycans found in a mucin monomer. ....	22
<b>Figure 18:</b> MUC5B and MUC5AC expression across the lungs. ....	24
<b>Figure 19:</b> The two models of the periciliary layer.....	26
<b>Figure 20:</b> Representation of a cilium beat (left) and modelisation of asynchronous beat (right). ....	26
<b>Figure 21:</b> Signaling in epithelial immunity. ....	28
<b>Figure 22:</b> Divisions of neural plate border and locations of the cranial placodes in a chick embryo. .	29
<b>Figure 23:</b> Embryonic lung patterning and development.....	30
<b>Figure 24:</b> Centriole amplification in multiciliated cells. ....	32
<b>Figure 25:</b> Multiciliogenesis pathway. ....	33
<b>Figure 26:</b> Mouse and human lung development. ....	34
<b>Figure 27:</b> Molecular repertoire of major signaling pathways in <i>in vitro</i> epithelial cells.....	37
<b>Figure 28:</b> Wnt/ $\beta$ -catenin signaling pathway.....	39
<b>Figure 29:</b> Wnt signaling and multiciliogenesis. ....	40
<b>Figure 30:</b> Canonical Hedgehog signaling.....	41
<b>Figure 31:</b> Epithelial Shh expression in the embryonic lung. ....	42
<b>Figure 32:</b> Epithelial cell trajectories. ....	43
<b>Figure 33:</b> SO <sub>2</sub> injury model.....	44

<b>Figure 34:</b> Xenopus mucociliary epithelium maturation.....	45
<b>Figure 35:</b> Epithelium culture at the Air-Liquid Interface.....	46
<b>Figure 36:</b> Bronchi on a chip model.....	46
<b>Figure 37:</b> Type 2 asthma classification.....	48
<b>Figure 38:</b> Asthma signaling pathway.....	50
<b>Figure 39:</b> Airway wall remodeling in asthma.....	51
<b>Figure 40:</b> Comparison between a normal epithelium and a goblet hyperplasia.....	52
<b>Figure 41:</b> IL-4 and IL-13 signaling pathways.....	54
<b>Figure 42:</b> Rhinovirus signaling in the airway epithelium.....	56
<b>Figure 43:</b> Monoclonal antibody treatments for asthma.....	57
<b>Figure 44:</b> Trained immunity and tolerance.....	59
<b>Figure 45:</b> Chromatin-related epigenetic functions.....	60
<b>Figure 46:</b> Polycomb and trithorax mechanisms.....	61
<b>Figure 47:</b> Experimental design of the project.....	63
<b>Figure 48:</b> Characterization of IL-13 induced remodeling of healthy and severe asthma epithelia.....	65
<b>Figure 49:</b> UMAP representation of the IL-13 perturbation dataset.....	66
<b>Figure 50:</b> Cell typing of single cell RNA sequencing dataset.....	68
<b>Figure 51:</b> Cell clusters correlations.....	69
<b>Figure 52:</b> Asthma remodeling is conserved in ALI cultures.....	70
<b>Figure 53:</b> Differential expression of genes between healthy and severe asthma cell types.....	71
<b>Figure 54:</b> Differential gene expression between healthy and severe asthma basal cells.....	72
<b>Figure 55:</b> Analysis comparison of regulated pathways across cell types.....	73
<b>Figure 56 :</b> Differential gene expression between healthy and severe asthma multiciliated cells.....	74
<b>Figure 57 :</b> Differential gene expression between healthy and severe asthma goblet cells.....	75
<b>Figure 58:</b> Differences in secretions ELISA detection of MUC5AC.....	77
<b>Figure 59:</b> IL-13 induces remodeling in healthy airway epithelial ALI cultures.....	78
<b>Figure 60:</b> IL-13 induces a strong inflammatory response in healthy goblet cells.....	79
<b>Figure 61:</b> Upregulated genes in IL-13 treated healthy goblet cells.....	80
<b>Figure 62:</b> Differential gene expression between untreated and IL-13 treated healthy multiciliated cells.....	81
<b>Figure 63:</b> IL-13 triggers deciliation of healthy multiciliated cells.....	83
<b>Figure 64:</b> IL-13 induces a population of mucus ciliated cells.....	84
<b>Figure 65:</b> IL-13 induces remodeling in severe asthma airway epithelial ALI cultures.....	86
<b>Figure 66:</b> Severe asthma epithelium undergoes a goblet to basal switch under chronic IL-13 treatment.....	87

<b>Figure 67</b> : Differential gene expression between untreated and IL-13 treated severe asthma goblet cells.....	89
<b>Figure 68</b> :IL-13 activation in severe asthma basal cells. ....	90
<b>Figure 69</b> : Differential gene expression between untreated and IL-13 treated severe asthma basal cells. ....	92
<b>Figure 70</b> : IL-13 induces mucus secretion in both healthy and severe asthma ALI cultures at timepoint 2.....	94
<b>Figure 71</b> : Differences in amplitude response between healthy and severe asthma epithelia. ....	95
<b>Figure 72</b> : Comparison of IL-13 response between healthy and severe asthma epithelia across timepoints. ....	97
<b>Figure 73</b> : How to infer cell trajectories among airway cell types? .....	98
<b>Figure 74</b> : Cell fate probabilities at baseline, timepoint 2. ....	101
<b>Figure 75</b> : Cell fate probabilities after IL-13 treatment, timepoint 2. ....	103
<b>Figure 76</b> : Visualization of pseudotime flow highlights IL-13 perturbations. ....	104
<b>Figure 77</b> : Cell fate probabilities at resolution (ILRV), timepoint 2. ....	105
<b>Figure 78</b> : UMAP representation of the rhinovirus A16 perturbation dataset. ....	107
<b>Figure 79</b> : RVA16 induces a strong viral response in healthy epithelia.....	108
<b>Figure 80</b> : Comparison between healthy and severe asthma response to RVA infection. ....	109
<b>Figure 81</b> : Preliminary result of epithelial trained immunity. ....	117
Figure 82: Principle of CRISPR-Cas9.....	121
Figure 83: Overview of the experimental set up. ....	123
<b>Figure 84</b> : Epithelial cell composition of BCi during IL13 treatment time course. ....	125
<b>Figure 85</b> : Effect of IL-13 treatment on expression of genes involved in epithelial remodeling and candidate genes.....	126
<b>Figure 86</b> : Validation of CRISPR/Cas9 efficacy by genomic PCR .....	127
Figure 87: Validation of gene invalidation by Nanopore sequencing.....	129
<b>Figure 88</b> : Characterization of invalidation at the protein level.....	130
<b>Figure 89</b> : Effect of invalidation on epithelial composition.....	132
<b>Figure 90</b> : Detection and quantification of MUC5AC in invalidated epithelia. ....	133
<b>Figure 91</b> : Effect of invalidation on expression of genes involved in epithelial remodeling. ....	134
<b>Figure 92</b> : Single cell atlas of CRISPR cells.....	136
<b>Figure 93</b> : EHF regulates GATA3 expression. ....	137
<b>Figure 94</b> : 10x Genomics multiplexing workflow. ....	153
<b>Figure 95</b> : CellRank2 general pipeline. ....	170

# Chapter I. Introduction

## A. Airway epithelium

The respiratory system has the crucial task of carrying and delivering oxygen-rich air to the blood. It comprises three main regions, the upper and lower airways and the alveoli:

- 1) The upper, or extra-thoracic, airways are made of the nose, nasal cavity, mouth, larynx and pharynx. With the exception of the mouth that serves as an alternative airway opening that cannot filter particles, the role of the upper airways is to filter, humidify and warm up inhaled air (Ximena et al., 2006). The nasal cavity lays on top of the hard palate and is split in half by the nasal septum. The lateral walls are made of three turbinates on each side (**Fig.1**) (Cardesa et al., 2017).

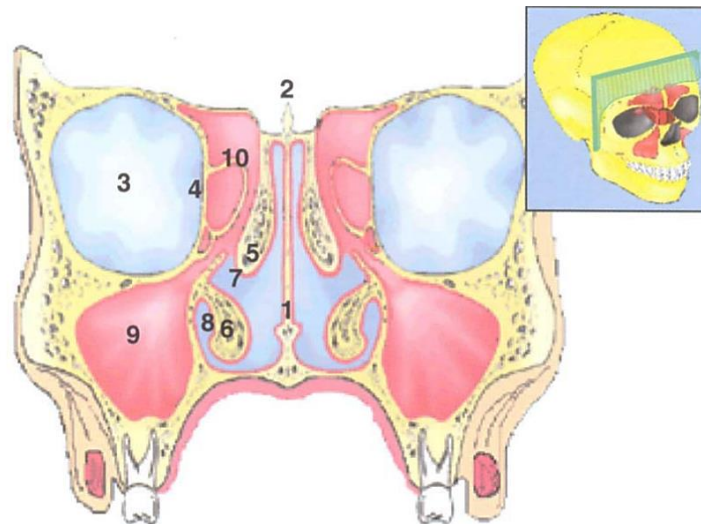


**Figure 1:** Frontal section of nasal and paranasal cavities.

1, Nasal septum; 2, crista galli; 3, orbit; 4, lamina papyracea; 5, middle turbinate; 6, inferior turbinate; 7, middle meatus; 8, inferior meatus; 9, maxillary sinus; 10, ethmoid sinus.

From Watelet & Van Cauwenberge, 1999.

- 2) The lower, or intra-thoracic, airways are composed of a succession of ducts that split into ducts of decreasing diameters (akin to a tree): the trachea, bronchi and bronchioles which make up the conducting airways (**Fig.2**). There are approximately 23 new branchings (called “generations”) in humans, compared to 13 in mice (**Fig.3**).
  - a. The trachea (generation 0) is the largest duct, with a diameter of approximately 2.5 cm and a length of ~10 cm. It is surrounded by ~18 C-shaped cartilage rings. Murine tracheas have a lumen of 1.5 mm in diameter.
  - b. The distal part of the trachea splits into two bronchi, the left and right main bronchi, that successively split to constitute the first three generations.



c. Once the diameter of the bronchi is inferior to 1 mm, they are considered as “bronchioles”. This section of the lung is often referred to as “small airways”. In human, the cartilage rings extend until the small airways, whereas in mice cartilage coverage stop at the main bronchus.

3) The respiratory bronchioles and alveoli which make up the acinar airway. The bronchioles transition progressively into alveoli to form the distal lung parenchyma, where oxygen from inhaled air is transferred to the blood stream in exchange for CO<sub>2</sub> which is then exhaled. The alveoli are the smallest functional units of the respiratory system. In human, alveoli have a diameter of 210 μm while in mice, they are about 80 μm across (Basil & Morrissey, 2020; P. R. Tata & Rajagopal, 2017; Weibel & Gomez, 1962).

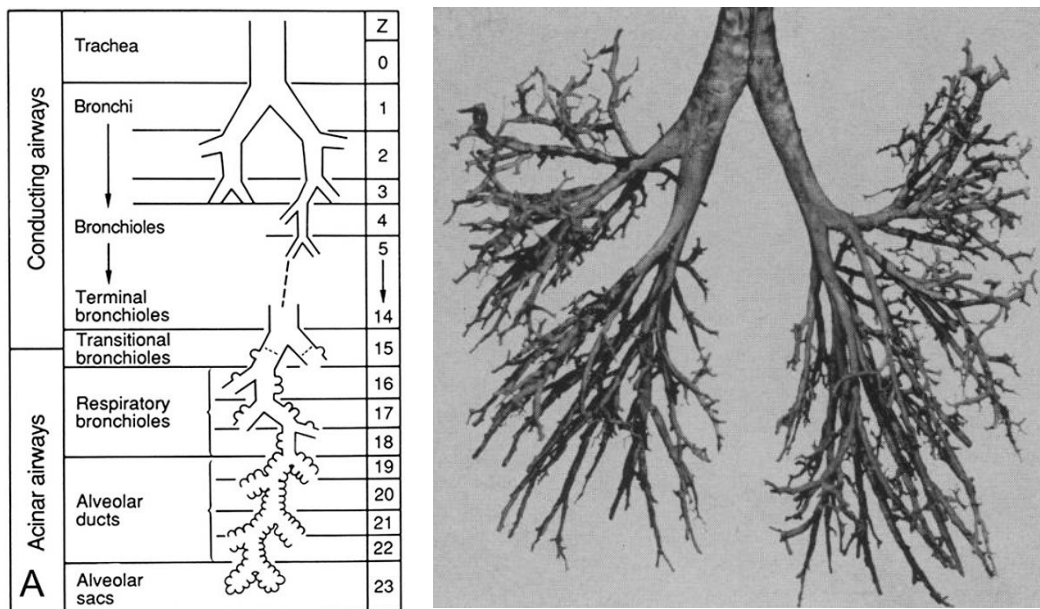


**Figure 2:** Organization of the human lung. Airway branching and their corresponding generations (z, left) and casting of an adult human lung (right). From Weibel, 2013 and Weibel, 1962.

Mammalian airways (upper and lower), are lined by a mucociliary epithelium constituting an effective first line of airway defense against a wide range of living or inert inhaled substances (Deprez et al., 2020; Hill et al., 2022; P. R. Tata & Rajagopal, 2017). In humans, this epithelium is pseudostratified from the nose to the terminal bronchioles, while in mice it transitions to a simple columnar epithelium in the distal part of the trachea (Rock et al., 2010).

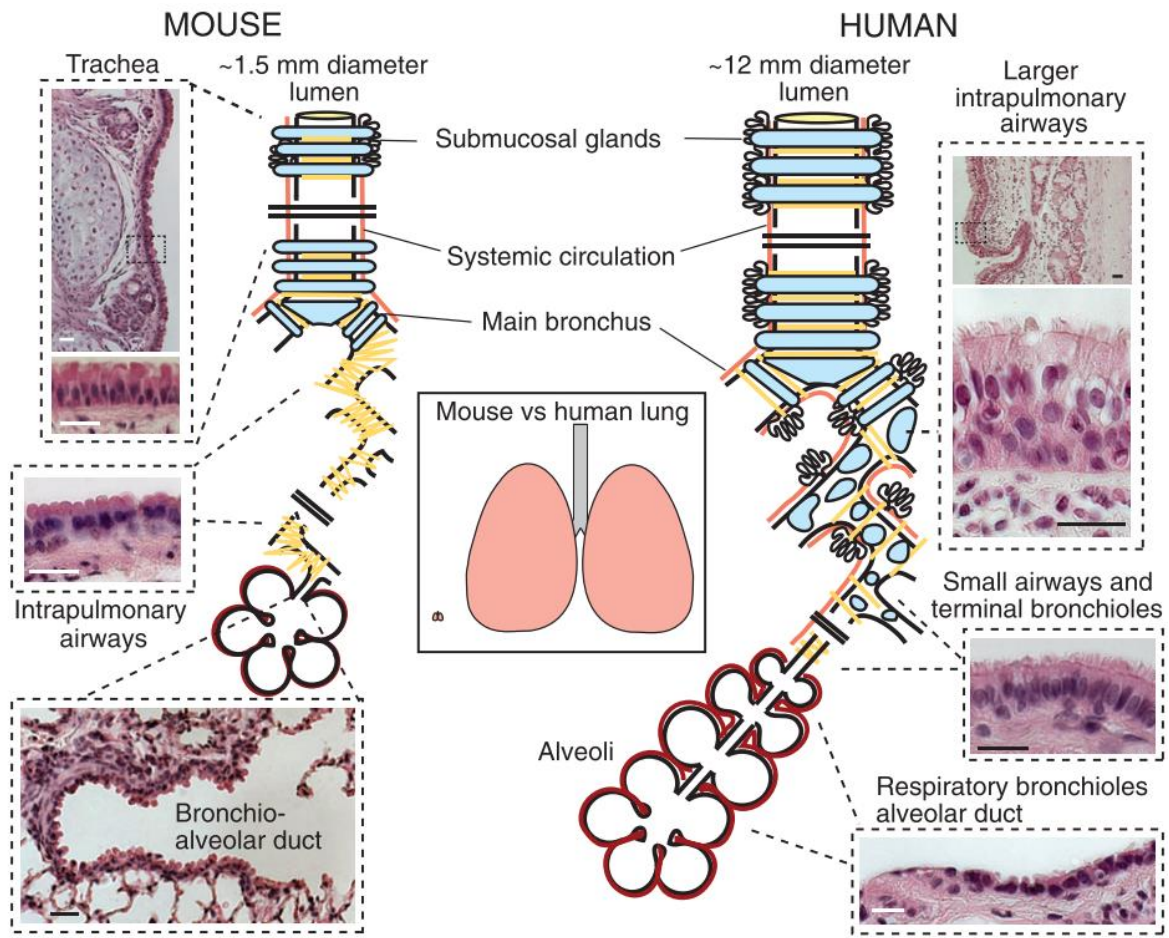


**Figure 3:** Anatomical comparison between mouse and human airways. From Rock et al., 2010.

This epithelium forms a complex ecosystem, with:

- basal cells playing a role in epithelial adhesion and stability (P. R. Tata & Rajagopal, 2017; L. E. Zaragosi et al., 2020),
- secretory cells such as club cells, producing antimicrobial and anti-inflammatory peptides (Wang et al., 2003) and goblet cells secreting protective mucins to the luminal surface (Chen et al., 2009),
- multiciliated cells (MCC), evacuating mucus through the coordinated beating of their cilia (mucociliary clearance) (Gras et al., 2013), which differentiate from a small population of deuterosomal cells (Deprez et al., 2020; Revinski et al., 2018; Ruiz García et al., 2019),
- as well as rarer cell types (ionocytes, pulmonary neuroendocrine cells, tuft cells) (**Fig. 4**).

The tracheal (mice) or the tracheal up to the bronchial (human) epithelium is punctuated by invaginations called submucosal glands (SMG) (**Fig.4**), playing an important role in mucus and fluid secretion and innate immunity (Widdicombe & Wine, 2015). The cellular composition of the epithelium

varies according to macro-anatomical location, with the greatest differences observed between nasal and tracheobronchial epithelia. In the tracheobronchial airways, cell distribution is relatively stable, with changes occurring in the most distal bronchioles (Deprez et al., 2020; Schiller et al., 2019).

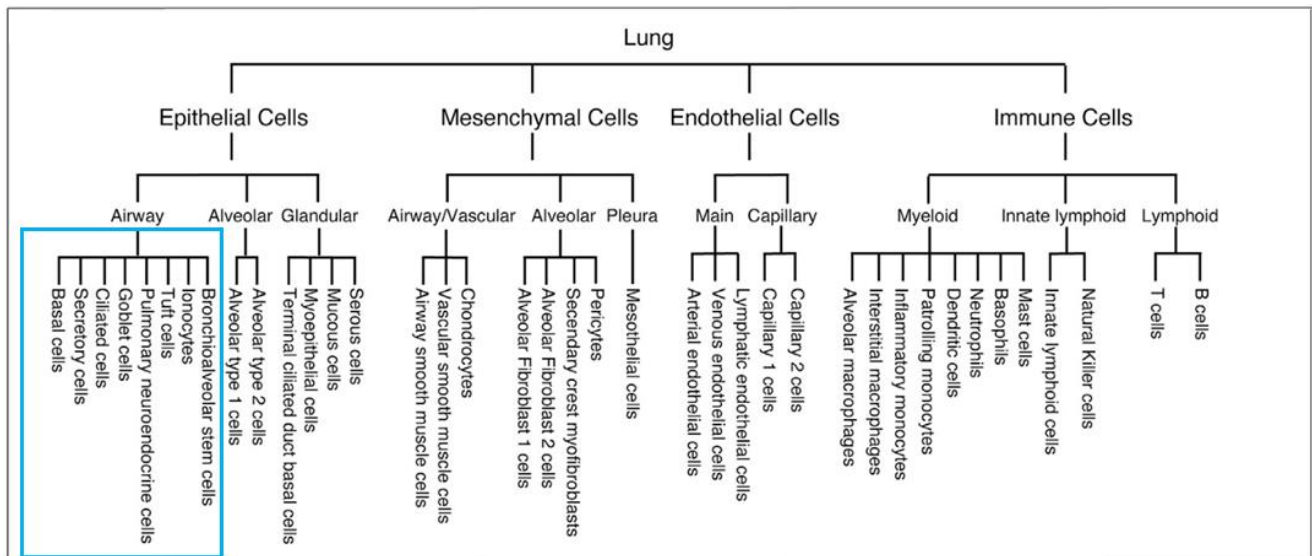


**Figure 4:** Overview of the different lung cell types featured in CellCards. This thesis is mainly focused on the airway epithelial cells (blue box). Adapted from Sun et al., 2022.

## 1. Composition

### Cell types

The airway epithelium is a complex ecosystem comprised of various cell types, each with specialized functions (**Fig.4&5**). When possible, I have provided here the proportions of different cell populations in the human or murine epithelium. However, achieving consensus across studies is often challenging due to conflicting conclusions. Some inconsistencies stem from direct extrapolations in humans of works done on rodents. Additionally, there is a confusion between epithelium composition and epithelium coverage. The former includes all epithelial cells from the basal lamina to the lumen, while the latter only considers lumen-facing cells (secretory and multiciliated). There are few studies quantifying human epithelial cell composition through histology. In recent years, several studies have attempted to map the human lung using single-cell RNA sequencing, which introduced its own biases; for example, the sampling method can skew estimations towards more apical cells (brushings) or basal cells (biopsies). **Figure 13** catalogues the markers and Cre lines of the main epithelial cell types.

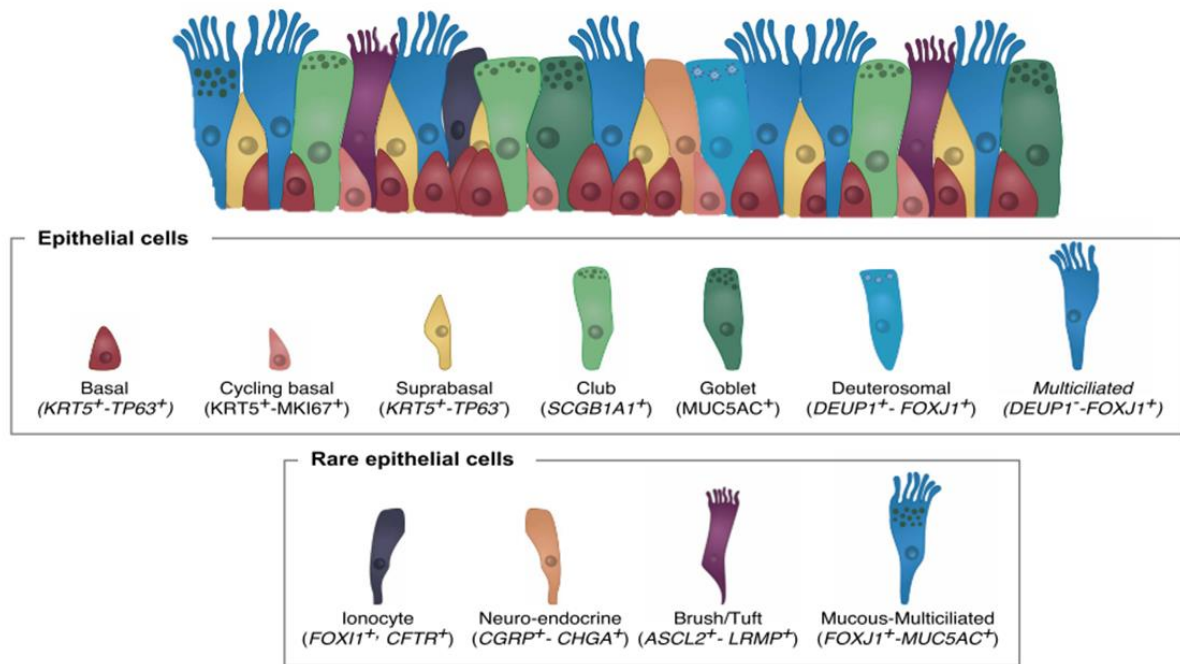


**Figure 5:** Cell composition of the surface airway epithelium. From Deprez et al., 2020.

### Basal cells

Basal cells are small, poorly differentiated cells that make up around 30% of the airway epithelium (**Fig.6A**) (Rock et al., 2009; P. R. Tata & Rajagopal, 2017). In humans, they are distributed all along the airway tract, although their number decreases distally, and is half as large in small airways (i.e. with a diameter of less than 0.5 mm) (Boers et al., 1999; Zaragosi et al., 2020). In mice, although abundant in the trachea (~30% of epithelial cells), basal cells are absent from the terminal airways (Rock et al., 2009, 2010). They line the basal lamina on which they are anchored via junctions called hemidesmosomes to ensure epithelium integrity (**Fig.6A**) (M. J. Evans et al., 1989; P. R. Tata & Rajagopal, 2017; L. E. Zaragosi et al., 2020). They specifically express the transcription factor TP63 and keratin 5 (KRT5) (X. Sun et al., 2022; P. R. Tata & Rajagopal, 2017).

Basal cells are the main stem cells of the airway epithelium: they can self-renew and give birth to the other resident epithelial cell populations. Indeed, a lineage tracing study by Rock and his team, used a Cre recombinase under the control of the *KRT5* promoter to demonstrate that the rate of labeled basal cells was similar in mice at 6 and 15 weeks, indicating that labeled cells renew themselves and are not diluted by the descendants of unlabeled cells. On the contrary, they found that the rate of labeled club and multiciliated cells increased over time, proving that basal cells generate secretory and ciliated cells with homeostasis (Rock et al., 2009). Similar results were obtained after administration of sulfur dioxide ( $SO_2$ ), a gas whose inhalation destroys the most apical part of the epithelium (Pardo-Saganta, Law, et al., 2015; Rock et al., 2009). Basal cells, considered to be relatively quiescent, are able to respond rapidly to aggression and proliferate to renew the epithelium, which is characteristic of stem cells

(Kotton & Morrisey, 2014; Rock et al., 2009). The cycling basal cells are identifiable by the expression of the marker of proliferation MKI67 and other cell cycle related genes (Deprez et al., 2020). In *in vitro* culture, these properties allow to reconstitute a mature, differentiated epithelium comprising the main cell types from a suspension of basal cells (Redman et al., 2024; Rock et al., 2009). Interestingly, however, it is not the proliferating basal cells that have the ability to differentiate. Ghosh et al. identify a unipotent population of proliferating basal cells (KRT5+/KRT14+/MKi67+), unable to generate a differentiated epithelium under conventional culture conditions (Air-Liquid Interface), unless in the presence of other tracheal cells (Ghosh et al., 2011).

Under homeostatic conditions, the airway epithelium is a relatively quiescent tissue with little turnover (Kotton & Morrisey, 2014). The rate of basal cell proliferation is controlled by the FGFR1-SPRY2 axis (Fig.6B), which inhibits the ERK and AKT pathways (Balasooriya et al., 2016), known to promote proliferation (Lavoie et al., 2020; McCubrey et al., 2007).

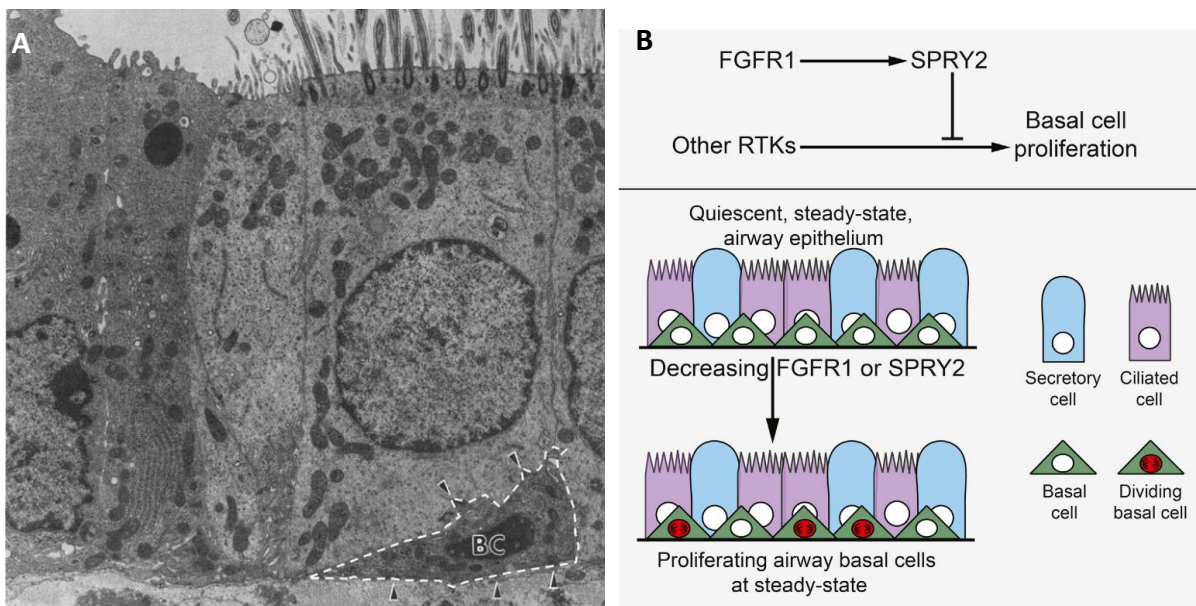


**Figure 6:** Basal cells.

**A:** Electron microscopy of a hamster tracheal epithelium with a basal cell outline in dotted lines, below a multiciliated cell (Magnification: x10,500). Adapted from Evans et al., 1989. **B:** Schematic representation of the FGFR1-SPRY2 axis limiting basal cell proliferation. Adapted from Balasooriya et al., 2016.

Finally, basal cells form a stem cell niche, which they maintain by preventing club cells (another progenitor population) from de-differentiating into basal cells. Indeed, Rao Tata has demonstrated *in vitro* that the presence of a single basal cell is sufficient to maintain club cell differentiation in organoids, and that basal cells therefore play a tissue-organizing role (Fig.7) (Rao Tata et al., 2013). This

niche regulates the fate of other cells and maintains the secretory/ciliary balance of the epithelium by sending certain signals (Pardo-Saganta, Tata, et al., 2015).

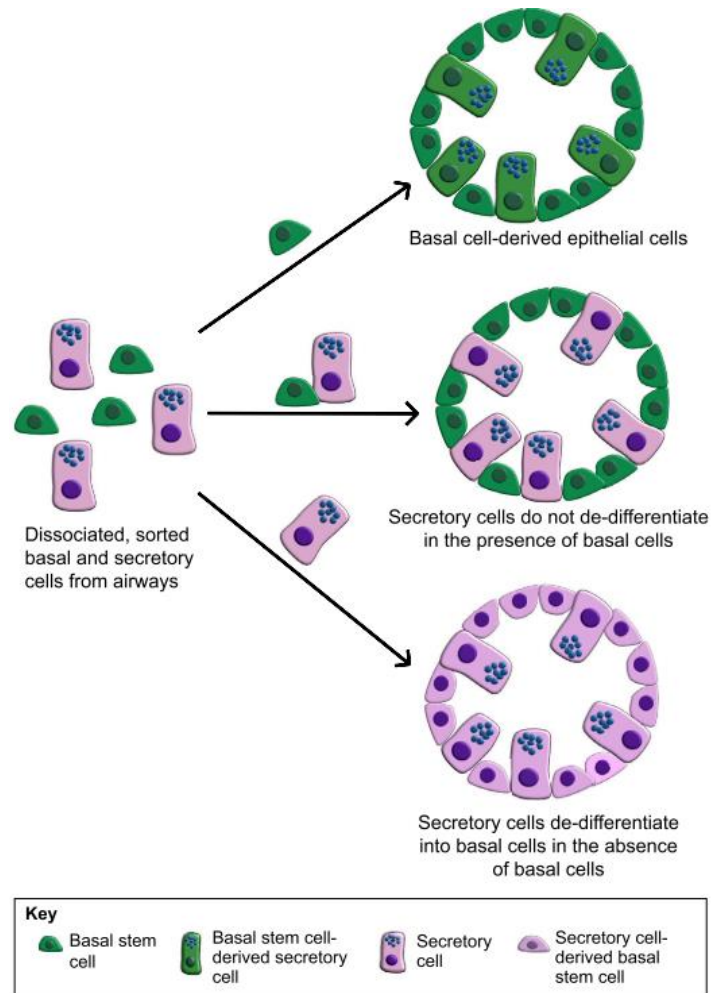


**Figure 7:** Basal cells maintain the stem cell niche.  
From Tata & Rajagopal, 2017.

### Suprabasal cells

As they differentiate, basal cells migrate towards the apical part of the epithelium. Before reaching the lumen, they pass through the "suprabasal" layer and lose TP63 expression, changing into the population of suprabasal cells, also called parabasal cells in some studies. This population, although important, is poorly characterized as it is morphologically identical to basal cells and differentiable from them only by its suprabasal location (above the basal cell layer) and by a negative marker: the low expression or absence of TP63 (Boers et al., 1998; Mori et al., 2015). Suprabasal cells are more often than not forgotten from reviews, even recent ones summarizing different populations of the airway epithelial ecosystem (Basil et al., 2020; Basil & Morrisey, 2020; Konkimalla et al., 2022; P. R. Tata & Rajagopal, 2017).

However, several studies have demonstrated the existence of this cell population. In a mouse model of basal cell lineage tracing where, after induction in adulthood, basal cells (*Krt5+*) become GFP positive, Watson et al. observed that luminal cells (secretory cells, multiciliated cells) known to be derived from basal cell differentiation, only became labeled once a basal cell generated a second *Krt5+GFP+* cell (J. K. Watson et al., 2015). Given that tracing is triggered in the adult mouse, if basal cells differentiated directly into luminal cells at homeostasis, new GFP+ luminal cells should have been able to appear without the first basal cell generating a second basal cell (*KRT5+ GFP+*). The authors concluded that basal cells were capable of asymmetric division, but that it was the second basal cell population that gave rise to luminal cells. They identified this population as "luminal precursor" basal cells on the basis of its expression of *Krt8* (luminal marker) and compared it with the "parabasal" cell population described by Mori et al. the same year, also *Krt8+*. Indeed, Mori et al. described the existence, in *in vitro* cultures, of a population of cells located above basal cells, resulting from *Notch3* activation in basal cells and showing a decrease in *Tp63* (Mori et al., 2015). In 2024 we know that Mori's population most likely corresponds to suprabasal cells (Ruiz García et al., 2019; L. E. Zaragosi et al., 2020). Watson's luminal precursor basal cells are therefore most likely suprabasal cells too, despite no decrease in *Tp63* and a slight increase in *Notch3* expressions in this population. It is important to note that expression analysis of these genes was performed by an early form of single-cell RNA sequencing (scRNA-seq), on an extremely small population of 67 cells due to the recent arrival of this technology in 2015 (J. K. Watson et al., 2015). This small proportion of cells may therefore not be representative of the entire study population.

With advances in scRNA-seq, sequencing a much larger number of cells allowed to characterize with greater granularity the different cell populations making up the airway epithelium. For example, in 2020, Depez et al. sequenced 77,969 cells from samples taken along the entire airway tract of 10 volunteers. Among these cells, 17.6% were positive for *KRT5* and *NOTCH3* and had low *TP63* expression, and were thus labeled as suprabasal (Depez et al., 2020).

### Club cells

Club cells, previously named Clara cells, are secretory cells present at the luminal part of the epithelium (Hogan et al., 2014). In humans, club cells are predominantly enriched in the distal part of the lungs, representing 11% of terminal bronchioles and 22% of respiratory bronchioles (Boers et al., 1999). In contrast, in mice, they are widely distributed from the trachea to the bronchioles (Hong et al., 2001; Rock & Hogan, 2011). They have a cuboid shape with a characteristic dome, sometimes called uterodome (Rock & Hogan, 2011). They possess electron-dense secretory granules on their membranes, containing antimicrobial and anti-inflammatory peptides (Boers et al., 1999; P. R. Tata & Rajagopal, 2017), which confer a protective function by enriching mucus to mediate the inflammatory

response. The most characteristic peptide secreted by club cells is SCGB1A1 (Rawlins, Okubo, et al., 2009), which contributes to xenobiotic metabolism (Jones et al., 1983). Additionally, club cells contribute to ion flow and express important ion transport molecules such as ENaC and CFTR (Hill et al., 2022).

In addition to their function as terminally differentiated cells, lineage tracing studies using transgenic mice possessing a Cre recombinase under the control of the *Scgb1a1* marker promoter have shown that club cells also function as airway epithelial progenitors. They can give rise to multiciliated cells (Rawlins, Okubo, et al., 2009) or to goblet cells (Chen et al., 2009), depending on whether the Notch pathway is repressed or activated, respectively (Lafkas et al., 2015). Moreover, they are capable of proliferation and self-renewal, which, by definition, make them stem cells (Boers et al., 1999; Hogan et al., 2014). In the event of severe aggression damaging basal cells, they can regenerate the epithelium by dedifferentiating into basal cells (Rao Tata et al., 2013). Indeed, Rao Tata et al. have developed a mouse model enabling the elimination of airway basal cells in the adult mouse while tracing club cells, with the conditional expression of the diphtheria toxin into *Krt5*<sup>+</sup> cells combined with lineage tracing using the YFP protein under the *Scgb1a1* promoter. After depletion of 80% of basal cells, the study showed a doubling in the number of proliferating *Scgb1a1*<sup>+</sup> cells, as well as ~8% YFP<sup>+</sup> basal cells, meaning that they originated from club cells that had dedifferentiated (Rao Tata et al., 2013).

In mice, a subset of *Upk3a* positive club cells termed variant-club has been identified after naphthalene injury, a chemical treatment used in mice to deplete the club cell population due to their conversion of naphthalene to a toxic product through the cytochrome P450 enzyme *Cyp2f2*. This rare subtype is located around neuroepithelial bodies and is able to survive naphthalene injury, probably because of a low expression of *Cyp2f2*. They can differentiate to repopulate the airway epithelium (Basil & Morrissey, 2020; Guha et al., 2017).

### Goblet cells

Goblet cells take their name from their characteristic vase-like shape (Rogers, 1994). They account for 12% of bronchial epithelial cells (or 23% of luminal cells) in humans (J. H. L. Watson & Brinkman, 1964), but are only slightly present in laboratory mice at homeostasis, probably due in part to the fact that they are raised in virtually pathogen-free environments, and that the development of these cells is at least partly linked to the presence of inhaled irritants (Basil & Morrissey, 2020; Hogan et al., 2014; Rock & Hogan, 2011; Rogers, 1994). Goblet cells arise from the differentiation of club cells under the effect of the expression of the transcription factor SPDEF (SAM pointed domain containing ETS transcription factor) (Chen et al., 2009).



Although often grouped together under the umbrella term "secretory" or mucus cells, goblet and club cells are cells with a distinct identity and function. Indeed, goblet cells possess large electron-lucent granules (~10µm) (Hill et al., 2022) at the apical side of their cytoplasm, containing mucus constituent molecules such as MUC5B and MUC5AC, two high-molecular-weight mucins, lipids and small glycoproteins (Rogers, 1994). Mucins are first synthesized as monomers that are dimerized then polymerized in the Golgi apparatus. The large mucin polymers are stored in secretory granules under a dehydrated form hundreds of times more compact than their hydrated form (**Fig.8A**). They are neutralized with positive Ca<sup>2+</sup> to avoid self-repulsion due to their negative charges (Fahy & Dickey, 2010; McShane et al., 2021). Low mucus secretion is continuous at baseline to ensure proper airway hydration and protection. However, vesicles can discharge in an explosive manner (within tenths of a millisecond) in response to various stimuli or irritants such as cigarette smoke, certain gases (SO<sub>2</sub>, ammonia vapor), prostaglandins or nervous signals (Jaramillo et al., 2018; Rogers, 1994). Vesicle transport from the cytoplasm to the apical membrane is partly mediated by the interaction of myristoylated alanine-rich C kinase substrate (MARCKS) with the cytoskeleton. Rab proteins on the vesicles interact with the tethering protein MUNC13-2 to dock the granules to the plasma membrane. Club cells of mice lacking *Munc13-2* accumulate Muc5b-filled secretory granules in their cytoplasm (Zhu et al., 2008). Once exocytosis is triggered, the SNARE complex and other molecules open the secretory pore. The instantaneous hydration of the mucins upon contact with the extracellular matrix leads to their ejection into the lumen (**Fig.8B**) (Jaramillo et al., 2018; Y. Li et al., 2001).

Goblet cells play an active role in protecting the airway tract against pathogens and other inhaled irritants. However, excessive or prolonged mucus secretion, or an imbalance in the ratio of goblet cells to multiciliated cells, can be pathological. Goblet cell hyperplasia, for example, is a telltale sign of chronic respiratory diseases such as asthma, chronic obstructive pulmonary disease (COPD) or cystic fibrosis (Chen et al., 2009; Gras et al., 2013; Tyner et al., 2006).

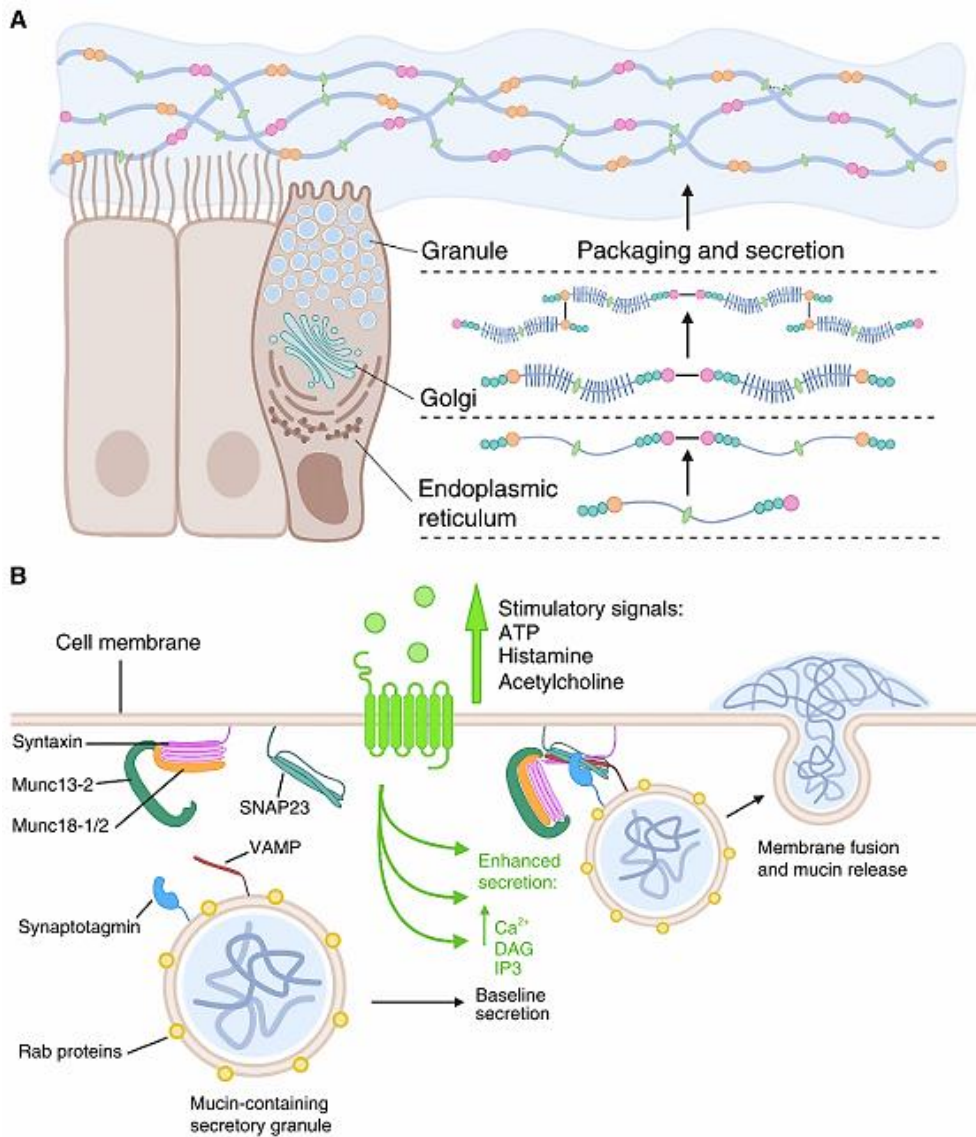


**Figure 8:** Mucus secretion.

**A:** Schematic representation of mucus secretion by goblet cells. **B:** Regulation of mucus exocytosis.

From McShane et al., 2021.

## Multiciliated cells

Multiciliated cells (MCCs) are pyramid-shaped luminal cells with hundreds (~300) of motile cilia on their surface. Cilia are hair-like structures projecting towards the lumen, with a highly organized internal structure composed of microtubules (axoneme), arranged in a 9+2 pattern (**Fig.9**). Their height varies from 7  $\mu\text{m}$  to 3-4  $\mu\text{m}$  in the bronchi, and they have a diameter of 0.3  $\mu\text{m}$ . Microvilli of about half the height of their height are interspersed between the cilia (Greenwood & Holland, 1975; Legendre et al., 2021). The distance between two neighboring cilia is around 200 nm (Widdicombe & Wine, 2015). Basal bodies anchoring the cilia are present beneath the luminal surface, accompanied by a high concentration of mitochondria, necessary to power the movement cilia (Ximena et al., 2006).

Multiciliated cells make up about 40 to 55% of murine tracheal epithelial cells (Rock et al., 2010; Roth et al., 2024). Several studies reveal contradicting estimations of the MCC repartition in humans: according to Mercer they make up 30% of human bronchial epithelial cells, which represent 60% of the apical coverage (Mercer et al., 1994). A study by Roth et al. published this year increased this estimates to almost 90% of total luminal surface area (Roth et al., 2024). These discrepancies might stem from the very different methods used in these studies, or for inter-individual variabilities, which are difficult to evaluate due to insufficient descriptions of tissue donors.

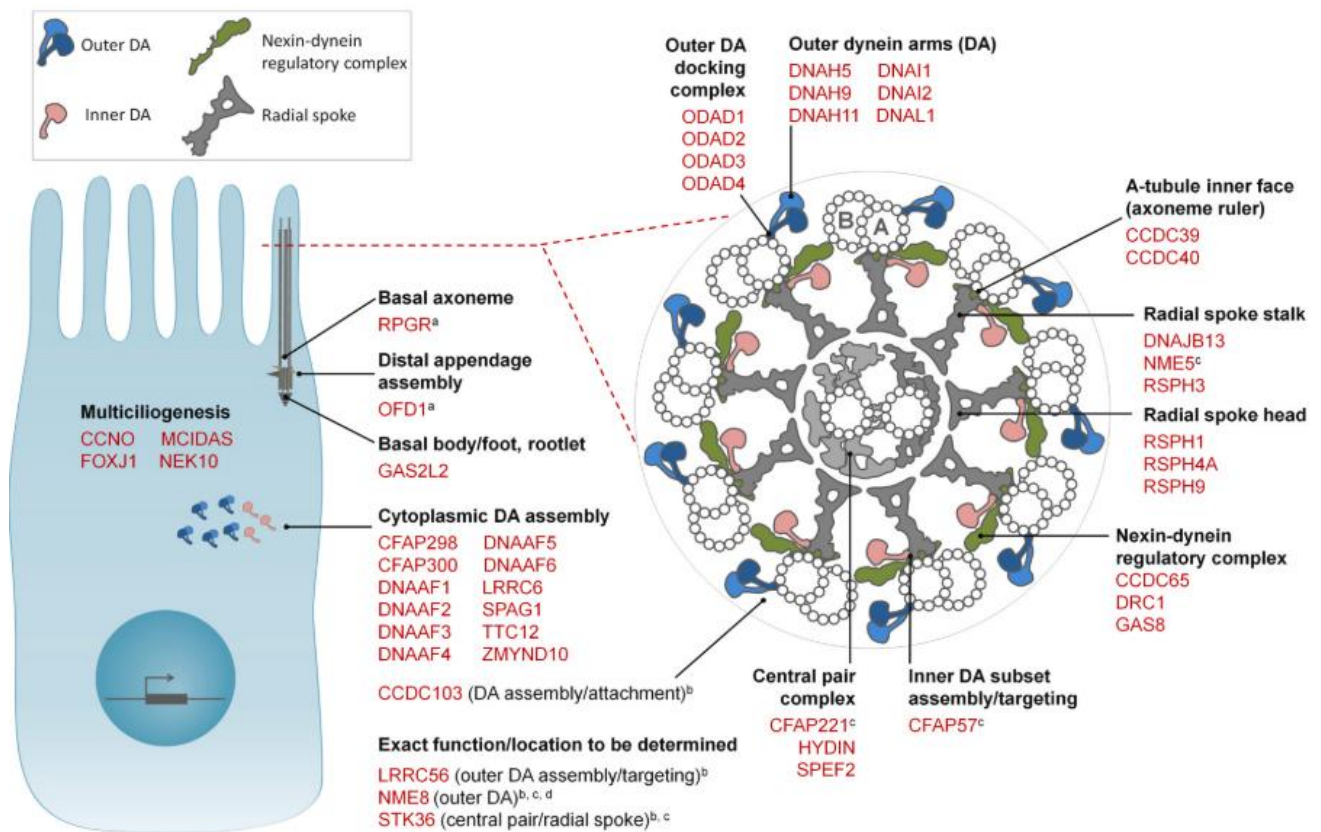


**Figure 9:** Multiciliated cells structure and components.  
From Legendre et al., 2021.

Multiciliated cells are post-mitotic, terminally differentiated cells with a half-life of 6 (trachea) to 17 months (bronchioles) in mice (Pardo-Saganta, Tata, et al., 2015; Rawlins & Hogan, 2008; X. Sun et al., 2022). They arise from the differentiation of club cells, when the Notch pathway is repressed, and the expression of their transcription factor *FOXJ1* is activated. More specifically, the generation of hundreds of cilia requires a complex process known as multiciliogenesis, which will be described in greater detail in the section on [multiciliogenesis](#). Among many specific genes, the Cell card study selected *FOXJ1* and *RSPH1* as marker genes in humans (X. Sun et al., 2022). MCCs play a crucial role in maintaining and protecting the airway tract, through the coordinated beating of their cilia, which evacuates the pathogen-trapping mucus.

## Deuterosomal cells

A key step in the process of multiciliogenesis corresponds to the rapid and extensive amplification of centrioles within a limited time frame, which occurs mainly around an acentriolar structure called the deuterosome (Barbry et al., 2020; Sorokin, 1968). Thus, deuterosomal cells form a necessary intermediate between club progenitor cells and multiciliated cells. This specific population also expresses *FOXJ1* but differs from mature MCCs in having a unique expression profile and at the same time sharing a signature with cycling basal cells, which is necessary to the biosynthesis of hundreds of centrioles. Among the markers specific to deuterosomal cells are *DEUP1*, which encodes a key component of deuterosomes, but also *CDC20B*, the host gene of miR-449abc, which has been shown to be a key regulator of centriole amplification (Revinski et al., 2018).

## Rare cells

In addition to the previous cell types, there are four cell types described as rare because of their low frequency in the epithelium (Deprez et al., 2020), that nonetheless possess important functions: ionocytes, pulmonary neuroendocrine cells (PNECs) and tuft/brush cells (L. E. Zaragosi et al., 2020).

### Ionocytes

Ionocytes are found on the luminal side of the epithelium. They represent between 0.5 and 1.5% of total human airway epithelial cells. In the mouse, Konkimalla et al. estimate that ionocytes represent only 0.42% of epithelial cells but are responsible for 54% of *Cftr* (Konkimalla et al., 2022). Murine ionocytes have been identified as the main source of *Cftr* (cystic fibrosis transmembrane conductance regulator), a critical chloride channel, many mutations of which are responsible for cystic fibrosis (Montoro et al., 2018). Ionocytes express genes encoding subunits of the proton pump V-ATPase, which plays an important role in the regulation of ion transport and pH, as well as the transcription factor *FOXJ1*, a crucial determinant of their lineage (Hewitt & Lloyd, 2021). *FOXJ1* and *ASCL3* are the two main markers of human ionocytes (X. Sun et al., 2022).

### Pulmonary neuroendocrine cells

Pulmonary neuroendocrine cells (PNECs) present microvilli at their apical pole, which protrude into the lumen. In the mouse, they are often grouped into innervated clusters called neuroepithelial bodies (NEBs) and located at branches of the airways (P. R. Tata & Rajagopal, 2017). PNECs also possess secretory granules containing various peptides such as bombesin or GRP (gastrin-releasing peptide), calcitonin gene-related peptide (CGRP) and even serotonin (5-HT). Specific markers of human PNECs are *GRP* and the Achaete-scute homolog 1 *ASCL1* (X. Sun et al., 2022). PNECs play a role in immune cell recruitment and can detect hypoxia or chemical and mechanical variations (P. R. Tata & Rajagopal, 2017).

In a club cell lineage tracing study (*Scgb1a1*), no labeling was detected in neuroendocrine cells (Rawlins, Okubo, et al., 2009), suggesting that they originate directly from basal cell differentiation. Indeed, in a basal cell lineage tracing model (*Krt5*), Watson et al. detected neuroendocrine cells labeled with the reporter (J. K. Watson et al., 2015). Furthermore, a study coupling a mouse model of PNEC lineage tracing (*Cgrp*) to naphthalene injury destroying club progenitor cells, showed that in a wounding context, neuroendocrine cells are able to proliferate and give rise to new club and multiciliated cells to restore the epithelium (Song et al., 2012). Thus, PNECs may also have a progenitor function in the event of injury.

### Tuft/brush cells

Although scarce (0.002 % of epithelial cells in humans), tuft cells (or brush cells), were identified as early as the 1950s on electron microscopy images due to their bottle shape and characteristic microvilli tuft (Billipp et al., 2021; Waghray et al., 2023). However, their function remained unknown until the 2010s, when they were identified as chemosensory cells that regulate immunity. They are located close to nerve fibers and mediate communication between the epithelium and the nervous system. They share similarities with taste cells, notably through the expression of *GNG13*. Tuft cell lineage is defined by the expression of the transcription factor *POU2F3* and *ASCL2* (Billipp et al., 2021; Hewitt & Lloyd, 2021; X. Sun et al., 2022). Recently, a deep lung single cell atlas identified a common progenitor between tuft cells and ionocytes, able to differentiate into tuft cells (at the expense of ionocytes), when treated with Type 2 or Type 17 cytokines (Waghray et al., 2023).

### Mucous-ciliated cells

Mucous-ciliated cells (or goblet-ciliated cells) are hybrid cells positive for *MUC5AC* and *FOXJ1*, possessing both secretory vesicles and cilia (**Fig.10**). They have been reported in humans under physiological (Deprez et al., 2020) and pathological (Vieira Braga et al., 2019) conditions both also in *in vitro* models of goblet hyperplasia (Gomperts et al., 2007; Turner et al., 2011; Tyner et al., 2006). That evasive cell type challenges the canonical cellular trajectories of the airway epithelium, and it is not clear whether they originate from the transdifferentiation of goblet cells, multiciliated cells or neither. No lineage-tracing study showed definitive proof of their origin. In a mouse model of ovalbumin challenge (that triggers goblet cell hyperplasia) coupled to a multiciliated cell lineage tracing (*Foxj1+*), no goblet cells were positive for YFP 48h after of OVA administration. Out of 16 YFP+ *Foxj1-* cells, 11 were positive for *Scgb1a1*, indicating that, in this model, multiciliated cells do not transdifferentiate to goblet cells but might dedifferentiate into club cells (Pardo-Saganta et al., 2013).

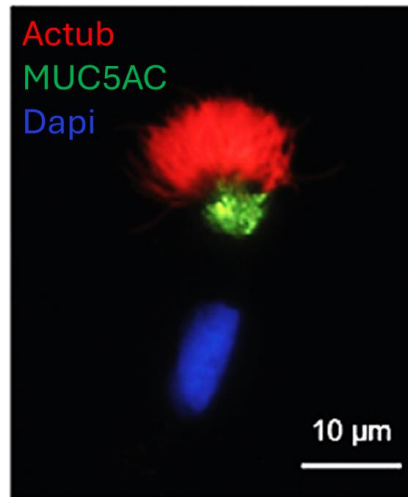


**Figure 10:** Mucous-ciliated cells.  
Immunofluorescence image of a mucous-ciliated cell isolated by cytopsin.  
From Deprez et al., AJRCCM 2020.

Ruiz-Garcia et al. identified mucous-ciliated cells expressing both *MUC5AC* and *FOXJ1* in healthy human bronchial biopsies, healthy human nasal epithelial cell (HNEC) cultures and newborn pig tracheas, confirming that these cells exist at homeostasis and without IL-13 treatment. Moreover, by sequencing single cells from HNEC cultures at different differentiation points and performing lineage inference, they placed goblet cells as putative precursors of multiciliated cells (**Fig.11**) (Ruiz García et al., 2019).

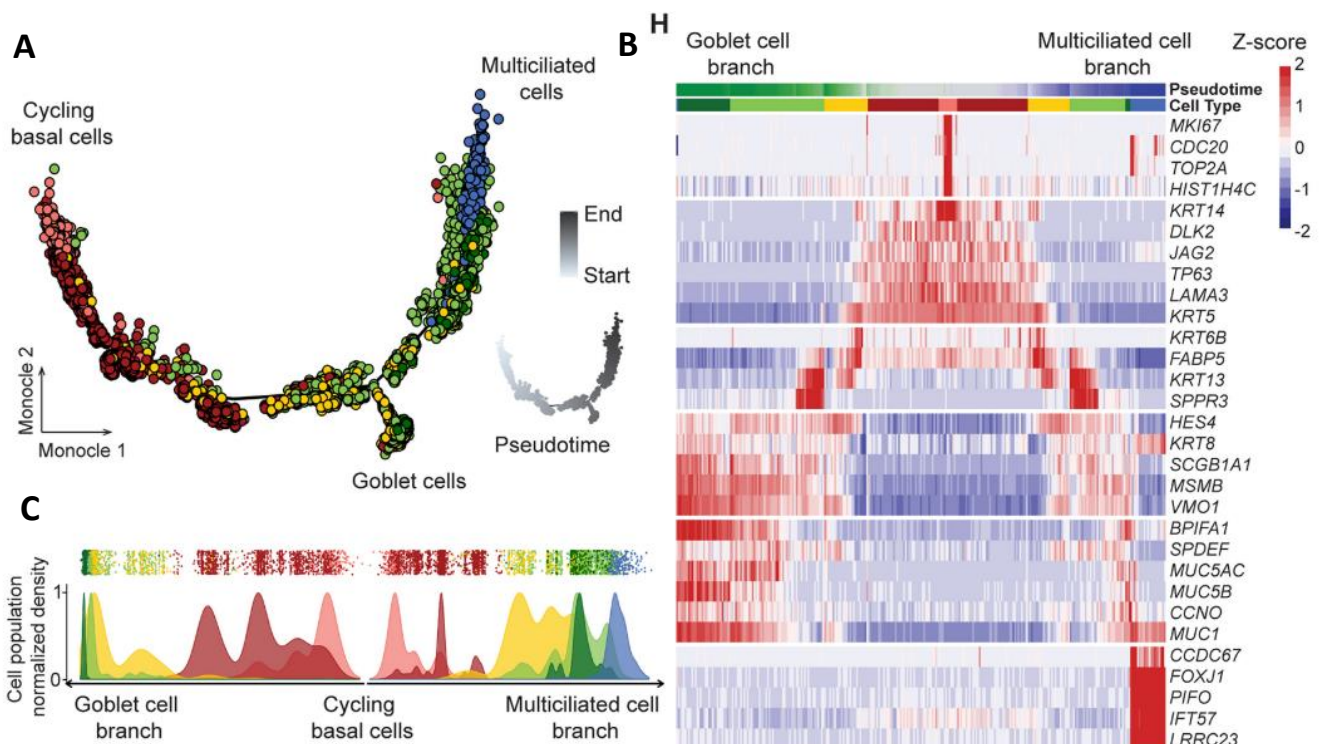


**Figure 11:** Goblet cells are precursors of multiciliated cells.  
**A.** Inference of goblet and multiciliated cell lineages. **B.** Cellular trajectories showing goblet and multiciliated cells on the same trajectory branch. **C.** Heatmap representing temporal expression pattern of cell type-specific markers.  
From Ruiz García et al., 2019.

## Structures

### Submucosal glands

Submucosal glands (SMG) are secretory structures found in the tracheal (mice) or the tracheal up to the bronchial (human) surface epithelium. They play an important role in fluid and mucus secretion and innate immunity. They form invaginations composed of a duct that branches into acini:

- 1) The duct is composed of the side walls connecting the surface epithelium to the distal part of the SMG and, as the surface epithelium, is composed of basal, club and multiciliated cells. Study of a single human SMG showed that the duct can start as a multiciliated duct that dilates into a collecting tube branching into a dozen of acini (Meyrick et al., 1969).
- 2) Acini are the distal part of the SMG. They host the majority of MUC5B+ goblet cells and some unique cell types described in **figure 12** (Anderson et al., 2017; Meyrick et al., 1969; X. Sun et al., 2022). MUC5B+ cells located in SMGs are most often termed “mucous cells”.

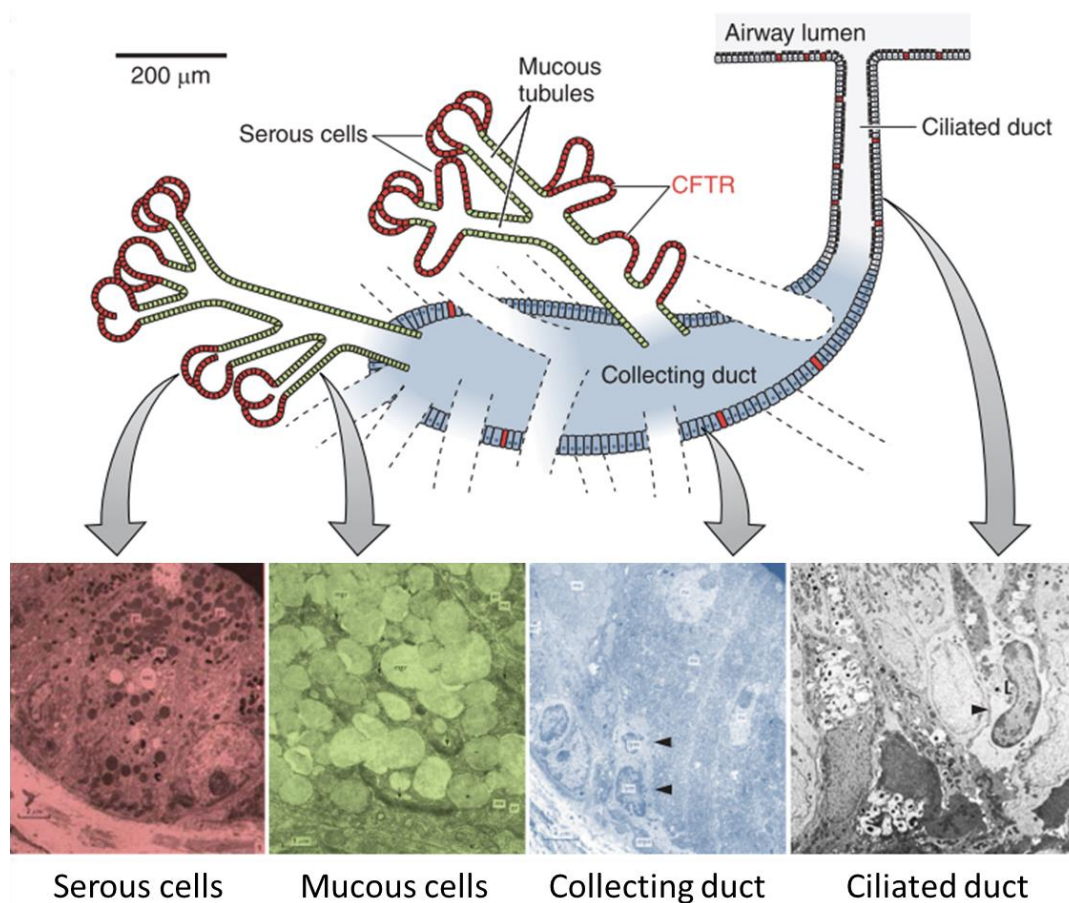


**Figure 12:** Schematic representation of a submucosal gland.  
From Widdicombe et al., 2015.

## Myoepithelial cells

Myoepithelial cells are flat and elongated cells found in the distal part of SMGs, that provide structural support to the acini. They can dedifferentiate into basal cells to replenish the surface epithelium (Lynch et al., 2018; A. Tata et al., 2018). They possess markers of both epithelial and muscle cells such as *KRT14*,  $\alpha$ -smooth muscle actin ( $\alpha$ SMA) and myosin heavy chain 11 (*MYH11*) (Anderson et al., 2017; X. Sun et al., 2022).

## Serous cells

Serous cells are secretory cells with small electron-dense granules. They participate in host defense by secreting antimicrobial lactoferrin and lysozyme and regulate fluid secretion as they are an important source of CFTR (Engelhardt et al., 1994; Widdicombe & Wine, 2015).

**Table 1. Markers and cre lines**

Cell lineage	Cell type	Marker genes <sup>#</sup>	Surface protein genes <sup>#</sup>	Antibodies	Cre lines <sup>*</sup>
Epithelium	Basal cell	<i>TP63, KRT5</i>	<i>NGFR<sup>H</sup>, TRPC6<sup>H</sup></i>	TRP63, KRT5	<i>Trp63<sup>creERT2</sup></i> (Lee et al., 2014) <i>Krt5<sup>creERT2</sup></i> (Van Keymeulen et al., 2011)
Epithelium	Secretory cell	<i>SCGB1A1, SCGB3A2</i>	<i>SLC4A7<sup>H</sup>, SCUBE2<sup>H</sup></i>	SCGB1A1	<i>Scgb1a1<sup>creERT2</sup></i> (Rawlins et al., 2009b)
Epithelium	Ciliated cell	<i>FOXJ1, RSPH1</i>	<i>CDHR3, CDHR4</i>	FOXJ1, Acetylated-Tubulin	<i>Foxj1<sup>creERT2</sup></i> (Rawlins and Hogan, 2008)
Epithelium	Goblet cell	<i>MUC5AC, SPDEF</i>	<i>PCDH7<sup>H</sup>, SLC4A11<sup>H</sup></i>	MUC5AC, AGR2	
Epithelium	Pulmonary neuroendocrine cell	<i>ASCL1, GRP<sup>H</sup>, Calca<sup>M</sup></i>	<i>NRXN1<sup>H</sup>, CDH18<sup>H</sup></i>	GRP <sup>H</sup> /Bombesin, CGRP <sup>M</sup>	<i>Ascl1<sup>creERT2</sup></i> (Kim et al., 2011) <i>Calca<sup>creERT2</sup></i> (Song et al., 2012)
Epithelium	Tuft cell	<i>POU2F3, ASCL2, Dclk1<sup>M</sup></i>	<i>TRPM5<sup>M</sup></i>	POU2F3, DCLK <sup>M</sup>	<i>Dclk1<sup>creERT2</sup></i> (Westphalen et al., 2014) <i>Pou2f3<sup>creERT2</sup></i> (McGinty et al., 2020)
Epithelium	Ionocyte	<i>FOXI1, ASCL3, Cfr<sup>M</sup></i>	<i>CFTR<sup>M</sup></i>		<i>Ascl3<sup>EGFP-Cre</sup></i> (Bullard et al., 2008)
Epithelium	Bronchoalveolar stem cell			Co-express low level SFTPC and SCGB1A1	Dual recombinases or split cre effector (Liu et al., 2019; Salwig et al., 2019)
Epithelium	Alveolar type 1 cell	<i>AGER<sup>H</sup>, RTKN2, Hopx<sup>M</sup></i>	<i>AGER, SEMA3B HTI-56<sup>H</sup> (MAB)</i>	AGER, HOPX	<i>Hopx<sup>creERT2</sup></i> (Jain et al., 2015) <i>Ager<sup>creERT2</sup></i> (Chung and Hogan, 2018) <i>Aqp5<sup>Cre</sup></i> (Flodby et al., 2010)
Epithelium	Alveolar type 2 cell	<i>SFTPC, LAMP3</i>	<i>KCNJ15 HTII-280<sup>H</sup> (MAB)</i>	SFTPC, ABCA3	<i>Sftpc<sup>creERT2</sup></i> (Chapman et al., 2011; Rock et al., 2011)
Epithelium	Ductal basal cell	<i>VIM, SOX9</i>		TRP63, KRT5	<i>Trp63<sup>creERT2</sup></i> (Lee et al., 2014) <i>Krt5<sup>creERT2</sup></i> (Van Keymeulen et al., 2011)
Epithelium	Myoepithelial cell	<i>KRT14, MYH11</i>		ACTA2/SMA	<i>Acta2<sup>creERT2</sup></i> (Anderson et al., 2017; Lynch et al., 2018; Tata et al., 2018) <i>Myh11-creERT2</i> (Anderson et al., 2017). (both are also active in smooth muscles and myofibroblasts)
Epithelium	Mucous cell	<i>MUC5B, SPDEF</i>		MUC5B	
Epithelium	Serous cell	<i>LYZ, LTF</i>			

**Figure 13:** Markers and cre lines of the main epithelial cell types. From Sun et al., 2022.

## Hillocks

Hillocks, although sometimes referred to as a cell type, are newly discovered stratifications of squamous-like (Krt13+) cells (Fig.14). They were first identified in murine epithelium by Montoro et al. in 2018 and are still poorly characterized in humans. Montoro et al. characterized hillocks as layers of Krt13+ Scgb1a1+ club cells stacked on top of Trp63+ Krt13+ basal cells, with concentrated EdU labeling



(**Fig.14A**). Authors speculated that the high proliferation observed in hillocks was indicative of an injury-responsive capacity (Montoro et al., 2018). Indeed, in 2024, they presented evidence that hillocks can withstand 80 mM HCl treatment and cryoinjury in mice. Moreover, they showed that hillock basal cells were able to repopulate the epithelium after naphthalene-induced epithelial denudation in mouse. Therefore, hillocks are a unique injury-resistant reservoir of epithelial stem cells (Lin et al., 2024). Hillocks might be implicated in asthma pathogenesis as hillock-like differentiation trajectory signature was identified in pre-asthmatic children (Koppelman et al., 2024).

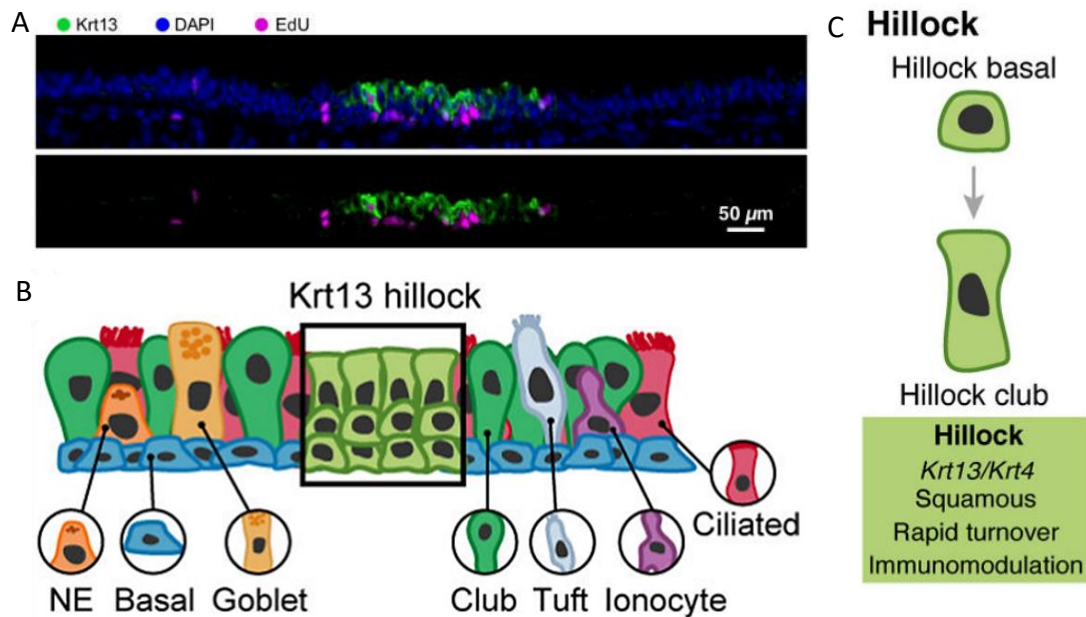


**Figure 14:** Hillocks.

**A:** Immunofluorescence image of Krt13+ hillock cells in mice. **B:** Schematic representation of a hillock structure.

**C:** Lineage hierarchy of hillock cells.

Adapted from Montoro et al., 2018.

## Cellular junctions

The airway epithelium is the first physical barrier against inhaled aggression. To ensure adequate protection, cells must form a cohesive unit that is impermeable to pathogens, through strong intercellular junctions (**Fig.15**).

### Tight junctions (zonula occludens)

Tight junctions are found in the most apical region of the lateral surface of epithelial cells (**Fig.15**). As their name suggests, these are the tightest junctions found in the epithelium, bringing two neighboring cells into close proximity. They form a distinct physiological barrier between the apical (outside the organism) and basolateral parts of the cells, but allow the polarized passage of certain molecules including ions, water and macromolecules, into the paracellular space (Gumbiner, 1993; Kageyama et al., 2024). Tight junctions are composed of transmembrane proteins such as claudins, occludin,

tricellulin and JAMs (junctional adhesion molecules), associated with cytoplasmic proteins such as zona occludens (ZO) -1, -2 and -3, themselves linked to the actin of the cytoskeleton (Kageyama et al., 2024).

### Intermediate junctions (zonula adhaerens)

Intermediate junctions provide resistance to mechanical forces between cells and regulate their morphology and movements (Perez-Moreno et al., 2003). They are located between the lateral surfaces of two neighboring cells (**Fig.15**) and form intercellular spaces about 200 Å wide (Farquhar & Palade, 1963). They belt the cells below the tight junctions and are composed of E-cadherin and  $\alpha$ - or  $\beta$ -catenin bridges, connected to the actin cytoskeleton (Perez-Moreno et al., 2003; Rezaee & Georas, 2014).

### Desmosomes (macula adhaerens)

Desmosomes are found along the basolateral half of cells, below the intermediate junctions (**Fig.15**). Unlike the latter, desmosomes do not form a belt but rather dense, punctually distributed plaques, where transmembrane proteins (desmogleins and desmocollins) are linked to the cytokeratin intermediate filaments of the neighboring cell via intracellular proteins such as desmoplakin. Desmosomes provide robust stability between cells (Kageyama et al., 2024).

### Hemidesmosomes

Hemidesmosomes are similar to desmosomes, but instead of connecting two cells to each other, they are located beneath the basal pole of cells and connect a cell to the extracellular matrix (basal lamina) (**Fig. 15**). For that reason, in the airway epithelium, they are only found on basal cells (M. J. Evans et al., 1989).

### Gap junctions

Gap junctions are intercellular, channel-like pores which, unlike other junctions, do not play a structural role, but enable direct and rapid communication between two cells, in the form of passive diffusion of ions, secondary messengers and small molecules (< 1 kDa). These pores are composed of two protein complexes called connexins (Goodenough et al., 1996).

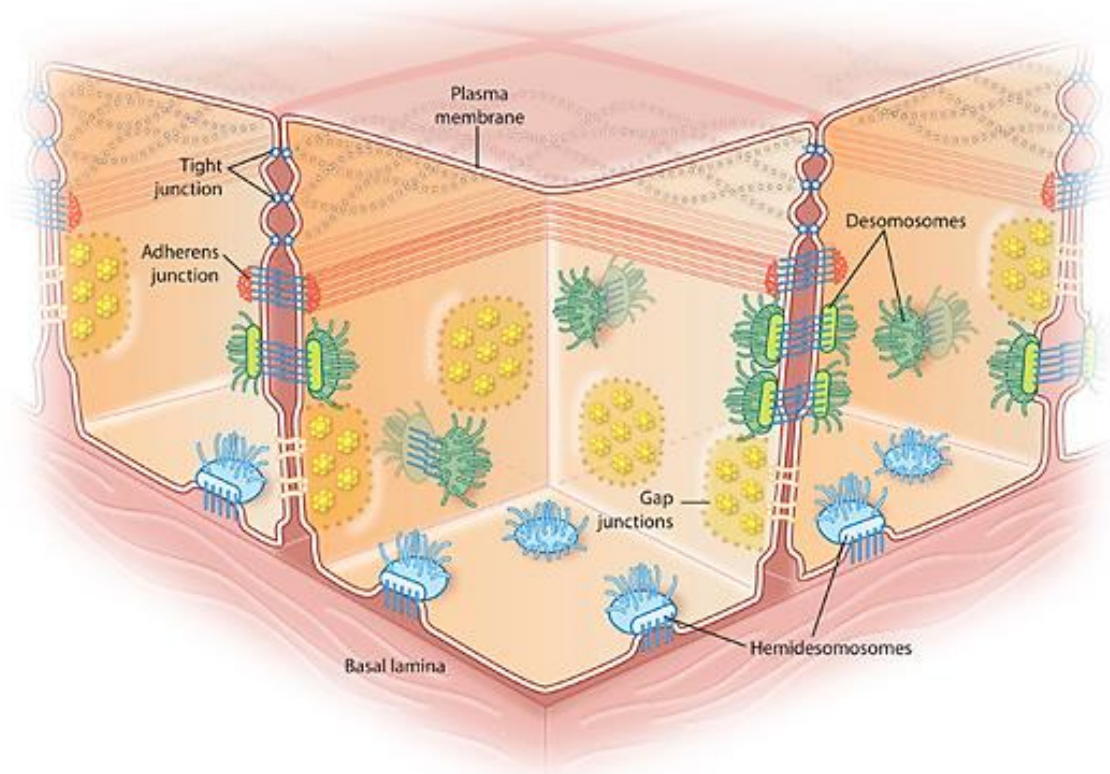


**Figure 15:** Schematic representation of the different epithelial junctions.  
From Nature Education, 2010.

## 2. Functions of the airway epithelium

As seen in part [IA1. Composition](#), the airway epithelium forms a rich ecosystem populated by cells specialized in protecting the lungs and the organism.

### Physical barrier

The section [Cellular junctions](#) detailed the structures of the airway epithelium allowing the formation of a tight physical barrier protecting the body from inhaled pathogens.

### Mucociliary clearance

Mucociliary clearance plays a major role in this defense, particularly against the  $10^6$  to  $10^9$  bacteria and other particles inhaled every day. Mucociliary clearance results from the coupling between mucus production by goblet cells from the surface epithelium and mucous cells from the SMGs, and the coordinated beating of motile cilia present on the apical surface of multiciliated cells. The mucus, rich in "sticky" glycosylated mucins (MUC5AC and MUC5B), traps viruses, bacteria, dust, pollen and other inhaled pathogens. The mucus is continuously displaced anteriorly by a current generated by the beating cilia of the multiciliated cells, at a speed of 5 mm/min, until it reaches the larynx, where it is

swallowed and digested or spat out (Hill et al., 2022; Legendre et al., 2021; Widdicombe & Wine, 2015). At the interface between the epithelium and the inhaled air is a liquid film of variable thickness (from 10  $\mu\text{m}$  in the trachea down to 0.1  $\mu\text{m}$  in the alveoli) and composed of two phases: the periciliary fluid (between the cilia of multiciliated cells) and the mucus, which is in contact with ciliary tips (Widdicombe & Wine, 2015).

### Mucus composition

At homeostasis, mucus is a hydrated gel composed of 97.5% water, 1.1% proteins, 0.9% salts and 0.5% high-molecular-weight mucin polymers (Hill et al., 2022). First synthesized as monomers, mucins are dimerized by disulfide bridging via their -COOH end chains, then polymerized in the Golgi apparatus by disulfide bridging via their -NH<sub>2</sub> terminal chains (Fig.16). The polymers formed are extremely large and rich in glycans (~75% of their total weight) (Fig.17). The extensive glycosylations (~4000 possible sites per dimer) provide:

- 1) hydroxyl sites for mucus hydration,
- 2) a negative charge to repel negative periciliary fluid,
- 3) an extensive catalog of modifications to hypothetically bind to and evacuate any inhaled foreign body (Hill et al., 2022; McShane et al., 2021).

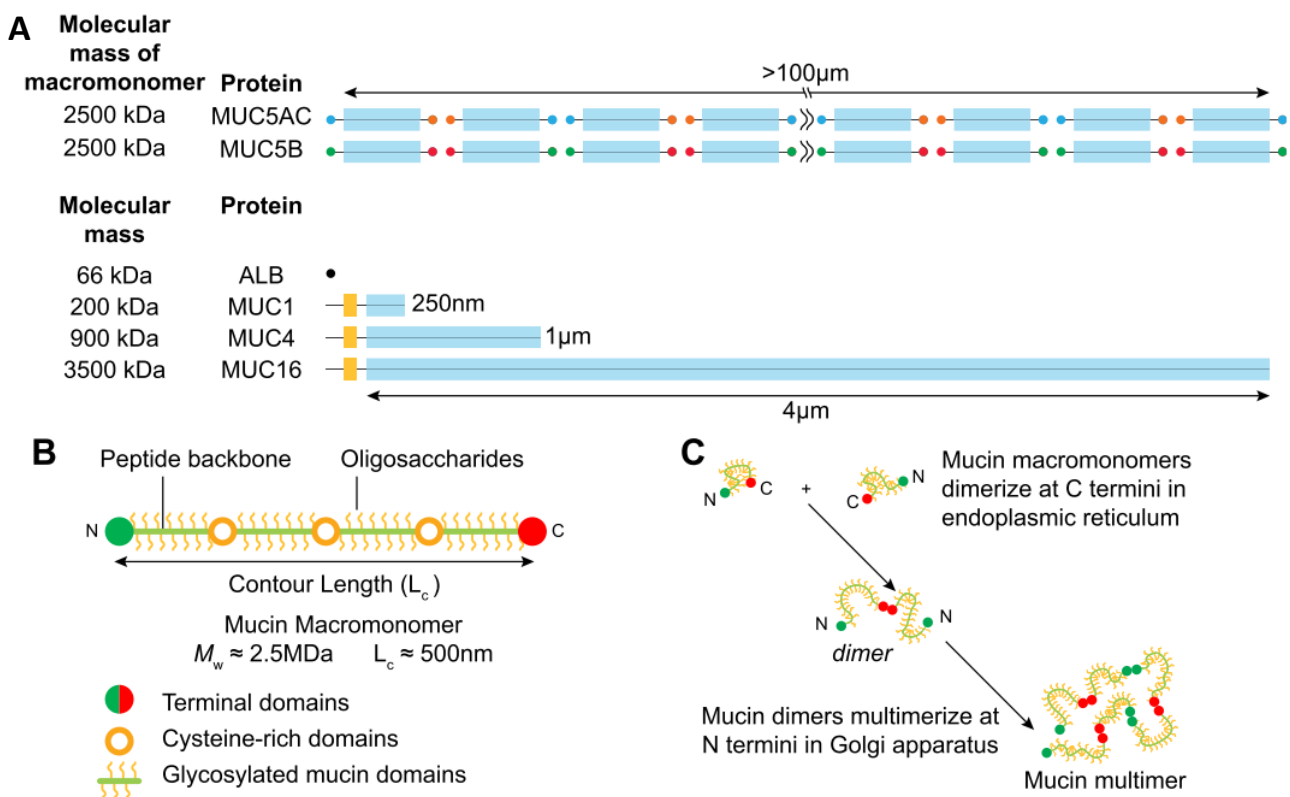


**Figure 16:** Characteristic of mucins.

**A:** Mass of different mucins. **B:** Structure of a mucin monomer. **C:** Dimerization of mucin monomers.

From Hill et al., 2022.

MUC5B and MUC5AC are the two main mucins in airway mucus. Their respective genes are coded in the same mucin genomic cluster along with the other secreted mucins MUC2 and MUC6, on the short arm of chromosome 11 (11p15) (Bansil & Turner, 2006; Whitsett & Alenghat, 2015). In the event of inflammation, the ratios between the two mucins can be altered, with notably MUC5AC expression increasing 50-fold (McShane et al., 2021).

The majority of authors agree that *in vivo*, MUC5B is predominantly expressed in submucosal glands, and MUC5AC is the dominant mucin in proximal and distal surface epithelial mucus (Hill et al., 2022; McShane et al., 2021). During human development, MUC5B appears early in the airways at 13 weeks of gestation, followed by MUC5AC expression at 17 weeks. As the airways mature and the submucosal glands develop, MUC5B expression migrates to the glands (Reid et al., 1997). However, a 2019 study by Okuda et al. contradicts this consensus by providing a regional characterization of the distribution of MUC5B and MUC5AC in normal human airways. The study shows that MUC5B is the predominant mucin secreted not only in submucosal glands but also in superficial airway epithelia (Fig.18). It also indicates that the principal region for MUC5AC production is the surface epithelium of proximal cartilaginous airways (Okuda et al., 2019). Moreover, location of mucus production could influence their glycosylation and sulfation content, leading to location-specific properties (Hill et al., 2022).

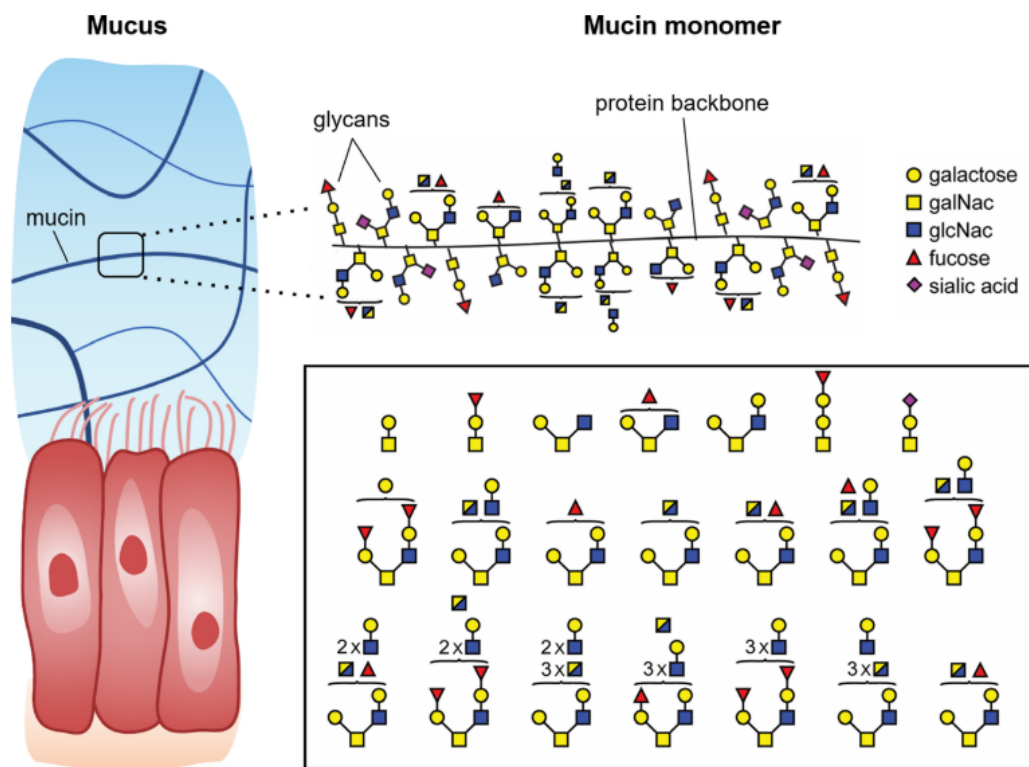


**Figure 17:** Representative glycans found in a mucin monomer. From Wang et al., 2021.

Interestingly, neither MUC5B nor MUC5AC was detected in terminal bronchioles (**Fig.18**), suggesting that proper gas exchange in alveoli requires an absence of mucins (Okuda et al., 2019). In 2011, Seibold and colleagues identified a gain-of-function rs35705950 SNP variant in the putative promoter of *MUC5B*, associated with pulmonary idiopathic fibrosis (IPF). They found an accumulation of MUC5B plugs in the cysts of patients and in the cytoplasm of the secretory columnar cells of their bronchi. One of their working theories is that this variant promoter could induce ectopic production of MUC5B in patients' alveoli, interfering with surfactants and/or perturbing alveolar repair (Seibold et al., 2011). David Schwartz's group has extensively studied the effect of rs35705950 on IPF initiation. Their latest works suggest that in small airways, alveolar cells get locked in a muco-secretory phenotype that results in progenitor depletion (Kurche et al., 2024). In agreement with that, an overexpression mouse model of *Muc5b* under an alveoli-specific reporter (surfactant protein C, *Sftpc*), coupled to bleomycin injury, demonstrated a correlation between overexpression of Muc5b in the distal lung and increased fibrotic response. In contrast *Muc5b*<sup>-/-</sup> mice presented less collagen deposits than control littermates (Hancock et al., 2018).

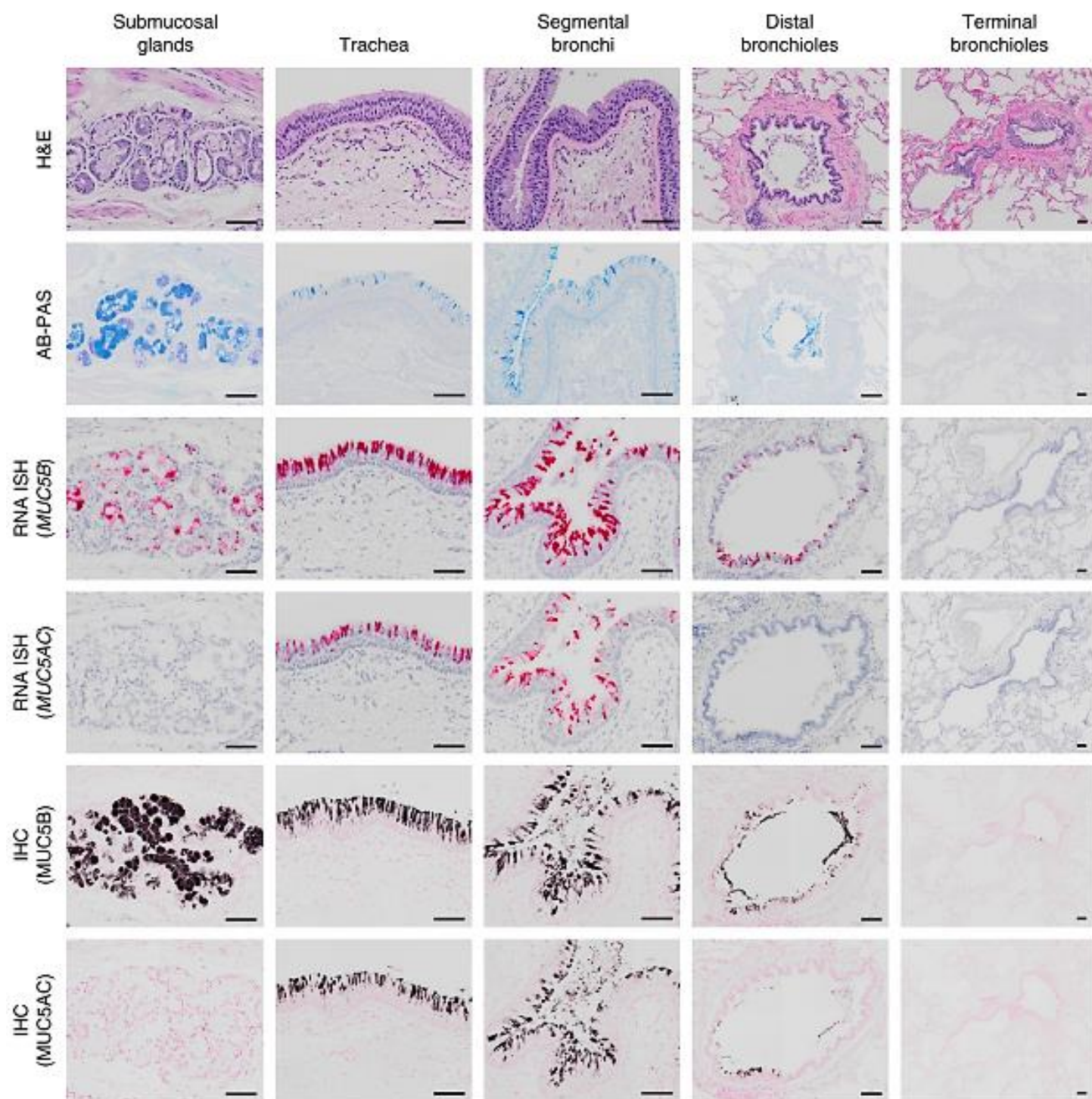


**Figure 18:** MUC5B and MUC5AC expression across the lungs.  
From Okuda et al., 2019.

## Periciliary layer

The periciliary layer is an aqueous layer necessary for proper ciliary beat. Its volume, composition and hydration levels must be strictly controlled to ensure efficient mucociliary clearance (Boucher, 2007). To regulate the hydration of the periciliary layer, the epithelium continuously secretes and absorbs ions through two main ion transporters: the epithelial Na<sup>+</sup> channel (ENaC) and CFTR, expressed by ionocytes and club cells (Hill et al., 2022). The major importance of this ion balance is illustrated by cystic fibrosis, a disease caused by mutations in the *CFTR* gene, which lead to mucus hyperconcentration (dehydration) in many organs. In particular it affects the lungs, where mucociliary clearance is impaired, leading to mucosal obstructions and repeated bacterial infections that can be fatal (Hill et al., 2022).

There are two models describing the interaction between mucus and the periciliary layer (**Fig.19**). The first, known as the "classical" model, dates back to the 1930s and equates the periciliary layer to a liquid in which the cilia beat freely, with the mucus layer above. Although intuitive, this model does not explain why mucus does not diffuse into this layer, nor why mucus does not detach from the interface in the event of high airway hydration (Dickey, 2012; Hill et al., 2022). A second model proposed by Button, known as "gel on brush", describes the periciliary layer not as a liquid but as a gel composed of membrane-bound mucins projecting toward the lumen, forming a brush along the cilia of MCCs (**Fig.19**). In human bronchial epithelial cell cultures, Button et al. identified MUC1 and MUC4 as the mucins forming a meshwork around cilia (Button et al., 2012). This gel on brush model has several advantages: 1) it helps explain why the mobile mucus layer does not diffuse into the periciliary layer: the compact membrane-bound mucins in the gel prevent the mobile mucins from intercalating into the cilia. 2) The mucins attached along the cilia create a spatial hindrance that allows neighboring cilia to repel and coordinate with each other. 3) The increasing density of anchored mucins from top to bottom helps expel particles from the periciliary layer and prevents particles larger than 25 nm from approaching the epithelium. 4) The negative charges of mucins make them excellent lubricants in aqueous environments, reducing friction between cilia and the mobile mucus layer. The negative charges of the periciliary layer also allow it to repel mucus (also negatively charged), and to be repelled by mucus, creating an osmotic force holding the periciliary layer in place (Dickey, 2012; Widdicombe & Wine, 2015).



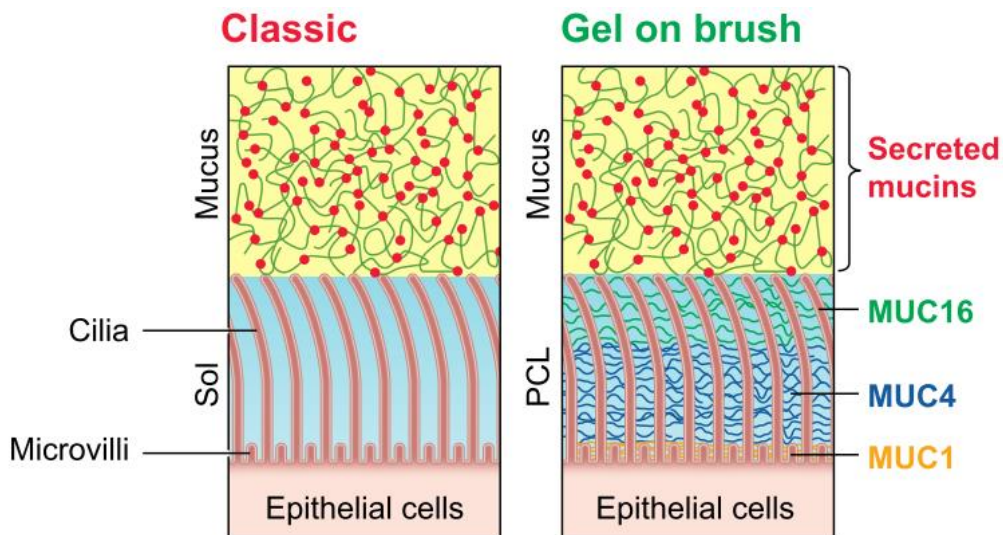


**Figure 19:** The two models of the periciliary layer.  
From Hill et al., 2022.

### Ciliary beating

Mucus evacuation is only possible owing to the cilia of multiciliated cells beating at a frequency between 10 and 20 Hz and according to a very specific pattern made up of two phases:

1. An effector phase in which the cilium is perpendicular to the epithelium, with its tip anchored in the mucus layer. It moves in one plane, in the direction of mucus evacuation.
2. A recovery phase in which the cilium curves like an arc to return to its initial position (Legendre et al., 2021).

The beating at the surface of the MCCs, although coordinated, is not synchronous. Their movement is slightly offset in time, creating a wave on the surface of the epithelium. According to a model by Elgeti, this asynchronous beating enables mucus to be propelled 10 times more efficiently and 3 times faster than a synchronous beating of the cilia would (**Fig.20**) (Elgeti & Gompper, 2013).

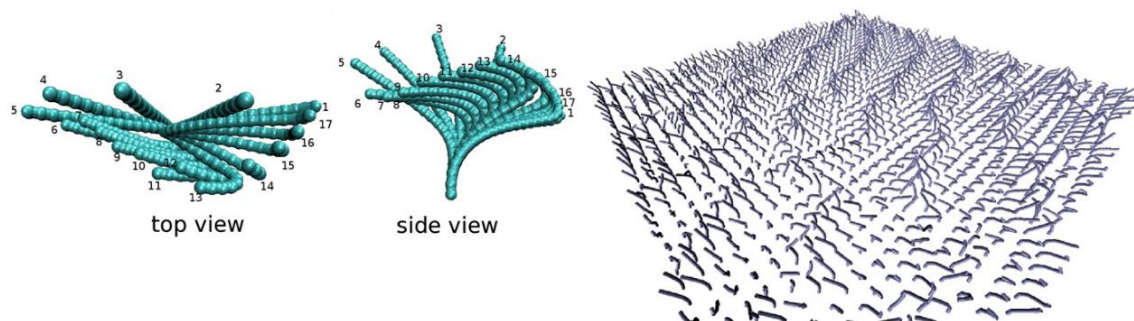


**Figure 20:** Representation of a cilium beat (left) and modelisation of asynchronous beat (right).  
From Elgeti & Gompper, 2013.

## Immune defense

Epithelial cells are in constant contact with external particles and pathogens carried by the inhaled air. In addition to forming a physical barrier to protect the lungs from injury, the airway epithelium is intimately linked to the plethora of immune cells hosted by the lungs (**Fig.21**):

- Neutrophils/granulocytes are small cells that patrol the lungs in search of pathogens to kill and remove.
- Macrophages are phagocytic scavengers that can be found in the alveolar or interstitial space. Alveolar macrophages are large and crucial for surfactant turnover, while interstitial macrophages are smaller and present antigens to trigger adaptive immunity.
- Dendritic cells are antigen presenting cells.
- Mast cells degranulate when they encounter IgE, releasing histamine.
- T cells can help the response of other immune cells (helper T cells) or kill virus-infected cells (cytotoxic T cells). When activated by an allergen, T cells become Th2 cells and trigger airway hyperresponsiveness by producing cytokines such as IL13 (X. Sun et al., 2022).

The role of the epithelial cells is to recognize pathogens, alert and recruit immune cells (**Fig.21**):

1. They express pattern recognition receptors (PRRs) such as Toll-like receptors -3, -4 (TLR3, -4) and NLRs, which enable them to detect foreign molecules (PAMPs and DAMPs) via the Janus kinase/signal transducer and activator of transcription 6 (JAK/STAT6), NF- $\kappa$ B and IRFs pathways.
2. Activation of TLRs and NLRs leads to the production of antimicrobial peptides (HBD-2, HBD-4), CXC chemokines (CXCL1-8, CXCL12) and CC chemokines (CCL2, CCL17, CCL18, CCL20), and cytokines (IL-33, TSLP, IL-25...) by epithelial cells, which will attract immune cells such as leukocytes, neutrophils, pulmonary dendritic cells, innate lymphoid cells type 2 (ILC2) or lymphocytes type 2 to the site (Hartl et al., 2018; Ordovas-Montanes et al., 2020; Whitsett & Alenghat, 2015).

Recently, a study presented an immunomodulatory role for epithelial SMG cells. Duct and serous cells can recruit immune cells (IgA plasma cells, B cells and CD4 T cells) and modulate their response through the secretion of cytokines and the expression of major histocompatibility complex class II (MHC-II) and CD40 (Madisson et al., 2023).

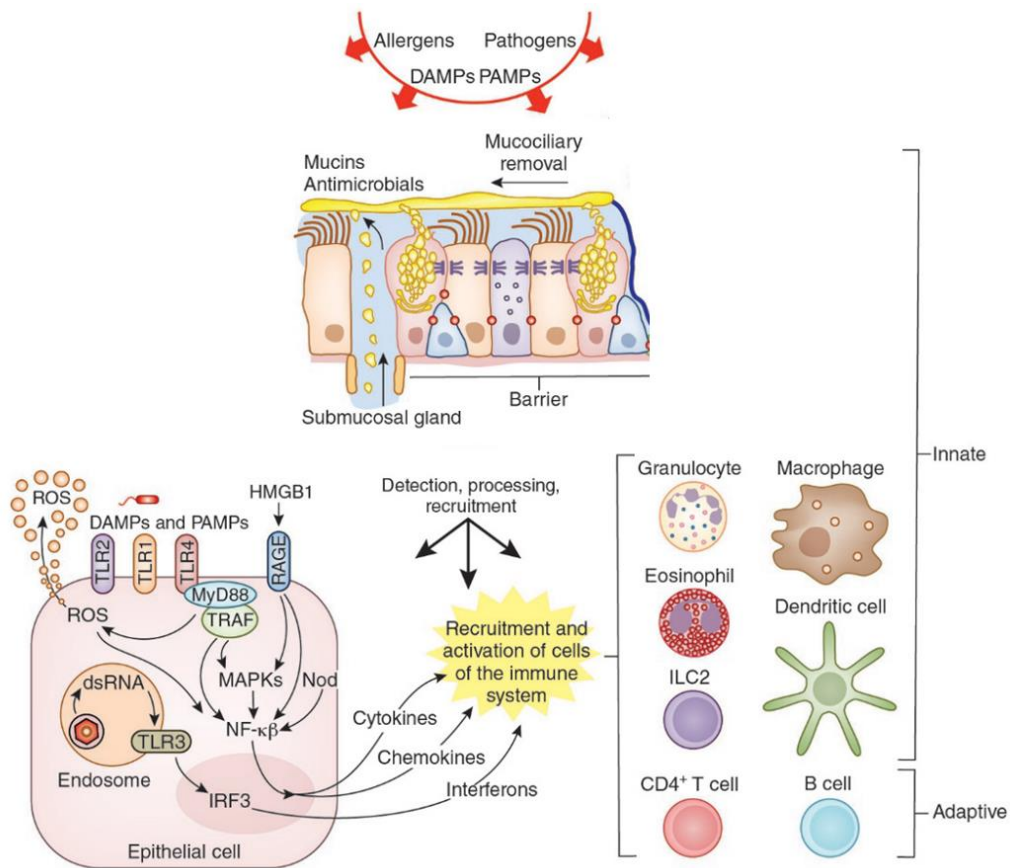


**Figure 21:** Signaling in epithelial immunity. Adapted from Whitsett et al., 2015.

### 3. Development of the lung and the respiratory airways

#### Embryonic origin of the upper airway epithelium

The development of the nasal cavity starts at embryonic day (E) 9.5 in mice or at the end of the 4<sup>th</sup> gestational week in humans, when the nasal/olfactory placodes emerge from the ectoderm. Between the 4<sup>th</sup> and 8<sup>th</sup> weeks, the nasal placodes thicken and invaginate to form the nasal epithelium and all midface structures (nostrils, nasal bones, nasal cartilage, sinuses) (Cardesa et al., 2017; Grindley et al., 1995). At week 5<sup>th</sup>, the nasal sacs form, and the primitive nasal and oral cavities separate. By the 8<sup>th</sup> week, the lateral nasal walls are well-developed. As the nasal pits deepen and expand, the nasal epithelium will differentiate into two distinct regions: the airway/respiratory and the olfactory epithelia. Although this divergence is not clearly reported, it can be assumed that it occurs around E10.5 to E12.5 in mice and between the 5<sup>th</sup> and 7<sup>th</sup> weeks of gestation in humans, during the formation of the primitive nose and the formation of the olfactory epithelium in the upper nasal cavities (Som & Naidich, 2013).

The development of the nasal airway epithelium has not been clearly described and the primitive nasal epithelium is often referred to as the olfactory epithelium, regardless of the developmental stage,

therefore in this paragraph I will assume that the primitive nasal epithelium is a progenitor of both tissues. Nasal epithelium development is under the tight control of several morphogens (**Fig.22**). Null homozygosity of the anteriorizing factor *Otx2* is lethal in mice as they fail to form midbrain and forebrain by E9.5 and heterozygous *Otx2*<sup>+/-</sup> mice do not develop nasal placodes (Acampora et al., 1995; Beby & Lamonerie, 2013). Similarly, *Pax6* expression in mice is detected in the head surface ectoderm at E8.0, around the time nasal placodes appear and *Pax6*<sup>-/-</sup> mice fail to form nasal placodes (Collinson et al., 2003).

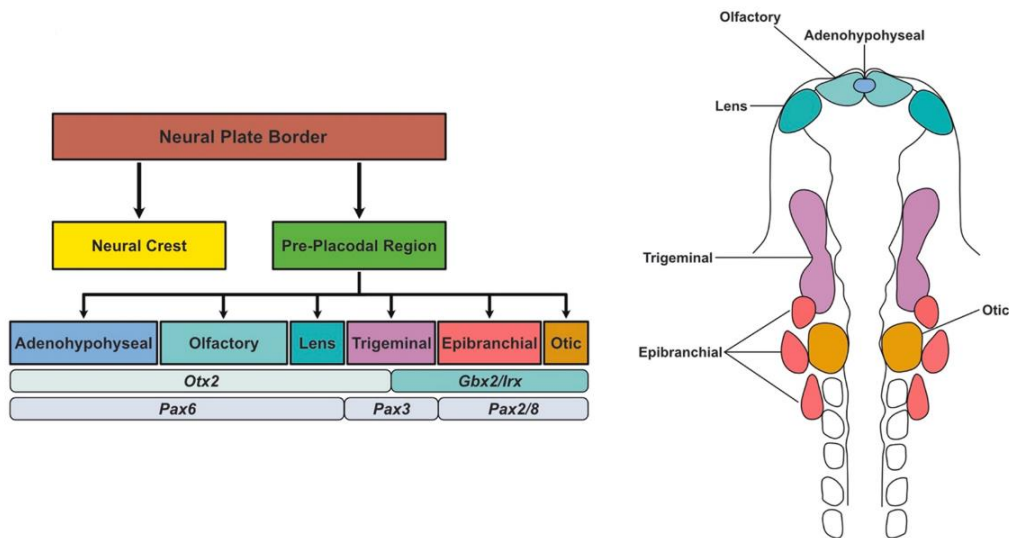


**Figure 22:** Divisions of neural plate border and locations of the cranial placodes in a chick embryo. From Koontz et al., 2023.

## Embryonic origin of the lower airway epithelium

The development of the lower airways (trachea, bronchi, parenchyma) begins in the endodermal layer of the embryo with the ventral expression of *Nkx2-1* in the primitive foregut endoderm, while *Sox2* is expressed dorsally in the future esophagus (**Fig.23A&B**). At E9.5 in mice or E28 in humans (4<sup>th</sup> week), two lung buds appear due to the expression of *Fgf10* in the adjacent mesoderm and *Fgfr2* in the endoderm. The localized expression of *Fgf10* relies on retinoic acid signaling and *Tgfβ* inhibition. Around the same period, the trachea and esophagus start separating. The lung buds then elongate and undergo branching morphogenesis (pseudoglandular stage), narrow (canalicular stage) and form small sacs (sacculi) that will develop into alveoli (saccular stage) (**Fig.23C**) (Cardoso, 2001; Morrisey & Hogan, 2010).

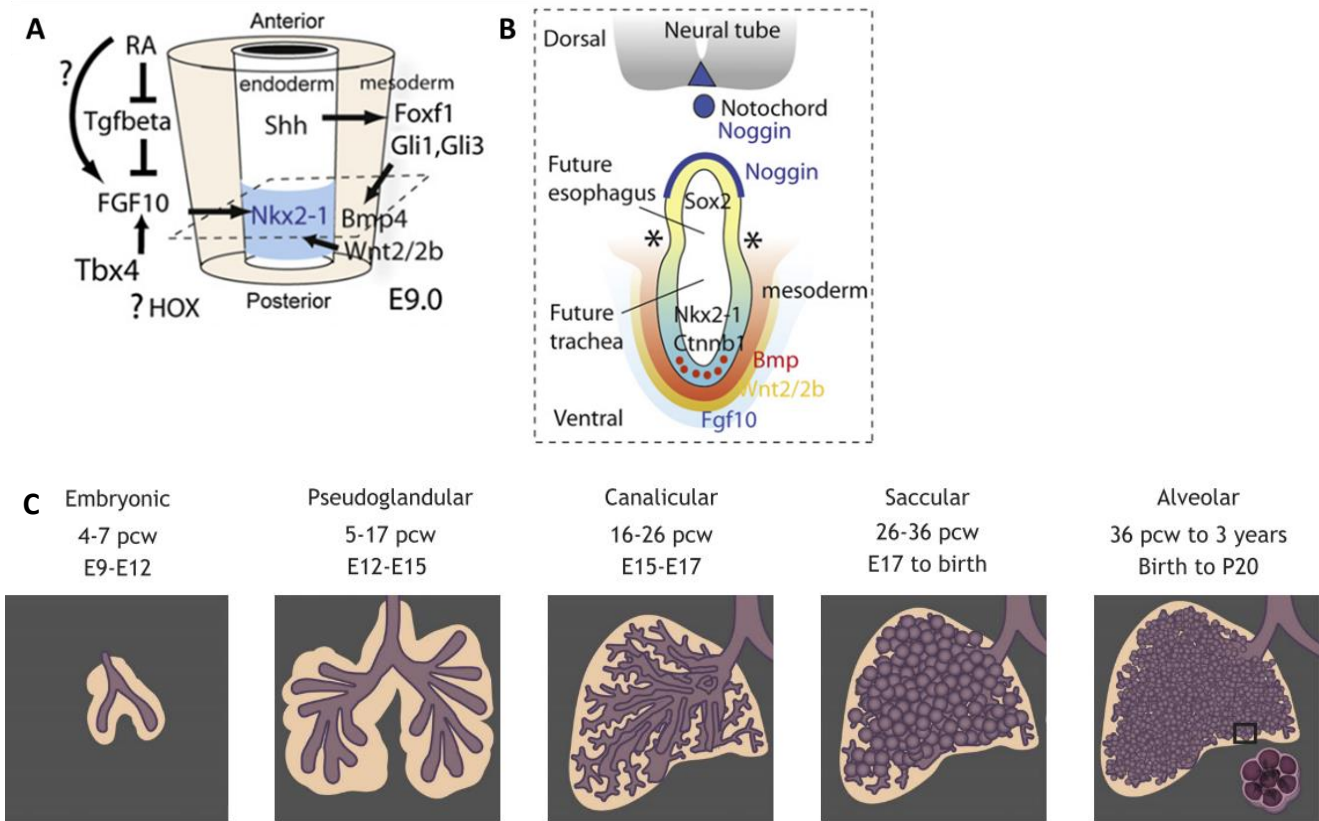


**Figure 23:** Embryonic lung patterning and development. Forgut (A) and dorsal (B) patterning, adapted from Morrisey et al., 2018. C: Main stages of lung development in human and mouse. From Nikolić et al., 2018.

## 4. Homeostasis and regeneration

### Multiciliogenesis

Multiciliogenesis is the process by which progenitor cells differentiate into multiciliated cells. It requires a centriole amplification step during which the cells generate ~300 of centrioles which mature into basal bodies from which will elongate motile cilia. Lineage tracing studies have shown that, at homeostasis, multiciliated cells originate from the differentiation of club cells (Rawlins, Okubo, et al., 2009). In a mouse model of apical sloughing, it has been shown that, in the absence of club cells, basal cells can differentiate directly into multiciliated cells (Pardo-Saganta et al., 2013). In both instances, during centriole amplification the progenitor transits through an intermediate cell type called the deuterosomal cell.

Centrosomes are core structures functioning as microtubule organizing centers (MTOC), made of a pair of half-micron centrioles arranged perpendicularly and surrounded by a cloud of proteins called the pericentriolar mass (PCM). Centrosomes are necessary for cell proliferation (Azimzadeh, 2014) (For review, Bettencourt-Dias Trends in genetics 2011). Chemical ablation of centrosomes by the PLK4 inhibitor centrinone lead to P53-mediated cell cycle arrest in the G1 phase (Wong et al., 2015). During

multiciliogenesis, centrioles are massively amplified before becoming the basal bodies that anchor cilia to the plasma membrane.

Multiciliogenesis can be recapitulated into several steps: cell cycle arrest, centriole amplification, apical network reorganization, centriole migration to the apical pole and cilia elongation.

- 1) Cell cycle arrest: To amplify their centrioles, progenitors must first exit the cell cycle as the centrosome is repurposed for centriole amplification. With a few exceptions, cilia are negative regulators of cell proliferation (Keeling et al., 2016).
- 2) Centriole amplification: There are two distinct but concomitant ways to increase centriole numbers from two to hundreds of centrioles:
  - a) Centriolar pathway: This is the pathway used by most cells to duplicate centrosomes in preparation for cell division. In multiciliated cell progenitors, one to multiple daughter procentrioles form around their mother centrioles in either an orthogonal, rosette or ectopic orthogonal fashion. The centriolar pathway is regulated by polo-like kinase 4 (PLK4). PLK4 is recruited to the mother centriole by centrosomal protein 152 (CEP152), then interacts with CEP63 to form a ring (Zhao et al., 2013).
    - i) Centriole duplication: Each of the two existing mother centrioles serves as a template for the formation of a new procentriole.
    - ii) Maturation: The new procentrioles elongate and mature by incorporating proteins from the PCM.
    - iii) Centrosomes separation (Werner et al., 2017).
  - b) Deuterosomal/acentriolar/*de novo* pathway: Deuterosomes are MCC-specific and membrane-less organelles that form *de novo*, independently from the centrosome, during multiciliogenesis. Cells undergoing massive centriole amplification through the deuterosomal pathway are called deuterosomal cells. Each deuterosome can nucleate tens of procentrioles, accounting for 90% of centrioles generated (**Fig.24**). Knocking out the gene coding for the deuterosome-specific protein Deup1 in mice and xenopus stops deuterosome formation but does not block centriole formation nor reduce the number of centrioles formed. It leads, however, to crowding of procentrioles in the centrosome region, indicating that deuterosome self-assembly could help sequester procentrioles into more compact flower arrangements to relieve parent centrioles from spatial hindrance. In addition, MCCs lacking both parent centrioles and deuterosomes still produce an appropriate number of centrioles inside a cloud of pericentriolar and fibrogranular material showing that centriole amplification can organize in an autonomous fashion without any specific organelle (Mercey, Levine, et al., 2019).

Al Jord et al. described three distinct stages during mouse ependymal cell differentiation (**Fig.24**).

- i) Halo stage or amplification A-phase: procentrioles form on deuterosome platforms;
  - ii) Flower stage or growth G-phase: procentrioles elongate and mature;
  - iii) Basal body stage or disengagement D-phase: mature centrioles disengage from the deuterosomes to then anchor at the apical pole of the plasma membrane and transform into basal bodies (Al Jord et al., 2014; Mercey, Al Jord, et al., 2019).
- 3) Apical network reorganization: To anchor and orientate basal bodies correctly, the actin cytoskeleton must be reorganized into a dense apical mesh network, through the repression of the small GTPase R-Ras by the miR-34/449 superfamily of microRNAs (Chevalier et al., 2015).
  - 4) Cilia elongation: The 9 outer doublet microtubules and 2 singlets axoneme structure of motile cilia (cilium proper, or core) are built and maintained through a process called intraflagellar transport (IFT). Tubulin is transported along the axoneme to the growing plus ends of the microtubules by motor proteins. Cilia are continuously being assembled and disassembled by IFT trains, maintaining a state of dynamic stability (Avasthi & Marshall, 2012).

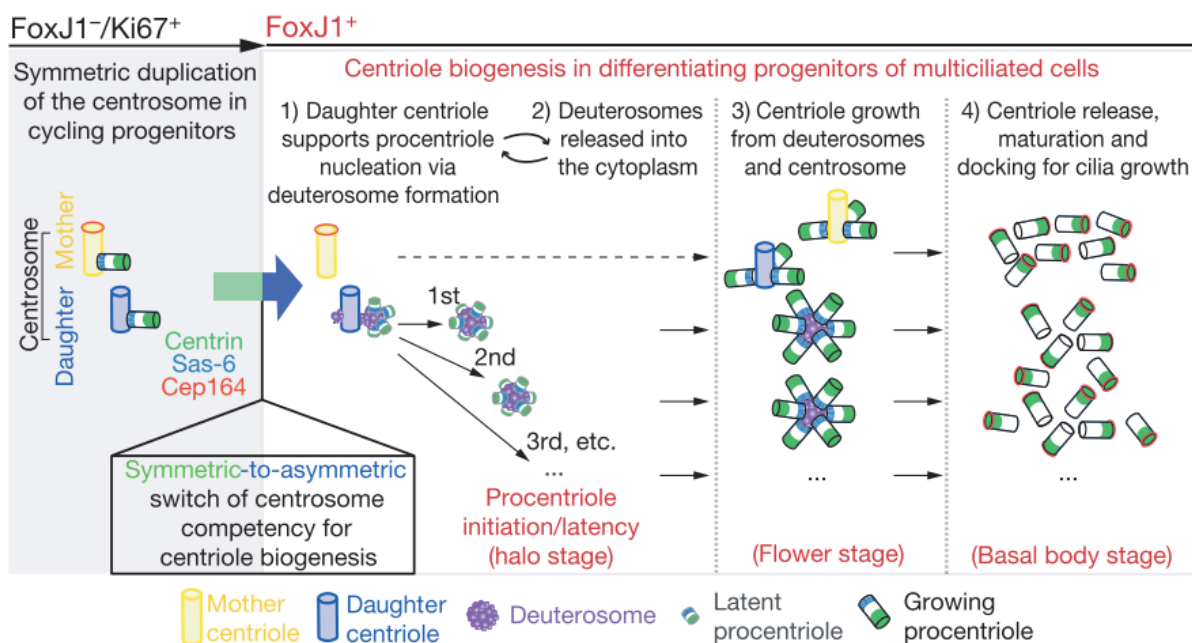


**Figure 24:** Centriole amplification in multiciliated cells.  
From Jord et al., 2014.

Multiciliogenesis is first triggered by the inhibition of Notch by miR-34/449 (Marcet, Chevalier, Luxardi, et al., 2011), which leads to the transcriptional induction of two major transcriptional regulators: Multicilin (MCIDAS) and Geminin (GMNC) (**Fig.25**). GMNC stimulates the expression of MCIDAS and interacts with E2F4/5-TFDP1 and MCIDAS to form a quaternary complex that regulates multiciliogenesis at an early-stage by inducing the expression of genes such as MYB, FOXJ1, FOXN4, or

RFX3 (Arbi et al., 2016; Kyrousi et al., 2015; Stubbs et al., 2012; Terré et al., 2016; F. Zhou et al., 2015). Another regulator of multiciliogenesis is TP73, which is expressed in a fraction of basal cells but mainly in multiciliated cells. TP73-deficient mice remain capable of centriole amplification, but these centrioles fail to anchor to the apical membrane, are not polarized, and do not develop axonemes (Nemajerova et al., 2016) The expression of TP73 is also controlled by MCIDAS and TP73 induces FOXJ1, RFX2/3 (Marshall et al., 2016). These transcription factors are both major inducers of late multiciliogenesis. FOXJ1 has been shown to be required for maturation, migration and/or apical anchoring of the centrioles, and for axoneme elongation and motility (Brody et al., 2000; J. Thomas et al., 2010; You et al., 2004; X. Yu et al., 2008). RFX factors promote the expression of numerous proteins that are integral to cilia structure, such as dyneins, and especially proteins involved in the intraflagellar transport of ciliary cargos (M. I. Chung et al., 2012; J. Thomas et al., 2010). In a possible co-regulatory mechanism involving the formation of a transcriptional complex, FOXJ1 can induce the expression of RFX2 and RFX3 (Didon et al., 2013). Conversely, RFX3 can bind to the FOXJ1 promoter and stimulate its expression (El Zein et al., 2009).

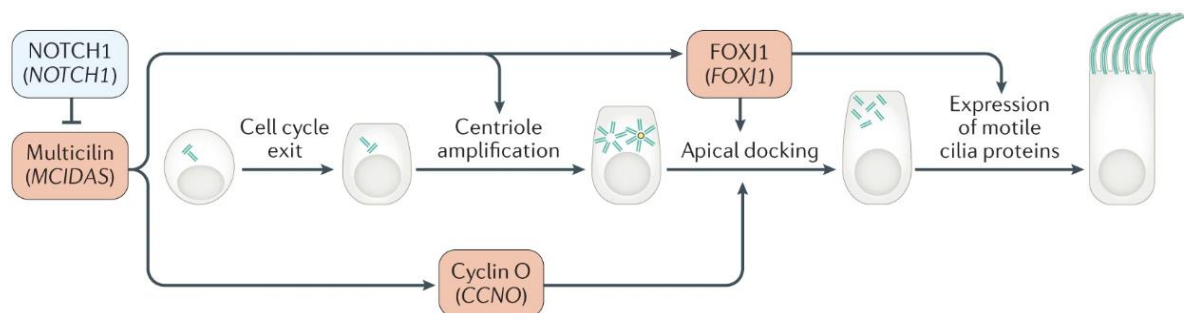


**Figure 25:** Multiciliogenesis pathway.  
From Wallmeier et al., 2020.

## Regeneration and remodeling

The adult lung is most often quiescent, with a low cellular turnover, but is still able to perform airway repair and maintenance at homeostasis, in response to minor injuries or normal wear and tear. Unlike pathological airway remodeling, which leads to structural changes that impair airway function and is associated with chronic diseases like asthma, IPF or COPD, regeneration is the ideal form of healing post injury as it maintains the normal structure and function of the airways (Kotton & Morrissey, 2014). Homeostatic epithelial regeneration is a dynamic process that ensures the maintenance and repair of the epithelium, preserving normal function and preventing disease progression. Upon injury, epithelial progenitors can be activated to replenish the defective cell populations. As seen in section [IA1: Composition](#), the epithelium is highly plastic and depending on the insult dedicated or facultative progenitors can differentiate or de-differentiate into one or several cell types to overcome the injury (Leach & Morrissey, 2018).



Regeneration can be limited or impaired by chronic inflammation or frequent damage and pathological remodeling can occur as a result. Remodeling is often associated with scarring or fibrosis, progressive loss of MCCs and increased goblet cell content (Kotton & Morrisey, 2014). Section [Remodeling in asthma](#) describes pathological remodeling in more details.

## Signaling pathways and molecular mechanisms controlling development and regeneration

Due to the limited access to human embryonic tissues, there is little information available on the molecular pathways involved in human embryonic lung development and the establishment of the airway epithelium (Nikolić et al., 2018). Therefore, this section will heavily rely on data from mice, with human data included wherever possible.

One stark difference between human and mice lung development is found at the pseudoglandular stage (5-17 pcw / E12-E15), a key step for airway epithelial differentiation emerging from lung endoderm progenitors (Nkx2.1+/Gata6+/Foxa1+/Foxa2+) (**Fig.26A**) (Herriges & Morrisey, 2014). During this stage, the airway tree structure is being laid down by branching of the distal part of the bud tips into the surrounding mesoderm. The lung buds are composed of a proximal Sox2+ zone and a distal Sox9+ Id2+ zone (the bud tip). In humans, the bud tip is SOX2+/SOX9+, but the role for SOX2 there is not known. At the canalicular stage (16-26 pcw / E15-E17), a transition zone Sox2-/Sox9-, called the stalk, appears in both species. As lungs mature, bud tip progenitor cells exit the tip for the stalk, switch from expressing Sox9 to Sox2 and differentiate into bronchiolar progenitor, while the bud tip extends distally. In humans, the bud tip progenitors turn off SOX9 but retain SOX2 (**Fig.26B**). Progenitors remaining in the bud tip are maintained in an immature state until later external cues signal for alveolar epithelial differentiation (He et al., 2022; Nikolić et al., 2018).

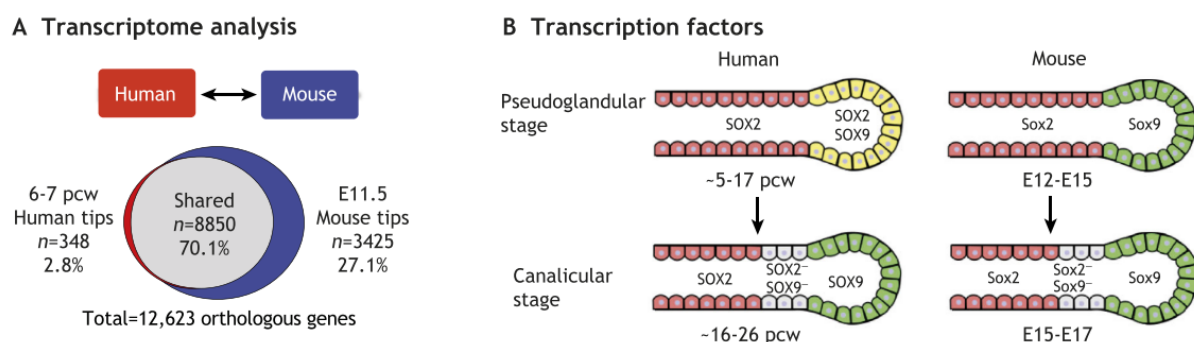


**Figure 26:** Mouse and human lung development.

**A:** Transcriptional differences between mouse and human bud tips. **B:** Human and mouse have different Sox2 expression patterns.

From Nikolić et al., 2018.

## Notch signaling

Notch signaling is a highly conserved pathway that operates through cell-cell contact. Notch is an essential player in embryonic epithelial development and is crucial for lung proximal-distal patterning and the specification of different lineages. The canonical pathway comprises four receptors (Notch1, Notch2, Notch3 and Notch4) and five membrane-bound ligands (Jagged1 and Jagged2, Delta-like ligand DLL1, DLL3 and DLL4). Upon binding of a ligand on the surface of one cell (activator cell) to a receptor on the surface of another cell (activated cell), the Notch Intracellular Domain (NICD) of the receptor is cleaved by the  $\gamma$ -secretase enzyme. NICD is then translocated to the nucleus, where it acts as a transcription factor to activate the expression of Notch target genes such as the Hes Family BHLH Transcription Factor 1 (Hes1) and Hey1 and Hey2. The activation of target genes is mediated by RBPJ (Gajjala & Madala, 2021).

### Notch signaling in embryonic development

**Notch signaling mediates club and multiciliated cell specification.** Disruption of canonical Notch signaling in embryonic mice results in the ablation of club cell and secretory lineages, and in a multiciliated cell hyperplasia (Morimoto et al., 2010; Tsao et al., 2009). Conversely, constitutive overexpression of NICD in embryonic mouse lungs induces goblet cell hyperplasia at the expense of multiciliated cells and prevents distal alveolarization. However, overexpression of Notch does not alter club cell frequency (Guseh et al., 2009).

**Notch1-activated progenitors become club and multiciliated cells, but not PNECs.** Lineage tracing of Notch1 activation marks club cells almost exclusively, suggesting that Notch1 is the Notch receptor at play in secretory lineage specification. Certain multiciliated cells are also labelled, probably because they arise from club cells (Morimoto et al., 2010).

**Notch2 signaling inhibits basal cell fate in favor of luminal specification.** An early p63<sup>+</sup> progenitor can generate both airway and alveolar epithelia before E10.5 (Yang et al., 2018). The progenitor commits to the airway lineage with the expression of Sox2 (Herriges & Morrissey, 2014). Of importance, this progenitor directly generates PNECs at E13.5. Next, Notch mediates a second lineage-restriction around E13.5/E14.5. Notch2 positive cells become airway luminal Scgb3a2<sup>+</sup> progenitors, and Notch2 negative cells become airway basal Krt17<sup>+</sup> progenitors. Notch2 specification of secretory and multiciliated lineage was also observed by Morimoto et al. (2012). Moreover, this differentiation pattern is similar to the one described by Morimoto and colleagues in 2010, therefore this progenitor might express Notch1 and Notch2 although the relationship between the two receptors is unclear.

Airway basal progenitors are committed to the basal cell fate before the apparition of Krt5, which happens around E16.5, time after which they can differentiate into luminal cells. Distal Scgb3a2

progenitors give rise to multiciliated and club cells (Kiyokawa et al., 2021). As Notch2 inhibits multiciliated cell specification when activated (Morimoto et al., 2012), it can be assumed that the Notch pathway is no longer active after basal/luminal specification. Moreover, Notch2 overexpression does not promote club cell specification (Morimoto et al., 2012), which suggests that more complex mechanisms are at work. A similar pSMAD+/TP63+/ KRT5- immature airway progenitor was identified in a single-cell atlas of human fetal lungs, suggesting that, at least in part, a related process occurs in humans.

### Notch signaling at homeostasis

**Notch repression is needed to maintain basal cell stemness.** Inhibition of Notch1 in mice after determination of ciliated fate does not influence the frequency of club and multiciliated cells, nor the viability of mice (Morimoto et al., 2010). Thus, Notch1 signaling does not seem to be involved in the maintenance of luminal cell identity at homeostasis, once differentiation has been established. Accordingly, *Notch1* mRNA enrichment was found in basal cells of mouse mature epithelial cultures. However, no differences in the expression of Notch2, Notch3 and Notch4 were found (Rock et al., 2011). Notch inhibition is however required to maintain basal cell stemness. Activation of the Notch pathway through constitutive expression of the target gene *HES1* in human primary basal cells *in vitro* triggered their differentiation in luminal cells (Rock et al., 2011). Constitutive expression of the *Notch1* intracellular domain in adult mice led to loss of basal cells and goblet cell hyperplasia (Rock et al., 2011).

**Notch3 specifies suprabasal cell fate.** Overexpression of Notch3 under the alveolar promoter SFTPC results in accumulation of “undifferentiated” cells (Scgb1a1-) (Dang et al., 2003). Although not characterized in this study, these cells are probably suprabasal cells. Indeed, Mori et al. described *in vitro* a population of cells present above the basal cell layer, presenting Notch3 activation and a decrease in Tp63 (Mori et al., 2015). Interestingly, disruption of Tp63 decreased the expression of Jag2 leading to incapacity for the cells to activate Notch3 (Yang et al., 2018), suggesting that Tp63-mediated activation of Notch3 is necessary for basal cell differentiation into suprabasal cells.

### Notch signaling in regeneration

**Notch is activated in response to injury.** Notch1 is reactivated following club cell ablation in a murine naphthalene injury model. However, no new club cells arising from Notch1+ cells were observed, suggesting that Notch1 does not directly participate into club cell regeneration (Morimoto et al., 2010).

**Notch regulates basal cell commitment after injury.** Following SO<sub>2</sub> injury (luminal sloughing), some basal cells display direct Notch activation (N2icd+) and differentiate directly into club cell, while some others present active Notch inhibition (cMyb+) and differentiate into multiciliated cells (Pardo-Saganta, Law, et al., 2015). An *in vitro* atlas of human airway epithelial cells, taken at different air-liquid interface (ALI) times, established a molecular repertoire of signaling pathways during regeneration (**Fig.27**). Basal

cells express *NOTCH1* but no target genes, suggesting an inactive pathway (Ruiz García et al., 2019). *NOTCH3* is expressed and activated exclusively in suprabasal cells, consistent with previous work linking *NOTCH3* to suprabasal cell specification (Dang et al., 2003; Yang et al., 2018). *NOTCH2* is expressed and activated in club cells, also in agreement with research identifying this receptor as crucial for secretory lineage establishment (Morimoto et al., 2012; Yang et al., 2018). Deuterosomal and multiciliated cells express *NOTCH4* and some ligands, but show clear signs of Notch inhibition with the expression of the NICD inhibitor *DYRK1A* (Ruiz García et al., 2019).

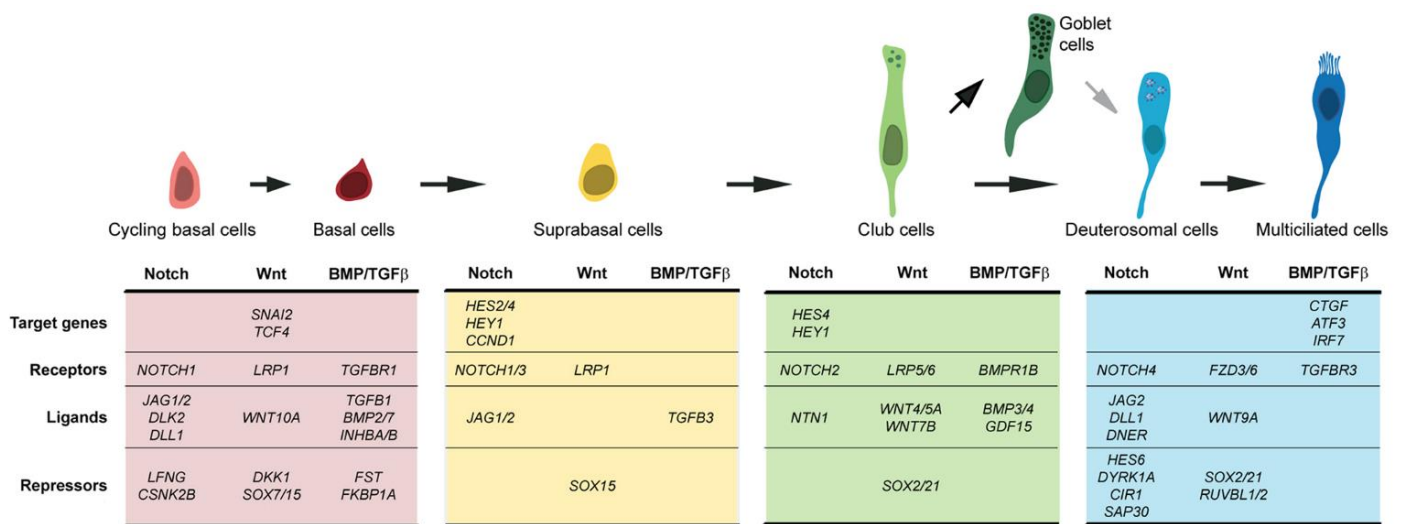


**Figure 27:** Molecular repertoire of major signaling pathways in *in vitro* epithelial cells. From Ruiz García et al., 2019.

## TGFβ signaling

### TGFβ signaling in embryonic development

One of the earliest epithelial progenitors in development are the Nkx2.1+ cells that are generated at E9.0 in mice, appearing at the ventral part of the foregut endoderm through the gradient expression of Wnt/Bmp ligands along the dorso-ventral axis (Kiyokawa et al., 2021). At E11.5, self-renewing Sox9+/Id2+ distal bud tip were detected and shown as progenitors for both bronchial and alveolar epithelial cells (Rawlins, Clark, et al., 2009). Then, before the canalicular stage (~E14.5), the progenitor diverges into an alveolar lineage (Id2+) (inhibitor of differentiation 2) and an airway lineage (Id2-) (Kiyokawa et al., 2021; Rawlins, Clark, et al., 2009). This bifurcation is mediated by the repression of Id2 through activation of Tgfr2 in the airway progenitor lineage (Kiyokawa et al., 2021). In 12-week human fetal lungs, TGFβ is strongly activated in airway epithelial cells (pSMAD+), but not in bud tip progenitors (A. J. Miller et al., 2020).

### TGF $\beta$ signaling at homeostasis

Id2 is a mediator of cell proliferation and is a marker of self-renewing embryonic progenitors (Kiyokawa et al., 2021; Rawlins, Clark, et al., 2009). In adults, Id2 is repressed by TGF $\beta$  activation to maintain tissue quiescence, at the exception of basal cells, where its expression is tightly maintained at low levels to ensure proliferative capacity of basal cells without triggering hyperplasia (Kiyokawa et al., 2021).

### TGF $\beta$ signaling in regeneration

In case of injury, TGF $\beta$  is downregulated to promote regeneration via cell proliferation. SO<sub>2</sub> treatment in adult mice decreased Smad2/3 phosphorylation and increased Id2 expression (Kiyokawa et al., 2021). In human cultures, TGF $\beta$  repressors (*FST* and *FKBP1A*) were only detected in the basal cell population (Ruiz García et al., 2019). TGF $\beta$ /BMP signaling inhibition, though SMAD inhibitors allowed long-term expansion of airway basal cells from several species (Mou et al., 2016).

### Wnt signaling

Wnt/ $\beta$ -catenin signaling is a highly conserved pathway involved in numerous biological processes, including cell proliferation, lung development and regeneration (Aros et al., 2021; Liu et al., 2022). The canonical wingless related-integration site (Wnt)/ $\beta$ -catenin signaling pathway signals through the co-receptors Frizzled (FZD) and leucine-rich repeat-containing G-protein coupled receptor (LGR). In its inactivated state,  $\beta$ -catenin is phosphorylated and ubiquitinated by the destruction complex to be degraded by the proteasome (**Fig.28**). The Wnt pathway is activated upon binding of one of the 19 mammalian Wnt ligands to the receptor complex. The destruction complex then phosphorylates the receptor complex instead of  $\beta$ -catenin, which stabilizes  $\beta$ -catenin and allows its accumulation into the cytosol.  $\beta$ -catenin can then translate into the nucleus, where it acts as a transcription factor to activate the transcription of Wnt target genes (Aros et al., 2021).

Due to its complexity, our current understanding of the specific roles of the Wnt pathway in the airway epithelium maintenance and regeneration remains limited (Aros et al., 2021). However, Wnt/planar cell polarity (Wnt/PCP) program, involving the noncanonical Wnt pathway which is independent from  $\beta$ -catenin, has been well described and regulates directional cell behaviors like polarized morphology, division, and migration via the cytoskeleton (Vladar et al., 2009). Here I will briefly review the implications of Wnt signaling in epithelial cell differentiation.

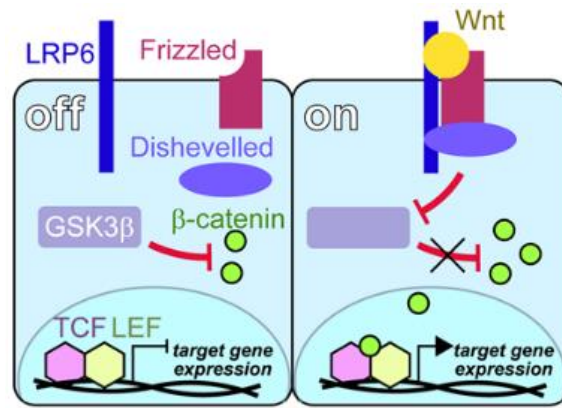


**Figure 28:** Wnt/ $\beta$ -catenin signaling pathway.  
From Walentek, 2022.

### Wnt signaling in embryonic development

The Wnt pathway is involved in the earliest stage of lung endoderm specification as *Wnt2/2b* is necessary for *Nkx2.1* endoderm expression. Murine embryos null for *Wnt2/2b* do not express *Nkx2.1* and fail to develop lungs (Goss et al., 2009). Wnt also controls Sox9 expression in tip bud progenitors in a positive-feedback loop to maintain progenitors self-renewal (D. Sun et al., 2022).

### Wnt signaling at homeostasis

In *Xenopus*, human and murine basal cells, a high level of Wnt signaling is required to promote stemness and inhibit differentiation, through the transcription of *Tp63* (Haas et al., 2019; Malleske et al., 2018). Moreover, excessive Wnt signaling in basal cells can drive basal hyperplasia (Aros et al., 2021). In other compartments, Wnt/ $\beta$ -catenin signaling is primarily inactive at homeostasis, with new  $\beta$ -catenin is either incorporated into adherens junctions or targeted for degradation by the destruction complex (Hogan et al., 2014). Activation of the pathway through expression of an activated form of  $\beta$ -catenin under the club cell promoter *Scgb1a1* in rats led to goblet cell hyperplasia and mucus hypersecretion (Mucenski et al., 2005). However, deletion of  $\beta$ -catenin in rats did not alter epithelial development (Zemke et al., 2009). Stabilization of  $\beta$ -catenin in murine club cells (Reynolds et al., 2008) or under the lung-specific promoter *Nkx2.1* (C. Li et al., 2009) disrupted epithelial cell differentiation and led to an accumulation of undifferentiated cells. Upon injury in mouse trachea, Wnt pathway activation has been shown to be required for basal cell proliferation. The source of secreted Wnt ligands has been identified as *Pdgfra*<sup>+</sup> fibroblasts from the intra-cartilaginous zone. On the other hand, secreted Wnt ligands from basal cells contribute to multiciliogenesis (Aros et al., 2020).

### Wnt signaling in multiciliogenesis

Tight regulation of Wnt signaling is necessary to ensure proper multiciliogenesis. Wnt activation is needed for multiciliogenesis, as it was found in *Xenopus* that the multiciliated cell transcription factor *Foxj1* is positively regulated by Wnt (Walentek et al., 2012). Moreover, a core framework mediated by

Wnt regulates the docking and maintenance of basal bodies to the apical pole of multiciliated cells in *Xenopus* (T. J. Park et al., 2008). However, overactivation of Wnt inhibits multiciliogenesis in favor of goblet cell differentiation, through the interaction of  $\beta$ -catenin with the co-factors cAMP response element binding (CREB)-binding protein (CBP) and P300 (Malleske et al., 2018). Recently, Cooney and colleagues demonstrated that a switch from canonical to non-canonical Wnt signaling, orchestrated by basal cells, is necessary for multiciliogenesis in primary human epithelial airway cells. Basal cells first inhibit canonical WNT/ $\beta$ -catenin signaling by secreting WNT4, which binds to the FZD6 non-canonical WNT/PCP receptor on progenitor cells. Subsequently, basal cells activate non-canonical WNT/PCP signaling by secreting the ligand DKK3, which binds to KREMEN1 (Fig.29) (Cooney et al., 2023). However, the study does not specify in which cell type the switch is executed. According to Ruiz et al., *FZD6* is expressed by deuterosomal cells (Ruiz García et al., 2019), which are already committed to the multiciliated cell fate. Therefore, while this switch from canonical to non-canonical Wnt signaling is necessary for multiciliogenesis, it might not initiate the process.

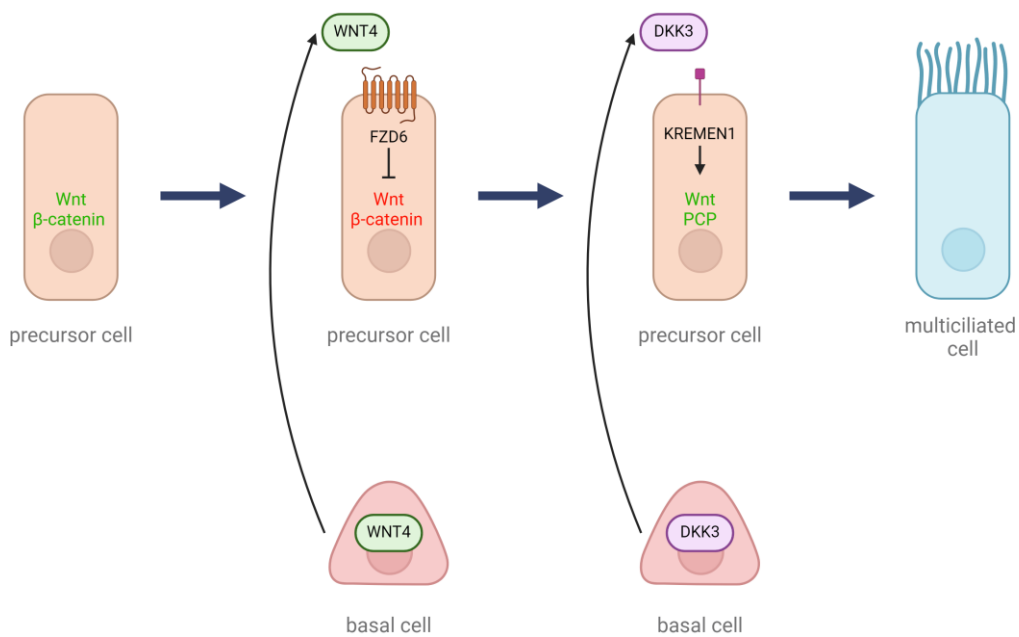


**Figure 29:** Wnt signaling and multiciliogenesis.

### Hedgehog signaling

Hedgehog signaling (HH) is crucial for respiratory system development. Sonic Hedgehog (SHH) is the best-studied ligand of the HH pathway in vertebrates. SHH binds to its receptor Patched 1 (PTCH1) present on its target cell. In the absence of SHH, PTCH1 inhibits the G protein-coupled receptor Smoothed (SMO), located downstream in the pathway, and the associated signaling cascade. Canonical HH signaling begins with SHH binding to PTCH1, which induces PTCH1 inactivation. As a result, SMO repression is lifted, triggering the signaling cascade and enabling SMO to localize and

accumulate in the primary cilium. This cascade leads to the activation of Glioma Oncogene (GLI1-2-3) transcription factors, which can migrate from the cilium to the nucleus to control the expression of the HH pathway target genes (**Fig.30**) (Gorojankina, 2016).

During embryogenesis, early development, and *in vitro* proliferation, each airway epithelial cell possesses a unique primary cilium (Jain et al., 2010). The primary cilium functions akin a cellular antenna capable of picking up various extracellular physical or chemical signals to amplify and modulate them. Huangfu and colleagues were the first to establish a functional link between the primary cilium and the Hedgehog signaling pathway, during embryonic development in the mouse (Huangfu et al., 2003). Since then, the HH signaling pathway has been extensively described in the primary cilium and the primary cilium has been found to be specifically enriched in receptors of the HH pathway.

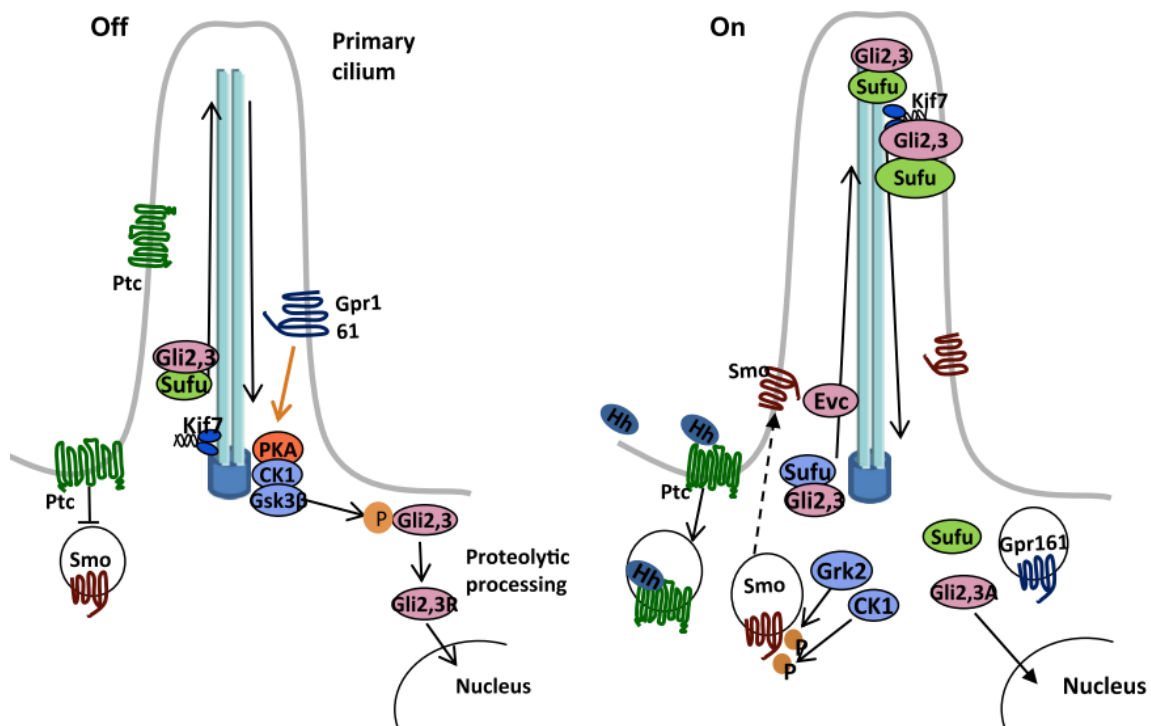


**Figure 30:** Canonical Hedgehog signaling.  
From Gorojankina, 2016.

### Hedgehog signaling during embryonic development.

Shh is expressed in airway epithelium throughout lung development, starting at E10 in mice. It is localized distally, at the tip of growing lung buds (**Fig.31**) (Kugler et al., 2015). Shh regulates esophagus and trachea separation during development as well as branching morphogenesis (L.-A. D. Miller et al., 2004; Pepicelli et al., 1998). Shh-null mice embryos present single-lobe hypoplastic lungs with disorganized cartilage rings and overall decreased mesenchyme (L.-A. D. Miller et al., 2004; Pepicelli et al., 1998). Moreover, although normal epithelial proximo-distal differentiation occurred, location of cell



types was perturbed, indicating that Shh is not needed for epithelial differentiation (Pepicelli et al., 1998).

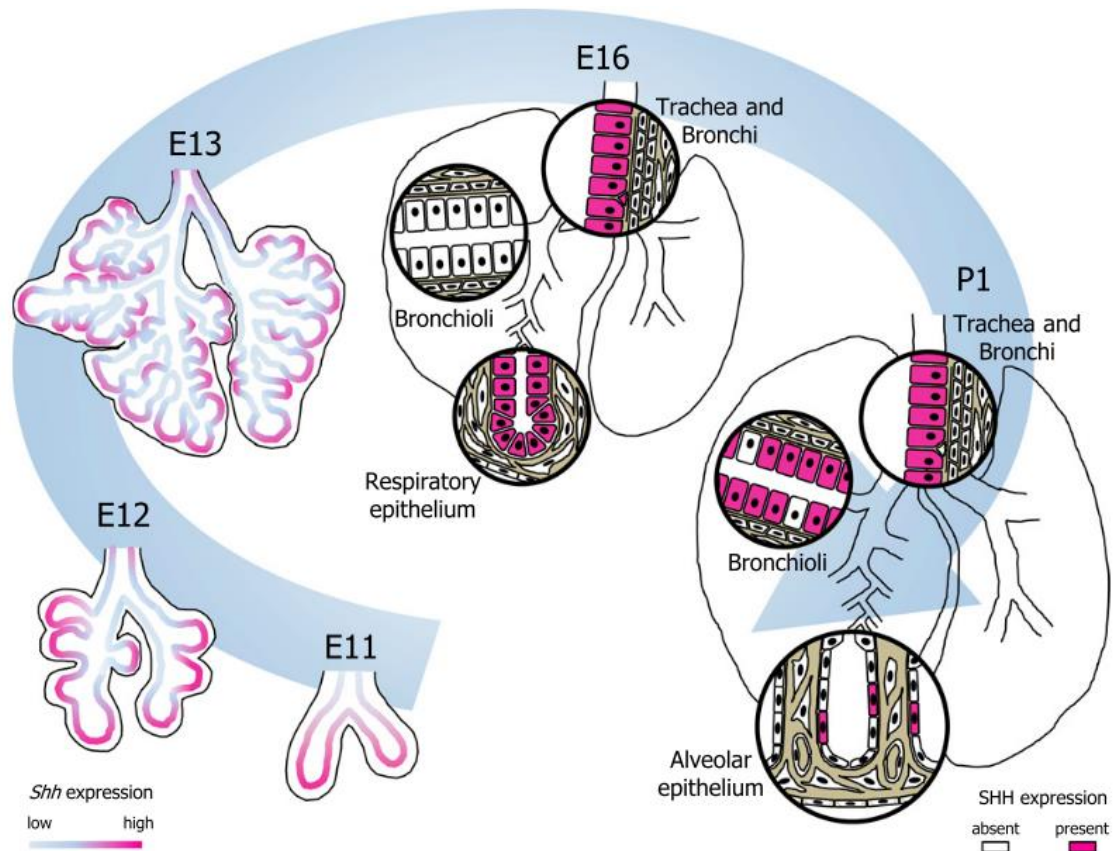


**Figure 31:** Epithelial Shh expression in the embryonic lung. From Kugler et al., 2015.

### Hedgehog signaling at homeostasis

Contrary to the extensive characterization that has been done for HH signaling in the primary cilium, the role of the HH pathway in motile cilia had not been described until recently. Mao et al. reported the expression of *SHH*, *SMO*, *SUFU*, *GLI2* and *GLI3* in fully differentiated bronchial airway epithelia cultured at ALI (Mao et al., 2018). *GLI1* was also detected, although at a very low level. At the protein level, SHH was detected in the apical pole of multiciliated cells, and in the apical and basolateral compartments. PTCH1, *SUFU*, *SMO*, *GLI2* and *GLI3* were localized in the cilia of multiciliated cells exclusively. Pharmacological activation and repression of HH did not result in an alteration in the activity of the GLI transcription factors, which led the authors to hypothesize that a non-canonical HH signaling was involved in motile cilia (Mao et al., 2018).

In nasal cultures derived from healthy subjects, PTCH1 and *SMO* were labeled in the cilia of multiciliated cells, and *GLI2* in the cilia but also the nucleus of MCCs. *GLI1* and *GLI3* were localized in the nucleus and apical region of MCCs. In COPD, *SMO* was not detected, *GLI3* detection was weaker and *GLI2* expression in the nucleus and cilia was lost, indicating an altered HH pathway in COPD (Belgacemi et

al., 2020). Indeed, the signaling pathway, normally quiescent in adults tissues, is reactivated in COPD (Cai et al., 2023). Cai and colleagues demonstrated the involvement of SHH signaling basal cell to ionocyte differentiation. Interestingly, the inhibition of SHH in fully differentiated healthy epithelia resulted in a significant decrease in the number of ionocytes and multiciliated cells, and in goblet cell hyperplasia (Cai et al., 2023), demonstrating a role for HH in the maintenance of mature epithelial cell types and the regulation of mucociliary clearance by controlling the balance between MCCs and goblet cells.

### Involvement of Hedgehog in multiciliogenesis

Previous work in the laboratory has shown that Notch and BMP signaling play a key role during multiciliogenesis (Cibois et al., 2015; Marcet, Chevalier, Coraux, et al., 2011; Marcet, Chevalier, Luxardi, et al., 2011). These two pathways can interact with the Hedgehog pathway to control a wide variety of processes during development or tumorigenesis (Gorojankina, 2016). In vertebrates, HH signaling is well described as contributing to primary cilium formation (Ruat et al., 2012), while its role in centriolar amplification and multiciliogenesis remains unexplored. Belgacemi et al. reported, in differentiating nasal airway epithelium cultured at ALI, the expression of *SMO*, *PTCH1*, *GLI2* and *GLI3*, which increased as differentiation progressed. In particular, protein expression of *GLI2* increased during differentiation, and preceded *FOXJ1*, indicating early involvement of the HH pathway in multiciliogenesis. Indeed, multiciliogenesis was affected by SHH inhibition, with an overall reduction in *FOXJ1* expression.

### Cellular trajectories

As seen in the chapter [IA1 Composition](#), the airway epithelium hosts both stem cell and terminally differentiated cells. In particular, basal cells can give rise to all surface airway epithelial cells. **Figure 32** recapitulates the main cell trajectories.

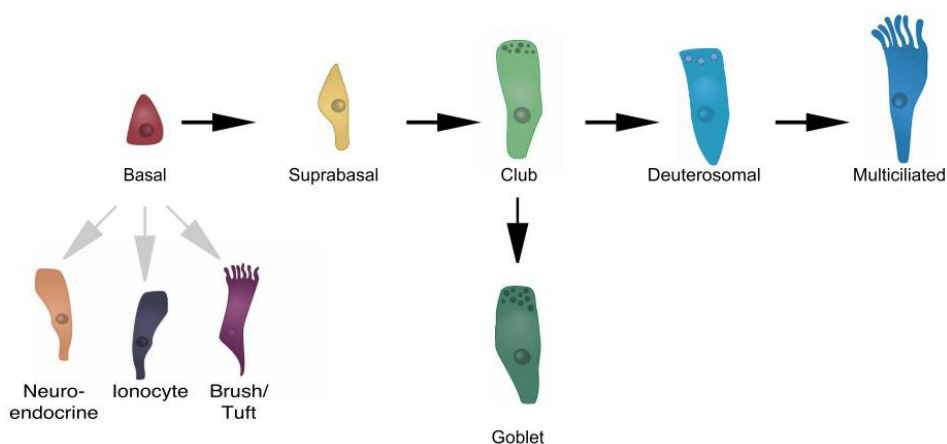


**Figure 32:** Epithelial cell trajectories.  
Adapted from Deprez et al., 2020.

## 5. Models for studying the airway epithelium regeneration

### Animal models

#### Mouse injury repair models

The airway epithelium is quiescent at homeostasis. Injury triggers a rapid repair response that can be used to study regeneration mechanisms (Konkimalla et al., 2022).

**Naphthalene injury:** Naphthalene is used to selectively ablates club cells, that convert naphthalene into a toxic product due to their expression of the Cyp2f2 enzyme. This model allows for the study of regenerative processes, including the proliferation and differentiation of remaining epithelial cells and led to the discovery of naphthalene-resistant variant club cells (Herriges & Morrissey, 2014).

**Sulfur Dioxide (SO<sub>2</sub>) inhalation:** SO<sub>2</sub> causes epithelial sloughing, exposing the remaining basal layer and is used to study the regeneration and repair mechanisms of the basal stem cells (**Fig.33**) (Pardo-Saganta, Law, et al., 2015).

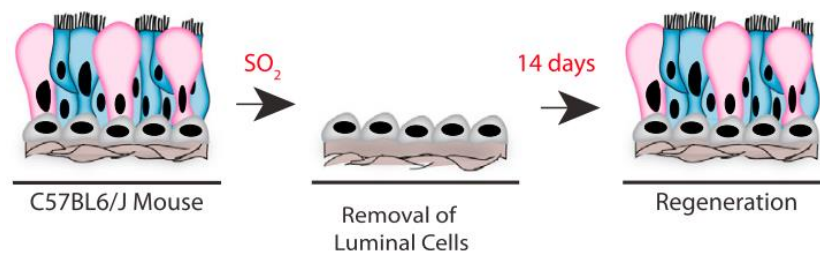


**Figure 33:** SO<sub>2</sub> injury model.  
From Pardo Saganta et al., 2015.

#### Xenopus

The large size, transparency and mucociliary epidermis of the *Xenopus* embryo makes it a good model organism to study multiciliogenesis and mucociliary development. Although multiciliogenesis processes are highly conserved across species, some differences, such as multiciliated cell intercalation, exist between species (**Fig.34**) (Walentek, 2018).

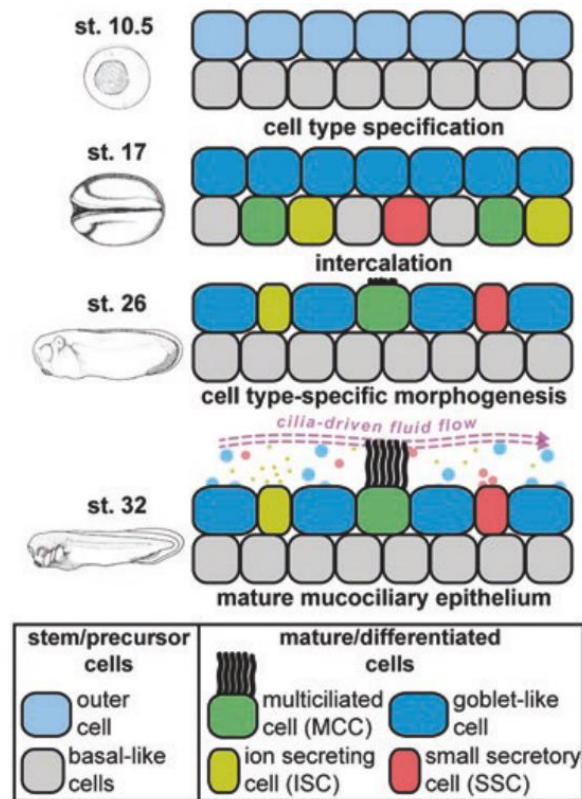


**Figure 34:** Xenopus mucociliary epithelium maturation. From Walentek, 2018.

## In vitro cultures

### Air-liquid interface culture

The mechanisms regulating epithelial regeneration from basal cells have been extensively documented *in vivo* in mice, and *in vitro* in humans using the 3D Air-Liquid Interface (ALI) culture model, which allows the reconstruction of a 3D epithelium that mimics *in vivo* cell composition (Gras et al., 2013). In the ALI model, basal cells are seeded on permeable inserts immersed in a proliferation medium. At confluence, the basal compartment medium is replaced by a differentiation medium, and the apical compartment is left without medium, in contact with air. This protocol allows basal cells to differentiate into a polarized, pseudostratified epithelium composed of the main airway epithelial cell types (**Fig.35**) (Redman et al., 2024). For human cultures, primary basal cells obtained from nose, trachea or bronchi sampled by brushing, biopsy or dissection can be used although for a limited number of passages. For convenience, a few immortalized cell lines were developed, such as the BCI NS-1.1 cell line (BCi), which was obtained from bronchial epithelial basal cells of a healthy non-smoking donor and transduced by a retrovirus expressing human telomerase (hTERT) (Walters et al., 2013).

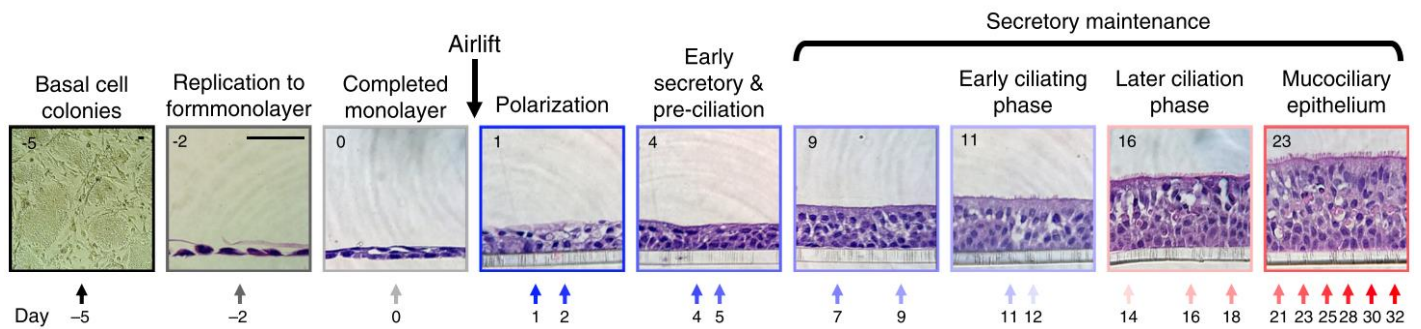


**Figure 35:** Epithelium culture at the Air-Liquid Interface.  
From Goldfarbmuren et al., 2020.

## Organoids

Organoids are spherical structures grown from stem or progenitor cells in a three-dimensional matrix, often in a Matrigel. They are especially useful for high-throughput drug screening, toxicity testing and stem cell lineage and developmental analyses but their variability in shape and size make them less appropriate for quantitative analyses (Lee et al., 2024; Lim et al., 2023).

## Bronchi on chip

Culture of airway cells on microfluidic chips is a novel culture system that allows the reproduction of a more physiological environment, with breathing-like stimuli such as airflow, mechanical stretch and perfusion, which seems to improve mucociliary clearance (**Fig.36**) (Nawroth et al., 2023) and trigger glycocalyx formation (S. Park et al., 2023). Gao and colleagues designed a tubular model that mimics the bronchiolar and alveolar duct environment (Gao et al., 2023).

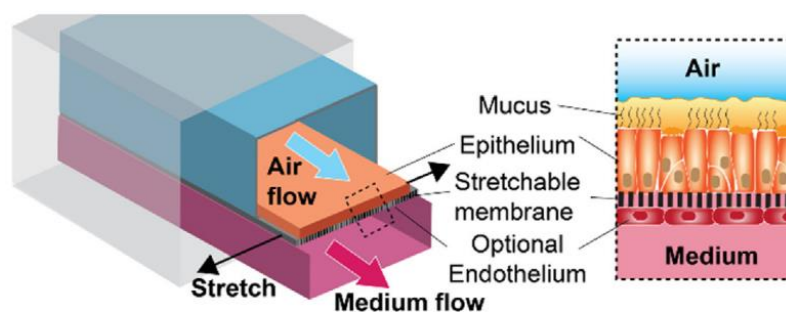


**Figure 36:** Bronchi on a chip model.  
From Nawroth et al., 2023.

## B. Asthma

### 1. Definition and clinical features

Asthma is a chronic respiratory and inflammatory disease affecting millions of people worldwide, with prevalence rates reaching up to 29 % of the population in some region. Asthma is strongly associated with genetics. It is estimated that genetics account for 60-70% of asthma susceptibility (Sayers et al., 2024). Genome-wide association studies (GWAS) have identified strongly regulated susceptibility genes such as *IL1RL1*, *IL33*, *TSLP*, *CDHR3* and *HLA*- (Stikker et al., 2023). People suffering from asthma experience wheezing, shortness of breath, limited expiratory airflow and chest tightness. The main feature of asthma is a narrowing of the lumen of the airways, due to mucus hypersecretion and thickening of the smooth muscle wall surrounding the bronchi (GINA, 2024; Woodruff et al., 2004). This narrowing is the result of strong airway remodeling, that might be the result of a defective regeneration due to chronic inflammation (Gras et al., 2011). Airway remodeling will be described in more detail below, in section [Remodeling in asthma](#).

Another key feature of asthma is airway hyperresponsiveness, an excessive sensibility of the airways to various stimuli, including allergens (such as pollen, dander, house dust mite...), infections (caused by virus, bacteria, fungi...), irritants (such as pollution, cigarette smoke, chemicals...) or other non-specific factors such as cold air or exercise. Triggering of the airways leads to exacerbations, also called asthma attacks. Exacerbations are acute episodes of sudden worsening of asthma symptoms, accompanied by bronchospasms (uncontrolled tightening of the smooth muscle surrounding the airways) and increased mucus production. This leads to moderate to severe airflow obstruction that can, in most cases, be spontaneously reversed or managed with bronchodilators ( $\beta$ -agonists) or inhaled corticosteroids. In severe cases, these attacks can be fatal. Symptoms can vary in intensity over time, either spontaneously or with treatment. Patients can go months without symptoms, or, on the contrary, they can suffer from periods of increased exacerbation rate (GINA, 2024; Papi et al., 2018).

### 2. Classification

The heterogeneity of asthma can make diagnosis difficult as no gold standard exists, and not all patients will present the same symptoms or the same form of asthma. Multiple subtypes of asthma have been proposed, based on the immune profile of the patient or the age of appearance of the symptoms (GINA, 2024; Hammad & Lambrecht, 2021; Papi et al., 2018).

Historically, asthma was split into two categories, allergic and non-allergic asthma. Allergic asthma is caused by allergen sensitization, or atopy, which predisposes a patient to develop asthma symptoms

when in contact with the allergen. The atopic status can be assessed by serum levels of immunoglobulin E (IgE). Allergic asthma is associated with eosinophil infiltration. The onset of this type is usually early, in childhood, but symptoms can also appear later in life with the encounter of a new allergen (Hammad & Lambrecht, 2021; Robinson et al., 2017). Non-allergic, or extrinsic, asthma, is usually late onset, is more preponderant in females and obese patients. Despite the lack of specific IgE, this type shares a lot of clinical features with allergic asthma, including an increase in T helper type 2 (Th2) cells. This categorization is now considered to be an oversimplification of asthma (Barnes, 2009; Hammad & Lambrecht, 2021; Robinson et al., 2017).

Since then, classification has evolved to divide asthma into endotypes, defined by pathophysiological mechanisms that are easier to correlate to treatment response. They are mainly based on the cytokine profile of the patient (type Th2-high and Th2-low) (**Fig.37**), and can be further divided into different phenotypes depending on the onset of the disease, the immune profile and other criteria (Hammad & Lambrecht, 2021).

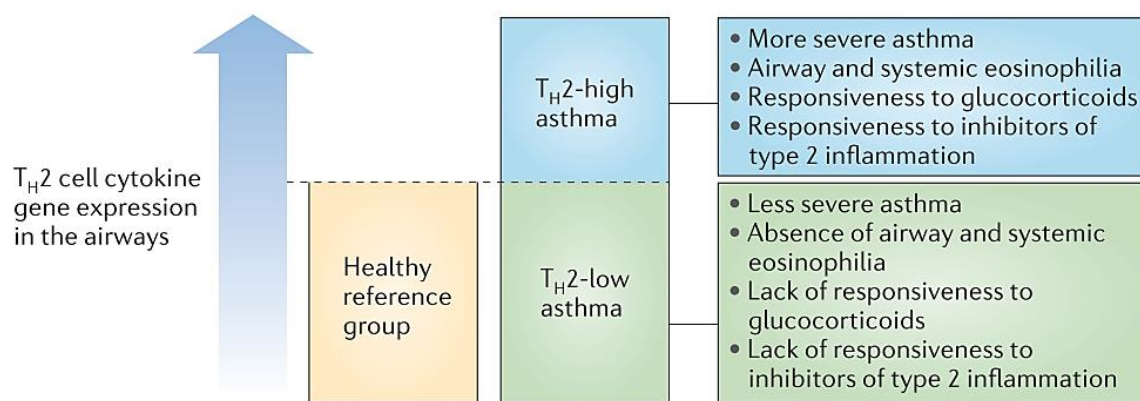


**Figure 37:** Type 2 asthma classification.  
From Fahy, 2015.

## Type 2-high

Type 2-high asthma is the most prevalent type. It is characterized by the presence of Th2-associated cytokines such as IL-4, IL-5 and IL-13, and cells such as eosinophils. It includes allergic forms of asthma that can appear before (early onset) or after (late onset) 12 years of age, the late onset being associated with more severe forms of asthma (Hammad & Lambrecht, 2021). In a transcriptomic study of sputum from asthmatic patients, an ultra-high type 2 with strong expression of all Th2 network genes was found in a subgroup of older patients with increased airflow obstruction (Peters et al., 2019).

## Type 2-low

Type 2-low asthma is more complex to define as it has no specific biomarkers. Thus, it groups all types of asthma that are not Type 2 high and non-eosinophilic. This type is less common and includes

endotypes that are late onset, linked to obesity or smoking and that are refractory to corticoid treatment (Hammad & Lambrecht, 2021).

## Severe asthma

Asthma severity is defined by how well a patient's asthma responds to conventional therapies. In severe asthma, symptoms remain uncontrolled despite optimized treatment (GINA, 2024). An estimated 5 to 10% of adults with asthma have severe asthma and suffer from debilitating and persistent symptoms (K. F. Chung et al., 2014; B. Thomas et al., 2010).

# 3. Pathophysiology

## Inflammation

Chronic inflammation is the main driver of asthma and leads to strong remodeling of the immune, smooth muscle and epithelial compartments, causing the narrowing of the airways. As type-2 high is the most prevalent form of asthma and that my work is centered around it, it will focus on this type for the rest of the manuscript. In asthma, the Th2 inflammatory cascade starts when an insult (dust, pollen, dander, virus, bacteria or mites such as *Dermatophagoides pteronyssinus* or *Dermatophagoides farinae*) reaches the airways and enters in contact with the epithelium (**Fig.38**). Epithelial cells are the main conductor of asthma pathogenesis by triggering the inflammatory response. They recognize pathogen-associated molecular patterns (PAMPs) and damage-associated molecular patterns (DAMPs) through pattern-recognition receptors (PRRs) such as toll-like receptors (TLRs) or protease-activated receptors. In response, epithelial cells produce alarmins such as TSLP, CXCL8, IL-1 $\beta$ , IL-6, IL-25 and IL-33 to alert and activate the immune system, in particular dendritic cells, group 2 innate lymphoid cells (ILC2), mast cells and basophils (Hammad & Lambrecht, 2021; Robinson et al., 2017). TSLP binds to its receptor TSLPR on dendritic cells, which migrate to the draining lymph node to activate naïve CD4+ T cells through OX40. These naïve CD4+ T cells then become T helper 2 (Th2) cells once in the blood circulation (Fahy, 2015). Th2 cells play a major part in asthma pathogenesis by secreting the pro-inflammatory cytokine interleukin-13 (IL-13), which triggers goblet cells hyperplasia and mucus hypersecretion (Guseh et al., 2009; Hammad & Lambrecht, 2021; León, 2023). Maturing Th cells also activate B cells to become antigen specific IgE-producing plasma cells. IgEs coat mast cells and basophils and act as receptors for antigens. The mast cells and basophils are activated upon binding of a pathogenic molecule to two adjacent IgEs. This activation triggers the release of allergic mediators through degranulation such as histamine, a contractile agonist that causes smooth muscle cells (SMCs) to contract (Fahy, 2015; Gour & Wills-Karp, 2015; Hammad & Lambrecht, 2021). Mast cells, basophils



and ILC2s also produce IL-13, increasing the pro-inflammatory response (Barlow & McKenzie, 2014; Hammad & Lambrecht, 2021). The role of IL13 will be described in more detail in section [Interleukin-13](#).

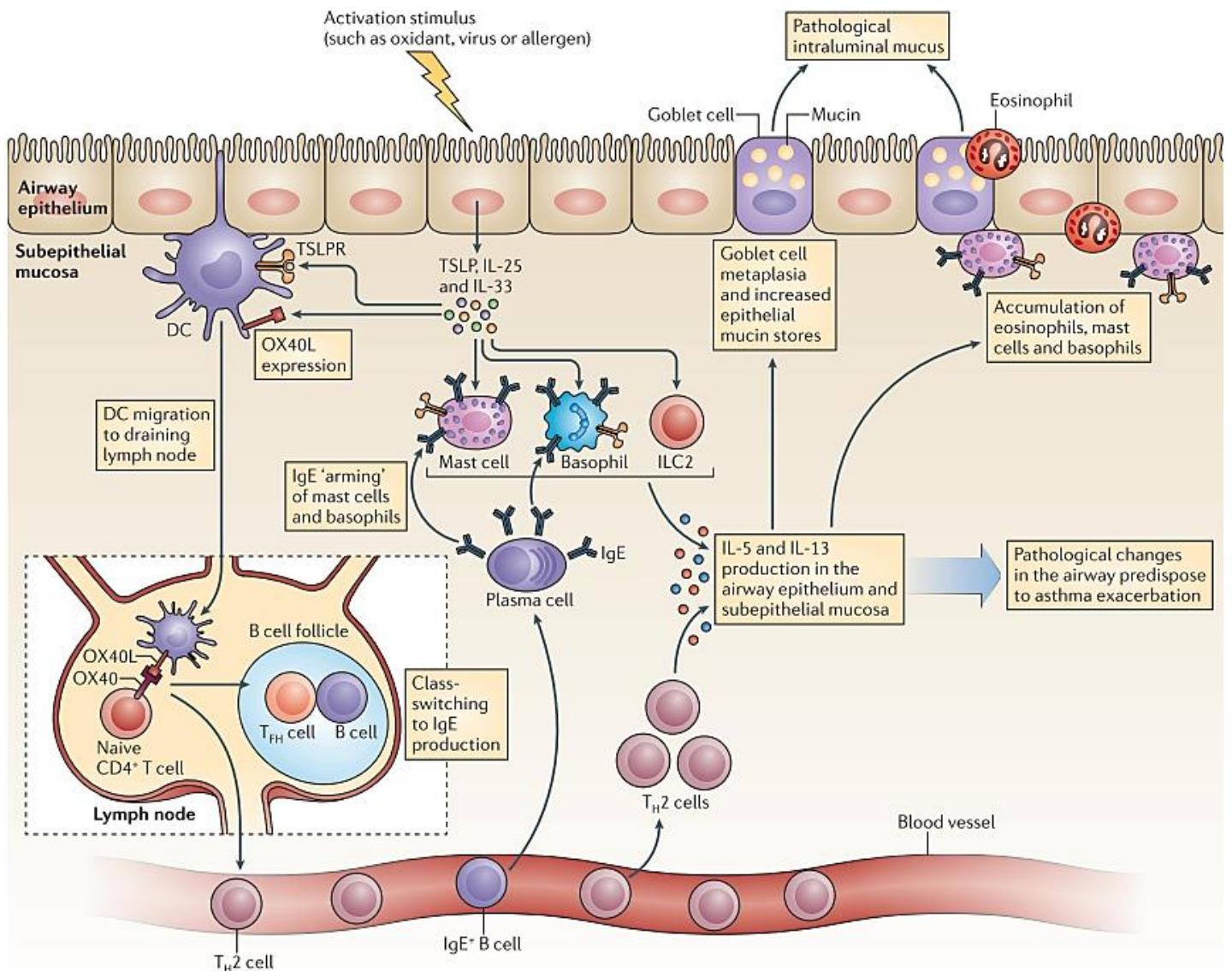


**Figure 38:** Asthma signaling pathway. From Fahy, 2015.

## Remodeling in asthma

In addition to immune cell recruitment described above, remodeling in asthma affects the airway walls (**Fig.39**). Hyperplasia of the smooth muscle cell layer reduces lumen diameter and airflow. The volume of the muscle layer is 83% greater in asthma patients than in healthy subjects (Woodruff et al., 2004). Asthma is accompanied by sub-epithelial fibrosis. The extracellular matrix is thickened due to an increased deposition of extracellular matrix (ECM) proteins such as collagen type I, III, V and fibronectin, contributing to the narrowing of the lumen (Gras et al., 2011).

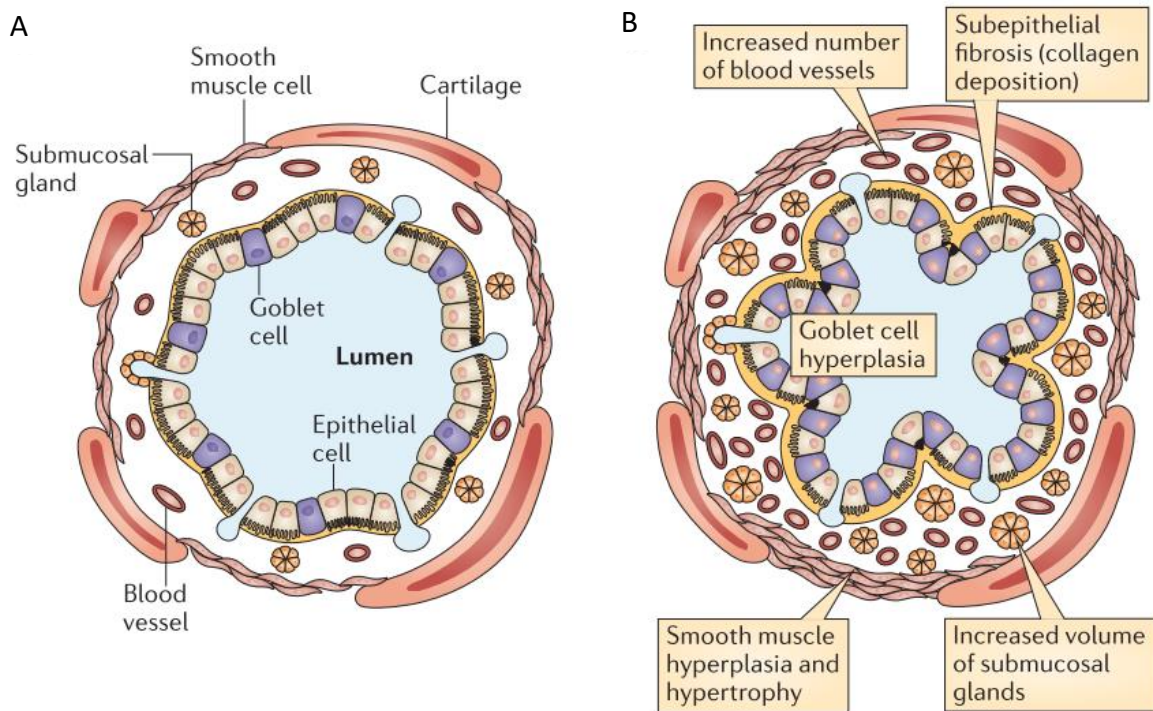


**Figure 39:** Airway wall remodeling in asthma.  
**A:** Healthy airway wall. **B:** Remodeled airway wall.  
 From Fahy, 2015.

### Epithelial remodeling in asthma

This study is centered around understanding the molecular and cellular mechanisms responsible for epithelial remodeling in asthma, therefore this section will focus on the epithelial compartment.

Epithelial remodeling in asthma is characterized by goblet cells hyperplasia accompanied by mucus hypersecretion (**Fig.39B & Fig.40**) and by a decrease in multiciliated cell number, leading to a mucociliary clearance defect that can severely affect patients' health. Indeed, marked goblet cell hyperplasia was found in the lungs of patients who died from severe asthma attack. Their airways presented a 30-fold increase in goblet cells compared to patients who did not die from acute asthma attack (Aikawa et al., 1992). Moreover, the volume of submucosal glands was also increased in fatal asthma lungs (Carroll et al., 1996). Autopsy of asthma patients who did not die from an asthma attack revealed the presence of mucus plugs in the bronchioles, obstructing partially the lumen (Saetta et al., 1991).

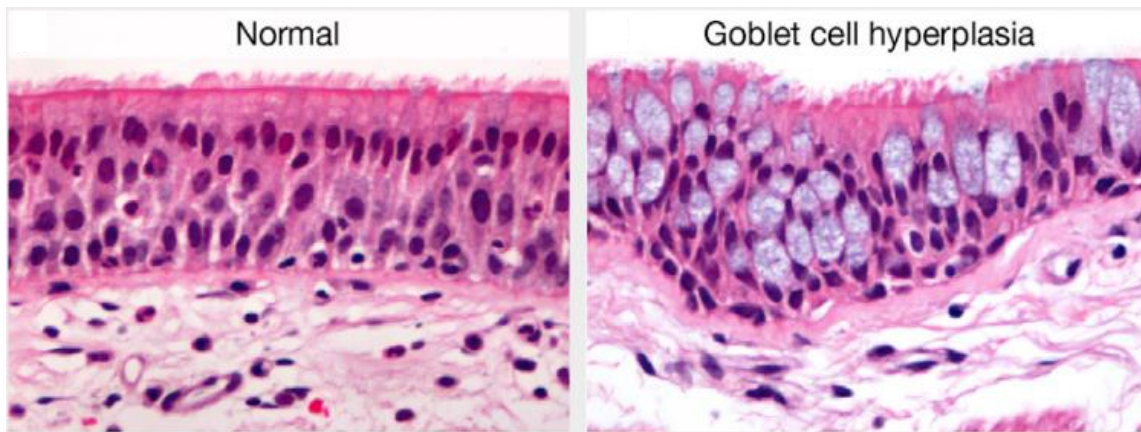


**Figure 40:** Comparison between a normal epithelium and a goblet hyperplasia.  
From Hogan et al., 2014.

Using bronchial brushes from healthy donors and donors with mild and severe asthma, Thomas and colleagues demonstrated that patients with asthma had a reduced number of multiciliated cells. These cells exhibited a lower beat frequency and increased ciliary disorientation compared to cells from healthy samples. Furthermore, these defects were more pronounced with increasing disease severity (B. Thomas et al., 2010). Similarly, in a cellular atlas of healthy and asthma lungs, the proportion of multiciliated cells was lower in the asthma condition than in the healthy one (Vieira Braga et al., 2019).

Epithelial remodeling was also reported in *in vitro* cultures of bronchial cells from pediatric asthma patients. The cultures presented an increased number of goblet cells and lower number of multiciliated cells, indicating that this remodeling is not age-dependent (J. Parker et al., 2010).

Additionally, loss of epithelial integrity is another important feature of asthma. Mis-localization or loss of tight junction proteins occludin and ZO-1 and intermediate junction protein E-cadherin have been observed in bronchial biopsies and cell cultures from asthma patients, and in murine models of asthma (T. L. Hackett et al., 2013; Tan et al., 2019; B. Thomas et al., 2010; Xiao et al., 2011). Asthma patient-derived cells cultures presenting defective epithelial junctions has elevated levels of TSLP and IL-33 (T. L. Hackett et al., 2013). In mice, conditional loss of E-cadherin in lung epithelial cells at birth resulted in progressive epithelial damage that mimicked asthma phenotype such as decrease in ZO-1 expression, loss of multiciliated cells, goblet cell hyperplasia and inflammation (Post et al., 2018).

### B-catenin and remodeling

Most importantly, loss of cell junctions does not only increase the risk of infection and inflammation by reducing epithelial barrier integrity, there is also evidence that it influences cell fate. Decrease in E-cadherin levels has been associated with activation of Wnt/ $\beta$ -catenin signaling (T. L. Hackett et al., 2013). Destabilization of intermediate cell-cell junctions may free  $\beta$ -catenin proteins into the cytoplasm, allowing them to activate the Wnt/ $\beta$ -catenin signaling.

## 4. Interleukin-13

As seen in part [Inflammation](#), the cytokine interleukin-13 is a major mediator of type-2 high asthma. IL-13 is produced by Th2 cells, mast cells, basophils and ILC2s in response to an insult to the airways and results in goblet cell hyperplasia. Administration of IL-13 *in vivo* (Grünig et al., 1998; Kuperman et al., 2002; Wills-Karp et al., 1998), or *in vitro* (Atherton et al., 2003; Jackson et al., 2020) is sufficient to reproduce asthma-like remodeling.

IL-13 shares a receptor with IL-4, another type 2 inflammatory cytokine. They are both encoded in the same genomic locus called the sTh2 cytokine locus, located on chromosome 5 in humans and in chromosome 11 in mice (Gour & Wills-Karp, 2015; Junntila, 2018). IL-13 and IL-4 have many overlapping roles in promoting Th2 immune responses and allergic inflammation, or inducing goblet cell hyperplasia *in vivo* (Dabbagh et al., 1999) and *in vitro* (Atherton et al., 2003). However, only IL-4 is essential in the initiation of an allergen sensitization, due to its ability to promote Th2 development and IgE production (Kopf et al., 1993). On the other hand, IL-13 is responsible for allergen-induced airway hyperresponsiveness, as blocking IL-4 during an antigen challenge does not fully resolve the allergic response but blocking IL-13 does (Gavett et al., 1997; Wills-Karp et al., 1998).

### Signaling pathway

IL-13 can bind to the type II IL-4 receptor IL-13R $\alpha$ 1, shared with IL-4 (**Fig.41**). This receptor is mainly expressed by non-hematopoietic cells such as epithelial cells. Once IL-13 has bound to IL-13R $\alpha$ 1, the newly formed complex recruits IL-4 $\alpha$  to form the complete receptor complex. The binding of the two subunits of the complex triggers the activation of Janus kinase 1 (JAK1; constitutively associated with IL-4R $\alpha$ ) and tyrosine kinase 2 (TYK2; constitutively associated with IL-13R $\alpha$ 1). JAK1 and TYK2 then phosphorylate IL-4R $\alpha$ , which in turns activates STAT6. Activated STAT6 homodimerize and translocate to the nucleus to activate the expression of IL-13-target genes (Junntila, 2018; Shankar et al., 2022). IL-13 can bind to IL-13R $\alpha$ 2, another receptor, with higher affinity (**Fig.41**). The role of IL-13R $\alpha$ 2 is unclear and it is considered as a putative decoy receptor with potential signaling activity (Junntila, 2018).

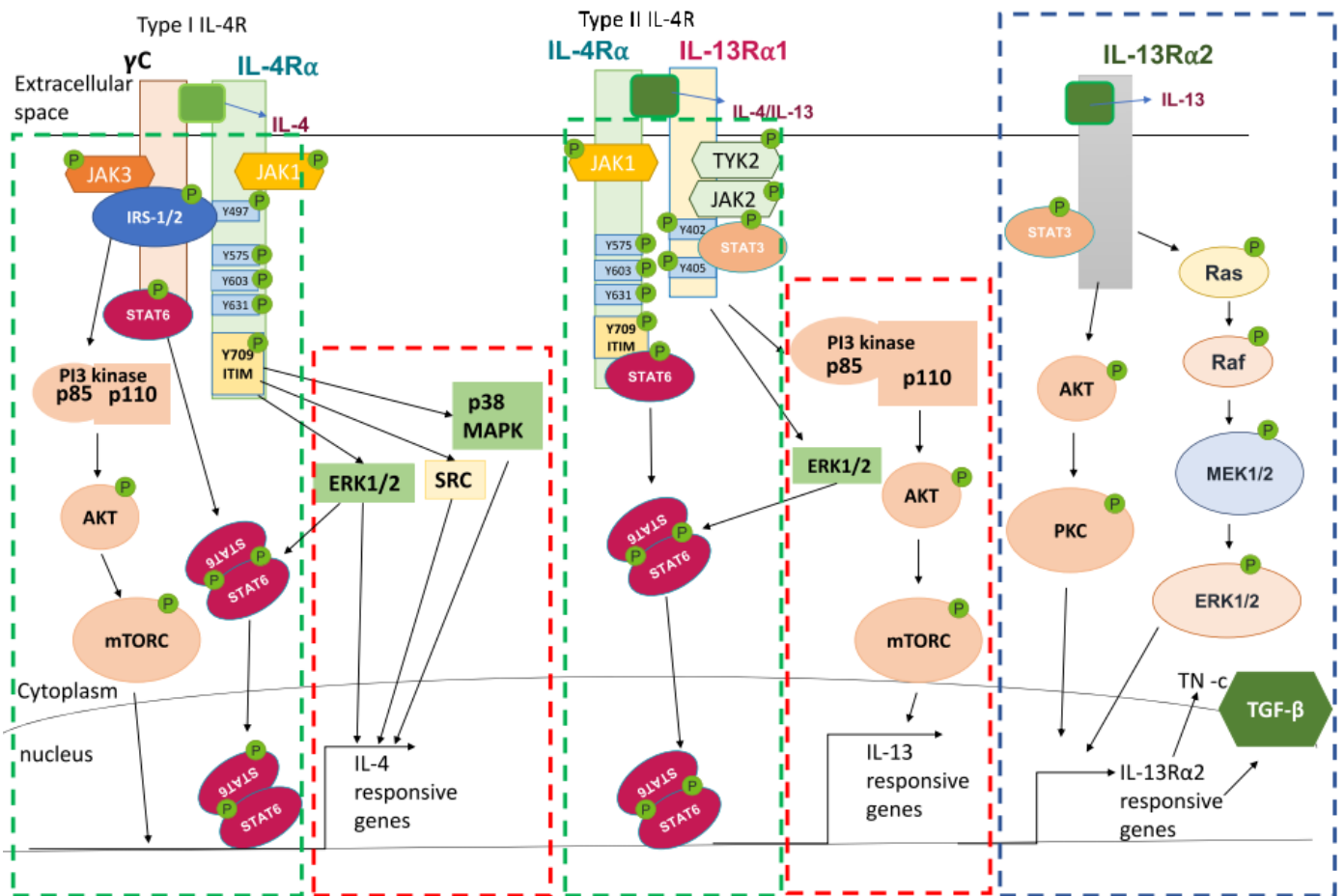


**Figure 41:** IL-4 and IL-13 signaling pathways. From Shankar et al., 2022.

## IL-13 in vitro

Chronic expression of IL-13 in murine lungs leads to inflammation, airway hyperresponsiveness and excessive mucus production (Kuperman et al., 2002). IL-13 treatment on healthy epithelial cell cultures is used to mimic *in vitro* the inflammatory remodeling seen in asthma and is a useful tool to investigate the epithelial response and the signaling pathways behind the disease. IL-13 treatment induces a strong transcriptional response in epithelial cells with pro-inflammatory expression programs including genes such as *ALOX15* and *CCL26*, *MUC5AC*, *HLA* genes, and others such as *POSTN*, *FETUB*, *STATH* (Giovannini-Chami et al., 2012; Jackson et al., 2020; Koh et al., 2023; McCauley et al., 2024; Zhen et al., 2007).

## Effect of IL-13 on goblet cells

Increase in SPDEF and *MUC5AC* expressions illustrates the induction of goblet cell hyperplasia and mucus hypersecretion following IL-13 treatment (Jackson et al., 2020; Laoukili et al., 2001; J. C. Parker et al., 2013; Zhen et al., 2007). Single-cell RNA sequencing provides a more precise appreciation of the remodeling of secretory or goblet cells (Jackson et al., 2020). In a recent study on primary human epithelial cell ALI cultures, the goblet cell population increased 36-fold after two weeks of treatment,

at the expense of club cells (McCauley et al., 2024). The goblet-specific transcription factors *SPDEF* and *FOXA3* are induced by IL-13 (Chen et al., 2009; Jackson et al., 2020; Zhen et al., 2007). Koh and colleagues identified an IL-13-responsive *SPDEF* promoter in humans and proposed a model where STAT6 activation by IL-13 triggers the recruitment of KLF5, which then mediates H3K27 acetylation to activate the *SPDEF* promoter (Koh et al., 2023). *SPDEF* positively regulates *FOXA3* and *MUC5AC*, while negatively regulating *MUC5B* and the club cell transcription factor *FOXA2* (Chen et al., 2009; Jackson et al., 2020; Koh et al., 2023). *FOXA2* promotes the expression of the club marker *SCGB1A1* (Bingle & Gitlin, 1993). In agreement with this, expression of *SCGB1A1* is decreased in IL-13 treated epithelia (Jackson et al., 2020). This regulatory switch from *FOXA2* to *FOXA3* could explain the transition from club to goblet cell upon IL-13 treatment.

### Effect of IL-13 on multiciliated cells

Human airway epithelial cells cultivated with IL-13 exhibit reduced number of multiciliated cells (Gerovac & Fregien, 2016; Gomperts et al., 2007; J. Parker et al., 2010). IL-13-treated multiciliated cells show a decrease in the number of cilia per cell, mislocalization of their basal bodies and altered ciliary beating (Gomperts et al., 2007; Jackson et al., 2020; Laoukili et al., 2001). IL-13 inhibits the differentiation of multiciliated cells through the repression of the transcription factor *FOXJ1*, directly by the putative interaction of STAT6 with a STAT-binding element located in the promoter of *FOXJ1* (Gomperts et al., 2007), and indirectly by repressing *MCIDAS*, which is a positive regulator of *FOXJ1* (Gerovac & Fregien, 2016; Stubbs et al., 2012). At the transcriptomic level, IL-13 treated multiciliated cells exhibit downregulation of cilium-assembly and microtubule motor activity signatures (Jackson et al., 2020).

## 5. Rhinovirus

Viral infections are known triggers of wheezing and asthma exacerbations (GINA, 2024). In particular, rhinovirus infections, responsible for the common cold (Rollinger & Schmidtke, 2011), are the first cause of exacerbation among children (Coleman et al., 2015) and adults (Gern, 2015) suffering from asthma. Different strains of rhinovirus infect cells through specific cell types. The majority of rhinovirus type A (RVA) and B (RVB) use ICAM1, which is mostly expressed by endothelial cells and macrophages. Other RVA types bind to low-density lipoprotein receptor family members (LDLR), most widespread in epithelial cells. RVC types bind to CDHR3, present on multiciliated cells (Basnet et al., 2019).

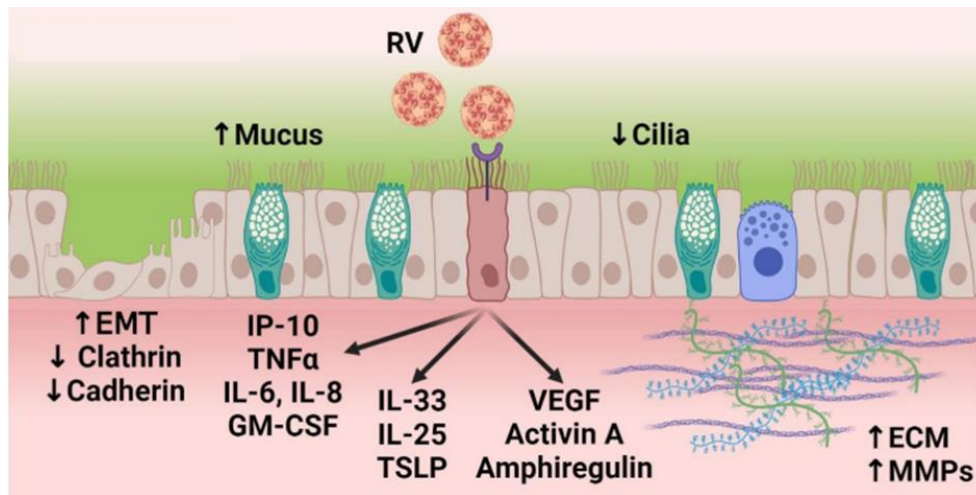


**Figure 42:** Rhinovirus signaling in the airway epithelium. Rhinoviruses use ICAM1 as entry factors, as depicted here by the purple symbol on multiciliated cells. From Spector et al., 2023.

*In vitro* studies of rhinovirus infection on primary epithelial cells have been extensively done as the respiratory epithelium is the primary target of rhinovirus infection (Spector et al., 2023). Rhinovirus infection triggers PRR activation, which leads to the type 2 immune response with production of interferons and alarmins such as chemoattractant C-X-C motif genes, C-C chemokine motif genes and TSLP by epithelial cells (**Fig.42**) (Bochkov et al., 2010; Jakiela et al., 2021; Spector et al., 2023). Upon infection, rhinoviruses can damage the epithelium due to their replication mechanism causing cell lysis (Gern, 2015). However, Warner and colleagues report no obvious damage in differentiated ALI culture, 6 days post infection (Warner et al., 2019). Rhinovirus infection of differentiated epithelial cells is associated with increased expression of the goblet cell genes *MUC5AC*, *MUC5B* and *SPDEF* and decrease in multiciliated-associated genes such as *FOXJ1* and *DNAI1*, although less pronounced than for IL-13 stimulation (Jakiela et al., 2014, 2021). Multiciliated cells are the target of rhinovirus infection (Jakiela et al., 2014; Warner et al., 2019), and the decrease in multiciliated cell markers after infection might be due in part to the death and extrusion of multiciliated cells. Rhinovirus also triggers ECM deposition in submerged epithelial cultures (Kuo et al., 2011) and disrupts the integrity of differentiated epithelial cells by reducing the expression of tight junction proteins claudin-1, occluding and ZO-1 (Gavala et al., 2011; Looi et al., 2018).

## 6. Treatments of asthma

As no definitive cure for asthma has been found yet, asthma treatments are focused on symptoms management. The Global Initiative for Asthma recommends the use, as-needed, of low-dose inhaled corticosteroids combined with a rapid-acting bronchodilator (ICS-formoterol) as a first line treatment. Alternatively, low dose of ICS with a short-acting beta2 agonist (SABA) can be used, even though the use of SABA has been associated with exacerbation in certain conditions (GINA, 2024). Oral

corticosteroids should only be used as a last-resort due to their side effects, but they are needed by ~30% of adults suffering from severe asthma (K. F. Chung et al., 2014).

## Biologics

In severe asthma, the addition of biologics targeting either IgE, IL-4 or IL-13 or IL-4R can help improve patients' quality of life (**Fig.43**).

- **Omalizumab** is a monoclonal antibody that inhibits the binding of IgE to its receptor on mast cells, basophils and dendritic cells. Treatment can reduce extracellular matrix remodeling and lower airway inflammation (Jesenak et al., 2023).
- **Dupilumab** is a monoclonal antibody raised against the  $\alpha$  chain present on type I and II IL-4 receptor complexes, effectively blocking IL-4 and IL-13 signaling. It has been shown to reduce the rate of asthma exacerbations (Varricchi et al., 2022).
- Anti-IL-13 monoclonal antibodies such as Anrukinzumab/IMA-638 (Gauvreau et al., 2012), Lebrikizumab (Austin et al., 2020), Tralokinumab (Russell et al., 2018), have had underwhelming effect on eosinophil count, airway hyperresponsiveness or asthma exacerbation.

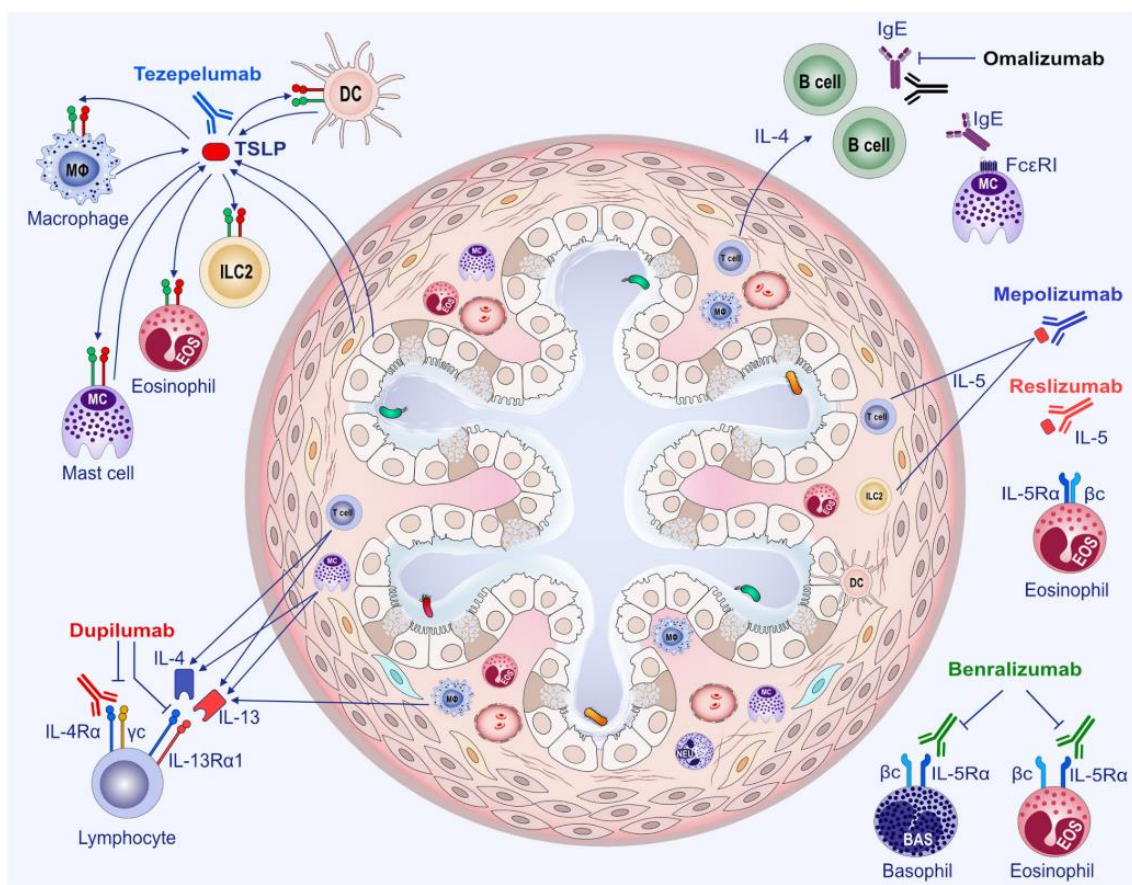


**Figure 43:** Monoclonal antibody treatments for asthma. From Varricchi et al., 2022.



## 7. Murine models of asthma

Mice models of asthma have been widely used to study the inflammation and airway hyperresponsiveness of asthma. The most common murine models of asthma are allergen-induced models. Mice must first be sensitized (introduced a first time) to an allergen to induce the production of allergen specific IgEs, then they can be challenged with the same allergen to trigger a reaction. Mouse strain and age, allergen type and dose, frequency, mean and duration of administration can be adapted based on the needs of the experiment. In particular, the duration of the challenge, can be adapted to mimic a more acute or chronic affection (Aun et al., 2018). Acute models of allergic airway inflammation (< 3 weeks) can present airway hyperresponsiveness and inflammation but typically do not manifest remodeling (Woo et al., 2018). Classically, ovalbumin (OVA) is used to induce a type 2 inflammation characterized by airway, eosinophilia and remodeling with increase collagen deposition, smooth muscle cell hyperplasia and mucus hypersecretion. This model however does not fully replicate the chronicity of asthma as airway hyperresponsiveness does not persist after arrest of chronic challenge (McMillan & Lloyd, 2004). Another commonly used allergen is house dust mite (HDM), which is a more clinically relevant allergen than OVA as OVA does not includes airway inflammation in humans (Aun et al., 2018).

## C. Cellular memory

Cells isolated from asthma patients and cultured *in vitro* in ALI retain specific disease characteristics, such as increased mucin and IL-8/CXCL8 secretion, asynchronous mitosis, impaired barrier function and elevated remodeling factors, even though basal cells isolated from tissue resections or nasal or bronchial brushings undergo several proliferation rounds before differentiation under standardized, non-inflammatory conditions (Freishtat et al., 2011; Gras et al., 2012; Lopez-Guisa et al., 2012). Ordovas-Montanes et al. have demonstrated that basal cells derived from nasal polyps of patients suffering from chronic rhinitis also retain a memory of inflammation (Ordovas-Montanes et al., 2018). These observations suggest that the information about epithelial defects and pathological remodeling associated with inflammatory diseases are preserved by basal cells and transmitted to their progeny.

## 1. Trained immunity

These inflammatory memory mechanisms have been described in the immune cells involved in innate immunity (monocytes/macrophages, NK cells, innate lymphoid cells). In contrast to adaptive immunity, which confers a specific response to each antigen, and a memory response enabling more efficient elimination of the same antigen on re-presentation, innate immunity can be triggered in a non-

pathogen-specific manner, and has been termed "trained immunity" (innate immune memory) or "tolerance" depending on whether the response to the second assault is respectively superior or inferior to that of the first (Netea et al., 2020). In non-immune cells, identifying this "memory" is still in its early stages. Stem cells in the intestinal epithelium, pancreas, or epidermis can develop a memory of inflammatory experiences, maintaining accessible chromatin at inflammation-activated loci long after the inflammation has resolved, and basal transcriptional levels have returned. These loci are reactivated during subsequent inflammatory episodes (Naik & Fuchs, 2022). Therefore, this cellular memory can have long-term beneficial or detrimental effects on the tissue by influencing epithelial stem cell responses (Gonzales et al., 2021).

Tolerance is an important mechanism preventing mucous membranes from systematically developing a large-scale immune response to each exposure to non-toxic foreign proteins (**Fig.44**). In non-immune cell types, identification of this memory is still in its infancy. Stem cells from intestinal epithelium, pancreatic epithelium and epidermis are able to develop a memory of their inflammatory experiences, maintaining accessible chromatin at inflammation-activated loci long after the inflammation has been resolved and returned to baseline transcriptional levels (Falvo et al., 2023). These loci are reactivated during a secondary assault (Naik et al., 2017; Naik & Fuchs, 2022). Thus, by influencing the responses of epithelial responses of epithelial stem cells, may have long-term beneficial or detrimental consequences for the tissue (Falvo et al., 2023; Gonzales et al., 2021). So far, trained immunity has been associated with epigenetics mechanisms.

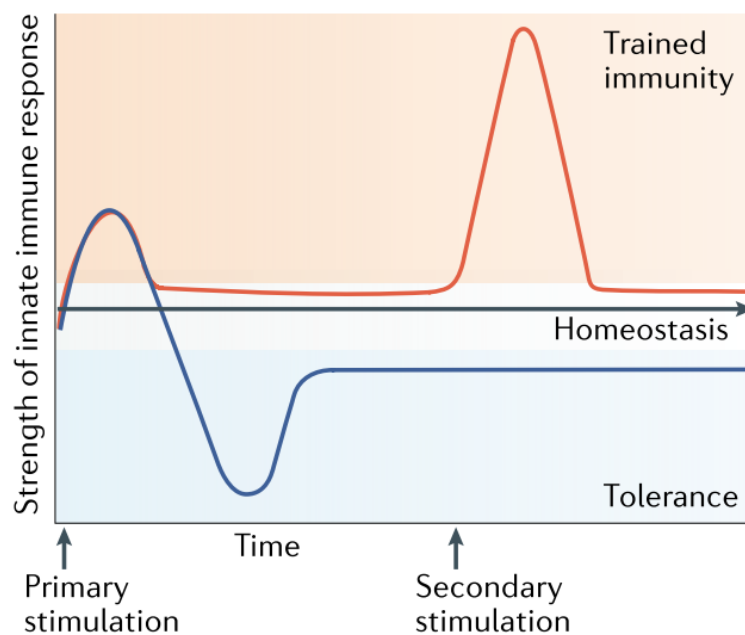


**Figure 44:** Trained immunity and tolerance.  
From Netea et al., 2020.

## 2. Epigenetics

Epigenetics is to nurture what genetics is to nature. Epigenetic marks are reversible and inheritable chemical modifications to chromatin that modulate gene expression (and thus the phenotype) without altering the genotype (**Fig.45**) (Allis & Jenuwein, 2016). Specifically, epigenetic marks explain how two cells from a same organism, such as a brain cell and a lung cell, can share the same genome while performing widely different functions. Changes in chromatin structure affect DNA transcription by altering the accessibility of DNA to the transcriptional machinery. Loosely packed euchromatin is generally associated with active transcription due to the presence of transcriptionally accessible regions of the genome, while condensed heterochromatin is associated with gene repression due to its inaccessibility (Allis & Jenuwein, 2016; Netea et al., 2020). Epigenetic marks include DNA methylation, histone modifications, chromatin remodeling, non-coding RNAs, and histone variants (**Fig.45**). The regulation and deposition of these marks are heavily influenced by the environment and allow cells to adapt to variable conditions (Allis & Jenuwein, 2016; Netea et al., 2020).

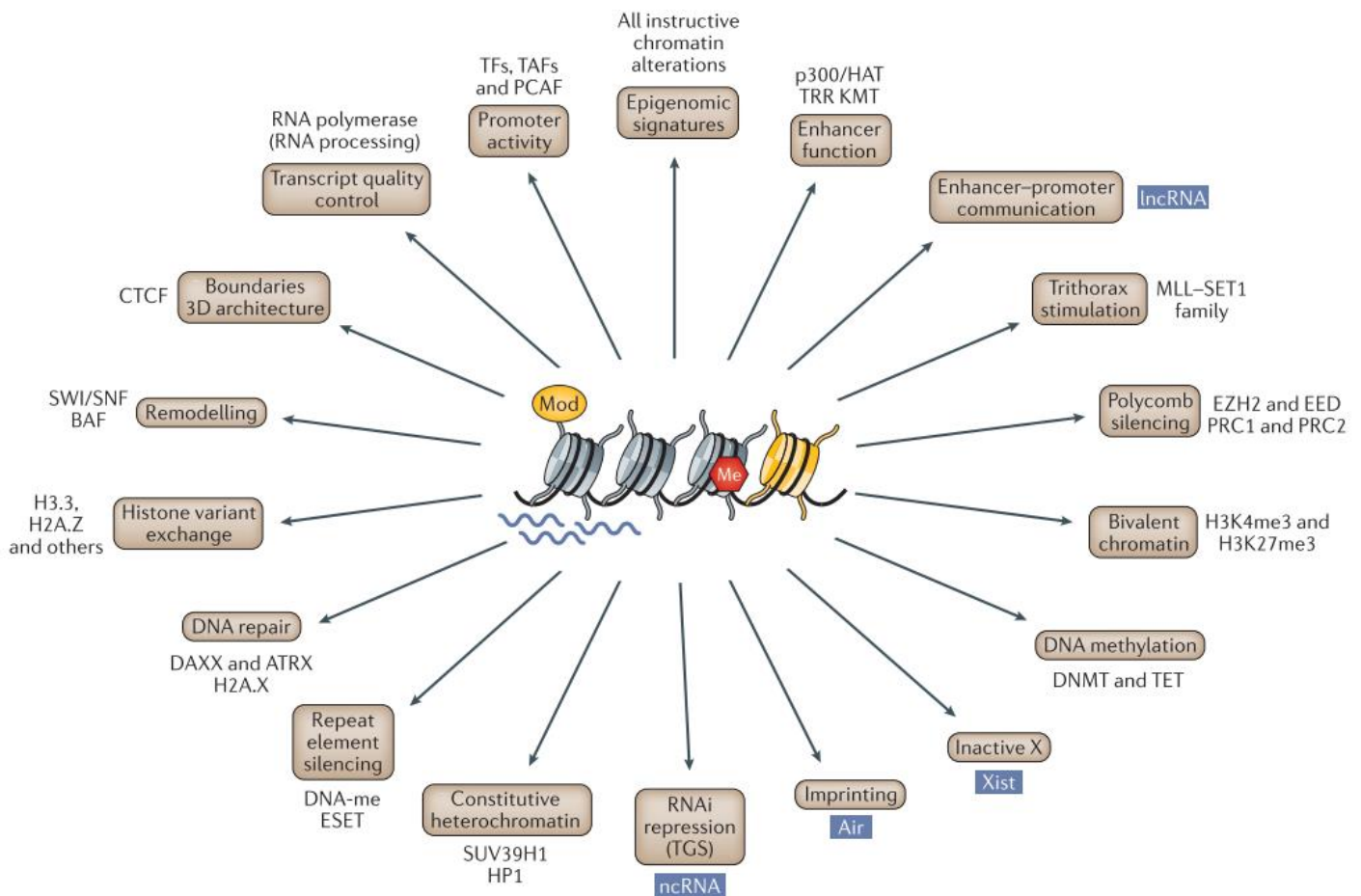


**Figure 45:** Chromatin-related epigenetic functions. From Allis and Jenuwein, 2016.

Trained immunity has been associated with key histone marks (**Fig.46**):

- 1) histone 3 lysine 27 trimethylation (H3K27me3), catalyzed by the polycomb group (PcG), is an abundant repressive mark associated with gene silencing (Piunti & Shilatifard, 2021),
- 2) histone 3 lysine 4 methylation (H3K4me1), deposited by the trithorax group (TrxG) at distal enhancers, associated with enhanced expression, and
- 3) histone 3 lysine 4 trimethylation (H3K4me3), also deposited by TrxG at the promoter of stimulated genes (Netea et al., 2020).

In the airway epithelium, the mechanisms behind this memory are yet to be identified. It is not understood how basal cells encode inflammation memory or how it is transmitted during cell divisions.

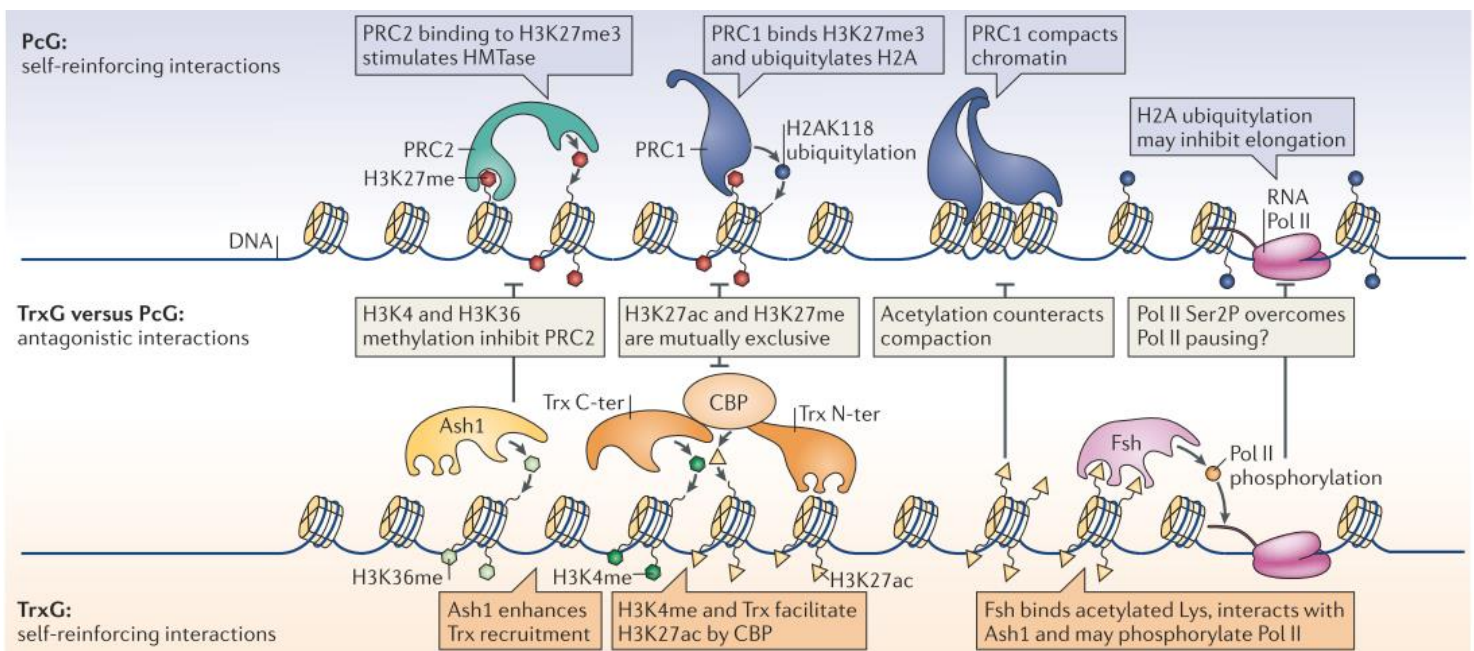


**Figure 46:** Polycomb and trithorax mechanisms.  
From Steffen and Ringrose, 2014.

# Chapter II. Results

## A. Single-cell Analysis of Human Airway Regeneration and Remodeling in Asthma

### Introduction

The study presented here was a continuation of the previous work of my team. My team is a leading team in pulmonary transcriptomic research and is the only French team to be part of the Human Cell Atlas (HCA), an international collaborating scientific initiative aimed at creating comprehensive reference maps of all human cells from all organs, through single cell RNA sequencing (Schiller et al., 2019). In the framework of this consortium, the team has already established a precise airway epithelium cell atlas referencing bronchial, tracheal and nasal cells sampled from 10 healthy living volunteers (Deprez et al., 2020). They also have created a comprehensive single-cell atlas of human nasal airway differentiation *in vitro* at several time points during differentiation and performed *in-silico* reconstruction of epithelial cell lineages (Ruiz García et al., 2019). To go deeper in the understanding of the mechanisms controlling the equilibrium of the airway epithelium, we studied pathological remodeling of the epithelium in the context of asthma.

The airway epithelium is a complex ecosystem that must be finely tuned to maintain the equilibrium between its various cell types to assure proper mucociliary clearance. In asthma, chronic inflammation dysregulates the molecular events controlling this equilibrium and causes remodeling, which reduces mucociliary clearance. The type 2 cytokine IL-13 and rhinovirus A16 (RVA) are two asthma-related triggers playing a role in epithelial remodeling in asthma. IL-13 treatment of ALI cultures has been widely used to monitor epithelial remodeling including goblet cell hyperplasia (Everman et al., 2018), however delineating the exact molecular mechanisms that contribute to mucus secreting cell hyper/metaplasia in asthma is still an open question. Moreover, the molecular events following recovery after inflammation have never been studied. No study has yet described at the single cell level the cellular and molecular alterations in severe asthmatics airways. The objectives of this project were to document the precise mechanisms that contribute to the severity and persistence of asthma, with an emphasis on the specific roles played by different subtypes of airway epithelial cells in the natural history of the disease. To this aim, I treated ALI cultures obtained from cells of either healthy or severe asthmatics donors with, IL-13 or RVA and performed single-cell RNA sequencing analysis.

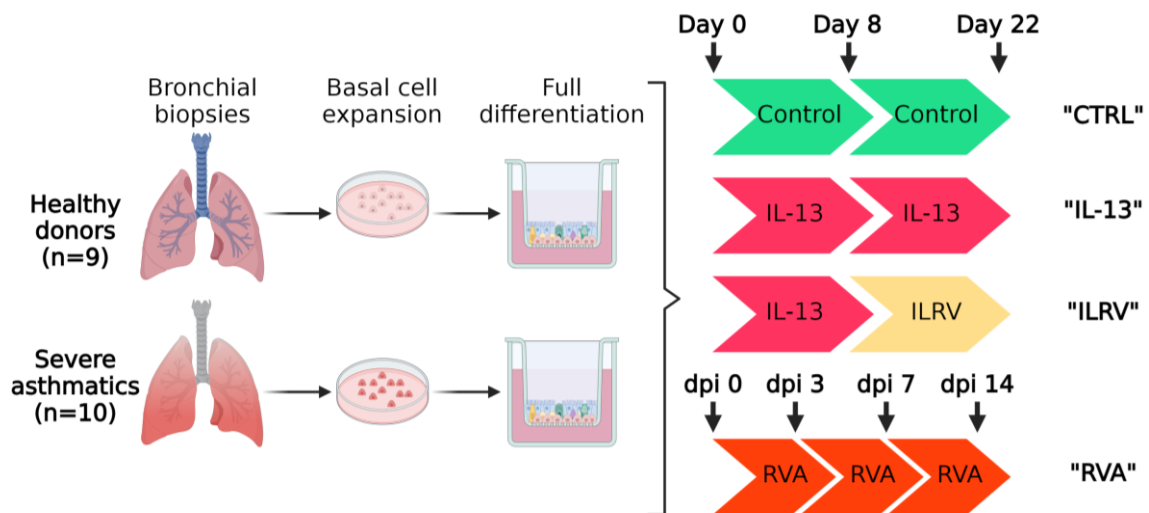


**Figure 47:** Experimental design of the project.

ALI culture obtained from bronchial biopsies of either healthy or severe asthmatics donors were treated with, IL-13 or RVA and analyzed by single-cell RNA sequencing.

To investigate the molecular events controlling airway epithelial cell balance and their dysregulation in severe asthma, bronchial biopsies from healthy and severe asthma donors were reconstructed in vitro using an Air-Liquid Interface (ALI) model. Severe asthma donors were selected on the basis of the persistence of the symptoms despite optimized treatment, as defined by the GINA guidelines (GINA, 2024). The fully differentiated ALI cultures were chronically treated with IL-13 (10 ng/mL) (n=6 healthy donors and 8 severe asthma donors) (**Fig.47**) or infected once with rhinovirus A16 (RVA) (n=3 healthy donors and 4 severe asthma donors) (**Fig.47A**) (**Table 1**). To monitor cellular and molecular events at the peak of treatment effects, single-cell RNA-seq was performed 8 days after IL-13 treatment (timepoint 1, IL-13 1) or 3 days post RVA infection (dpi 3). Then, to monitor cellular and molecular events taking place during epithelial recovery (resolution), part of the cultures was washed out of IL-13 and single-cell RNAseq was performed 14 days later (timepoint 2, ILRV), or remained treated with IL-13, for a total of 22 days (timepoint 2, IL-13 2). For RVA16 infection, ALI cultures were allowed to recover with no additional treatment nor infection. Single-cell RNAseq was performed 7 and 14 days later (dpi7 and dpi 14) (**Fig.47B**). In total over 260,000 cells from 9 healthy and 11 severe asthma donors were obtained, from two distinct datasets:

- 129,306 cells in the IL-13 treated dataset and
- 61,913 cells in the RVA treated dataset (**Table 1**).

**Table 1:** Cohort of the study.

	IL-13 experiments			Rhinovirus A16 experiments		
	Age (year)	Donor (number)	Cell (number)	Age (year)	Donor (number)	Cell (number)
<b>Healthy</b>	56.5 ± 12.3	6	54685	61.6 ± 4.9	3	25631
<b>Asthma</b>	53.5 ± 13	8	74621	66.2 ± 6.7	4	36282
<b>Total</b>	53.4 ± 12.5	14	129306	64.28 ± 6.2	7	61913

Two main hypotheses were tested:

- 1) Epithelia reconstructed from cells of severe asthma patients have a different cellular and molecular response from healthy epithelia during asthma-related remodeling (IL-13 or RVA) and resolution after treatment withdrawal.
- 2) During remodeling and resolution, there are transdifferentiation events between already differentiated cell types (goblet and multiciliated).

The following comparisons were performed to test the hypothesis:

- **Asthma CTRL vs Healthy CTRL:** to identify the differences in cell composition and gene expression between healthy and asthma epithelia at baseline.
- **Healthy IL-13 vs Healthy CTRL:** to identify the events triggered by IL-13 treatment in healthy epithelia.
- **Healthy IL-RV vs Healthy CTRL:** how do healthy epithelia recover after IL-13 induced remodeling?
- **Asthma IL-13 vs Asthma CTRL:** to identify the events triggered by IL-13 treatment in severe asthma epithelia.
- **Asthma IL-RV vs Asthma CTRL:** how do severe asthma epithelia recover after IL-13 treatment?
- **Asthma IL-13 vs Healthy IL-13:** do the severe asthma epithelia respond differently to IL-13 than the healthy ones?
- **Healthy RVA dpi 3 vs Healthy CTRL:** how do healthy epithelia respond to RVA infection?
- **Asthma RVA dpi 3 vs Asthma CTRL:** how do severe asthma epithelia respond to RVA infection?
- **Asthma RVA dpi 3 vs Healthy RVA dpi 3:** do the severe asthma epithelia respond differently to RVA infection than the healthy ones?
- **Healthy RVA dpi 14 vs Healthy CTRL:** how do healthy epithelia recover from RVA infection?
- **Asthma RVA dpi 14 vs Asthma CTRL:** how do severe asthma epithelia recover from RVA infection?

The first part of this section will focus on the IL-13 dataset.

## Building of an asthma-centric perturbation atlas

### IL-13 induces remodeling in healthy and severe asthma epithelia.

Epithelia from healthy or severe asthma donors were treated with IL-13 for 8 (IL-13 1) or 22 (IL-13 2) days. Epithelial remodeling was first monitored at each timepoint by immunofluorescence staining of MUC5AC (goblet cells), acetylated alpha-tubulin (actub, cilia) and phalloidin (actin) (**Fig. 48**).

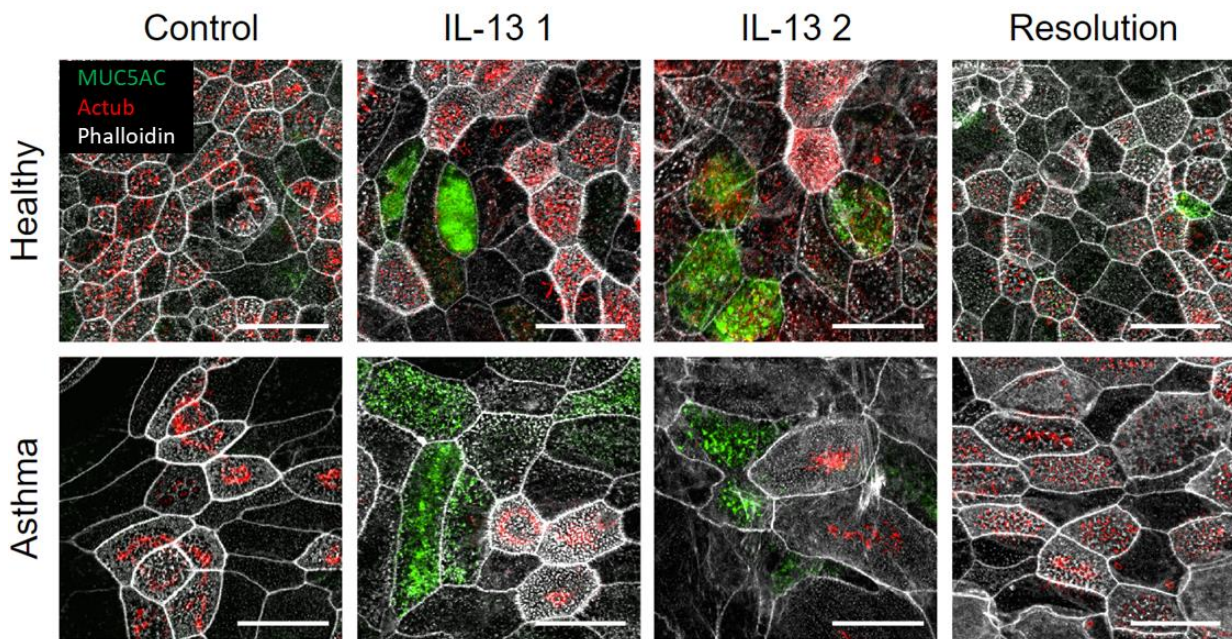


**Figure 48:** Characterization of IL-13 induced remodeling of healthy and severe asthma epithelia. Confocal immunofluorescence images stained for goblet (MUC5AC, green) and multiciliated cells (actub, red). Actin-F is marked with phalloidin, white. Scale bars = 25 $\mu$ m.

IL-13 treatment of healthy epithelia triggered remodeling after 8 days with goblet cell hyperplasia, identified by an increase in MUC5AC+ cells and a decrease in multiciliated cell (MCC) number, identified by a decrease in acetylated alpha-tubulin staining. Fourteen days after IL-13 washout (resolution), healthy epithelia seemed to have recovered their initial cell composition. Contrary to what has been reported in other studies of severe asthma ALL cultures, untreated severe asthma epithelia did not display overt goblet cell hyperplasia (**Fig.48**) (Gras et al., 2012). Severe asthma basal cells seemed to have differentiation defects, in addition to lower proliferation abilities (not shown). Overall, severe asthma epithelia displayed a phenotype distinct from that of healthy cultures at baseline, but also showed goblet cell hyperplasia and loss of MCC upon IL-13 treatment. Severe asthma epithelia also seemed to recover their initial phenotype after resolution (**Fig.48**), demonstrating a certain cell plasticity.



## Single-cell RNA-sequencing dataset

To understand the cellular and molecular events at play during IL-13 induced remodeling and resolution, I performed single-cell RNA sequencing at timepoints 1 and 2 (**Fig.49**). I obtained 129,306 cells from healthy and severe asthma bronchial ALI cultures (**Fig.49A:C**). I also treated and sequenced nasal ALI cultures from 3 healthy and 3 severe asthma donors from the cohort for future comparison between bronchial and nasal remodeling events (**Fig.49B**).

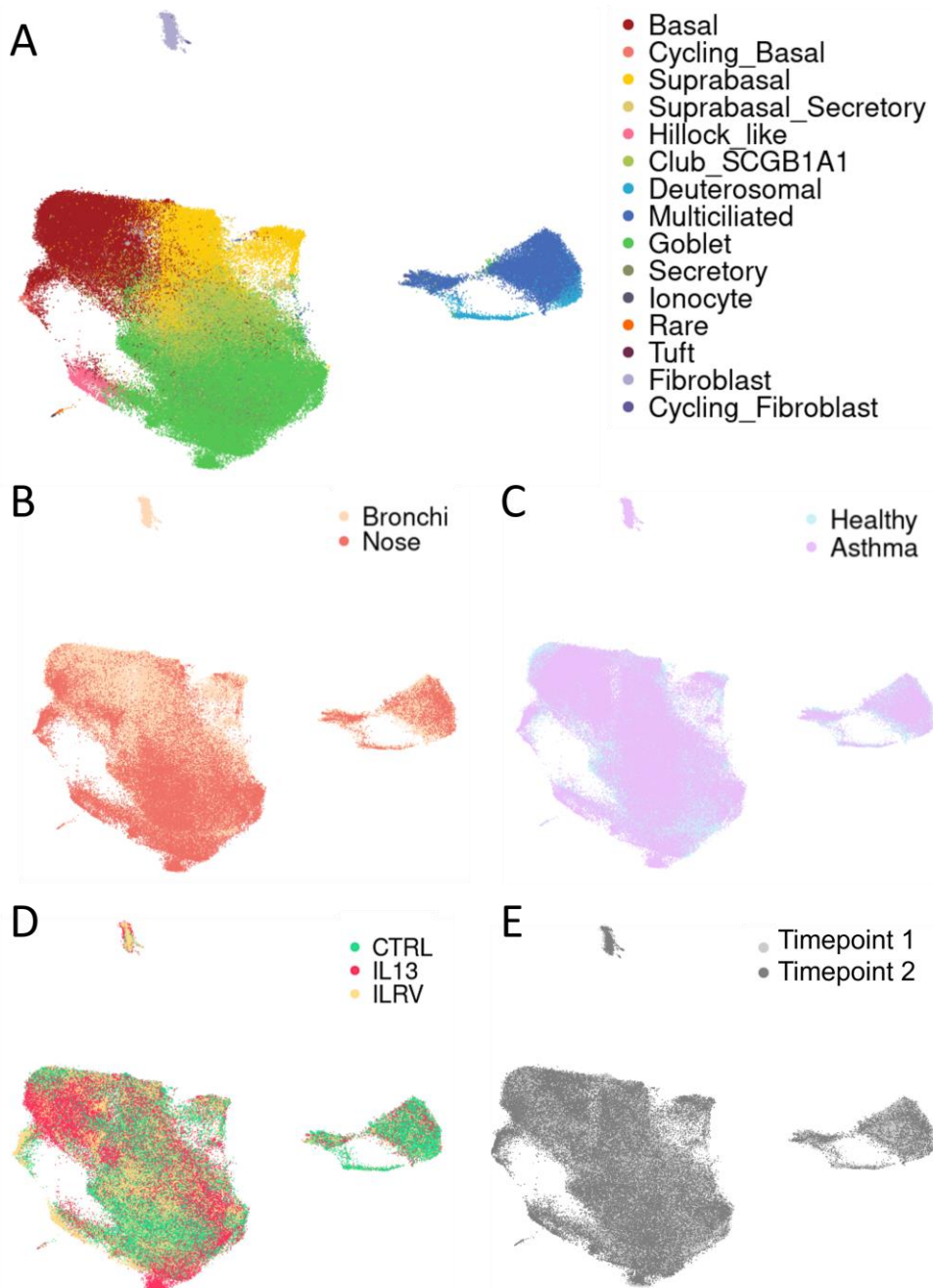


**Figure 49:** UMAP representation of the IL-13 perturbation dataset. UMAPs colored by cell types (A), organ (B), health status (C), treatment condition (D) and timepoint (E).

I identified 13 main epithelial cell types such as basal (*KRT5+/TP63+*), suprabasal (*KRT5+/TP63-*), club (*SCGB1A1+*), deuterosomal (*DEUP1+*), multiciliated (*FOXJ1+*) and goblet cells (*SPDEF+/MUC5AC+*) (**Fig.49A & Fig.50**). Of note, *MUC5AC* was poorly detected in the scRNA-seq datasets, which was surprising given immunostainings intensities, but which is consistent to what we and other found previously (Jackson et al., 2020). Surprisingly, in 2 cultures from severe asthmatic donors, I also identified fibroblasts (*PDGFR+*) and cycling fibroblasts with a strong collagen signature, that might be carryover from the 2 corresponding biopsies that persisted in culture. Fibroblasts were removed from the dataset for subsequent analysis, in order to remain focused on epithelial signatures. Moreover, there was also a “hillock-like” population of *SCGB1A1+/KRT13+* cells enriched in nasal samples (**Fig.49A**).

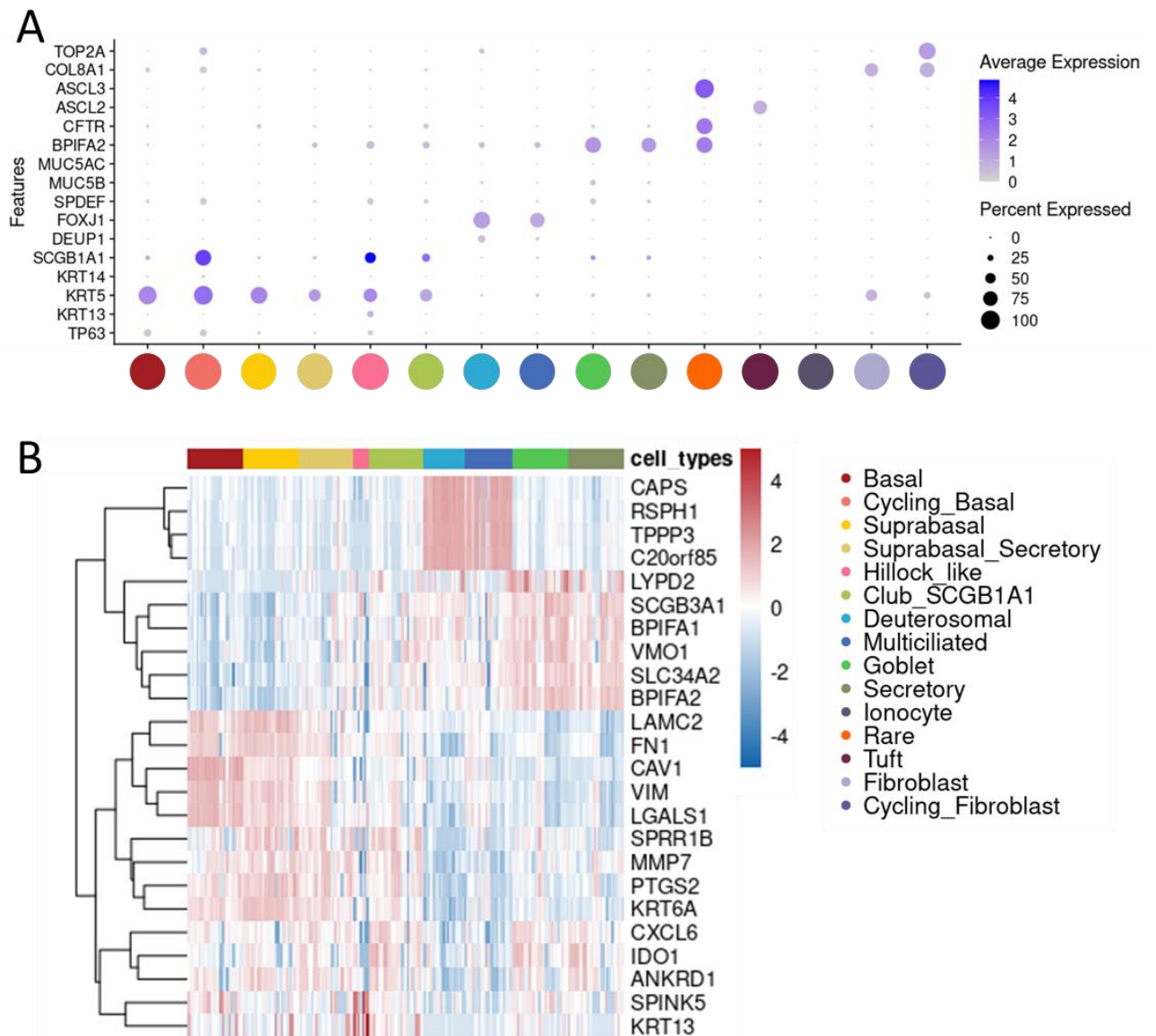


**Figure 50:** Cell typing of single cell RNA sequencing dataset.

**A:** Dotplot of canonical markers. **B:** Heatmap of top markers for each cell type selected on  $p\text{-val} \leq 0.05$ ,  $\log_{2}FC > 0$ ,  $\text{pct.1} \geq 0.3$  and  $\text{pct.2} < 0.5$ . Plots are obtained with the dataset of untreated bronchial cells.

Lastly, assessment of correlation between cell types divided by health status, treatment and timepoint shows that cellular typing takes precedence over the other conditions. Groups cluster first by similar cell type before treatment or healthy status, at the exception of some small subgroups such as deuterosomal and cycling basal cells that may be more heterogeneous due to their small size. Overall, this validates cell type robustness (**Fig.51**).

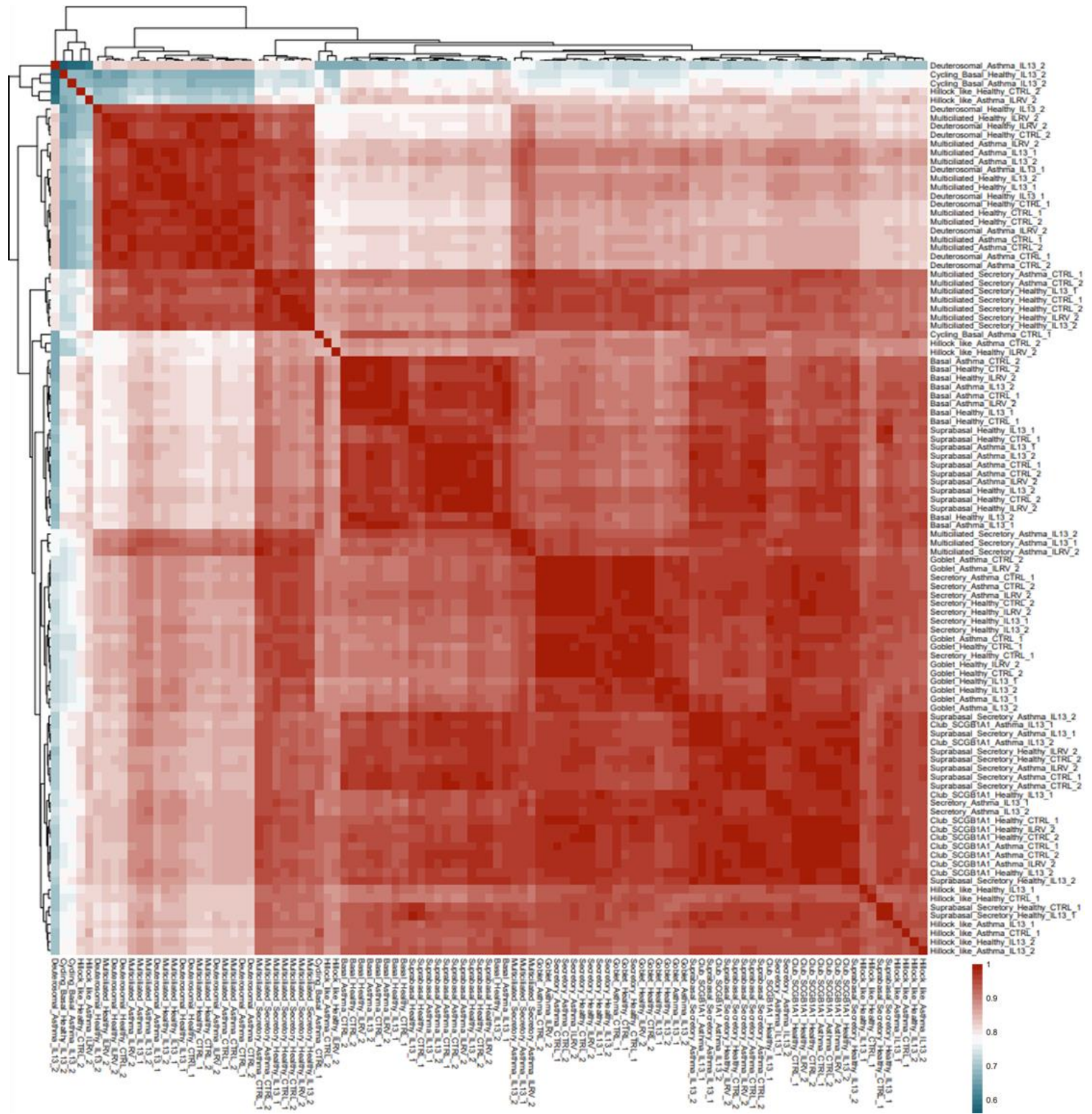


**Figure 51: Cell clusters correlations.**  
Heatmap of correlations between cell types sub-divided by health status, treatment and timepoint.

## Differences of composition and transcriptomic profiles between *in vitro* severe asthma and healthy cells

### Asthma epithelium maintains a phenotype of disease *in vitro*

To identify specific events occurring in cultures obtained from severe asthmatics compared to healthy ones, I first compared cultures at baseline without treatment. I used 2 distinct analyses to assess remodeling: the milo package (**Fig.52A**) that uses partially overlapping neighborhoods of cells for cell type abundance enrichment analysis and the speckle package (**Fig.52B**), which uses the discrete cell clusters that I annotated (**Fig.49**) and pairwise comparisons as statistical tests for cell proportion analysis. The milo plot showed a significant ( $p\text{-val} < 0.05$ ) enrichment in basal, club and suprabasal populations in asthma (red dots) and a significant enrichment of a suprabasal secretory cell population (blue dots). Goblet and multiciliated cells both had mixed profiles with one side enriched in healthy samples and one side enriched in asthma ones, suggesting discrete subclusters specific to each condition. Cell proportion analysis by speckle found that the healthy epithelium had a greater population of goblet and deuterosomal cells ( $p\text{-val} = 4.2\text{e-}04$  and  $0.02$ , respectively), and confirmed that the asthma epithelium was significantly enriched in more immature cell types such as basal ( $p\text{-val} = 0.001$ ), suprabasal ( $p\text{-val} = 2.1\text{e-}04$ ) and club cells ( $p\text{-val} = 8.4\text{e-}06$ ) (**Fig.52B**). Overall, both approaches confirmed the observations done on immunofluorescence image.

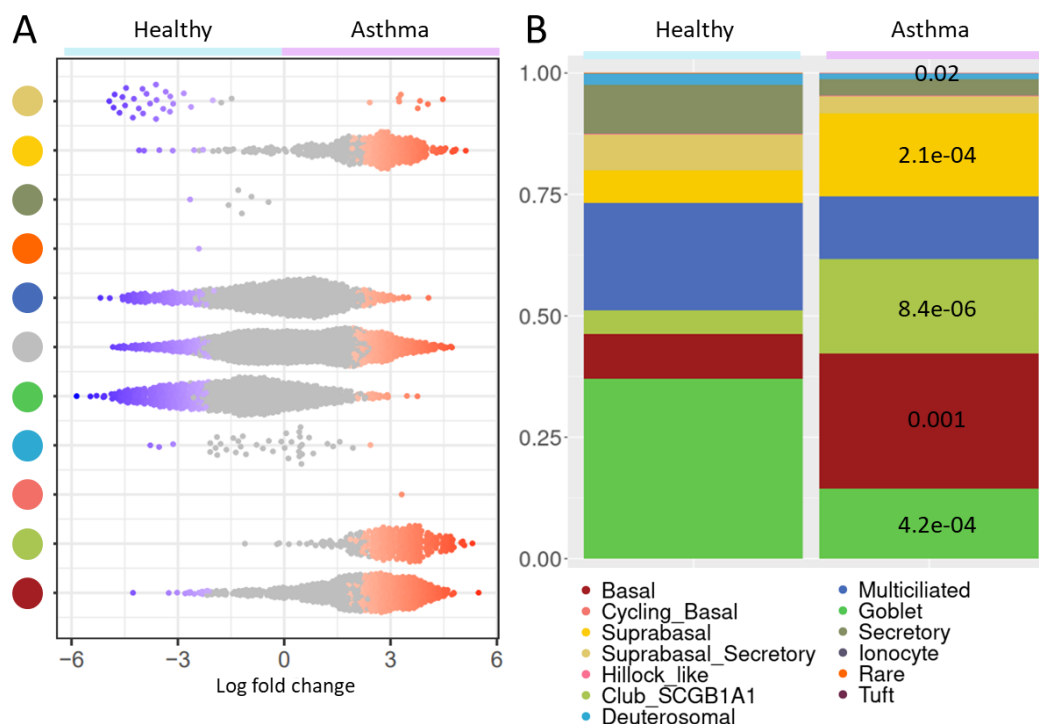


**Figure 52:** Asthma remodeling is conserved in ALI cultures.

**A:** Beeswarm plot of differential abundance between healthy and asthma cell populations with Milo. Gray cell type indicates mixed cell neighborhoods. **B:** Proportion plot of cell types.  $p\text{-val}$ ues obtained by t-test.

Then, I performed differential gene expression for each cell cluster, between healthy and asthma cultures. I used a pseudobulk approach which compared gene expression between 2 conditions by aggregating cells by sample and by cell cluster and not at the single cell level. This allows to take into consideration the inter-donor variability by considering each sample as an individual sample, as opposed to approaches using single cells as individual samples.

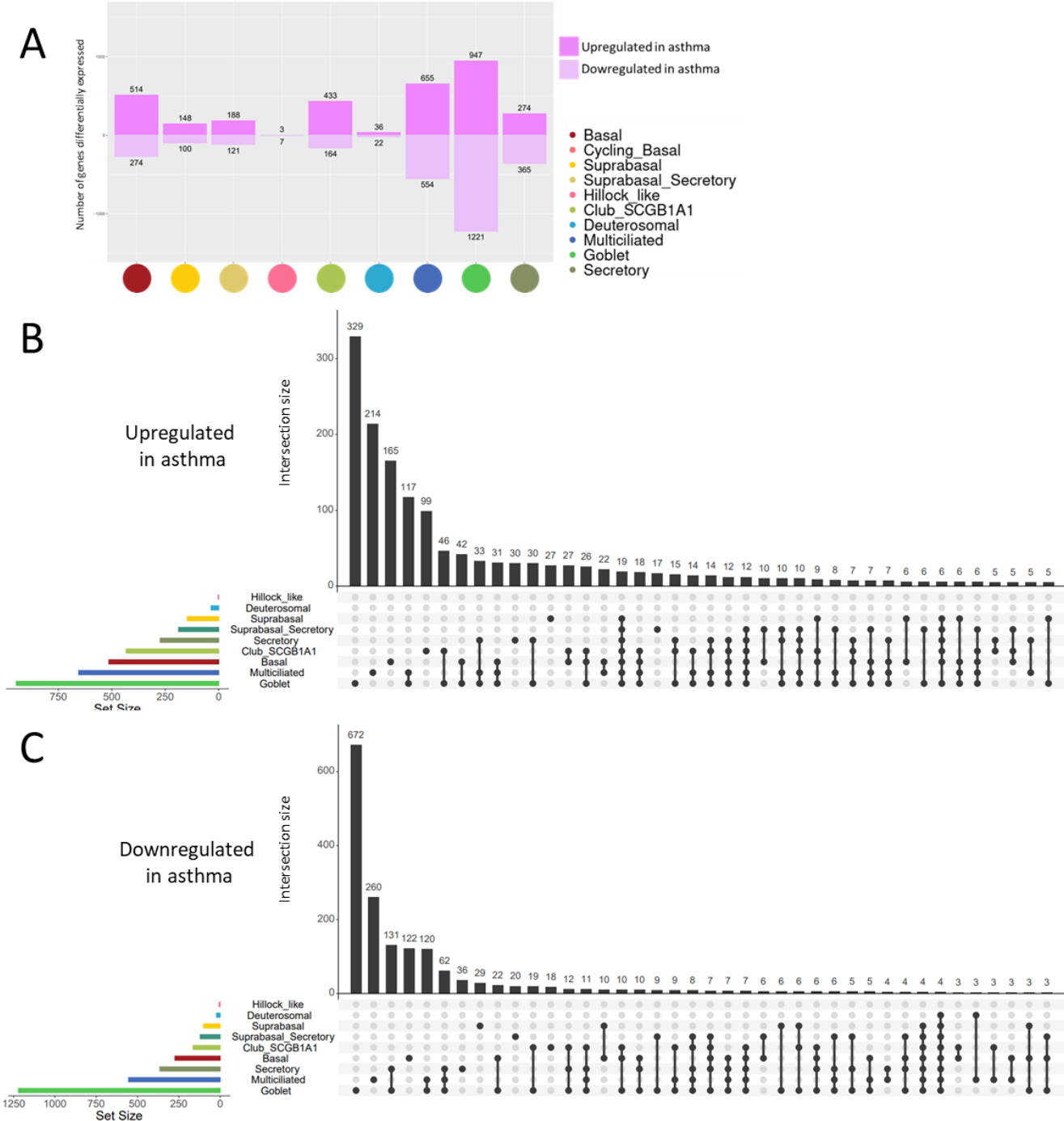


**Figure 53:** Differential expression of genes between healthy and severe asthma cell types. **A:** Bar plot of gene up- and downregulated in severe asthma cells populations performed on merged data from timepoint 1 and 2 ( $p\text{-val} < 0.05$ ). **B:** Upset plot of genes differentially upregulated between healthy and severe asthma cell populations performed on merged data from timepoint 1 and 2 ( $p\text{-val} < 0.05$ ,  $\log\text{FC} > 0$ ). **C:** Upset plot of genes differentially downregulated between healthy and severe asthma cell populations performed on merged data from timepoint 1 and 2 ( $p\text{-val} < 0.05$ ,  $\log\text{FC} < 0$ ).

Differential gene expression showed that the basal and goblet cell populations had the most distinct transcriptome compared to healthy populations, with 514 and 947 genes upregulated, respectively (Fig.53A). Goblet cells also had the most downregulated genes with 1221, including 672 only downregulated in this population (Fig.53A&C).

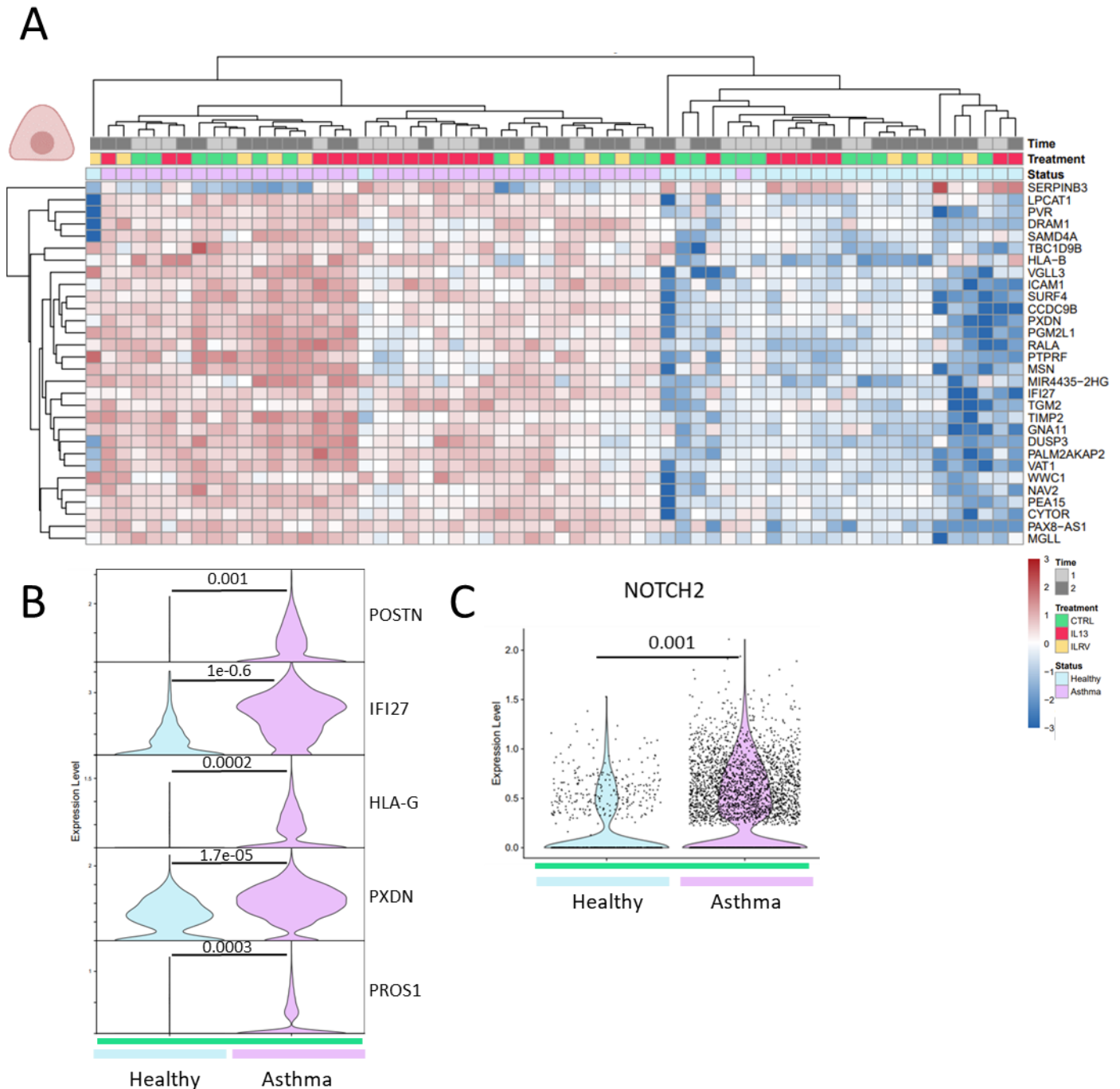


**Figure 54:** Differential gene expression between healthy and severe asthma basal cells.

**A:** Heatmap of the top 30 most differentially expressed genes in basal cells, timepoints merged ( $p$ -val < 0.05, pct.1 > 0.3). **B:** Violin plot of Th2 genes significantly upregulated in asthma basal cells. **C:** Violin plot of *NOTCH2* expression in asthma basal cells.

Among the genes most upregulated in the basal asthma population were Th2-associated genes such as the host response to virus gene *IFI27*, major histocompatibility complex class II (MHC-II) genes *HLA-B* and *HLA-G*, the asthma marker *POSTN* (logFC 2.2) (**Fig.54A&B**) and matrix-related genes such as collagens (*COL1A1*, *COL4A1*, *COL4A2*) and metalloproteinases (*ADAM9*, *ADAM19*) (not shown). Interestingly, the gene encoding the receptor *NOTCH2* was also strongly upregulated in asthma basal cells (**Fig.54C**). This receptor is usually found on club cells and its activation triggers the differentiation of club cells into goblet cells (Ruiz García et al., 2019).

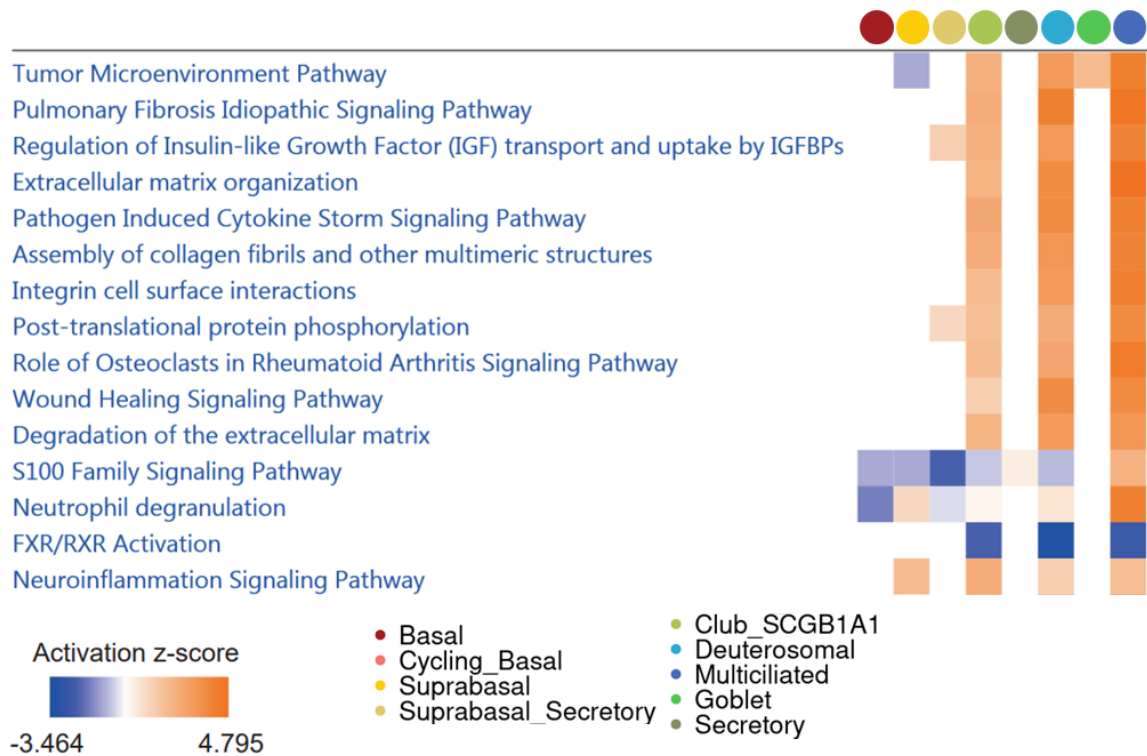


**Figure 55:** Analysis comparison of regulated pathways across cell types.

Analysis comparison of regulated pathways across cell types revealed common pathways activated between club, deuterosomal and multiciliated cells, with the strongest activation z-score in the latest. In particular, the pulmonary fibrosis idiopathic signaling pathway was strongly activated in the three cell types, suggesting common interactors between respiratory diseases (**Fig.55**). The pathogen induced cytokine storm signaling pathway was also strongly activated in MCCs, in agreement with the expression of *IFI27* significantly upregulated in the population (**Fig.56A**). The dynein light chain *DYNLT4* and mitochondria-associated genes *SDHD*, *HIGD2A* and *CIAO2A* (Morgenstern et al., 2021; Spinelli & Haigis, 2018) were downregulated, which could suggest a decrease in cilia mobility, as motile cilia are powered by mitochondria (Ximena et al., 2006). Interestingly asthma MCC transcriptome was also enriched in *SNF* and *LAMC2* that have been associated with squamous metaplasia (Goldfarbmuren et



al., 2020), and numerous basal cell markers such as laminins (*LAMB3*, *LAMC2*), integrins (*ITGB1*, *ITGA3*, *ITGB6*), filamin (*FLNB*), actinin (*ACTN1*) and *HSPG2* (**Fig.56A**). Moreover, the basal-associated keratins *KRT5* and *KRT6A*, and suprabasal-associated *KRT16* were also upregulated (**Fig.56B**). To go further, I plotted the expression score of the top expressed asthma MCC genes across all cell types (first dendrogram row of **Fig.56A**) and noticed that this “MCC asthma” signature was consistently highest in asthma samples. It scored the highest in basal and suprabasal cells. (**Fig.56C**). Put together, these results suggest that asthma MCCs are more immature than healthy ones.

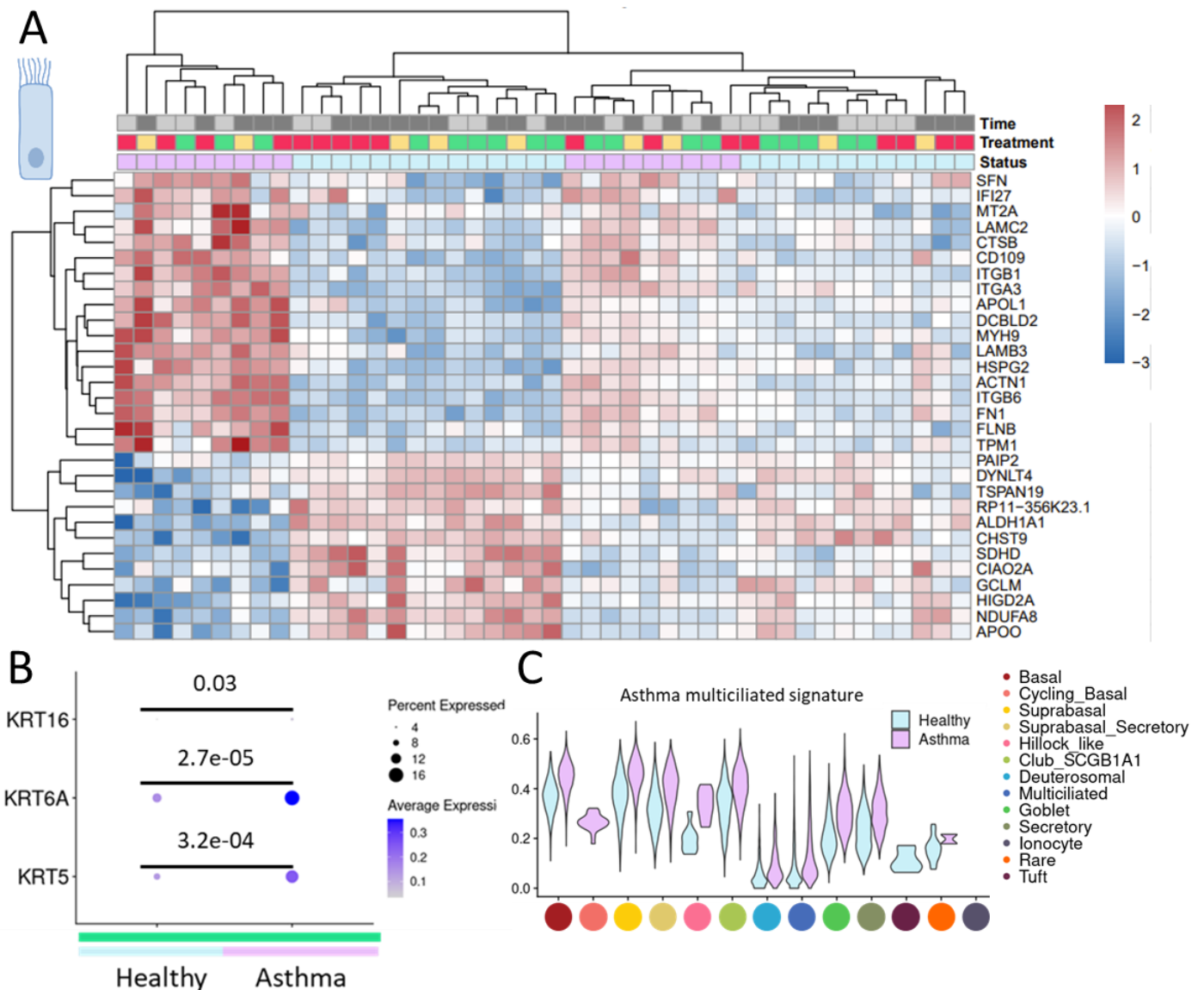


**Figure 56** : Differential gene expression between healthy and severe asthma multiciliated cells.

**A:** Heatmap of the top 30 most differentially expressed genes in MCCs, timepoints merged ( $p\text{-val} < 0.05$ ,  $\text{pct.1} > 0.3$ ). **B:** Dot plot of keratin genes in MCCs.  $p\text{-values}$  obtained by LRT test. **C:** Violin plot of the asthma MCC signature composed of the top genes from heatmap A.

Asthma goblet cells were enriched in genes related to immunity such as transporter associated with antigen processing 1 (*TAP1*), which plays a role in antigen presentation by transporting peptides to MHC class I molecules (Kaer et al., 1992), and type I or type III interferon signaling with upregulation of *STAT2* and *IFI27* (Au-Yeung et al., 2013) (Fig.57A). Similarly to MCCs, asthma goblet cells were also strongly enriched in basal cell markers and ECM-related genes such as the laminins *LAMC2* and *LAMB3*, filamin B (*FLNB*), *HSPG2*, *ITGB6*, *ACTN1* and fibronectin (*FN1*) (N. R. Hackett et al., 2011), and *KRT5*, *KRT6A* and *KRT16* (Fig.57B). The asthma goblet cell signature also scored high in basal and suprabasal cells (Fig.57C).

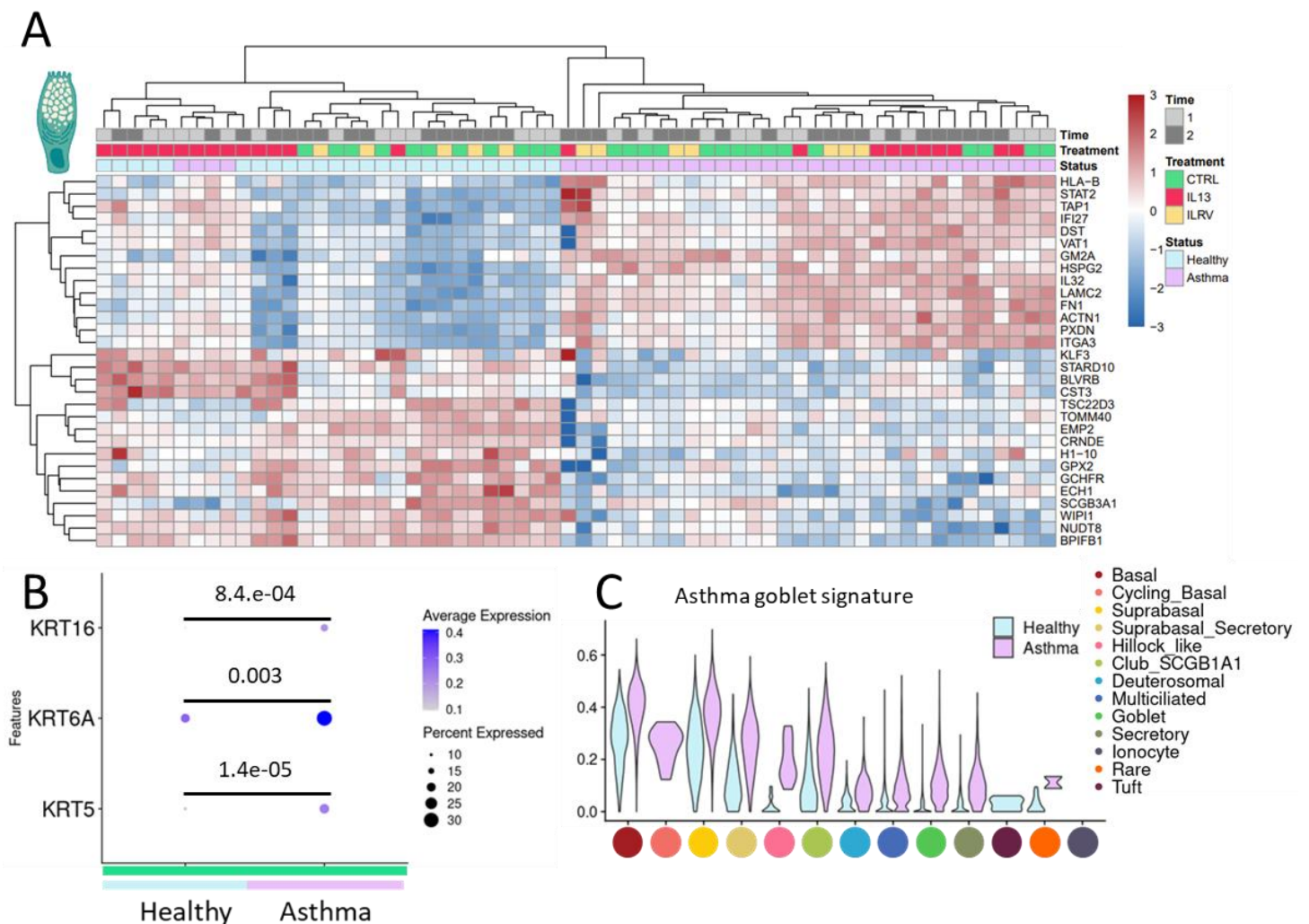


**Figure 57** : Differential gene expression between healthy and severe asthma goblet cells.  
**A:** Heatmap of the top 30 most differentially expressed genes in goblet cells, timepoints merged ( $p\text{-val} < 0.05$ ,  $\text{pct.1} > 0.3$ ). **B:** Dot plot of keratin genes in goblet cells.  $p\text{-values}$  obtained by LRT-test. **C:** Violin plot of the asthma goblet cell signature composed of the top genes from heatmap A.

For all cell types, plotting of the topmost differentially expressed genes on a heatmap with an expression matrix of cells of the same cell type but from all conditions (healthy, asthma, treatments and timepoints combined) (Fig.54A, Fig.56A and Fig.57A) showed an unsupervised clustering of sample per health status. The samples clustering by cell type and not by treatment demonstrated that

the asthma signature is stronger than the IL-13 signature and that IL-13 treated healthy cells do not cluster with the asthma samples.

To have a more comprehensive view of the biological processes differing between healthy and asthma epithelia, we performed a secretome analysis on apical washes from the surface epithelia that we collected before dissociating ALI cultures for scRNA-seq. Secretions of the basal compartments of the culture inserts were also collected and analyzed but as no significant changes were detected, only results of the apical secretions are presented in the manuscript. No difference in MUC5AC expression was detected with ELISA analysis of mucus secretion between healthy and asthma samples (**Fig.58A:C**). Mucus of asthma epithelia was significantly enriched in MUC5B, but its RNA expression was significantly decreased in goblet cells. This discrepancy could be due to differential secretion mechanisms between healthy and asthma epithelia or to experimental issues such as antibody cross reaction. Cytokine secretions were assessed by LEGENDplex™ assay. Among the most differentially regulated cytokines, the growth factors CSF1 and PDGFB were upregulated both in secretions (**Fig.58D&E**) and RNA expression from the scRNA-seq data (**Fig.58F**) of asthma samples. CSF1 is a lineage-specific growth factor for macrophages that is expressed by fibroblasts and PDGFB is a fibroblast growth factor expressed by macrophages. Macrophages and fibroblasts hence regulate each other's population through paracrine signals, *in vitro* and *in vivo* (Bonnardel et al., 2019; X. Zhou et al., 2018, 2022). Given the expression and different levels in asthma samples, it is tempting to speculate that asthma epithelial cells can similarly signal to the mesenchymal and immune niches of the lungs.

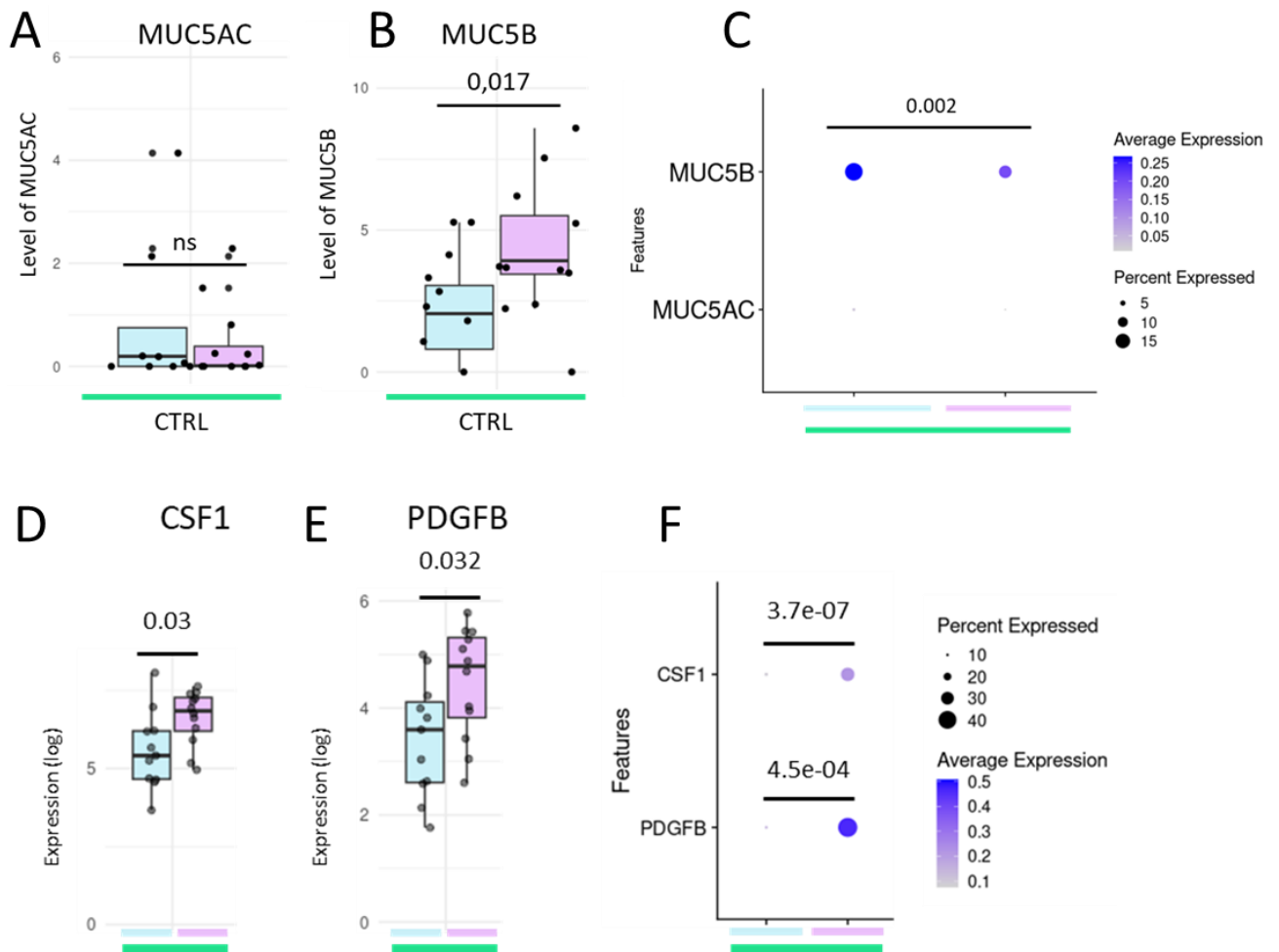


**Figure 58:** Differences in secretions ELISA detection of MUC5AC.

(A) and MUC5B (B) in apical washes of healthy and asthma cultures at baseline C: mRNA levels of *MUC5AC* and *MUC5B* in goblet cells. Legendplex detection of *CSF1* (D) and *PDGFB* (E) in apical washes at baseline. F: mRNA levels of *CSF1* and *PDGFB* in the whole dataset.

# Characterization of cell types and states induced during remodeling and regeneration events

## Characterization of cell types and states induced by IL-13 in healthy epithelium

Our working hypothesis was that during remodeling and resolution, there are transdifferentiation events between already differentiated cell types such as goblet cells and multiciliated cells.

### IL-13 induces goblet cell hyperplasia in healthy epithelium

To identify specific remodeling events such as putative transdifferentiation between multiciliated and goblet cells, I treated healthy airway epithelial ALI cultures with IL13 (10 ng/mL). Milo enrichment analysis shows goblet cell hyperplasia after 8 days of IL-13 treatment in healthy epithelia as expected, as well as basal cell hyperplasia and a decrease in multiciliated cell population in healthy epithelium. This remodeling persisted through timepoint2 (**Fig.59A&B**).

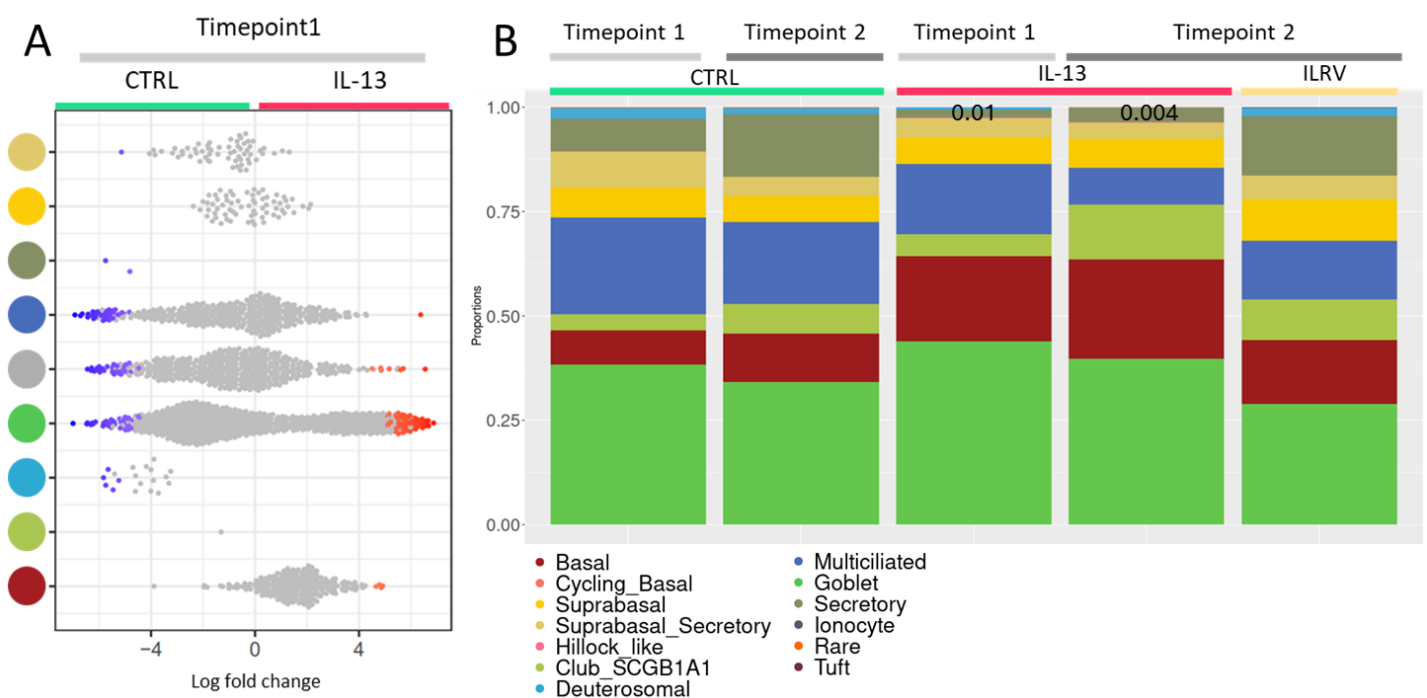


**Figure 59:** IL-13 induces remodeling in healthy airway epithelial ALI cultures.

**A:** Beeswarm plot of differential abundance of cell types between IL-13 treated and untreated healthy cells at timepoint 1 with Milo. Gray cell type indicates mixed cell neighborhoods. **B:** Proportion plot of cell types between IL-13 treated, untreated (CTRL) and ILRV (resolution) healthy cells at timepoint 1 and 2. *P* values obtained by t-test.

### Goblet cells are the main responder of IL-13 in healthy epithelium

IL-13 induced a strong response in goblet cells at the transcriptome level, with 683 genes upregulated at timepoint1 (**Fig.60A**), including typical IL-13 epithelial response with genes such as *ALOX15*, *FETUB* or *CDH26*. This was reflected with Ingenuity Pathway Analysis predicting strong activation of the IL-13 pathway in goblet cells and associated genes such as *SPDEF*, *ALOX15*, *CCL26* or *ANO1* (**Fig.60B**).

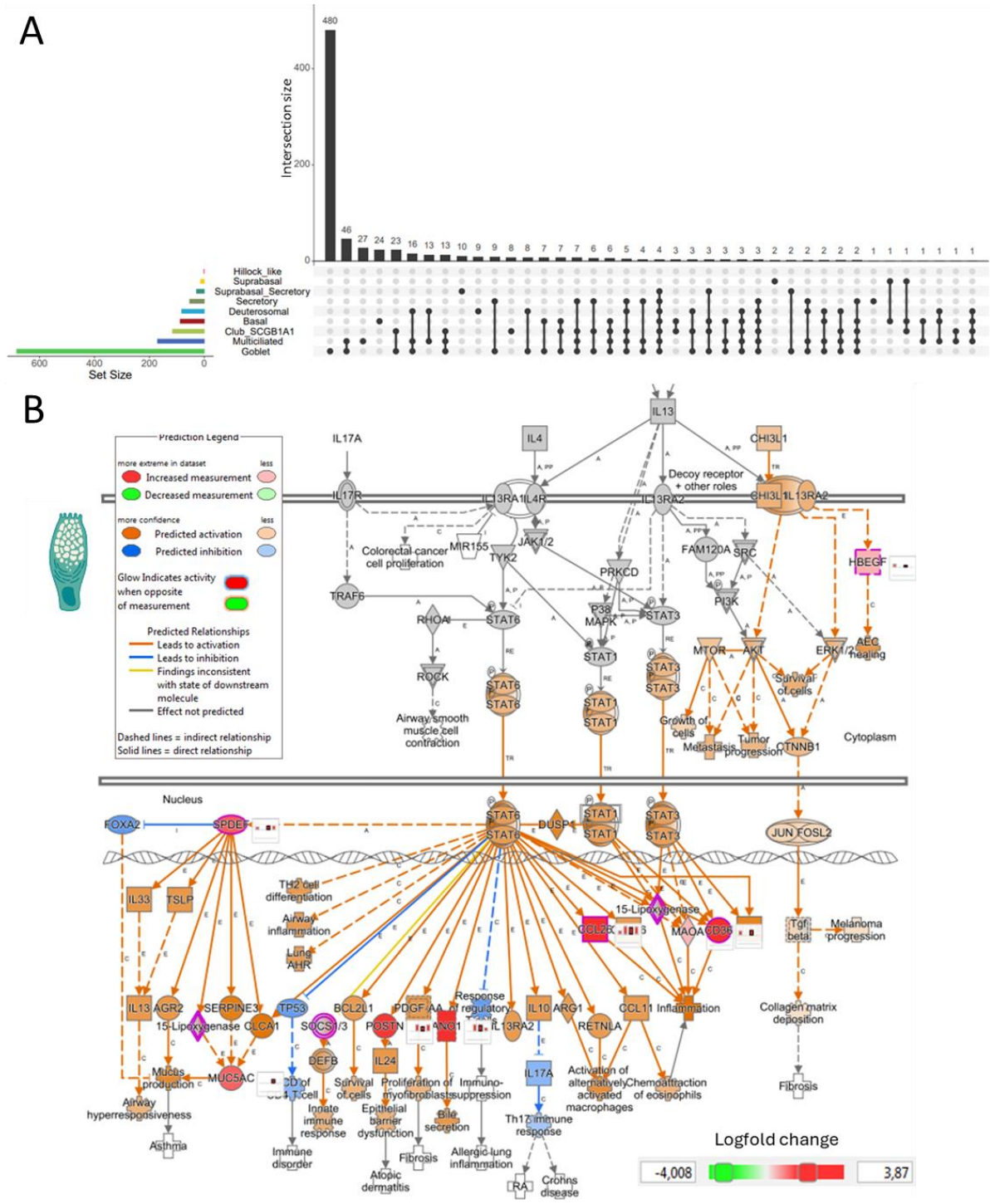


**Figure 60:** IL-13 induces a strong inflammatory response in healthy goblet cells. **A:** Upset plot of genes significantly upregulated ( $P$  val < 0.05, logFC > 0) by IL-13 in healthy cells at timepoint 1. **B:** Ingenuity Pathway Analysis (IPA) prediction of IL-13 pathway activation in IL-13 treated healthy goblet cells at timepoint 1.

Among the upregulated genes found in the differential expression analysis in goblet cells at timepoint 1, 480 were uniquely found in this population, including cystatin C (*CST3*) (Fig.60A and Fig.61A&B), an antiprotease involved in epithelial fluid balance and mucociliary clearance (T. I. A. Evans et al., 2016). Significant increase in *CST3* protein expression was detected in apical washes of IL-13 treated healthy ALI cultures at timepoint 2 (Fig.61B). Other genes involved in fluid balance like *ANO1*,

involved in chloride ion transport (Widdicombe & Wine, 2015) and *SLC12A2*, a basolateral  $\text{Na}^+/\text{K}^+/\text{2Cl}^-$  cotransporter were also upregulated (Hill et al., 2022). Interestingly, by plotting the top 50 most upregulated genes in healthy goblet cells after IL-13 treatment on a heatmap representing all samples, I noticed that the top genes of this response were also upregulated in IL-13 treated asthma goblet cells but at a lower intensity (**Fig.61C**). This difference in response will be explored in more details in part [Comparison of the differences in response to IL-13 between asthmatic and healthy epithelia](#).

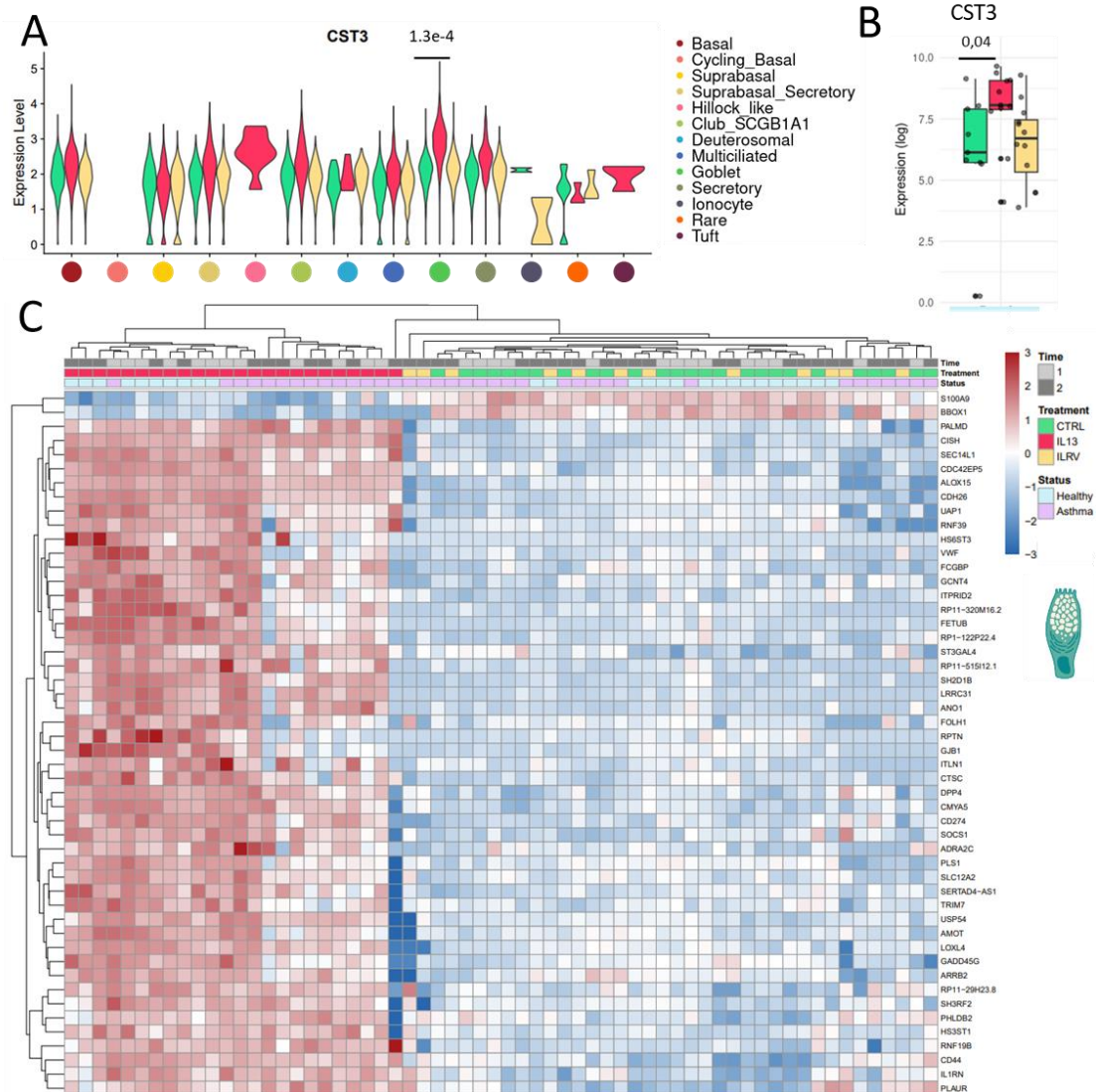


**Figure 61:** Upregulated genes in IL-13 treated healthy goblet cells.

**A:** Violin plot of *CST3* mRNA levels across healthy cell types at timepoint 2. **B:** Protein level of *CST3* in apical washes of healthy epithelia at timepoint 2. **C:** Heatmap of the top 50 most upregulated genes ( $P$  val < 0.05,  $\log_{2}FC > 0$ ) by IL-13 in healthy goblet cells at timepoint 1.

## IL-13 triggers deciliation in healthy epithelia

To understand the events causing the decrease in the MCC population observed both in immunofluorescence microscopy and in single cell RNA sequencing, I then focused the analysis on the

MCC population. IL-13 treatment induced the expression of ion transporter genes such as *TRPM6* and *ATP12A* (Schlingmann et al., 2007; Shah et al., 2016) and serine peptidase inhibitors (SERPINs) like *SERPINB2* and *SERPINB10* that have been linked to asthma (Mo et al., 2019) (**Fig.62**). Interestingly, when plotting the top 50 most differentially expressed genes in response to IL-13 in healthy MCCs at timepoint 1, on an expression matrix of all conditions and timepoints merged, I noticed that these genes were not expressed by severe asthma MCCs at baseline and were less upregulated in severe asthma MCCs after IL-13 treatment (**Fig.62**), similarly to what was observed in the goblet cells (**Fig.62C**).

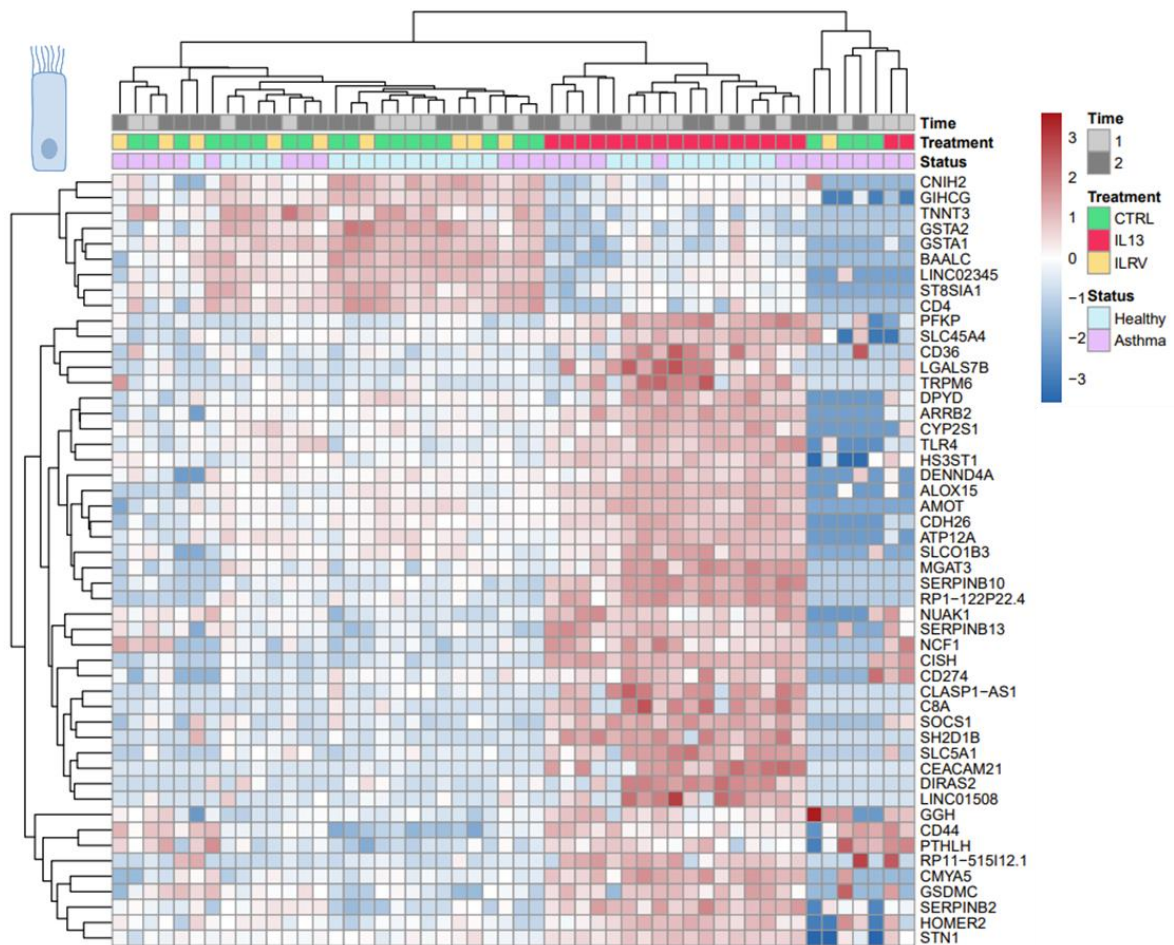


**Figure 62:** Differential gene expression between untreated and IL-13 treated healthy multiciliated cells. Heatmap of the top 50 most differentially expressed genes ( $P$  val  $< 0.05$ ) in response to IL-13 in healthy MCCs at timepoint 1, projected on an expression matrix of all conditions and timepoints merged.

The MCC population was also affected by IL-13 treatments, with a decreased expression of cilia components such as dynein light chain roadblock-type 2 (*DYNRLB2*) or *SNTN* as well as a decrease in the expression of the tubulin polymerization promoting protein family member 3 (*TPPP3*) (**Fig.63B**). Deuterosomal and MCC populations exhibited decreased SYSCILIA Gold Standard signatures of ciliary components (**Fig.63C**) (Suly Saray Villa Vasquez, John van Dam, 2021). To understand if this decrease in the expression of cilia genes was only the reflection of decreased MCC numbers, or could also reflect lower numbers of cilia per cell, I further characterized the loss of cilia that I observed by



immunofluorescence on **Figure 48**. I performed a time course study and imaged IL-13 treated healthy ALI cultures at several timepoints. I observed a disorganization of the apical mesh and a decrease in cilia density for each MCC after 3 days of treatment which became more important after 7 days. At this point the IL-13 was washed out and a rescue of the phenotype was visible as soon as 3 days after resolution. I continued the treatment on the remaining epithelia until day 17 when some MCCs only harbored a couple of cilia (**Fig.63A**), confirming loss of cilia in MCCs.

Interestingly, almost half of the genes induced by IL-13 in MCCs were shared with goblet cells, including the goblet cell transcription factor *SPDEF* (**Fig.63D**). Therefore, I decided to increase the resolution of the analysis of the MCC population by performing a subclustering step.

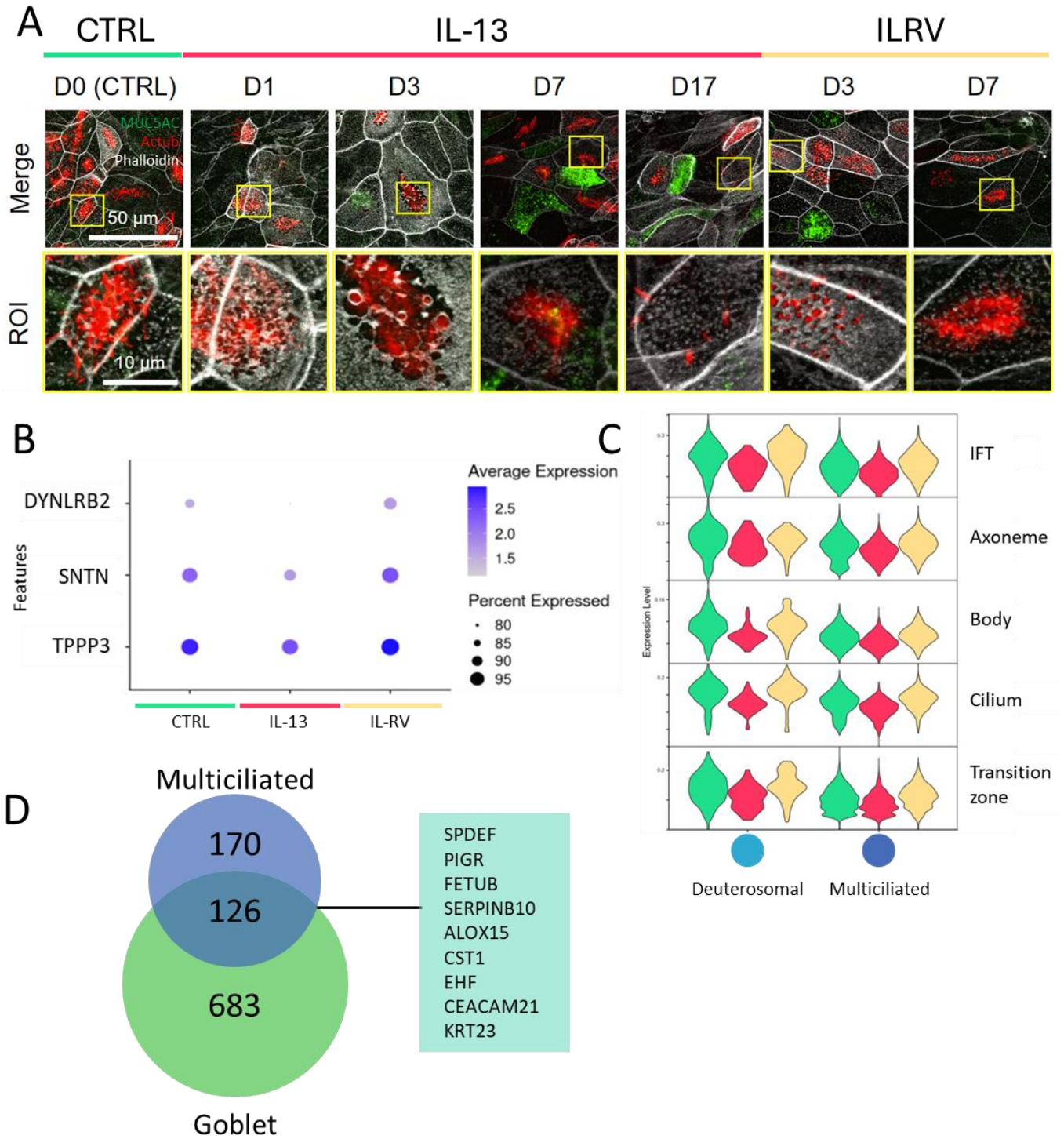


**Figure 63: IL-13 triggers deciliation of healthy multiciliated cells.**

**A:** Confocal microscopy images of healthy epithelia after IL-13-time course treatment, stained for MUC5AC (goblet cells, green); acetylated alpha-tubulin (Actub, cilia, red), and actin-F (cell outline, white). Lower panel: x3 zoom on yellow ROI. Scale bar: 50  $\mu$ m (upper panel) and 10  $\mu$ m (lower panel). **B:** Dot plot of multiciliated markers in the healthy multiciliated population at timepoint 2. **C:** SYSCILIA Gold Standard signatures in healthy deuterosomal and multiciliated cells at timepoint 2. **D:** Venn diagram of genes significantly upregulated ( $P$  val < 0.05, logFC > 0) by IL-13 in healthy goblet and multiciliated cells, and curated list of genes at the intersection.

## A hybrid mucous-ciliated population is induced by IL-13

Subclustering of MCCs by scANVI revealed two distinct subclusters (**Fig.64A**), both *FOXJ1+*. One subcluster expressed typical MCC markers (*FOXJ1+*, *RFX2+*) and was labeled as the main MCC population, however the second one expressed on top of these MCC markers, goblet-specific markers such as *SPDEF* and *MUC5B*. Thus, this cell population was labeled “mucous-ciliated” (**Fig.64C-E**). Additionally, the mucous-ciliated population shared the calcium-dependent cysteine protease *CAPN13* with goblet cells. This calpain is poorly characterized (Spinozzi et al., 2021) but could play a role in mucosal immunity by modulating the activity of certain proteins. Interestingly, mucous-ciliated cells also expressed *KRT5*, indicating a level of immaturity (**Fig.64F**). Cell proportion analysis showed that the mucous-ciliated cell population was enriched both in IL-13 treated healthy and asthma epithelia, although not significantly, probably due to its small size (**Fig.64G**).

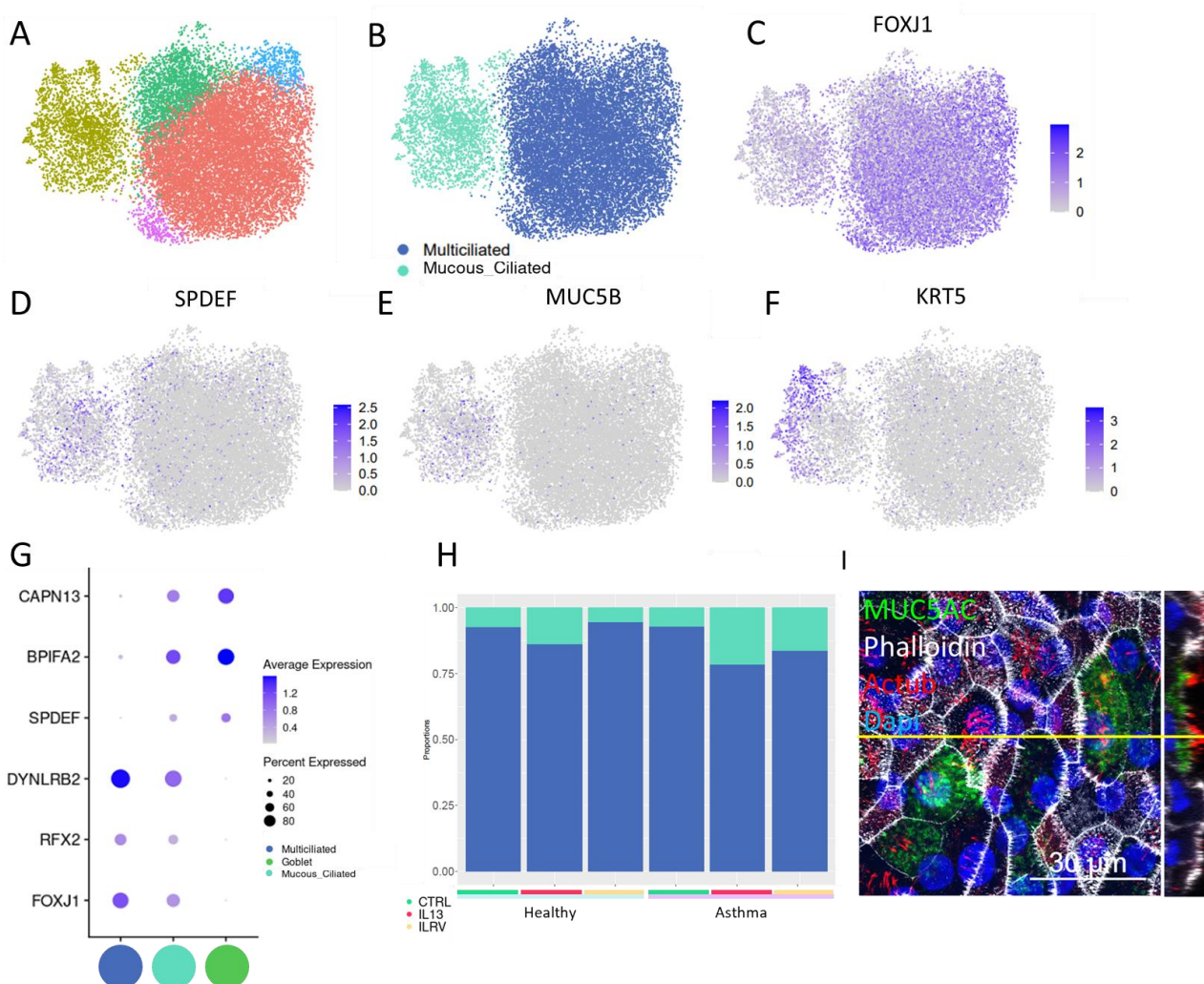


**Figure 64:** IL-13 induces a population of mucus ciliated cells.

UMAPs of subcluster multiciliated cells colored by leiden clustering (**A**) or new cell typing (**B**). Feature plots of *FOXJ1*(**C**), *SPDEF* (**D**), *MUC5B* (**E**) and *KRT5* (**F**). **G**: Dot plot of MCC and goblet markers shared by mucus-ciliated cells. **H**: Proportion plot of MCC and mucous-ciliated cells across conditions. **I**: Confocal immunofluorescence image of mucus-ciliated cells in a IL-13 treated healthy epithelium, stained for goblet (*MUC5AC*, green) and multiciliated cells (actub, red). Actin-F is marked with phalloidin, in white and nuclei with dapi in blue. Scale bars = 30  $\mu$ m.

Overall, IL-13 treatment of healthy ALI-cultured epithelium triggered a clear remodeling with a goblet cell hyperplasia and a decrease in deuterosomal and multiciliated cells, that was reversible after two weeks without IL-13 (timepoint 2). The transcriptomic response was carried in majority by the goblet cells with notably the upregulation of the expression of genes related to ion transport. Most interesting was the induction of a hybrid, mucous-secretory cell population expressing transcription factors specific of MCCs and goblet cells. For all cell types, plotting of the topmost differentially expressed genes on a heatmap with an expression matrix of cells of the same cell type but from all conditions (healthy, asthma, treatments and timepoints combined) (**Fig.61A** and **Fig.62A**) showed an unsupervised clustering of sample per treatment. IL-13 treated samples clustered alone while CTRL and ILRV (resolution) samples clustered together, indicating a complete resolution of the transcriptomic signature of samples that are no longer treated (ILRV) and is now undistinguishable from the CTRL one.

## Characterization of cell types and states induced by IL-13 in severe asthma epithelium

### Severe asthma epithelium can respond to IL-13 inflammation and recover after resolution

Next, I analyzed the effect of IL-13 treatment on severe asthma cultures. The goblet cell population was increased and the multiciliated cell population was decreased after 8 days of IL-13 treatment (timepoint 1), as seen by abundance (**Fig.65A**) and cell proportion (**Fig.65B**) analyses. However, after 22 days (timepoint 2), the basal cell population increased and became the dominant population (**Fig.65B**), highlighting a different dynamic between healthy and severe asthma epithelia during IL-13 treatment. Comparison of the proportions of control (CTRL) and resolution (ILRV) severe asthma epithelia at timepoint 2 shows no significant differences. Thus, the recovery of the initial cell proportions after resolution demonstrates plasticity despite impaired differentiation capacities of severe asthma epithelium.

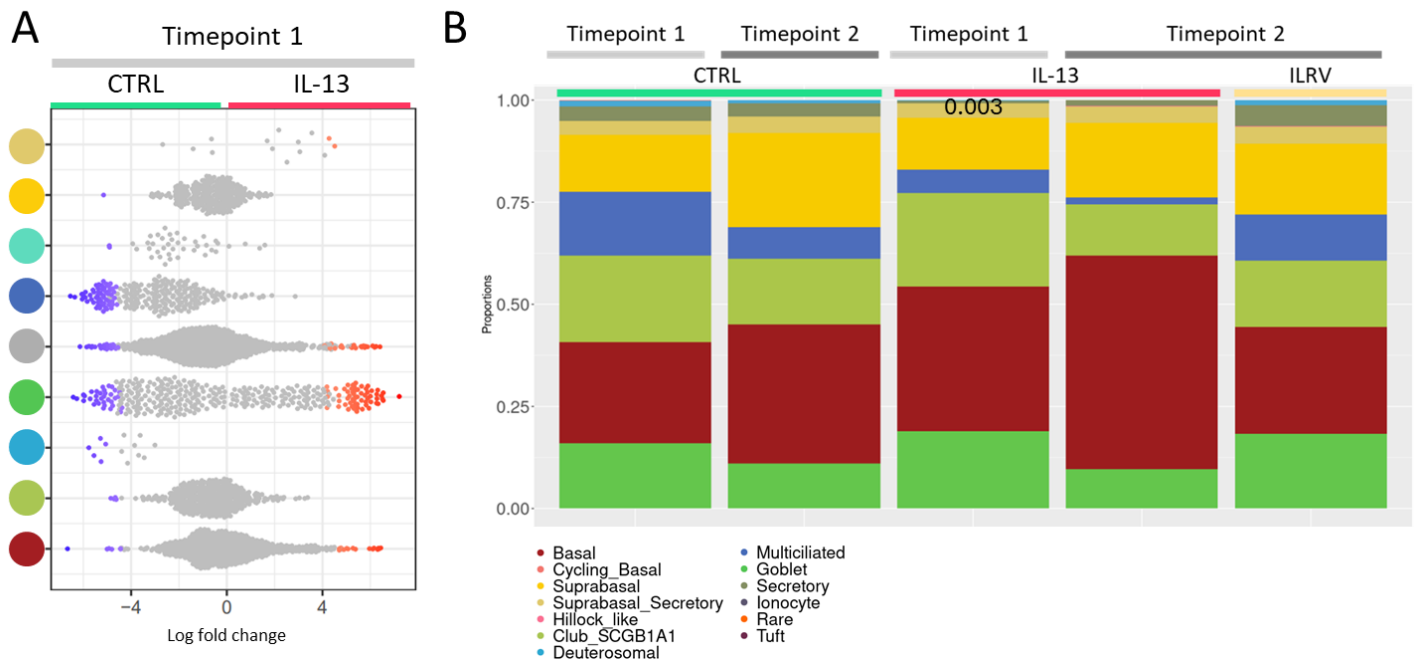


**Figure 65:** IL-13 induces remodeling in severe asthma airway epithelial ALI cultures.

**A:** Differential abundance of cell types between IL-13 treated and untreated severe asthma cells at timepoint 1 with Milo. Gray cell type indicates mixed cell neighborhoods. **B:** Proportion plot of cell types between IL-13 treated, untreated (CTRL) and ILRV (resolution) severe asthma cells at timepoint 1 and 2. *p-values* obtained by t-test.

### Severe asthma epithelia undergo a goblet to basal switch in response to chronic IL-13

Differential gene expression analysis at timepoint 1 revealed that similarly to healthy ALI cultures, goblet cells displayed the strongest transcription response with the most genes upregulated by IL-13 (**Fig.66A**). At timepoint2 however, the goblet cell response was decreased, and the basal cell response was dominant (**Fig.66B**). This is in agreement with what was observed with cell proportions with timepoint 1 centered around goblet cells and timepoint 2 dominated by basal cells, indicating a goblet to basal switch in the cellular and molecular response of asthma epithelia subjected to chronic IL-13.

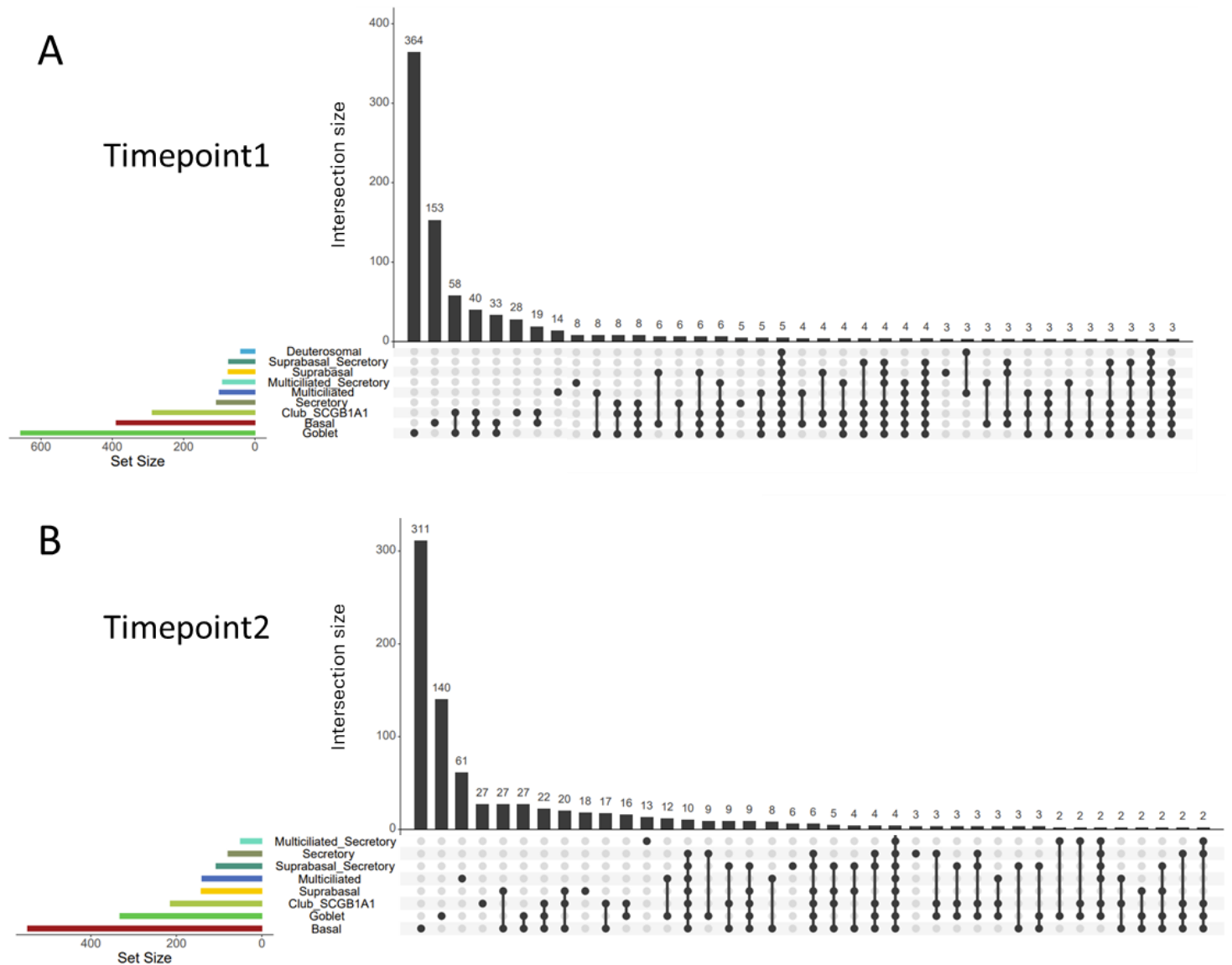


**Figure 66:** Severe asthma epithelium undergoes a goblet to basal switch under chronic IL-13 treatment. Upset plot of significantly upregulated genes ( $p$ -val < 0.05, logFC > 0) in IL-13 treated severe asthma airway epithelial cells at timepoint 1 (A) and timepoint 2 (B).

A closer look at goblet cells showed that, at timepoint 1, IL-13 treatment induced characteristic Th2 genes such as *LOXL4*, *CISH*, *ALOX15*, *CDH6*, *CDH26* and *FETUB* (Giovannini-Chami et al., 2012; Woodruff et al., 2009). Galectin genes such as *GALNT5* and *GALNT7* were also upregulated. Galectins are glycosyltransferase enzymes involved in the O-linked glycosylation of mucins (Fig.67A) (Tian et al., 2023). Thus, these genes could participate in IL-13-induced mucus hypersecretion. As expected, the goblet cell transcription factor *SPDEF* was strongly upregulated at timepoint 1 and 2 (Fig.67B) (K. S. Park et al., 2007). Interestingly, it also induced *KRT16* (Fig.67C). This keratin, that is usually specific to the suprabasal cell population, was already upregulated in asthma goblet cells compared to healthy goblet cells. Among the genes specifically induced at timepoint 1 but not timepoint 2 were genes involved in ion transport like *KCNK6* and *TRPM4* (potassium and calcium, respectively) (Nechipurenko,

2020; Toczyłowska-Mamińska & Dołowy, 2012) and vesicle trafficking such as *EXOC3*, a subunit of the exocyst complex (Wu & Guo, 2015) (**Fig.67D**). Fewer genes were specifically upregulated at timepoint 2 and not timepoint 1, among them *RAMP1*, which has been found to be negatively correlated to bronchial hyperresponsiveness in mice (M. Li et al., 2014), and *SCRN1*, involved in vesicle trafficking (Lindhout et al., 2019) (**Fig.67E**). Heatmap of the topmost differentially expressed genes projected on an expression matrix of goblet cells from all conditions (healthy, asthma, treatments and timepoints combined) showed an unsupervised clustering of CTRL and ILRV samples, indicating identical expression profiles between the two conditions and resolution of goblet cells transcriptome post IL-13 treatment (**Fig.67A**).

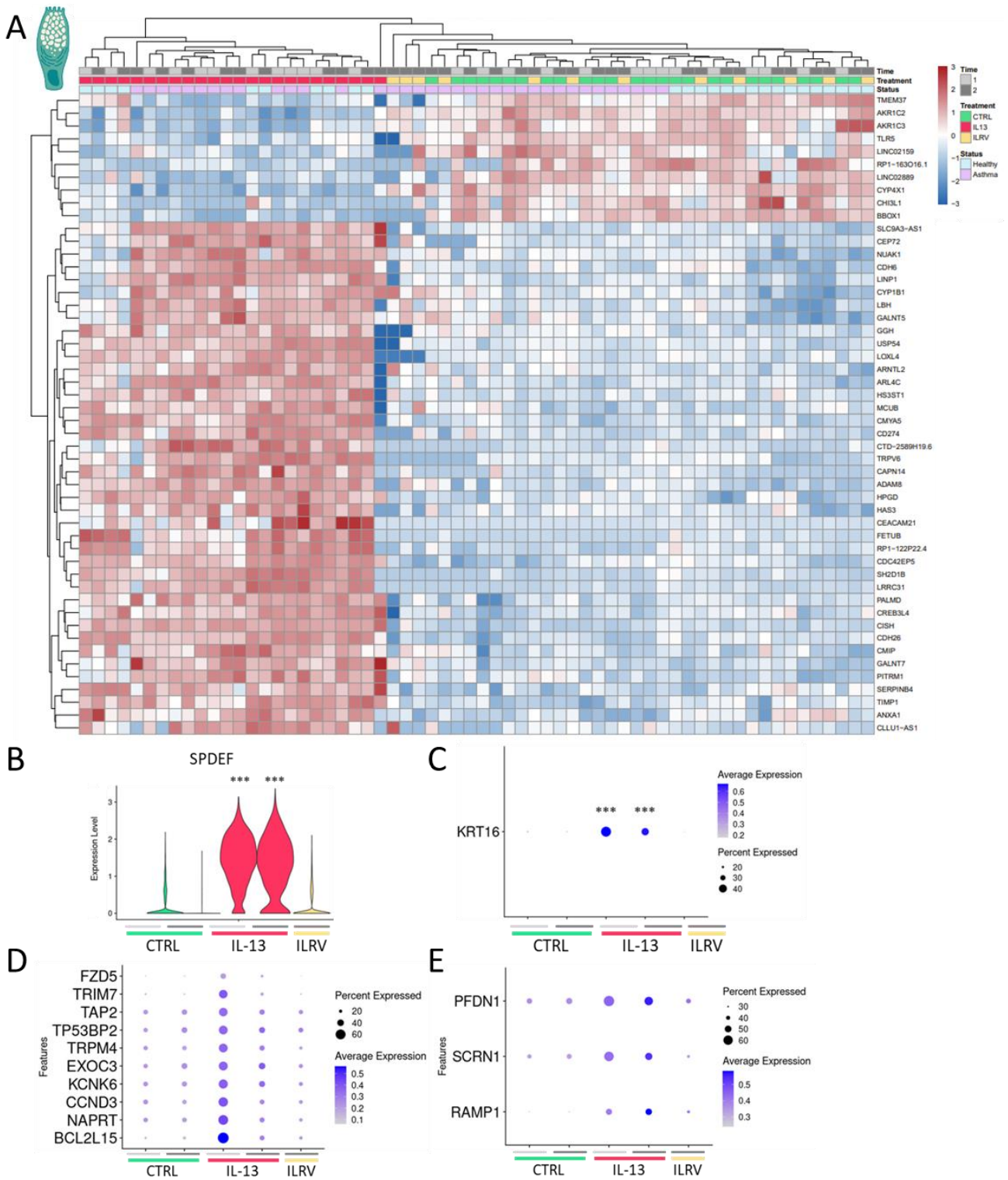


**Figure 67** : Differential gene expression between untreated and IL-13 treated severe asthma goblet cells.

**A:** Heatmap of the top 50 most differentially expressed genes ( $P$  val  $< 0.05$ ) in goblet cells at timepoint 1, projected on an expression matrix of all conditions and timepoints merged. **B:** Violin plot of *SPDEF* expression in severe asthma goblet cells depending on treatment and timepoint. **C:** Dot plot of *KRT16* expression in severe asthma goblet cells. **D:** Dot plot of some genes significantly upregulated ( $P$  val  $< 0.05$ ) in IL-13 treated goblet cells at timepoint 1 compared to untreated goblet cells (CTRL) at timepoint 1, that are not upregulated at timepoint 2. **E:** Dot plot of some genes significantly upregulated ( $P$  val  $< 0.05$ ) in IL-13 treated goblet cells at timepoint 2 compared to untreated goblet cells (CTRL) at timepoint 2, that are not upregulated at timepoint 1.  $p$ -values obtained by LRT-test.



As IL-13 treated severe asthma epithelia underwent basal cell hyperplasia at timepoint 2, I next focused my analysis on this population. IPA predicted a strong activation of the IL-13 pathway in IL-13 treated severe asthma basal cells at timepoint 1, through STAT6, STAT1 and STAT3 signaling (Fig.68).

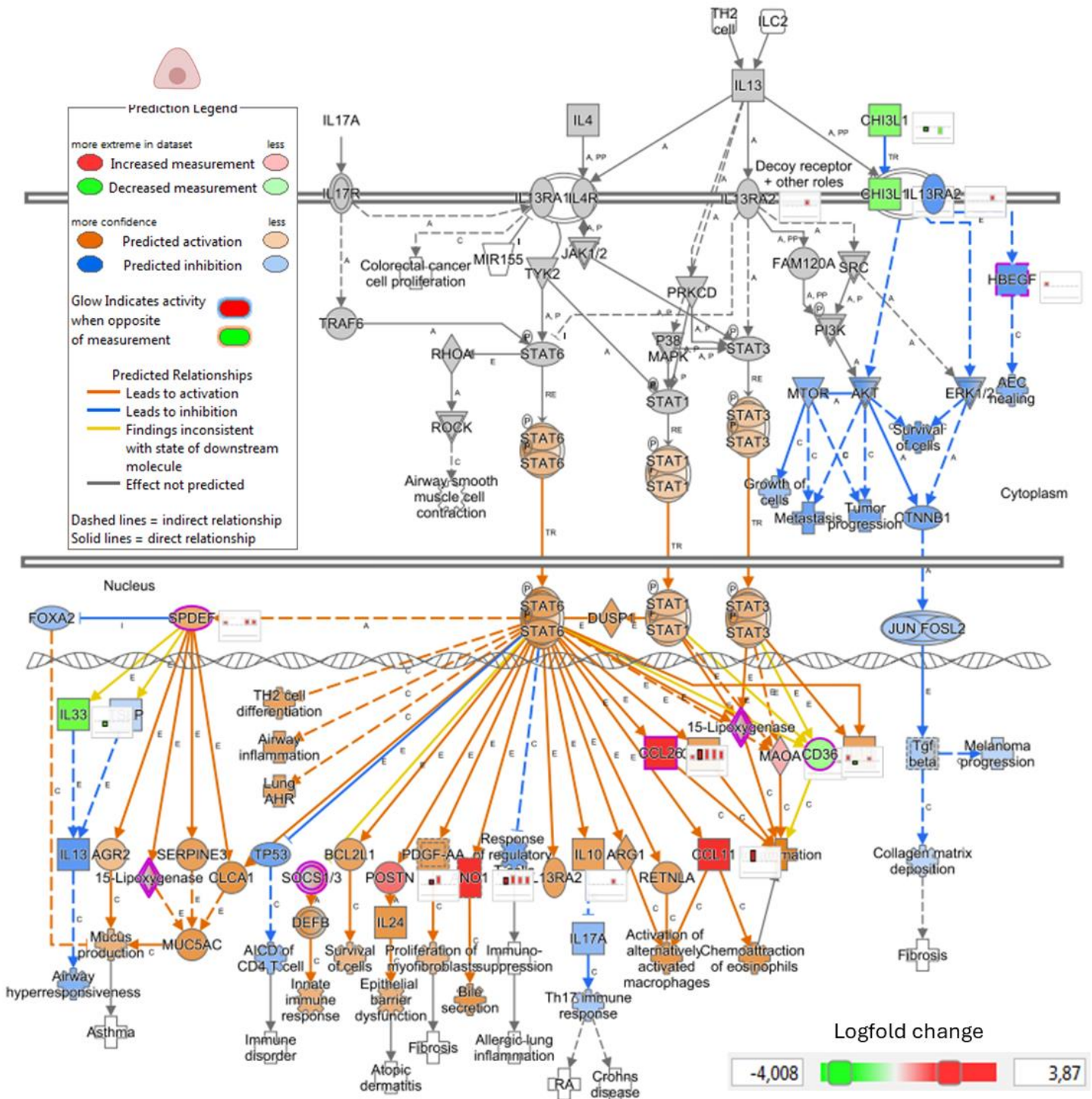


**Figure 68:** IL-13 activation in severe asthma basal cells. Ingenuity Pathway Analysis (IPA) prediction of IL-13 pathway activation in IL-13 treated severe asthma basal cells at timepoint 1.

At timepoint 2, in severe asthma basal, IL-13 induced the expression of typical Th2 genes similarly to what I observed in the other IL-13 treated cell types (*CDH6*, *CISH*, *CCL26*, *LOXL4*...) (**Fig.69A**). Basal and suprabasal specific keratins *KRT5*, *KRT6A* and *KRT16* were significantly downregulated in severe asthma basal cells after IL-13 treatment at timepoint 1 and/or 2 (**Fig.69B**), which could indicate a defective epithelial differentiation. Moreover, several developmental signaling pathways were dysregulated. Looking at the Notch pathway for example, the Notch ligands *DLL1* and *DLK2* were downregulated at timepoint 2. On the other hand, the hedgehog signaling was activated with the upregulation of the ligand *SHH* (**Fig.69C**). Moreover, the transcription factor *FOXA1*, upstream of *SPDEF*, was upregulated at both timepoints and some *SPDEF* transcripts were detectable, although not significantly, indicating an early specification of basal cells toward the goblet cell lineage (**Fig.69D**). Lastly, I also noticed a specific epithelial to mesenchymal transition (EMT) signature extracted from the GSEA HALLMARK\_EPITHELIAL\_MESENCHYMAL\_TRANSITION signature, in a subset of basal and suprabasal IL-13 treated asthma cells. This signature comprised collagen genes (*COL11A1*, *COL5A3*, *COL6A3*...) and fibroblasts marker like *DCN* and *CTHRC1* which is associated with fibrosis (**Fig.69E**) (Tsukui et al., 2020).

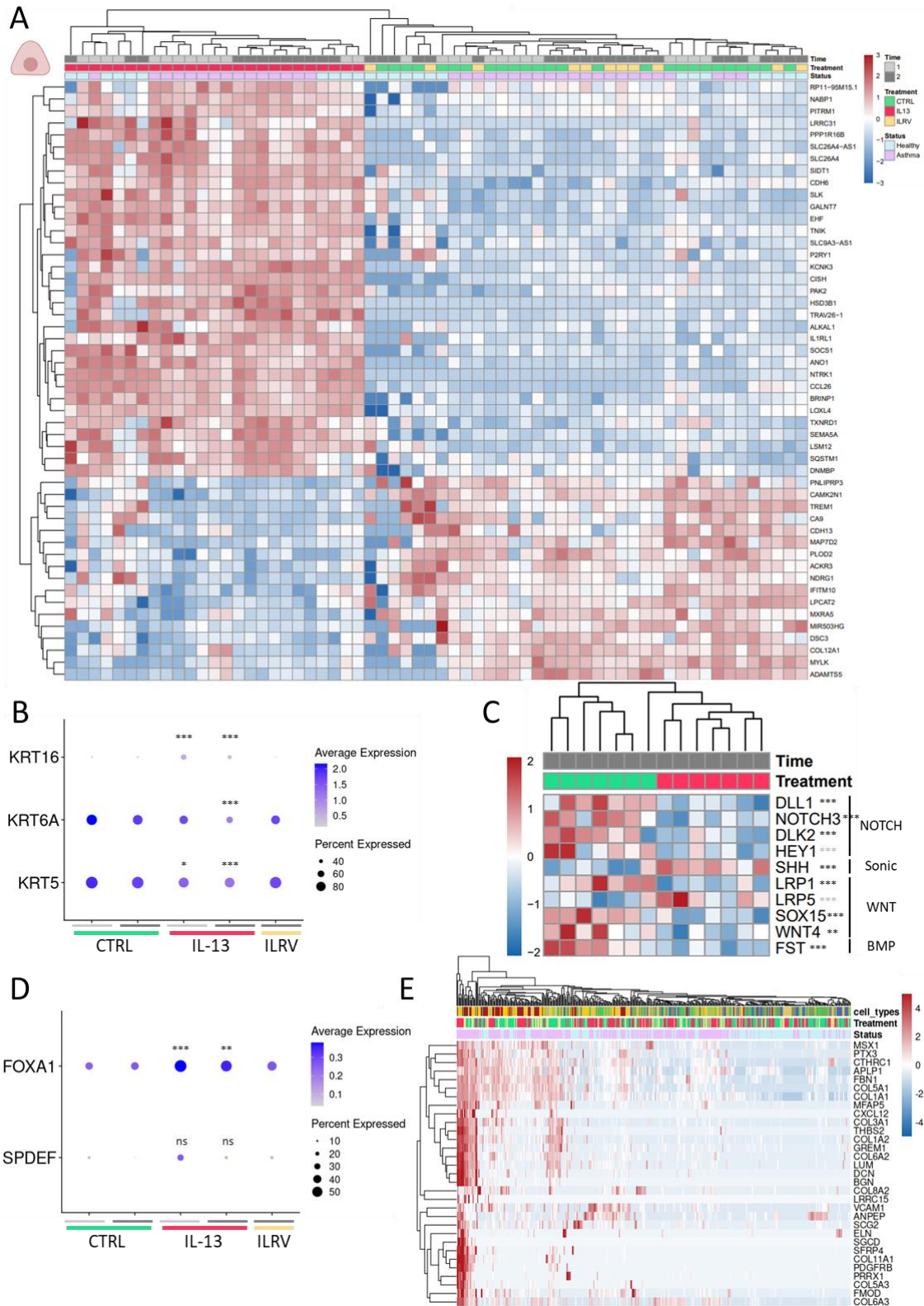


**Figure 69:** Differential gene expression between untreated and IL-13 treated severe asthma basal cells.

**A:** Heatmap of the top 50 most differentially expressed genes ( $p$ -val < 0.05) in basal cells at timepoint 2, projected on an expression matrix of all conditions and timepoints merged. **B:** Dot plot of KRT genes expression in severe asthma basal cells. **C:** Heatmap of developmental signaling pathways genes in severe asthma basal cells at timepoint 2. Black stars indicate statistical significance at timepoint 2, and gray stars indicate statistical significance at timepoint 1 only. **D:** Dot plot of goblet cells related genes expression in severe asthma basal cells. Stars indicate statistical significance of a condition compared to its timepoint-matched control. **E:** Heatmap of EMT related genes projected on an expression matrix of all conditions and timepoints merged.  $p$ -values obtained by LRT-test.

Taken together, these results show that severe asthma ALI-cultured epithelium can respond to IL-13 treatment and that IL-13 triggered a goblet to basal switch with a remodeling going from a goblet cell hyperplasia at timepoint 1 to a basal cell hyperplasia at timepoint 2. The response to IL-13 is robust, with hundreds of genes induced in most cell types. Interestingly, goblet and MCCs appeared to transition toward a somewhat dedifferentiated state by gaining basal cell markers while basal cells acquired secretory markers. Similarly to what was observed in healthy epithelium, in all severe asthma cell types, plotting of the topmost differentially expressed genes on a heatmap with an expression matrix of cells of the same cell type but from all conditions (healthy, asthma, treatments and timepoints combined) (**Fig.67A** and **Fig.69A**) showed an unsupervised clustering of sample per treatment. IL-13 treated samples clustered alone while CTRL and ILRV (resolution) samples clustered together, indicating a complete resolution of the transcriptomic signature of samples that are no longer treated (ILRV) and is now undistinguishable from the CTRL ones.

## Comparison of the differences in response to IL-13 between asthmatic and healthy epithelia

### Asthma epithelium is more reactive to IL-13

After I characterized the individual response of healthy and of severe asthma to IL-13, I compared directly the two responses to identify asthma-specific mechanisms of the airway epithelium to inflammation. IL-13 induced *MUC5AC* mRNA expression in healthy and in asthma epithelia ( $p\text{-val} = 1.2\text{e-}05$  and  $1\text{e-}06$ , respectively) (**Fig.70A**). This induction was also observed at the protein level by performing ELISA assay on the apical secretions collected from the ALI culture inserts although not significantly for asthma secretions, which might be due to sample variation (**Fig.70B**). No significant changes in *MUC5B* mRNA were detected, although *MUC5B* levels seem to decrease in both healthy and severe asthma conditions after IL-13. Surprisingly, expression of *MUC5B* protein level was increased in asthma apical secretions, and a non-significant increase trend was observed in healthy secretions (**Fig.70C**). This discrepancy between mRNA and protein levels could be explained by differential regulation in mucin expression such as glycosylation and exocytosis. Another, simpler explanation would be a technical issue such as poor detection of *MUC5B* by the antibody or interference with other secreted proteins.

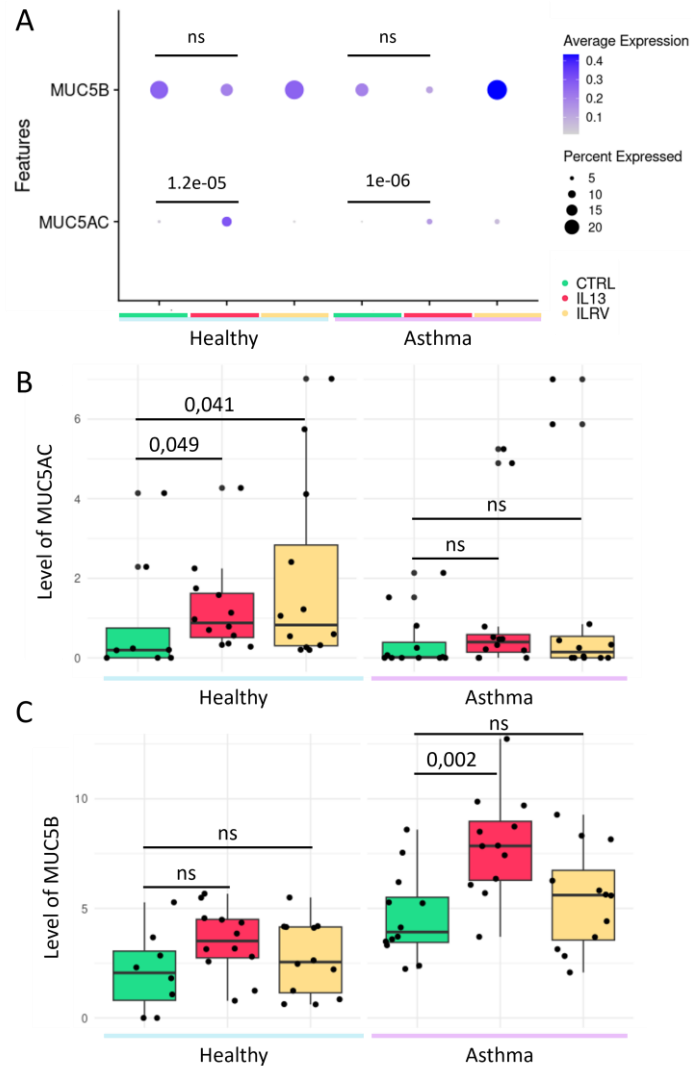


**Figure 70:** IL-13 induces mucus secretion in both healthy and severe asthma ALI cultures at timepoint 2.

**A:** Dot plot of *MUC5AC* and *MUC5B* mRNA expression in healthy and severe asthma goblet cells. ELISA detection of MUC5AC (**B**) and MUC5B (**C**).

Comparison of the number of genes differentially expressed in IL-13 treated asthma and healthy epithelia revealed that asthma epithelium had a broader response to treatment with more genes upregulated in each cell type, at the exception of MCCs and goblet cells that had more IL-13 upregulated genes in healthy samples (**Fig71A**). To appreciate the distribution of the genes differentially expressed I plotted the same data by strip plot and noticed that the asthma epithelium also has a stronger response to IL-13, as in all cell types at the exception of the deuterosomal cells, genes in IL-13 severe asthma cells had a higher maximum log fold change than in healthy epithelia, with CCL11 (coding for eotaxin) and CCL26 (coding for eotaxin-3) having a log fold change superior to 10 in certain asthma cell types. Eotaxins are eosinophil-attracting chemokines that contribute to the inflammation observed in asthma airways by promoting the recruitment eosinophils and other immune cells (Pease & Williams, 2001) (**Fig71B**).

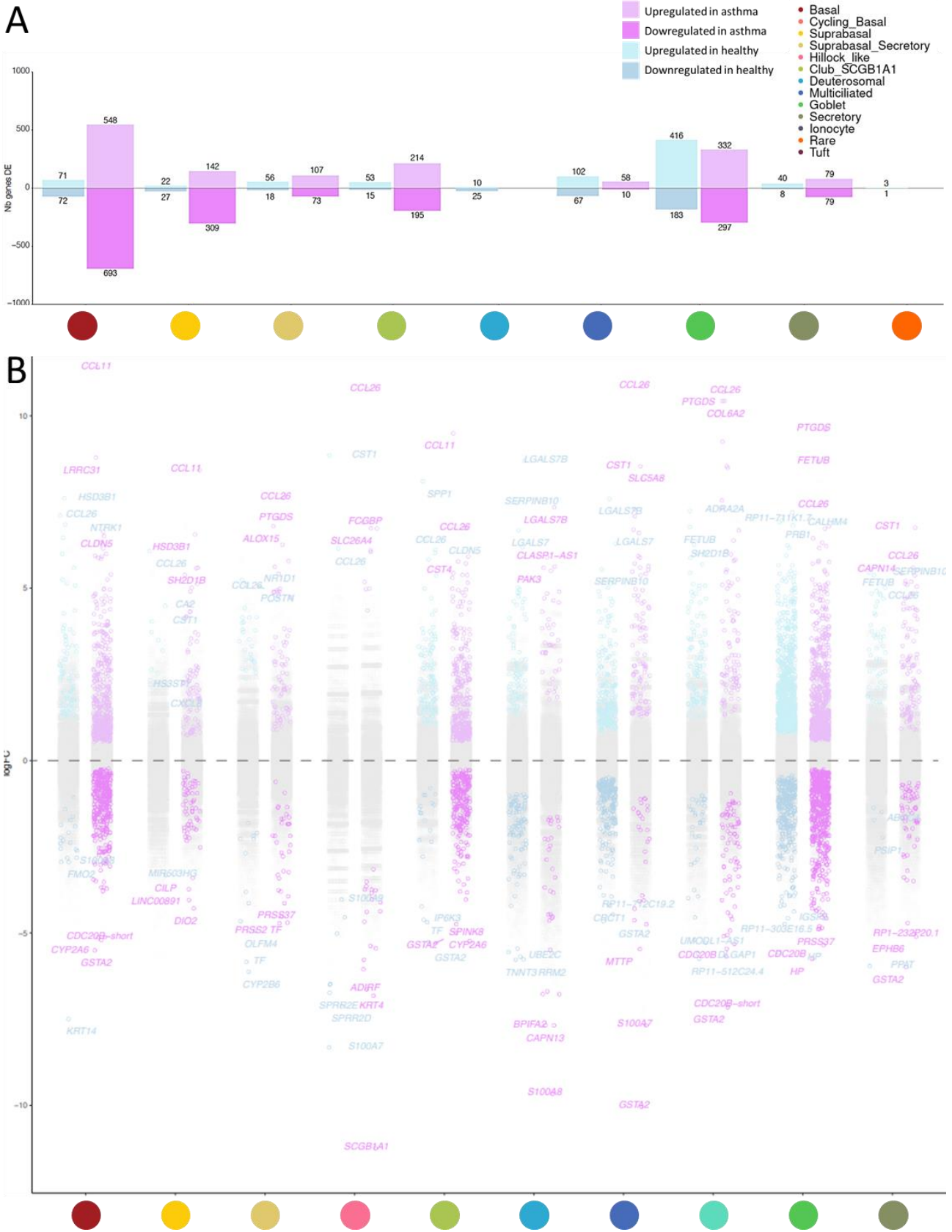


**Figure 71:** Differences in amplitude response between healthy and severe asthma epithelia.

**A:** Bar plot showing the number of upregulated and downregulated genes between healthy and severe asthma epithelia, per cell type.  
**B:** Strip plot showing the number of upregulated and downregulated genes between healthy and severe asthma epithelia, per cell type.

Next, among the differentially regulated genes, I compared those that were unique or common to each condition (healthy epithelium treated with IL-13 at timepoint 1 or 2 and asthma epithelium treated with IL-13 at timepoint 1 or 2) in basal (**Fig.72A**), goblet (**Fig.72C**) and MCCs (**Fig.72E**). In basal cells, *POSTN*, a well-known marker of asthma (Woodruff et al., 2007), was only upregulated in the healthy condition (**Fig.72B**). This could suggest that severe asthma basal cells are already at their maximal transcriptional capacity for *POSTN* and that it cannot be more upregulated or that the induction is not strong enough to be statistically significant. The upregulation of genes involved in calcium signaling such as *TENM2* (Silva et al., 2011) and *CAMK1D* (Verploegen et al., 2005) could participate in fluid secretion or generation of reactive oxygen species. Genes specifically upregulated in severe asthma basal cells were related to immune signaling (*PIGR*, *IFIT2*, *TMPRSS2* or *IL1RL1*) (**Fig.72B**). Among the most upregulated genes in basal cells of both conditions were *EHF*, an epithelial-specific transcription factor that may play a role in the regulation and differentiation of certain epithelial tissues (Reehorst et al., 2021), *GATA3*, a gene coding for an important regulator of T cell development (Koretzky et al., 2002) and *TNIK*, an activator of the WNT pathway (Mahmoudi et al., 2009) that has been implicated in asthma (Legaki et al., 2022) (**Fig.72B**).

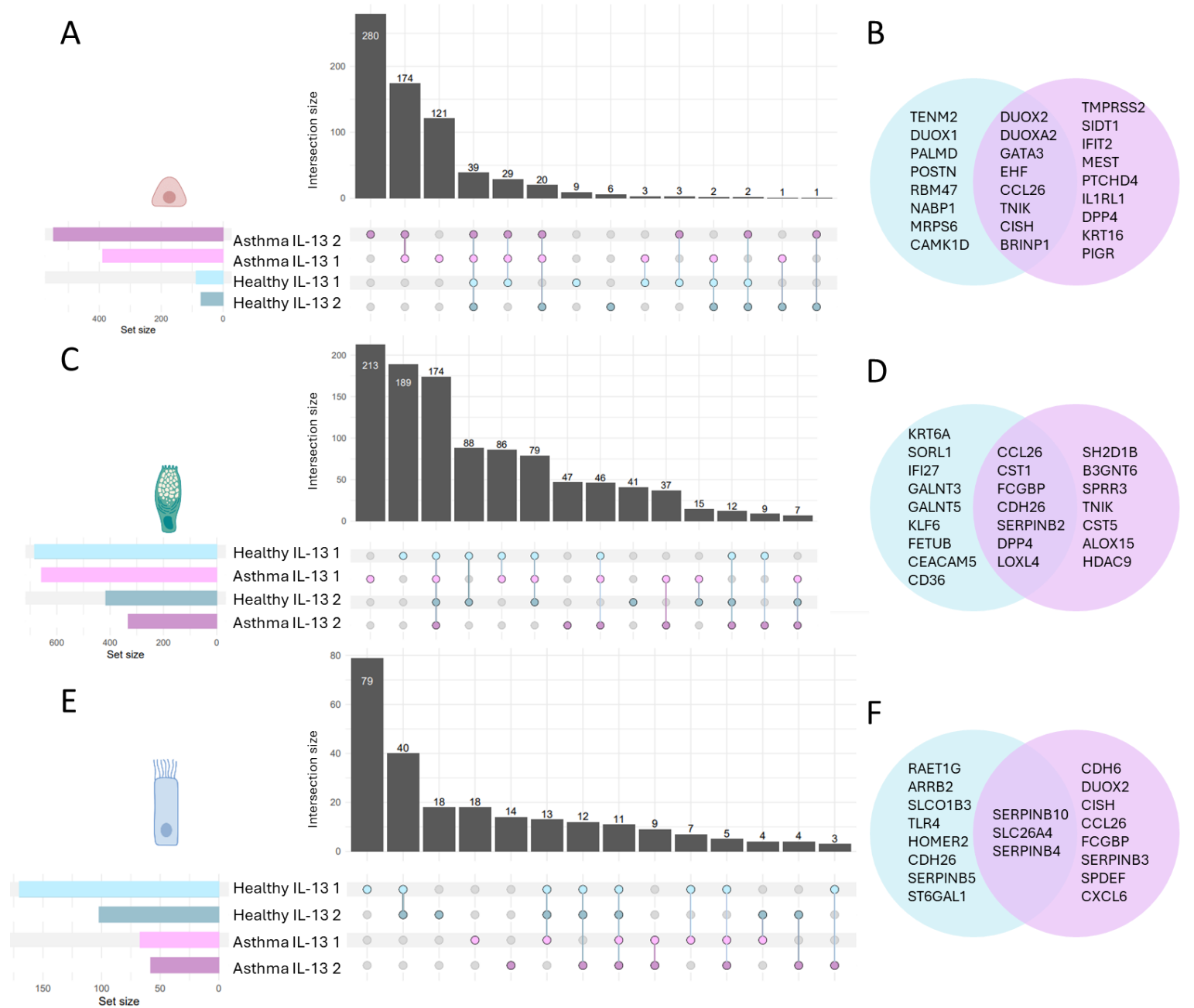


**Figure 72:** Comparison of IL-13 response between healthy and severe asthma epithelia across timepoints. Upset plot of upregulated genes between healthy and severe asthma epithelia, at timepoint 1 or 2 in basal (A), goblet (C) or MCC (E). Venn diagrams displaying curated selections of genes in healthy (light blue) or asthma (light pink) cells at either timepoint, in basal (B), goblet (D) or MCC (F).



## Cell trajectories inference

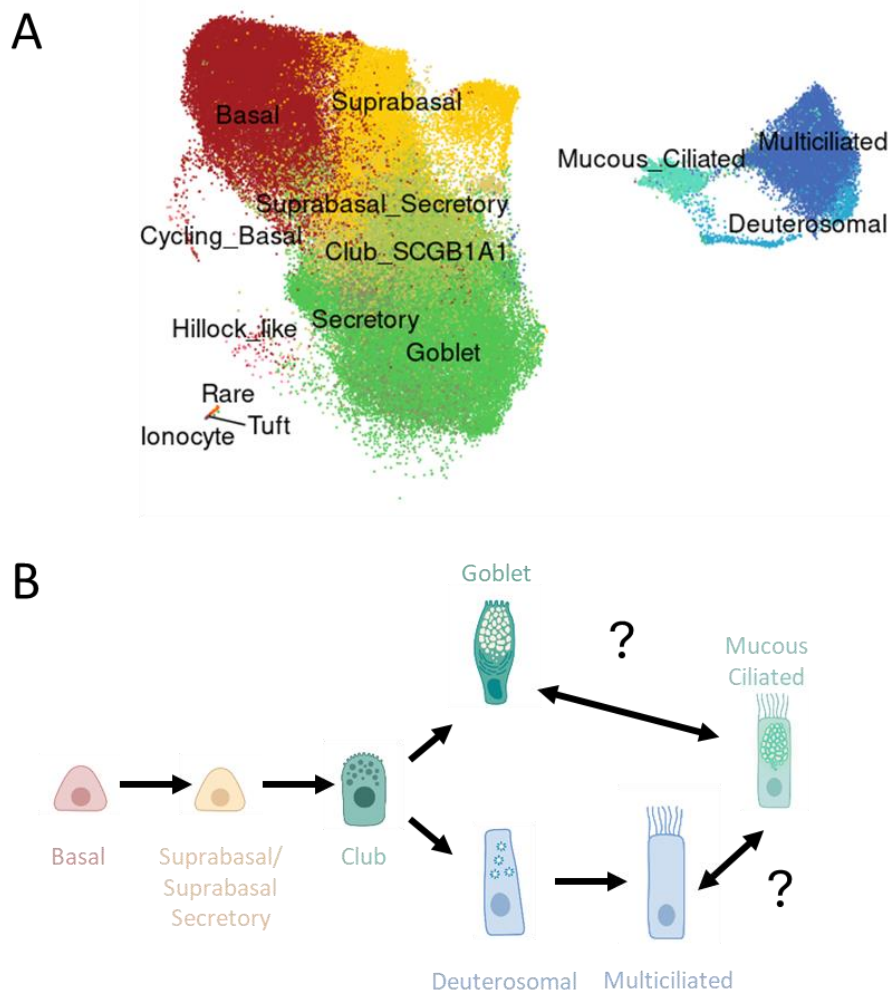


**Figure 73:** How to infer cell trajectories among airway cell types?  
**A:** UMAP of the IL-13 dataset labeled by cell type. **B:** Canonical and putative (question mark) airway epithelial cell trajectories.

The analysis of my asthma-centric perturbation atlas revealed molecular events related to IL-13 induced remodeling and allowed me to identify a discrete population of hybrid goblet/MCC cells (**Fig73A**) that are enriched in IL-13 treated conditions. Although similar hybrid cells have been identified by my team (Deprez et al., 2020) and others (Vieira Braga et al., 2019), it is unclear whether these cells emerge from the transdifferentiation of goblet cells, the transdifferentiation of MCCs, or both (**Fig.73B**). To better characterize this remodeling, I analyzed and compared the cellular trajectories (paths taken from cells transitioning from one state to another) taken by epithelial cells with or without IL-13 induced remodeling.

## Introduction to cell trajectories

Cell differentiation trajectories describe the paths that cells take as they transition from one cell state to another, usually a progenitor or stem cell state to a more final differentiated state. These trajectories capture the dynamic process of cell fate decisions, showing how cells progress through various intermediate states before reaching their mature form. To adapt to injuries and insults, tissues can undergo remodeling and cells adopt new trajectories. Under pathological conditions, these trajectories can be disturbed and lead to tissue dysfunction such as defective mucociliary clearance in asthma (see [Remodeling in asthma](#)).

While traditional lineage tracing such as mice with specific reporter cell lines offers direct and unambiguous lineage relationships by directly tracking cell divisions and migrations, no equivalent system exists for human primary cell models. The only robust approach available to us to perform “cell trajectories” was lineage inference through computational analysis of single-cell transcriptomes. Cells can be analyzed through pseudotime analysis, that orders cells along a continuous trajectory based on their gene expression profiles to see the progression of cells along the inferred trajectory, with pseudotime values assigning cells a relative distance from one cell determined as an initial point, regardless of its lineage and terminal fates. This information is then used for trajectory inference. Here I used a computational method using CellRank to perform the trajectory inference visualizable in low dimensions (i.e. 2D plots). The CellRank framework predicts lineage-specific fates using transition matrices that can be produced by different kernels (such as velocity-based or connectivity-based kernels) depending on the data and research focus. To infer trajectories, we chose the Pseudotime kernel, using information from the Palantir pseudotime. This kernel is used to generate a cell-cell transition matrix. From the transition matrix are defined “macrostates”, which are distinct cell states that represent groups of cells with similar fate potential, based on transition probabilities. Among the macrostates, Palantir then identified groups of most stable or terminally differentiated cells as the terminal macrostates. We chose our parameters based on the results obtained in the “Healthy CTRL timepoint 2” group, that we selected as reference since it was our most physiologically relevant group. Analysis of one timepoint was sufficient to reconstruct cell trajectories in our ALI model, as mature *in vitro* epithelia retain all transitory cells. All cell trajectories inference results are presented at timepoint 2 for simplicity. Goblet and multiciliated terminal macrostates defined by CellRank are represented in **Figure74A&B** for healthy CTRL and asthma CTRL, **Figure75A&B** for healthy IL13 and asthma IL13 and **Figure77A&B** for healthy ILRV and asthma ILRV. The fate probabilities toward goblet or MCC state according to conditions are summarized in **Table 2** below, for better comprehension.

### Multiciliated cells are more likely to transition to goblet cells in asthma

The probabilities of any cell to differentiate into a given cell type is represented on a fate probability map that color code cells with the lowest fate probability in dark blue (0%) and cells with the highest fate probability in yellow (100% = already differentiated into the state analyzed). Here I looked, in all conditions, at the probability of one of the cell types I have annotated (**Fig.73A**) of becoming either a “goblet terminal macrostate” or a “multiciliated terminal macrostate”, which are subpopulations identified by CellRank as being the most terminally differentiated cells (most stable RNA velocity) among the other cells. To avoid confusion, I will refer to the cell populations I have annotated as “types” and the cell macrostates identified by CellRank as “states”.

When observing the fate probability of untreated healthy cells at timepoint 2 (reference group) to reach a goblet state (goblet terminal macrostate), most cells were dark green (medium probability) at the exception of the goblet cell type (yellow, already differentiated to goblet cells) and MCCs which were dark blue (very low probability) (**Fig.74C**). Interestingly, a couple of cells situated at the mucous-ciliated cell type cluster location had a higher probability than the rest of the MCCs to become a goblet state cell (**Fig.74C**, red arrow). By representing this score on a violin plot (**Fig.74G**), I estimated that most cell types had a probability of about 40% to become a goblet state cell, including goblet cells, which suggests that at baseline, most cells typed as goblet are not terminally committed to their cell state and remain plastic. Deuterosomal cells and MCCs had the lowest score (<10 and close to 0%, respectively) (**Fig.74G**, red box). Most cells had a higher fate probability of becoming multiciliated state cells, as represented by the light green score on the fate probability map (**Fig.74D**, red arrow) of basal, suprabasal and secretory cells, and by the yellow score of deuterosomal and MCCs (in agreement with the fact that they are already committed to becoming MCCs). The goblet terminal macrostate was the least likely to transition to MCCs as it was dark blue, confirming that this subpopulation was indeed terminally differentiated (**Fig.74D**). Looking at the violin plot of fate probability of becoming a MCC state revealed that rare cells were the least likely to transition to a MCC state, while all other cell types had a ~60% probability. Deuterosomal and multiciliated cell types had a ~100% fate probability of becoming an MCC, indicating that they are fully committed to the MCC lineage (**Fig.74I**).

Next, I analyzed the fate probabilities in the asthma CTRL condition (**Fig.74B**). Interestingly, the fate probability of becoming a goblet state cell was much higher than in healthy CTRL cells, as most cell types scored at around 90 to 100% (**Fig.74E&H**). Cells located at the mucous-secretory cluster score higher than the rest of the MCCs (~60% compared to ~10%, respectively) (**Fig.74E**, red arrow). Severe asthma MCCs had a higher probability of becoming a goblet cell than healthy ones (**Fig.74H**, red box compared to **Fig.74G**, red box).

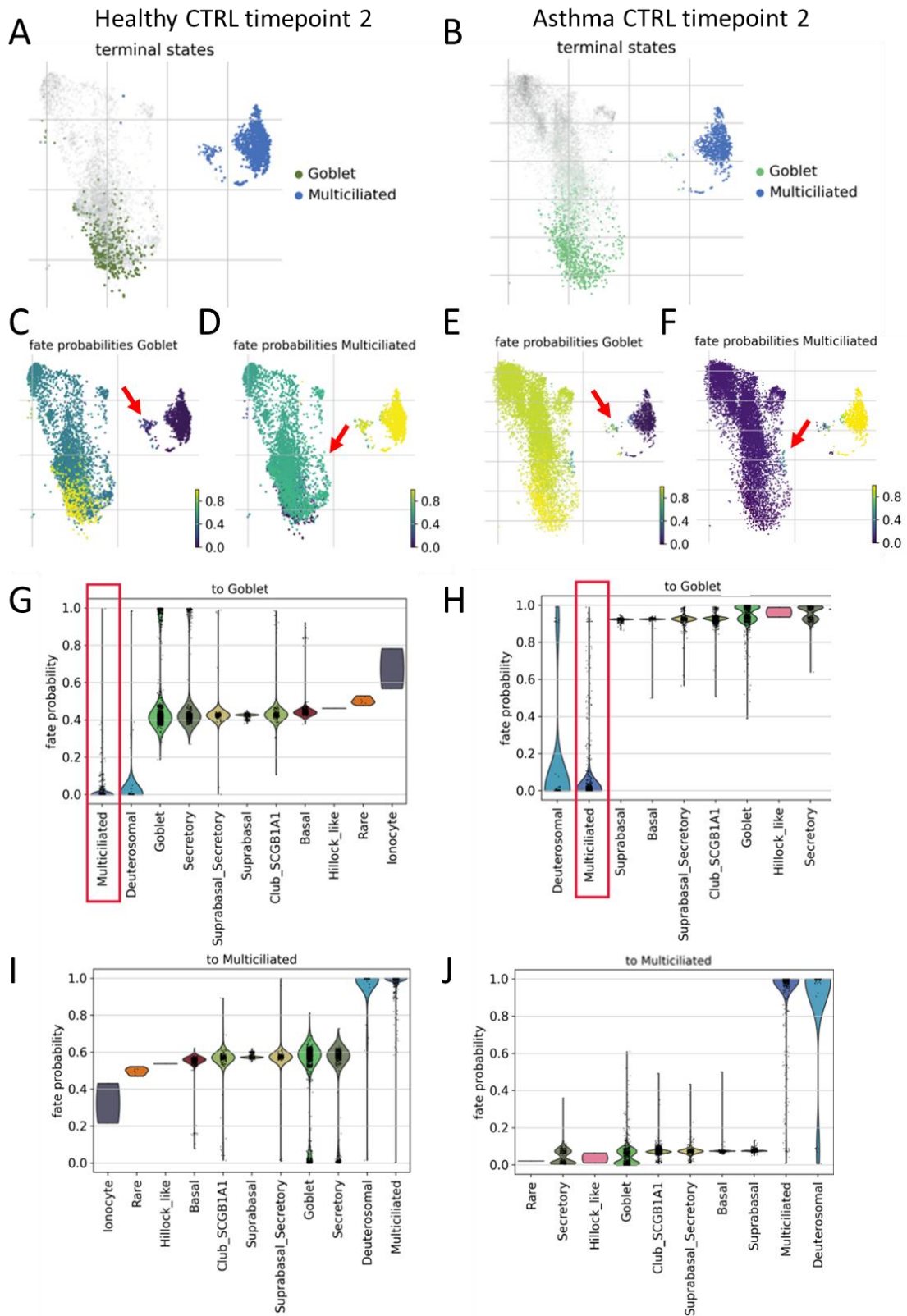


**Figure 74:** Cell fate probabilities at baseline, timepoint 2. Map of terminal state cells in healthy CTRL 2 epithelium (A) and severe asthma CTRL 2 epithelium (B). Fate probability map of a cell to become a goblet terminal macrostate in healthy CTRL 2 epithelium (C) and severe asthma CTRL 2 epithelium (E). Fate probability map of a cell to become a MCC terminal macrostate in healthy CTRL 2 epithelium (D) and severe asthma CTRL 2 epithelium (F). Violin plot of the fate probability of a cell to become a goblet terminal macrostate in healthy CTRL 2 epithelium (G) and severe asthma CTRL 2 epithelium (H). Violin plot of the fate probability of a cell to become a MCC terminal macrostate in healthy CTRL 2 epithelium (I) and severe asthma CTRL 2 epithelium (J).

Reciprocally, severe asthma cells had a lower fate probability of becoming a multiciliated state cell than healthy cells, all cell types scored lower than 10%, at the exception of a subgroup of goblet cells (**Fig.74F**, red arrow, and **Fig74H.**) and of deuterosomal and MCCs that score between 80 and 100% (**Fig.74J**).

Overall, compared to a healthy epithelium, the severe asthma epithelium is strongly skewed toward a secretory fate.

### IL-13 increases multiciliated cell to goblet cell transition probability

After IL-13 treatment, the probability of most cell types to become a goblet state rose to 80% in the healthy epithelium (**Fig.75C&G**) and to more than 80% in severe asthma epithelium (**Fig.75E&H**). MCCs fate probability to differentiate to the goblet state increased in both conditions, most noticeably in asthma IL-13 where it exceeded 20% (**Fig.75H**, red box). Reciprocally, the probability of most cell types to differentiate to a MCC state dropped to 20% in healthy epithelium (**Fig.75D&I**) and <20% in the severe asthma epithelium (**Fig.75F&J**). This probability also decreased in MCCs of both conditions. Interestingly, in severe asthma, the violin plot of the probability of MCCs to become a goblet state of MCC state became bimodal. A second discrete MCC population seemed to detach from the first one after IL-13 treatment and could possibly be the mucous-ciliated cell population.

Cell trajectories and pseudotime progression can be visualized on diffusion maps, where arrows indicate the inferred direction of cell differentiation through pseudotime (pseudotime flow). I compared the two most extreme conditions of timepoint 2, healthy CTRL (reference) and asthma IL-13 to highlight the perturbations caused by IL-13 remodeling (**Fig76.**). At homeostasis (healthy CTRL) differentiation starts with basal cells that differentiate into suprabasal then club cells which then either turn into goblet cells (secretory trajectory) or into deuterosomal cells and finally MCCs (MCC trajectory) (**Fig76.A**, highlighted by magenta arrows). In IL-13 treated asthma epithelium the secretory trajectory is conserved, however, the pseudotime flow of MCCs is direct toward the secretory and goblet cells, indicating that the MCC trajectory is diverted toward the secretory lineage (**Fig76.B**, highlighted by magenta arrows). This strongly suggests that, in asthma, multiciliated cells differentiate to goblet cells.

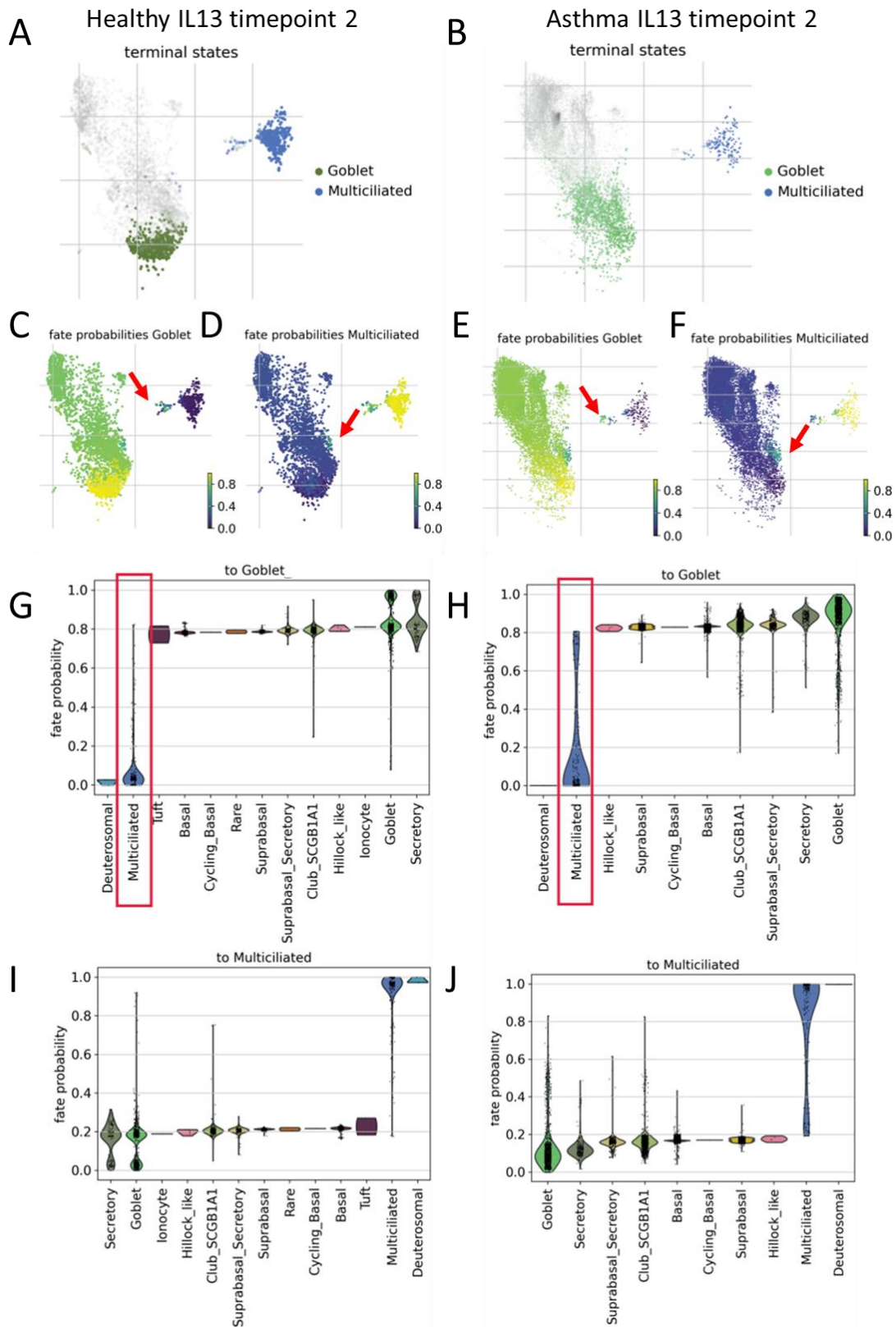


**Figure 75:** Cell fate probabilities after IL-13 treatment, timepoint 2.

Map of terminal state cells in healthy IL-13 2 epithelium (**A**) and severe asthma IL-13 2 epithelium (**B**). Fate probability map of a cell to become a goblet terminal macrostate in healthy IL-13 2 epithelium (**C**) and severe asthma IL-13 2 epithelium (**E**). Fate probability map of a cell to become a MCC terminal macrostate in healthy IL-13 2 epithelium (**D**) and severe asthma IL-13 2 epithelium (**F**). Violin plot of the fate probability of a cell to become a goblet terminal macrostate in healthy IL-13 2 epithelium (**G**) and severe asthma IL-13 2 epithelium (**H**). Violin plot of the fate probability of a cell to become a MCC terminal macrostate in healthy IL-13 2 epithelium (**I**) and severe asthma IL-13 2 epithelium (**J**).

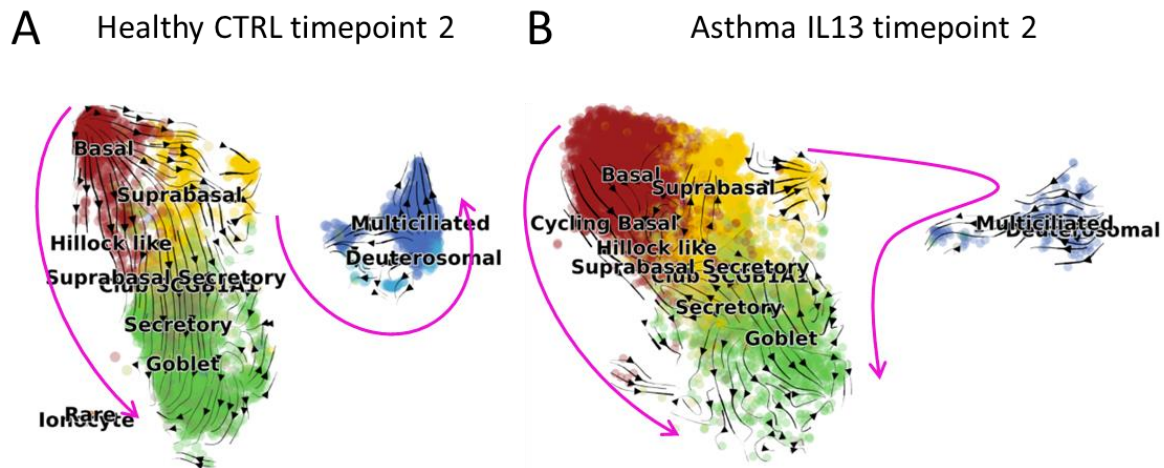


**Figure 76:** Visualization of pseudotime flow highlights IL-13 perturbations. Diffusion maps of healthy CTRL epithelium (A) compared to IL-13 treated epithelium (B) at timepoint 2. Magenta arrows represent the flow of the two major cell trajectories in each condition.

### Differences in recovery dynamics between healthy and severe epithelia

Lastly, I compared the two resolution conditions (healthy ILRV and asthma ILRV) to apprehend the cell trajectories leading to the recovery of the initial state of the epithelium after IL-13 induced inflammation in healthy and severe asthma epithelia. In healthy epithelium, fate probabilities of most cell types (basal, suprabasal, club, secretory, goblet, rare) toward the goblet state or the MCC state went back to their initial state (40% and 60% respectively), at the exception of a subgroup of goblet and secretory cells that remained ~100% committed to goblet cell state (**Fig.77C&G**) (or 0% committed to the MCC state, **Fig.77D&I**). This subgroup of fully committed cells could serve as a “quick starter” to induce a fast secretory response in case of a future new insult. The MCC cell type also recovered its initial probabilities of 0% toward the goblet state (**Fig.77C&G**) and 100% toward the MCC state (**Fig.77D&I**).

On the contrary, fate probabilities of the severe asthma epithelium were not completely back to their CTRL levels. Most cell types were less committed to the goblet state with 80-100% at resolution (**Fig.77E&H**), compared to 90-100% in the control condition. Reciprocally, cells were more committed to the MCC state with 20% for the ILRV condition compared to 10% in the control condition. This could indicate that severe asthma cells are slower at recovery than the healthy ones and that some severe asthma cells are still in the process of re-ciliating the epithelium 14 days after the last IL-13 treatment (timepoint 2).

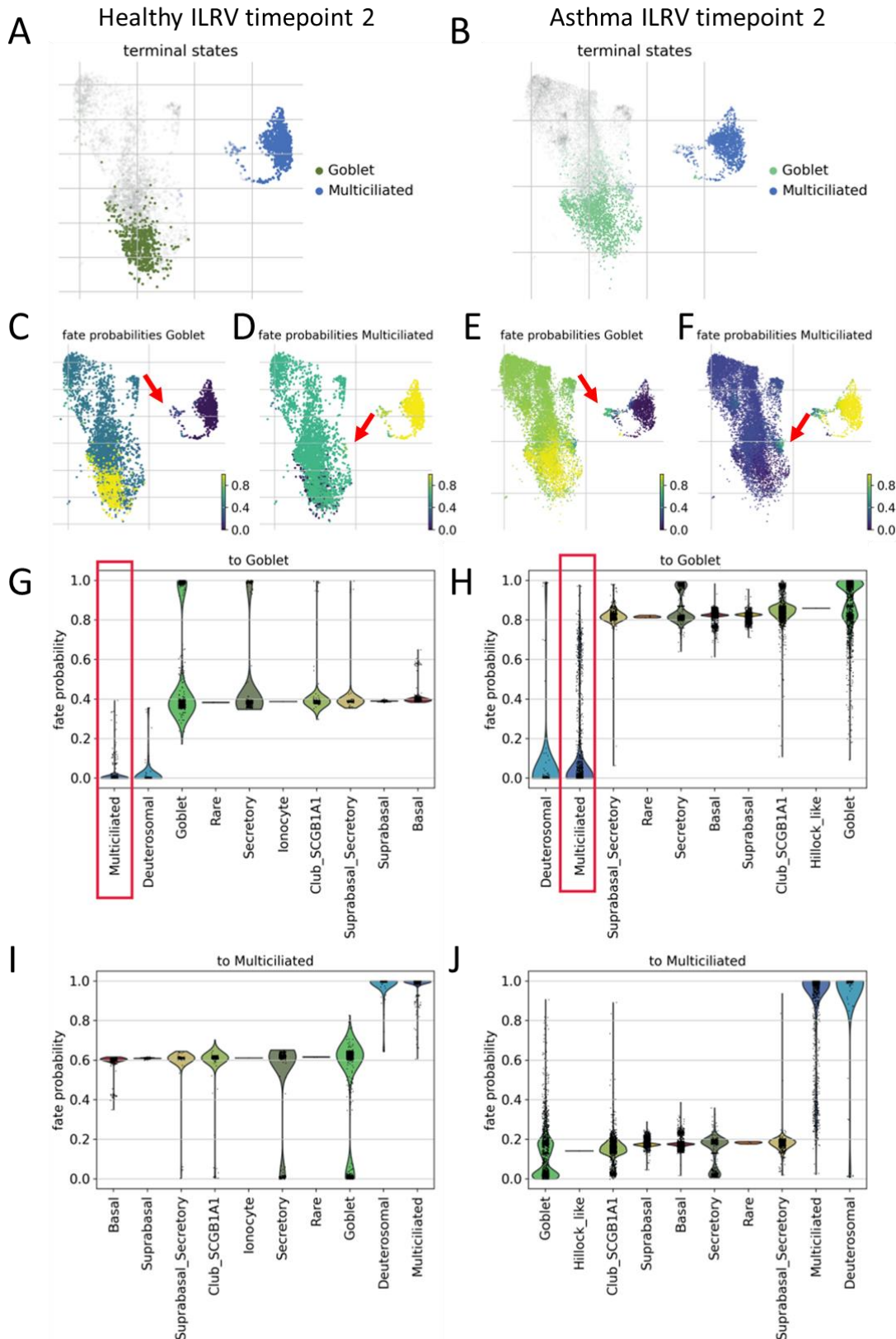


**Figure 77** : Cell fate probabilities at resolution (ILRV), timepoint 2.

Map of terminal state cells in healthy ILRV 2 epithelium (**A**) and severe asthma ILRV 2 epithelium (**B**). Fate probability map of a cell to become a goblet terminal macrostate in healthy ILRV 2 epithelium (**C**) and severe asthma ILRV 2 epithelium (**E**). Fate probability map of a cell to become a MCC terminal macrostate in healthy ILRV 2 epithelium (**D**) and severe asthma ILRV 2 epithelium (**F**). Violin plot of the fate probability of a cell to become a goblet terminal macrostate in healthy ILRV 2 epithelium (**G**) and severe asthma ILRV 2 epithelium (**H**). Violin plot of the fate probability of a cell to become a MCC terminal macrostate in healthy ILRV 2 epithelium (**I**) and severe asthma ILRV 2 epithelium (**J**).



**Table 2:** Summary of fate probabilities toward goblet or MCC state according to conditions.

Condition	Cell type	Fate probability to goblet state (%)	Fate probability to MCC state (%)
Healthy CTRL	Goblet	40	60
	MCC	<10	100
	Other	40	60
Asthma CTRL	Goblet	90-100	0-10
	MCC	>10	90-100
	Other	90	10
Healthy IL-13	Goblet	80-100	0-20
	MCC	10	90-100
	Other	80	20
Asthma IL-13	Goblet	90	0-20
	MCC	0-80	20-100
	Other	>80	<20
Healthy ILRV	Goblet	30-100	0-80
	MCC	0	100
	Other	30-100	60
Asthma ILRV	Goblet	80-100	0-30
	MCC	15-20	80-100
	Other	80-100	20

## Characterization of cell types and states induced by rhinovirus A16 in healthy and severe asthma epithelia

### Rhinovirus A16 infection does not induce remodeling in ALI cultures

Lastly, I compared the response of healthy and severe asthma epithelia to another asthma-related triggered, the rhinovirus infection, by infecting cultures with rhinovirus A16 (RVA) in an independent experiment. Single-cell RNA-sequencing was performed at 3-, 7- and 14-days post infection (dpi) to monitor epithelial remodeling during and after viral infection (**Fig.78A**). Viral infection was confirmed and monitored by analyzing virus replication at 1, 3, 7 and 14 dpi (**Fig.78B**). 61,913 cells from 3 healthy and 4 severe asthma donors were sequenced, and 9 major epithelial cell types were identified (**Fig.78C:E**). Club and goblet cells were not distinguishable in this dataset as only one secretory SCGB1A1+/MUC5AC+/MUC5B+ population was identified and labelled “mucous secretory” (**Fig.78C**).

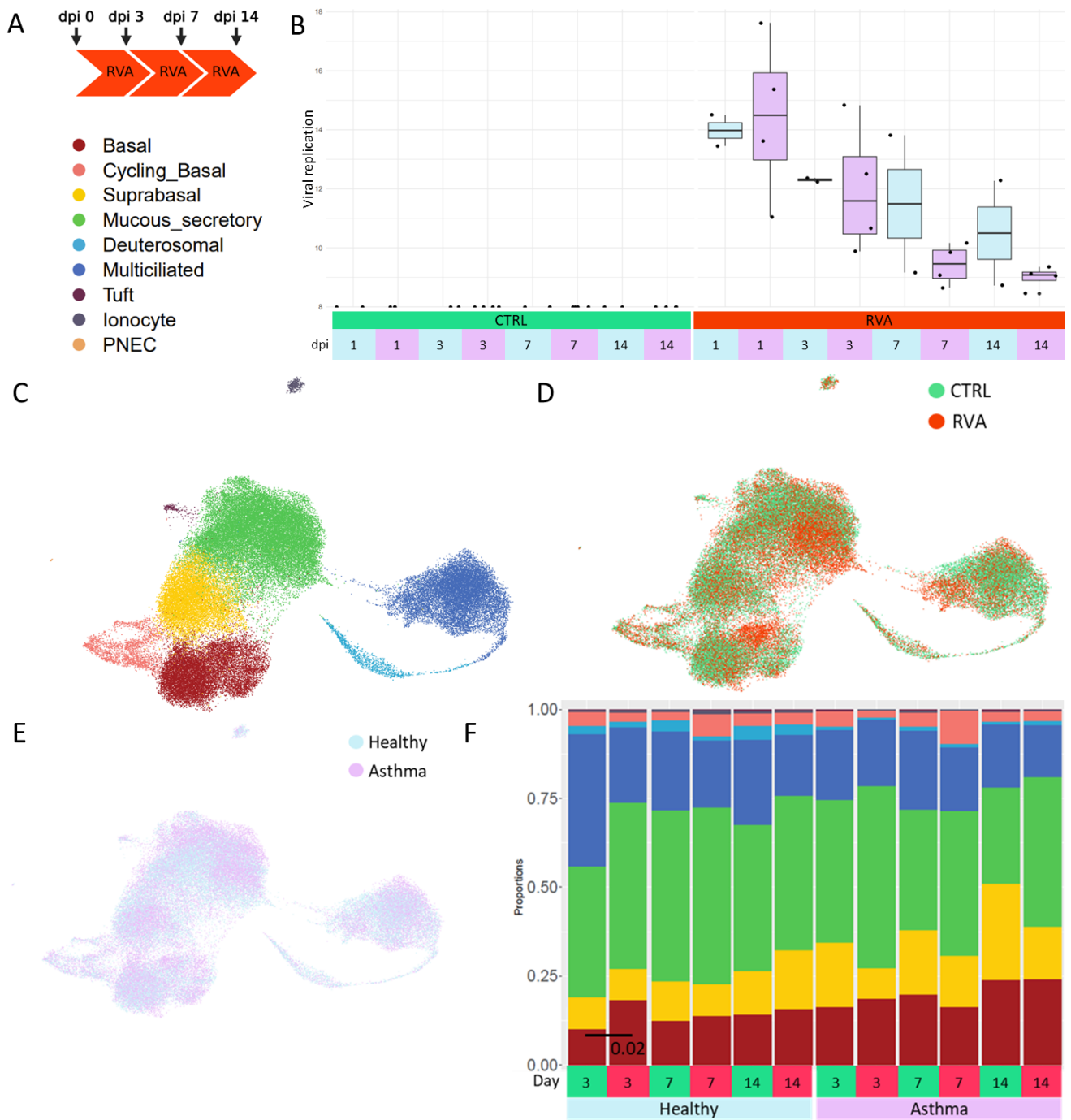


**Figure 78:** UMAP representation of the rhinovirus A16 perturbation dataset.

**A:** Experimental design. **B:** Viral replication detection. UMAPs colored by cell types (**C**), treatment (**D**) or health status (**E**), **F:** Proportion plot of cell types across samples. *p*-values obtained by t-test.

I first analyzed the epithelial cell proportions to check if rhinovirus A16 infection induced remodeling in ALI cultures. Cell proportion analysis did not reveal any RVA-induced remodeling, at the exception of a slight increase of healthy basal cells at dpi 3, compared to healthy basal cell proportions (**Fig.78A**).

## Airway epithelial response to RVA16 is reduced in severe asthma

Next, I analyzed the gene expression responses to the infection to study the differences between healthy and severe asthma ALI cultures. Healthy epithelia had a strong response to RVA with genes mainly upregulated in basal, mucous secretory, deuterosomal and MCCs. The maximum induction was of 1262 genes upregulated in mucous secretory cells at dpi 3, the peak of infection (**Fig.79A**). Severe asthma epithelia had a weaker response across all cell types compared to healthy epithelia, with a maximum of 202 genes upregulated in MCCs at dpi 3. Regardless, both healthy and severe epithelia produced typical interferon (IFN) and TNF responses (**Fig.79B**). Visual inspection of the violin plots illustrating the responses also revealed a bi- or tri-modal response of asthma cells with low, mid and high responding cells, thus revealing that part of the severe asthma cells do not respond to RVA infection.

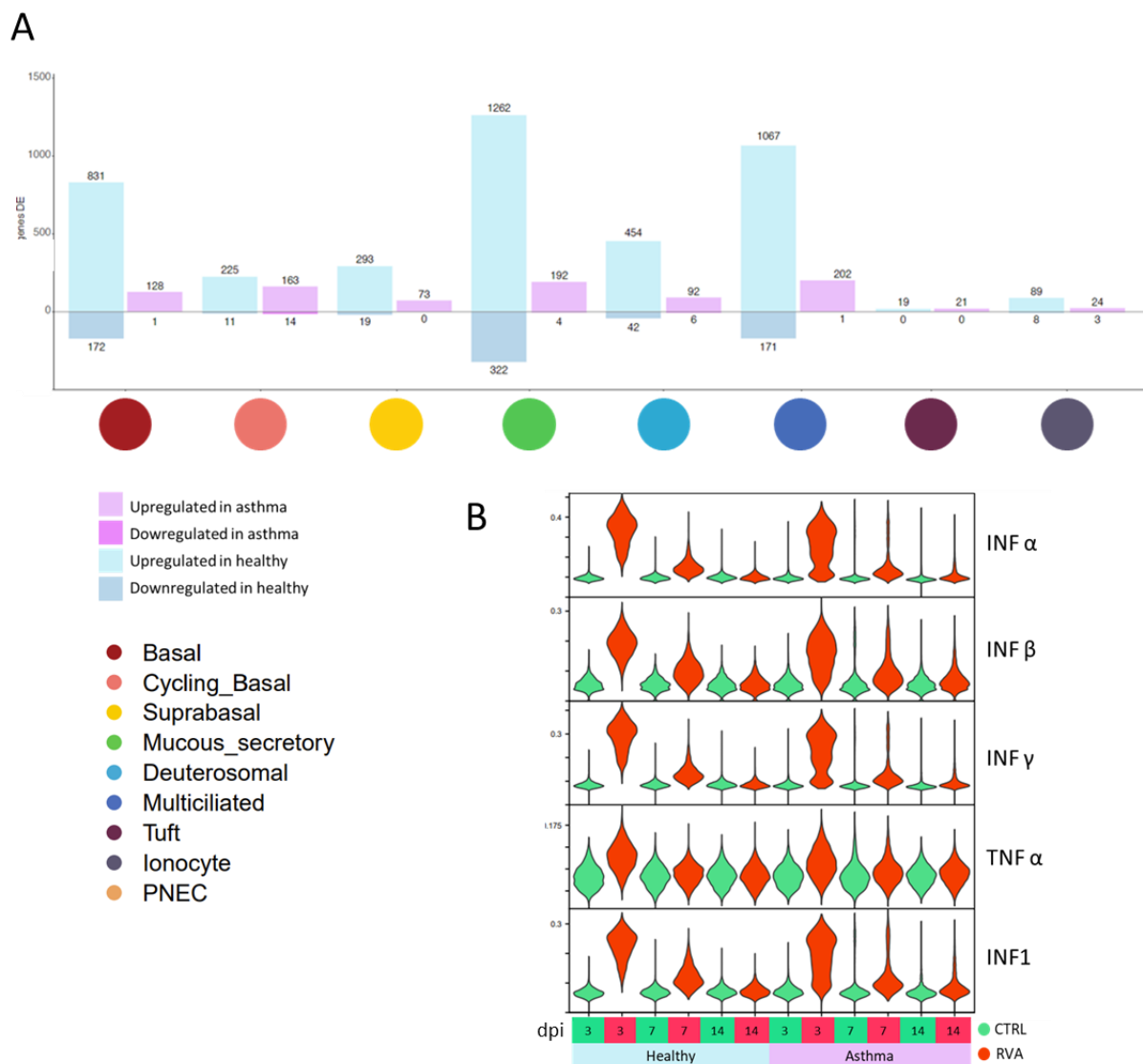


**Figure 79:** RVA16 induces a strong viral response in healthy epithelia.

**A:** Bar plot showing the number of upregulated and downregulated genes between infected healthy and severe asthma epithelia, per cell type. **B:** Violin plots of INF and TNF signatures.

## NF-kappa B signaling is impaired in severe asthma

To determine if the asthma viral response differed not only in intensity but also in nature, I compared the responses between healthy and asthma samples across basal, mucous secretory and MCCs. Interestingly, almost the entirety of genes upregulated in asthma were also upregulated in healthy cells, in all three cell types. Comparison of enrichment analysis by enrichR of genes uniquely upregulated in healthy cell types and genes upregulated in both healthy and asthma revealed that NF-kappa B pathway was enriched in healthy RVA epithelia only (**Fig.80D**). NF-kappa B genes such as *RIPK1*, *NFKBIA* and *TNFAIP3* were upregulated in healthy RVA but not in asthma RVA (**Fig.80E**).

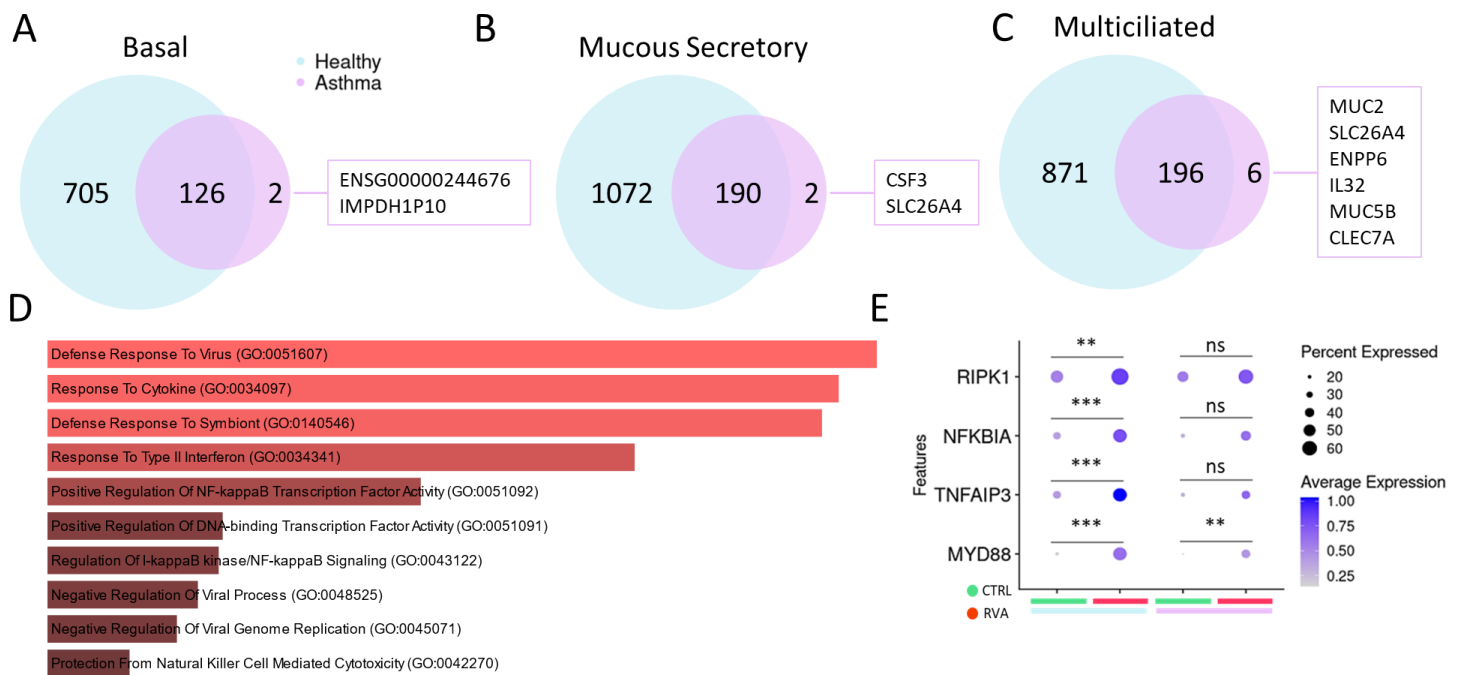


**Figure 80:** Comparison between healthy and severe asthma response to RVA infection.

Venn diagrams showing genes upregulated in healthy (light blue) or severe asthma (light pink) epithelia in basal (**A**), mucus secretory (**B**) or multiciliated (**C**) cells at dpi 3. **D:** Top GO terms enriched in RVA healthy only basal cells at dpi 3. **E:** Dot plot of NF kappa B genes upregulated in healthy epithelia at 3 dpi.

## Discussion and opening

### Context

Global feature differences between ALI cultures from asthmatic and healthy subjects had previously been described. No study has yet described at the single-cell level, the cellular and molecular alterations in airways from healthy and severe asthmatics, and in particular the molecular mechanisms that contribute to mucus secreting cell hyper/metaplasia in asthma. Moreover, the molecular events following recovery after inflammation have been poorly studied. Therefore, the principal aim of my project was to identify genes, pathways or modulators that contribute to the establishment of a healthy airway epithelium, and which are altered in pathological epithelia derived from patients suffering from severe asthma. To gain more insight and catch the different molecular features that are altered in asthmatic epithelium, I also characterized the cellular responses to two asthma-relevant stimuli, IL-13 and rhinovirus A16. To this aim, I treated Air-Liquid Interface cultures obtained from bronchial cells of either healthy or severe asthma donors with IL-13 or RVA and performed single-cell RNA sequencing analysis. Our rationale was to use ALI cultures in order to perform our entire multiscale work program on a same batch of cells from the same donor, and then to reproduce experiments on independent donors. Cells dissociated from 1 single biopsy can be sufficient to generate up to 60 individual Transwell™ inserts. Performing the same analyses on cells directly after isolation from fresh biopsies would require much more biopsies, something that would not be feasible from an ethical point of view and would in any case certainly increase the experimental noise. Moreover, *in vitro* culture allowed the isolation of epithelial cells from their diseased niche and the focus on epithelial-specific mechanisms of the disease. Finally, this model eliminates the influence of treatments taken by asthmatic patients (e.g. high doses of corticosteroids that severe asthma patients cannot abstain from), which are likely to interfere with measurements of expression profiles.

### Reconstituted epithelia from severe asthmatics have a different cellular and molecular composition

ALI cultures derived from asthmatic patients have been studied by traditional methods (immunohistology, RNA-sequencing...). They display some features of the disease such as upregulation of MUC5AC (Gras et al., 2012), inflammation, dyssynchronous mitosis, decreased resolution processes, defects in junctional proteins, and upregulation of remodeling factors (Freishtat et al., 2011; Lopez-Guisa et al., 2012), indicating that epithelial defects found in asthma can be conserved *in vitro*.

In my hands, I did observe striking differences between healthy and severe asthma cultures. Basal cells from some severe asthma donors proliferated more slowly and differentiated into a thinner epithelium.

In my single-cell RNA dataset, this was reflected by a higher ratio of basal and suprabasal cells to other cell types, compared to the healthy epithelium. However, in absolute values the healthy condition might have had more basal cells and other cell types overall, as the healthy donors generated denser and thicker epithelia, while the severe asthma cells appeared more spread out and stretched out. This is noticeable on immunofluorescence microscopy images as the asthma cells are much bigger than the healthy ones. I am currently improving the characterization of these differences in epithelial morphology by performing sections of ALI cultures followed by classical stainings. I am also working on an automated pipeline to quantify changes in cell shape from the immunofluorescence images that I have already acquired. I am combining confocal images preprocessing with Fiji (Schindelin et al., 2012) using macro scripts and cell segmentation with the Cellpose algorithm (a generalist algorithm for cellular segmentation using artificial intelligence and human-in-the-loop capabilities on python) (Pachitariu & Stringer, 2022; Stringer et al., 2020) to segment and quantify automatically the surface area of each cell. Basal cell hyperplasia has been reported in inflammatory respiratory diseases such as Chronic Obstructive Pulmonary Disease (COPD) (Coraux et al., 2008; Herfs et al., 2012). One of the earliest alterations of epithelial composition in asthmatics is the thickening of the basal cell layer, with increased production of matrix components including fibronectin but the role of the basal cells in this thickening is unclear (Burgess et al., 2016). I found that in severe asthma basal cells the Notch pathway was dysregulated, the gene encoding the receptor *NOTCH2* was strongly upregulated in the population while this receptor is usually only expressed by club cells (Ruiz García et al., 2019). The activation of a Notch receptor triggers the differentiation of the club cell carrying the receptor into a goblet cell (Lafkas et al., 2015). Hence, severe asthma basal cells might be pre-committed toward the secretory lineage. Indeed, despite having less goblet cells than the healthy epithelium, the severe asthma epithelium was strongly enriched in club cells. Moreover, in addition to carrying typical Th2 inflammatory signatures, severe asthma goblet and MCCs displayed an overexpression of *KRT5*, *KRT6A* and *KRT16*, which are normally found in more undifferentiated basal and suprabasal cells (Ruiz García et al., 2019), and in other basal cell markers, which could indicate a defective differentiation which an incapacity to lose undifferentiated markers. *KRT6A* and *KRT16* have also been associated with wound-response in the olfactory epithelium (Gadye et al., 2017).

## Memory of disease

The conservation of a distinct phenotype in the severe asthma cells cultivated *in vitro* in conditions identical to the healthy ones suggests that cells retain a “memory of disease”. In non-immune cell types, the identification of this “memory” is still in its infancy. Ordovas-Montanes et al. have shown that basal cells derived from nasal polyps of patients suffering chronic rhinitis also retain a memory of inflammation (Ordovas-Montanes et al., 2020). We do not know how basal cells encode the memory

of inflammation, nor how it is transmitted during cell divisions. Our hypothesis however, it that this memory is encoded and transmitted through epigenetic marks. To investigate this memory of disease, I collected basal cells from all donors before differentiation and performed epigenetic analysis with the CUT&Tag protocol (Kaya-Okur et al., 2020) to analyze differential chromatin marks between healthy and severe asthma basal cells. We have chosen to study a combination of histone marks that have been shown to be related to cell memory (H3K4me1, H3K4me3 and H3K27me3). So far, I have sequenced 6 donors (3 healthy + 3 severe asthma), and the results suggest a difference in the regulation of the circadian rhythm, insulin pathway, AMPK and FoxO signaling pathways. Interestingly, severe asthma basal cells have an enrichment of the activation histone mark H3K4me1 near the *ID2* gene (**Table 3**), a mediator of cell proliferation and a marker of self-renewing embryonic progenitors, repressed in homeostatic basal cells (Kiyokawa et al., 2021; Rawlins, Clark, et al., 2009). To consolidate these results, I plan on processing the remaining samples of the cohort and perform RNA sequencing on cells from the same samples to compare epigenetic regulation and gene transcription.

**Table 3: Differential enrichment of epigenetic mark in severe asthma basal cells.**

Histone mark	Width	Peak Annotation	Nearest gene	adj. P value	log2 Fold Change	Peak intensity
H3K4me1 (activation)	4470	Distal Intergenic	PARP11	0,0002	-1,27	99,28
	5506	3' UTR	YKT6	0,0002	-1,20	178,22
	3030	Distal Intergenic	FBXW8	0,0015	-2,87	25,76
	1924	Intron (uc001twf.1/26259, intron 1 of 10)	FBXW8	0,0062	-2,59	21,76
	2952	Distal Intergenic	CSF3R	0,0116	-2,80	25,54
	3417	Intron (uc002itv.4/56934, intron 3 of 9)	CA10	0,0116	1,94	50,29
	4493	Distal Intergenic	ZNF469	0,0177	-1,05	109,12
	2785	Distal Intergenic	SLITRK1	0,0195	-2,08	28,53
	6385	Promoter (<=1kb)	NPBWR2	0,0261	-0,96	163,46
	1240	Promoter (2-3kb)	ZNF639	0,0261	-2,71	16,42
	556	Distal Intergenic	FBXW8	0,0271	-3,06	13,64
	1722	Distal Intergenic	NRG2	0,0295	1,77	46,54
	2096	Intron (uc003wwm.2/10395, intron 2 of 17)	DLC1	0,0295	-2,41	19,41
	4600	Promoter (<=1kb)	INS	0,0328	-0,97	109,28
	1486	Distal Intergenic	ID2	0,0328	3,23	14,81
	3132	3' UTR	SLC4A11	0,0410	1,29	49,54
	5315	Distal Intergenic	MYT1	0,0438	-1,06	71,68
	1324	Intron (uc031qlb.1/100874167, intron 3 of 4)	LINC00423	0,0530	-2,89	14,26
	853	Intron (uc002tap.1/4862, intron 2 of 20)	NPAS2	0,0542	2,41	19,78
	847	Intron (uc011kvl.2/51422, intron 1 of 13)	PRKAG2	0,0582	2,50	16,86
	1211	Distal Intergenic	PCDH18	0,0779	-3,09	13,38
	3250	3' UTR	IPO5	0,0826	-1,27	57,22
	3250	Intron (uc002tma.3/6344, intron 1 of 12)	SCTR	0,0847	-1,05	66,23
	3673	Intron (uc003tkp.2/816, intron 17 of 20)	YKT6	0,0847	-1,20	65,64
802	Distal Intergenic	METRNL	0,0930	2,19	16,72	
H3K4me3 (activation)	1998	Intron (uc001twf.1/26259, intron 1 of 10)	FBXW8	0,0000	-4,42	48,68
	7407	Distal Intergenic	ELF3	0,1004	0,89	301,01
H3K27me3 (repression)	2355	Distal Intergenic	LINC00457	0,0200	-2,09	25,80
	1969	Distal Intergenic	YWHAEP7	0,0200	1,70	35,64
	4396	Distal Intergenic	LINC00620	0,0200	-1,26	77,64
	7233	Intron (uc011eak.1/57107, intron 7 of 7)	BEND3	0,0200	-0,92	151,61
	1834	Distal Intergenic	CCND2	0,0235	1,89	30,24
	2104	Distal Intergenic	RBM43	0,0383	-1,57	37,12

## Severe asthma epithelia have a different cellular and molecular response to IL-13 than healthy epithelia

In the healthy condition, IL-13 induced atypical remodeling with goblet cell hyperplasia and decreased multiciliated cells and deciliation. Goblet cells had the strongest transcriptional response with the induction of a canonical Th2 signature (*ALOX15*, *FETUB*) (Giovannini-Chami et al., 2018). It is unclear



why and how MCCs lose their cilia following IL-13 treatment. Deciliation can be partial (particle shedding through ectocytosis, decapitation) or total (cilia shedding by autotomy) and the length of the particle shed can trigger different events. Cilia can also be disassembled and resorbed by a cell (Doornbos & Roepman, 2021; Liang et al., 2016; Quarmby, 2004; Werner et al., 2017). Based on the observations of the immunofluorescence images of my kinetic study, it seems that some cilia were shortened, and the apical mesh was disturbed, which could suggest cilia resorption. It would be interesting to replicate the experiment and acquire electron microscopy images to obtain a better resolution of the ciliary structures.

No study has ever reported the effect of IL-13 treatment on severe asthma epithelial cell cultures at the single cell level and few studies have mentioned IL-13 treatment of asthma epithelial cultures. Parker and colleagues treated of pediatric bronchial epithelial cells with 20 ng/mL IL-13 (two times the concentration that I used), during differentiation (which is unclear if the epithelia were mature at the time of treatment) and assessed remodeling by immunohistochemistry and RT-qPCR. They reported a decrease in MCCs but no statistically significant goblet hyperplasia (J. C. Parker et al., 2013). Another study stimulated adult mild and severe asthma ALI cultures with IL-13 and briefly assessed remodeling by immunofluorescence and RNA-sequencing. They reported goblet hyperplasia after treatment (Jakiela et al., 2014). We therefore had no expectations on what could result from this experiment. We did not know if severe asthma epithelium would have a strong reaction to IL-13 due to the cells being already “primed” for a quick response, or on the contrary if they would have no response at all due to being already at their maximal inflammatory state. My results show that the former is likely true, severe asthma epithelium was able to respond to the IL-13 induced inflammation and even had a more intense transcriptional response than the healthy epithelium. Interestingly, the severe asthma epithelium had a biphasic response with a goblet to basal cell switch. At timepoint 1, after 8 days of IL-13 treatment there was a goblet cell hyperplasia that was replaced by a majority of basal cells at timepoint 2, after 22 days of treatment. This could indicate that basal cells had a reduced capacity to have a “traditional” secretory-oriented remodeling, perhaps due to a limited differentiation capacity. After a prolonged inflammation cells have lost their capacity to differentiate and maintain a differentiated state and dedifferentiate into basal and suprabasal cells. This theory is in agreement with the inactivation of the Notch signaling pathway in basal cells with IL-13 at timepoint 2. IL-13 also induced the expression of the ligand *SHH*. The hedgehog signaling pathway participates in the regulation of goblet and MCC differentiation and is normally quiescent in mature epithelium. It is however reactivated in COPD (Cai et al., 2023).

## A mucous-ciliated cell population is increased after IL-13 treatment

The work of two previous students of my team showed the existence of these cells *in vivo* (Deprez et al., 2020) and *in vitro*, which allowed the demonstration that goblet cells appeared as possible precursors of MCCs (Ruiz García et al., 2019). This indeed corresponds to one of the first examples of a fully differentiated cell type with specialized functions that also acts as differentiation intermediate toward another and very distinct type of specialized cells (MCCs). These cells were found *in vitro* and *in vivo*, and we have proposed that they could correspond to differentiation intermediates between goblet and multiciliated cells (Deprez et al., 2020). They have however never been comprehensively characterized and have never been reported in lineage tracing studies. A 2019 study has mentioned the presence of this hybrid cell population in only one asthmatic patient (Vieira Braga et al., 2019). There is no convincing data showing the fate of each cell population upon stimuli-induced remodeling in the human epithelium. Turner and colleagues (Turner et al., 2011) proposed that MCCs could trans-differentiate into goblet cells after performing *in vitro* lentiviral transduction of ALI cultures with a vector containing a Cre recombinase under the control of the FOXJ1 promoter. However, these results remain very controversial since FOXJ1 promoter leakage completely biases lineage tracing, as shown by Rajagopal's group which showed no goblet arising from MCCs in a context of OVA-induced mucous metaplasia in mouse airways in a lineage tracing experiment of a *Foxj1-cre* mice (Pardo-Saganta et al., 2013).

A careful analysis of the healthy MCCs after IL-13 revealed a subpopulation of cells expressing markers of both MCCs and goblet cells, including their respective transcription factors *FOXJ1* and *SPDEF*. Due in part to its length, the transcript of *MUC5AC* is poorly detected by 10x Genomics single-cell RNA sequencing, therefore I could not detect this mucin in mucous-ciliated cells. I was however able to detect the expression of *MUC5B*. The mucous-ciliated cell population was present in the asthma CTRL and asthma IL-13 conditions. They were more numerous in the asthma conditions in terms of raw numbers, but the differences were not statistically significant, perhaps due to the small size of the population.

## Cell trajectory inferences show that multiciliated cells can transdifferentiate into goblet cells

Cellular trajectory inference allowed to better characterize the differences in remodeling between healthy and severe asthma epithelia at baseline and after IL-13 treatment. We first tested the use of RNA velocity as it has been used successfully in other studies (Bergen et al., 2020). “RNA velocity” refers to the time derivative of gene expression states. It is inferred by quantifying unspliced and spliced mRNAs, based on the assumption that unspliced transcripts predict a cell's state in the next few hours. The unspliced fraction of all transcripts in all cells is represented as a vector indicating the future state of a cell, specifically the spliced state. Thus, RNA velocity is a high-dimensional vector that predicts the future state of individual cells over a timescale of hours. When testing the pipeline on our reference group (healthy CTRL timepoint 2) and the projected dynamics and downstream results obtained using the pseudotime Palantir, unlike those based on RNA velocity, corresponded more accurately to the biological reality. We therefore chose to use the pseudotime kernel, where the transition matrix is calculated from the pseudotime Palantir. The pseudotime Palantir also showed in subsequent analyses, using estimators, that the results did indeed correspond to the known biological reality. By also correctly identifying basal cells as the initial state and as the least stable macrostate (from which the cells therefore have a greater probability to differentiate), and goblet cells and multiciliated cells were identified as terminal macrostates with greater stability.

Calculation of fate probabilities toward the goblet or multiciliated cell fate confirmed that severe asthma epithelium is skewed toward the goblet cell lineage. Administration of IL-13 increased this probability in both conditions and visualization of pseudotime flow with a diffusion map illustrated the redirection of cell trajectories of the multiciliated cells toward the goblet cells. This strongly suggests that multiciliated cells can transdifferentiate into goblet cells under pathological remodeling. This result will be further validated by the team by experimental approaches that will be set-up, such as live imaging to observe such a transition. Our data showed that both healthy and severe asthma epithelia were able to recover their initial cell composition and transcriptional signature. This result was surprising considering the apparent defective differentiation capacities of the severe asthma cells. However, the trajectory inference analysis showed that at resolution, severe asthma fate probabilities were not restored back to normal, compared to the healthy condition, which indicates a slower resolution process for the severe asthma condition. It would be interesting to perform a time course analysis during resolution to confirm this observation. A small subgroup of healthy goblet cells conserved a level of fate probability similar to the one during IL-13 treatment. This small subcluster of “preactivated” cells could serve as a “quick starter” to induce a fast secretory response in case of a future new insult, as suggested by the trained immunity principle. If true, applying successive phases

of resolution and IL-13 treatments should result in more intense responses over treatment cycles. I tested this theory in a preliminary experiment that indicated that, in healthy cells, the goblet hyperplasia and mucus hypersecretion were more important after a second cycle of IL-13 treatment (**Fig.81**). These promising results granted us a funding from the Fondation du Souffle to pursue the trained immunity project.

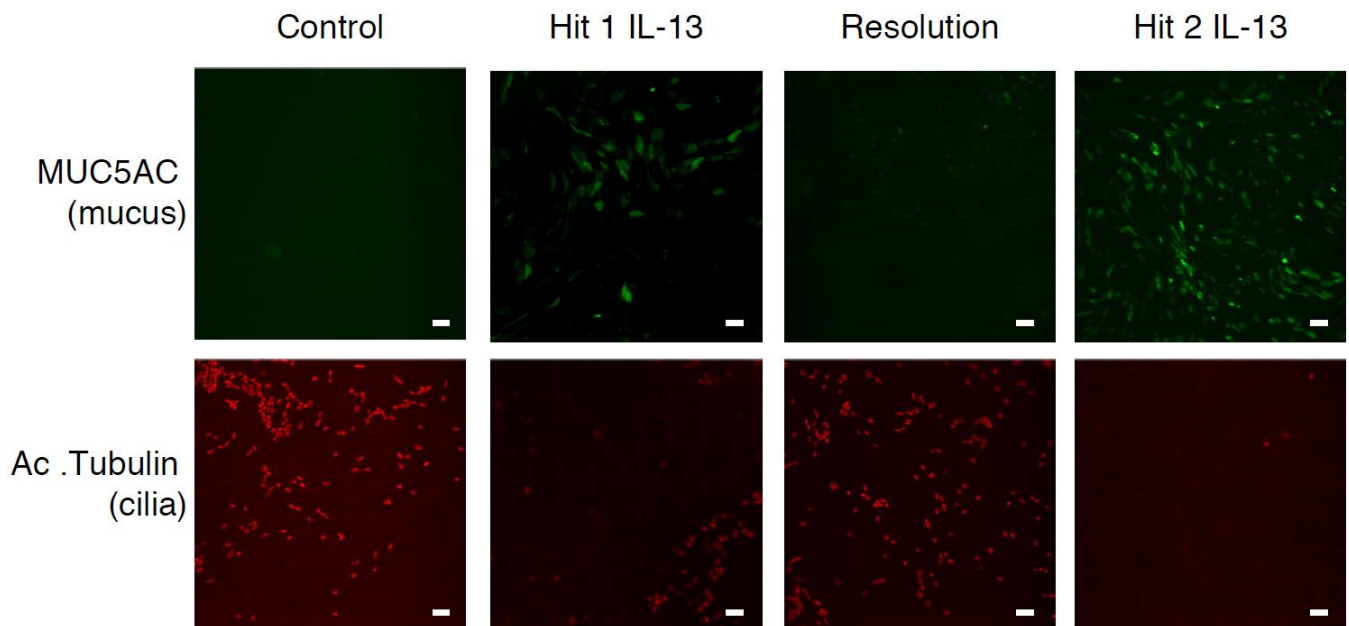


**Figure 81:** Preliminary result of epithelial trained immunity.  
Scale bar 10  $\mu\text{m}$ .

## Characterization of cell types and states induced by rhinovirus A16 in healthy and severe asthma epithelia

Lastly, I conducted an independent experiment to compare the response of healthy and severe asthma epithelia to a rhinovirus A16 infection, a common asthma-related trigger. Cultures were infected with rhinovirus A16 (RVA), and single-cell RNA sequencing was performed at 3-, 7-, and 14-days post-infection (dpi) to monitor epithelial remodeling during and after the viral infection. Monitoring of epithelial resolution after RVA infection had never been done at the single cell level before.

The cell cultures and rhinovirus infections for this experiment were done by our collaborators in Aix-Marseille Université, who are experienced in viral infections. Since our sequencing platform is in Nice, we did not perform the single cell RNA-sequencing on fresh cells as we routinely do to avoid damaging live cells in transport. Instead, we chose a new sequencing approach that allows the sequencing of fixed single cells. Our collaborators cultivated, infected, dissociated, fixed and froze the cells for

shipping. We prepared, sequenced and analyzed the samples. Because of these experimental differences, we decided to not combine this experiment with the IL-13 dataset but to analyze it separately instead.

RVA infection did not trigger any noticeable remodeling in healthy or severe asthma epithelia at any timepoint, beside a slight increase of healthy basal cells at dpi 3, compared to healthy basal cell proportions. In the literature, RVA-induced remodeling is compared to a weaker version of IL-13 remodeling (Jakiela et al., 2021). The RVA infection still induced an intense IFN and TNF response in healthy epithelium at the peak of infection (3 dpi). The severe asthma response was very weak in comparison, but in agreement with the work of Jakiela and colleagues who combined IL-13 treatment and RVA infection in healthy cells and also saw a weaker response due to the asthma-related inflammation (Jakiela et al., 2014). By comparing the healthy and severe asthma responses to RVA I noticed a defect in NF-kappa B signaling in severe asthma cells. Interestingly, corticosteroids can crosstalk and repress NF-kappa B signaling (Bekhbat et al., 2017; Salter et al., 2007). Although unlikely, residual effects of corticosteroids (taken by all severe asthma volunteers of the cohort) could explain the repression of NF-kappa B observed here. Due to time constraints this dataset has not been fully exploited yet and will be analyzed more in depths in the future.

## Organ-specific differences in the asthmatic response

Bronchial and nasal epithelial cells generate similar mucociliary epithelia after 3D *in vitro* differentiation and display similar responses to viral infection and IL-13 stimulation (Brewington et al., 2018; Roberts et al., 2018). However, in these studies, similarities were deduced from equivalent cell proliferation and global composition of the *in vitro* regenerated epithelia. In the dataset collected in the framework of the Human Cell Atlas, we have found differences between nose and bronchi biopsies, especially at the level of the club cell population. I have processed identically to the rest of the IL-13 cohort 3 healthy and 3 severe asthma nasal sample to evaluate, at the single-cell level, whether the differences observed *in vivo* between nose and bronchi are maintained *in vitro* in ALI cultures and then to compare cultures from control and asthmatic patients. These samples will be analyzed shortly.

## Dosage of secreted mucus

Mucins are very high molecular weight glycoproteins with a highly glycosylated structure, which play a crucial role in the protection and lubrication of epithelial surfaces (Carpenter et al., 2021). Due to their size and complexity, their detection and analysis pose significant challenges. Western blotting has significant limitations for the detection of mucins. In the electrophoresis gel, proteins are separated according to their molecular weight. The high molecular weight of mucins severely impairs their entry

into the gel. As a result, the proteins detected represent the least glycosylated fraction. Moreover, variations in glycosylation can alter the net charge of proteins, which can lead to differences in migration in the gel and band distortions, making their quantification and accurate analysis difficult (Ramsey et al., 2016). In this context, we attempted to assess the differences in mucus secretion between conditions by ELISA with mixed results. mRNA and protein trends of MUC5AC levels were coherent and both single-cell RNA-seq and ELISA indicated an increase in MUC5AC after IL-13 treatment in healthy and severe asthma epithelia. However, for MUC5B, results were contradictory. mRNA analysis indicated a (non-significant) decrease in *MUC5B* after IL-13, while ELISA indicated an increase in MUC5B. Jackson and colleagues showed a sharp decrease of MUC5B in IL-13 treated healthy epithelia at the transcriptome and secretome levels, which suggests that our detection of MUC5B by ELISA was incorrect and could be due to technical issues such as poor detection of MUC5B by the antibody or interference with other secreted proteins.

## miRNA

Studies have also focused on epithelial miRNAs. MiRNAs are known for their ability to regulate multiple target genes with complex cellular functions. Experiments have shown that repression of miR-141 caused a decrease in goblet cells in response to IL-13, demonstrating its involvement in this process (Siddiqui et al., 2021). It would therefore be interesting to explore the role of miRNAs in IL-13-induced epithelial remodeling in future projects.

## Functional analysis of human airway regeneration and remodeling in asthma by CRISPR-Cas9

Efficacy of gene manipulation in 3D cultures of airway epithelial cells has always been a problem. New approaches, based on the use of Cas9 nuclease RNP complexes, have dramatically improved the situation, resulting in up to 95% efficiency. This approach is much more efficient and generate less off-target effects than the delivery of sgRNA and Cas9 by lentivirus, or other silencing techniques (L.-E. Zaragosi et al., 2024), and allowed us to perform a functional analysis to characterize the role of two gene candidates in regeneration and remodeling in asthma. The results are presented in part [B. Functional Analysis Of Human Airway Regeneration And Remodeling In Asthma By CRISPR-Cas9](#)

# B. Functional analysis of human airway regeneration and remodeling in asthma by CRISPR-Cas9

## Introduction and objectives

From the *in vitro* single-cell RNA-seq atlas of healthy and asthma epithelial cells described in [A. Single-cell Analysis of Human Airway Regeneration and Remodeling in Asthma](#), I have established a list of candidates for putative regulators of epithelial remodeling in health and asthma. In order to identify whether these genes are active players in epithelial remodeling, I have conducted a functional study by invalidating the expression of selected candidates. For a first evaluation, 2 transcription factors were selected based on their strong induction by IL-13:

- *EHF* (Ets Homologue Factor). This gene encodes a protein known for its specific expression in the epithelium (ESE). This poorly characterized protein acts as a transcriptional regulator and is involved in keratinocyte differentiation and certain cancers. *EHF* is structurally close to *SPDEF*, the goblet cell transcription factor (Luk et al., 2018).
- *GATA3*. This gene codes for a protein containing two GATA-type zinc fingers and is an important regulator of T cell development (Koretzky et al., 2002). We did not detect *GATA3* in epithelial cells at homeostasis, but its expression was induced after IL-13 treatment.

To identify the involvement of *EHF* and *GATA3* in IL-13-mediated respiratory epithelial remodeling, we invalidated these genes by CRISPR-Cas9 RNP (RiboNucleoProtein). We have previously developed a CRISPR-Cas9 RNP technique that has proven to be particularly efficient in our 3D model, enabling functional studies that were previously impossible (L.-E. Zaragosi et al., 2024). CRISPR-Cas9 allows the targeted inactivation of a gene with a Cas9 endonuclease loaded with a SgRNA (Single-guide RNA). Each target SgRNA contains a gene-specific sequence (crRNA for crisprRNA) fused to the "tracrRNA" (trans-activating crRNA) Cas9 chaperone sequence. Together with the Cas9 protein, they are integrated into cells by electroporation or nucleofection. Once in the cell, the Cas9 causes a DNA double-strand break to a specific target genomic region (**Fig.82**) (Doudna & Charpentier, 2014). The CRISPR/Cas9-RNP (ribonucleoprotein) method, which uses a recombinant Cas9, is a "quick and dirty" method that avoids the need to clone SgRNA and Cas9 into expression vectors. Although this approach does not select for clones, thus does not remove non-invalidated cells, it has been validated by our team as the most efficient invalidation technique in airway epithelial cells as it generates multiple cuts in DNA (L.-E. Zaragosi et al., 2024).

Experiments were conducted using the BCI NS-1.1 cell line (hereafter referred to as BCI), which was obtained from bronchial epithelial basal cells of a healthy non-smoking donor and immortalized by transduction of a retrovirus expressing human telomerase (hTERT) (Walters et al., 2013). We previously validated the proper differentiation of this cell line in our hands (data not shown). The choice of the BCI cell line for this functional analysis was due to its ability to undergo multiple passages without loss of differentiation potential, enabling the generation of a larger cell stock compared to primary cells and allowing for cryopreservation for future experiments.

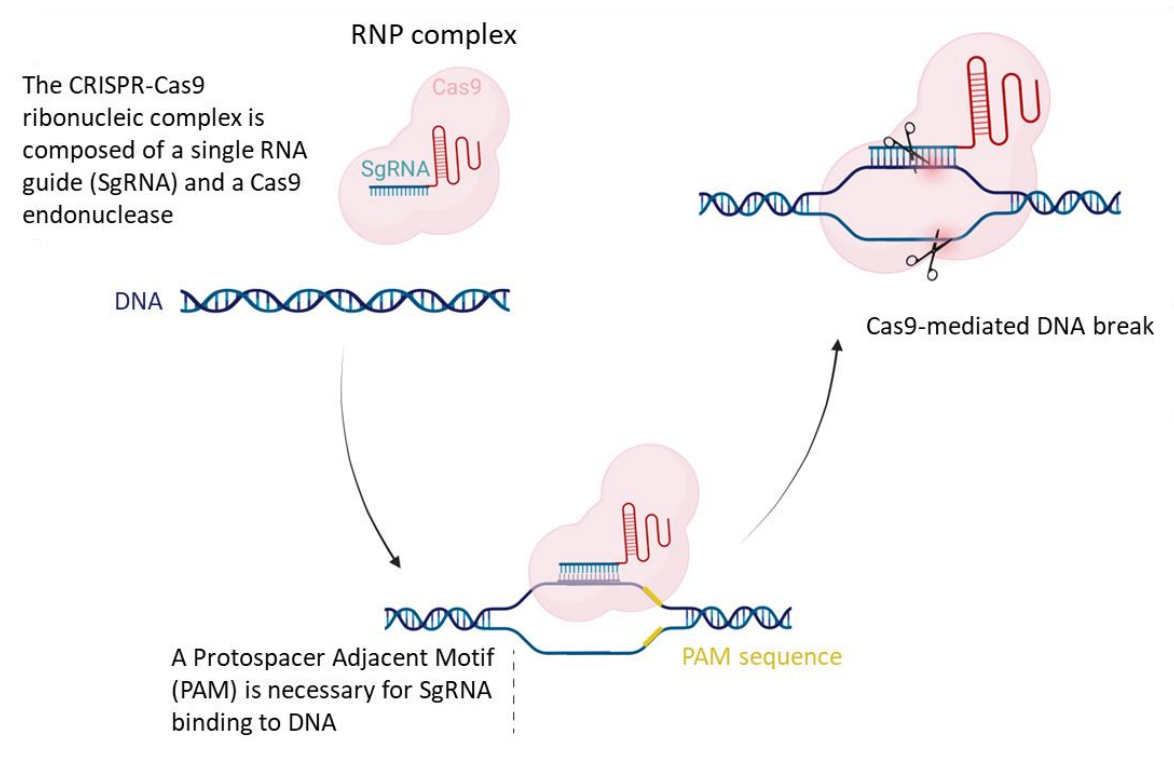


**Figure 82:** Principle of CRISPR-Cas9.

**The experimental plan was the following:**

1. Validate the BCI model
  - a. Validate *EHF* and *GATA3* gene expression in the BCI cell line.
  - b. Test the induction of *EHF* and *GATA3* by IL-13 treatment in BCI cultures.
  - c. Determine the kinetics of IL-13-induced epithelial remodeling in BCI.
2. Invalidate the candidate genes:
  - a. Invalidate the *EHF* and *GATA3* using the CRISPR-Cas9 RNP technique.
  - b. Confirm invalidation of *EHF* and *GATA3*.
3. Analyze the effect of the invalidation on epithelia:
  - a. Characterize IL-13 epithelial remodeling on invalidated epithelia.



- b. Perform single-cell RNAseq to define the individual IL-13 response of each cell type within the invalidated epithelia.

Six experimental conditions were performed:

- Negative controls:
  - NoNuc: Cells were not nucleofected.
  - Scrambled (SgScrb1): Cells were nucleofected with an equimolar mixture of 2 SgRNAs with random sequences that have no genome matches (negative control SgRNA #1, #2, Synthego).
- Positive controls with an easy readout to measure the effectiveness of the invalidation:
  - CRISPR *FOXJ1* (SgFOXJ1): Cells were nucleofected with SgRNAs targeting *FOXJ1*. Previous studies, including one carried out in the team, have demonstrated that *FOXJ1* invalidation leads to a strong decrease in the number of multiciliated cells within the respiratory epithelium (L.-E. Zaragosi et al., 2024).
  - CRISPR *SPDEF* (SgSPDEF): Cells were nucleofected with SgRNAs targeting *SPDEF*. Targeting *SPDEF* has been shown to abolish *MUC5AC* expression, thereby strongly reducing mucus levels in bronchial epithelial cells (Koh et al., 2020). This type of invalidation had never been performed in the team prior to this.
- Candidate genes:
  - CRISPR *EHF* (SgEHF): Cells were nucleofected with SgRNAs targeting *EHF*.
  - CRISPR *GATA3* (SgGATA3): Cells were nucleofected with SgRNAs targeting *GATA3*.

Two independent experiments were performed from the same batch of nucleofected cells (**Fig.83**):

- Experiment #1 consisted in seeding the cells on inserts directly after transfection.
- Experiment #2 consisted in proliferating the cells on flask after transfection to obtain a stock of invalidated cells that could be frozen for future experiments. After a couple of passages the cells were seeded and differentiated as usual.

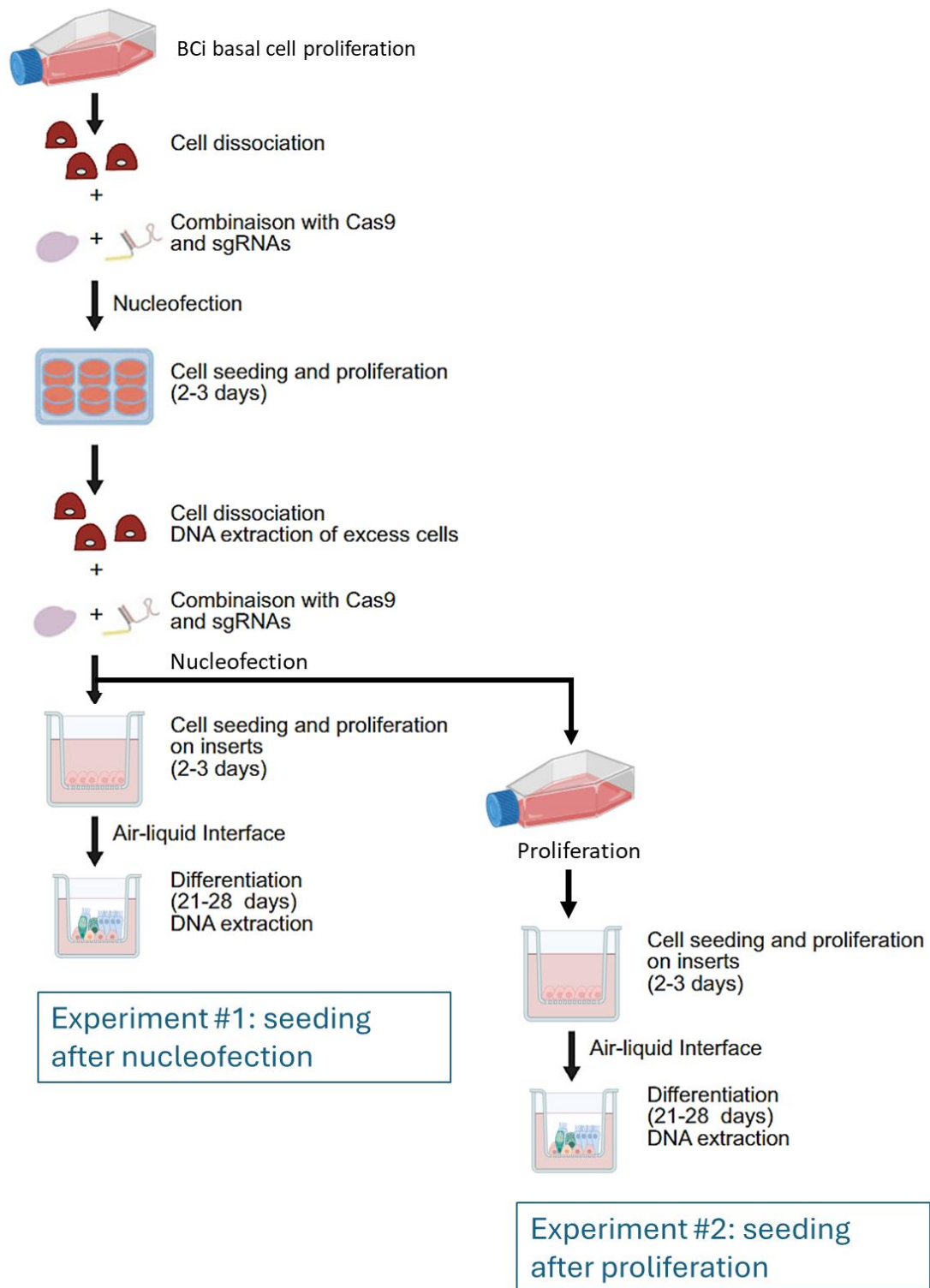


**Figure 83:** Overview of the experimental set up.

## Results

### Characterization of IL-13-induced epithelial remodeling in BCI cell cultures

Although IL-13-induced epithelial remodeling of primary cultures has been extensively studied by our team and others, it has, to my knowledge, never been reported in the BCI cell line. Thus, to determine if IL-13 treatment on BCI cells induced a remodeling similar to the one observed in primary cultures, a time course study was performed, with timepoints selected at 2, 4, 7 and 10 days of IL-13 treatment. At each time point, changes in gene and protein expression or secretions associated with epithelial remodeling were assessed.

#### IL-13 induces remodeling in BCI cultures

Immunofluorescence stainings for MUC5AC (goblet cells) and acetylated alpha-tubulin (AcTub, multiciliated cells) were done to characterize epithelial composition during IL-13 treatment. Analysis by confocal microscopy and epifluorescence revealed a clear increase of MUC5AC in IL-13-treated epithelia from day 7 onwards, compared with control epithelia (**Fig.84A**). Quantitative measurements of fluorescence intensity of images taken by epifluorescence microscopy revealed a significant increase in MUC5AC in IL-13-treated samples, compared with controls, from 2 days of treatment. This increase continued until day 10 (**Fig.84B**). Quantitative analysis of fluorescence intensity for Actub staining showed no significant variation during IL-13 treatment, compared with control (**Fig.84C**). However, a decrease that is more difficult to appreciate on images obtained by confocal microscopy was observed at the end of the 10<sup>th</sup> day of treatment (**Fig.84A**). This initial characterization revealed a significant goblet hyperplasia, as well as a slight, although non-significant decrease in ciliation in response to IL-13 treatment in BCI.

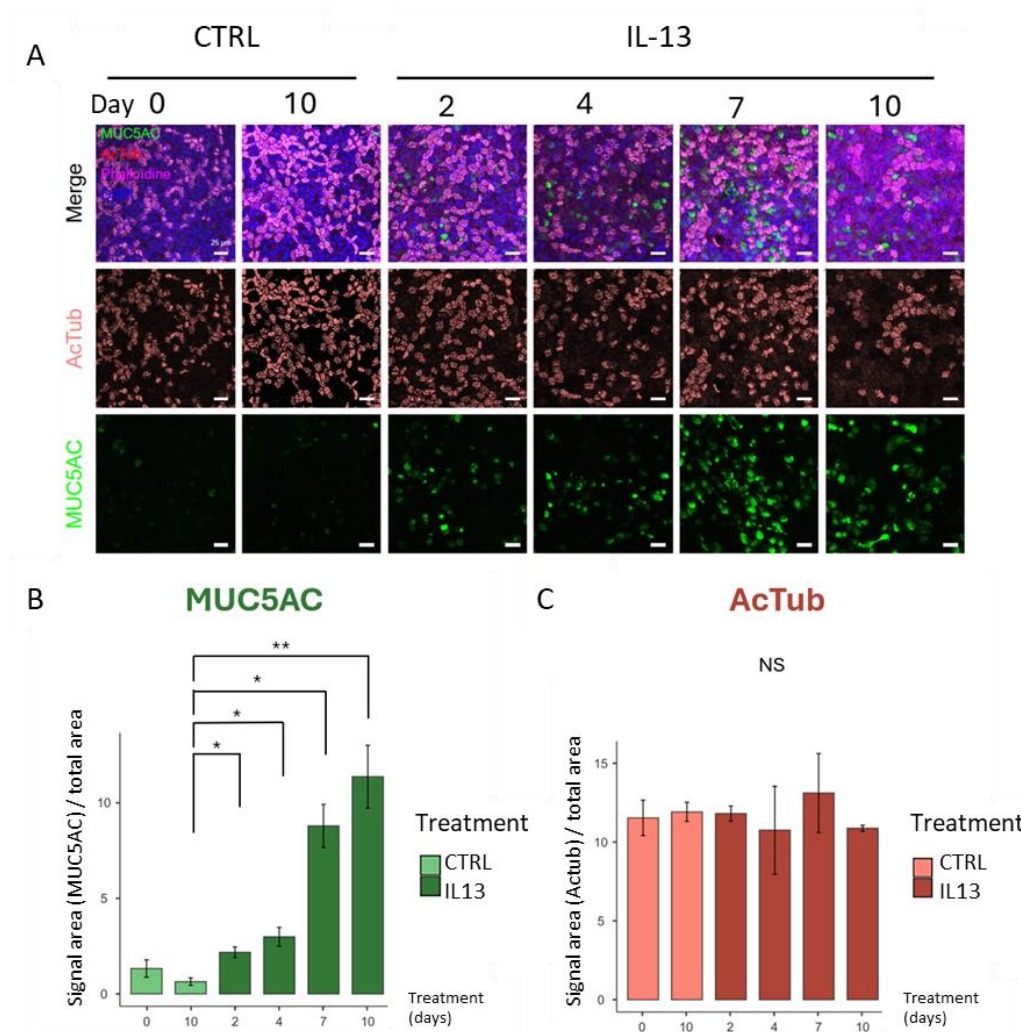


**Figure 84:** Epithelial cell composition of BCI during IL13 treatment time course.

**A:** Confocal microscopy images of differentiated epithelia after different IL13 treatment times stained for MUC5AC (mucus, green); Acetylated alpha-tubulin (AcTub, cilia, red), and DAPI (nuclei, blue). Scale bar: 25  $\mu$ m. Measurement of the mean fluorescence intensity of 3 fields per condition obtained by epifluorescence microscopy at 10X objective for MUC5AC (**B**) and for ciliary labeling (AcTub) (**C**). \*:  $p$ -val $\leq$ 0.05; \*\*:  $p$ -val $\leq$ 0.01. Results are averages of 3 culture inserts.

### IL-13 induces MUC5AC expression in BCI cultures

RT-PCR analysis was performed to assess BCI response to IL-13 at the transcriptomic level. An increase in MUC5AC expression in IL-13-treated epithelia was observed, with a significant 3-fold increase at 4 days of IL-13 treatment and non-significant peak reach at day 7 (**Fig.85A**), in agreement with the increase in MUC5AC staining observed with immunofluorescence. In multiciliated cells, there was a non-significant downward trend in the expression of their transcription factor *FOXJ1* after treatment (**Fig.85B**). A slight but non-significant increase in the expression of the two candidate genes *EHF* and *GATA3* was observed after 10 days of treatment, suggesting a potential difference in the transcriptional response to IL-13 between primary and BCI cells (**Fig.85C&D**). Of note, preliminary RNAseq results of our team depicts a 1.4-fold increase ( $p$ -value =  $8.16 \cdot 10^{-09}$ ) in *EHF* expression upon IL-13 treatment in BCI. Based on these results, and to match the experimental plan of the course of IL-13 treatment done

on primary cells during the first part of the thesis, we chose a 7-day long treatment plan for the subsequent experiments.

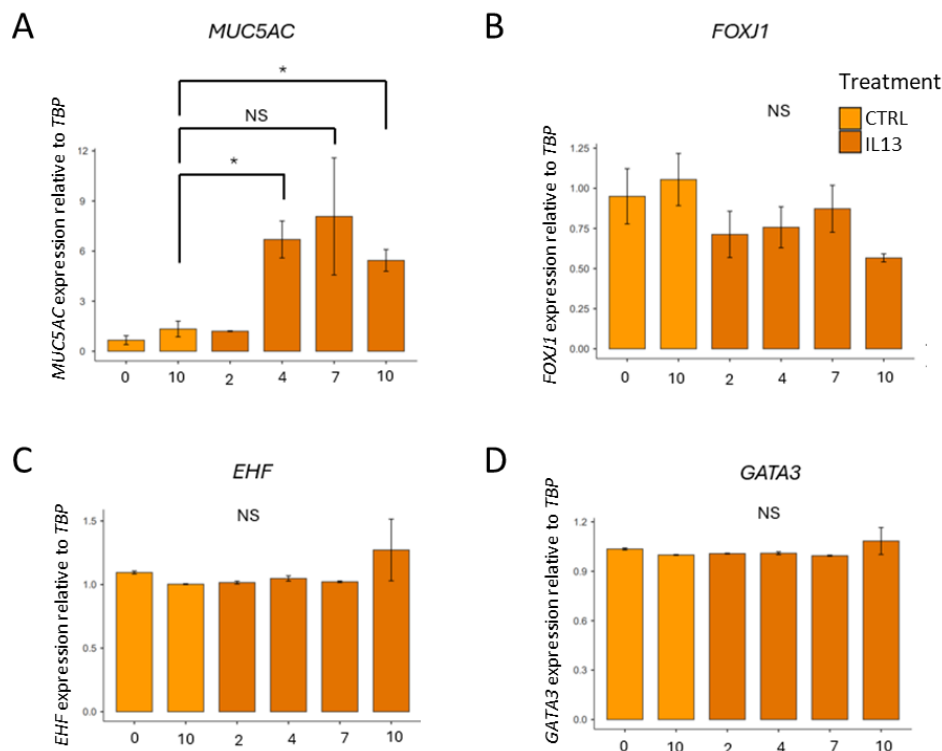


**Figure 85:** Effect of IL-13 treatment on expression of genes involved in epithelial remodeling and candidate genes. Relative expressions of  $2^{-\Delta\Delta Ct}$  *MUC5AC* (A), *FOXJ1* (B), *EHF* (C) and *GATA3* (D) relative to *TBP*. \*:  $p$ -val  $\leq 0.05$  (Student's t-test). Crossbars represent standard deviation. Results are averages of 3 culture inserts.

## Invalidation of *EHF* and *GATA3* genes by CRISPR-Cas9 RNP

In order to identify the putative role of *EHF* and *GATA3* in the epithelial remodeling process and if their absence can attenuate epithelial remodeling in the context of asthma, these genes were knocked down by CRISPR-Cas9 RNP. Two independent experiments were performed from the same batch of invalidated cells (Fig.83):

- Experiment #1 consisted in seeding the cells on inserts directly after transfection.
- Experiment #2 consisted in proliferating the cells on flask after transfection to obtain a stock of invalidated cells that could be frozen for future experiments. After a couple of passages the cells were seeded and differentiated as usual. Thus, invalidation conditions are identical as in experiment #1, at the exception of SgFOXJ1, which is absent due to an insufficient number of cells.

The propagation and storage of invalidated cells had never been carried out by the team, as we usually work on primary cells that do not tolerate more than 3 or 4 passages before losing their differentiation potential.

### Confirmation of invalidation by PCR

To assess the efficiency of the invalidations, we performed PCRs on the genomic regions targeting the candidate genes using DNA extracted from the basal cells directly after the second round of CRISPR invalidation. Comparison of amplicon migration profiles revealed distinct changes in amplicon size between control (Scrambled: SgScrbl) and invalidated conditions. The SgScrbl condition is a negative control using a pair of SgRNA composed of random sequences with no genome match that does not resolve in any deletion. The band obtained in the SgScrbl lane represents the expected size of the wild-type amplicon, according to the pair of primers used per targeted gene. For all 4 invalidated genes, an almost total reduction in amplicon size was observed compared with the SgScrbl condition, suggesting efficient invalidation. Observation of the profiles of invalidated samples showed several amplification bands of different sizes, suggesting the generation of multiple deletions (**Fig.86**). The state of the invalidation was also analyzed after proliferation and full differentiation for both experiments #1 and #2. The same deletion profiles were observed, indicating that the genetic modifications were conserved after proliferation and differentiation and after several passages in culture.

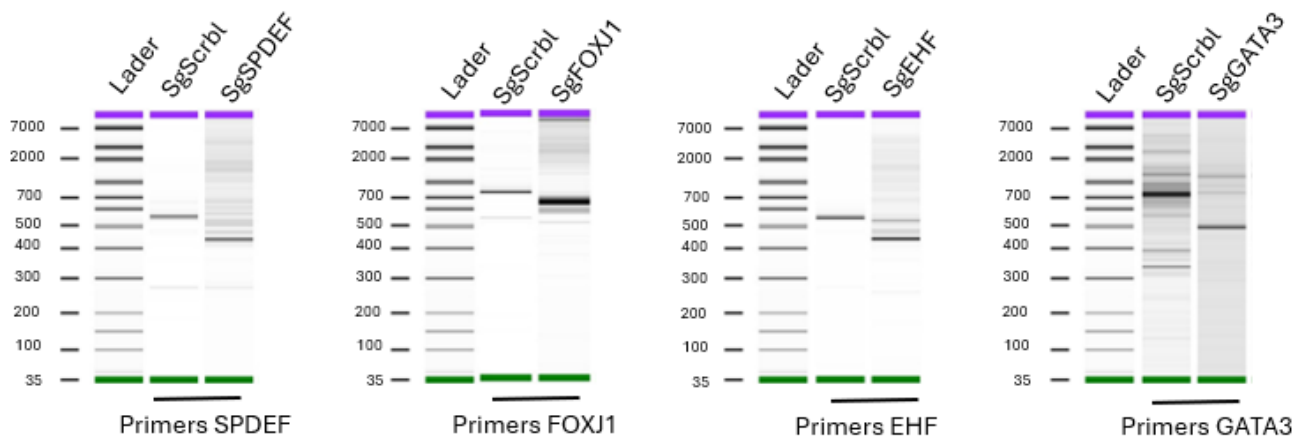


**Figure 86:** Validation of CRISPR/Cas9 efficacy by genomic PCR

Capillary electrophoresis analysis of purified PCR products revealing a size shift, attributed to deletions generated by the action of Cas9/SgRNA pairs on target genomic regions, for each gene of interest. SgScrbl track serves as a control for each invalidation condition, providing a sequence reference. Results of experiment #1, which were identically reproduced in experiment #2.

### Confirmation of invalidation by Nanopore sequencing

To better characterize and quantify the deletions made for each gene of interest, we sequenced the PCR amplicons using the Nanopore technique, obtaining full-size reads of each amplicon. The reads obtained were aligned with the human genome and visualized using a genome browser. We observed that within the *EHF* gene, deletions were heterogeneous although all localized to the genomic region comprising the SgRNAs. This heterogeneity is due to the use of 3 different SgRNAs that produce 7 possible combinations of cuts within a cell (**Fig.87A**). To quantify CRISPR efficiency, we used a script developed by the team which counts the number of reads with deletion(s) as a function of deletion size. We determined the invalidation efficiency by calculating the percentage of deletions in each condition (sum of reads with deletions / sum of total reads) (**Fig.87B**). Here the percentage of deletions was of 87%, 88% and 92% for the *SPDEF*, *GATA3* and *EHF* genes, respectively (**Fig87.C-E**).

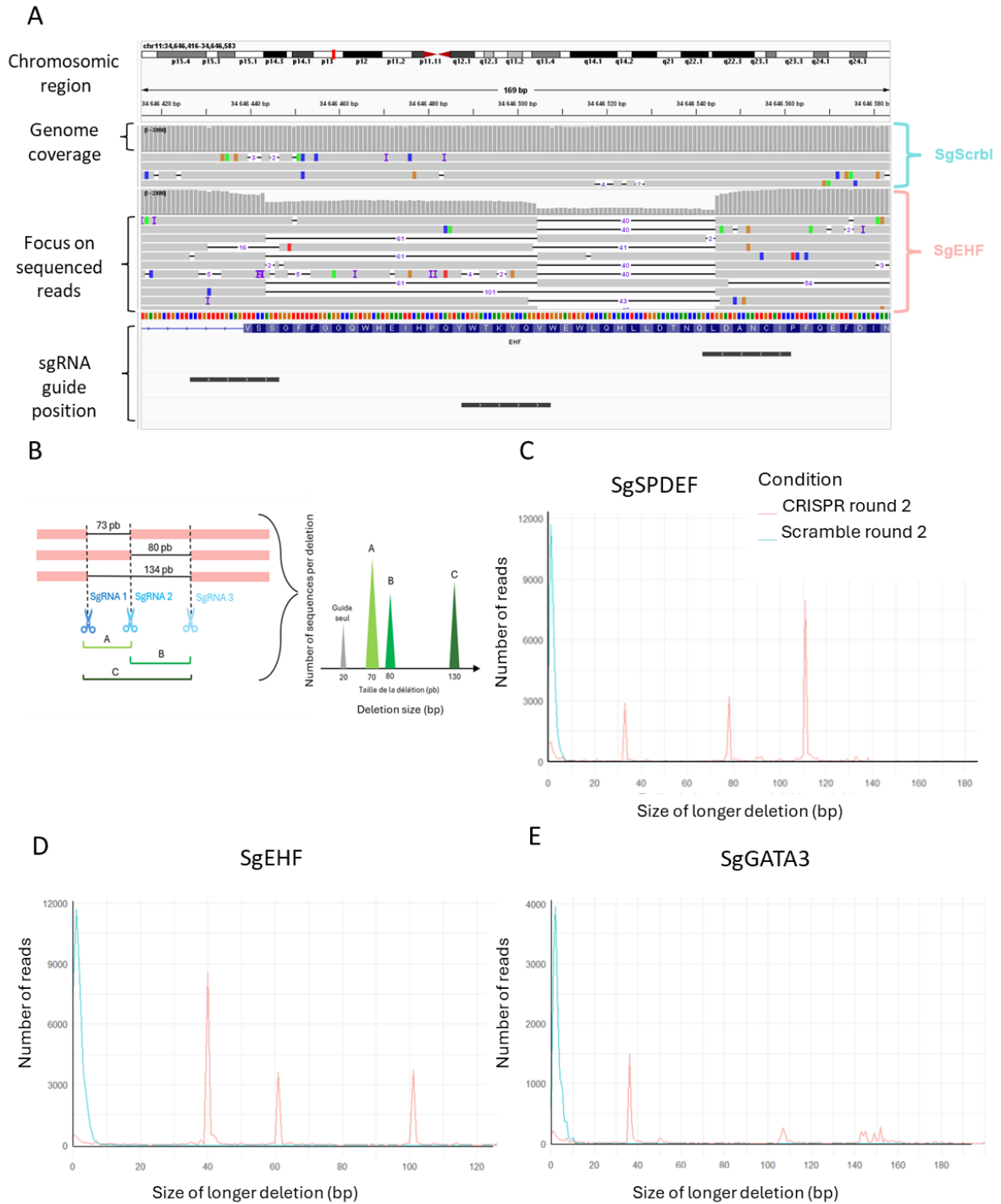


**Figure 87:** Validation of gene inactivation by Nanopore sequencing.

**A:** Visualization of the alignment of reads obtained on the reference genome (IGV). This visualization shows the size of the deletions and the location of the deleted region. **B:** Schematic representation of the effect of combined SgRNAs on target genomic sequences. The induced deletion can vary in size depending on the active SgRNA, which explains the different deletion sizes that can be identified by sequencing. **C:** Graphical representation of the number of reads obtained as a function of the length of the deletions (in base pairs). Blue = Condition SgScrb1, a single peak observed demonstrating the absence of a deletion; Orange = Condition SgSPDEF, SgEHF, SgGATA3, the peaks obtained demonstrate the presence of deletions of different sizes. Results obtained from cells of experiment #2.



## Western blot verification of invalidation

Western blots were performed to determine whether invalidation of *EHF* and *GATA3* observed at the genomic level affected the proteins encoded by these genes. Our results show that invalidation of the *EHF* gene resulted in an absence of a band at the expected size for its protein under SgEHF conditions, indicating a significant reduction in EHF protein, thus confirming effective invalidation of the gene. However, a lower band could be observed, suggesting the presence of a truncated form of the EHF protein. This truncated form could be the consequence of the CRISPR-induced deletion (**Fig.88A&B**). According to the cut sites, this protein should be deprived of its DNA-binding domain, which is at the C-ter of the protein. No band for *GATA3* was observed in the SgGATA3 condition and in the SgScrbl condition at the expected size, therefore we could not conclude as to the effect of the invalidation at the protein level. This absence of band might be due to the low to null level of *GATA3* expression in the homeostatic epithelium. Interestingly, in conditions where *EHF* has been invalidated (SgEHF), there was a notable band for *GATA3*, particularly in the control condition (**Fig.88A&C**). It was not possible to verify the effect of SgSPDEF on SPDEF protein levels, as there are no efficient antibodies available. Thus, gene invalidation was confirmed for the control genes, *SPDEF* and *FOXJ1*, as well as for the genes of interest, *EHF* and *GATA3*.

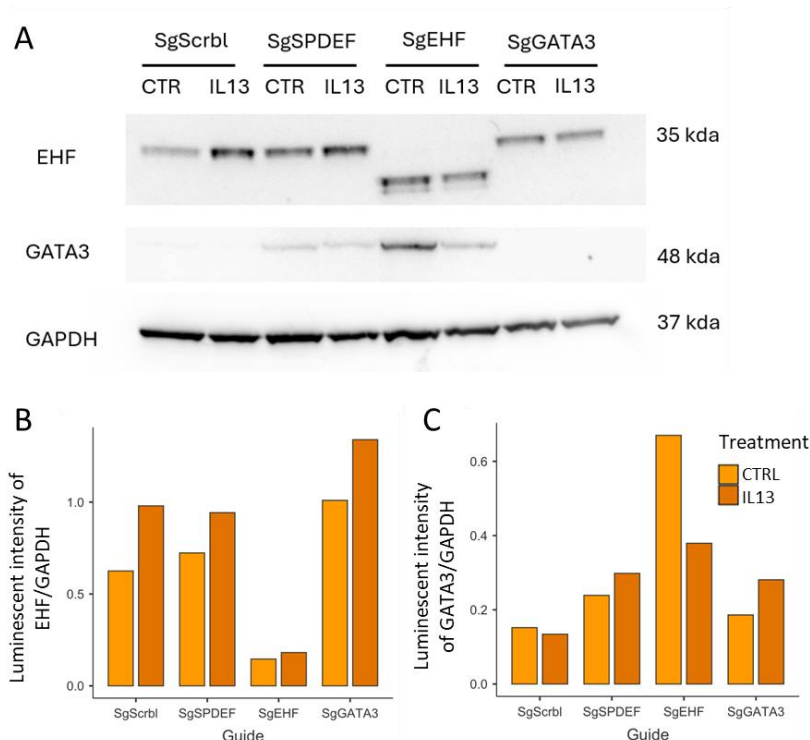


**Figure 88:** Characterization of invalidation at the protein level.

**A:** Western blots for EHF and GATA3 under the conditions indicated, for experiment #2. Measurement of luminescence intensity of bands obtained by Western blot for EHF (**B**) and for GATA3. (**C**) GAPDH was used as a normalizer of luminescence intensities.

## Characterization of the effect of target gene invalidation on epithelial remodeling

ALI35 invalidated epithelia were treated with IL-13 (10 ng/mL) for 7 days to study the impact of target gene invalidation on epithelial remodeling. Remodeling assessment was performed by examining cell composition, gene expression and protein levels of goblet and multiciliated cell-specific markers.

### Effect of invalidation on epithelial composition

First, we checked that neither *EHF* nor *GATA3* invalidations affected epithelial differentiation, under control conditions. According to the numbers of MUC5AC<sup>+</sup> and AcTub<sup>+</sup> cells, and the total signal for these stainings, we found no statistical difference between SgScrbl and SgEHF or SgGATA3, although *GATA3* invalidation seems to increase MUC5AC signal. In the absence of *SPDEF*, mucus production was significantly lower than in all other invalidation conditions, with or without IL-13. As *SPDEF* is the transcription factor activating *MUC5AC* expression, the absence of mucus on the apical surface functionally demonstrated the efficacy of its invalidation, and the use of this gene as a positive control for an absence of remodeling (**Fig.89A&B**). Also, as expected, invalidation of *FOXJ1* resulted in a significant reduction in the number of multiciliated cells, validating our experimental set-up (**Fig.89A&C**). As expected, IL-13 treatment induced a marked increase in mucus production in the SgScrbl epithelia. Similar results were obtained for SgEHF and SgGATA3: confocal microscopy observations did not seem to show any difference in the quantity of MUC5AC compared with the SgScrbl after treatment with IL-13, confirmed by quantification performed on several fields at low magnification, which showed no decrease in mucin due to invalidation of these genes (**Fig.89**). Thus, invalidation of *EHF* and *GATA3* did not prevent IL-13-induced mucus hypersecretion.

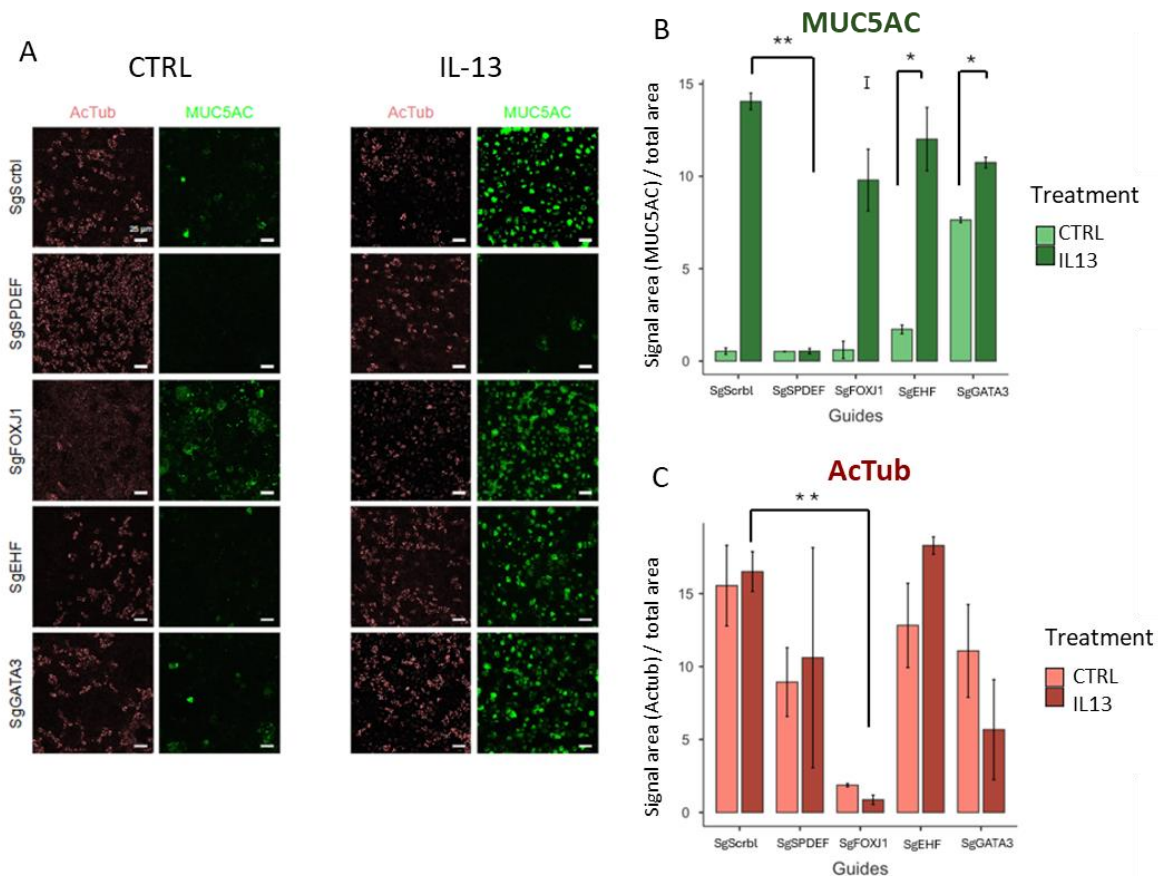


**Figure 89:** Effect of invalidation on epithelial composition.

**A:** Confocal microscopy images of differentiated invalidated epithelia. Immunostaining of MUC5AC (mucus, green); acetylated alpha-tubulin (AcTub, cilia of multiciliated cells, red) Scale: 25  $\mu$ m. Measurement of the mean fluorescence intensity of 3 fields per condition obtained by epifluorescence microscopy of MUC5AC (**B**) and Actub (**C**). \*  $p$ -val  $\leq$  0.05 (Student's t-test), \*\*  $p$ -val  $\leq$  0.01 (Student's t-test). Results are averages of 3 culture inserts from experiment #1, which were replicated identically for experiment #2.

### Effect of invalidation on mucus production

Western blots on total lysates were performed to quantify MUC5AC at the whole epithelium scale. **Fig.90C&D** shows an induction of MUC5AC under SgScrb1, SgGATA3 and SgEHF conditions, and an absence of MUC5AC detection under SgSPDEF. To better quantify the effects of *EHF* and *GATA3* invalidation at the mucus level, MUC5AC secretions in apical compartments were analyzed by dot blot. This method detects and quantifies the presence of protein in supernatants, without separating them by size and can be better adapted to study high molecular weight mucins, as their quantification by Western blot is not optimal due to their size and their abundant glycosylations. Quantification of the dot blot signals revealed an increase in the amount of MUC5AC following IL-13 treatment for SgScrb1, SgEHF and SgGATA3 epithelia, indicating apically secreted mucus production (**Fig.90A&B**). These observations are consistent with immunostaining data. However, it is crucial to note that these results came from a single replicate, which limits the robustness of this observation. Nevertheless, this trend is in line with the expected effects of IL-13 on mucus production and corroborates our previous observations. Luminescence intensity of SgSPDEF, was low, demonstrating little mucus in the

supernatants. Interestingly, an unexpected decrease in mucus was observed in supernatants from SgFOXJ1 epithelia (**Fig.90A**).

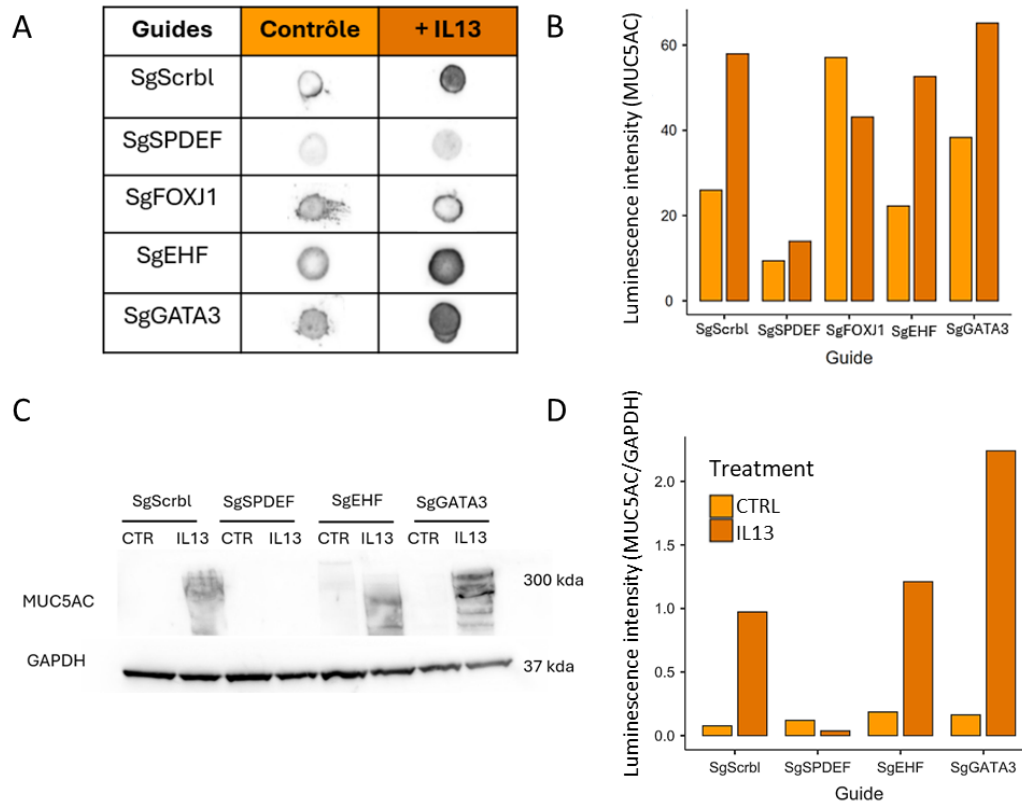


**Figure 90:** Detection and quantification of MUC5AC in invalidated epithelia.

**A:** Dot blot analysis of MUC5AC in supernatants from cultures of experiment #1. **B:** Quantification of luminescence signals from Dot blot spots. **C:** Western blots of protein extracts from total lysates of different invalidated epithelia stained with anti-MUC5AC (experiment #2). (Same membrane as in figure 7.) **D:** Measurement of luminescence intensity of MUC5AC Western blot bands. GAPDH was used as a normalizer for luminescence intensities.

### Effect of invalidation on gene expression

To complement the observations made at protein level, the relative expression of the various genes involved in epithelial remodeling within the invalidated epithelia, were analyzed by qPCR. In the SgSPDEF condition, positive control of absence of remodeling, IL-13 treatment completely abolished the increase in *MUC5AC* (**Fig.90**). In contrast, no significant decrease in *MUC5AC* expression was detected between SgScrb1 and the SgEHF, SgGATA3 and SgFOXJ1 conditions, upon IL-13 treatment. This confirmed the mucus hypersecretion observed at the protein level in invalidated epithelia, which would imply that the epithelia underwent remodeling despite gene invalidation. There was, however, a significant decrease (\*  $p$ -value  $\leq 0.05$ ) in *SPDEF* expression compared with SgScrb1, in the SgEHF epithelium, after IL-13 treatment (**Fig.90**). It is known that *EHF* transcriptionally stimulates *SPDEF* expression, thus implicating *EHF* in the activation of goblet cell differentiation (Fossum et al., 2017). It was to be expected that in the absence of *EHF*, *SPDEF* expression would be decreased, but this was not

reflected by a decrease in the amount of *MUC5AC* in the experiments. Lastly, the effect of *EHF* and *GATA3* invalidation on the number of multiciliated cells were also investigated, by quantifying the expression of the transcription factor, *FOXJ1*, that predominantly regulates multiciliogenesis. IL-13 treatment induced a significant decrease in this gene in all epithelia, including SgEHF and SgGATA3 (SgEHF: \*  $p$ -value  $\leq 0.05$ ; SgGATA3: \*\*\*  $p$ -value  $\leq 0.001$ ) (**Fig.90**). Therefore, there was also no multiciliated cell related remodeling after invalidation of *EHF* and *GATA3*. Taken together, the data suggest that neither *EHF* nor *GATA3* appear to have any effect on mucus secretion or on the number of multiciliated cells after IL-13 treatment.

The gene expression of *EHF* and *GATA3* was also quantified in these experiments, even though a decrease in the detection of invalidated genes by qPCR is not necessarily expected, as the region targeted by SgRNAs is different from the region detected by qPCR. Moreover, the creation of a deletion in a given DNA region does not always destabilize the entire mRNA of the targeted gene. *EHF* was detected in the SgScrbl condition (\*  $p$ -value  $\leq 0.05$ ), indicating that this gene is significantly induced by IL-13. This was expected based on the primary culture data but had not been observed in the preceding time course assay (**Fig.74C**). Interestingly, invalidation of each gene (*SPDEF*, *FOXJ1*, *GATA3* and *EHF*) induced a significant decrease in *EHF* after IL-13 (SgSPDEF, SgFOXJ1:  $p$ -value  $\leq 0.05$ ; SgEHF, SgGATA3:  $p$ -value  $\leq 0.01$ ). On the other hand, no induction of *GATA3* expression was detected following IL-13 treatment, except in SgEHF (**Fig.91**), which was not expected but corroborated the increase in *GATA3* observed at the protein level with Western blot (**Fig.77A**).

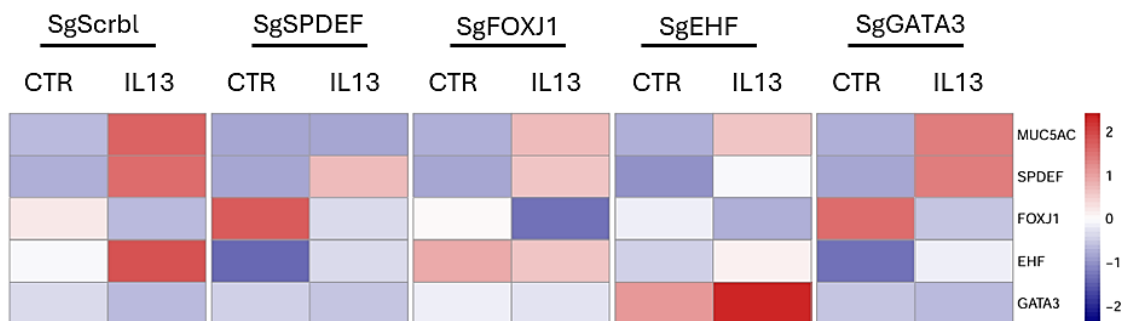


**Figure 91:** Effect of invalidation on expression of genes involved in epithelial remodeling. Heatmap of relative expressions measured by qPCR of  $2^{-\Delta\Delta Ct}$  *MUC5AC*, *FOXJ1*, *EHF*, *GATA3* and *SPDEF* relative to *TBP* gene within epithelia. Results are averages of 3 culture inserts of experiment #1.

## Single-cell RNA sequencing analysis of invalidated epithelia

### Invalidation of *EHF* and *GATA3* does not prevent *MUC5AC* expression in response to IL-13 at the single cell level

We sequenced 70 000 cells from mature epithelia of experiment #2 (SgScrbl, SgSPDEF, SgEHF and SgGATA3), with or without IL-13, to quantify cell type distribution and gene expression variation at a

more granular level (**Fig.92A**). Proportion analysis confirmed the absence of MUC5AC+ goblet cells in condition SgSPDEF, which was accompanied by an absence of *MUC5AC*, even after IL-13 stimulation (**Fig.92B&E**). On the other hand, there were no significant differences between SgScrb1, SgEHF and SgGATA3 (**Fig.91B, C, D, F**), confirming the absence of prevention of goblet hyperplasia without *EHF* or *GATA3*.

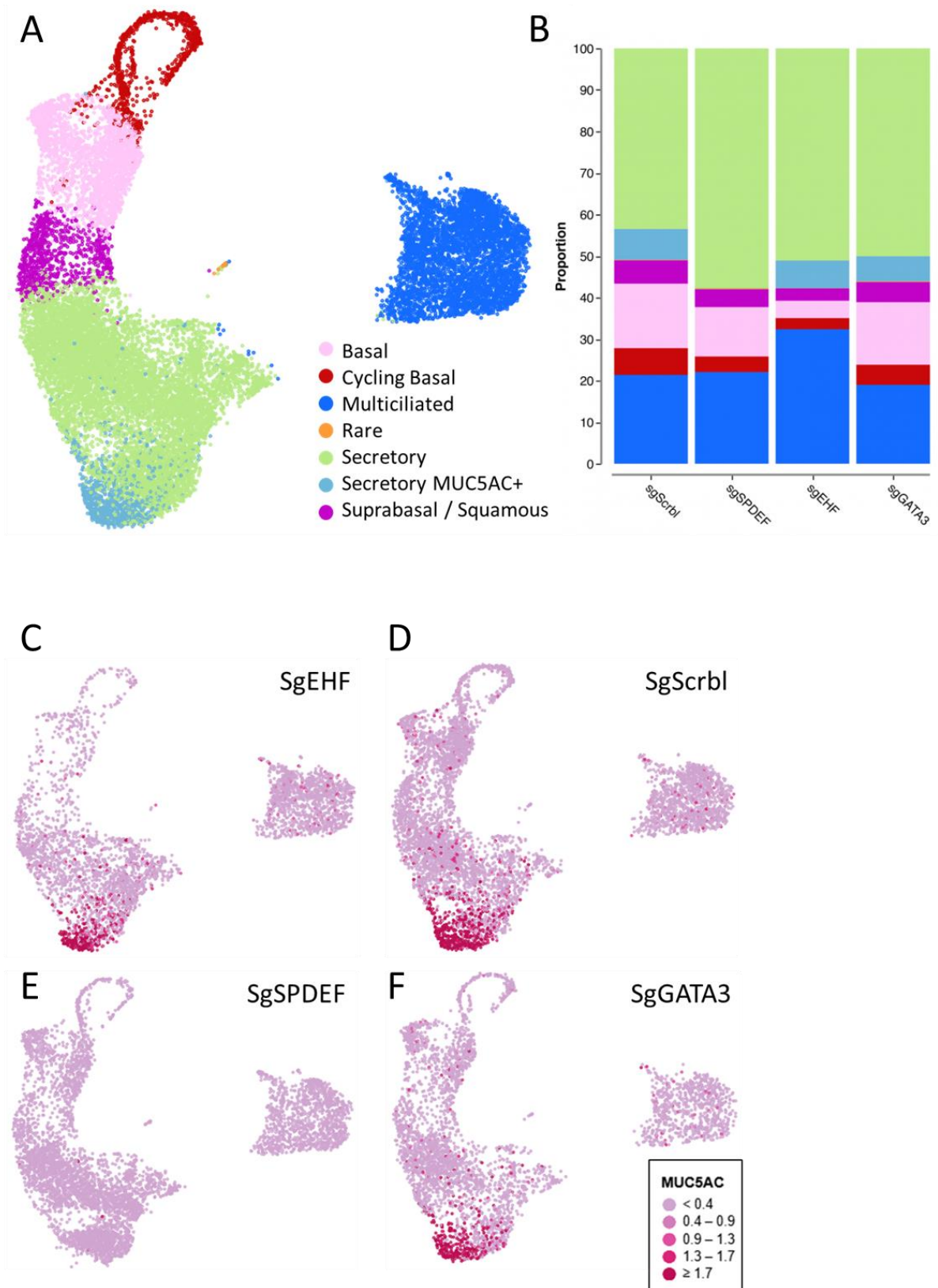


**Figure 92:** Single cell atlas of CRISPR cells.

**A:** UMAP representation of the CRISPR single-cell atlas colored by cell types. **B:** Proportion plot of cell type in percentage, according to sg condition in untreated cells. Feature plot of *MUC5AC* expression in IL-13 treated cells of condition SgEHF (**C**), SgScrb1 (**D**), SgSPDEF (**E**) and SgGATA3 (**F**).

## EHF regulates GATA3 expression

Interestingly, we observed several differentially expressed genes in the basal cell population in condition SgEHF. Compared to SgScrbl, a strong interleukin-1 pro-inflammatory signature was detected in SgEHF basal cells after IL-13 treatment, with induction of genes such as *IL1RN*, *IL32*, *IL1A* and *IL1R1*, accompanied by neutrophil-attracting cytokines such as *CXCL1*, -2 and -8 (**Fig.93A**). Most strikingly, we detected an upregulation of *GATA3* in this condition, which was confirmed by qPCR and Western blot (**Fig.93A-C**). Therefore, *EHF* appears to repress the expression of *GATA3* in basal cells.

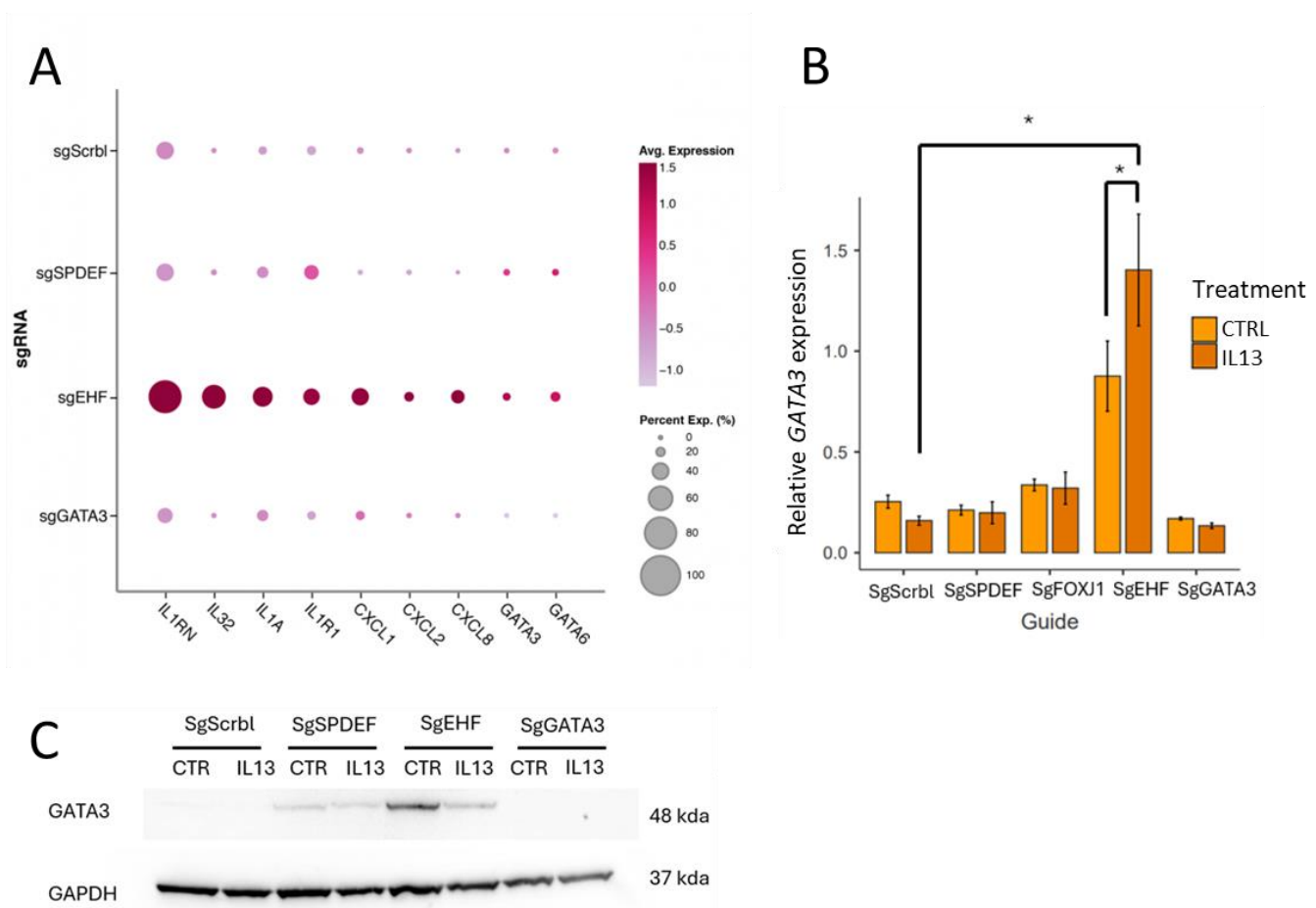


**Figure 93:** EHF regulates GATA3 expression.

**A:** Dot plot of selected genes in IL-13 basal cells. **B:** qPCR of relative *GATA3* expression over *TBP* across different conditions from experiment #1. **C:** Western blot for *GATA3* in conditions from experiment #2.



## Discussion

The goal of this project was to identify the involvement of two candidate genes, *EHF* and *GATA3*, in epithelial remodeling in the context of type 2 asthma, in the BCI cell line. Several studies comparing this cell line with primary cultures demonstrated its similarity in terms of morphology, cell type composition and overall gene expression patterns (Prescott et al., 2023). The use of this immortalized cell line enabled two sequences of manipulations, one in which the cells were used directly after their invalidation, as is routinely done with primary cultures in our team, and a second one in which the cells were propagated for several passages after their invalidation. Both experiments showed the same results, validating the stability through time of gene invalidation in this cellular model. Moreover, this cell line successfully reproduced IL-13-induced epithelial remodeling, with its typical features, i.e. a decrease in the number of multiciliated cells and a goblet cell hyperplasia.

In this study, the use of the CRISPR-Cas9 RNP technique to invalidate the genes of interest proved effective, enabling us to observe significant effects on the phenotype obtained. The CRISPR-Cas9 RNP method, by offering rapid genome editing, stands out for its increased specificity (between 80 and 95% depending on the genes targeted), which considerably improves the reliability of the results. Another major advantage of this technique is that it does not require clonal selection of invalidated cells. This is crucial, as it maintains the cellular equilibrium of the respiratory epithelium, avoiding the enrichment of clones that could introduce biological artifacts and disrupt the differentiation process. Moreover, the use of a recombinant Cas9, whose presence in the cells is only transient, reduces off-target effects.

Various mucin detection methods were applied to characterize the effect of gene invalidation on epithelial remodeling. Mucins are very high molecular weight glycoproteins with a highly glycosylated structure, which play a crucial role in the protection and lubrication of epithelial surfaces (Carpenter et al., 2021). Due to their size and complexity, mucins are hard to detect and analyze (Ramsey et al., 2016). In this context, we used a technique favored for mucin detection, the dot blot. In this method the samples are applied directly to a membrane, without electrophoretic separation, thus simplifying the detection of very high molecular weight proteins such as mucins. This technique can detect the presence of mucins secreted at the apical side of epithelia (Ahmed et al., 2022). Some improvements are still needed to improve the homogeneity of the signal per spot. Thus, the multi-methodological approach used here ensured better quantification and characterization of these complex proteins.

These different methods demonstrated that despite the absence of *EHF* and *GATA3*, there was no decrease in mucus production after IL-13 treatment. The working hypothesis was that invalidation of *EHF* decreases mucus production via regulation of its cousin the goblet cell transcription factor, *SPDEF* (Fossum et al., 2017). *SPDEF* expression has been shown to be sufficient to induce goblet cell

differentiation (K. S. Park et al., 2007). However, the results obtained in my study show that *EHF* invalidation does induce a decrease in *SPDEF* expression but does not translate into an effect on *MUC5AC* expression. The remaining *SPDEF* level, although decreased, may be sufficient to maintain induction of *MUC5AC* expression in response to IL-13. Studies have demonstrated that the effects of *SPDEF* on IL-13-induced *MUC5AC* expression are *STAT6*-dependent (H. Yu et al., 2010). Binding of IL-13 to its receptor complex, including IL-13R $\alpha$ 1, activates JAK kinases. These kinases phosphorylate *STAT6*, leading to the transcription of *SPDEF* (Tsiogka et al., 2022), without the involvement of *EHF*. Importantly, it is also possible that other signaling pathways and regulators play a role in modulating *MUC5AC* independently of *EHF*.

Invalidation of *GATA3* had no effect on epithelial remodeling when treated with IL-13. *GATA3* is critically involved in regulating the differentiation of Th2 cells (Skapenko et al., 2004), the immune cells predominantly involved in severe type 2 asthma. In certain pathologies, *GATA3* and *FOXA1* are coexpressed. *FOXA1* depletion is associated with a significant decrease in *SPDEF* levels (Paranjapye et al., 2020). The working hypothesis was that *GATA3* invalidation decreases mucus production. However, the lack of effect of *GATA3* invalidation, despite its relationship with *FOXA1*, demonstrates that *GATA3* is not directly involved in the regulation of mucus production. The increase in *GATA3* in SgEHF epithelia may be explained by the fact that *EHF* is known to repress *GATA6* expression (Fossum et al., 2017). Being part of the same family, it could be assumed that *GATA3* and *GATA6* share common regulators such as *EHF*.

To better understand the roles of *EHF* and *GATA3* in epithelial remodeling, IL-13-treated and invalidated cells were sequenced by scRNA-seq. This technique offers the advantage of studying transcriptional responses at the single-cell level, without a priori detection. It is thus able to reveal effects specific to each cell type, without being limited to the study of a single parameter, such as the detection of *MUC5AC*. Analysis of the results is currently underway and will enable the detection of changes in the epithelium at the level of parameters that we have not been able to analyze until now, such as the differential regulation of certain genes or a change in the number of cells of other cell types. By combining scRNA-seq with our current methods, we hope to gain a more detailed and precise understanding of the regulatory mechanisms involved in IL-13-induced epithelial remodeling, and the impact of *EHF* and *GATA3* gene invalidation on these processes.

Beyond the roles of *EHF* and *GATA3*, my results include some very interesting elements for the team's projects. Looking closely at the results for genes used as negative controls for remodeling, I observed that in the absence of *FOXJ1*, the multiciliated transcription factor, there was an increase in the number of goblet cells, suggesting that invalidation of *FOXJ1*, which is known to inhibit multiciliated

differentiation, would also have an impact on the regulation of the goblet cell differentiation pathway. Conversely, the absence of *SPDEF*, the goblet cell transcription factor, led to a marked increase in the number of multiciliated cells. These observations highlight the equilibrium of the epithelial ecosystem: inhibition of the goblet cell pathway would stimulate the multiciliated cell pathway, and vice versa. This phenomenon has never been demonstrated before and is now beginning to be studied by the team.

## C. Cell culture differentiation and proliferation conditions influence the *in vitro* regeneration of the human airway epithelium

*In vitro* regeneration of airway epithelium at the Air/Liquid Interface (ALI) is a system widely used for functional studies in cell and molecular biology, pharmacology, and physio-pathological studies of chronic respiratory diseases such as asthma, COPD and cystic fibrosis. Recently, the COPD drug Kalydeco (Vertex Pharmaceuticals Incorporated) was approved by the U.S. Food and Drug Administration based on work using primary cultures (Durmowicz et al., 2018). Since 2020, it has also become the most appropriate model for severe acute respiratory syndrome coronavirus 2 (SARS-CoV-2) *in vitro* infectivity studies. Given the significant differences in the experimental conditions of ALI cultures used in the numerous studies in the literature, it was necessary to precisely define the impact of these different experimental protocols on the final composition of the reconstituted epithelia.

For multiciliogenesis studies, our team has used a commercial medium, Pneumacult-ALI™ (STEMCELL technologies) for cell differentiation, as it generates a densely ciliated epithelium. However, this medium is not well adapted for goblet cell hyperplasia studies as the amount of goblet cells at baseline in this medium is almost at its maximum capacity. Thus, goblet cell stimulation with IL-13 in the case of my project, or other remodeling agents, would not be effective. In addition, the composition of this medium is not known as it is proprietary, hindering the possibility to use it in studies necessitating the use of agonist or antagonists for signaling pathways. To counteract this problem, we compared different culture media among the most commonly used ones: two commercially available and widely used media PneumaCult-ALI™ (STEMCELL Technologies) and BEGM™ (Lonza), and two “homemade” medium. Half & Half (H&H), developed by Susan Reynolds’s group, it is considered to produce fewer biases compared with other media (Malleske et al., 2018), and “Clancy’s”, used by Clancy’s group to perform electrophysiological studies (Brewington et al., 2018).

We realized that to date, no study had compared in detail, the impact of these 4 media on the cellular composition of the airway epithelium in ALI culture, at the single cell level. We thus used single-cell RNA-sequencing to analyze epithelial cells obtained after ALI differentiation in these 4 media and we also compared epithelial composition after proliferation (immersed). We found variations in cell composition, gene expression, and secretome transcripts that were illustrated more precisely with the differential expression of the SARS-CoV-2 entry factor ACE2. Proliferation in PneumaCult-Ex Plus favored secretory cell fate, highlighting the key influence of proliferation media on epithelial

differentiation. Our data provide a comprehensive repertoire for evaluating culture condition influence on airway epithelial differentiation.



# MAJOR TECHNICAL ADVANCES

## Cell Culture Differentiation and Proliferation Conditions Influence the *In Vitro* Regeneration of the Human Airway Epithelium

Elisa Redman<sup>1,2</sup>, Morgane Fierville<sup>1,2,3</sup>, Amélie Cavard<sup>1</sup>, Magali Plaisant<sup>1</sup>, Marie-Jeanne Arguel<sup>1,2</sup>, Sandra Ruiz Garcia<sup>1</sup>, Eamon M. McAndrew<sup>1,2</sup>, Cédric Girard-Riboulleau<sup>1</sup>, Kevin Lebrigand<sup>1,2</sup>, Virginie Magnone<sup>1,2</sup>, Gilles Ponzio<sup>1,2</sup>, Delphine Gras<sup>4</sup>, Pascal Chanez<sup>4</sup>, Sophie Abelanet<sup>1</sup>, Pascal Barbry<sup>1,2,3</sup>, Brice Marcet<sup>1,2\*</sup>, and Laure-Emmanuelle Zaragosi<sup>1,2\*</sup>

<sup>1</sup>Institut de Pharmacologie Moléculaire et Cellulaire, Centre National de la Recherche Scientifique (CNRS), Institut National de la Santé et de la Recherche Médicale (INSERM), and Université Côte d'Azur, <sup>2</sup>IHU RespirERA, and <sup>3</sup>Interdisciplinary Institute for Artificial Intelligence (3IA Côte d'Azur), Université Côte d'Azur, Sophia Antipolis, France; and <sup>4</sup>Centre de Recherche en Cardiovasculaire et Nutrition, Institut National de la Santé et de la Recherche Médicale (INSERM), and Institut National de Recherche pour L'agriculture, L'alimentation et L'environnement (INRAE), Université Aix-Marseille, Marseille, France

ORCID IDs: 0000-0001-9632-6483 (P.B.); 0000-0001-6747-7928 (L.-E.Z.).

### Abstract

The human airway mucociliary epithelium can be recapitulated *in vitro* using primary cells cultured in an air–liquid interface (ALI), a reliable surrogate to perform pathophysiological studies. As tremendous variations exist among media used for ALI-cultured human airway epithelial cells, the aim of our study was to evaluate the impact of several media (BEGM, PneumaCult, Half & Half, and Clancy) on cell type distribution using single-cell RNA sequencing and imaging. Our work revealed the impact of these media on cell composition, gene expression profile, cell signaling, and epithelial morphology. We found higher proportions of multiciliated cells in PneumaCult-ALI and Half & Half, stronger EGF signaling from basal cells in BEGM-ALI, differential expression of the severe acute

respiratory syndrome coronavirus 2 (SARS-CoV-2) entry factor *ACE2*, and distinct secretome transcripts depending on the media used. We also established that proliferation in PneumaCult-Ex Plus favored secretory cell fate, showing the key influence of proliferation media on late differentiation epithelial characteristics. Altogether, our data offer a comprehensive repertoire for evaluating the effects of culture conditions on airway epithelial differentiation and will aid in choosing the most relevant medium according to the processes to be investigated, such as cilia, mucus biology, or viral infection. We detail useful parameters that should be explored to document airway epithelial cell fate and morphology.

**Keywords:** airway epithelium; single-cell RNA sequencing; air–liquid interface cell culture; culture medium; differentiation

(Received in original form October 9, 2023; accepted in final form June 6, 2024)

Ⓞ This article is open access and distributed under the terms of the Creative Commons Attribution Non-Commercial No Derivatives License 4.0. For commercial usage and reprints, please e-mail Diane Gern.

\*These authors contributed equally to this work.

Supported by Fondation pour la Recherche Médicale grant DEQ20180339158; Institut National de la Santé et de la Recherche Médicale Inserm Cross-Cutting Scientific Program HuDeCA 201; Chan Zuckerberg Initiative grant 2017-175159-5022; H2020 Health DiscovAIR; Canceropôle PACA Innovation Technologique 2018; Centre National de la Recherche Scientifique; Agence Nationale de la Recherche grant 21-ESRE-0052, ANR-19-P3IA-0002, ANR-19-CE14-0027, ANR-23-IAHU-0007, ANR-10-INBS-09-02, ANR-10-INBS-09-03; and HORIZON EUROPE Marie Skłodowska-Curie Actions grant 101072892. Conseil Départemental 06 016-294DGADSH-CV; Fondation du Souffle.

Author Contributions: E.R. designed and performed experiments and wrote the manuscript. A.C., M.P., M.-J.A., S.R.G., G.P., V.M., and D.G. performed experiments. S.A. performed some image acquisition. M.F. and E.M.M. performed transcriptomics data analysis and wrote the manuscript. C.G.-R. and K.L. performed transcriptomics data analysis. P.B. and P.C. performed data analysis and edited the manuscript. B.M. supervised the study and edited the manuscript. L.-E.Z. supervised the study, performed experiments, and wrote and edited the manuscript.

Correspondence and requests for reprints should be addressed to Laure-Emmanuelle Zaragosi, Ph.D., Université Côte d'Azur, Centre National de la Recherche Scientifique, Institute Pharmacology Moléculaire et Cellulaire, 06560 Sophia-Antipolis, France. E-mail: zaragosi@ipmc.cnrs.fr. Brice Marcet, Ph.D., Université Côte d'Azur, Centre National de la Recherche Scientifique, Institute Pharmacology Moléculaire et Cellulaire, 06560 Sophia-Antipolis, France. E-mail: marcet@ipmc.cnrs.fr.

This article has a data supplement, which is accessible at the Supplements tab.

Am J Respir Cell Mol Biol Vol 71, Iss 3, pp 267–281, September 2024

Copyright © 2024 by the American Thoracic Society

Originally Published in Press as DOI: 10.1165/rcmb.2023-0356MA on June 6, 2024

Internet address: www.atsjournals.org

## Clinical Relevance

The human airway mucociliary epithelium can be recapitulated *in vitro* using primary cells cultured in an air-liquid interface, a reliable surrogate to perform pathophysiological studies. Our study provides a comprehensive repertoire for evaluating the effects of culture conditions on airway epithelial differentiation and will aid in choosing the most relevant medium according to the processes to be investigated.

The mammalian airways are lined by a mucociliary epithelium, composed of basal cells, club cells, goblet cells, multiciliated cells (MCCs), and rarer cell types (deuterosomal cells, ionocytes, pulmonary neuroendocrine and tuft cells, and microfold cells) (1–3). The cell composition of the epithelium varies according to the macroanatomical location, with the highest differences found between the nasal and tracheobronchial epithelia (4). Within the tracheobronchial airways, cellular distribution is relatively stable, with modifications occurring in the most distal bronchioles (4–7). The airway epithelium is frequently challenged by the inhalation of noxious compounds, chemicals, microorganisms, and viruses, which alter its integrity. Specific repair mechanisms allow full epithelial restoration so that normal physiological function can be reestablished (see Figure E1A in the data supplement). In chronic lung diseases, such as cystic fibrosis (CF), asthma, and chronic obstructive pulmonary disease, frequent injuries and chronic inflammation induce remodeling of the epithelium, often associated with a progressive loss of MCCs and an increased content of goblet cells. Studying the regeneration of the epithelium in normal or pathological conditions is necessary to identify mechanisms regulating the physiological regeneration and pathological remodeling of the airway epithelium. The development of cell cultures at the air-liquid interface (ALI) of nasal or bronchial epithelial cells has been crucial in many mechanistic studies (8, 9, 10). These cultures are not just convenient surrogates of *in vivo* epithelium (11–14); they were extensively used to establish the cellular roadmap of airway regeneration (11, 15) (see Figure E1A). This is illustrated by the

recent approval of Kalydeco (Vertex Pharmaceuticals Incorporated) by the U.S. Food and Drug Administration, on the basis of work using primary cultures to predict clinical response in patients with CF bearing ultrarare CFTR mutations, for whom direct clinical trial studies are not feasible (16). Over the past three years, it has also become the most appropriate model for severe acute respiratory syndrome coronavirus 2 (SARS-CoV-2) *in vitro* infectivity studies. Although most studies have identified MCCs as the major entry cell type (17–22), others have shown a more widespread distribution (23, 24), some with nonciliated cells being infected preferentially over MCCs (25, 26). One striking difference between these studies was indeed the culture medium that was used.

Considering the large differences existing in cell culture conditions across the many studies using ALI cultures, it is important to define exactly the impact of the different experimental setups in terms of cellular composition (8). Some studies have already performed direct comparison of cell culture media on ALI culture structure and/or function (27–34), but none has combined quantitative assessment of cell type distribution with differential gene expression profiles. The effect of using distinct commercial proliferation media during the cell expansion stage has never been reported either. We thus investigated the impact of four distinct proliferation and differentiation media on the epithelial structure and cellular composition of the reconstructed airway epithelium. We selected two commercially available and widely used media (PneumaCult and BEGM; Lonza), which we compared with Half & Half (H&H), which has been described by Susan Reynolds's group and is considered to produce fewer biases compared with other media (35). The last medium is used by Clancy's group to perform electrophysiological investigations (36). We used single-cell RNA sequencing (scRNA-seq) to quantify cell type distribution and gene expression profile variations across the four media. We also evaluated the impact of proliferation media on ALI differentiation and the variations caused by the use of distinct porous membranes. Given the widespread use of ALI culture in SARS-CoV-2 studies, we also evaluated the effect of these media on viral entry factor expression.

Some of the results of these studies have been previously reported in preprint form ([www.biorxiv.org/content/10.1101/2024.03.16.584842v1.full](http://www.biorxiv.org/content/10.1101/2024.03.16.584842v1.full)).

## Methods

To evaluate the impact of cell culture media on cell composition of fully differentiated ALI-regenerated airway epithelium, we first used primary cells that were freshly dissociated from human bronchi and set up proliferation and differentiation in four culture media: PneumaCult-ALI (hereafter Pneuma-ALI) and BEGM-ALI (i.e., the two most widely used media) in parallel with H&H (35) and Clancy medium (36). Freshly isolated human bronchial epithelial cells (HBECs) underwent one passage in PneumaCult-Ex Plus medium, then were split and seeded on Transwell (Corning) membranes in four distinct proliferation media: PneumaCult-Ex Plus (hereafter Pneuma-Ex+), BEGM, Wu medium, and Clancy medium. Once cells reached confluence, differentiation was induced by removing the medium in the apical chamber and adding matched differentiation medium in the basal chamber. The differentiation media were Pneuma-ALI, H&H, BEGM-ALI, and Clancy. scRNA-seq was performed at three time points: after the initial propagation step in plastic flasks, at the onset of the ALI (ALI0), and at full differentiation (ALI28) (see Figure E1B). To evaluate whether some differences in ALI differentiation might stem from the medium used at the initial cell propagation steps, we amplified human nasal epithelial cells (HNECs) for two passages on plastic, in either BEGM or Pneuma-Ex+ (Stemcell Technologies). We then seeded them on membranes, maintained cell amplification in the same medium until reaching confluence, and then set up the ALI in either BEGM-ALI or Pneuma-ALI (see Figure E1C). We evaluated epithelial composition using quantitative PCR (qPCR) and immunostaining. The effects of using alternative semiporous membranes were also evaluated. Detailed methods are described in the data supplement. scRNA-seq data are available at <http://carra.ipmc.cnrs.fr:3838/CultureMedia2024/> and <https://cellxgene.cziscience.com/collections/73cf6939-3caa-4105-bc57-e073ee885a28>.

## Results

### ALI Differentiation Medium Influences Epithelial Morphology and Cell Type Distributions

After full differentiation of HBECs, epithelia were fixed for histological analysis and



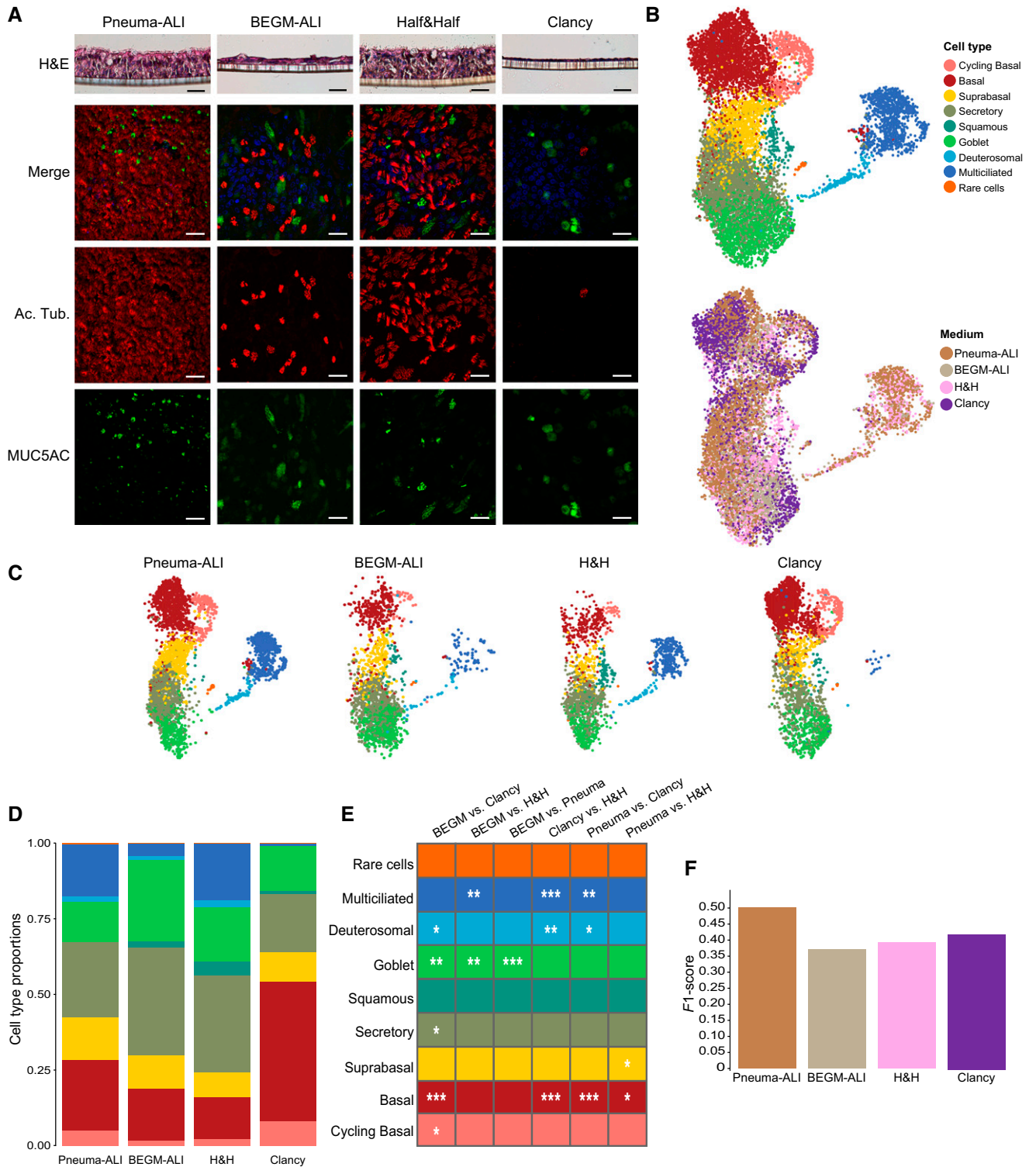


**Figure 1.** Single-cell RNA sequencing analysis of human bronchial epithelial cells (HBECs) at 28 days of differentiation (ALI28) in four distinct media. (A) General characterization of HBEC differentiation in four cell culture media. (Top) Representative images of H&E staining of sections of HBECs at ALI28. Scale bars, 100  $\mu$ m. For each condition and each of the two independent cell cultures, two inserts were sectioned and imaged. (Bottom) Representative images of immunostaining of HBECs at ALI28 for acetylated  $\alpha$ -tubulin and MUC5AC. Scale bars, 30  $\mu$ m. Nuclei were stained with DAPI and shown in blue on the merged images. For each condition and each of the two independent cell cultures, three inserts were stained and imaged. (B) Uniform manifold approximation and projection (UMAP) of the integrated dataset of HBECs at ALI28 containing all cells from the four distinct conditions, from two independent cultures from two healthy donors. (Top) UMAP colored by cell type.

immunostaining. Hematoxylin and eosin staining on epithelia sections revealed large differences in tissue structures (Figure 1A). Pneuma-ALI and H&H media generated thicker epithelia with an apical surface covered with cilia. BEGM-ALI and Clancy media generated much thinner epithelia, with this effect more prevalent for Clancy medium. Cilia immunostaining with acetylated  $\alpha$ -tubulin suggested a higher content of MCCs in Pneuma-ALI and H&H media than in BEGM-ALI and Clancy media (Figure 1A).  $MUC5AC^+$  goblet cell content was difficult to compare among culture media because staining patterns differed according to media with, for instance, smaller and more intense  $MUC5AC$  patches in Pneuma-ALI (Figure 1A).

Thus, to obtain a more quantitative and detailed description of the regenerated epithelia in each culture medium, we performed 3' scRNA-seq on fully differentiated HBEC cultures in each medium (ALI28). To reduce batch effects, we multiplexed all conditions using cell hashing (37). Datasets for all conditions and all donors were aggregated for subsequent analyses, allowing cell type quantification and differential gene expression among culture media (Figure 1B). Cell types were determined on the basis of the expression of known marker genes (see Figures E2A–E2C and Table E1). Basal cells were identified by high expression of *KRT5* and *TP63* and cycling basal cells by typical proliferation markers such as *MKI67*. Suprabasal cells were defined as cells located at the basal side of the epithelium but not directly lying on the basal lamina, expressing *KRT5* but very low *TP63*. Secretory cells included not only club cells that were *SCGB1A1*<sup>+</sup> and *CYP2F1*<sup>+</sup> but also other cell types that did not necessarily express *SCGB1A1* but instead markers such as *AQP5* and *FAM3D*. Squamous cells were characterized by an intermediate signature between suprabasal and secretory cells and also through expression of specific genes such as *SPRR1A*, *IVL*, and *SCEL*. Goblet cells displayed a typical secretory cell gene expression program, with *SCGB1A1*, *BPIFA1*, and *BPIFB1* together with the expression of

*MUC5B* and/or *MUC5AC*. Of note, the length of the *MUC5AC* and *MUC5B* transcripts can affect their detection in scRNA-seq datasets and probably contributed to an underestimation of  $MUC5AC^+$  and  $MUC5B^+$  cells. MCCs were identified as *FOXJ1*<sup>+</sup> and *DYNLRB2*<sup>+</sup>, while deuterosomal cells, which are cells amplifying centrioles, were *FOXJ1*<sup>+</sup>, *CDC20B*<sup>+</sup>, and *DYNLRB2*<sup>-</sup>. Rare cells formed a small but distinct cell cluster, characterized by the expression of the ionocyte-specific *FOXJ2*, as well as *HEPACAM2* and *NREP*, which we previously detected expressed by both ionocytes and neuroendocrine cells. We also detected *STMN1*, a specific marker of tuft cells, and *MARCKSL1* and *CRYM*, expressed by both tuft and neuroendocrine cells as expected (1, 4).

Figure 1B shows the distribution of the different cell type clusters at ALI28, after aggregation of the four datasets (top) and colored according to the differentiation media (bottom). The uniform manifold approximation and projection representation is split in Figure 1C according to the four media, with the corresponding cell type distributions quantified in Figure 1D. Pneuma-ALI and H&H cultures displayed similar distribution profiles (Figures 1C and 1D) with, for instance, 15.7% and 19.5% of MCCs, respectively, and 13.1% and 17.7% of goblet cells, respectively (Figure 1D and Table E2). BEGM-ALI and Clancy media cultures displayed more diverse profiles characterized by much lower MCC content (3.8% for BEGM-ALI and 0.6% for Clancy medium) and a higher goblet cell proportion in BEGM-ALI (26.6%). We assessed the statistical significance of the differences among scRNA-seq conditions by performing pairwise comparisons using the propeller package (38, 39), which confirmed the significance of the observations for the multiciliated and goblet cell populations (Figure 1E). The Clancy medium also yielded a significant difference in basal cell content against all other media (Figure 1E). Compared with the luminal immunostaining from Figure 1A, the higher proportion of goblet cells and the absence of a significant decrease of MCCs in BEGM-ALI might

seem surprising but can be explained by the greater tissue thickness in Pneuma-ALI and H&H. As the scRNA-seq dataset quantifies all cells, from the basal to the luminal compartment, the proportion of luminal cells in thick epithelia is decreased compared with thin epithelia. In addition, immunostaining detected  $MUC5AC^+$  cells only, as opposed to scRNA-seq, which identified goblet cells on the basis of the entire set of enriched genes, including *MUC5B*. We quantified goblet cells expressing *MUC5AC* alone, *MUC5B* alone, or both and found some significant differences between differentiation media, with BEGM and H&H producing more *MUC5B*-only and *MUC5AC*-only goblet cells, respectively (see Figures E3A and E3B).

We next sought to compare the regenerated epithelia with *in vivo* data to identify the *in vitro* conditions that best reproduced the healthy airway environment. We used a label transfer tool based on universal cell embeddings (39) to map each medium-specific dataset onto the Human Lung Cell Atlas (HLCA) core reference (1). We computed an *F1* score by comparing the predicted labels, obtained through the universal cell embeddings label transfer method, against those manually annotated using marker genes and clustering. The *F1* score evaluates the classification performance of the method, and the method should perform best on cells most resembling the *in vivo* reference. Figure 1F shows that the best *F1* score was obtained by Pneuma-ALI media (0.5), followed by Clancy (0.42), H&H (0.39), and BEGM (0.37). We used label transfer to obtain prediction proportions between our *in vitro* and the *in vivo* reference, and we observed variable results depending on cell clusters (see Figure E4). Despite high mapping with HLCA basal cells, basal cells from BEGM-ALI and H&H also mapped with HLCA suprabasal cells, suggesting diverse gene expression profiles in these media. On the other hand, suprabasal cells from Pneuma-ALI and Clancy media better mapped onto their HLCA counterparts. MCCs from all media mapped almost perfectly with HLCA MCCs, but in Clancy and BEGM-ALI, MCCs also displayed high scores for deuterosomal cells,

**Figure 1.** (Continued). (Bottom) UMAP colored by medium. (C) UMAPs for each medium, colored by cell type, with color code identical to A. (D) Quantification of cell type proportions in each medium. (E) *P* value of *t* test using the propeller package, using the arcsine transformation, for each two-to-two medium comparison of cell type proportions. (F) *F1* score derived from universal cell embeddings (UCE) label transfer against the Human Lung Cell Atlas core reference (8). The *F1* score is calculated by comparing the predicted labels, obtained through the UCE label transfer method, against those manually annotated using marker genes and clustering; the maximal score is 1. Ac. Tub = acetylated  $\alpha$ -tubulin; ALI = air-liquid interface; H&E = hematoxylin and eosin; H&H = Half & Half.

suggesting more immature MCCs in these media. Finally, the most striking difference was observed for Pneuma-ALI goblet cells, which did not map with HLCA goblet cells. Instead, cells that we classified as secretory in Pneuma-ALI mapped with goblet cells from HLCA (see Figure E4). These data indicate that secretory and goblet cells, which share very close expression profiles (see Figure E2B), might carry subtle differences between media that influence their classification.

Thus, scRNA-seq allowed the identification of differences among differentiation media, with a higher MCC content in Pneuma-ALI and H&H, as well as gene expression differences shown by differential mapping to an *in vivo* reference. To investigate further these findings, we next aimed to identify more specific effects of each differentiation medium on gene expression profiles within each cell cluster.

### ALI Differentiation Medium Influences Gene Expression Profiles

We first performed media pairwise comparison using a pseudobulk strategy. The largest number of differentially expressed genes was obtained when comparing Pneuma-ALI with BEGM-ALI and Clancy (see Figure E5 and Table E3). In contrast, the smallest number of differentially expressed genes was observed when comparing H&H with Pneuma-ALI. We then displayed the top expressed genes in all pairwise comparisons. Some genes were specifically enriched in one medium, such as *IL33* and *ZBTB16* for Pneuma-ALI and Clancy, respectively (Figure 2A). *IL33* is expressed *in vivo* in healthy lung, in basal and suprabasal cells, and in endothelial cells (1, 4). Interestingly, it is a T-helper cell type 2-oriented cytokine that is involved in asthma susceptibility (40). *ZBTB16* encodes a zinc finger transcription factor that may play a role in the transcriptional memory of hormone stimulation (41). *CYP26A1* was also expressed only by basal cells from Pneuma-ALI medium. This cytochrome-encoding gene contributes to retinoic acid clearing (42). As Pneuma-ALI is the only of the four media for which the composition is not publicly available, interpreting this difference concerning retinoic acid clearing was difficult. *VIM* was also enriched in cycling basal cells from Clancy medium, suggesting a mesenchymal-like phenotype. Pneuma-ALI and H&H shared several differentially enriched genes compared with the other media, such as the secreted

peptides *TFF3*, *ELAPOR1*, and *SCGB1A1*. They also shared the upregulation of *GLIPR2*, a Golgi-associated protein that negatively regulates autophagy (43). On the other hand, BEGM-ALI and Clancy media shared enriched genes such as several anion exchangers (*SLC5A5* and *SLC34A2*), secreted proteins (*STATH*, *VSTM2L*, and *BPIFA2*), and *GCNT3*, an N-acetylglucosaminyltransferase contributing to mucin glycosylation. Altogether, these data suggest significant differences in the secretomes by Pneuma-ALI and H&H on one hand and BEGM-ALI and Clancy on the other.

Given the tremendous number of possible comparisons, we used CellChat (<https://github.com/sqjin/CellChat>) to stratify the different expressed pathways. CellChat quantifies outgoing and incoming signals per signaling pathway, at the level of each cell cluster, thus identifying cells involved in sending and receiving signals for each pathway in an autocrine and paracrine manner. When comparing the number of inferred interactions within each culture medium, we found that BEGM-ALI generated the largest number of interactions compared with all other media and that basal and suprabasal cells are the source of the major incoming signals (shown by top bars of incoming signaling patterns in Figure E6 and by Figures E7A and E7B). However, the communication probability of these interactions, represented by the interaction strength or “weight” calculated by CellChat, appeared equivalent among all media (see Figure E7A, right, and Figure E7B). Some pathways showed striking differences in communication probabilities, such as the EGF, NOTCH, BMP, and WNT pathways (Figures 2B and E7C). The EGF pathway showed stronger outgoing signals in BEGM-ALI and H&H media (see Figure E6) with basal and cycling basal cells sending EGF signals to all other cell types of the epithelium, including themselves (Figure 2B). This signal is consistent with the strong expression of *AREG* in cycling basal and basal cells of BEGM-ALI and H&H, together with the specific *AREG* and *HBEGF* signals in BEGM-ALI only (see Figure E8A). Contribution of each ligand–receptor pair could be inferred from the expression data and showed high contribution of *AREG* signaling toward *EGFR* or *EGFR* together with *ERBB2* in BEGM-ALI (see Figures E8B and E8C). We also looked more closely at differences observed for the NOTCH pathway. Expression of ligands and

receptors were modulated by differentiation media (see Figure E9A), which produced large differences in the inferred interactions (see Figures E9B and E9C). We found that suprabasal, deuterosomal, multiciliated, and squamous cells were predicted as receiving high Notch pathway signals in BEGM compared with Pneuma-ALI (see Figure E9C). As *AREG* has been reported to increase cell proliferation and mediate the upregulation of mucus-related genes in the mouse lung and airway epithelial cell lines (44–47), and as the NOTCH pathway favors the secretory fate over the multiciliated fate (48–51), the differences we report here might explain the greater number of goblet cells and smaller number of MCCs detected in BEGM-ALI.

Hence, the choice of differentiation media can strongly influence signaling pathways between the distinct cell types of the epithelium, which might affect the balance between the different cell types.

### Identification of Cell Types at the Onset of Differentiation

As differentiation media influenced epithelial composition and gene expression, we next assessed whether the cell composition at the onset of differentiation was equivalent among all culture conditions.

We first analyzed HBECs from the same donors as previously, immediately after the initial amplification step in Pneuma-Ex+ (see Figure E1B) to identify the different cell identities that were seeded on the culture membranes. Among the 1,716 cells we analyzed, we found a majority of basal and cycling basal cells (see Figure E10 and Table E4). Interestingly, *KRT13*<sup>+</sup> basal cell types were identified and comprised some proliferative cells, on the basis of *MKI67* expression. A small fraction (3.50%) of goblet cells was also detected, identified by the expression of *SCGB1A1* and *MUC5AC*. No proliferation was detected among goblet cells, as evidenced by the absence of *MKI67* expression (see Figures E10A and E10B).

We then evaluated whether the use of the four distinct proliferation media during the HBEC propagation step on Transwell membranes could influence epithelial cell composition at ALI0, using scRNA-seq. Although basal and cycling basal cells composed the majority of the cultures, we also detected secretory cells (*SCGB1A1*<sup>+</sup> and *SLPI*<sup>+</sup>) and suprabasal cells with a secretory signature (*LY6D*<sup>+</sup> and *SLPI*<sup>+</sup>) (Figures 3A and 3B). No *MUC5AC*<sup>+</sup> goblet cells were detected at this stage. Few cells that we

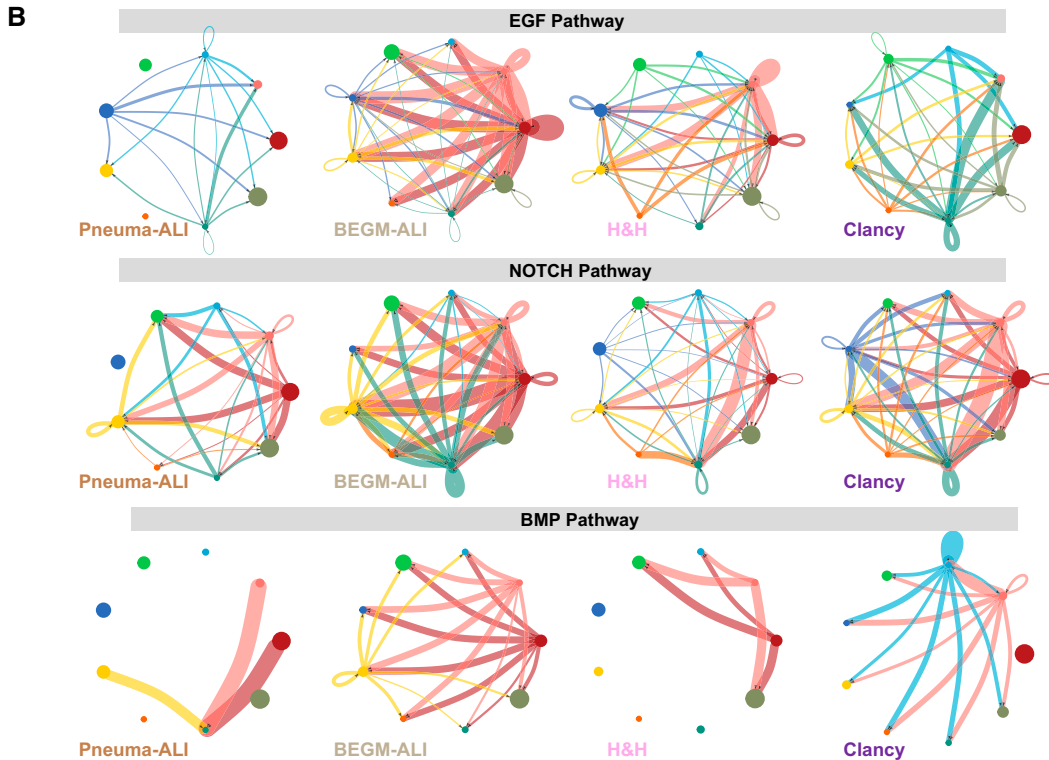
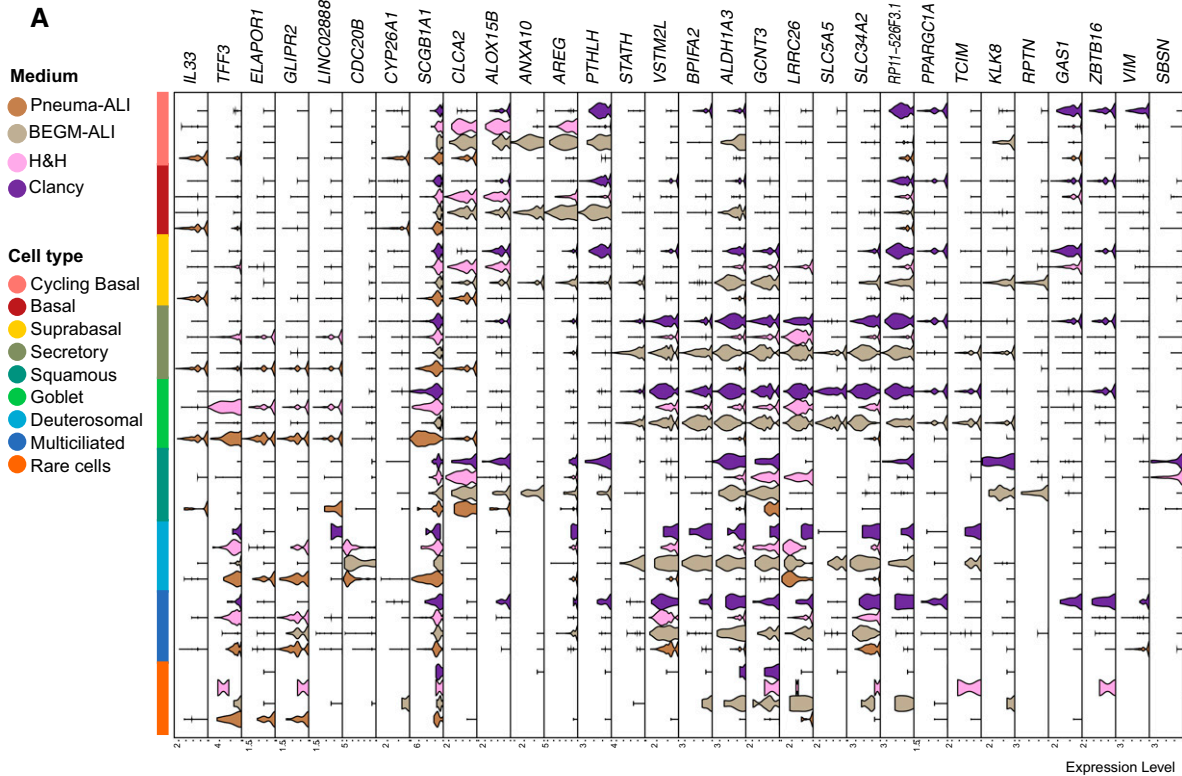


**Figure 2.** Genes and pathways regulated by each cell culture medium at ALI28 of bronchial epithelial cell differentiation. (A) Violin plot showing the top 30 regulated genes among all medium comparisons by pairs. Only genes expressed in at least 30% of cells of at least one cell cluster were selected. The top 30 genes were sorted by the lowest adjusted *P* value of each comparison by pair. For each gene, expression in the four tested media is shown. (B) Circle plots showing the inferred intercellular communication networks for EGF, NOTCH, and BMP signaling. The edge width is proportional to inferred interaction strengths considering ligand-receptor pairs. Black arrowheads show directionality of the inferred interactions. For B, the color code for cell types is identical to A. BMP = bone morphogenetic protein; EGF = epidermal growth factor; NOTCH = notch receptor.

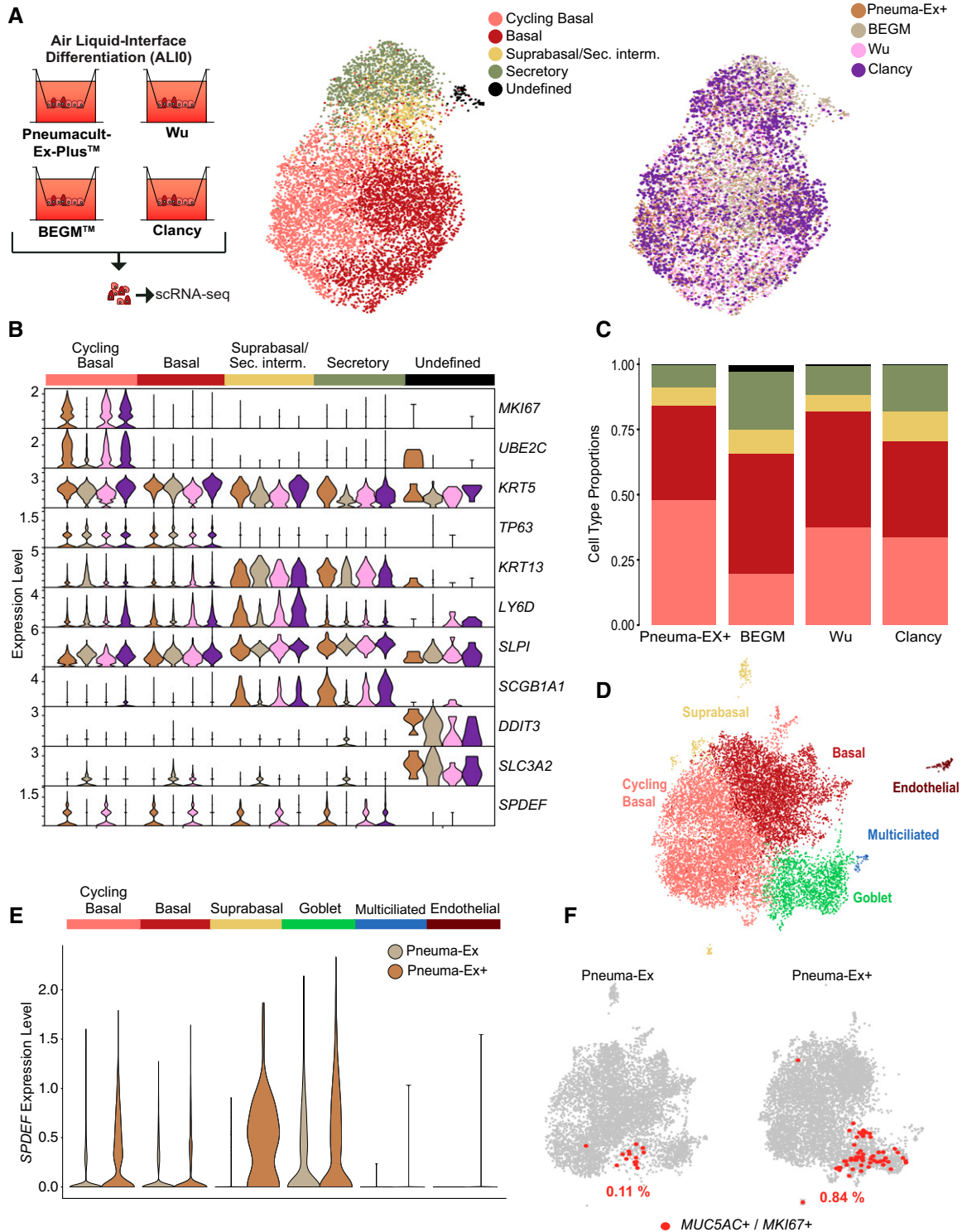


**Figure 3.** Impact of distinct proliferation media on cell type composition and cell expression at ALIO of epithelial cell differentiation. (A) Experimental strategy (left) and UMAPs of the integrated dataset at the onset of differentiation of HBECs containing all cells from the four distinct conditions, colored by cell type and by medium according to the indicated color codes (right). (B) Expression of the top 10 marker genes and of *SPDEF* for the five detected cell populations from A, displayed for each proliferation medium. (C) Quantification of cell type proportions from A for each proliferation medium. (D) UMAP of the integrated dataset composed of human nasal epithelial cell (HNECs) analyzed after the first expansion stage in either PneumaCult-Ex (Pneuma-Ex) or PneumaCult-Ex Plus (Pneuma-Ex+), colored by cell type. (E) Expression of *SPDEF* by each cell type of dataset from D in either Pneuma-Ex or Pneuma-Ex+, as indicated by color code displayed in D. (F) Identification of *MUC5AC*<sup>+</sup> / *MKI67*<sup>+</sup> cells in the integrated dataset composed of HNECs analyzed after the first expansion stage in either

named “undefined” were detected predominantly in the BEGM condition and did not match with any cell type usually found *in vivo*. These cells are negative for all basal cell markers and positive for *DDIT3*, *SLC3A2*, *ISG15*, and *SQSTM1*, among other specifically expressed genes (Figures 3A–3C and Table E5) that seem related to DNA damage, endoplasmic reticulum stress, negative regulation of RNA transcription, and protein ubiquitination. Cell composition was affected by proliferation medium: the BEGM medium generated a smaller fraction of proliferative cells, which is consistent with the lower cell densities observed in this medium, despite reaching confluence. Indeed, contact inhibition appeared higher in BEGM (data not shown). BEGM generated more secretory cells, with lower expression of *SCGB1A1* than all other media (Figures 3B and 3C). In the absence of proliferation in these secretory cells, they probably emerged from differentiation during the expansion process. Wu and Pneuma-Ex+ generated similar cell compositions (Figure 3C). We noticed at this stage a ubiquitous expression of the goblet cell–specific transcription factor *SPDEF* in Pneuma-Ex+ and Wu media (Figure 3B). *SPDEF* was not detected in either BEGM or Clancy medium in basal, cycling basal, or suprabasal/secretory intermediates but was detected in secretory cells from Clancy medium. To explore further this finding, we set up cultures on four independent batches of HNECs, from four distinct healthy donors, either in BEGM or in Pneuma-Ex+. HNECs were used at this stage as a convenient material for experimental replication and were shown as reliable surrogates to HBECs (10). qPCR analysis confirmed strong upregulation of *SPDEF* in all four HNEC cultures at the proliferation stage (see Figure E10C). We then repeated this experiment with three additional HNEC cultures either in Pneuma-Ex+ or PneumaCult-Ex, which is equivalent to BEGM for proliferation, and performed scRNA-seq analysis. In this dataset, we could identify cell populations that were similar to those we found in HBECs, and we detected few multiciliated and endothelial cells, which were probably carried over from tissue isolation (Figures 3D and E10D and Table E6). We confirmed that proliferation in Pneuma-Ex+ for one passage was sufficient

to induce *SPDEF* expression (Figure 3E). Surprisingly, we found few proliferative goblet cells at this stage of cell propagation, with a clear enrichment in Pneuma-Ex+ compared with PneumaCult-Ex (Figure 3F).

Altogether, these results indicate that proliferation conditions could affect cell type distribution and gene expression profiles. Thus, we next evaluated whether some differences in ALI differentiation might stem from the initial cell propagation step.

### Effect of Proliferation Medium on Features of Differentiated Cultures

HNECs were amplified in either BEGM or Pneuma-Ex+, in plastic flasks, and on Transwell membranes and then induced to differentiate at the ALI in either BEGM-ALI or Pneuma-ALI (see Figure E1C). We evaluated epithelial composition by qPCR and immunostaining using the MCC-specific markers *FOXJ1* and acetylated  $\alpha$ -tubulin and the goblet cell–specific marker *MUC5AC*. Both qPCR and immunostaining showed that although Pneuma-ALI yielded more MCCs than BEGM as expected, the proliferation medium had no effect on the MCC content. However, when differentiation was performed in BEGM-ALI, the use of Pneuma-Ex+ for proliferation increased *MUC5AC* content, as shown by qPCR (Figure 4A), immunostaining (Figure 4B), western blot (Figures 4C, 4D, E11A, and E11B). When differentiation was performed in Pneuma-ALI, although qPCR did not show any difference in *MUC5AC* expression comparing proliferation in BEGM or Pneuma-Ex+ (Figure 4A), western blot did show a significant increase in *MUC5AC* content when cells were amplified in Pneuma-Ex+ (Figures 4C, 4D, E11A, and E11B). *MUC5B* content tended to also be increased by proliferation in Pneuma-Ex+, although not significantly (see Figures E11C–E11E).

Thus, even though proliferation in Pneuma-Ex+ did not favor goblet or secretory cell content during proliferation (Figures 3 and E10D), this proliferation medium favored goblet cell differentiation or mucin production. This increase might be due to the proliferative goblet cells that we detected during the initial cell propagation of nasal cultures in Pneuma-Ex+ (Figure 3F), although there is no evidence that these cells

were retained during the amplification step on Transwell membranes. For HBECs, even though we detected some goblet cells at the initial propagation step (see Figures E10A and E10B), these cells were not retained after amplification on membranes (Figure 3A). Another possibility is that Pneuma-Ex+ induced basal cells’ imprinting toward a subsequent goblet fate, as suggested by increased expression of *SPDEF* (Figures 3B and 3E).

### Effect of Cell Culture Media on SARS-CoV-2 Entry Factors

The ALI model is appropriate for SARS-CoV-2 *in vitro* infectivity studies, but discrepancies in major entry cell types have been described (17–25). As various cell culture media have been used in past studies, we wondered whether SARS-CoV-2 entry factor expression varied according to differentiation and proliferation media. Although *ACE2* was very poorly detected in scRNA-seq data of HBECs at ALI28 (Figure 5A), other entry factors, such as *TMPRSS2*, *FURIN*, *BSG*, *CTSB*, *ANPEP*, *ST6GAL1*, and *ST3GAL4*, were well detected. *TMPRSS2* was well expressed in MCCs from all media but was detected only in BEGM-ALI for secretory and goblet cells and in H&H for squamous cells. Other entry factors showed some medium-specific expression, such as *FURIN* in BEGM-ALI and Clancy medium; *ANPEP*, which was restricted to Clancy medium in goblet cells; and *ST3GAL4*, which was detected in BEGM-ALI and H&H for goblet cells and H&H only in squamous cells (Figure 5A). *ACE2* expression was then investigated using qPCR and western blot, for the two proliferation and differentiation commercial media, in HNECs. Although proliferation media did not produce significant effects (Figures 5B, 5C, and E12A), qPCR showed that *ACE2* expression was significantly lower in Pneuma-ALI. The western blot analysis showed a decreased expression of the main isoform in Pneuma-ALI compared with BEGM-ALI, which appears as a ~135-kD band, and an increased expression of a ~100-kD differentially glycosylated isoform (52) (Figures 5C and E12B).

Thus, both *ACE2* expression and glycosylation displayed medium-specific effects.

**Figure 3.** (Continued). Pneuma-Ex or Pneuma-Ex+. Cells were selected if they had normalized expression of *MUC5AC* of  $> 1$  and *MKI67* of  $> 0.5$ . The percentage of *MUC5AC*<sup>+</sup>/*MKI67*<sup>+</sup> cells for each sample is indicated on the plot. ALI0 = onset of air–liquid interface; scRNA-seq = single-cell RNA sequencing; Sec. interm. = secretory intermediate.

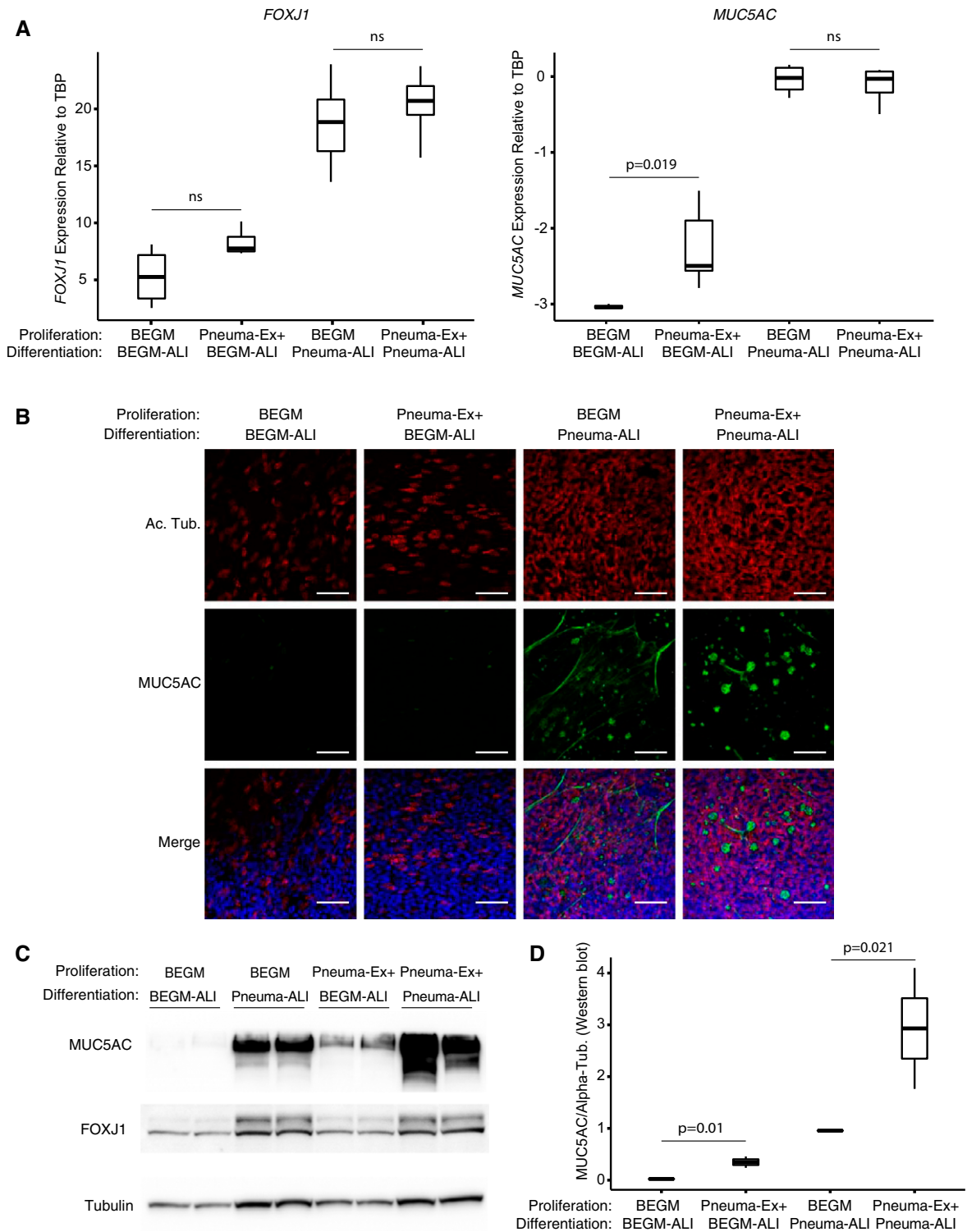


**Figure 4.** Effect of distinct proliferation media on epithelial composition after ALI differentiation of nasal epithelial cultures. (A) Expression of *FOXJ1* and *MUC5AC* (quantitative PCR) on ALI cultures after full differentiation of nasal epithelial cells in the indicated media. Data shown are the values for  $2^{Ct}(\text{FOXJ1-TBP})$  and  $\log_{10}[2^{Ct}(\text{MUC5AC-TBP})]$  for three independent cultures from three donors. *P* values are the results of Mann-Whitney *U* tests. (B) Representative images for immunostaining of MUC5AC and acetylated  $\alpha$ -tubulin on HNEC ALI cultures after full differentiation in the indicated media. Scale bars, 30  $\mu\text{m}$ . Nuclei were stained with DAPI and are shown in blue on the merge images. For each condition, three independent cell cultures were performed, and three inserts were stained and imaged for each. (C) Western blot for MUC5AC and FOXJ1 on HNEC ALI cultures after full differentiation in the indicated media. Tubulin was used as loading control. For each condition,

### Effect of Membranes and Media Alternatives

The pandemic crisis and the development of ALI models in respiratory virus studies led to reagent shortages. Alternative media or porous membranes other than Transwell were evaluated. PneumaCult-ALI-S (Pneuma-ALI-S), an additional commercial medium, designed for the differentiation of small airways, and ThinCert membranes (Greiner Bio-One), a commercial membrane, were assessed on HNECs. The morphology of multiciliated and goblet cells and content in reconstructed epithelium were compared between Pneuma-ALI-S and Pneuma-ALI. Figures 6 and E13 show that the use of the Pneuma-Ex+/Pneuma-ALI combination appeared to yield more MUC5AC<sup>+</sup> cells than the Pneuma-Ex/Pneuma-ALI combination. In addition, when comparing epithelial layer morphology, the use of Pneuma-Ex+ during the proliferation phase generated thick epithelia, with invaginations within the layer, as shown by actin, hematoxylin–eosin, and nuclei staining (Figures 6 and E13), which is not the case when cells proliferate in PneumaCult-Ex. In contrary, despite the use of Pneuma-Ex+ for proliferation, the use of Pneuma-ALI-S restored the epithelial morphology, as shown by the absence of invaginations in the reconstructed tissue, and a flat epithelial surface. MUC5AC<sup>+</sup> cell content appeared similar to that obtained with Pneuma-ALI (Figures 6 and E13). Although further experiments are needed to precisely evaluate the effects of the use of Pneuma-ALI-S on cell composition of ALI cultures, this medium can be used to generate apparent healthy epithelia after HNEC expansion in Pneuma-Ex+. We also evaluated the effect of using alternative polyethylene terephthalate membranes, which are very similar to Transwell filters that carry 0.4- $\mu\text{m}$  pores. The difference between these products is in the pore density, which is  $2.10^6$  pores/cm<sup>2</sup> for ThinCert membranes and  $4.10^6$  pores/cm<sup>2</sup> for Transwell membranes. We evaluated these membranes after HNEC proliferation in Pneuma-Ex+ medium, as above, and induced differentiation with either Pneuma-ALI or PromoCell-ALI (Promo-ALI; PromoCell) (whose composition is identical to that of BEGM-ALI). As previously

mentioned, thick and invaginated epithelia were obtained when using Transwell membranes with the Pneuma-Ex+/Pneuma-ALI combination (Figure 7). Promo-ALI generated thinner epithelia, but they still displayed invaginations. The basal and suprabasal cell layers, stained with KRT5, seemed expanded in both media. The use of ThinCert membranes strongly reduced the overall thickness of the epithelia and yielded epithelia with the expected morphology together with the expected basal cell, goblet cell, and MCC disposition in Pneuma-ALI. Nonetheless, the use of Promo-ALI on ThinCert membranes produced thin epithelia containing few multiciliated and MUC5AC<sup>+</sup> cells (Figure 7).

Together, these results show that if using Pneuma-Ex+ for basal cell expansion, restoration of the expected epithelial morphology and gross composition can be achieved by using ThinCert membranes if differentiating in Pneuma-ALI or by using Pneuma-ALI-S instead of Pneuma-ALI on Transwell membranes.

### Discussion

In this study we analyzed, at the single-cell level, the effects of five distinct cell culture media and two types of insert membranes for ALI differentiation of nasal and bronchial epithelial cells. All media allowed the detection of all major cell types present in the airway epithelium. We have shown that two cell culture media, Pneuma-ALI and H&H, generated ALI cultures with high MCC content. H&H contains half PneumaCult-ALI medium, minus the 100 $\times$  supplement, which has a proprietary composition. We assumed that this supplement includes retinoic acid. The other half of this medium is composed of Wu medium, which itself contains retinoic acid. According to the authors who developed this medium, it was intended to create conditions that are more similar to *in vivo* conditions (35). However, except for some subtle differences, we found that cell identities and distributions were highly similar between Pneuma-ALI and H&H. On the contrary, the BEGM-ALI and Clancy media yielded many fewer MCCs. Thus, the choice of the culture conditions

should be conditioned by the study to be performed. For cilia biology, Pneuma-ALI and H&H should be largely preferred, as the MCC content was much higher in these conditions, with a neat deuterosomal cell cluster. However, if studying secretory cells, BEGM-ALI and Clancy media should be considered, taking into consideration the differences we found in secreted mucin expression. We also noticed the rare occurrence of ionocytes, brush cells, and pulmonary neuroendocrine cells, which were found in too small proportions to allow a comparison among media (8). Future investigations analyzing higher cell numbers should better identify the impact of differentiation media on the amounts and gene expression profiles of these cells.

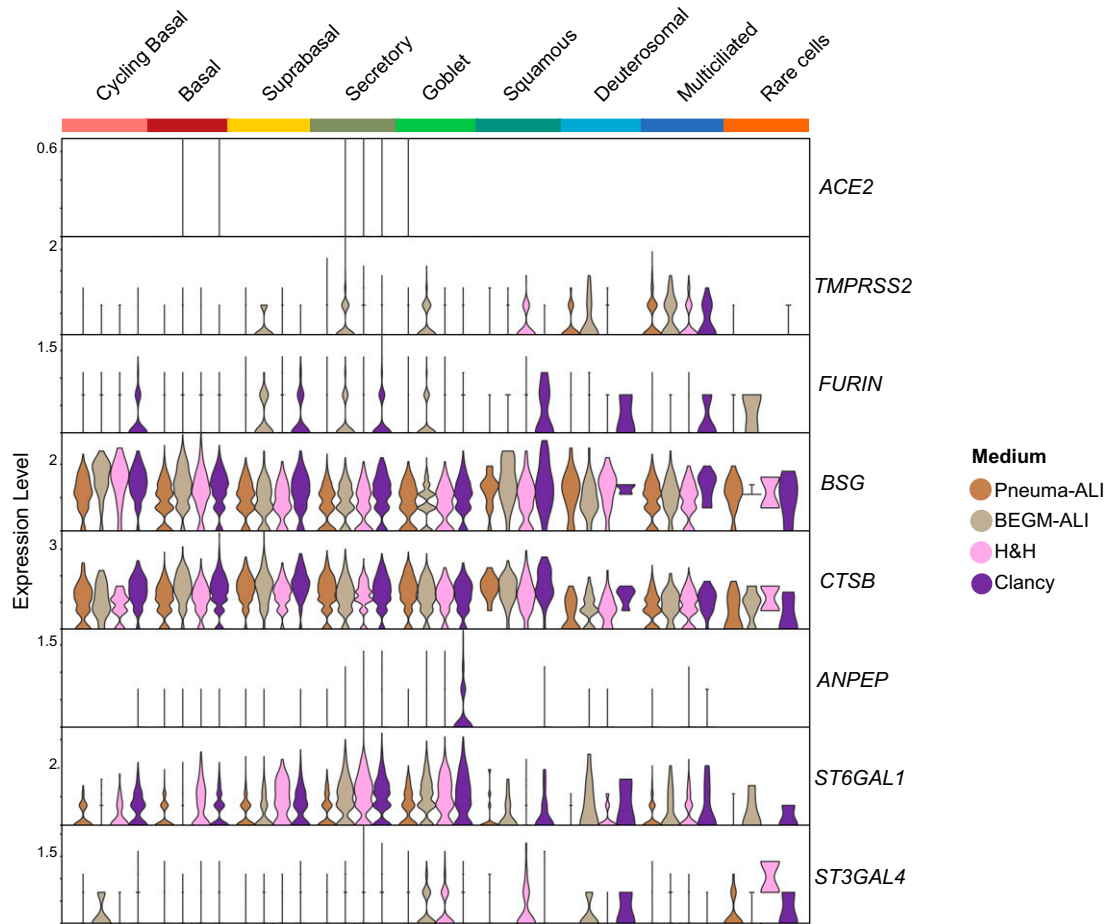
We used a label transfer method that incorporates reference similarity beyond marker genes alone to compare cells from the ALI model with *in vivo* airway cells. Given the very wide use of this culture model, such a comparison could be very useful. We have found some cell type and medium-dependent differences, mainly in basal, suprabasal, secretory, and goblet cells, which are cell types showing continuous expression profiles, as opposed to MCCs, which have very distinct expression profiles and the largest number of marker genes. These data highlight the difficulty to annotate cell types on the basis of automatic clustering followed by manual annotation and illustrate that using automatic annotations with label transfer that allow datasets to be compared with a reference in an unbiased manner tools could be a very useful complement.

Leung and colleagues recently published a comparative study of Pneuma-ALI and BEGM-ALI (27). Their findings, in terms of multiciliated, goblet cell content and epithelial thickness, were very similar to ours. Saint-Criq and colleagues also compared Pneuma-ALI to University of North Carolina at Chapel Hill medium, which is quite similar to BEGM. They also obtained thicker epithelia with Pneuma-ALI, and their differential gene expression analysis also showed increased expression of *IL33* and *TFF3* in Pneuma-ALI and increased expression of ion transport genes in

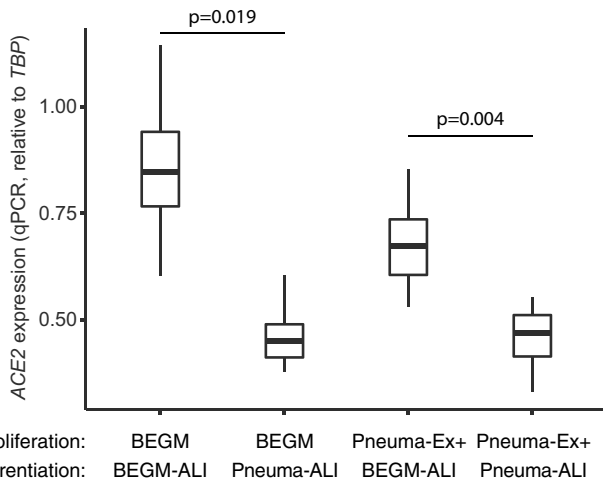
**Figure 4.** (Continued). two lanes were loaded, each with an independent Transwell membrane from the same culture. (D) Quantification of the MUC5AC signal from C; P values are the results of Welch's *t* tests. For each condition, three independent cell cultures were performed, and two inserts were used for western blot. Data from the additional cultures are shown in Figure E11. ns = not significant.



A



B



C

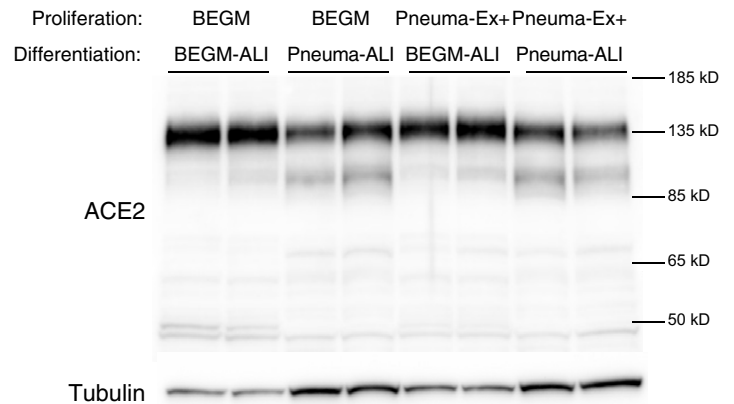


**Figure 5.** Effect of proliferation and differentiation media on ACE2 expression at ALI28 of epithelial cell differentiation. (A) Violin plot showing expression of severe acute respiratory syndrome coronavirus 2 (SARS-CoV-2) entry factors in each of the four media conditions used for HBECS at ALI28 (Figure 1B). (B) qPCR for ACE2 on three independent HNEC ALI cultures from three donors after proliferation and full differentiation in the indicated media. Data shown are the values for  $2^{Ct}(ACE2-TBP)$  for three independent cultures from three donors. *P* values are the results of Mann-Whitney *U* tests. (C) Western blot for ACE2 on HNEC ALI cultures after full differentiation in the indicated media. Tubulin was used as loading control. For each condition, three independent cell cultures were performed, and two inserts were used for western blot. Data from two additional independent cultures are shown in Figure E12. qPCR = quantitative polymerase chain reaction.

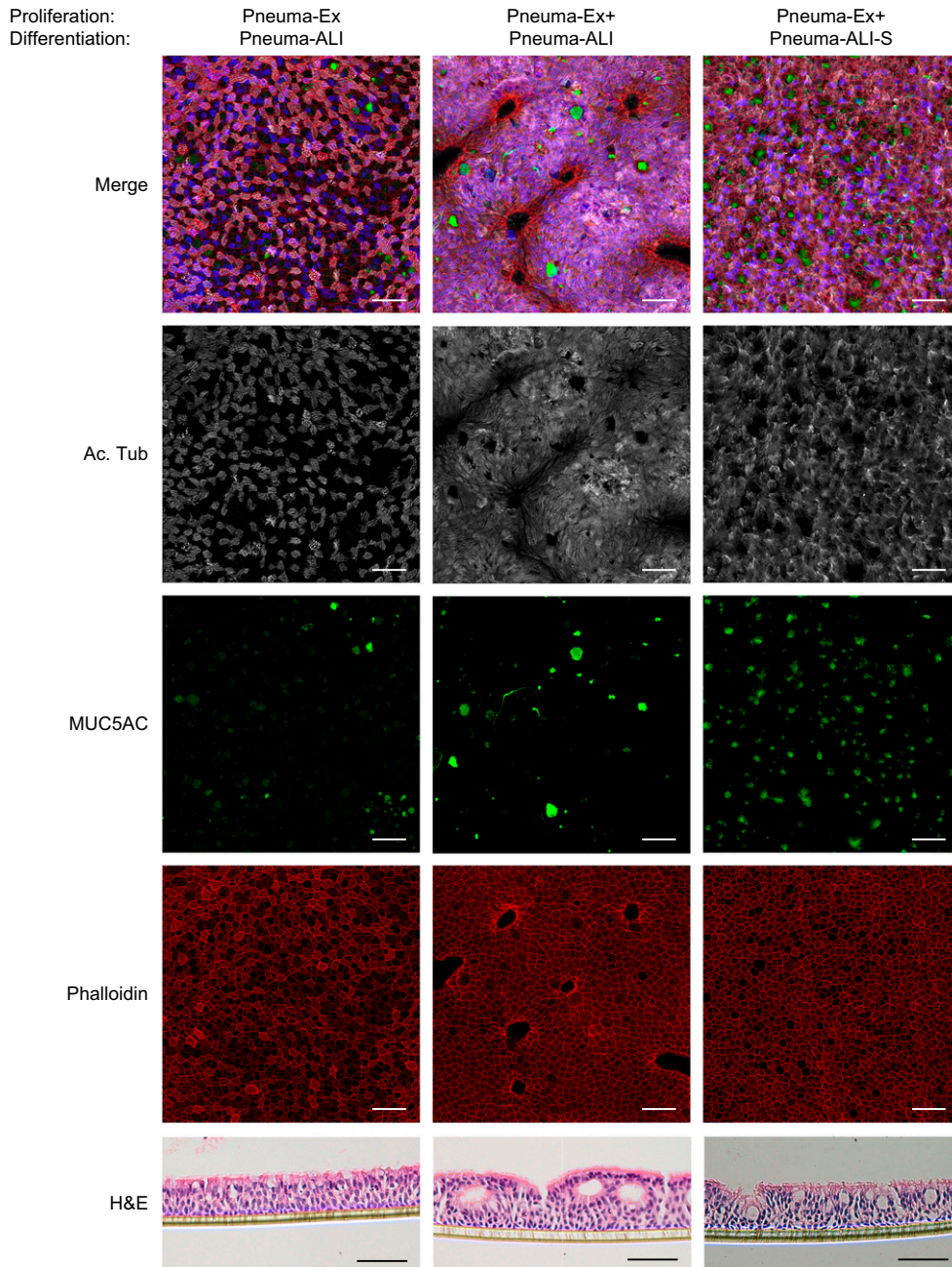


**Figure 6.** Effect of an alternative differentiation medium on epithelial composition after ALI differentiation of nasal epithelial cells. (Top) Representative images of immunostaining for MUC5AC and Ac. Tub. on HNEC ALI cultures after full differentiation in the indicated media. Phalloidin was used to stain for actin. Nuclei were stained with DAPI and are shown in blue on the merge images. Scale bars, 30  $\mu\text{m}$ . (Bottom) H&E staining of sections of paraffin-embedded epithelia. Scale bars, 100  $\mu\text{m}$ . For each condition, one cell culture was performed, and two inserts were stained and imaged. Additional images are shown in Figure E13.

University of North Carolina at Chapel Hill medium, similar to our findings with BEGM and Clancy media. Importantly, they showed that differentiation media can influence CF cell cultures responses to CFTR modulators (29). We add here that the choice of differentiation medium can also modify the

expression of SARS-CoV-2 entry factors: ACE2 expression appeared lower in Pneuma-ALI, with a distinct glycosylation profile, and *TMPRSS2* was restricted to MCCs in this medium, whereas it showed wider expression in BEGM-ALI. Most studies have used Pneuma-ALI and shown

higher SARS-CoV-2 tropism toward MCCs (17–22). However, V'kovski and colleagues (25) and Johansen and colleagues (26) used BEGM and found a higher tropism toward nonmulticiliated cells. Thus, medium selection might be a crucial parameter for viral infection studies.

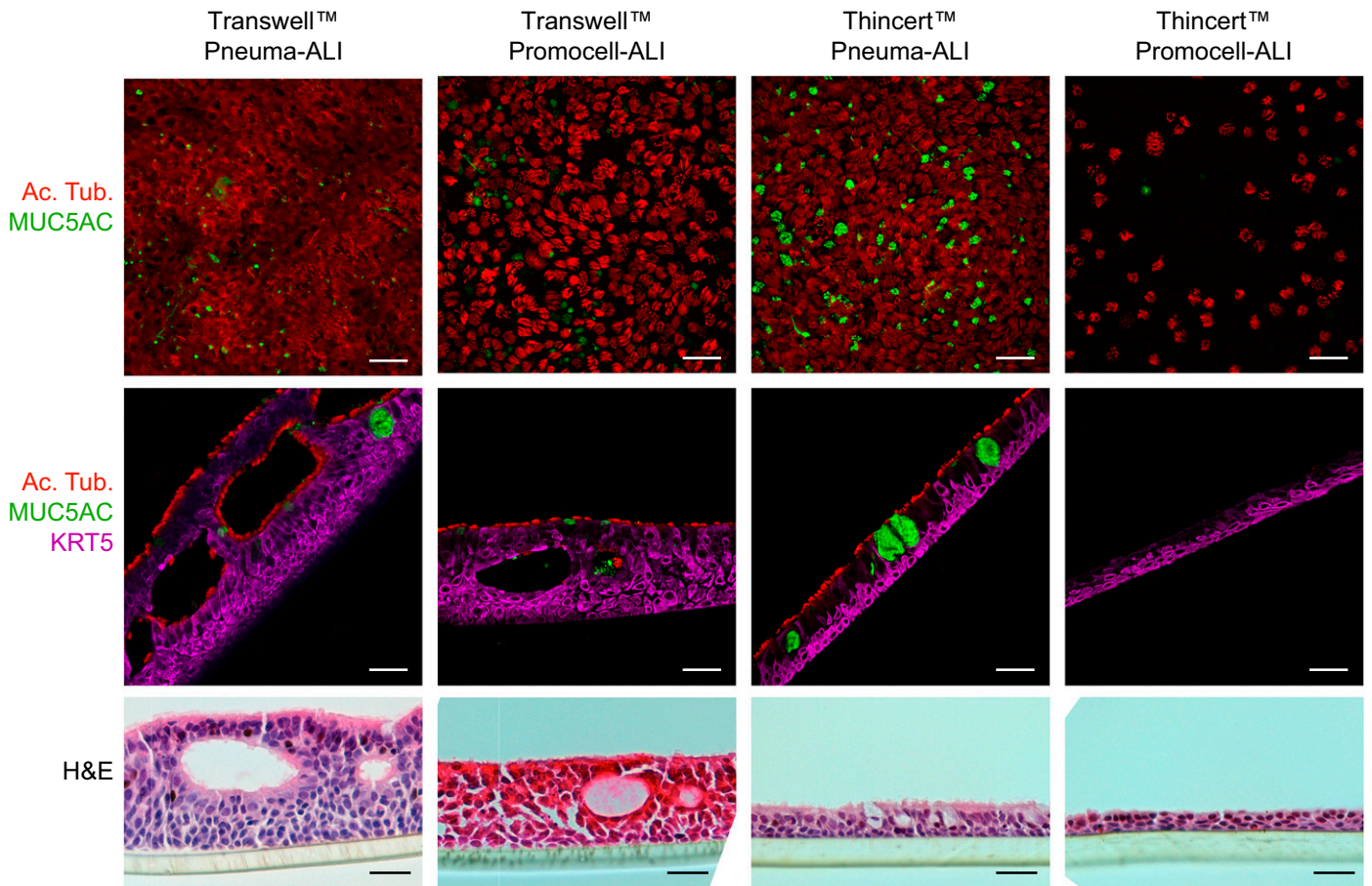


**Figure 7.** Effect of cell culture inserts and differentiation media on epithelial composition after ALI differentiation of nasal epithelial cultures. (Top) Representative images of immunostaining on whole inserts for MUC5AC and Ac. Tub. on HNEC ALI cultures after full differentiation in the indicated media. Scale bars, 30  $\mu$ m. (Middle) Representative images of immunostaining on sections of inserts for MUC5AC and Ac. Tub. on ALI cultures after full differentiation in the indicated media. Scale bars, 30  $\mu$ m. (Bottom) Representative images of H&E staining of sections of paraffin-embedded inserts. Scale bars, 100  $\mu$ m. For each condition, two inserts were stained and imaged.

We extended our investigation to the stages occurring before differentiation. With the exception of a few studies describing conditional reprogramming of epithelial cells (coculture with irradiated fibroblast feeder cells and a Rho kinase inhibitor) (53, 54), or the use of dual SMAD signaling inhibition (55), these stages have been largely ignored in previous works using ALI cultures. Yet proliferation conditions might influence cell fate by modifying the identity and/or potency of basal cells, which are the stem cells generating the entire epithelium upon setting up the ALI. Here, scRNA-seq was instrumental to identify the precise cell composition of epithelial cell cultures during the initial propagation steps. We have shown that after a first stage in plastic flasks, cycling basal and basal cells are highly dominant in

both bronchial and nasal cultures, but secretory, goblet, multiciliated, and even endothelial cells were detected, with variations depending on the proliferation medium that was used. For nasal epithelial cells in Pneuma-Ex+ medium, we detected few proliferative goblet cells. These findings should be considered when using this medium, and a more accurate characterization of these cells would be required. Interestingly, we found that gene expression profiles of basal cells were affected, with, for instance, the upregulation of *SPDEF* by Pneuma-Ex+, which could influence the fate of these cells. In line with these findings, we found that proliferation in Pneuma-Ex+ favored the goblet cell lineage after differentiation.

Finally, we evaluated the effects of using an alternative differentiation medium

(Pneuma-ALI-S) and alternative porous membranes (ThinCert) on epithelial morphology after proliferation in Pneuma-Ex+. We found that both restored the normal epithelial morphology which was lost with the use of Pneuma-Ex+ for all proliferation stages, followed by Pneuma-ALI differentiation. As the composition of PneumaCult products is not known, it is not possible to identify the differential cues that produced these effects. The use of alternative porous membranes has also been very informative and suggests that the pore density influences cell morphology. ThinCert membranes having a lower pore density, we speculate that the flow of nutrient might be slower in these conditions and might account for the difference in epithelial morphology.

## Conclusions

Our study provides a reference for evaluating the influence of culture conditions on airway epithelial differentiation. Our scRNA-seq data could be further analyzed

and could lead to the identification of other pathways regulating differentiation. Beyond the technical usefulness of our results, our study also identifies parameters that should be further

explored to study cell fate and epithelial morphology. ■

**Author disclosures** are available with the text of this article at [www.atsjournals.org](http://www.atsjournals.org).

## References

- Sikkema L, Ramírez-Substage C, Strobl DC, Gillett TE, Zappia L, Madissoon E, et al.; Lung Biological Network Consortium. An integrated cell atlas of the lung in health and disease. *Nat Med* 2023;29:1563–1577.
- Surve MV, Lin B, Reedy JL, Crossen AJ, Xu A, Klein BS, et al. Single-cell transcriptomes, lineage, and differentiation of functional airway microfold cells. *Am J Respir Cell Mol Biol* 2023;69:698–701.
- Hogan B, Tata PR. Cellular organization and biology of the respiratory system. *Nat Cell Biol* 2019 [accessed 2024 Jan 5]. Available from: <https://doi.org/10.1038/s41556-019-0357-7>.
- Deprez M, Zaragosi L-E, Truchi M, Bécavin C, Ruiz García S, Arguel MJ, et al. A single-cell atlas of the human healthy airways. *Am J Respir Crit Care Med* 2020;202:1636–1645.
- Zepp JA, Morrissey EE. Cellular crosstalk in the development and regeneration of the respiratory system. *Nat Rev Mol Cell Biol* 2019;20:551–566.
- Sun X, Perl AK, Li R, Bell SM, Sajti E, Kalinichenko VV, et al.; NHLBI LungMAP Consortium. A census of the lung: CellCards from LungMAP. *Dev Cell* 2022;57:112–145.e2.
- Rustam S, Hu Y, Mahjour SB, Rendeiro AF, Ravichandran H, Urso A, et al. A unique cellular organization of human distal airways and its disarray in chronic obstructive pulmonary disease. *Am J Respir Crit Care Med* 2023;207:1171–1182.
- Cavard A. Contribution des gènes des loci 5q11 et 11q23 à la multiciliogenèse et régulation de l'équilibre mucociliaire dans l'épithélium des voies respiratoires au cours de la régénération in vitro. Villeurbanne, France: Centre pour la Communication Scientifique Directe; 2020 [accessed 2024 Jan 5]. Available from: <https://theses.hal.science/tel-03200434/>.
- Yamaya M, Finkbeiner WE, Chun SY, Widdicombe JH. Differentiated structure and function of cultures from human tracheal epithelium. *Am J Physiol* 1992;262:L713–L724.
- Lopez-Souza N, Avila PC, Widdicombe JH. Polarized cultures of human airway epithelium from nasal scrapings and bronchial brushings. *In Vitro Cell Dev Biol Anim* 2003;39:266–269.
- Ruiz Garcia S, Deprez M, Lebrigand K, Cavard A, Paquet A, Arguel M, et al. Novel dynamics of human mucociliary differentiation revealed by single-cell RNA sequencing of nasal epithelial cultures. *Development* 2019;146:dev177428.
- Greaney AM, Adams TS, Brickman Raredon MS, Gubbins E, Schupp JC, Engler AJ, et al. Platform effects on regeneration by pulmonary basal cells as evaluated by single-cell RNA sequencing. *Cell Rep* 2020;30:4250–4265.e6.
- Gras D, Chanez P, Vachier I, Petit A, Bourdin A. Bronchial epithelium as a target for innovative treatments in asthma. *Pharmacol Ther* 2013;140:290–305.
- Carlini F, Picard C, Garulli C, Piquemal D, Roubertoux P, Chiaroni J, et al. Bronchial epithelial cells from asthmatic patients display less functional HLA-G isoform expression. *Front Immunol* 2017;8:6.
- Zaragosi LE, Deprez M, Barbry P. Using single-cell RNA sequencing to unravel cell lineage relationships in the respiratory tract. *Biochem Soc Trans* 2020;48:327–336.
- Durmowicz AG, Lim R, Rogers H, Rosebraugh CJ, Chowdhury BA. The US Food and Drug Administration's experience with ivacaftor in cystic fibrosis: establishing efficacy using in vitro data in lieu of a clinical trial. *Ann Am Thorac Soc* 2018;15:1–2.
- Ravindra NG, Alfajaro MM, Gasque V, Huston NC, Wan H, Szigeti-Buck K, et al. Single-cell longitudinal analysis of SARS-CoV-2 infection in human airway epithelium identifies target cells, alterations in gene expression, and cell state changes. *PLoS Biol* 2021;19:e3001143.
- Beucher G, Blondot ML, Celle A, Pied N, Recordon-Pinson P, Esteves P, et al. Bronchial epithelia from adults and children: SARS-CoV-2 spread via syncytia formation and type III interferon infectivity restriction. *Proc Natl Acad Sci U S A* 2022;119:e2202370119.
- Fiege JK, Thiede JM, Nanda HA, Matchett WE, Moore PJ, Montanari NR, et al. Single cell resolution of SARS-CoV-2 tropism, antiviral responses, and susceptibility to therapies in primary human airway epithelium. *PLoS Pathog* 2021;17:e1009292.
- Hou YJ, Okuda K, Edwards CE, Martinez DR, Asakura T, Dinnon KH III, et al. SARS-CoV-2 reverse genetics reveals a variable infection gradient in the respiratory tract. *Cell* 2020;182:429–446.e14.
- Zhu N, Wang W, Liu Z, Liang C, Wang W, Ye F, et al. Morphogenesis and cytopathic effect of SARS-CoV-2 infection in human airway epithelial cells. *Nat Commun* 2020;11:3910.
- Morrison CB, Edwards CE, Shaffer KM, Araba KC, Wykoff JA, Williams DR, et al. SARS-CoV-2 infection of airway cells causes intense viral and cell shedding, two spreading mechanisms affected by IL-13. *Proc Natl Acad Sci U S A* 2022;119:e2119680119.
- Purkayastha A, Sen C, Garcia G Jr, Langerman J, Shia DW, Meneses LK, et al. Direct exposure to SARS-CoV-2 and cigarette smoke increases infection severity and alters the stem cell-derived airway repair response. *Cell Stem Cell* 2020;27:869–875.e4.
- Hao S, Ning K, Kuz CA, Vorhies K, Yan Z, Qiu J. Long-term modeling of SARS-CoV-2 infection of in vitro cultured polarized human airway epithelium. *mBio* 2020;11:e02852-20.
- V'kovski P, Gultom M, Kelly JN, Steiner S, Russeil J, Mangeat B, et al. Disparate temperature-dependent virus–host dynamics for SARS-CoV-2 and SARS-CoV in the human respiratory epithelium. *PLoS Biol* 2021;19:e3001158.
- Johansen MD, Mahbub RM, Idrees S, Nguyen DH, Miemczyk S, Pathinayake P, et al. Increased SARS-CoV-2 infection, protease, and inflammatory responses in chronic obstructive pulmonary disease primary bronchial epithelial cells defined with single-cell RNA sequencing. *Am J Respir Crit Care Med* 2022;206:712–729.
- Leung C, Wadsworth SJ, Yang SJ, Dorscheid DR. Structural and functional variations in human bronchial epithelial cells cultured in air-liquid interface using different growth media. *Am J Physiol Lung Cell Mol Physiol* 2020;318:L1063–L1073.
- Rayner RE, Makena P, Prasad GL, Cormet-Boyaka E. Optimization of normal human bronchial epithelial (NHBE) cell 3D cultures for in vitro lung model studies. *Sci Rep* 2019;9:500.
- Saint-Criq V, Delpiano L, Casement J, Onuora JC, Lin J, Gray MA. Choice of differentiation media significantly impacts cell lineage and response to CFTR modulators in fully differentiated primary cultures of cystic fibrosis human airway epithelial cells. *Cells* 2020;9:2137.
- Morgan R, Manfredi C, Easley KF, Watkins LD, Hunt WR, Goudy SL, et al. A medium composition containing normal resting glucose that supports differentiation of primary human airway cells. *Sci Rep* 2022;12:1540.
- Awatade NT, Reid AT, Nichol KS, Budden KF, Veerati PC, Pathinayake PS, et al. Comparison of commercially available differentiation media on cell morphology, function, and anti-viral responses in conditionally reprogrammed human bronchial epithelial cells. *Sci Rep* 2023;13:11200.
- Luengen AE, Kniebs C, Buhl EM, Cornelissen CG, Schmitz-Rode T, Jockenhoevel S, et al. Choosing the right differentiation medium to develop mucociliary phenotype of primary nasal epithelial cells in vitro. *Sci Rep* 2020;10:6963.
- Broadbent L, Manzoor S, Zarcone MC, Barabas J, Shields MD, Saglani S, et al. Comparative primary paediatric nasal epithelial cell culture differentiation and RSV-induced cytopathogenesis following culture in two commercial media. *PLoS One* 2020;15:e0228229.

34. Lee DDH, Petris A, Hynds RE, O'Callaghan C. Ciliated epithelial cell differentiation at air-liquid interface using commercially available culture media. *Methods Mol Biol* 2020;2109:275–291.
35. Malleske DT, Hayes D Jr, Lallier SW, Hill CL, Reynolds SD. Regulation of human airway epithelial tissue stem cell differentiation by  $\beta$ -catenin, P300, and CBP. *Stem Cells* 2018;36:1905–1916.
36. Brewington JJ, Filbrandt ET, LaRosa FJ III, Moncivaiz JD, Ostmann AJ, Strecker LM, et al. Brushed nasal epithelial cells are a surrogate for bronchial epithelial CFTR studies. *JCI Insight* 2018;3:e99385.
37. Stoeckius M, Zheng S, Houck-Loomis B, Hao S, Yeung BZ, Mauck WM III, et al. Cell hashing with barcoded antibodies enables multiplexing and doublet detection for single cell genomics. *Genome Biol* 2018;19:224.
38. Phipson B, Sim CB, Porrello ER, Hewitt AW, Powell J, Oshlack A. propeller: testing for differences in cell type proportions in single cell data. *Bioinformatics* 2022;38:4720–4726.
39. Simmons S. Cell type composition analysis: comparison of statistical methods [preprint]. bioRxiv; 2022 [accessed 2022 Feb 10]. Available from: <https://www.biorxiv.org/content/10.1101/2022.02.04.479123v1>.
40. Chan BCL, Lam CWK, Tam LS, Wong CK. IL33: roles in allergic inflammation and therapeutic perspectives. *Front Immunol* 2019;10:364.
41. Bothe M, Buschow R, Meijnsing SH. Glucocorticoid signaling induces transcriptional memory and universally reversible chromatin changes. *Life Sci Alliance* 2021;4:1–17.
42. Osanai M, Takasawa A, Takasawa K, Kyuno D, Ono Y, Magara K. Retinoic acid metabolism in cancer: potential feasibility of retinoic acid metabolism blocking therapy. *Med Mol Morphol* 2023;56:1–10.
43. Zhao Y, Zou Z, Sun D, Li Y, Sinha SC, Yu L, et al. GLIPR2 is a negative regulator of autophagy and the BECN1-ATG14-containing phosphatidylinositol 3-kinase complex. *Autophagy* 2021;17:2891–2904.
44. Manzo ND, Foster WM, Stripp BR. Amphiregulin-dependent mucous cell metaplasia in a model of nonallergic lung injury. *Am J Respir Cell Mol Biol* 2012;47:349–357.
45. Val S, Belade E, George I, Boczkowski J, Baeza-Squiban A. Fine PM induce airway MUC5AC expression through the autocrine effect of amphiregulin. *Arch Toxicol* 2012;86:1851–1859.
46. Zuo W-L, Yang J, Gomi K, Chao I, Crystal RG, Shaykhiev R. EGF-amphiregulin interplay in airway stem/progenitor cells links the pathogenesis of smoking-induced lesions in the human airway epithelium. *Stem Cells* 2017;35:824–837.
47. Wang J, Zhu M, Wang L, Chen C, Song Y. Amphiregulin potentiates airway inflammation and mucus hypersecretion induced by urban particulate matter via the EGFR-PI3K $\alpha$ -AKT/ERK pathway. *Cell Signal* 2019;53:122–131.
48. Mori M, Mahoney JE, Stupnikov MR, Paez-Cortez JR, Szymaniak AD, Varelas X, et al. Notch3-Jagged signaling controls the pool of undifferentiated airway progenitors. *Development* 2015;142:258–267.
49. Rock JR, Gao X, Xue Y, Randell SH, Kong Y-Y, Hogan BLM. Notch-dependent differentiation of adult airway basal stem cells. *Cell Stem Cell* 2011;8:639–648.
50. Kuchibhotla VNS, Heijink IH. Join or leave the club: Jagged1 and Notch2 dictate the fate of airway epithelial cells. *Am J Respir Cell Mol Biol* 2020;63:4–6.
51. Laffkas D, Shelton A, Chiu C, de Leon Boenig G, Chen Y, Stawicki SS, et al. Therapeutic antibodies reveal Notch control of transdifferentiation in the adult lung. *Nature* 2015;528:127–131.
52. Li W, Moore MJ, Vasilieva N, Sui J, Wong SK, Berne MA, et al. Angiotensin-converting enzyme 2 is a functional receptor for the SARS coronavirus. *Nature* 2003;426:450–454.
53. Reynolds SD, Rios C, Wesolowska-Andersen A, Zhuang Y, Pinter M, Happoldt C, et al. Airway progenitor clone formation is enhanced by Y-27632-dependent changes in the transcriptome. *Am J Respir Cell Mol Biol* 2016;55:323–336.
54. Supryniewicz FA, Upadhyay G, Krawczyk E, Kramer SC, Hebert JD, Liu X, et al. Conditionally reprogrammed cells represent a stem-like state of adult epithelial cells. *Proc Natl Acad Sci U S A* 2012;109:20035–20040.
55. Mou H, Vinarsky V, Tata PR, Brazauskas K, Choi SH, Crooke AK, et al. Dual SMAD signaling inhibition enables long-term expansion of diverse epithelial basal cells. *Cell Stem Cell* 2016;19:217–231.


## D. The MIR34B/C genomic region contains multiple potential regulators of multiciliogenesis

MiR-34b/c and miR-449a/b/c, two miRNA families belonging to the same superfamily, and both involved in multiciliogenesis, are located on 2 distinct genomic loci. The miR-449 family is located on locus 5q11 and are encoded by the second intron of *CDC20B*, a gene involved in the disengagement of centrioles formed within deuterosomes (Revinski et. al, 2018). The 5q11 locus encompasses *MCIDAS*, which also plays a role in multiciliogenesis, activating the expression of *FOXJ1*, *CCNO* and *DEUP1* as well as itself in cooperation with *GemC1* and *E2F4/5*. This locus also bears *CCNO*, whose expression is required for deuterosome formation and centriole amplification. Interestingly, *MCIDAS*, *CCNO* and *CDC20B* are activated at the same time as a self-activating loop of the locus. The shared location of several genes all involved in multiciliogenesis, led the team to define the 5q11 locus as a “multiciliary locus” (Revinski et al., 2018). We thus wondered whether the logic applied for the miR-34b/c locus (11q23) where three proximal genes are located: *C11ORF88*, *LAYN* and *BTG4*. *C11ORF88* murine ortholog *Hoatz* has recently been characterized. *Hoatz* knockout (KO) mice developed motile cilia related disorders such as hydrocephalus and male infertility, which suggests a functional role in multiciliated cells (Narita et al., 2020). *LAYN* has been described as a receptor for hyaluronic acid located apically in the airway epithelium. It is thought to signal through the ROCK/Rho pathway to inhibit transcriptional and protein expression of E-cadherin (Forteza et al., 2012). This gene is also thought to be a downstream effector of TP53, which can enable the differentiation of secretory cells into multiciliated cells (McConnell et al., 2016). *BTG4* has been described as a negative regulator of the cell cycle (Auer et al., 2005), and its expression has only been detected in tissues with multiciliated cells (pharynx, trachea, oviduct and testes) (Mano et al., 2015). Using scRNA-seq and super-resolution microscopy, we demonstrated that the MIR34B/C locus, like its homolog MIR449, is a multiciliary locus encompassing genes that are potential regulators of multiciliogenesis.



## RESEARCH LETTER

# The *MIR34B/C* genomic region contains multiple potential regulators of multiciliogenesis

Amélie Cavard<sup>1</sup>, Elisa Redman<sup>1</sup>, Olivier Mercey<sup>2</sup>, Sophie Abelanet<sup>1</sup>, Magali Plaisant<sup>1</sup>, Marie-Jeanne Arguel<sup>1</sup>, Virginie Magnone<sup>1</sup>, Sandra Ruiz García<sup>1</sup>, Géraldine Rios<sup>1</sup>, Marie Deprez<sup>1</sup>, Kévin Lebrigand<sup>1</sup>, Gilles Ponzio<sup>1</sup>, Ignacio Caballero<sup>3</sup>, Pascal Barbry<sup>1</sup>, Laure-Emmanuelle Zaragosi<sup>1</sup>  and Brice Marcet<sup>1</sup>

<sup>1</sup> Université Côte d'Azur, CNRS, IPMC, Sophia-Antipolis, France

<sup>2</sup> Institut de Biologie de l'École Normale Supérieure, Paris, France

<sup>3</sup> ISP, INRA, Université Tours, Nouzilly, France

## Correspondence

L.-E. Zaragosi and B. Marcet, IPMC-CNRS, UMR-7275, 660 Route des Lucioles, 06560 Sophia-Antipolis, Valbonne, France  
 Tel: +33 (0)4 93 95 77 03  
 E-mail: zaragosi@ipmc.cnrs.fr (L-EZ); marcet@ipmc.cnrs.fr (BM)

Laure-Emmanuelle Zaragosi and Brice Marcet contributed equally to this article

(Received 8 November 2022, revised 11 April 2023, accepted 12 April 2023, available online 8 May 2023)

doi:10.1002/1873-3468.14630

Edited by Tamas Dalmay

The *MIR449* genomic locus encompasses several regulators of multiciliated cell (MCC) formation (multiciliogenesis). The miR-449 homologs miR-34b/c represent additional regulators of multiciliogenesis that are transcribed from another locus. Here, we characterized the expression of *BTG4*, *LAYN*, and *HOATZ*, located in the *MIR34B/C* locus using single-cell RNA-seq and super-resolution microscopy from human, mouse, or pig multiciliogenesis models. *BTG4*, *LAYN*, and *HOATZ* transcripts were expressed in both precursors and mature MCCs. The Layilin/LAYN protein was absent from primary cilia, but it was expressed in apical membrane regions or throughout motile cilia. *LAYN* silencing altered apical actin cap formation and multiciliogenesis. *HOATZ* protein was detected in primary cilia or throughout motile cilia. Altogether, our data suggest that the *MIR34B/C* locus may gather potential actors of multiciliogenesis.

**Keywords:** BTG4; HOATZ; LAYN; miR-34b/c; motile cilia; multiciliated cells

The airway epithelium is the first line of defense of airways against external stress and is constituted by several cell types including basal, club, goblet, and multiciliated cells (MCCs), as well as rare cells such as ionocytes [1-3]. MCCs carry hundreds of motile cilia at their apical surface which orchestrate mucociliary clearance [4,5]. Ciliary disorders are observed in ciliopathies and chronic respiratory diseases [4]. The formation of MCCs

(a process called multiciliogenesis) requires the production of tens to hundreds of centrioles in a shallow time window, mostly through a structure named the deuterosome, composed, in part, by DEUP1 proteins [5,6]. Neosynthesized centrioles migrate apically to dock at the plasma membrane to initiate cilium elongation [5]. Over the last decade, the complex mechanisms underlying multiciliogenesis have begun to be unraveled.

## Abbreviations

Ac. Tub., acetylated alpha-tubulin; ALI, air-liquid interface; APC/C, anaphase-promoting complex/cyclosome; BEBM, bronchial epithelial cell basal medium; BEGM, bronchial epithelial cell growth medium; BTG, B-cell translocation gene; Cas9, CRISPR-associated protein 9; CCNO, cyclin O; CDC20B, cell division cycle protein 20 homolog B; CRISPR, clustered regularly interspaced short palindromic repeats; DAPI, 4',6-diamidino-2-phenylindole; DEUP1, deuterosome assembly protein 1; ENO4, enolase 4; FOXJ1, forkhead box J1; GAPDH, glyceraldehyde-3-phosphate dehydrogenase; HBEC, human bronchial epithelial cell; HNEC, human nasal epithelial cell; HOATZ, hydrocephalus and oligoastheno-terato-zoospermia; IFT, intraflagellar transport; LAYN, Layilin; MCC, multiciliated cell; MCIDAS, multiciliate differentiation and DNA synthesis associated cell cycle protein; MiRNA or miR, microRNA; mTEC, mouse tracheal epithelial cell; PLK1, polo-like kinase 1; RhoA, Ras homolog family member A; ROCK, Rho-associated, coiled-coil-containing protein kinase; scRNA-seq, single-cell RNA-sequencing; siRNA, small interfering RNA; SNTN, Sentan; STED, stimulated emission depletion; UMI, unique molecular identifier.



Multiciliogenesis involves a coordinated expression of hundreds of genes. Some, such as *MCIDAS*, *CCNO*, *CDC20B*, and *MIR449A/B/C*, are located in the same evolutionarily conserved genomic locus (5q11 in human) and all participate in multiciliogenesis [7-9]. This complementary contribution of genes located in the same locus in the same biological process led us to propose that this locus acts as a 'multiciliary locus' [9]. The miR-34/449 microRNA (miRNA or miR) superfamily, largely conserved across vertebrates, is encoded by six miRNA genes located in three distinct loci: (a) *MIR449A/B/C* are located in the second intron of the host gene *CDC20B* (5q11 in human) [8-10], (b) *MIR34B/C* are located on a second conserved locus between *C11orf88* and *BTG4* (11q23 in human), (c) *MIR34A* is located on a third locus (1p36 in human) [8,10]. Whereas miR-34a seems to be the only member of the family that has not been associated with MCC differentiation, we and others have previously described the role of miR-34b/c together with miR-449 miRNAs as conserved regulators of multiciliogenesis [7,8,10-23].

In this study, we investigated the hypothesis of a second 'multiciliary locus' corresponding to the genomic locus around *MIR34B/C*. In humans, *MIR34B/C* genes are located near *C11orf88*, *LAYN*, and *BTG4*. *C11orf88*, of unknown function, has not yet been characterized in humans while *4833427G06Rik*, its murine ortholog, has been recently designated as *Hoatz* due to the Hydrocephalus and Oligo-Astheno-Terato-Zoospermia phenotype of *Hoatz* knockout mice [24]. HOATZ is required in flagellar and motile ciliogenesis notably by mediating the maturation of the flagellar glycolytic enzyme ENO4, though HOATZ may be involved in ciliogenesis with additional undetermined mechanisms [24]. *LAYN* gene codes for Layilin protein that has been described as a receptor of hyaluronan [25]. Finally, B cell translocation gene 4 (*BTG4*) belongs to the *BTG/Tob* protein family that controls transcription and mRNA turnover [26]. Although the *BTG/Tob* gene family has been examined in differentiation processes in other cellular contexts [26], the expression of *BTG4* during MCC differentiation remains still unexplored. In the present study, our findings provide evidence that (a) transcripts of *BTG4*, *LAYN*, and *HOATZ*, three proximal genes of the *MIR34B/C* locus, are expressed in both precursors and mature MCCs from human, mouse and pig models, (b) HOATZ protein is specifically and highly expressed in MCCs from the bottom to the tip of motile cilia, (c) *LAYN* proteins are expressed in both multiciliated and non-multiciliated cells and (4) *LAYN* silencing alters apical actin cap formation and multiciliogenesis.

## Methods

### Animals

All experiments were performed following the Directive 2010/63/EU of the European Parliament and of the council of 22 September 2010 on the protection of animals used for scientific purposes.

### Mouse tracheal epithelial cell cultures

Each trachea was dissected from 12 weeks-old C57BL/6 mice (Charles River Laboratories, Wilmington, MA, USA) and placed in cold DMEM : F12 medium (1 : 1) supplemented with 15 mM HEPES, 100 U·mL<sup>-1</sup> penicillin, 100 µg·mL<sup>-1</sup> streptomycin, 50 µg·mL<sup>-1</sup> gentamycin sulfate, and 2.5 µg·mL<sup>-1</sup> amphotericin B. Each trachea was cleared under a binocular microscope to remove as much conjunctive tissue as possible and was opened longitudinally. Tracheas were then immersed overnight at 4 °C in supplemented DMEM : F12 containing 0.15% protease XIV from *Streptomyces griseus*. After incubation, tubes with the tracheas were agitated by inverting five times and let 10 min to reach room temperature. Tubes were reversed 10 times, FBS was added to a final concentration of 10%, and tubes were reversed again 20 times. Tracheas were transferred in a tube with supplemented DMEM-F12 containing 10% FBS, inverted 20 times, and the operation was repeated one more time in another tube. After discarding the tracheas, all the cell suspensions in the separate tubes were pooled and centrifuged at 500 g for 10 min at 4 °C. The pellet was resuspended in supplemented DMEM : F12 with 10% FBS and the cells were plated on regular cell culture plates and incubated in a humidified atmosphere of 5% CO<sub>2</sub> at 37 °C for 4 h to allow attachment of putative contaminating fibroblast. Cells in suspension were collected and centrifuged at 400 g for 5 min and were resuspended in DMEM-F12 containing BEGM Singlequot™ kit supplements (Lonza, Basel, Switzerland) and 5% FBS. Cells were then plated apically on rat-tail collagen I-coated Transwells® with medium in the basal side at ~ 30 000 cells per Transwell®. Medium was changed 48 h after, and every other day until confluency. Confluency was detected through the measure of the transepithelial electrical resistance (with EVOM2; World Precision Instruments, Sarasota, FL, USA). Once the resistance had reached a minimum of 1000 ohms·cm<sup>-2</sup>, the apical medium was removed, and the basal medium was changed by Pneumacult-ALI™ medium (STEMCELL Technologies, Vancouver, Canada) to create ALI culture. This day corresponded to the differentiating step at day 0 (ALI0). Medium was then changed every other day. We analyzed mTEC differentiation at several time points (which were different from HNECs) including ALI0, ALI2, ALI3, ALI5, ALI6, ALI7, ALI9, ALI14 or ALI27, as indicated in figures and legends.

## Mouse ependymal cell cultures

For the mouse ependymal cell cultures, experiments were performed using mouse Centrin-2-GFP-tagged ependymal cells as previously described [27]. Briefly, P0–P2 mice were sacrificed by decapitation. Brains were dissected in Hank's solution (10% HBSS, 5% HEPES, 5% sodium bicarbonate, 100 U·mL<sup>-1</sup> penicillin, 100 µg·mL<sup>-1</sup> streptomycin), and the telencephalon was manually cut into pieces, followed by enzymatic digestion (DMEM GlutaMAX, 3% papain (Worthington Biochemical, Lakewood, NJ, USA), 1.5% 10 mg·mL<sup>-1</sup> DNase, and 2.4% 12 mg·mL<sup>-1</sup> cystein) for 45 min at 37 °C in a humidified 5% CO<sub>2</sub> incubator. The digestion was stopped by the addition of a solution of trypsin inhibitors (Leibovitz's L15 medium, 10% 1 mg·mL<sup>-1</sup> ovomucoid, and 2% 10 mg·mL<sup>-1</sup> DNase). The cells were then washed in L15 medium and resuspended in DMEM GlutaMAX supplemented with 10% FBS and 1% penicillin/streptomycin in a poly-L-lysine-coated flask. The ependymal progenitors were allowed to proliferate for 4–5 days, until confluence was reached, before being incubated overnight under shaking (250 r.p.m.). Cells were grown on 12-mm glass coverslips and were fixed on differentiation day 5.

## Human samples

Inferior nasal turbinates were collected from patients with nasal obstruction (surgical intervention performed by L. Castillo at the Nice University Hospital, France) in Ca<sup>2+</sup>/Mg<sup>2+</sup>-free HBSS supplemented with 25 mM HEPES, 200 U·mL<sup>-1</sup> penicillin, 200 µg streptomycin, 50 µg·mL<sup>-1</sup> gentamicin sulfate, and 2.5 µg·mL<sup>-1</sup> amphotericin B (all reagent from Gibco/Thermo Fisher Scientific, Waltham, MA, USA). Human bronchial tissue samples were collected from healthy adult volunteers during bronchoscopy under local anesthesia. All procedures were administered by the same pulmonologist at Nice University Hospital, France. The process, location, and type of specimens (brushing or biopsy) were compatible with future use in daily clinical practice. These procedures have been performed according to the guidelines of the Declaration of Helsinki, after approval by the institutional review board 'Comité de Protection des Personnes Sud Méditerranée V' (06/06/2015, approval number: 17/081). The use of human tissues was authorized by bioethics law 94-654 of the French Public Health Code after written consent from the patients.

## Human nasal epithelial cell cultures

Nasal turbinates were washed three times with cold-supplemented HBSS (Hepes 25 mM, 200 U·mL<sup>-1</sup> penicillin, 200 µg·mL<sup>-1</sup> streptomycin, 2.5 µg·mL<sup>-1</sup> amphotericin B, 50 µg·mL<sup>-1</sup> gentamycin sulfate) and immersed in

supplemented HBSS containing 0.1% protease XIV from *S. griseus* (Sigma-Aldrich, Saint-Louis, MO, USA) overnight at 4 °C for epithelial digestion. Gentle agitation allowed to collect detached cells in inactivation buffer (DMEM supplemented with 10% FBS, 100 U·mL<sup>-1</sup> penicillin, 100 µg·mL<sup>-1</sup> streptomycin, 50 µg·mL<sup>-1</sup> gentamicin sulfate, and 2.5 µg·mL<sup>-1</sup> amphotericin B). After centrifugation at 150 g for 5 min, cells were resuspended in supplemented DMEM, centrifuged again, and then resuspended in bronchial epithelium basal medium (BEBM; Lonza) supplemented with BEGM SingleQuot™ Kit supplements (Lonza). Cell suspension was passed through a 21G needle, then plated (~20 000 cells·cm<sup>-2</sup>) on 75 cm<sup>2</sup>-flasks coated with rat-tail collagen I (Sigma-Aldrich), in and incubated in a humidified atmosphere of 5% CO<sub>2</sub> at 37 °C. After 24 h, cells were rinsed with PBS to remove erythrocytes and debris from the culture and immersed again in BEGM medium. After 4–5 days of culture, cells reached 70% confluence. They were detached using trypsin–EDTA 0.05% (Gibco) for 5–10 min, collected in inactivation buffer, centrifuged at 150 g for 5 min, and resuspended in BEGM medium. Cells were seeded on human placenta collagen IV-coated Transwell® permeable supports (6.5 mm diameter; 0.4 µm pore size; Corning, Corning, NY, USA) in the apical part with a density of ~30 000 cells per Transwell® and with medium in the basal part. Once the cells have reached confluence (~5 days after seeding), the medium was removed from the apical side of the Transwell® and the basal medium, replaced by Pneumacult-ALI™ (STEM-CELL Technologies) to create ALI cultures as previously described [3,8,9]. This day corresponded to the differentiating step at day 0 (ALI0). Culture medium was changed every other day. We analyzed HNEC differentiation at several time points including ALI0, ALI6, ALI7, ALI10, ALI14, ALI15, ALI20, ALI22, and ALI28, as indicated in corresponding figures and legends. ALI day 0 (ALI0) is the time point at which cell cultures are switched to ALI in both HNECs and mTECs. Solitary primary cilia are detected in early ALI cultures usually from ALI0 to ALI12 before resorbing [28,29]. Then, a step of massive centriole amplification typically occurs around ALI1–ALI10 or ALI7–ALI14 in mTEC and HNEC cultures, respectively [3,9,29]. Then, the first motile cilia appear around ALI2–ALI7 or ALI15 in mTECs and HNECs or HBECs, respectively [3,8,9,28,29,30]. Fully-differentiated MCCs are detected around ALI5–ALI14 and ALI21–ALI28 for mTECs and HNECs or HBECs, respectively [3,7,8,9,28,29,30].

## Human bronchial epithelial cell cultures

ALI HBECs were purchased from Epithelix® Sarl (Geneva, Switzerland) and cultured at ALI following the manufacturer's instructions.

## Tissue processing for embedding

Human bronchial tissue biopsies were fixed in paraformaldehyde 4% (15 min at room temperature) and then extensively rinsed with PBS. Fixed tissues were then prepared for paraffin embedding. Cutting of paraffin-embedded sections was performed using a rotary microtome MICROM HM 340E (Thermo Fisher Scientific). Before staining, deparaffinization and antigen retrieval process were carried out on bronchial sections using citrate buffer at pH6. Sections and cytopspins were permeabilized with 0.5% Triton X-100 in PBS. A following blocking treatment was performed with 3% bovine serum albumin (BSA) in PBS for 30 min. The incubation with primary antibodies was carried out at 4 °C overnight. Incubation with secondary antibodies was carried out during 1 h at room temperature. Nuclei were stained with 4,6-diamidino-2-phenylindole (DAPI).

## Cytopspins from human airway epithelial cell cultures

Cells dissociated from differentiated human nasal and bronchial epithelium cultured in ALI were cytocentrifuged at 72 g (800 r.p.m.) for 10 min onto SuperFrost™ Plus slides using a Shandon Cytospin™ 4 cytocentrifuge. Cytospin™ slides were fixed for 10 min in 4% paraformaldehyde at room temperature for further immunostaining.

## Single-cell RNA-sequencing of HNECs, mTECs, and pig samples

Data used in the present study were generated from our previous study [3].

## Cell dissociation of HNECs and mTECs

To perform single-cell analysis, cells on Transwells® at different days of ALI culture were incubated with 0.1% protease type XIV *S. griseus* (Sigma-Aldrich) in HBSS for 4 h at 4 °C. Then, cells were gently detached from the Transwell® by pipetting and transferred in a microtube. Cells were incubated at room temperature for 10 min with 50 units of DNase I (EN0523; Thermo Fisher Scientific) per 250 µL directly added in the tube. Cells were centrifuged at 150 g for 5 min and resuspended in 500 µL of supplemented HBSS containing 10% FBS, centrifuged again at 150 g for 5 min, and resuspended in 500 µL HBSS with 10% FBS and dissociated mechanically four times through a 26-G syringe. Finally, cell suspensions were filtered through a 40-µm porosity Flowmi™ Cell Strainer (Bel-Art, Wayne, NJ, USA), centrifuged at 150 g for 5 min, and resuspended in 500 µL of HBSS. Cell concentration was measured with Scepter™ 2.0 Cell Counter (Merck Millipore, Darmstadt, Germany) and Countess™ automated cell counter (Thermo Fisher Scientific). Cell viability was checked with Countess™ automated

cell counter (Thermo Fisher Scientific). All steps except the DNase I incubation were performed on ice. Cell concentration was adjusted to 300 cells·µL<sup>-1</sup> in HBSS for the cell capture by 10× Genomics device, in order to capture 1500 cells for HNECs and 5000 cells for mTECs.

## Single-cell isolation and library construction

We followed the manufacturer's protocol (Chromium™ Single-Cell 3' Reagent Kit, v2 Chemistry, 10X Genomics, Pleasanton, CA, USA) to obtain single-cell 3' libraries for Illumina sequencing. Libraries were sequenced with a Next-Seq 500/550 High Output v2 kit (75 cycles) (Illumina, San Diego, CA, USA) that allows up to 91 cycles of paired-end sequencing: Read 1 had a length of 26 bases that included the cell barcode and the unique molecular identifier (UMI); Read 2 had a length of 57 bases that contained the cDNA insert; Index reads for sample index of 8 bases.

## Single-cell RNA-seq data analysis

CELL RANGER SINGLE-CELL Software Suite v1.3 (10X Genomics) was used to perform sample demultiplexing, barcode processing, and single-cell 3' gene counting using standards default parameters and human build hg 38, pig build sus scrofa 11.1 and mouse build mm10. Individual dataset analysis was performed using SEURAT standard analysis pipeline [31]. Briefly, cells were first filtered based on the number of expressed features, dropout percentage, library size, and mitochondrial gene percentage. Thresholds were selected by visually inspecting violin plots in order to remove the most extreme outliers. Genes expressing less than 5 UMI across all cells were removed from further analysis. Cell-level normalization was performed using the median UMI counts as a scaling factor. Highly variable genes (hvg) were selected for the following analysis based on their expression level and variance. PCA analysis was performed on those hvgs, and the number of PCs to use was chosen upon visual inspection of the PC variance elbow plot (~10–20 PCs depending on the dataset). Clustering was first performed with the default parameter and then increasing the resolution parameter above 0.5 to identify small clusters (but with the knowledgeable risk of splitting big cluster due to high gene expression variability). Differential analysis was again performed using SEURAT FindAllMarkers and FindMarkers functions based on the nonparametric Wilcoxon rank-sum test. All graphs were generated using SEURAT and GGPLOT2 [32] in the free software environment R (<http://www.r-project.org>).

## RNA interference

Before seeding (60 000 cells per Transwell®) HNECs were transfected with a mixture of four individual siRNAs against human *LAYN* transcript or siRNAs scrambled

(5 nM final concentration) (ON-Target plus SMARTpool; Dharmacon Horizon Discovery, Lafayette, CO, USA) using Lipofectamine RNAi Max Reagent (Invitrogen) in OPTIMEM (Invitrogen/Thermo Fisher Scientific) according to the manufacturer's instructions. The cells were then harvested as in normal conditions.

## Immunostainings

Human and mouse airway epithelial samples were fixed with 4% paraformaldehyde (20 min, 4 °C), washed in PBS, permeabilized with 0.5% Triton X-100 (5 min, room temperature), and blocked with 3% BSA in PBS (30 min, room temperature). Incubation with primary antibodies was carried out at 4 °C overnight, as follows: rabbit polyclonal anti-LAYN (1 : 200, HPA-040087; Sigma-Aldrich), goat polyclonal anti-HOATZ (C11orf88) (1 : 100, SC-270467; Santa Cruz Biotechnology, Dallas, TX, USA), rabbit polyclonal anti-C11orf88-DNAXpab (HOATZ) (1 : 100, H00399949-W01P; Abnova, Taipei City, Taiwan), mouse monoclonal antiacetylated alpha-tubulin (1 : 1000, Clone 6-11B-1; Sigma-Aldrich), rabbit polyclonal anti-SNTN (sentan) (1/50, ab122845; Abcam, Cambridge, UK), mouse monoclonal anticentrin-2 (1 : 200, clone (N-17)-R; Santa Cruz Biotechnology). Incubation with secondary antibodies (1 : 500, Alexa Fluor; Thermo Fisher Scientific) was carried out for 1 h at room temperature and protected from light. Transwell® membranes were cut with a razor blade and mounted on slides with Fluoromount-G™ mounting medium with DAPI (Thermo Fisher Scientific).

Mouse ependymal cells were fixed for 10 min in either 4% paraformaldehyde at room temperature or 100% ice-cold methanol at -20 °C. Cells were preblocked in PBS with 0.2% Triton X-100 and 10% FBS before incubation with the primary and secondary antibodies. Centrin-2-GFP-tagged ependymal cells were co-stained with mouse anti-GT335 to detect cilia (1 : 500, AG-20B-0020-C100; Adipogen, San Diego, CA, USA) and with goat polyclonal anti-HOATZ (C11orf88) (1 : 100, SC-270467; Santa Cruz Biotechnology), followed by an incubation with species-specific Alexa Fluor secondary antibodies (1 : 400; Life Technologies/Thermo Fisher Scientific). Cells were counterstained with DAPI (10 µg·mL<sup>-1</sup>; Sigma-Aldrich) and mounted in Fluoromount (Thermo Fisher Scientific).

Images were acquired using the Olympus Fv10i (Olympus, Tokyo, Japan) or Leica SP5 or Leica SP8 (Leica Microsystems, Nanterre, France) confocal imaging systems.

## Confocal and stimulated emission depletion microscopy

Samples were mounted either in Fluoromount-G mounting medium with DAPI (for confocal) or in Abberior Mount Solid Antifade (Abberior GmbH, Göttingen, Germany) (for STED). Images were acquired using a Leica SP8 STED

3× (Leica Microsystems), at 700 Hz either through a 63×/1.4 NA Oil objective (for confocal) or through a 93×/1.3 NA Glyc objective (for STED), using the LAS X software (Leica Microsystems). Confocal images were obtained by a 405-, 488-, and 561-nm laser excitation, respectively. All images have a 72-nm pixel size. Super-resolution images were obtained using STED microscopy with 561 and 633-nm excitations and the depletion at 775 nm for both fluorophores (20–30% of power). Images obtained in STED had a 17-nm pixel size. The images were deconvolved using Huygens Professional (version 18.10; Scientific Volume Imaging, Hilversum, The Netherlands, <http://svi.nl>), using the CML algorithm with SNR:20 and 40 iterations (for confocal) or with SNR:100 and 5 iterations (for STED).

## Western blot experiments

Cells were collected by scrapping in antiprotease supplemented RIPA lysis Buffer (Pierce/Thermo Fisher Scientific), ultrasonicated, and cleared by centrifugation. Protein concentration was determined using the BCA assay (Thermo Fisher Scientific), and 25 µg of protein was resolved on SDS polyacrylamide gels using gradient Bolt SDS/PAGE Gel System following the manufacturer's instructions. Proteins were transferred to PVDF membranes; membranes were blocked with 5% milk in TBS-Tween buffer for 1 h. Incubation with primary antibodies (mouse monoclonal anti-LAYN 1 : 500, Santa Cruz, sc377389; goat polyclonal anti-HOATZ 1 : 100, Santa Cruz Biotechnology, SC-270467; rabbit polyclonal anti-HOATZ-DNAXpab 1 : 100, H00399949-W01P, Abnova; mouse monoclonal anti-GAPDH 1 : 20 000, 60004-1, ProteinTech, San Diego, CA, USA; and goat polyclonal anti-HSP60 1 : 5000, sc-1052, Santa Cruz Biotechnology, Inc), in 5% milk in TBS-Tween buffer, was carried out at 4 °C overnight. After three washes with TBS-Tween buffer during 10 min at room temperature, membranes were incubated with HRP-conjugated secondary antibodies (diluted at the required concentration) at room temperature for 1 h. After three washes, immunoreactive bands were detected using Immobilon ECL kit (Merck Millipore) on Fusion-FX imager (Vilber, Marne-La-Vallée, France).

## Results

### Transcript expression of the MIR34B/C gene members during airway epithelium regeneration

In order to identify cell type-specific expression of *HOATZ* (C11orf88), *LAYN*, and *BTG4*, three proximal genes of the conserved *MIR34B/C* genomic locus (Fig. 1A), we have used single-cell RNA-seq (scRNA-seq) *in vitro*, on both human nasal epithelial cells (HNECs) and mouse tracheal epithelial cells (mTECs) differentiated at the air-liquid interface (ALI), and *in vivo*, in human airway biopsies and

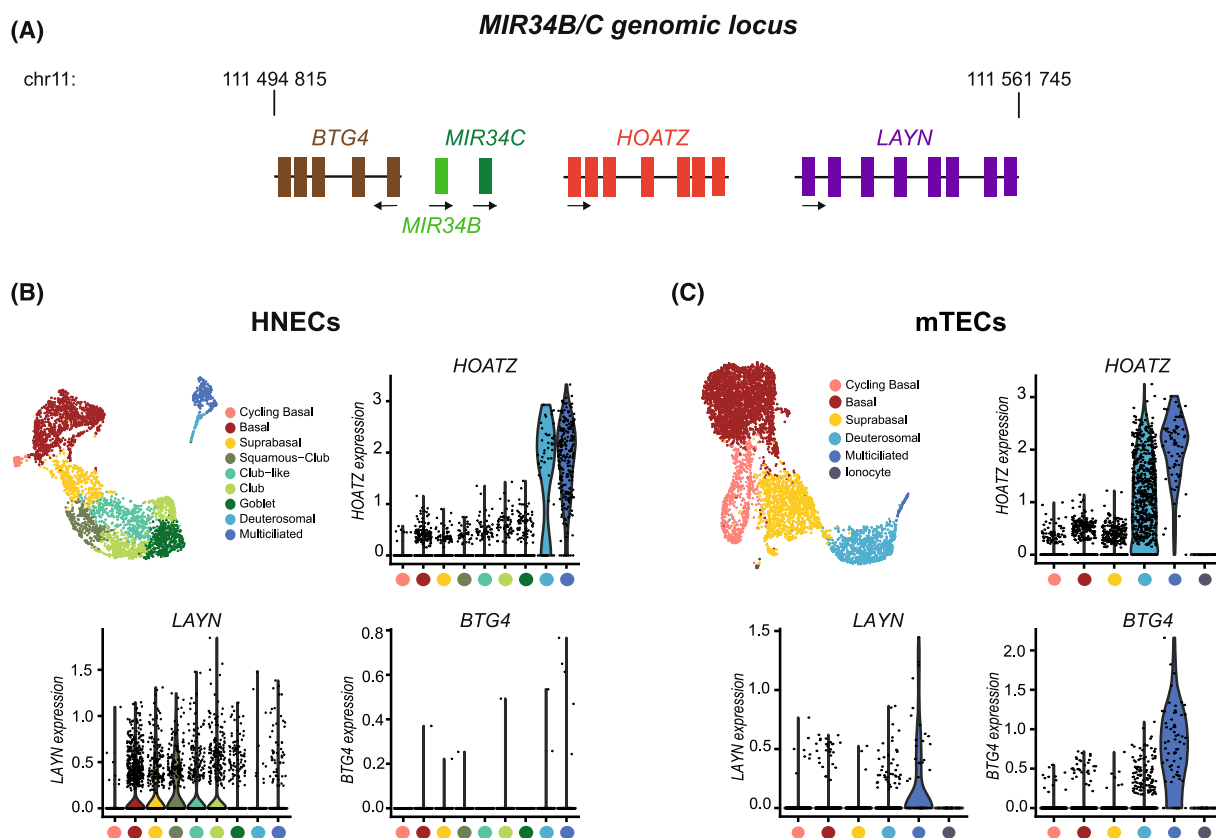


**Fig. 1.** Expression and localization of the *MIR34B/C* locus members in multiciliated epithelia from human and mouse. (A) Illustration of the positioning of three proximal genes around the *MIR34B/C* genomic locus. Exon lengths and positions are not strictly proportional to actual annotations. Genomic start and end positions of the locus are accurate and indicated on the top. (B) Transcript expression of the *MIR34B/C* locus members is enriched in MCCs of the human airway epithelium: UMAP (top left panel) illustrating single-cell RNA-sequencing data from fully-differentiated HNECs in Pneumacult-ALI™ medium (ALI28) clustered 9-cell populations. Violin plots (top right and bottom panels) representing the level of normalized gene expression in each cell population for *HOATZ*, *LAYN*, and *BTG4*. (C) Transcript expression of the *MIR34B/C* locus members is enriched in MCCs of the murine tracheal epithelium: UMAP (top left panel) illustrating single-cell RNA-sequencing data obtained with mouse tracheal epithelial cells (mTECs) at mid-differentiation (ALI3). Violin plots (top right and bottom panels) representing the level of normalized gene expression in each cell population for *HOATZ*, *LAYN*, and *BTG4*.

brushings [2], as well as in newborn pig airways. All scRNA-seq datasets showed that *HOATZ* transcripts were specifically and strongly expressed in both mature MCCs and their precursors (deuterosomal cells) in all models: human (Fig. 1B; Fig. S1A for *in vitro* data; Fig. S2A,B for *in vivo* data), mouse (Fig. 1C; Fig. S1B) or pig (Fig. S3A, B,E,F). Two isoforms of human *HOATZ* transcripts were described in Ensembl Genome Browser: *HOATZ-201* (ENST00000332814) with 7 exons and *HOATZ-202* (ENST00000375618) with 6 exons (Fig. S4A). Using long-read RNA-sequencing and RT-PCR, our data showed that both *HOATZ* transcript isoforms were expressed in differentiated HNECs (Fig. S4A,B), with an overrepresentation of *HOATZ-202* compared with *HOATZ-201* (Fig. S4A).

*LAYN* expression was also specific to MCCs in mice and pigs but was more ubiquitous in human with

detection in all cell types (Fig. 1B,C; Figs S2C and S3C,G).

*BTG4* was expressed in a few cells in humans and pigs, most of them being MCCs, both *in vitro* and *in vivo* (Fig. 1B,C; Figs S2D and S3D,H). Fortunately, we found out that *BTG3*, another gene belonging to the BTG/Tob family, for which the level of expression and the number of *BTG3*-expressing cells were much higher than the one of *BTG4* in human cells, was markedly expressed in human deuterosomal cells and also moderately expressed in mature MCCs (Fig. S5).

When analyzing transcript expression in a time-course manner, by RNA-seq and RT-qPCR, the expression of *HOATZ* and *BTG4* increased concomitantly to *FOXJ1* (a marker of MCCs) and *CDC20B* (a

marker of deuterosomal cells) in both HNECs and mTECs (Fig. S1C–F) [9,33]. In agreement with the scRNA-seq data, *Layn* expression was increased during multiciliogenesis of mTECs and remained constant in HNECs (Fig. S1C–F).

### HOATZ proteins are localized in motile cilia in human and mouse MCCs

HOATZ protein subcellular localization was assessed from ALI cultures (HNECs, human bronchial epithelial cells (HBECs) or mTECs), native human bronchial tissue (biopsy sections), and mouse ependymal cells by immunostaining followed by confocal or stimulated emission depletion (STED) microscopy. Antibodies against HOATZ were validated by western blot (Fig. S4C,D). In early ALI cultures, HOATZ was first detected in a punctate manner in the primary cilium of mTECs, while it was not detected in the primary cilium of HNECs (Fig. 2A). At early steps of the formation of motile cilia, when cilia have not fully elongated, HOATZ was mainly detected at the tip of cilia (Fig. 2B,C) and partially co-localized with Sentan (SNTN) (Fig. 2C), the first described molecular component of the ciliary tip of vertebrate motile cilia [34]. This was well observed using confocal and super-resolution STED microscopy at 12–14 days of differentiation for HNECs (Fig. 2B,C), 2 days for mTECs (Fig. 3A) and 5 days for ependymal cells (Fig. 3B). Later in differentiation, mature MCCs displayed longer motile cilia in which HOATZ was highly detected from the bottom of cilia until the ciliary tip, with a punctate pattern in all models, including on ALI cultures or cytospin-isolated HNECs and HBECs (Fig. 2B,D,E), as well as on native human bronchial tissue sections (Fig. 2F) and mouse ependymal cells (Fig. 3B).

### Localization of LAYN proteins in both human and mouse models of airway epithelium

As shown by immunostaining, LAYN protein was absent from the primary cilium in mTECs but appeared as a punctate distribution along the motile cilia in mid- and fully-differentiated MCCs (Fig. 4A). A distinct pattern of expression was observed in HNECs, where LAYN expression was not restricted to MCCs and was detected in the cytoplasmic region with an apical polarization in fully-differentiated MCCs (Fig. 4B). An apical surface localization of LAYN has already been reported in human airway epithelial cells [25]. In HNECs, LAYN was also expressed in other cells than MCCs, which is consistent with our scRNA-

seq data (Fig. 1B; Fig. S2C). The distinct expression and localization of LAYN in mouse and human airway epithelium may refer to distinct roles in the two species. To assess the role of LAYN in HNEC differentiation, we performed siRNA silencing using siRNAs against human *LAYN* transcripts 4 days before ALI differentiation. Expression analysis from ALI0 to ALI14 showed that siRNAs efficiently knocked-down LAYN both at the RNA and protein levels (Fig. S6A–C) and that *LAYN* RNA levels started to reverse back to control level from day 7 (Fig. S6A). Upon differentiation, the level of *FOXJ1* transcripts (ALI14, Fig. S6C) and the proportion of centrin-2-positive (ALI20, Fig. 4C,D) or acetylated alpha-tubulin-positive MCCs (ALI20, Fig. 4E,F) were significantly lower in cultures transfected with siRNAs against *LAYN* transcripts compared with control. In addition, the apical actin meshwork was strongly altered in si*LAYN* conditions (Fig. 4G), revealed by a reduction of the enrichment of the phalloidin-stained apical actin cap and a decrease in the number of cells exhibiting an enrichment of apical actin meshwork corresponding to MCCs. These observations also suggest defects in polarization and basal body anchoring. Therefore, inhibition of *LAYN* expression at an early stage of differentiation appears sufficient to alter the subsequent formation of MCCs.

### Discussion

This work represents the first characterization of the expression of three genes belonging to the *MIR34B/C* genomic locus. The first observation is that *HOATZ* expression was strikingly increased in both deuterosomal and MCCs during human, mouse, or pig airway epithelium regeneration. It is noteworthy that *HOATZ* expression was maintained in MCCs, while gene expression from the *MIR449* genomic locus rapidly decreased after the deuterosomal stage. The punctate pattern of HOATZ proteins in the primary cilium of mTECs is probably related to a functional role played in the primary cilium before multiciliogenesis. Indeed, cells with a primary cilium acquire markers of motile ciliogenesis and MCCs may originate from primary ciliated cells as previously described elsewhere [28]. The ciliary tip, at the distal end of the cilium, is a putative site of axonemal growth and resorption and may be involved in the regulation of the intraflagellar transport (IFT) [35]. Using super-resolution microscopy, we showed that HOATZ was partially co-localized with SNTN in the ciliary tip region, suggesting a role of HOATZ either in the assembly of the microtubule doublets during the elongation of axoneme, in the

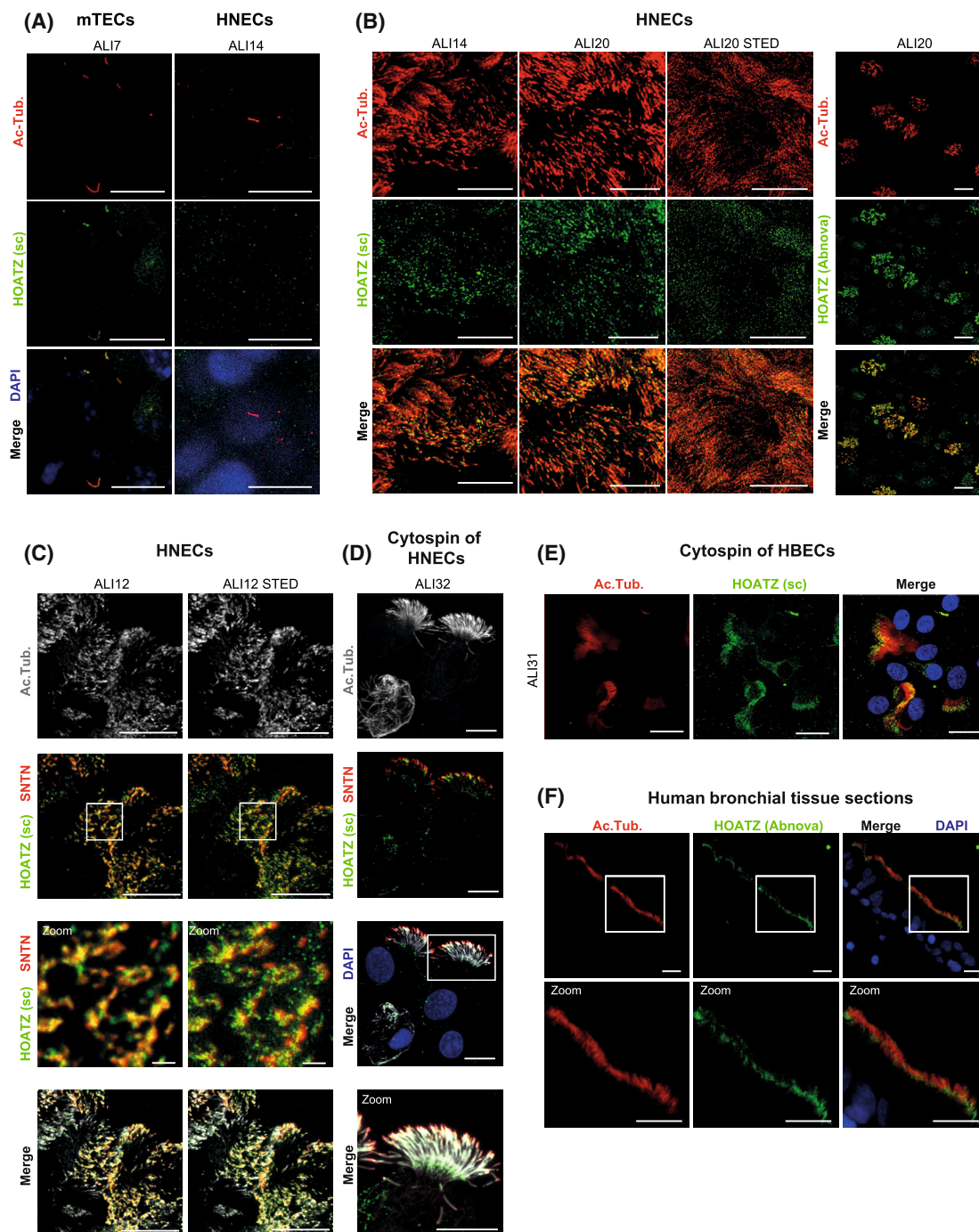


**Fig. 2.** Expression of HOATZ in primary and motile cilia in mouse and human airway cells. (A) Immunostainings performed on mTECs at ALI7 or in HNECs at ALI14, for acetylated alpha-tubulin (Ac. Tub.) and HOATZ. Regions of the cell culture devoid of MCCs were selected to show immunostaining of solitary primary cilium. (B) Immunostainings carried out on HNECs at ALI14 and ALI20 for acetylated alpha-tubulin (Ac. Tub.) and HOATZ. (C) Immunostainings carried out on HNEC cultures (ALI12) for HOATZ, SNTN, and acetylated alpha-tubulin (Ac. Tub.). (D) Immunostainings performed on cytospin-isolated HNECs (ALI32) for HOATZ, SNTN, and acetylated alpha-tubulin (Ac. Tub.). (E) Immunostainings performed on cytospin-isolated HBECs (ALI31) for HOATZ and acetylated alpha-tubulin (Ac. Tub.). (F) Immunostainings performed on human bronchial tissue sections for HOATZ and acetylated alpha-tubulin (Ac. Tub.). Scale bars for all images: 10  $\mu$ m, except for zoom images in (C), scale bars: 1  $\mu$ m. sc: Santra Cruz sc-270467 antibody; Abnova: DNAXPab, H00399949 antibody. Images were obtained by confocal microscopy or, when indicated, by super-resolution STED microscopy.

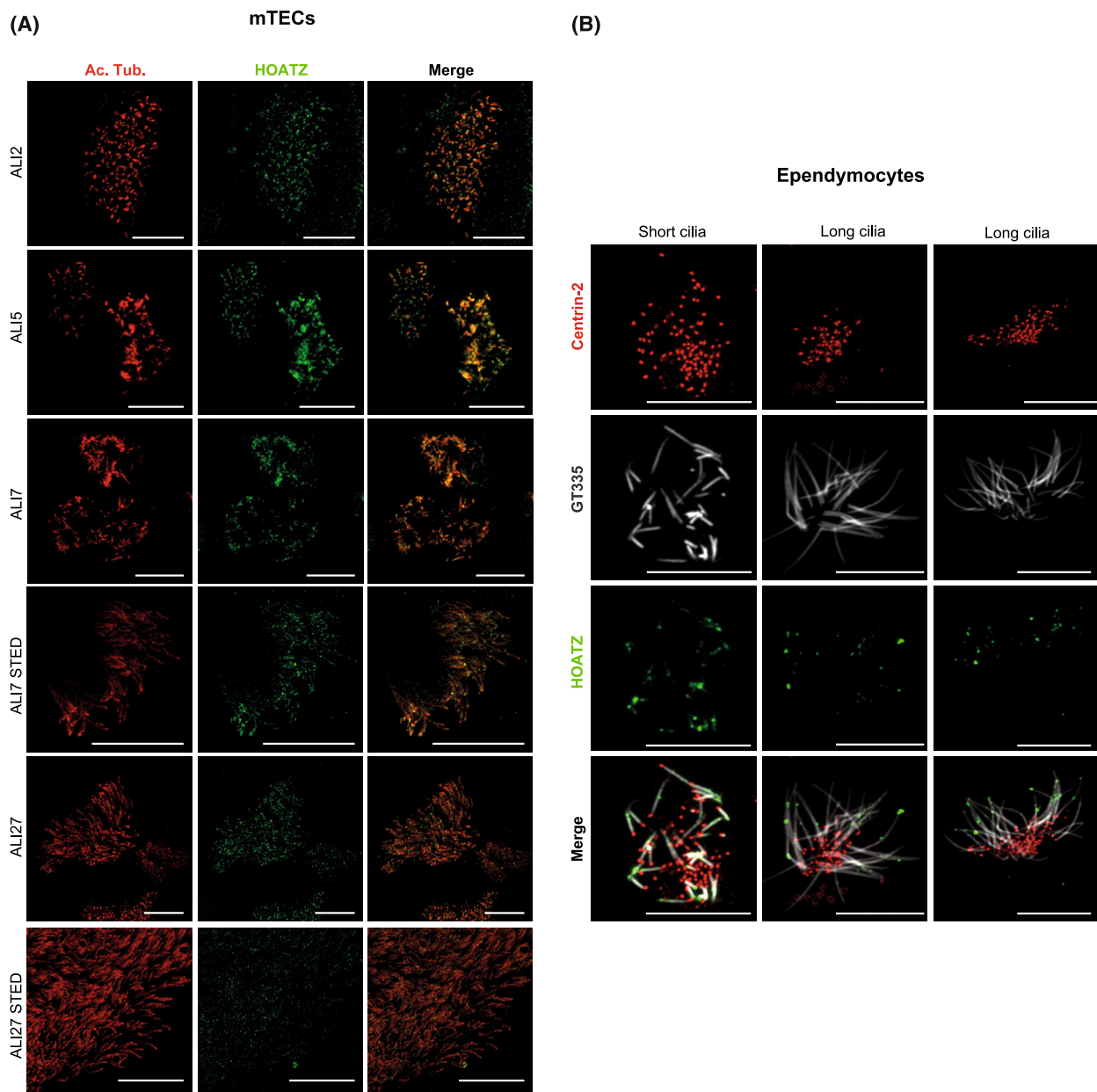
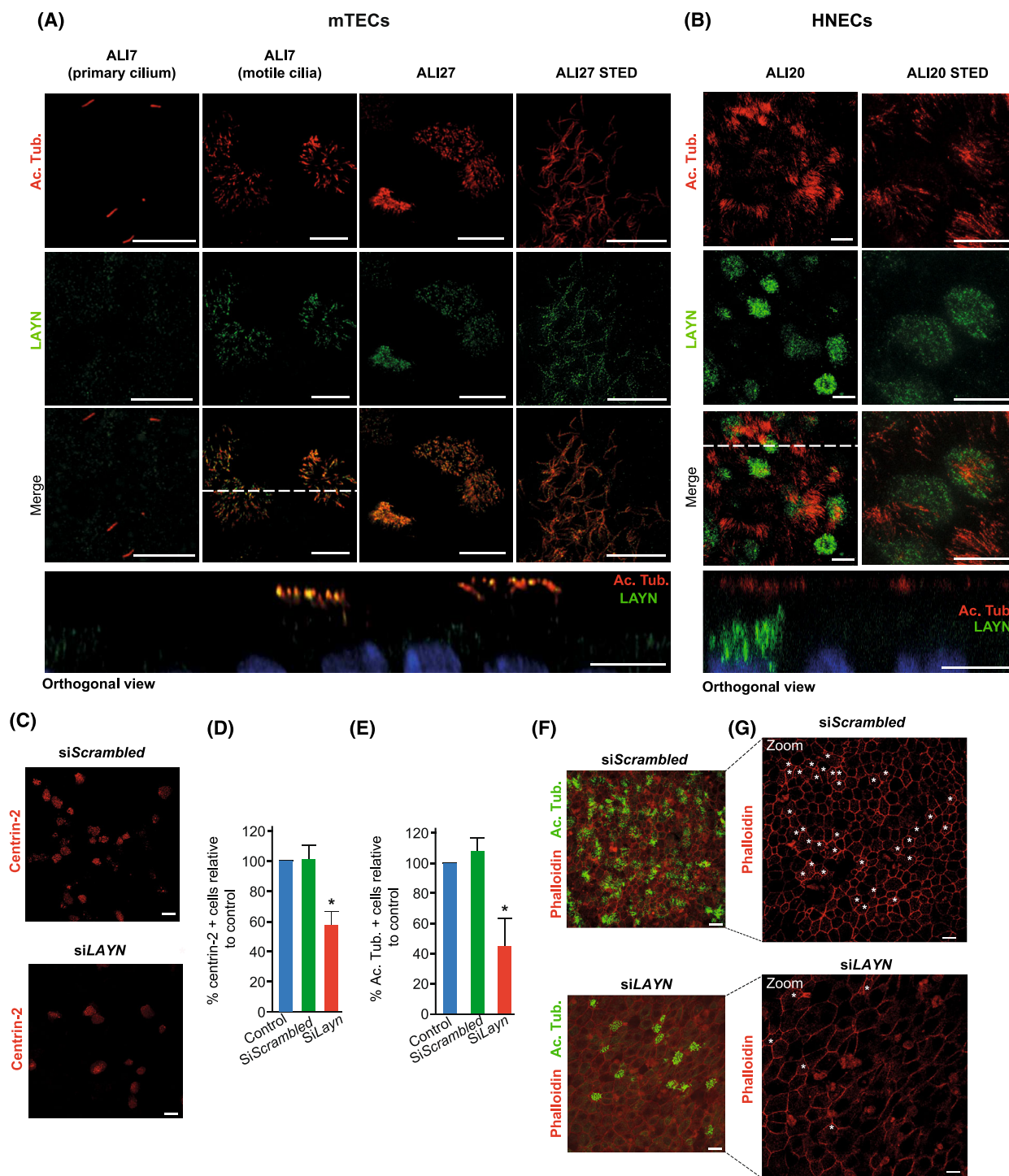


**Fig. 3.** Expression of HOATZ in motile cilia throughout the differentiation of mouse tracheal epithelial cells (mTECs) and in mouse ependymal cells. (A) Immunostainings performed on mTECs at ALI2, ALI5, ALI7, and ALI27 for HOATZ and acetylated alpha-tubulin (Ac. Tub.). (B) Immunostainings performed on mouse ependymal cells expressing Centrin-2-GFP (shown in red) at day 5 of differentiation, with antibodies against GT335, a marker of cilia glutamylation, and against HOATZ. The first line of panels illustrates maturing MCCs exhibiting shorter cilia. The second and third lines of panels illustrate mature MCCs with longer cilia. Scale bars for all images: 10  $\mu$ m. Images were obtained by confocal microscopy or, when indicated, by super-resolution STED microscopy.

control of the ciliary length or in the formation of the ciliary cap at the tip. Moreover, the punctate pattern of HOATZ in motile cilia may evoke a role in the transport of components during the building and maintenance of cilia. HOATZ may be a component of trains, or cargo of this transport, or may be carried by IFT along the cilia to play a role in the axoneme. A

recent study in mice showed that *Hoatz* was required for motile ciliogenesis in ependymal cells and sperm flagella genesis by mediating the maturation of the flagellar glycolytic enzyme enolase-4 ENO4. Indeed, ENO4, which is specifically expressed in ciliated cells, is actively transported along the motile cilia in mice, suggesting the importance of glycolytic enzymes in





local ATP production in highly energy-demanding cell types such as MCCs [24]. In agreement with this, we also observed in our datasets that *ENO4* transcripts were mainly detected in deuterosomal and MCC populations: about 30% (in HNECs) and 37% (in mTECs)

of MCC/deuterosomal cells co-expressed *HOATZ* and *ENO4*. A small proportion of deuterosomal cells or MCCs (0.6% in HNECs and 4.6% in mTECs) expressed *ENO4* without *HOATZ* (Table S1). These observations corroborate the previous conclusions of

**Fig. 4.** LAYN expression and function during multiciliogenesis. (A) Immunostainings performed on mTECs at ALI7 and ALI27 for LAYN and acetylated alpha-tubulin (Ac. Tub.). (B) Immunostainings carried out on HNECs at ALI20 for LAYN and acetylated alpha-tubulin (Ac. Tub.). The bottom panel is an orthogonal view from the top image, performed at the level of dashed line. Scale bars: 10  $\mu\text{m}$ . (C) Immunostainings performed on HNECs (ALI20) for centrin-2 after LAYN knock-down by siRNAs (siLAYN). (D) The bar plot indicates the percentage of centrin-2+ cells (over nuclei numbers), relative to the control set to 100%, and calculated from immunostainings on HNECs (ALI20) after LAYN knock-down by siRNAs (siLAYN). The control condition refers to nontransfected cells. siScrambled: transfection with scrambled siRNAs. Data are mean  $\pm$  SD from 10 fields per insert,  $n = 3$  independent experiments ( $*P < 0.05$ ; Student's *t*-test). (E) The bar plot indicates the percentage of Ac. Tub. + cells (over nuclei numbers), relative to the control set to 100%, and calculated from immunostainings on HNECs (ALI20) after LAYN knock-down by siRNAs (siLAYN). The control condition refers to nontransfected cells. siScrambled: transfection with scrambled siRNAs. Data are mean  $\pm$  SD from 10 fields per insert,  $n = 3$  independent experiments ( $*P < 0.05$ ; Student's *t*-test). (F) Immunostainings performed on HNECs (ALI20) for acetylated alpha-tubulin (Ac. Tub.) and actin network (Alexa Fluor™ Phalloidin-647) after LAYN knock-down by siRNAs (siLAYN). (G) Blow-up images from phalloidin staining in (F). White asterisks indicate in a nonexhaustive manner MCC with enriched apical actin cap in siScrambled compared with siLAYN conditions, in representative images. Scale bars: 10  $\mu\text{m}$ . Images were obtained by confocal microscopy or, when indicated, by super-resolution STED microscopy.

Narita *et al.* [24], which proposed that HOATZ was involved in the maturation of ENO4 and contributed to metabolic pathways for energy production in the cilia.

The second gene of the *MIR34B/C* locus that we investigated was *LAYN*. In humans, *LAYN* transcripts were expressed in deuterosomal cells and, to a lesser extent, in mature MCCs, but they were also detected in other cell types including basal, suprabasal, and secretory cells. We detected the Layilin protein as punctate spots along the motile cilia in mouse tracheal MCCs, whereas it was localized in a cytoplasmic region, with an apical polarization in human airway MCCs. An apical surface localization of *LAYN* in airway epithelial cells has already been reported in human airway epithelium in ALI cultures. This previous study has described that the signal of hyaluronan binding on *LAYN* acted through RhoA/ROCK pathway [25]. We showed that *LAYN* silencing at an early stage of differentiation was sufficient to alter the subsequent formation of MCCs with defects in apical actin network. This observation suggests that the early absence of *LAYN* may prevent some key events, which will be detrimental to the rest of MCC differentiation, such as polarization and actin network formation. So, it is possible that in siLAYN conditions, the MCC differentiation may be prevented because of these early stages that the cells did not go through. In these conditions, restoration of *LAYN* levels at ALI14 may not be sufficient to fully restore MCC differentiation. The dependence of multiciliogenesis on the actin cytoskeleton has been well documented by numerous studies including ours. The apical surface of MCCs is enriched with a dense meshwork of actin composed of two distinct parts, the apical and the subapical actin networks. This apical actin network is essential for both polarization and motility of the cilia. Defects in this apical actin network have been shown to impair

basal body transport, localization, polarity, docking, and stability [7,19,36,37,38]. Previously, we have reported that miR-34/449 controls apical actin network reorganization by modulating small GTPase pathways, including RhoA [7,19]. The localization of *LAYN* near the apical membrane in MCCs, combined with the alteration of the apical actin web and MCC formation in response to *LAYN* silencing and with the previously described interaction of *LAYN* with RhoA/ROCK signal [25] are consistent with a putative role played by *LAYN* in the remodeling of apical cytoskeleton that contributes to the basal body anchoring in MCCs. Hyaluronic acid is secreted by submucosal glands, but its function in airway secretions other than influencing the rheology of mucus is not fully understood. Since hyaluronic acid has already been shown to contribute to ciliary differentiation and beating in human airway epithelium [39,40], we can speculate that *LAYN* might also contribute to ciliary beating in fully-differentiated airway epithelium.

Finally, we provide some observations about *BTG4*, the third gene of the *MIR34B/C* locus. However, due to the weak *BTG4* expression in our different models and the lack of available antibodies giving a specific signal for *BTG4* in our models, a more descriptive study is limited at this time. We, however, noticed that MCCs express higher levels of *BTG4* compared with deuterosomal cells. In addition, a previous study indicated that *BTG4* was highly expressed in ciliated epithelial tissues of juvenile mice such as pharynx, trachea, oviduct, and testis but expressed at lower levels in adult mice [41]. While human diseases caused by mutations in *BTG4* have not been clearly identified, some homozygous mutations in *BTG4* have been associated with zygotic cleavage failure and female infertility through a mechanism involving the maternal mRNA decay in mammalian oocytes [42]. Nevertheless, these authors did not examine the MCC

phenotype in the reproductive tract of women carrying *BTG4* mutations and diagnosed with infertility. *BTG4* also prevents the progression of oocytes into anaphase II by ensuring that the anaphase-promoting complex/cyclosome (APC/C) is completely inhibited during the arrest [43]. Furthermore, *PLK1* controls the onset of spindle assembly and formation and is essential for APC/C activation before anaphase onset in mouse zygotes [44]. This mechanism could be connected to our previous work showing that the *MIR449* gene member *CDC20B* cooperates around deuterosomes with *PLK1* and APC/C activation to trigger centriole disengagement in maturing MCCs [9]. Moreover, the expression of *BTG3*, another gene belonging to the BTG/Tob family, was stronger than *BTG4* in both deuterosomal cells and MCCs. In another context, *BTG3* has been shown to inhibit BMP2 signaling during osteoblast differentiation [26], and we have previously shown that BMP2 signal inhibition strongly stimulated the formation of MCCs [30]. The role of the BTG/Tob family as negative regulators of the cell cycle [45] and the use of cell cycle actors for the amplification of centrioles in MCCs reported in our recent studies [3,9] may suggest a putative role of some members of the BTG/Tob family such as *BTG4* or *BTG3* in MCC differentiation.

In conclusion, our study demonstrates that the transcripts of *BTG4*, *LAYN*, and *HOATZ*, three proximal genes of the *MIR34B/C* locus, are expressed in human, mouse, and pig MCCs. Especially, we have described in different models, human and mouse, the precise site of *HOATZ* expression in motile cilia, its enrichment at the tip of the cilia, more particularly in developing epithelium, and its more punctiform profile from the bottom to the tip of motile cilia in fully-differentiated epithelium (Fig. S7). Using a knockout mouse model, *HOATZ* has been shown by others to be required for the motile cilia function of ependymal cells or sperm flagellum formation [24]. These data collectively argue that *HOATZ* represents a novel conserved motile ciliogenesis actor. We have also observed that early inhibition of *LAYN* expression dramatically impairs apical actin cap formation and MCC differentiation, probably through indirect mechanisms given the expression pattern of *LAYN*. Altogether, our data indicate that, as previously observed for *MIR449* genomic locus [8,9,10,46,47], the *MIR34B/C* locus also encompasses some genes that may be involved in MCC biology. Further investigations of loss or gain of function using approaches such as CRISPR-Cas9 in different models would be needed to elucidate the precise role of each of these genes in multiciliogenesis.

## Acknowledgements

We are grateful to the UCAGenomiX platform for fruitful discussions and technical help with single-cell RNA-sequencing and to the IPMC imaging platform for fruitful discussions and technical help with imaging.

## Author contributions

BM, L-EZ, and PB involved in conceptualization and design; AC, ER, SRG, OM, GP, MD, MP, M-JA, VM, IC, L-EZ, and BM involved in investigation and data interpretation; AC, SRG, MD, KL, M-JA, VM, GR, L-EZ, BM, and PB involved in sequencing experiments and analysis; AC, OM, ER, GP, BM, and L-EZ involved in cell biology experiments; AC, OM, ER, SA, GP, MP, BM, and L-EZ involved in cell imaging experiments; BM, L-EZ, and PB involved in validation and formal analysis; BM involved in writing—original manuscript; BM, L-EZ, and PB involved in writing—review and editing; BM and L-EZ involved in supervision; BM and PB involved in project administration; BM and PB involved in funding acquisition.

## Funding

This work supported by CNRS, Inserm, and the French Government (Agence Nationale de Recherche, ANR) was funded by grants from ANR (21EQUI09Z6RCHX, ANR-19-P3IA-0002, ANR-19-CE14-0027, ANR-11-BSV2-021-02, ANR-13-BSV4-0013, ANR-15-CE13-0003), the Fondation pour la Recherche Médicale (DEQ20180339158, DEQ20141231765, DEQ20130326464), the Labex Signallife (ANR-11-LABX-0028-01), the Association Vaincre la Mucoviscidose (RF20180502280, RF20150501288, RF20140501158, RF20120600738), the Fondation ARC (PJA 20161204865, PJA 20161204542), the Ligue Nationale contre le Cancer (15BDO003SCSR), the H2020 Health (Discovair) and the Chan Zuckerberg Initiative (Silicon Valley Community Foundation, 2017–175159-5022). The UCAGenomiX platform, a partner of the National Infrastructure France Génomique, is supported by the Commissariat aux Grands Investissements (ANR-10-INBS-09-03 and ANR-10-INBS-09-02) and Canceropôle PACA.

## Data accessibility

Single-cell RNA-seq datasets used in the present study were generated from our previous studies [2,3]. All scRNA-seq data generated from our previous study [2] are currently available through the European Genome-

phenome Archive (EGAS00001004082), and sequence-free data will be linked to the Data Central Repository of the Human Cell Atlas, in order to ensure the openness of information. Data are also available through a dedicated web interface (<https://www.genomique.eu/cellbrowser/HCA/>). Datasets generated from our previous study [3] have been previously deposited in GEO under the series number GSE121600. Links to the UCSC cell browser for data visualization are [genomique.info/cellbrowser/Differentiation/Pneumacult/](https://genome.ucsc.edu/cgi-bin/hgCellBrowser?h=cellbrowser/Differentiation/Pneumacult/) and [genomique.info/cellbrowser/Differentiation/BEGM/](https://genome.ucsc.edu/cgi-bin/hgCellBrowser?h=cellbrowser/Differentiation/BEGM/). All other data are available from the authors.

## References

- Zaragosi LE, Deprez M and Barbry P (2020) Using single-cell RNA sequencing to unravel cell lineage relationships in the respiratory tract. *Biochem Soc Trans* **48**, 327–336.
- Deprez M, Zaragosi LE, Truchi M, Becavin C, Ruiz García S, Arguel MJ, Plaisant M, Magnone V, Lebrigand K, Abelanet S *et al.* (2020) A single-cell atlas of the human healthy airways. *Am J Respir Crit Care Med* **202**, 1636–1645.
- Ruiz Garcia S, Deprez M, Lebrigand K, Cavard A, Paquet A, Arguel M-J, Magnone V, Truchi M, Caballero I, Leroy S *et al.* (2019) Novel dynamics of human mucociliary differentiation revealed by single-cell RNA sequencing of nasal epithelial cultures. *Development* **146**, dev177428.
- Legendre M, Zaragosi LE and Mitchison HM (2021) Motile cilia and airway disease. *Semin Cell Dev Biol* **110**, 19–33.
- Spassky N and Meunier A (2017) The development and functions of multiciliated epithelia. *Nat Rev Mol Cell Biol* **18**, 423–436.
- Zhao H, Zhu L, Zhu Y, Cao J, Li S, Huang Q, Xu T, Huang X, Yan X and Zhu X (2013) The Cep63 paralogue *Deup1* enables massive de novo centriole biogenesis for vertebrate multiciliogenesis. *Nat Cell Biol* **15**, 1434–1444.
- Chevalier B, Adamiok A, Mercey O, Revinski DR, Zaragosi L-E, Pasini A, Kodjabachian L, Barbry P and Marcet B (2015) miR-34/449 control apical actin network formation during multiciliogenesis through small GTPase pathways. *Nat Commun* **6**, 8386.
- Marcet B, Chevalier B, Luxardi G, Coraux C, Zaragosi LE, Cibois M, Robbe-Sermesant K, Jolly T, Cardinaud B, Moreilhon C *et al.* (2011) Control of vertebrate multiciliogenesis by miR-449 through direct repression of the Delta/Notch pathway. *Nat Cell Biol* **13**, 693–699.
- Revinski DR, Zaragosi L-E, Boutin C, Ruiz-Garcia S, Deprez M, Thomé V, Rosnet O, Gay A-S, Mercey O, Paquet A *et al.* (2018) CDC20B is required for deuterosome-mediated centriole production in multiciliated cells. *Nat Commun* **9**, 4668.
- Loukas I, Skannelou M, Tsaridou S, Bournaka S, Grigoriadis S, Taraviras S, Lygerou Z and Arbi M (2021) Fine-tuning multiciliated cell differentiation at the post-transcriptional level: contribution of miR-34/449 family members. *Biol Rev Camb Philos Soc* **96**, 2321–2332.
- Wu YJ, Liu Y, Hu YQ, Wang L, Bai FR, Xu C and Wu JW (2021) Control of multiciliogenesis by miR-34/449 in the male reproductive tract through enforcing cell cycle exit. *J Cell Sci* **134**, jcs253450.
- Yuan S, Liu Y, Peng H, Tang C, Hennig GW, Wang Z, Wang L, Yu T, Klukovich R, Zhang Y *et al.* (2019) Motile cilia of the male reproductive system require miR-34/miR-449 for development and function to generate luminal turbulence. *Proc Natl Acad Sci USA* **116**, 3584–3593.
- Mercey O, Popa A, Cavard A, Paquet A, Chevalier B, Pons N, Magnone V, Zangari J, Brest P, Zaragosi L-E *et al.* (2017) Characterizing isomiR variants within the microRNA-34/449 family. *FEBS Lett* **591**, 693–705.
- Yuan S, Tang C, Zhang Y, Wu J, Bao J, Zheng H, Xu C and Yan W (2015) mir-34b/c and mir-449a/b/c are required for spermatogenesis, but not for the first cleavage division in mice. *Biol Open* **4**, 212–223.
- Wu J, Bao J, Kim M, Yuan S, Tang C, Zheng H, Mastick GS, Xu C and Yan W (2014) Two miRNA clusters, miR-34b/c and miR-449, are essential for normal brain development, motile ciliogenesis, and spermatogenesis. *Proc Natl Acad Sci USA* **111**, E2851–E2857.
- Comazzetto S, Di Giacomo M, Rasmussen KD, Much C, Azzi C, Perlas E, Morgan M and O'Carroll D (2014) Oligoasthenoteratozoospermia and infertility in mice deficient for miR-34b/c and miR-449 loci. *PLoS Genet* **10**, e1004597.
- Wang L, Fu C, Fan H, Du T, Dong M, Chen Y, Jin Y, Zhou Y, Deng M, Gu A *et al.* (2013) miR-34b regulates multiciliogenesis during organ formation in zebrafish. *Development* **140**, 2755–2764.
- Bao J, Li D, Wang L, Wu J, Hu Y, Wang Z, Chen Y, Cao X, Jiang C, Yan W *et al.* (2012) MicroRNA-449 and microRNA-34b/c function redundantly in murine testes by targeting E2F transcription factor-retinoblastoma protein (E2F-pRb) pathway. *J Biol Chem* **287**, 21686–21698.
- Mercey O, Kodjabachian L, Barbry P and Marcet B (2016) MicroRNAs as key regulators of GTPase-mediated apical actin reorganization in multiciliated epithelia. *Small GTPases* **7**, 54–58.
- Marcet B, Chevalier B, Coraux C, Kodjabachian L and Barbry P (2011) MicroRNA-based silencing of Delta/Notch signaling promotes multiple cilia formation. *Cell Cycle* **10**, 2858–2864.

- 21 Song R, Walentek P, Sponer N, Klimke A, Lee JS, Dixon G, Harland R, Wan Y, Lishko P, Lize M *et al.* (2014) miR-34/449 miRNAs are required for motile ciliogenesis by repressing cp110. *Nature* **510**, 115–120.
- 22 Lize M, Klimke A and Dobbelstein M (2011) MicroRNA-449 in cell fate determination. *Cell Cycle* **10**, 2874–2882.
- 23 Wildung M, Esser TU, Grausam KB, Wiedwald C, Volceanov-Hahn L, Riedel D, Beuermann S, Li L, Zylla J, Guenther A-K *et al.* (2019) Transcription factor TAp73 and microRNA-449 complement each other to support multiciliogenesis. *Cell Death Differ* **26**, 2740–2757.
- 24 Narita K, Nagatomo H, Kozuka-Hata H, Oyama M and Takeda S (2020) Discovery of a vertebrate-specific factor that processes flagellar glycolytic enolase during motile ciliogenesis. *iScience* **23**, 100992.
- 25 Forteza RM, Casalino-Matsuda SM, Falcon NS, Valencia Gattas M and Monzon ME (2012) Hyaluronan and layilin mediate loss of airway epithelial barrier function induced by cigarette smoke by decreasing E-cadherin. *J Biol Chem* **287**, 42288–42298.
- 26 Winkler GS (2010) The mammalian anti-proliferative BTG/Tob protein family. *J Cell Physiol* **222**, 66–72.
- 27 Delgehr N, Meunier A, Faucourt M, Bosch Grau M, Strehl L, Janke C and Spassky N (2015) Ependymal cell differentiation, from monociliated to multiciliated cells. *Methods Cell Biol* **127**, 19–35.
- 28 Jain R, Pan J, Driscoll JA, Wisner JW, Huang T, Gunsten SP, You Y and Brody SL (2010) Temporal relationship between primary and motile ciliogenesis in airway epithelial cells. *Am J Respir Cell Mol Biol* **43**, 731–739.
- 29 Vladar EK and Brody SL (2013) Analysis of ciliogenesis in primary culture mouse tracheal epithelial cells. *Methods Enzymol* **525**, 285–309.
- 30 Cibois M, Luxardi G, Chevalier B, Thomé V, Mercey O, Zaragosi L-E, Barbry P, Pasini A, Marcet B and Kodjabachian L (2015) BMP signalling controls the construction of vertebrate mucociliary epithelia. *Development* **142**, 2352–2363.
- 31 Stuart T, Butler A, Hoffman P, Hafemeister C, Papalexi E, Mauck WM 3rd, Hao Y, Stoeckius M, Smibert P and Satija R (2019) Comprehensive integration of single-cell data. *Cell* **177**, 1888–1902.e21.
- 32 Wickham, H. (2009). ggplot2. <https://doi.org/10.1007/978-0-387-98141-3>
- 33 Nemajerova A, Kramer D, Siller SS, Herr C, Shomroni O, Pena T, Gallinas Suazo C, Glaser K, Wildung M, Steffen H *et al.* (2016) TAp73 is a central transcriptional regulator of airway multiciliogenesis. *Genes Dev* **30**, 1300–1312.
- 34 Kubo A, Yuba-Kubo A, Tsukita S, Tsukita S and Amagai M (2008) Sentan: a novel specific component of the apical structure of vertebrate motile cilia. *Mol Biol Cell* **19**, 5338–5346.
- 35 Fisch C and Dupuis-Williams P (2011) Ultrastructure of cilia and flagella – back to the future! *Biol Cell* **103**, 249–270.
- 36 Antoniadou I, Stylianou P and Skourides PA (2014) Making the connection: ciliary adhesion complexes anchor basal bodies to the actin cytoskeleton. *Dev Cell* **28**, 70–80.
- 37 Yasunaga T, Wiegel J, Bergen MD, Helmstädter M, Epting D, Paolini A, Çiçek Ö, Radziwill G, Engel C, Brox T *et al.* (2022) Microridge-like structures anchor motile cilia. *Nat Commun* **13**, 2056.
- 38 Hoffman HK and Prekeris R (2022) Roles of the actin cytoskeleton in ciliogenesis. *J Cell Sci* **135**, jcs259030.
- 39 Lieb T, Forteza R and Salathe M (2000) Hyaluronic acid in cultured ovine tracheal cells and its effect on ciliary beat frequency in vitro. *J Aerosol Med* **13**, 231–237.
- 40 Huang TW, Cheng PW, Chan YH, Yeh TH, Young YH and Young TH (2010) Regulation of ciliary differentiation of human respiratory epithelial cells by the receptor for hyaluronan-mediated motility on hyaluronan-based biomaterials. *Biomaterials* **31**, 6701–6709.
- 41 Mano H, Nakatani S, Kimira Y, Mano M, Sekiguchi Y, Im RH, Shimizu J and Wada M (2015) Age-related decrease of IF5/BTG4 in oral and respiratory cavities in mice. *Biosci Biotechnol Biochem* **79**, 960–968.
- 42 Zheng W, Zhou Z, Sha Q, Niu X, Sun X, Shi J, Zhao L, Zhang S, Dai J, Cai S *et al.* (2020) Homozygous mutations in BTG4 cause zygotic cleavage failure and female infertility. *Am J Hum Genet* **107**, 24–33.
- 43 Pasternak M, Pfender S, Santhanam B and Schuh M (2016) The BTG4 and CAF1 complex prevents the spontaneous activation of eggs by deadenylating maternal mRNAs. *Open Biol* **6**, 160184.
- 44 Baran V, Brzakova A, Rehak P, Kovarikova V and Solc P (2016) PLK1 regulates spindle formation kinetics and APC/C activation in mouse zygote. *Zygote* **24**, 338–345.
- 45 Auer RL, Starczynski J, McElwaine S, Bertoni F, Newland AC, Fegan CD and Cotter FE (2005) Identification of a potential role for POU2AF1 and BTG4 in the deletion of 11q23 in chronic lymphocytic leukemia. *Genes Chromosomes Cancer* **43**, 1–10.
- 46 Stubbs JL, Vladar EK, Axelrod JD and Kintner C (2012) Multicilin promotes centriole assembly and ciliogenesis during multiciliate cell differentiation. *Nat Cell Biol* **14**, 140–147.
- 47 Funk MC, Bera AN, Menchen T, Kualess G, Thriene K, Lienkamp SS, Dengjel J, Omran H, Frank M and Arnold SJ (2015) Cyclin O (Ccn0) functions during deuterosome-mediated centriole amplification of multiciliated cells. *EMBO J* **34**, 1078–1089.

## Supporting information

Additional supporting information may be found online in the Supporting Information section at the end of the article.

**Appendix S1.** Supplemental methods.

**Fig. S1.** Expression of deuterosomal, multiciliated cell markers and *MIR34B/C* locus members during multiciliogenesis.

**Fig. S2.** *HOATZ*, *LAYN* and *BTG4* expression *in vivo* in human airway tissues from Human Cell Atlas data.

**Fig. S3.** *HOATZ* transcript expression is enriched in multiciliated cells of newborn pig airways, *in vitro* and *in vivo*.

**Fig. S4.** *HOATZ* isoform detection and ectopic expression.

**Fig. S5.** *BTG3* transcript expression is specific to human deuterosomal cells.

**Fig. S6.** Effect of *LAYN* silencing on multiciliogenesis.

**Fig. S7.** Schema illustrating *HOATZ* and *LAYN* protein localization in maturing (short cilia) and mature (long cilia) multiciliated cells (MCCs) in both human and mouse models.

**Fig. S8.** Uncropped Western blots.

**Table S1.** Single-cell correlation of gene expression of *HOATZ*, *FOXJ1* and *ENO4* in mTECs and HAECs.

# Chapter III: Materials and methods

## Cell culture

### Primary cells

Human bronchial biopsies and brushings were collected from healthy adult volunteers or severe asthma patients during bronchoscopy under local anesthesia. All procedures were administered either by one pulmonologist at Centre Hospitalier Universitaire de Nice, France or by another pulmonologist at Aix-Marseille Université, France. Biopsies were collected in DPBS (Gibco™), rotated overnight (O/N) at 4°C and centrifuged 5 min at 200 g the next day before being minced with a scalpel and resuspended in 1 mL in Pneumacult Ex+ proliferation medium (PneumaCult-Ex™ Plus Basal Medium, StemCell Technologies, Cat#05041) supplemented with penicillin (100 U/mL), streptomycin (100 µg/mL), gentamicin (50 µg/mL) and amphotericin B (2.5 µg/mL), and plated in a 12 well-plate well coated with Fibronectin at 10 µg/ml, collagen type I at 30 µg/ml, BSA at 10 µg/ml. Brushings (one per donor) were collected in HBSS (Gibco™) supplemented with 200 U/mL penicillin, 200µg/mL streptomycin, amphotericin B 2.5 µg/mL and gentamycine 50µg/mL. Tubes were very gently vortexed then centrifuged 10 min at 400 g before being resuspended in 1mL in Pneumacult Ex+ proliferation medium and plated in a 12 well-plate well coated with the fibronectin/collagen coating detailed above. Medium was renewed every other day and cells were maintained in culture in an incubator at 37°C and 5% CO<sub>2</sub>. Cells were dissociated with trypsin when reaching ~ 80% confluence and plated in a 75 cm culture flask previously coated with type I collagen 50 µg/mL (Merck catalog #C3867). At ~ 80% confluence cells were dissociated again and were seeded on semi-permeable Transwell™ inserts (Corning reference CLS3470), previously coated with type IV collagen 0.2 mg/mL (Merck catalog #C7521) and maintained in Pneumacult Ex+ medium until full confluence. At confluence, the apical medium was removed, and the basal medium replaced with PromoCell® Airway Epithelial Cell Growth Medium, replacing retinoic acid from the kit in order to reach a final concentration of 30 nM (Sigma Aldrich reference R2625) for the IL-13 experiments, or with PneumaCult™-ALI Medium (StemCell Technologies, Cat#05001) for the rhinovirus A16 experiments, to trigger differentiation. Differentiation medium was replaced every other day and epithelia were considered mature after 28 days of ALI.

**Table 4:** Severe asthma donors' clinical data.

Donor	Gender	Age	Exacerbation over the last year	VEMS (%)	Eosinophils/mm <sup>3</sup>	Rhinosinusitis	Allergy	IgE (kUI/l)	Smoking	Treatments						
										ICS	SAB	LAB	OCS	LAMA	Azithromycin	Immunotherapy
551	M	49	No	60	220	Yes	No	-	Ex > 20 years	Yes	No	Yes	No	Yes	No	No
552	M	57	No	90	0 (max 4000)	Yes	Yes	415	No	Yes	No	Yes	No	Yes	No	Anti-IL5R
569	F	63	No	90	0	Yes	No	-	No	Yes	No	Yes	No	No	Yes	Anti-IL5R
568	F	61	6	80	220 (max 600)	Yes	Yes	206	Ex	Yes	No	Yes	No	Yes	No	No
535	F	36	2	59	0 (max 2000)	Yes	Yes	-	No	Yes	No	Yes	No	Yes	No	Anti-IL5
576	F	69	2	100	160	Yes	Yes	3	No	Yes	No	Yes	Yes	No	Yes	No
567	M	58	2	46	100 (max 230)	Yes	-	-	No	Yes	No	Yes	Yes	No	Yes	anti-IL5
636	F	73	3	81	1280	-	-	2638	No	Yes	No	Yes	No	No	Yes	No
637	F	71	3	45	0 (max 640)	Yes	-	-	No	Yes	No	Yes	No	No	Yes	anti-IL5R

### BCi NS-1.1 immortalized cells

BCi NS-1.1 cells (passage 16) were seeded in 75 cm culture flasks previously coated with type I collagen (Merck catalog #C3867), at a density of 2 million cells per flask and grown in Pneumacult Ex+ proliferation medium (PneumaCult-Ex™ Plus Basal Medium, StemCell Technologies, Cat#05041), supplemented with penicillin (100 U/mL), streptomycin (100 µg/mL), gentamicin (50 µg/mL) and amphotericin B (2.5 µg/mL). Experiments were conducted using passage 17 cells and epithelia were considered mature after 28 days of ALI. At full confluence, cells were differentiated in PromoCell® Airway Epithelial Cell Growth Medium, identically as described above for the primary cells.

### IL-13 treatment

ALI35-50 (primary cells) or ALI35 (BCi) epithelia were treated with 10 ng/mL of interleukin-13 (R&D Systems) diluted in PBS BSA 0.1%, added to the basal compartment at each medium change. For the primary cells, 10 µL of IL-13 solution were added to the apical part during the first 3 days.

### Rhinovirus infection

For rhinovirus infection, the apical side of all inserts was washed by adding 500 µL PBS (+ Calcium + Magnesium) followed by a 45 min to 1 h incubation at 37°C. The medium from the basal compartment was changed with fresh Pneumacult-ALI medium and transepithelial resistance (TEER) was measured (n=3 MOCK and n= 3 RVA16). TEER will be measured in these same wells at dpi 2, 4, 7 and 14 (days post-infection). Cells were infected by applying 100 µL of either viral solution containing 1.10<sup>6</sup> copies of RVA16 RNA in Pneumacult-ALI medium or Pneumacult-ALI medium only (MOCK), on the apical part of each insert. Cells were incubated for 4 h at 33°C, 5% CO<sub>2</sub>. Then, the infecting solution was removed, and inserts were washed 3 times with PBS (+ Calcium + Magnesium, 500µL/insert). A final wash was performed with 500 µL of Pneumacult-ALI apically for 20 min at 33°C. Finally, the apical medium was



removed, and cells were incubated at 33°C overnight. The day after, the apical side of inserts was washed again with 400 µL of Pneumacult-ALI for 20 min at 33°C. Then, this apical medium was removed and 60 µL were stored at -80°C for subsequent virus quantitation. The basal medium of inserts was changed with Pneumacult-ALI. Cells were then placed at 37°C. At dpi 3, 4, 5, 6, 7 and 14, a similar apical wash was performed, and the medium was stored for subsequent virus quantitation.

## Virus replication quantification

From the collected apical washes, viral RNA was extracted with the QiAmp Viral RNA kit (Qiagen). One-step RT-qPCR was performed with the QuantiTect Probe RT-PCR Kit (Qiagen) with the following oligonucleotides: 5'-AGC CTG CGT GGC KGC C-3' (forward primer), 5'- GAA ACA CGG ACA CCC AAA GTA GT-3' (reverse primer), 5'-[FAM]CTC CGG CCC CTG AAT GYG GCT AA [TAM]-3' (Taqman Probe).

## Cytokine quantification with LEGENDplex™

Quantification of a custom panel of 14 cytokines (Eotaxin-2, IL-1β, PAI-1, SAA, CXCL1, PDGF-BB, BMP2, IL-8, M-CSF, IGFBP-4, Ceruloplasmin, MRP14, Cystatin C, CCL20) was done using the LEGENDplex™ multiplex immunoassay (BioLegend, Inc.), following the manufacturer's instructions. Quantifications were performed in apical and basal washes at the timepoints that are indicated in figures.

## MUC5AC and MUC5B quantification with ELISA

To quantify MUC5AC and MUC5B in apical washes, an ELISA was performed using the following antibodies: anti-MUC5AC (mouse Monoclonal clone 45M1 MA1-35706, Fischer scientific) 1/500, anti-MUC5B (mouse Monoclonal clone 5B19-2E, Fischer Scientific) 1/2000, secondary antibody: Goat Anti Mouse-HRP (c-2005, SantaCruz) 1/10 000. A 96-well flat-bottomed plate was coated with a mix of 50 µL of each sample and 50 µL Carbonate Bicarbonate Buffer 0.05 M pH 9.6 (Sigma Aldrich C3041). For MUC5AC, a 1/5 dilution was applied (10 µL Apical Wash + 40 µL PBS calcium- magnesium-). For MUC5B, a 1/2 dilution was applied (25 µL Apical Wash + 25 µL PBS calcium- magnesium-). The plate was incubated overnight at 37°C until complete evaporation. Wells were then washed 3 times with 300 µL PBS Tween 20 0.05% (wash buffer), incubated in 300 µL PBS 2% BSA, 0.05% Tween 20 (blocking buffer) for 1h at room temperature. Wells were washed 3 times with 300 µL wash buffer before being incubated with 100 µL of primary antibody in PBS 2% BSA, for 1 h at room temperature. Wells were washed 3 times with 300 µL wash buffer then incubated with 100 of secondary antibody in PBS BSA 2%, for 1h at room temperature. Wells were washed 3 times with 300 µL wash buffer then 100 µL of tetramethylbenzidine substrate (TMB) was added to each well and the plate was incubated in the dark for 10 min at room temperature while monitoring color change. The reaction was stopped by adding 100 µL of H2SO4 2N (stop solution). The plate was read at 450 nm with reference.

## Immunofluorescence microscopy

Epithelia were fixed for 15 min at room temperature in 4% paraformaldehyde and permeabilized for 5 min in 0.5% PBS Triton X100 and saturated with 3% PBS-BSA for 45 min. They were then incubated overnight at 4°C, with primary antibodies against acetylated alpha-tubulin (AcTub) and MUC5AC (**Table 5**). Secondary antibodies (**Table 6**) and ALEXA594-coupled phalloidin (1/500) and DAPI (1/500), were incubated for 2h at RT in the dark. Images were acquired with a Zeiss Axioplan2 epifluorescence microscope using a x10 objective and a Leica TCS SP5 MP confocal microscope (Leica) using a x63 oil objective (HCX PL APO 63x/1.40-0.60 Oil, 11506192). Images were processed via OMERO and analyzed with Fiji.

**Table 5:** Primary antibody references and dilutions.

Target	Clone	Supplier	Catalog number	Dilution	Host species/ Isotype
Acetylated Alpha-tubulin	6B11	Merck	T7451	1/1000	Mouse / IgG2b
MUC5AC	45M1	Abnova	MAB11324	1/250	Mouse / IgG1
EHF	Antibody kindly provided by Dr Antonio Tugores (Tugores et al., 2001).			1/250	Mouse
GATA3	D13C9	Cell Signaling	13411	1/250	Rabbit / IgG
GAPDH	1E6D9	Proteintech	60004-1	1/20000	Mouse / IgG2b

**Table 6:** Secondary antibody references and dilutions.

Antibody	Supplier	Catalog number	Dilution	Application
Anti-mouse IgG1 - Alexa Fluor 488	Invitrogen	A-21121	1/500	Immunofluorescence
Anti-mouse IgG2b - Alexa Fluor 647	Invitrogen	A-21242	1/500	Immunofluorescence
Anti-mouse -HRP	Dako	P0447	1/5000	Western blot / Dot Blot
Anti-Rabbit -HRP	Dako	P0448	1/5000	Western blot

## CRISPR Cas9 RNP

### Invalidation of target genes by CRISPR Cas9 RNP

Proliferating BCI cells were transiently transfected, with recombinant Cas9, using an electroporator and following the instructions of the Amaxa P3 primary Cell 4D-Nucleofector X Kit S (Lonza Catalog #V4XP-3032). For each targeted gene, we used a mixture of 3 SgRNAs supplied by Synthego. Briefly, 150,000 BCI basal cells per condition were resuspended in 15 µL of nucleofector P3 buffer. To this cell suspension was added 15 µL of Cas9 mix (Recombinant Cas9 2NLS nuclease, 20 µM, Synthego #Cas9 2NLS nuclease) and 3 µL of guide SgRNA per targeted gene (*FOXJ1*, *SPDEF*, *EHF* or *GATA3*; 100 µM, Knockout kit V2,

Synthego) or scrambled control (Scrb1; negative control SgRNA #1, #2, Synthego). Cells were then placed in cuvettes for transfection by electroporation/nucleofection (DC-100 -Nucleofector program, Lonza). The transfected cells were resuspended in Pneumacult Ex+ proliferation medium in one well of a 6-well plate. Three days later, a second identical round of nucleofection was performed, to maximize invalidation efficiency. After this second round, cells were directly seeded on Transwell™ inserts (Experiment #1) or expanded on flask for three passages before seeding (Experiment #2).

## Quality control

### DNA extraction

DNAs from mature epithelia were extracted by cell lysis directly on inserts with QuickExtract™ (QuickExtract™ DNA Extraction Solution, Epicentre). Extracts were heated to 68°C for 6 minutes, vortexed and heated to 97°C before being frozen at -20°C until analysis.

### Genomic PCR

Presence of deletions was analyzed by PCR amplification of a region encompassing the sequence of the SgRNAs used for each CRISPR condition (**Table 7**). Amplification was performed with Primestarc polymerase (Primestarc GXL DNA Polymerase, Takara). PCR cycles were: 10 s at 98°C, 35 cycles at 98°C for 10 s, 55°C for 15 s, 68°C for 60 s, followed by 5 min at 68°C. For each gene, the scrambled condition was used as a reference for absence of deletion. PCR amplicons were quantified by Qubit fluorometric assay (Qubit™ 1X high sensitivity (HS) and wide range (BR) dsDNA assay kits (Q33231, ThermoFisher Scientific). Finally, amplicon size was confirmed by high-sensitivity capillary electrophoresis using a Bioanalyzer (Bioanalyzer High Sensitivity DNA Analysis, 5067-4626, Agilent).

### Nanopore sequencing

To better characterize genomic DNA cuts, 150 ng of PCR product from each condition was sequenced by Nanopore using the “Native Barcoding Genomic DNA” kit (Nanopore Technologies, Ref: SQK-NBD114.24), on a Flongle cell (Nanopore Technology, Ref: FLO-FLG114). Base calling was carried out using MinKnow software on a Promethion sequencer. Read alignments were done on the Human GRCh38/hg38 reference genome using MiniMap2 software.

## Quantitative RT-PCR

ALI-differentiated epithelia were lysed in QIAzol Lysis Reagent (Qiagen), and RNA was extracted using the miRNeasy Mini kit (Qiagen, 217004). Total RNA purification was automated on the QIAcube Connect robot. RNA concentration was quantified by Qubit fluorometric assay and spectrometry with a NanoDrop. RNA integrity was checked by Bioanalyzer (RNA 6000 Nano Kit & Reagents, Agilent, 5067-1511). RNAs were retro-transcribed using the RNA-to-cDNA™ high-capacity kit (ThermoFisher

Scientific, 4387406). Retro-transcription was performed in three successive steps: 10 minutes at 25°C, followed by 1 hour at 37°C and 5 minutes at 85°C. Quantitative PCRs were performed using SYBR Green reagent (FastStart SYBR Green Master) and the primers detailed in **Table 8**, on a lightcycler 40 (Roche). Expressions were normalized using the *TBP* housekeeping gene.

**Table 7:** Primer sequences used for genomic PCR.

Target gene	Primer sequences
SPDEF	5'- CCATCCGCCAGTATTACAAG - 3' 5'- GGGTGCACGAACTGGTAGAC - 3'
FOXJ1	5'- GCTGCGGGGATGATGTTAGA - 3' 5'- CTTGTAGATGGCCGACAGGG - 3'
EHF	5'- TGACCTGTTCCAGTCCACAC - 3' 5'- GGGTTCTTGTCTGGGTTCAA - 3'
GATA3	5'- GCGGGCTCTATCACAAAATGA - 3' 5'- GCCTTCGCTTGGGCTTAAT - 3'

**Table 8:** Primer sequences used for qPCR.

Target gene	Primer sequences
SPDEF	5'- GTCTGACTTCCTCCAGCAC - 3' 5'- CTTGGAGGACTGGGTCTGTG - 3'
FOXJ1	5'- TGGATCACGGACAACCTCTG - 3' 5'- GAGGCACTTTGATGAAGCAC - 3'
MUC5AC	5'- CCAAATACGCCAACCAAGACC - 3' 5'- ATTCCATGGGTGTCAGCTTG - 3'
TBP	5'- ACGCCAGCTTCGGAGAGTTC - 3' 5'- CAAACCGCTTGGGATTATATTCG - 3'

## Western blot

Proteins were extracted by lysing differentiated epithelia in a RIPA solution containing protease and phosphatase inhibitors (1/100) and EDTA (1/100) (Pierce™ BCA Protein Assay Kits, ThermoFisher Scientific, Ref: 23225). Protein extracts were sonicated and assayed with protein assay dye reagent concentrate (BioRad, 5000006) and a luminometer at 595 nm. After migration and transfer to PVDF (polyvinylidene difluoride) membranes, amido Black staining was performed to check the homogeneity of the deposits (Staining Solution 2X, Sigma, A8181). After wash, membranes were saturated in 5% TBS-milk and incubated with primary antibodies overnight at 4°C (**Table 5**). HRP-coupled secondary antibodies were incubated for 2h at room temperature (**Table 6**). Revelation was performed with the

Fusion FX Imager using the Immobilon Western kit (Chemiluminescent HRP Substrate, Millipore, WBKLS0500).

## Dot Blot

Secreted proteins were collected by incubating the apical compartment of the inserts in 200  $\mu$ L of PBS for 20 min. Supernatants were collected and deposited on a Hybond-C-extra nitrocellulose membrane. Once saturated in 5% TBS-milk, the membrane was incubated with an anti-MUC5AC primary antibody (**Table 5**). After wash, the membrane was incubated with an HRP-coupled secondary antibody (**Table 6**). Revelation was carried out identically as for Western blotting.

## Single-cell RNA-sequencing of primary cells

### IL-13 experiment sequencing approach

To perform single-cell analysis, cells grown on Transwell™ inserts were harvested by O/N at 4°C with 0.1% protease type XIV *Streptomyces griseus* in HBSS. Then, cells were gently detached from the Transwell™ by pipetting and transferred into a microtube. Two inserts were pooled per condition. An excess of HBSS containing 2% BSA was added. Cells were centrifuged at 150 g for 5 min and resuspended in 100  $\mu$ L of supplemented HBSS containing 1% BSA.

To reduce cost and optimize experiments (increased cell throughput, reduction of sample-specific batch effects), we multiplexed samples before applying the single-cell protocol. This was made possible by cell-hashing technologies which uses oligo-tagged antibodies against ubiquitously expressed surface proteins (TotalSeq™, BioLegend) (Stoeckius et al., 2018) or Cell Multiplexing Oligo (CMO) that are tagged lipids designed to bind to cell membranes (10x Genomics CellPlex technology) to uniquely label cells from distinct samples (**Fig.94**). Later we moved to single nucleotide polymorphisms (SNP) based multiplexing, which consists in pooling samples from different donors and demultiplexing them based on their individual SNPs.

Cells were hashed either by hashtag antibody (TotalSeq™, BioLegend), CellPlex CMO (10X Genomics) or nothing (SNP). Cell concentration of each cell suspension was determined, and 500 000 cells of each were centrifuged and resuspended in 100  $\mu$ L of HBSS containing 2% BSA. Each cell suspension was then incubated with 0.5  $\mu$ g of a distinct hashtag antibody (TotalSeq™-A0251, A0252, A0253 and A0254, BioLegend) or CMO (CMO 301, 302, 303, 304, 305, 306, 307, 308, 309, 310, 311, 312, 10X Genomics) or nothing if pool based on SNP. Each cell suspension was washed thrice with HBBS + 1% BSA with 5 min of centrifugation at 300 g in between, and cell concentration was measured again. For hashtag antibody or CMO hashing, cells from different conditions of one donor (CTRL, IL13 and ILRV) were

pooled together. For SNP based hashing, cells from the same condition but of different donors were pooled together. In all cases pool were prepared to obtain a final cell suspension containing identical cell concentrations of each condition. Cell suspensions were then filtered with either a 40  $\mu\text{m}$  porosity Flowmi™ Cell Strainer (Bel-Art) or a 15  $\mu\text{m}$  ÜberStrainer (pluriSelect) and centrifuged at 150 for 5 min and resuspended in 50-100  $\mu\text{L}$  of HBSS. Cell concentration and viability were measured with a Countess™ automated cell counter (ThermoFisher Scientific), after incubation with NucGreen to detect dead cells (ThermoFisher Scientific). All steps were performed on ice. We aimed at reaching a total concentration of 1000 cells/ $\mu\text{L}$  in HBSS for the cell capture by 10X genomics Chromium, to capture 10 000 cells by a droplet-based approach.

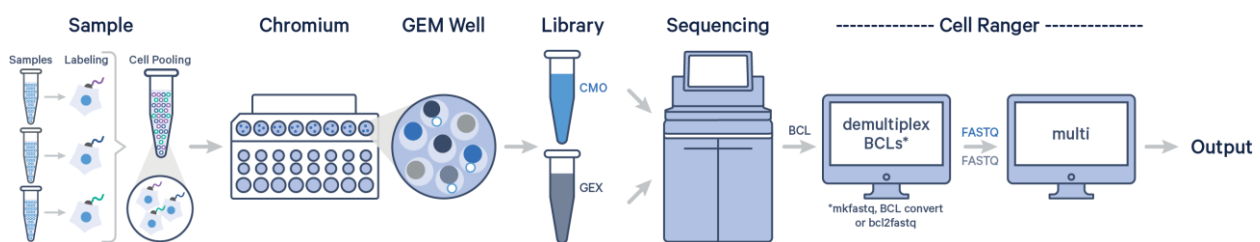


**Figure 94:** 10x Genomics multiplexing workflow. From 10x Genomics.

We followed the manufacturer's protocol (Chromium™ Single Cell 3' Reagent Kits, v3.1 Chemistry) to obtain single cell 3' libraries for Illumina sequencing. Libraries were sequenced with either a

- NextSeq 500/550 High Output v2 kit (75 cycles):
  - Read 1 (R1) had a length of 28 bases that included the cell barcode (10 bases) and the UMI (12 bases);
  - Read 2 (R2) had a length of 55 bases that contained the cDNA insert;
  - Single index read of 8 bases.
- Or a NextSeq 2000 P2 (100 cycles) or P3 Reagents (100 cycles) in paired-end mode at length of 28 bases for R1 (cell barcode [10 bases], and UMI [12 bases]) and 90 bases for R2 with 2 index reads of 10 bases.

Raw sequencing data were processed using the 10x Cell Ranger count pipeline v7.0.0 with default parameters and aligned to the GRCh38 human reference genome (Gencode Release 38).

## RVA experiment sequencing approach

As the rhinovirus infections were done by our collaborators in Marseille but our sequencing platform is in Nice, we decided to use the Evercode™ Wild Type (WT) (Parse Biosciences) sequencing technology

that allows single-cell RNA sequencing on fixed samples, therefore allowing us to process samples in Marseille and sequence them in Nice, without having to worry about transporting live cells from one site to another. Moreover, this technology uses a two-level split-pool combinatorial barcoding system to multiplex cells and allows the processing of a large number of cells in a single experiment. Cells are first labeled with one set of barcodes, and then split and re-labeled with another set, creating a unique combination for each cell.

Cells were harvested identically to the IL-13 experiment cells. Then cells were fixed and prepared according to the Evercode™ WT v2 protocol (Parse Biosciences) to obtain single cell 3' libraries for Illumina sequencing. Libraries were sequenced on a NextSeq 2000 P3 (100 cycles) or P3 Reagents (100 cycles) in paired-end mode at length of 98 \* 8 \* 8 \* 86 bases.

### Preprocessing, integration, normalization and clustering

We have generated a dataset from 54 experiments that included 122 samples (divided by donors, health status, treatment, day of sequencing, and locations), summarized in **Table 9**.

**Table 9:** Summary of samples sequenced.

Sample	Donor ID	Day	Location	Timepoint	Treatment	Condition	Status	Organ	Sampling	Multiplexing	ID_Multiplexing
D486_D08_NTUR_CTRL	D486	D08	NTUR	1	CTRL	CTRL_1	Healthy	Nose	NTUR	HTO	B1,B2
D486_D08_NTUR_IL13	D486	D08	NTUR	1	IL13	IL13_1	Healthy	Nose	NTUR	HTO	B3,B4
D486_D22_NTUR_CTRL	D486	D22	NTUR	2	CTRL	CTRL_2	Healthy	Nose	NTUR	HTO	B1,B2
D486_D22_NTUR_IL13	D486	D22	NTUR	2	IL13	IL13_2	Healthy	Nose	NTUR	HTO	B5,B6
D486_D22_NTUR_ILRV	D486	D22	NTUR	2	ILRV	ILRV_2	Healthy	Nose	NTUR	HTO	B3,B4
D487_D08_NTUR_CTRL	D487	D08	NTUR	1	CTRL	CTRL_1	Asthma	Nose	NTUR	HTO	B3,B4
D487_D08_NTUR_IL13	D487	D08	NTUR	1	IL13	IL13_1	Asthma	Nose	NTUR	HTO	B5,B6
D487_D22_NTUR_CTRL	D487	D22	NTUR	2	CTRL	CTRL_2	Asthma	Nose	NTUR	HTO	B1,B2
D487_D22_NTUR_IL13	D487	D22	NTUR	2	IL13	IL13_2	Asthma	Nose	NTUR	HTO	B5,B6
D487_D22_NTUR_ILRV	D487	D22	NTUR	2	ILRV	ILRV_2	Asthma	Nose	NTUR	HTO	B3,B4
D497_D08_B10D_CTRL	D497	D08	B10D/B10R	1	CTRL	CTRL_1	Healthy	Bronchi	BBIO	HTO	B1,B2
D497_D08_B10D_HDMM	D497	D08	B10D/B10R	1	HDMM	HDMM_1	Healthy	Bronchi	BBIO	HTO	B3,B4
D497_D08_B10D_IL13	D497	D08	B10D/B10R	1	IL13	IL13_1	Healthy	Bronchi	BBIO	HTO	B5,B6
D497_D22_B10D_CTRL	D497	D22	B10D/B10R	2	CTRL	CTRL_2	Healthy	Bronchi	BBIO	HTO	B1,B2
D497_D22_B10D_HDMM	D497	D22	B10D/B10R	2	HDMM	HDMM_2	Healthy	Bronchi	BBIO	HTO	B3,B4
D497_D22_B10D_HDRV	D497	D22	B10D/B10R	2	HDRV	HDRV_2	Healthy	Bronchi	BBIO	HTO	B5,B6
D497_D22_B10D_IL13	D497	D22	B10D/B10R	2	IL13	IL13_2	Healthy	Bronchi	BBIO	HTO	B7,B8
D497_D22_B10D_ILRV	D497	D22	B10D/B10R	2	ILRV	ILRV_2	Healthy	Bronchi	BBIO	HTO	B9,B10
D501_D08_B09R_CTRL	D501	D08	B09R	1	CTRL	CTRL_1	Healthy	Bronchi	BBIO	HTO	B1,B2
D501_D08_B09R_HDMM	D501	D08	B09R	1	HDMM	HDMM_1	Healthy	Bronchi	BBIO	HTO	B3,B4
D501_D08_B09R_IL13	D501	D08	B09R	1	IL13	IL13_1	Healthy	Bronchi	BBIO	HTO	B5,B6
D501_D23_B09R_CTRL	D501	D23	B09R	2	CTRL	CTRL_2	Healthy	Bronchi	BBIO	HTO	B1,B2
D501_D23_B09R_HDMM	D501	D23	B09R	2	HDMM	HDMM_2	Healthy	Bronchi	BBIO	HTO	B3,B4
D501_D23_B09R_HDRV	D501	D23	B09R	2	HDRV	HDRV_2	Healthy	Bronchi	BBIO	HTO	B5,B6
D501_D23_B09R_IL13	D501	D23	B09R	2	IL13	IL13_2	Healthy	Bronchi	BBIO	HTO	B7,B8
D501_D23_B09R_ILRV	D501	D23	B09R	2	ILRV	ILRV_2	Healthy	Bronchi	BBIO	HTO	B9,B10
D534_D08_B08D_CTRL	D534	D08	B08D/B08R	1	CTRL	CTRL_1	Healthy	Bronchi	BBIO	CMO	CMO307
D534_D08_B08D_IL13	D534	D08	B08D/B08R	1	IL13	IL13_1	Healthy	Bronchi	BBIO	CMO	CMO308
D534_D23_B08D_CTRL	D534	D23	B08D/B08R	2	CTRL	CTRL_2	Healthy	Bronchi	BBIO	CMO	CMO309
D534_D23_B08D_IL13	D534	D23	B08D/B08R	2	HDMM	HDMM_2	Healthy	Bronchi	BBIO	CMO	CMO310
D534_D23_B08D_ILRV	D534	D23	B08D/B08R	2	IL13	IL13_2	Healthy	Bronchi	BBIO	CMO	CMO311
D534_D23_B08D_HDMM	D534	D23	B08D/B08R	2	ILRV	ILRV_2	Healthy	Bronchi	BBIO	CMO	CMO312
D535_D09_BBIO_CTRL	D535	D09	BBIO	1	CTRL	CTRL_1	Asthma	Bronchi	BBIO	CMO	CMO309
D535_D09_BBIO_IL13	D535	D09	BBIO	1	IL13	IL13_1	Asthma	Bronchi	BBIO	CMO	CMO310
D528_D03_B02R_CTRL	D528	D03	B02R	1	CTRL	CTRL_1	Healthy	Bronchi	BBIO	NO	
D528_D03_B02R_HDMM	D528	D03	B02R	1	HDMM	HDMM_1	Healthy	Bronchi	BBIO	NO	
D554_D08_BBRU_CTRL	D554	D08	BBRU	1	CTRL	CTRL_1	Healthy	Bronchi	BBRU	CMO	CMO301
D554_D08_BBRU_IL13	D554	D08	BBRU	1	IL13	IL13_1	Healthy	Bronchi	BBRU	CMO	CMO302
D554_D08_NBRU_CTRL	D554	D08	NBRU	1	CTRL	CTRL_1	Healthy	Nose	NBRU	CMO	CMO309
D554_D08_NBRU_IL13	D554	D08	NBRU	1	IL13	IL13_1	Healthy	Nose	NBRU	CMO	CMO310
D554_D23_B03R_CTRL	D554	D23	B03R	2	CTRL	CTRL_2	Healthy	Bronchi	BBIO	CMO	CMO301
D554_D23_B03R_IL13	D554	D23	B03R	2	IL13	IL13_2	Healthy	Bronchi	BBIO	CMO	CMO302
D554_D23_B03R_ILRV	D554	D23	B03R	2	ILRV	ILRV_2	Healthy	Bronchi	BBIO	CMO	CMO303
D554_D23_B03R_HDMM	D554	D23	B03R	2	HDMM	HDMM_2	Healthy	Bronchi	BBIO	CMO	CMO304
D554_D23_NBRU_CTRL	D554	D23	NBRU	2	CTRL	CTRL_2	Healthy	Nose	NBRU	CMO	CMO310
D554_D23_NBRU_IL13	D554	D23	NBRU	2	IL13	IL13_2	Healthy	Nose	NBRU	CMO	CMO311
D554_D23_NBRU_ILRV	D554	D23	NBRU	2	ILRV	ILRV_2	Healthy	Nose	NBRU	CMO	CMO312
D554_D24_B05R_CTRL	D554	D24	B05R	2	CTRL	CTRL_2	Healthy	Bronchi	BBIO	CMO	CMO305
D554_D24_B05R_IL13	D554	D24	B05R	2	IL13	IL13_2	Healthy	Bronchi	BBIO	CMO	CMO306
D554_D24_B05R_ILRV	D554	D24	B05R	2	ILRV	ILRV_2	Healthy	Bronchi	BBIO	CMO	CMO307
D554_D24_B05R_HDMM	D554	D24	B05R	2	HDMM	HDMM_2	Healthy	Bronchi	BBIO	CMO	CMO308
D554_D24_BBRU_CTRL	D554	D24	BBRU	2	CTRL	CTRL_2	Healthy	Bronchi	BBRU	CMO	CMO311
D554_D24_BBRU_IL13	D554	D24	BBRU	2	IL13	IL13_2	Healthy	Bronchi	BBRU	CMO	CMO312
D554_D24_BBRU_ILRV	D554	D24	BBRU	2	ILRV	ILRV_2	Healthy	Bronchi	BBRU	CMO	CMO303
D555_D08_B02R_CTRL	D555	D08	B02R	1	CTRL	CTRL_1	Healthy	Bronchi	BBIO	CMO	CMO307
D555_D08_B02R_IL13	D555	D08	B02R	1	IL13	IL13_1	Healthy	Bronchi	BBIO	CMO	CMO308
D555_D08_B09L_CTRL	D555	D08	B09L	1	CTRL	CTRL_1	Healthy	Bronchi	BBIO	CMO	CMO305
D555_D08_B09L_IL13	D555	D08	B09L	1	IL13	IL13_1	Healthy	Bronchi	BBIO	CMO	CMO306
D555_D08_BBRU_CTRL	D555	D08	BBRU	1	CTRL	CTRL_1	Healthy	Bronchi	BBRU	CMO	CMO303
D555_D08_BBRU_IL13	D555	D08	BBRU	1	IL13	IL13_1	Healthy	Bronchi	BBRU	CMO	CMO304



D555_D08_NBIO_CTRL	D555	D08	NBIO	1	CTRL	CTRL_1	Healthy	Nose	NBIO	CMO	CMO307
D555_D08_NBIO_IL13	D555	D08	NBIO	1	IL13	IL13_1	Healthy	Nose	NBIO	CMO	CMO308
D555_D08_NBRU_CTRL	D555	D08	NBRU	1	CTRL	CTRL_1	Healthy	Nose	NBRU	CMO	CMO309
D555_D08_NBRU_IL13	D555	D08	NBRU	1	IL13	IL13_1	Healthy	Nose	NBRU	CMO	CMO310
D555_D23_B09L_CTRL	D555	D23	B09L	2	CTRL	CTRL_2	Healthy	Bronchi	BBIO	CMO	CMO301
D555_D23_B09L_IL13	D555	D23	B09L	2	IL13	IL13_2	Healthy	Bronchi	BBIO	CMO	CMO302
D555_D23_B09L_ILRV	D555	D23	B09L	2	ILRV	ILRV_2	Healthy	Bronchi	BBIO	CMO	CMO303
D555_D23_B09L_HDMM	D555	D23	B09L	2	HDMM	HDMM_2	Healthy	Bronchi	BBIO	CMO	CMO304
D555_D23_NBIO_CTRL	D555	D23	NBIO	2	CTRL	CTRL_2	Healthy	Nose	NBIO	CMO	CMO310
D555_D23_NBIO_IL13	D555	D23	NBIO	2	IL13	IL13_2	Healthy	Nose	NBIO	CMO	CMO311
D555_D23_NBIO_ILRV	D555	D23	NBIO	2	ILRV	ILRV_2	Healthy	Nose	NBIO	CMO	CMO312
D555_D23_NBRU_CTRL	D555	D23	NBRU	2	CTRL	CTRL_2	Healthy	Nose	NBRU	CMO	CMO301
D555_D23_NBRU_IL13	D555	D23	NBRU	2	IL13	IL13_2	Healthy	Nose	NBRU	CMO	CMO302
D555_D23_NBRU_ILRV	D555	D23	NBRU	2	ILRV	ILRV_2	Healthy	Nose	NBRU	CMO	CMO309
D555_D24_BBRU_CTRL	D555	D24	BBRU	2	CTRL	CTRL_2	Healthy	Bronchi	BBRU	CMO	CMO304
D555_D24_BBRU_IL13	D555	D24	BBRU	2	IL13	IL13_2	Healthy	Bronchi	BBRU	CMO	CMO305
D555_D24_BBRU_ILRV	D555	D24	BBRU	2	ILRV	ILRV_2	Healthy	Bronchi	BBRU	CMO	CMO306
D569_D08_BBIO_CTRL	D569	D08	BBIO	1	CTRL	CTRL_1	Asthma	Bronchi	BBIO	NO	
D569_D08_BBIO_IL13	D569	D08	BBIO	1	IL13	IL13_1	Asthma	Bronchi	BBIO	NO	
D569_D23_BBIO_CTRL	D569	D23	BBIO	2	CTRL	CTRL_2	Asthma	Bronchi	BBIO	NO	
D569_D23_BBIO_IL13	D569	D23	BBIO	2	IL13	IL13_2	Asthma	Bronchi	BBIO	NO	
D569_D23_BBIO_ILRV	D569	D23	BBIO	2	ILRV	ILRV_2	Asthma	Bronchi	BBIO	NO	
D551_D09_BBIO_CTRL	D551	D09	BBIO	1	CTRL	CTRL_1	Asthma	Bronchi	BBIO	NO	
D568_D09_BBIO_CTRL	D568	D09	BBIO	1	CTRL	CTRL_1	Asthma	Bronchi	BBIO	NO	
D551_D08_BBIO_IL13	D551	D08	BBIO	1	IL13	IL13_1	Asthma	Bronchi	BBIO	SNP	
D568_D08_BBIO_IL13	D568	D08	BBIO	1	IL13	IL13_1	Asthma	Bronchi	BBIO	SNP	
D551_D23_BBIO_CTRL	D551	D23	BBIO	1	CTRL	CTRL_1	Asthma	Bronchi	BBIO	SNP	
D568_D23_BBIO_CTRL	D568	D23	BBIO	1	CTRL	CTRL_1	Asthma	Bronchi	BBIO	SNP	
D551_D23_BBIO_IL13	D551	D23	BBIO	1	IL13	IL13_1	Asthma	Bronchi	BBIO	SNP	
D568_D23_BBIO_IL13	D568	D23	BBIO	1	IL13	IL13_1	Asthma	Bronchi	BBIO	SNP	
D551_D23_BBIO_ILRV	D551	D23	BBIO	1	ILRV	ILRV_1	Asthma	Bronchi	BBIO	SNP	
D568_D23_BBIO_ILRV	D568	D23	BBIO	1	ILRV	ILRV_1	Asthma	Bronchi	BBIO	SNP	
D552_D08_BBIO_CTRL	D552	D08	BBIO	1	CTRL	CTRL_1	Asthma	Bronchi	BBIO	SNP	
D576_D08_BBIO_CTRL	D576	D08	BBIO	1	CTRL	CTRL_1	Asthma	Bronchi	BBIO	SNP	
D552_D08_BBIO_IL13	D552	D08	BBIO	1	IL13	IL13_1	Asthma	Bronchi	BBIO	SNP	
D576_D08_BBIO_IL13	D576	D08	BBIO	1	IL13	IL13_1	Asthma	Bronchi	BBIO	SNP	
D552_D22_BBIO_CTRL	D552	D22	BBIO	1	CTRL	CTRL_1	Asthma	Bronchi	BBIO	SNP	
D576_D22_BBIO_CTRL	D576	D22	BBIO	1	CTRL	CTRL_1	Asthma	Bronchi	BBIO	SNP	
D552_D22_BBIO_IL13	D552	D22	BBIO	1	IL13	IL13_1	Asthma	Bronchi	BBIO	SNP	
D576_D22_BBIO_IL13	D576	D22	BBIO	1	IL13	IL13_1	Asthma	Bronchi	BBIO	SNP	
D552_D22_BBIO_ILRV	D552	D22	BBIO	1	ILRV	ILRV_1	Asthma	Bronchi	BBIO	SNP	
D576_D22_BBIO_ILRV	D576	D22	BBIO	1	ILRV	ILRV_1	Asthma	Bronchi	BBIO	SNP	
D577_D08_NBRU_CTRL	D577	D08	NBRU	1	CTRL	CTRL_1	Asthma	Nose	NBRU	SNP	
D578_D08_NBRU_CTRL	D578	D08	NBRU	1	CTRL	CTRL_1	Asthma	Nose	NBRU	SNP	
D577_D08_NBRU_IL13	D577	D08	NBRU	1	IL13	IL13_1	Asthma	Nose	NBRU	SNP	
D578_D08_NBRU_IL13	D578	D08	NBRU	1	IL13	IL13_1	Asthma	Nose	NBRU	SNP	
D577_D23_NBRU_CTRL	D577	D23	NBRU	2	CTRL	CTRL_2	Asthma	Nose	NBRU	SNP	
D578_D23_NBRU_CTRL	D578	D23	NBRU	2	CTRL	CTRL_2	Asthma	Nose	NBRU	SNP	
D577_D23_NBRU_IL13	D577	D23	NBRU	2	IL13	IL13_2	Asthma	Nose	NBRU	SNP	
D578_D23_NBRU_IL13	D578	D23	NBRU	2	IL13	IL13_2	Asthma	Nose	NBRU	SNP	
D577_D23_NBRU_ILRV	D577	D23	NBRU	2	ILRV	ILRV_2	Asthma	Nose	NBRU	SNP	
D578_D23_NBRU_ILRV	D578	D23	NBRU	2	ILRV	ILRV_2	Asthma	Nose	NBRU	SNP	
D577_D08_BBRU_CTRL	D577	D08	BBRU	1	CTRL	CTRL_1	Asthma	Bronchi	BBRU	SNP	
D578_D08_BBIO_CTRL	D578	D08	BBIO	1	CTRL	CTRL_1	Asthma	Bronchi	BBIO	SNP	
D577_D08_BBRU_IL13	D577	D08	BBRU	1	IL13	IL13_1	Asthma	Bronchi	BBRU	SNP	
D578_D08_BBIO_IL13	D578	D08	BBIO	1	IL13	IL13_1	Asthma	Bronchi	BBIO	SNP	
D577_D23_BBRU_CTRL	D577	D23	BBRU	2	CTRL	CTRL_2	Asthma	Bronchi	BBRU	SNP	
D578_D23_BBIO_CTRL	D578	D23	BBIO	2	CTRL	CTRL_2	Asthma	Bronchi	BBIO	SNP	
D577_D23_BBRU_IL13	D577	D23	BBRU	2	IL13	IL13_2	Asthma	Bronchi	BBRU	SNP	
D578_D23_BBIO_IL13	D578	D23	BBIO	2	IL13	IL13_2	Asthma	Bronchi	BBIO	SNP	
D577_D23_BBRU_ILRV	D577	D23	BBRU	2	ILRV	ILRV_2	Asthma	Bronchi	BBRU	SNP	
D578_D23_BBIO_ILRV	D578	D23	BBIO	2	ILRV	ILRV_2	Asthma	Bronchi	BBIO	SNP	

# Sequencing, alignment, demultiplexing and count table generation

## Library preparation and sample multiplexing of IL-13 experiments

Fastq files are obtained as output of the sequencer. These raw sequencing data were processed using the 10x Cell Ranger count pipeline (v6) and multi pipeline (v6) according to the following explanation on multiplexing data. This pipeline was used with default parameters and aligned to the Genome Reference Consortium Human Build 38 (GRCh38) (Gencode Release 38).

### Sample multiplexing

Samples were multiplexed, enabling several samples to be multiplexed together and run in a single experiment. The main approach that was used was feature barcoding technology which uses either: (i) hashtag oligos (HTOs) which are antibodies against ubiquitously expressed surface proteins and that are covalently linked to a sample barcode sequence (feature barcode) (BioLegend TotalSeq™-B Antibodies) or (ii) Cell Multiplexing Oligos (CMOs) which contain a proprietary lipid that inserts in the membrane of all cells and that are conjugated to feature barcodes (10x genomics 3' CellPlex).

Another approach that we used for some sample was the pooling of cells from 2 distinct donors without any HTO or CMO labeling. Assignment of cells to each donor was performed using the Single Nucleotide Polymorphisms (SNP) that are specific to each donor.

Library preparation was always performed according to the manufacturer's instructions. For both approaches, 2 libraries were built: one for the gene expression (GEX), which is similar to libraries for non-multiplexed samples and another library for the cell multiplexing (PLEX). This PLEX library contains read 1 (R1) which is similar to that of the GEX library, to get a correspondence between both libraries; and read 2 (R2) on which the first 15 bases correspond to the feature barcode, thus identifying the sample of origin of each cell.

#### 1. Analysis using feature barcoding with Hashtag Oligos (HTOs):

We used the 10x Cell Ranger count pipeline (v6) with the following parameters:

- id: name of the sample
- libraries: csv (Comma Separated Values) which indicate the path where both libraries fastq are located (Gene Expression and Antibody Capture)
- feature-ref: csv which indicates the association sample-barcode (**Table 10**)

The output is a count matrix of the tags found for each HTO barcode in each cell.

**Table 10:** TotalSeqTM-B barcodes.

Id	Name	Read	Pattern	Sequence	Feature type
B1	B1	R2	5PNNNNNNNNNN(BC)	GTCAACTCTTTAGCG	Antibody
B2	B2	R2	5PNNNNNNNNNN(BC)	TGATGGCCTATTGGG	Antibody
B3	B3	R2	5PNNNNNNNNNN(BC)	TTCCGCCTCTCTTG	Antibody
B4	B4	R2	5PNNNNNNNNNN(BC)	AGTAAGTTCAGCGTA	Antibody
B5	B5	R2	5PNNNNNNNNNN(BC)	AAGTATCGTTTCGCA	Antibody
B6	B6	R2	5PNNNNNNNNNN(BC)	GGTTGCCAGATGTCA	Antibody
B7	B7	R2	5PNNNNNNNNNN(BC)	TGTCTTCTCTGCCAG	Antibody
B8	B8	R2	5PNNNNNNNNNN(BC)	CTCCTCTGCAATTAC	Antibody
B9	B9	R2	5PNNNNNNNNNN(BC)	CAGTAGTCACGGTCA	Antibody
B10	B10	R2	5PNNNNNNNNNN(BC)	ATTGACCCGCGTTAG	Antibody

## 2. Analysis using feature barcoding with Cell Multiplexing Oligos (CMOs):

We used the 10x Cell Ranger multi pipeline (v6) with the following parameters:

- id: name of the sample
- csv: the multi config file containing the path to both libraries fastq files, the reference genome and the association sample-CMO ids (specific to 10x genomics) (**Table11**)

The output is a count matrix of the tags found for each CMO barcode in each cell.

**Table 11:** 10x genomics CellPlex CMO barcodes.

Id	Name	Read	Pattern	Sequence	Feature type
CMO301	CMO301	R2	5P(BC)	ATGAGGAATTCCTGC	Multiplexing
CMO302	CMO302	R2	5P(BC)	CATGCCAATAGAGCG	Multiplexing
CMO303	CMO303	R2	5P(BC)	CCGTCGTCGAAGCAT	Multiplexing
CMO304	CMO304	R2	5P(BC)	AACGTTAATCACTCA	Multiplexing
CMO305	CMO305	R2	5P(BC)	CGCGATATGGTCGGA	Multiplexing
CMO306	CMO306	R2	5P(BC)	AAGATGAGGTCTGTG	Multiplexing
CMO307	CMO307	R2	5P(BC)	AAGCTCGTTGAAGA	Multiplexing
CMO308	CMO308	R2	5P(BC)	CGGATTCCACATCAT	Multiplexing

CMO309	CMO309	R2	5P(BC)	GTTGATCTATAACAG	Multiplexing
CMO310	CMO310	R2	5P(BC)	GCAGGAGGTATCAAT	Multiplexing
CMO311	CMO311	R2	5P(BC)	GAATCGTGATTCTTC	Multiplexing
CMO312	CMO312	R2	5P(BC)	ACATGGTCAACGCTG	Multiplexing

### 3. Analysis using SNP demultiplexing:

We used the 10x Cell Ranger count pipeline (v6). Secondly, for donor demultiplexing, we used demuxafy pipeline (Neavin et al., 2024). This pipeline uses several tools to find a consensus on the cell donor based on SNP genotype and doublet detection. We chose to combine Vireo (Huang et al., 2019), Souporcell (Heaton et al., 2020) and Scds (Bais & Kostka, 2020) with the MajoritySinglet mode, following the software selection tool. Finally, after cell assignment to each donor, some cells remain annotated as “unknown” by demuxafy, meaning that no donor could be assigned based on the detected SNPs.

### **Library preparation and sample multiplexing for the rhinovirus experiments**

For the rhinovirus experiments, we used the combinatorial Split-seq (Rosenberg et al., 2018) approach (Parse Biosciences technology). This technology allows to combine 48 samples in the same experiment without any cell labeling. We followed the manufacturer’s protocol for “Evercode™ WT v2 Kits” (Parse Biosciences) to obtain single cell 3’ libraries for Illumina sequencing. The libraries were sequenced with NextSeq 2000 P3 Reagents (200 cycles) in paired-end mode at the length of 98 bases for R1 (10 bases barcode and 12 bases UMI) and 86 bases for R2 with dual index reads of 8 bases. Fastq files are obtained as the output of the sequencer. These raw sequencing data were processed using the Parse Biosciences pipeline “split-pipe” (v1.0.3). This pipeline was used with default parameters and aligned to the GRCh38 (Ensembl Release 108). We added the Rhinovirus A 16 sequence in the annotation file to count the number of reads that map the virus in each cell.

## Quality control and cell filtering

Each individual dataset was preprocessed using Seurat standard analysis pipeline v4.3.1 (Hao et al., 2021).

### 1. Filtering

For each experiment, cells were filtered out based on:

- nFeature\_RNA: number of expressed genes (features) in each cell

- dropouts: percentage of genes with 0 counts in a cell, ie. inverse of the nFeature\_RNA
- nCount\_RNA: number of reads/transcripts in each cell, ie. library size
- percent.mito: percentage of mitochondrial genes in a cell

Thresholds were selected by visually inspecting violin plots to remove the most extreme outliers (for sample details and filtering see **Table 12**).

## 2. Cell assignments to each sample

### Cell hashing (HTO + CMO)

Demultiplexing separate cells according to the feature barcodes that were used for each sample. After cell quality control and filtering, each cell then gets assigned to each sample of origin. We used the function “demuxmix\_calls\_all” (default parameters) from demuxmix R package (Klein, 2023) to assign antibody tags for each cell based on the antibody count matrices. Cellranger multi performs the demultiplexing step and returns a csv file ‘assignment\_confidence\_table.csv’. However, for some experiments, very low CMO barcode assignments were found. So, to overcome this problem, we used demuxmix to rescue some unassigned cells.

### SNP demultiplexing

The Demuxafy tool returns a ‘combined\_results\_w\_combined\_assignments.tsv’ file containing the assignment of each cell to a “generic” donor, or alternatively to a doublet, or left unassigned. The next step is to make the correspondence between the “generic” donors and the actual donors. To improve donor assignment, we have multiplexed 1 woman and 1 man together, so that we can identify donors based on the expression of the sexual chromosomal genes.

We have used the following sex specific genes:

- X chromosome : XIST
- Y chromosome : RPS4Y1, ZFY, ZFY-AS1, LINC00278, PCDH11Y, USP9Y, DDX3Y, UTY, TMSB4Y, TTTY14, KDM5D, EIF1AY, RPS4Y2

For the Y chromosome, we calculated the number of reads aligning to this chromosome by summing all counts assigned to the above genes. We created a function to rescue some cells that were not assigned to a donor based on SNP demultiplexing. A cell was assigned as a "XIST cell" if it expressed XIST but did not express Y chromosome genes. Conversely, we assigned a cell as a "chrY cell" if it expressed Y chromosome genes but did not express XIST. Next, we could assign cells annotated "cell XIST" to the female donor and those annotated "cell chrY" to the male donor.

### 3. Cell cycle score

We also use the CellCycleScoring function from Seurat to assign each cell to a phase of the cell cycle between “G1”, “S” and “G2M”.

### 4. Doublet detection

Single-cell separation does not guarantee that 2 or more cells cannot be labeled with the same cell barcode. These doublets can be due to imperfect cell dissociation or can be generated during separation in the droplets (10x), or by the combinatorial barcoding (Parse Biosciences).

We used 2 distinct functions to detect doublets:

- scDbfFinder (default parameters) from scDbfFinder R package (Germain et al., 2022)
- cxds\_bcdrs\_hybrid (default parameters) from scds R package which combines both annotations into a hybrid annotation (Bais & Kostka, 2020) [8]. We considered as a doublet a cell with a score > 1.

To increase robustness, we labeled cells as doublets if at least one of the methods above labeled a cell as a doublet. As our dataset may contain transitional cell types that express genes from 2 distinct canonical cell types, we chose to use this stringent method in order to preclude the labeling of doublets as transitional cells.

## Integration / Annotation

After the preprocessing step, the data from the experiments were merged in a single dataset through an integration step that corrects batch effects. We performed integration with the package “scVI” integration on raw counts from all the individual datasets (latent space of 50 dimensions) (v0.14.6) (Gayoso et al., 2022). Then, we used the package “scanpy” from Python to construct the nearest neighbor graph on the space latent from scVI, and visualize it in two dimensions with the Uniform Manifold Approximation and Projection (UMAP) (Wolf et al., 2018). To obtain the UMAP, we used “min\_dist=0.1” and “spread=0.5” as parameters. We chose these parameters to optimize inter-cluster and intra-cluster distances. Clustering was performed by using the Leiden function from scanpy package. We performed the clustering using several resolution levels, which were generally 0.4, 0.8, or 1.2. Then, we manually annotated each cluster based on known marker genes and we re-run scVI on each cluster for better resolution at the subcluster level. We also used Seurat FindAllMarkers function based on non-parametric Wilcoxon rank sum test, to find gene markers for each cluster previously established. Finally, after having carefully examined and validated the annotation, we ran scANVI to improve the accuracy of the final integration, and better suited latent space for downstream tasks like

visualization (Xu et al., 2021). We normalized and log-transformed our data using the `normalize_total` (`target_sum = 10000`) and the `log1p` functions from the `scanpy` package. Finally, we have reached 4 annotation levels. After the filtering and integration steps, our dataset comprised 208,156 cells for the IL-13 experiment, and 61,913 cells for the rhinovirus experiment.

**Table 12:** scRNA-seq sample metrics and cut offs used.

Sample	Mean Reads Per Cell	Median Genes Per Cell	percent.mito<	dropouts<	nFeature_RNA>	nCount_RNA<	Nb cells after filtering
D486_D08_NTUR_CTRL	24458	2726	30	0.99		25000	1736
D486_D08_NTUR_IL13	24458	2726	30	0.99		25000	1933
D486_D22_NTUR_CTRL	13443	1965	30	0.99		15000	2515
D486_D22_NTUR_IL13	13443	1965	30	0.99		15000	2465
D486_D22_NTUR_ILRV	13443	1965	30	0.99		15000	2277
D487_D08_NTUR_CTRL	47586	3512	30	0.98		40000	2530
D487_D08_NTUR_IL13	47586	3512	30	0.98		40000	1648
D487_D22_NTUR_CTRL	30794	2985	30	0.98		30000	2523
D487_D22_NTUR_IL13	30794	2985	30	0.98		30000	1952
D487_D22_NTUR_ILRV	30794	2985	30	0.98		30000	2717
D497_D08_B10D_CTRL	30794	3060	30	0.98		40000	1165
D497_D08_B10D_HDMM	30794	3060	30	0.98		40000	1082
D497_D08_B10D_IL13	30794	3060	30	0.98		40000	954
D497_D22_B10D_CTRL	27874	454	30	0.96		60000	565
D497_D22_B10D_HDMM	27874	454	30	0.96		60000	626
D497_D22_B10D_HDRV	27874	454	30	0.96		60000	580
D497_D22_B10D_IL13	27874	454	30	0.96		60000	453
D497_D22_B10D_ILRV	27874	454	30	0.96		60000	676
D501_D08_B09R_CTRL	45604	1228	30	0.96		60000	502
D501_D08_B09R_HDMM	45604	1228	30	0.96		60000	799
D501_D08_B09R_IL13	45604	1228	30	0.96		60000	411
D501_D23_B09R_CTRL	31831	656	30	0.96		75000	82
D501_D23_B09R_HDMM	31831	656	30	0.96		75000	105
D501_D23_B09R_HDRV	31831	656	30	0.96		75000	107
D501_D23_B09R_IL13	31831	656	30	0.96		75000	68
D501_D23_B09R_ILRV	31831	656	30	0.96		75000	94
D534_D08_B08D_CTRL	21190	2537	30	0.98		20000	1951
D534_D08_B08D_IL13	21190	2537	30	0.98		20000	1849
D534_D23_B08D_CTRL	17377	2350	30	0.98		20000	1163
D534_D23_B08D_IL13	17377	2350	30	0.98		20000	917
D534_D23_B08D_ILRV	17377	2350	30	0.98		20000	1144
D534_D23_B08D_HDMM	17377	2350	30	0.98		20000	1382
D535_D09_BBIO_CTRL	38570	2030	30		3000	70000	1158
D535_D09_BBIO_IL13	38570	2030	30		3000	70000	1673
D528_D03_B02R_CTRL	21613	3373	30		1000	40000	3750
D528_D03_B02R_HDMM	19819	2972	30		800	30000	2901
D554_D08_BBRU_CTRL	15290	2055	30	0.98		20000	1932
D554_D08_BBRU_IL13	15290	2055	30	0.98		20000	1772
D554_D08_NBRU_CTRL	28383	2740	30	0.97		30000	2540
D554_D08_NBRU_IL13	28383	2740	30	0.97		30000	2127
D554_D23_B03R_CTRL	28923	2055	30	0.98		30000	1444
D554_D23_B03R_IL13	28923	2055	30	0.98		30000	558
D554_D23_B03R_ILRV	28923	2055	30	0.98		30000	665
D554_D23_B03R_HDMM	28923	2055	30	0.98		30000	1087
D554_D23_NBRU_CTRL	26394	2624	30	0.98		30000	1793
D554_D23_NBRU_IL13	26394	2624	30	0.98		30000	977
D554_D23_NBRU_ILRV	26394	2624	30	0.98		30000	1602
D554_D24_B05R_CTRL	20929	2770	30	0.98		30000	1148
D554_D24_B05R_IL13	20929	2770	30	0.98		30000	1288
D554_D24_B05R_ILRV	20929	2770	30	0.98		30000	894
D554_D24_B05R_HDMM	20929	2770	30	0.98		30000	1257
D554_D24_BBRU_CTRL	26474	2713	30	0.97		40000	776
D554_D24_BBRU_IL13	26474	2713	30	0.97		40000	701
D554_D24_BBRU_ILRV	26474	2713	30	0.97		40000	1160
D555_D08_B02R_CTRL	21689	1755	30	0.99		15000	2382
D555_D08_B02R_IL13	21689	1755	30	0.99		15000	1604
D555_D08_B09L_CTRL	21235	1945	30	0.99		20000	2195
D555_D08_B09L_IL13	21235	1945	30	0.99		20000	2353
D555_D08_BBRU_CTRL	20145	2413	30	0.97		25000	1884
D555_D08_BBRU_IL13	20145	2413	30	0.97		25000	2327



D555_D08_NBIO_CTRL	21255	2102	30	0.97		40000	1938
D555_D08_NBIO_IL13	21255	2102	30	0.97		40000	1136
D555_D08_NBRU_CTRL	20206	2496	30	0.97		40000	2386
D555_D08_NBRU_IL13	20206	2496	30	0.97		40000	1130
D555_D23_B09L_CTRL	25414	3120	30	0.98		40000	1031
D555_D23_B09L_IL13	25414	3120	30	0.98		40000	811
D555_D23_B09L_ILRV	25414	3120	30	0.98		40000	842
D555_D23_B09L_HDMM	25414	3120	30	0.98		40000	1242
D555_D23_NBIO_CTRL	21838	1793	30	0.98		30000	877
D555_D23_NBIO_IL13	21838	1793	30	0.98		30000	393
D555_D23_NBIO_ILRV	21838	1793	30	0.98		30000	803
D555_D23_NBRU_CTRL	21679	2834	30	0.99		30000	1329
D555_D23_NBRU_IL13	21679	2834	30	0.99		30000	1003
D555_D23_NBRU_ILRV	21679	2834	30	0.99		30000	1327
D555_D24_BBRU_CTRL	21237	2117	30	0.98		30000	1210
D555_D24_BBRU_IL13	21237	2117	30	0.98		30000	712
D555_D24_BBRU_ILRV	21237	2117	30	0.98		30000	724
D569_D08_BBIO_CTRL	35349	3701	30	0.97		50000	4006
D569_D08_BBIO_IL13	52417	3996	30	0.97		50000	3247
D569_D23_BBIO_CTRL	34156	864	30	0.97		40000	1451
D569_D23_BBIO_IL13	42143	905	30	0.96		50000	1753
D569_D23_BBIO_ILRV	32127	950	30	0.97		40000	2370
D551_D09_BBIO_CTRL	34081	1804	30	0.97		40000	2233
D568_D09_BBIO_CTRL	18966	2309	30	0.98		30000	4186
D551_D08_BBIO_IL13	46284	1391	30	0.95		60000	1305
D568_D08_BBIO_IL13	46284	1391	30	0.95		60000	1395
D551_D23_BBIO_CTRL	62904	1424	30	0.95		40000	786
D568_D23_BBIO_CTRL	62904	1424	30	0.95		40000	1262
D551_D23_BBIO_IL13	55165	1438	30	0.95		60000	1462
D568_D23_BBIO_IL13	55165	1438	30	0.95		60000	940
D551_D23_BBIO_ILRV	30990	3198	30	0.96		40000	1957
D568_D23_BBIO_ILRV	30990	3198	30	0.96		40000	3510
D552_D08_BBIO_CTRL	32184	2507	30	0.97		40000	2102
D576_D08_BBIO_CTRL	32184	2507	30	0.97		40000	2282
D552_D08_BBIO_IL13	44095	3540	30	0.97		50000	949
D576_D08_BBIO_IL13	44095	3540	30	0.97		50000	2267
D552_D22_BBIO_CTRL	61235	2322	30	0.97		40000	1183
D576_D22_BBIO_CTRL	61235	2322	30	0.97		40000	1302
D552_D22_BBIO_IL13	48196	3332	30	0.97		50000	2610
D576_D22_BBIO_IL13	48196	3332	30	0.97		50000	2395
D552_D22_BBIO_ILRV	36644	2352	30	0.98		30000	1413
D576_D22_BBIO_ILRV	36644	2352	30	0.98		30000	3523
D577_D08_NBRU_CTRL	36469	2345	30	0.97		60000	2646
D578_D08_NBRU_CTRL	36469	2345	30	0.97		60000	2602
D577_D08_NBRU_IL13	36251	2154	30	0.97		60000	3430
D578_D08_NBRU_IL13	36251	2154	30	0.97		60000	2047
D577_D23_NBRU_CTRL	32172	1358	30	0.96		50000	2449
D578_D23_NBRU_CTRL	32172	1358	30	0.96		50000	3168
D577_D23_NBRU_IL13	39913	2792	30	0.95		50000	2513
D578_D23_NBRU_IL13	39913	2792	30	0.95		50000	2406
D577_D23_NBRU_ILRV	29359	2673	30	0.96		40000	3678
D578_D23_NBRU_ILRV	29359	2673	30	0.96		40000	4118
D577_D08_BBRU_CTRL	39924	3149	30	0.96		40000	1954
D578_D08_BBRU_CTRL	39924	3149	30	0.96		40000	3097
D577_D08_BBRU_IL13	27253	2154	30	0.95		40000	2798
D578_D08_BBRU_IL13	27253	2154	30	0.95		40000	2367
D577_D23_BBRU_CTRL	48759	2800	30	0.95		40000	2672
D578_D23_BBRU_CTRL	48759	2800	30	0.95		40000	2852
D577_D23_BBRU_IL13	45073	3603	30	0.95		50000	3650
D578_D23_BBRU_IL13	45073	3603	30	0.95		50000	2022
D577_D23_BBRU_ILRV	65780	1405	30	0.95		60000	622
D578_D23_BBRU_ILRV	65780	1405	30	0.95		60000	1471

## Differential expression analysis

We performed differential expression analysis by using the `run_de` function from `Libra` package (v1.0.0) (<https://github.com/neurorestore/Libra>) and using the pseudobulk method with `edgeR`.

## Analysis of cell type proportions

We used the `propeller` function (with `asin` transformation) from the “`speckle`” package (v0.0.3) to compare cell type proportions between the different conditions and timepoints (Phipson et al., 2022). We also used `miloR`, a tool for differential abundance on K-Nearest Neighbors (KNN) graph (Dann et al., 2022). A mixed cell type is defined as a heterogeneous neighborhoods (ie. a mix of cell types) with a “`celltype_fraction`” smaller than 0.7.

## Enrichment analysis

Enrichment analysis was performed with `EnrichR` online (<https://maayanlab.cloud/Enrichr/>).

## Cell trajectory inference pipeline

Cell trajectories were inferred for the conditions of interest that are displayed in **Table 13**. Only bronchi samples were included in this analysis.

**Table 13:** Conditions selected for trajectory inference analysis.

	<b>CTRL_1</b>	<b>IL13_1</b>	<b>CTRL_2</b>	<b>IL13_2</b>	<b>ILRV_2</b>
<b>Healthy</b>	Healthy_CTRL_1	Healthy_IL13_1	Healthy_CTRL_2	Healthy_IL13_2	Healthy_ILRV_2
<b>Asthma</b>	Asthma_CTRL_1	Asthma_IL13_1	Asthma_CTRL_2	Asthma_IL13_2	Asthma_ILRV_2

The pipeline contains all the scripts from pre-processing of data to the inference of trajectories. All scripts were launched in a `conda` (v.22.9.0) environment specially created for the pipeline. The codes were written in `Python` for the majority of the steps, and in `bash` for a smaller part. To interactively see the results of each step and work on the choice of the parameters, the `Python` scripts were launched in `.ipynb` notebook files.

The input of the pipeline was a `.h5ad` file containing cells from all conditions to analyze. Each condition was analyzed independently, so we performed one subset per condition at the very beginning of the pipeline. We kept the global annotation and the coordinates of the global Uniform Manifold Approximation and Projection (UMAP) in each condition for comparison. Originally, counts data contained 199606 cells for 36602 genes. This data was already normalized, and log transformed, this is essential for the majority of the functions of the pipeline to work. Trajectories were calculated in `Python`, for this reason data was manipulated as an `AnnData` object. These objects can be treated using

the library of the same name Anndata. The package handles annotated data matrices. For each condition separated, in this paragraph, we will refer to this AnnData object as “adata” (Virshup et al., 2021).

The pipeline is composed of the following steps:

- A. Verifying and subsetting data
- B. Velocity for RNA velocity calculation
- C. scVelo
- D. CellRank kernels
- E. CellRank estimators

## A. Verifying and subsetting data

This step consisted in exploration of the input data, and verification that the count matrixes were normalized, and log transformed. Then we filtered cells to separate the 10 conditions. The pipeline, from this step on, was run separately on each subset. In order to set the optimal parameters and establish a standard pipeline, we started from the subset healthy\_CTRL\_2, to verify which parameters corresponded better to the expected cell trajectory.

## B. Velocity for RNA velocity calculation

The first step is to run Velocity, a package to analyze RNA velocity.

RNA velocity can be defined as the time derivative of the gene expression state. This velocity can be estimated using the ratio of spliced and unspliced mRNAs. RNA velocity is particularly useful because it can predict the future state of each cell (La Manno et al., 2018). We chose Velocity because it is the golden standard for RNA velocity calculation and because its results are directly usable by the CellRank pipeline, for trajectory inference. We used the CLI (Command Line) tool from Velocity (La Manno et al., 2018), and then directly analyzed the Velocity output with the scVelo Python package (v.0.3.2) (Bergen et al., 2020), as described in “C. scVelo”.

### **Velocity CLI**

This command line tools performs read counting and generates .loom files with spliced and unspliced counts separated. We ran Velocity in a for loop, for all the experiments in adata, as follow:

```
velocity run \  
"$DATAPATH"/"$sample"/outs/possorted_genome_bam.bam \  
/data/analysis/data_porracciolo/2023_2024/SAHARRA/data/gtf/ucagenomix_cellranger_refdata-gex-GRCh38-release-104-gencode.v38/genes/genes.gtf \  

```

```
--bcfile ${sample_folder}/outs/filtered_gene_bc_matrices/barcodes.tsv.gz \  
--outputfolder $OUTPUTPATH/"$sample" \  
-vvv \  
--mask /data/analysis/data_porracciolo/2023_2024/SAHARRA/data/gtf/GRCh38_hg38_rmsk.gtf
```

In detail:

- **BAMFILE.** "\$DATAPATH"/"\$sample"/outs/possorted\_genome\_bam.bam: bam file with sorted reads from which velocity extracted read counts.
- **GTFFILE.**  
/data/analysis/data\_porracciolo/2023\_2024/SAHARRA/data/gtf/ucagenomix\_cellranger\_refdata-gex-GRCh38-release-104-gencode.v38/genes/genes.gtf: the genome annotation file.
- **--bcfile.** \${sample\_folder}/outs/filtered\_gene\_bc\_matrices/barcodes.tsv.gz: the barcode file to filter the bam.
- **--outputfolder.** \$OUTPUTPATH/"\$sample": the output folder to store the loom file.
- **-vvv** : Verbosity level: (warnings, info and debug)
- **--mask.**  
/data/analysis/data\_porracciolo/2023\_2024/SAHARRA/data/gtf/GRCh38\_hg38\_rmsk.gtf : .gtf file containing intervals to mask. : Elements to mask (5683690 in our case), like expressed repetitive elements, since they can be a confounding factor in downstream analysis.

The output .loom files contain the spliced and unspliced count data.

## C. scVelo

From spliced and unspliced counts obtained by the Velocity CLI, we estimated RNA velocity to study the cellular dynamics of the differentiation. The first step consisted in merging the loom files into a single one using the function `loompy.combine()`. Then we read the merged loom file as an `AnnData` object. We preprocessed the `.obs_names` (the name of the cell entries, containing the barcodes), to make sure they matched between the `adata` and the merged loom. We merged the `adata` and the merged loom using `scvelo.utils.merge()`. To visualize the proportions of spliced and unspliced counts, we used the function `scvelo.pl.proportions()`. For each cell, for each gene, 3 matrices (spliced, unspliced and ambiguous counts) are stored in `adata`.

### *scVelo preprocessing*

The first step to obtain data ready for velocity calculation, is:

- The filtering of genes that do not have enough spliced and unspliced counts.
- The normalization of each cell by total counts over all genes.

We used the following function: `scvelo.pp.filter_and_normalize()`, with default parameters used in the tutorial from CellRank (Lange et al., 2022), available at :

[https://github.com/theislab/CellRank\\_notebooks/blob/main/tutorials/kernels/200\\_rna\\_velocity.ipynb](https://github.com/theislab/CellRank_notebooks/blob/main/tutorials/kernels/200_rna_velocity.ipynb)

The function was launched as follow:

```
scvelo.pp.filter_and_normalize (adata, min_shared_counts = 20, n_top_genes = 2000,  
subset_highly_variable = False, log = False)
```

where:

- **min\_shared\_counts**: is the minimum number of counts required for a gene (both unspliced and spliced), before normalization.
- **n\_top\_genes**: the number of top genes to keep.
- **subset\_highly\_variable**: whether to subset adata keeping only `n_top_genes`, or to store the information of the `n_top_genes` in `adata.var["highly_variable"]`.
- **log**: wheter adata.X is to logarithmize or not.

Then we computed principal components and moments for velocity estimation. Using the functions `scanpy.tl.pca(adata)`, where all parameters were those by default.

Based on the `pca`, we calculated the nearest neighbors distance matrix and a neighborhood graph of observations, using the function `scanpy.pp.neighbors()`. The parameters were the same as those from the CellRank tutorial, which correspond to the default parameters of the same function from `scVelo` library:

```
scanpy.pp.neighbors(adata, n_pcs=30, n_neighbors=30)
```

where:

- **n\_pcs**: are the number of principal components from the PCA to use.
- **n\_neighbors**: are the neighbor data points.

From the connectivities calculated by the previous function, we computed moments of un/spliced abundances for velocity estimation. For each cell, we computed the mean (first-order moments) and variance (second-order moments) of its neighboring cells ([https://nbisweden.github.io/single-cell\\_sib\\_scilifelab\\_2021/project\\_velocity/RNA\\_velocity\\_group2.html](https://nbisweden.github.io/single-cell_sib_scilifelab_2021/project_velocity/RNA_velocity_group2.html)). We used `scvelo.pp.moments` using the full space of the precomputed PCA, with all default parameters:

```
scv.pp.moments(adata)
```

### ***scVelo velocity calculation***

At first, we recovered the splicing kinetics of specified genes, using the function `scvelo.tl.recover_dynamics()`, as follow:

```
scvelo.tl.recover_dynamics(adata, n_jobs=8)
```

where:

- **n\_jobs**: specifies the number of parallel jobs.

Since we did not specify genes to use for the fitting, the function estimated velocity genes, these genes are used for modeling the cell fate transition probabilities. In particular, this function infers: transcription rates, splicing rates, degradation rates, cell-specific latent time and transcriptional states.

All the information gathered, and in particular the fitted parameters for splicing dynamics, was used to compute the actual velocities using the function `scvelo.tl.velocityscv.tl.velocity()`, as follow:

```
scvelo.tl.velocity(adata, mode="dynamical")
```

where:

- **mode**: indicates the model for the estimation of the transcriptional dynamics. Compared to the other modes, the “dynamical” mode do not rely on a linear assumption, but a more complex set of information: the gene rates of transcription, splicing and degradation. In addition to that, it considers transient cell-states.

## **D. CellRank kernels**

The connection between scVelo and CellRank is that the resulting calculated velocity is the input of CellRank, to generate a transition matrix. This transition matrix can be defined as matrix of dimensions `nb_cells x nb_cells`, where each row represents a cell, and the values are the assumed transition probabilities of that cell to the others. The transition matrix is then used as input of the CellRank estimators (see next paragraph) to perform the trajectory inference. To generate the transition matrix, CellRank supplies different methods, called « kernels » by the authors, referring, in essence, to units of calculation. All the kernels give a transition matrix as output, what differs is the input information to calculate it.

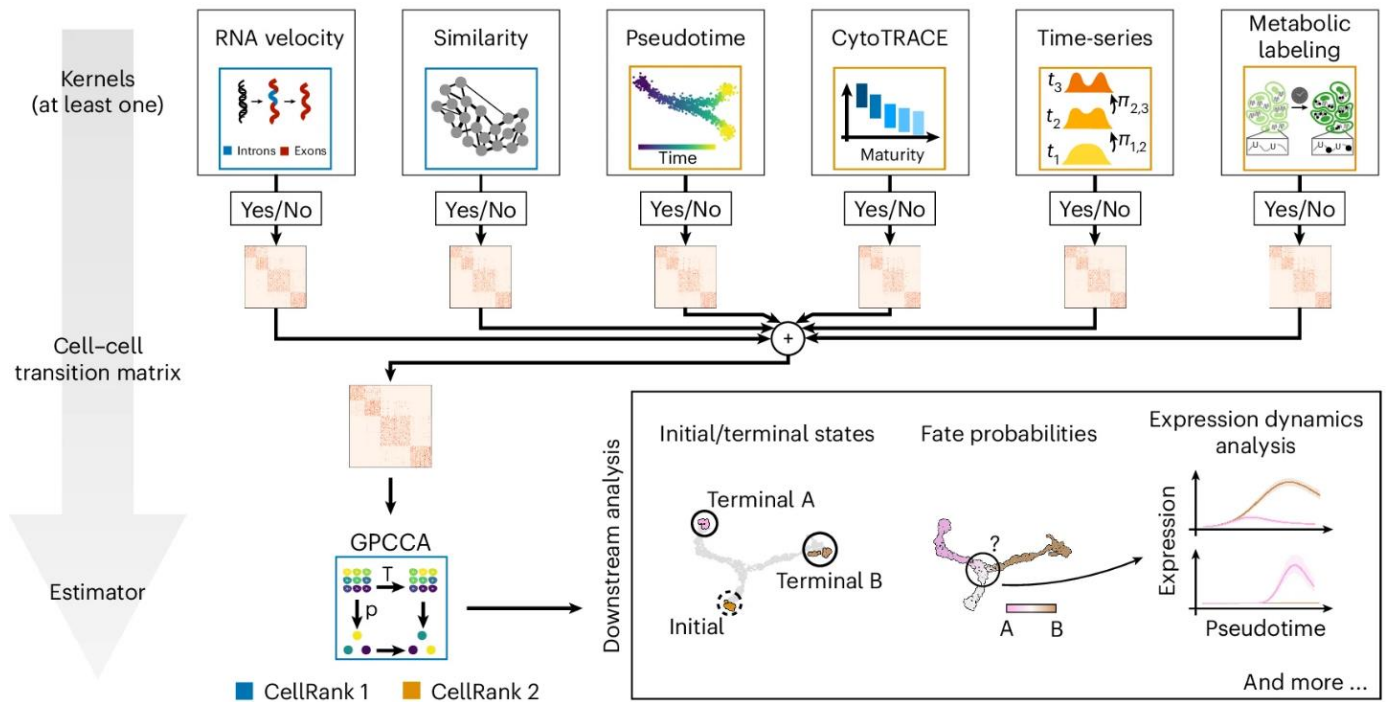


**Figure 95:** CellRank2 general pipeline.  
From Weiler et al., 2024.

### ***Choice of the CellRank kernels***

Among the kernels available (Velocity Kernel, Connectivity Kernel, Real-time Kernel, CytoTRACE Kernel, and the Pseudotime Kernel), we used the Pseudotime Kernel.

In particular, this kernel is based on the calculation of the pseudotime, which can be defined as the ranking of cells along an inferred transition path. To generate a transition matrix with this kernel, it is necessary to provide the results of pseudotime algorithms as input. This is the kernel that worked the best with the healthy CTRL dataset, reflecting the biological truth as best as possible. For this reason, we decided to use this kernel for the generation of the matrix.

### ***Pseudotime Kernel***

The first steps before calculating the pseudotime itself are the selection of the high variable genes, and the calculation of the PCA, which had already been performed before. The second step is the determination of the diffusion maps to estimate the low dimensional space of the data with the Palantir algorithm (Setty et al., 2019), using the function `palantir.utils.run_diffusion_maps()` as follow:

```
palantir.utils.run_diffusion_maps (adata, n_components=5)
```

where:

- **n\_components:** indicates the number of principal components.

Afterwards, we used the `palantir.utils.determine_multiscale_space()` function to find the best low-dimensional version of the data space with default values. By observing the violin plots showing the order of the cell types based on the calculated pseudotime and the pseudotime representation on the umap, we decided to calculate the transition matrix based on the Palantir pseudotime, using the function `CellRankkernels.PseudotimeKernel()`:

```
CellRankkernels.PseudotimeKernel(adata, time_key="palantir_pseudotime")
```

where:

- `time_key`: indicates the key in the adata where we can find the pseudotime values to generate the transition matrix.

## E. CellRank estimators

CellRank estimators are used to quantitatively analyze the transition matrix to mainly detect initial and terminal states, compute fate probabilities and gene expression trends.

### *Computing Initial and Terminal States*

Computing initial and terminal states involves the determination of macrostates, which are groups of stable cells. The first step is to initialize the estimator, by providing the transition matrix obtained from the Pseudotime kernel as input. The pyGPCCA - Generalized Perron Cluster Cluster Analysis method was adapted to identify the most stable macrostates from the transition matrix. We launched the method using the function `CellRank.estimators.GPCCA()` as follow:

```
CellRank.estimators.GPCCA(pk)
```

where:

- **object**: the input to recover cell dynamics, here: `pk` was the name of the variable containing the result of the Pseudotime Kernel transition matrix calculation.

Afterwards, as an advanced use, we computed a Schur decomposition of the transition matrix, to obtain an indication of the optimal number of stable macrostate. We used the function `g.compute_schur()` with default parameters, and to plot the results we used the function `g.plot_spectrum()`, where “`g`” is the variable containing the results of `CellRank.estimators.GPCCA(pk)`. However, the choice of the number of macrostates can be manual, aiming to choose macrostates as stable as possible. The number of macrostates, and of the terminal states are the only parameters in this section that were not set automatically for all conditions, but that had to be adapted for each condition.

The functions used to define the macrostates was `g.fit()`, employed as follow:



```
g.fit(cluster_key="Celltype_lv_2", n_states=[n, 11])
```

where:

- **cluster\_key**: cluster labels can be given (macrostate labels will be based on these labels)
- **n\_states**: is either the precise number of states to identify, or a range of numbers. Here n was set as the optimal given by the calculated Schur decomposition.

To predict the initial and terminal macrostates, we employed the functions: `g.predict_initial_states()` and `g.predict_terminal_states()`, where we can define the most n stable macrostates as terminal states. These functions are based on the stability of the macrostates, where the most stable are the terminal states and the least is the initial state.

### ***Estimating Fate Probabilities and Driver Genes***

In this step, ran right after computing macrostates, we estimated fate probabilities, as the probability of any cell that is not in a terminal state, towards this last. This involves the use of the function `g.compute_fate_probabilities()`, we tested all the solvers, but we found no difference, hence we launched the function with default parameters. When multiple terminal states are present, we explored the probabilities towards each state separately. We defined the terminal states as the most 2 stable ones, separately for each condition. We employed the function `CellRank.pl.aggregate_fate_probabilities()`, to investigate how likely a cluster goes towards a terminal state. Afterwards, we used the `g.compute_lineage_drivers()`, specifying each time the terminal state and the cluster key to uncover putative driver genes. The method does that by correlating fate probabilities with gene expression. For 2 terminal states at a time (each time we have only 2), it was possible to plot the best drivers for a terminal state against those of the other terminal state, to see their correlation by using the function `g.plot_lineage_drivers_correlation()`.

### ***Visualizing and Clustering Gene Expression trends***

In this step, the aim was the computation of gene expression trends through differentiation trajectories. These trends were then clustered to detect those genes with similar dynamics. The first step is the initialization of a model of the type Generalized Additive Models (GAMs), using the function `CellRank.models.GAMR()` as follow:

```
CellRank.models.GAMR(adata, smoothing_penalty=10.0)
```

where:

- **smoothing\_penalty**: indicates the penalty for smoothing the fitting curve (the higher the smoother).

By selecting the putative driver genes previously calculated and a pseudotime (for us the Palantir pseudotime), we could plot the trends by using the function `CellRank.pl.gene_trends()`, separately for each terminal state. It was then possible to cluster gene trends by using the function `CellRank.pl.cluster_trends()`, plotting the GAMR model for the high variable genes. By finding in which cluster/clusters we had the majority of the genes, we could select the best of those genes, and replot their trends by using again `CellRank.pl.gene_trends()`.

## Flex single-cell RNA sequencing (BCi cells)

To perform single-cell analysis, cells differentiated on Transwell™ inserts (3 per experimental condition) were harvested by incubating with 0.1% protease type XIV *Streptomyces griseus* in HBSS at 4°C overnight. Then, cells were gently detached from the inserts by pipetting and transferred into a microtube, pooling cells from 3 inserts. An excess of HBSS containing 2% BSA was added. Cells were centrifuged at 150 g for 5 min and resuspended in 1 mL of PBS containing 0.04% BSA and filtered through a 20 µm mesh filter (miltenyi). Cell concentration and viability were measured with a Countess™ automated cell counter (ThermoFisher Scientific), after incubation with NucGreen to detect dead cells (ThermoFisher Scientific). Cells were centrifuged at 150 g for 5 min and resuspended in 1 mL fixation buffer from the “Chromium Next GEM Single Cell Fixed RNA Sample Preparation” (PN-1000414). Fixation procedure was performed following manufacturer’s instructions. All steps were performed on ice. Fixed cells were frozen and conserved at -80°C for 3 days before using the “Chromium Fixed RNA Kit, Human Transcriptome” kit (PN1000475) for single-cell library preparation. Libraries were sequenced to achieve a minimum of 10 000 paired reads per cell, on a P2 100 cycles Flowcell (Illumina).

## CUT&Tag chromatin analysis

In order to identify the chromatin modifications that differ between asthmatic vs healthy patients, we performed a CUT&Tag analysis of a selection of histone marks (H3K27me3, H3K4me3 and H3K4me1). CUT&Tag is a technique to identify genome-wide chromatin regions bound to specific histone marks, in cells or nuclei, with low background noise. It uses a Tn5 transposase fused to a protein A, enabling it to bind to the secondary antibody targeting the marker of interest (histone modification or transcription factor) and to cut and insert indexes into the chromatin regulated by this marker. The indexed reads are then sequenced and analyzed by bio-computational analysis.

## Sample preparation

The CUT&Tag experiments were carried out on healthy and severe asthma CTRL basal cells from the IL-13 experiment and four conditions were observed: H3K27me3, H3K4me3, H3K4me1 and rabbit anti-mouse IgG (negative control). At the passage from flask to inserts basal cells were set aside and frozen in preparation for the CUT&Tag experiment. I adapted the Bench top CUT&Tag V.3 protocol of Dr. Henikoff to our samples (<https://www.protocols.io/view/bench-top-cut-amp-tag-kqdg34qdp125/v3>) (Kaya-Okur et al., 2019). Aliquots of one million cells per donor were thawed in Pneumacult-Ex+ and resuspended into wash buffer (20 mM HEPES pH 7.5; 150 mM NaCl; 0.5 mM Spermidine; 1× Roche Complete Protease Inhibitor EDTA-Free tablet [Sigma-Aldrich, cat. no. 5056489001]). CUTANA™ Concanavalin A Conjugated Paramagnetic Beads (EpiCypher, 21-1401) were washed and resuspended in binding buffer (20 mM HEPES pH 7.9; 10 mM KCl; 1 mM CaCl<sub>2</sub>; 1 mM MnCl<sub>2</sub>) and 10 µL of activated beads per sample were added and incubated for 15 min at RT to bind cells to the beads. Bead and cells suspension was divided into four and immobilized on a magnetic rack. Supernatant were removed and bead-bound cells were resuspended into 200 µL antibody buffer (wash buffer + 1% digitonin + 2 mM EDTA + 0.01% BSA) with 1 µL of the corresponding primary antibody (anti-H3K27me3 rabbit monoclonal antibody [EpiCypher, Inc. 19-1002], anti-H3K4me3 rabbit monoclonal antibody [EpiCypher, Inc., 13-0041] and anti-H3K4me1 rabbit monoclonal antibody [EpiCypher, Inc., 13-0057]) or a negative control (CUTANA™ IgG Negative Control Antibody for CUT&RUN and CUT&Tag, EpiCypher, Inc., 13-0042). Incubation was performed on a rotating platform overnight at 4 °C. After clearing on a magnetic rack, beads were resuspended in 100 µL secondary antibody solution (wash buffer + 0.05% digitonin + 1/50 anti-rabbit guinea pig secondary antibody [Antibodies online cat. no. ABIN101961] and cells were incubated at RT on a nutator for 1h. Then cells were washed using the magnet stand 3x in 2 mL dig-dash buffer (wash buffer + 0.05% digitonin) and 100 µL of pre-loaded pA-Tn5 adapter complex (CUTANA™ pAG-Tn5 for CUT&Tag; EpiCypher, Inc. 15-1017) diluted 1/20 in dig-300 buffer (20 mM HEPES pH 7.5; 300 mM NaCl; 0.5 mM Spermidine; 0.01% digitonin; 1× Roche Complete Protease Inhibitor EDTA-Free tablet) was added to each sample and incubated at RT for 1 h on a nutator. Beads were washed 3x times with dig-300 buffer and resuspended in 300 µL tagmentation buffer (dig-300 buffer + 10 mM MgCl<sub>2</sub>) and incubated at 37 °C for 1 h. To stop tagmentation, 2.5 µL of 0.5 M EDTA, 3 µL of 10% SDS and 0.5 µL of 20 mg/mL Proteinase K was added directly to each sample. Samples were then incubated un a dry bath 1 h at 55°C to solubilize DNA fragments. DNA was purified by phenol-chloroform extraction and quantified using a Bioanalyzer and Qubit.

## Sequencing

Samples were indexed using the primers described by Buenrostro, J.D. et al. (Buenrostro et al., 2015), with a common i5 and individual i7 indexes. The indexes used are summarized in **Table 14**:

**Table 14:** Indexes used for the CUT&Tag experiment.

Index	Sequence
i7_2.1	TAAGGCGA
i7_2.2	CGTACTAG
i7_2.3	AGGCAGAA
i7_2.4	TCCTGAGC
i7_2.5	GGACTCCT
i7_2.6	TAGGCATG
i7_2.7	CTCTCTAC
i7_2.8	CAGAGAGG
i7_2.9	GCTACGCT
i7_2.10	CGAGGCTG
i7_2.11	AAGAGGCA
i7_2.12	GTAGAGGA
i7_2.13	TGGATCTG
i7_2.14	CCGTTTGT
i7_2.15	TGCTGGGT
i7_2.16	AGGTTGGG
i7_2.17	GTGTGGTG
i7_2.18	TGGGTTTC
i7_2.19	TGGTCACA
i7_2.20	TTGACCCT
i7_2.21	CGCGGACA
i7_2.22	TTCCATAT
i7_2.23	AATTCGTT
i7_2.24	GGCGTCGA
i5	TAGATCGC

PCR amplification was performed with the following parameters:

- Cycle 1: 72 °C for 5 min (gap filling)
- Cycle 2: 98 °C for 30 sec
- [Cycle 3: 98 °C for 10 sec
- Cycle 4: 63 °C for 10 sec]
- Repeat Cycles 3-4 13 times
- 72°C for 1 min

Samples were sequenced on a NextSeq 2000 P1 (100 cycles) in paired-end mode with a length of 28\*10\*10\*90 bases.

## Analysis

### **1. Input**

The input consisted in 24 samples, 12 healthy and 12 asthmatics. For each condition, 3 patients were sequenced and for each patient, 3 histone marks were targeted: H3K4me3, H3K4me1 and H3K27me3.

## **2. Steps of the pipeline**

After sequencing, the libraries were analyzed using a bioinformatics pipeline we set up. First the analysis started with peak identification (calling). This step included: pre-processing, alignment and peak calling (identification of genomic regions that are significantly enriched), using the nf-core/cutandrun pipeline (DOI 10.5281/zenodo.5653535).

The command was run with the following parameters:

- nextflow : the nf-core pipeline was written using the Nextflow workflow language.
- -bg run /export/apps/nf-core/cutandrun: to launch the background pipeline, indicating the location of the program.
- --input  
/export/data2/porracciolo/SAHARRA/cutandrun/samplesheet/240409\_samplesheet.csv: to specify the samplesheet file which indicates the location of the samples.
- -profile singularity: to specify configuration presets.
- --outdir seacr\_mac2\_RPKM\_mac2narrowpeakfalse: to specify the output folder for analyses.
- --genome GRCh38: the reference genome.
- --peakcaller seacr, macs2: the peak calling methods.
- --normalisation\_mode RPKM: reads normalization method, here : Reads Per Kilobase per Million mapped reads.
- --macs2\_narrow\_peak false: for peak calling macs2 determines whether wide or narrow mode is used. Wide peaks were chosen as they are more suitable for histone marks.

Genomic annotation of the peaks (identification of the gene closest to the peak), was done using the R ChIPseeker library (G. Yu et al., 2015). Differential analysis of peaks to test, for each mark, whether regions were more enriched in one condition compared to the other, was performed using the R DESeq2 library (Love et al., 2014). Regions were considered differentially enriched in a condition if adjusted  $p$ -value  $< 0.05$  and  $\log_2\text{FoldChange} > 0$  (enriched in asthmatic) or  $< 0$  (enriched in healthy).

# References

- Acampora, D., Mazan, S., Lallemand, Y., Avantaggiato, V., Maury, M., Simeone, A., & Brûlet, P. (1995). Forebrain and midbrain regions are deleted in *Otx2*<sup>-/-</sup> mutants due to a defective anterior neuroectoderm specification during gastrulation. *Development*, *121*(10), 3279–3290. <https://doi.org/10.1242/dev.121.10.3279>
- Ahmed, E., Fieldes, M., Bourguignon, C., Mianné, J., Petit, A., Jory, M., Cazevieille, C., Boukhaddaoui, H., Garnett, J. P., Hirtz, C., Massiera, G., Vachier, I., Assou, S., Bourdin, A., & De Vos, J. (2022). Differentiation of Human Induced Pluripotent Stem Cells from Patients with Severe COPD into Functional Airway Epithelium. *Cells*, *11*(15), 2422. <https://doi.org/10.3390/CELLS11152422/S1>
- Aikawa, T., Shimura, S., Sasaki, H., Ebina, M., & Takishima, T. (1992). Marked goblet cell hyperplasia with mucus accumulation in the airways of patients who died of severe acute asthma attack. *Chest*, *101*(4), 916–921. <https://doi.org/10.1378/chest.101.4.916>
- Al Jord, A., Lemaître, A. I., Delgehyr, N., Faucourt, M., Spassky, N., & Meunier, A. (2014). Centriole amplification by mother and daughter centrioles differs in multiciliated cells. *Nature*, *516*(7529), 104–107. <https://doi.org/10.1038/nature13770>
- Allis, C. D., & Jenuwein, T. (2016). The molecular hallmarks of epigenetic control. *Nature Reviews Genetics*, *17*(8), 487–500. <https://doi.org/10.1038/nrg.2016.59>
- Anderson, P. J., Lynch, T. J., & Engelhardt, J. F. (2017). Multipotent myoepithelial progenitor cells are born early during airway submucosal gland development. *American Journal of Respiratory Cell and Molecular Biology*, *56*(6), 716–726. <https://doi.org/10.1165/rcmb.2016-0304OC>
- Arbi, M., Pefani, D.-E., Kyrousi, C., Lalioti, M.-E., Kalogeropoulou, A., Papanastasiou, A. D., Taraviras, S., & Lygerou, Z. (2016). GemC1 controls multiciliogenesis in the airway epithelium. *EMBO Reports*, *17*(3), 400–413. <https://doi.org/10.15252/embr.201540882>
- Aros, C. J., Pantoja, C. J., & Gomperts, B. N. (2021). Wnt signaling in lung development, regeneration, and disease progression. *Communications Biology*, *4*(1), 1–13. <https://doi.org/10.1038/s42003-021-02118-w>
- Aros, C. J., Vijayaraj, P., Pantoja, C. J., Bisht, B., Meneses, L. K., Sandlin, J. M., Tse, J. A., Chen, M. W., Purkayastha, A., Shia, D. W., Sucre, J. M. S., Rickabaugh, T. M., Vldar, E. K., Paul, M. K., & Gomperts, B. N. (2020). Distinct Spatiotemporally Dynamic Wnt-Secreting Niches Regulate Proximal Airway Regeneration and Aging. *Cell Stem Cell*, *27*(3), 413-429.e4. <https://doi.org/10.1016/j.stem.2020.06.019>
- Atherton, H. C., Jones, G., & Danahay, H. (2003). IL-13-induced changes in the goblet cell density of human bronchial epithelial cell cultures: MAP kinase and phosphatidylinositol 3-kinase regulation. *American Journal of Physiology - Lung Cellular and Molecular Physiology*, *285*(3 29-3), 730–739. <https://doi.org/10.1152/ajplung.00089.2003>
- Au-Yeung, N., Mandhana, R., & Horvath, C. M. (2013). Transcriptional regulation by STAT1 and STAT2 in the interferon JAK-STAT pathway. *JAK-STAT*, *2*(3), e23931. <https://doi.org/10.4161/JKST.23931>
- Auer, R. L., Starczynski, J., McElwaine, S., Bertoni, F., Newland, A. C., Fegan, C. D., & Cotter, F. E. (2005). Identification of a potential role for POU2AF1 and BTG4 in the deletion of 11q23 in chronic lymphocytic leukemia. *Genes, Chromosomes and Cancer*, *43*(1), 1–10. <https://doi.org/10.1002/GCC.20159>
- Aun, M. V., Bonamichi-Santos, R., Arantes-Costa, F. M., Kalil, J., & Giavina-Bianchi, P. (2018). Animal

- models of asthma: Utility and limitations. In *Journal of Asthma and Allergy* (Vol. 10, pp. 293–301). Dove Press. <https://doi.org/10.2147/JAA.S121092>
- Austin, C. D., Gonzalez Edick, M., Ferrando, R. E., Solon, M., Baca, M., Mesh, K., Bradding, P., Gauvreau, G. M., Sumino, K., FitzGerald, J. M., Israel, E., Bjermer, L., Bourdin, A., Arron, J. R., Choy, D. F., Olsson, J. K., Abreu, F., Howard, M., Wong, K., ... Woodruff, P. G. (2020). A randomized, placebo-controlled trial evaluating effects of lebrikizumab on airway eosinophilic inflammation and remodelling in uncontrolled asthma (CLAVIER). *Clinical and Experimental Allergy*, *50*(12), 1342–1351. <https://doi.org/10.1111/cea.13731>
- Avasthi, P., & Marshall, W. F. (2012). Stages of ciliogenesis and regulation of ciliary length. *Differentiation*, *83*(2). <https://doi.org/10.1016/j.diff.2011.11.015>
- Azimzadeh, J. (2014). Exploring the evolutionary history of centrosomes. *Philosophical Transactions of the Royal Society B: Biological Sciences*, *369*(1650), 20130453. <https://doi.org/10.1098/rstb.2013.0453>
- Bais, A. S., & Kostka, D. (2020). scds: computational annotation of doublets in single-cell RNA sequencing data. *Bioinformatics*, *36*(4), 1150–1158. <https://doi.org/10.1093/bioinformatics/btz698>
- Balasoorya, G. I., Johnson, J. A., Basson, M. A., & Rawlins, E. L. (2016). An FGFR1-SPRY2 Signaling Axis Limits Basal Cell Proliferation in the Steady-State Airway Epithelium. *Developmental Cell*, *37*(1), 85–97. <https://doi.org/10.1016/j.devcel.2016.03.001>
- Bansil, R., & Turner, B. S. (2006). Mucin structure, aggregation, physiological functions and biomedical applications. *Current Opinion in Colloid and Interface Science*, *11*(2–3), 164–170. <https://doi.org/10.1016/j.cocis.2005.11.001>
- Barbry, P., Cavard, A., Chanson, M., Jaffe, A. B., & Plasschaert, L. W. (2020). Regeneration of airway epithelial cells to study rare cell states in cystic fibrosis. *Journal of Cystic Fibrosis*, *19*(March 2019), S42–S46. <https://doi.org/10.1016/j.jcf.2019.09.010>
- Barlow, J. L., & McKenzie, A. N. J. (2014). Type-2 innate lymphoid cells in human allergic disease. *Current Opinion in Allergy and Clinical Immunology*, *14*(5), 397–403. <https://doi.org/10.1097/ACI.0000000000000090>
- Barnes, P. J. (2009). Intrinsic asthma: Not so different from allergic asthma but driven by superantigens? In *Clinical and Experimental Allergy* (Vol. 39, Issue 8, pp. 1145–1151). John Wiley & Sons, Ltd. <https://doi.org/10.1111/j.1365-2222.2009.03298.x>
- Basil, M. C., Katzen, J., Engler, A. E., Guo, M., Herriges, M. J., Kathiriya, J. J., Windmueller, R., Ysasi, A. B., Zacharias, W. J., Chapman, H. A., Kotton, D. N., Rock, J. R., Snoeck, H.-W., Vunjak-Novakovic, G., Whitsett, J. A., & Morrissey, E. E. (2020). The Cellular and Physiological Basis for Lung Repair and Regeneration: Past, Present, and Future. *Cell Stem Cell*, *26*(4), 482–502. <https://doi.org/10.1016/j.stem.2020.03.009>
- Basil, M. C., & Morrissey, E. E. (2020). Lung regeneration: a tale of mice and men. *Seminars in Cell & Developmental Biology*, *100*, 88–100. <https://doi.org/10.1016/j.semcd.2019.11.006>
- Basnet, S., Palmenberg, A. C., & Gern, J. E. (2019). Rhinoviruses and Their Receptors. *Chest*, *155*(5), 1018. <https://doi.org/10.1016/J.CHEST.2018.12.012>
- Beby, F., & Lamonerie, T. (2013). The homeobox gene *Otx2* in development and disease. *Experimental Eye Research*, *111*, 9–16. <https://doi.org/10.1016/j.EXER.2013.03.007>
- Bekhat, M., Rowson, S. A., & Neigh, G. N. (2017). Checks and balances: The glucocorticoid receptor

- and NFκB in good times and bad. *Frontiers in Neuroendocrinology*, 46(1), 15–31. <https://doi.org/10.1016/j.yfrne.2017.05.001>
- Belgacemi, R., Luczka, E., Ancel, J., Diabasana, Z., Perotin, J. M., Germain, A., Lalun, N., Birembaut, P., Dubernard, X., Mérol, J. C., Delepine, G., Polette, M., Deslée, G., & Dormoy, V. (2020). Airway epithelial cell differentiation relies on deficient Hedgehog signalling in COPD. *EBioMedicine*, 51. <https://doi.org/10.1016/j.ebiom.2019.11.033>
- Bergen, V., Lange, M., Peidli, S., Wolf, F. A., & Theis, F. J. (2020). Generalizing RNA velocity to transient cell states through dynamical modeling. *Nature Biotechnology*, 38(12), 1408–1414. <https://doi.org/10.1038/s41587-020-0591-3>
- Billipp, T. E., Nadsombati, M. S., & von Moltke, J. (2021). Tuning tuft cells: new ligands and effector functions reveal tissue-specific function. *Current Opinion in Immunology*, 68, 98–106. <https://doi.org/10.1016/j.coi.2020.09.006>
- Bingle, C. D., & Gitlin, J. D. (1993). Identification of hepatocyte nuclear factor-3 binding sites in the Clara cell secretory protein gene. *Biochem. J*, 295, 227.
- Bochkov, Y. A., Hanson, K. M., Keles, S., Brockman-Schneider, R. A., Jarjour, N. N., & Gern, J. E. (2010). Rhinovirus-induced modulation of gene expression in bronchial epithelial cells from subjects with asthma. *Mucosal Immunology*, 3(1), 69–80. <https://doi.org/10.1038/mi.2009.109>
- Boers, J. E., Ambergen, A. W., & Thunnissen, F. B. J. M. (1998). Number and proliferation of basal and parabasal cells in normal human airway epithelium. *American Journal of Respiratory and Critical Care Medicine*, 157(6 PART I), 2000–2006. <https://doi.org/10.1164/ajrccm.157.6.9707011>
- Boers, J. E., Ambergen, A. W., & Thunnissen, F. B. J. M. (1999). Number and Proliferation of Clara Cells in Normal Human Airway Epithelium. *Am J Respir Crit Care Med*, 159, 1585–1591. [www.atsjournals.org](http://www.atsjournals.org)
- Bonnardel, J., T'Jonck, W., Gaublumme, D., Browaeys, R., Scott, C. L., Martens, L., Vanneste, B., De Prijck, S., Nedospasov, S. A., Kremer, A., Van Hamme, E., Borghgraef, P., Toussaint, W., De Bleser, P., Mannaerts, I., Beschin, A., van Grunsven, L. A., Lambrecht, B. N., Taghon, T., ... Guilliams, M. (2019). Stellate Cells, Hepatocytes, and Endothelial Cells Imprint the Kupffer Cell Identity on Monocytes Colonizing the Liver Macrophage Niche. *Immunity*, 51(4), 638–654.e9. <https://doi.org/10.1016/j.immuni.2019.08.017>
- Boucher, R. C. (2007). Cystic fibrosis: a disease of vulnerability to airway surface dehydration. *Trends in Molecular Medicine*, 13(6), 231–240. <https://doi.org/10.1016/j.molmed.2007.05.001>
- Brewington, J. J., Filbrandt, E. T., LaRosa, F. J., Moncivaiz, J. D., Ostmann, A. J., Strecker, L. M., & Clancy, J. P. (2018). Brushed nasal epithelial cells are a surrogate for bronchial epithelial CFTR studies. *JCI Insight*, 3(13). <https://doi.org/10.1172/JCI.INSIGHT.99385>
- Brody, S. L., Yan, X. H., Wuerffel, M. K., Song, S. K., & Shapiro, S. D. (2000). Ciliogenesis and left-right axis defects in forkhead factor HFH-4-null mice. *American Journal of Respiratory Cell and Molecular Biology*, 23(1), 45–51. <https://doi.org/10.1165/ajrcmb.23.1.4070>
- Buenrostro, J. D., Wu, B., Litzenburger, U. M., Ruff, D., Gonzales, M. L., Snyder, M. P., Chang, H. Y., & Greenleaf, W. J. (2015). Single-cell chromatin accessibility reveals principles of regulatory variation. *Nature*, 523(7561), 486–490. <https://doi.org/10.1038/nature14590>
- Burgess, J. K., Mauad, T., Tjin, G., Karlsson, J. C., & Westergren-Thorsson, G. (2016). The extracellular matrix – the under-recognized element in lung disease? *The Journal of Pathology*, 240(4), 397–409. <https://doi.org/10.1002/PATH.4808>



- Button, B., Cai, L.-H., Ehre, C., Kesimer, M., Hill, D. B., Sheehan, J. K., Boucher, R. C., & Rubinstein, M. (2012). A Periciliary Brush Promotes the Lung Health by Separating the Mucus Layer from Airway Epithelia. *Science*, 337(6097), 937–941. <https://doi.org/10.1126/science.1223012>
- Cai, Q., Luo, M., Tang, Y., Yu, M., Yuan, F., Gasser, G. N., Liu, X., & Engelhardt, J. F. (2023). Sonic Hedgehog Signaling Is Essential for Pulmonary Ionocyte Specification in Human and Ferret Airway Epithelia. *American Journal of Respiratory Cell and Molecular Biology*, 69(3), 295–309. <https://doi.org/10.1165/rcmb.2022-02800C>
- Cardesa, A., Alos, L., Nadal, A., & Franchi, A. (2017). Nasal cavity and paranasal sinuses. In *Pathology of the Head and Neck: Second Edition* (pp. 49–127). [https://doi.org/10.1007/978-3-662-49672-5\\_2](https://doi.org/10.1007/978-3-662-49672-5_2)
- Cardoso, W. V. (2001). Molecular regulation of lung development. In *Annual Review of Physiology* (Vol. 63, pp. 471–494). <https://doi.org/10.1146/annurev.physiol.63.1.471>
- Carpenter, J., Wang, Y., Gupta, R., Li, Y., Haridass, P., Subramani, D. B., Reidel, B., Morton, L., Ridley, C., O’Neal, W. K., Buisine, M. P., Ehre, C., Thornton, D. J., & Kesimer, M. (2021). Assembly and organization of the N-terminal region of mucin MUC5AC: Indications for structural and functional distinction from MUC5B. *Proceedings of the National Academy of Sciences of the United States of America*, 118(39), e2104490118. [https://doi.org/10.1073/PNAS.2104490118/SUPPL\\_FILE/PNAS.2104490118.SAPP.PDF](https://doi.org/10.1073/PNAS.2104490118/SUPPL_FILE/PNAS.2104490118.SAPP.PDF)
- Carroll, N., Lehmann, E., Barret, J., Morton, A., Cooke, C., & James, A. (1996). Variability of Airway Structure and Inflammation in Normal Subjects and in Cases of Nonfatal and Fatal Asthma. *Path. Res. Pract*, 192, 238–248. [https://doi.org/10.1016/S0344-0338\(96\)80227-5](https://doi.org/10.1016/S0344-0338(96)80227-5)
- Chen, G., Korfhagen, T. R., Xu, Y., Kitzmiller, J., Wert, S. E., Maeda, Y., Gregorieff, A., Clevers, H., & Whitsett, J. A. (2009). SPDEF is required for mouse pulmonary goblet cell differentiation and regulates a network of genes associated with mucus production. *Journal of Clinical Investigation*, 119(10), 2914–2924. <https://doi.org/10.1172/JCI39731>
- Chevalier, B., Adamiok, A., Mercey, O., Revinski, D. R., Zaragosi, L. E., Pasini, A., Kodjabachian, L., Barbry, P., & Marcet, B. (2015). MiR-34/449 control apical actin network formation during multiciliogenesis through small GTPase pathways. *Nature Communications*, 6. <https://doi.org/10.1038/ncomms9386>
- Chung, K. F., Wenzel, S. E., Brozek, J. L., Bush, A., Castro, M., Sterk, P. J., Adcock, I. M., Bateman, E. D., Bel, E. H., Bleecker, E. R., Boulet, L. P., Brightling, C., Chanez, P., Dahlen, S. E., Djukanovic, R., Frey, U., Gaga, M., Gibson, P., Hamid, Q., ... Teague, W. G. (2014). International ERS/ATS guidelines on definition, evaluation and treatment of severe asthma. *European Respiratory Journal*, 43(2), 343–373. <https://doi.org/10.1183/09031936.00202013>
- Chung, M. I., Peyrot, S. M., LeBoeuf, S., Park, T. J., McGary, K. L., Marcotte, E. M., & Wallingford, J. B. (2012). RFX2 is broadly required for ciliogenesis during vertebrate development. *Developmental Biology*, 363(1), 155–165. <https://doi.org/10.1016/J.YDBIO.2011.12.029>
- Cibois, M., Luxardi, G., Chevalier, B., Thomé, V., Mercey, O., Zaragosi, L. E., Barbry, P., Pasini, A., Marcet, B., & Kodjabachian, L. (2015). BMP signalling controls the construction of vertebrate mucociliary epithelia. *Development (Cambridge)*, 142(13), 2352–2363. <https://doi.org/10.1242/dev.118679>
- Coleman, A. T., Jackson, D. J., Gangnon, R. E., Evans, M. D., Lemanske, R. F., & Gern, J. E. (2015). Comparison of risk factors for viral and nonviral asthma exacerbations. *Journal of Allergy and Clinical Immunology*, 136(4), 1127–1129.e4. <https://doi.org/10.1016/j.jaci.2015.05.038>
- Collinson, J. M., Quinn, J. C., Hill, R. E., & West, J. D. (2003). The roles of Pax6 in the cornea, retina, and olfactory epithelium of the developing mouse embryo. *Developmental Biology*, 255(2), 303–312.

[https://doi.org/10.1016/S0012-1606\(02\)00095-7](https://doi.org/10.1016/S0012-1606(02)00095-7)

- Cooney, R. A., Saal, M. L., Geraci, K. P., Maynard, C., Cleaver, O., Hoang, O. N., Moore, T. T., Hwang, R. F., Axelrod, J. D., & Vldar, E. K. (2023). A WNT4 and DKK3 driven canonical to noncanonical Wnt signaling switch controls multiciliogenesis. *Journal of Cell Science*. <https://doi.org/10.1242/jcs.260807>
- Coraux, C., Roux, J., Jolly, T., & Birembaut, P. (2008). Epithelial Cell-Extracellular Matrix Interactions and Stem Cells in Airway Epithelial Regeneration. *Proceedings of the American Thoracic Society*, 5(6), 689–694. <https://doi.org/10.1513/pats.200801-010AW>
- Dabbagh, K., Takeyama, K., Lee, H.-M., Ueki, I. F., Lausier, J. A., & Nadel, J. A. (1999). IL-4 Induces Mucin Gene Expression and Goblet Cell Metaplasia In Vitro and In Vivo. *The Journal of Immunology*, 162(10), 6233–6237. <https://doi.org/10.4049/jimmunol.162.10.6233>
- Dang, T. P., Eichenberger, S., Gonzalez, A., Olson, S., & Carbone, D. P. (2003). Constitutive activation of Notch3 inhibits terminal epithelial differentiation in lungs of transgenic mice. *Oncogene*, 22(13), 1988–1997. <https://doi.org/10.1038/sj.onc.1206230>
- Dann, E., Henderson, N. C., Teichmann, S. A., Morgan, M. D., & Marioni, J. C. (2022). Differential abundance testing on single-cell data using k-nearest neighbor graphs. *Nature Biotechnology*, 40(2), 245–253. <https://doi.org/10.1038/s41587-021-01033-z>
- Deprez, M., Zaragosi, L. E., Truchi, M., Becavin, C., García, S. R., Arguel, M. J., Plaisant, M., Magnone, V., Lebrigand, K., Abelanet, S., Brau, F., Paquet, A., Pe'er, D., Marquette, C. H., Leroy, S., & Barbry, P. (2020). A single-cell atlas of the human healthy airways. *American Journal of Respiratory and Critical Care Medicine*, 202(12), 1636–1645. <https://doi.org/10.1164/rccm.201911-2199OC>
- Dickey, B. F. (2012). Walking on Solid Ground. *Science*, 337(6097), 924–925. <https://doi.org/10.1126/science.1227091>
- Didon, L., Zwick, R. K., Chao, I. W., Walters, M. S., Wang, R., Hackett, N. R., & Crystal, R. G. (2013). RFX3 Modulation of FOXJ1 regulation of cilia genes in the human airway epithelium. *Respiratory Research*, 14(1), 1–13. <https://doi.org/10.1186/1465-9921-14-70/FIGURES/7>
- Doornbos, C., & Roepman, R. (2021). Moonlighting of mitotic regulators in cilium disassembly. *Cellular and Molecular Life Sciences*, 78(11), 4955–4972. <https://doi.org/10.1007/s00018-021-03827-5>
- Doudna, J. A., & Charpentier, E. (2014). The new frontier of genome engineering with CRISPR-Cas9. *Science*, 346(6213). <https://doi.org/10.1126/SCIENCE.1258096>
- Durmowicz, A. G., Lim, R., Rogers, H., Rosebraugh, C. J., & Chowdhury, B. A. (2018). The U.S. food and drug administration's experience with ivacaftor in cystic fibrosis: Establishing efficacy using in vitro data in lieu of a clinical trial. In *Annals of the American Thoracic Society* (Vol. 15, Issue 1, pp. 1–2). American Thoracic Society. <https://doi.org/10.1513/AnnalsATS.201708-668PS>
- El Zein, L., Ait-Lounis, A., Morlé, L., Thomas, J., Chhin, B., Spassky, N., Reith, W., & Durand, B. (2009). RFX3 governs growth and beating efficiency of motile cilia in mouse and controls the expression of genes involved in human ciliopathies. *Journal of Cell Science*, 122(17), 3180–3189. <https://doi.org/10.1242/jcs.048348>
- Elgeti, J., & Gompper, G. (2013). Emergence of metachronal waves in cilia arrays. *Proceedings of the National Academy of Sciences*, 110(12), 4470–4475. <https://doi.org/10.1073/pnas.1218869110>
- Engelhardt, J. F., Zepeda, M., Cohn, J. A., Yankaskas, J. R., & Wilson, J. M. (1994). Expression of the cystic fibrosis gene in adult human lung. *Journal of Clinical Investigation*, 93(2), 737–749. <https://doi.org/10.1172/JCI117028>

- Evans, M. J., Cox, R. A., Shami, S. G., Wilson, B., & Plopper, C. G. (1989). The role of basal cells in attachment of columnar cells to the basal lamina of the trachea. *American Journal of Respiratory Cell and Molecular Biology*, 1(6), 463–469. <https://doi.org/10.1165/ajrcmb.1.6.463>
- Evans, T. I. A., Joo, N. S., Keiser, N. W., Yan, Z., Tyler, S. R., Xie, W., Zhang, Y., Hsiao, J. J., Cho, H. J., Wright, M. E., Wine, J. J., & Engelhardt, J. F. (2016). Glandular proteome identifies antiprotease cystatin c as a critical modulator of airway hydration and clearance. *American Journal of Respiratory Cell and Molecular Biology*, 54(4), 469–481. <https://doi.org/10.1165/rcmb.2015-0090OC>
- Everman, J. L., Rios, C., & Seibold, M. A. (2018). *Utilization of Air–Liquid Interface Cultures as an In Vitro Model to Assess Primary Airway Epithelial Cell Responses to the Type 2 Cytokine Interleukin-13* (pp. 419–432). [https://doi.org/10.1007/978-1-4939-7896-0\\_30](https://doi.org/10.1007/978-1-4939-7896-0_30)
- Fahy, J. V. (2015). Type 2 inflammation in asthma—present in most, absent in many. *Nature Reviews Immunology*, 15(1), 57–65. <https://doi.org/10.1038/nri3786>
- Fahy, J. V., & Dickey, B. F. (2010). Airway Mucus Function and Dysfunction. *New England Journal of Medicine*, 363(23), 2233–2247. <https://doi.org/10.1056/nejmra0910061>
- Falvo, D. J., Grimont, A., Zumbo, P., Fall, W. B., Yang, J. L., Osterhoudt, A., Pan, G., Rendeiro, A. F., Meng, Y., Wilkinson, J. E., DüNDAR, F., Elemento, O., Yantiss, R. K., Hissong, E., Koche, R., Betel, D., & Chandwani, R. (2023). A reversible epigenetic memory of inflammatory injury controls lineage plasticity and tumor initiation in the mouse pancreas. *Developmental Cell*, 58(24), 2959–2973.e7. <https://doi.org/10.1016/j.DEVCEL.2023.11.008>
- Farquhar, M. G., & Palade, G. E. (1963). Junctional complexes in various epithelia. *The Journal of Cell Biology*, 17, 375–412. <https://doi.org/10.1083/jcb.17.2.375>
- Forteza, R. M., Casalino-Matsuda, S. M., Falcon, N. S., Gattas, M. V., & Monzon, M. E. (2012). Hyaluronan and layilin mediate loss of airway epithelial barrier function induced by cigarette smoke by decreasing. *Journal of Biological Chemistry*, 287(50), 42288–42298. <https://doi.org/10.1074/jbc.M112.387795>
- Fossum, S. L., Mutolo, M. J., Tugores, A., Ghosh, S., Randell, S. H., Jones, L. C., Leir, S. H., & Harris, A. (2017). Ets homologous factor (EHF) has critical roles in epithelial dysfunction in airway disease. *Journal of Biological Chemistry*, 292(26), 10938–10949. <https://doi.org/10.1074/jbc.M117.775304>
- Freishtat, R. J., Watson, A. M., Benton, A. S., Iqbal, S. F., Pillai, D. K., Rose, M. C., & Hoffman, E. P. (2011). Asthmatic airway epithelium is intrinsically inflammatory and mitotically dyssynchronous. *American Journal of Respiratory Cell and Molecular Biology*, 44(6), 863–869. <https://doi.org/10.1165/rcmb.2010-0029OC>
- Gadye, L., Das, D., Sanchez, M. A., Street, K., Baudhuin, A., Wagner, A., Cole, M. B., Choi, Y. G., Yosef, N., Purdom, E., Dudoit, S., Risso, D., Ngai, J., & Fletcher, R. B. (2017). Injury Activates Transient Olfactory Stem Cell States with Diverse Lineage Capacities. *Cell Stem Cell*, 21(6), 775–790.e9. <https://doi.org/10.1016/j.stem.2017.10.014>
- Gajjala, P. R., & Madala, S. K. (2021). Notch3: A new culprit in fibrotic lung disease. In *American Journal of Respiratory Cell and Molecular Biology* (Vol. 64, Issue 4, pp. 403–404). American Thoracic Society. <https://doi.org/10.1165/rcmb.2021-0024ED>
- Gao, W., Kanagarajah, K. R., Graham, E., Soon, K., Veres, T., Moraes, T. J., Bear, C. E., Veldhuizen, R. A., Wong, A. P., & Günther, A. (2023). Collagen Tubular Airway-on-Chip for Extended Epithelial Culture and Investigation of Ventilation Dynamics. *BioRxiv*, 1–26. <https://doi.org/10.1002/sml.202309270>

- Gauvreau, G. M., Boulet, L. P., Cockcroft, D. W., Fitzgerald, J. M., Carlsten, C., Davis, B. E., Deschesnes, F., Duong, M., Durn, B. L., Howie, K. J., Hui, L., Kasaian, M. T., Killian, K. J., Strinich, T. X., Watson, R. M., Nathalie, Y., Zhou, S., Raible, D., & O'Byrne, P. M. (2012). Effects of Interleukin-13 Blockade on Allergen-induced Airway Responses in Mild Atopic Asthma. *Https://Doi.Org/10.1164/Rccm.201008-1210OC*, 183(8), 1007–1014. <https://doi.org/10.1164/RCCM.201008-1210OC>
- Gavala, M. L., Bertics, P. J., & Gern, J. E. (2011). Rhinoviruses, allergic inflammation, and asthma. *Immunological Reviews*, 242(1), 69–90. <https://doi.org/10.1111/j.1600-065X.2011.01031.x>
- Gavett, S. H., O'Hearn, D. J., Karp, C. L., Patel, E. A., Schofield, B. H., Finkelman, F. D., & Wills-Karp, M. (1997). Interleukin-4 receptor blockade prevents airway responses induced by antigen challenge in mice. *American Journal of Physiology - Lung Cellular and Molecular Physiology*, 272(2 16-2). <https://doi.org/10.1152/ajplung.1997.272.2.1253>
- Gayoso, A., Lopez, R., Xing, G., Boyeau, P., Valiollah Pour Amiri, V., Hong, J., Wu, K., Jayasuriya, M., Mehlman, E., Langevin, M., Liu, Y., Samaran, J., Misrachi, G., Nazaret, A., Clivio, O., Xu, C., Ashuach, T., Gabitto, M., Lotfollahi, M., ... Yosef, N. (2022). A Python library for probabilistic analysis of single-cell omics data. *Nature Biotechnology* 2022 40:2, 40(2), 163–166. <https://doi.org/10.1038/s41587-021-01206-w>
- Germain, P. L., Robinson, M. D., Lun, A., Garcia Meixide, C., & Macnair, W. (2022). Doublet identification in single-cell sequencing data using scDblFinder. *F1000Research*, 10. <https://doi.org/10.12688/f1000research.73600.2>
- Gern, J. E. (2015). How rhinovirus infections cause exacerbations of asthma. In *Clinical and Experimental Allergy* (Vol. 45, Issue 1, pp. 32–42). John Wiley & Sons, Ltd. <https://doi.org/10.1111/cea.12428>
- Gerovac, B. J., & Fregien, N. L. (2016). IL-13 inhibits multicilin expression and ciliogenesis via janus kinase/signal transducer and activator of transcription independently of notch cleavage. *American Journal of Respiratory Cell and Molecular Biology*, 54(4), 554–561. <https://doi.org/10.1165/rcmb.2015-0227OC>
- Ghosh, M., Helm, K. M., Smith, R. W., Giordanengo, M. S., Li, B., Shen, H., & Reynolds, S. D. (2011). A single cell functions as a tissue-specific stem cell and the in vitro niche-forming cell. *American Journal of Respiratory Cell and Molecular Biology*, 45(3), 459–469. <https://doi.org/10.1165/rcmb.2010-0314OC>
- GINA. (2024). *Global Strategy for Asthma Management and Prevention*.
- Giovannini-Chami, L., Marcet, B., Moreilhon, C., Chevalier, B., Illie, M. I., Lebrigand, K., Robbe-Sermesant, K., Bourrier, T., Michiels, J. F., Mari, B., Crénesse, D., Hofman, P., De Blic, J., Castillo, L., Albertini, M., & Barbry, P. (2012). Distinct epithelial gene expression phenotypes in childhood respiratory allergy. *European Respiratory Journal*, 39(5), 1197–1205. <https://doi.org/10.1183/09031936.00070511>
- Giovannini-Chami, L., Paquet, A., Sanfiorenzo, C., Pons, N., Cazareth, J., Magnone, V., Lebrigand, K., Chevalier, B., Vallauri, A., Julia, V., Marquette, C. H., Marcet, B., Leroy, S., & Barbry, P. (2018). The “one airway, one disease” concept in light of Th2 inflammation. *European Respiratory Journal*, 52(4), 1–12. <https://doi.org/10.1183/13993003.00437-2018>
- Goldfarbmuren, K. C., Jackson, N. D., Sajuthi, S. P., Dyjack, N., Li, K. S., Rios, C. L., Plender, E. G., Montgomery, M. T., Everman, J. L., Bratcher, P. E., Vladar, E. K., & Seibold, M. A. (2020). Dissecting the cellular specificity of smoking effects and reconstructing lineages in the human airway epithelium. *Nature Communications*, 11(1). <https://doi.org/10.1038/s41467-020-16239-z>

- Gomperts, B. N., Kim, L. J., Flaherty, S. A., & Hackett, B. P. (2007). IL-13 regulates cilia loss and foxj1 expression in human airway epithelium. *American Journal of Respiratory Cell and Molecular Biology*, 37(3), 339–346. <https://doi.org/10.1165/rcmb.2006-0400OC>
- Gonzales, K. A. U., Polak, L., Matos, I., Tierney, M. T., Gola, A., Wong, E., Infarinato, N. R., Nikolova, M., Luo, S., Liu, S., Novak, J. S. S., Lay, K., Pasolli, H. A., & Fuchs, E. (2021). Stem cells expand potency and alter tissue fitness by accumulating diverse epigenetic memories. *Science*, 374(6571). <https://doi.org/10.1126/science.abh2444>
- Goodenough, D. A., Goliger, J. A., & Paul, D. L. (1996). Connexins, connexons, and intercellular communication. In *Annual Review of Biochemistry* (Vol. 65, pp. 475–502). <https://doi.org/10.1146/annurev.bi.65.070196.002355>
- Gorojankina, T. (2016). Hedgehog signaling pathway: a novel model and molecular mechanisms of signal transduction. *Cellular and Molecular Life Sciences: CMLS*, 73(7), 1317. <https://doi.org/10.1007/S00018-015-2127-4>
- Goss, A. M., Tian, Y., Tsukiyama, T., Cohen, E. D., Zhou, D., Lu, M. M., Yamaguchi, T. P., & Morrisey, E. E. (2009). Wnt2/2b and  $\beta$ -Catenin Signaling Are Necessary and Sufficient to Specify Lung Progenitors in the Foregut. *Developmental Cell*, 17(2), 290–298. <https://doi.org/10.1016/j.devcel.2009.06.005>
- Gour, N., & Wills-Karp, M. (2015). IL-4 and IL-13 signaling in allergic airway disease. *Cytokine*, 75(1), 68–78. <https://doi.org/10.1016/j.cyto.2015.05.014>
- Gras, D., Bourdin, A., Chanez, P., & Vachier, I. (2011). Airway remodeling in asthma: Clinical and functional correlates. *Medecine/Sciences*, 27(11), 959–965. <https://doi.org/10.1051/medsci/20112711011>
- Gras, D., Bourdin, A., Vachier, I., De Senneville, L., Bonnans, C., & Chanez, P. (2012). An ex vivo model of severe asthma using reconstituted human bronchial epithelium. *Journal of Allergy and Clinical Immunology*, 129(5), 1259–1266.e1. <https://doi.org/10.1016/j.jaci.2012.01.073>
- Gras, D., Chanez, P., Vachier, I., Petit, A., & Bourdin, A. (2013). Bronchial epithelium as a target for innovative treatments in asthma. *Pharmacology and Therapeutics*, 140(3), 290–305. <https://doi.org/10.1016/j.pharmthera.2013.07.008>
- Greenwood, M. F., & Holland, P. (1975). Scanning Electron Microscopic Observations of the Human Respiratory Tract. *American Journal of Diseases of Children*, 129(3), 289–294. <https://doi.org/10.1001/ARCHPEDI.1975.02120400007002>
- Grindley, J. C., Davidson, D. R., & Hill, R. E. (1995). The role of Pax-6 in eye and nasal development. *Development*, 121(5), 1433–1442. <https://doi.org/10.1242/dev.124.8.1433>
- Grünig, G., Warnock, M., Wakil, A. E., Venkayya, R., Brombacher, F., Rennick, D. M., Sheppard, D., Mohrs, M., Donaldson, D. D., Locksley, R. M., & Corry, D. B. (1998). Requirement for IL-13 independently of IL-4 in experimental asthma. *Science*, 281(5399), 2261–2263.
- Guha, A., Deshpande, A., Jain, A., Sebastiani, P., & Cardoso, W. V. (2017). Uroplakin 3a+ Cells Are a Distinctive Population of Epithelial Progenitors that Contribute to Airway Maintenance and Post-injury Repair. *Cell Reports*, 19(2), 246–254. <https://doi.org/10.1016/j.celrep.2017.03.051>
- Gumbiner, B. M. (1993). Breaking through the tight junction barrier. In *Journal of Cell Biology* (Vol. 123, Issue 6 PART 2, pp. 1631–1633). <https://doi.org/10.1083/jcb.123.6.1631>
- Guseh, J. S., Bores, S. A., Stanger, B. Z., Zhou, Q., Anderson, W. J., Melton, D. A., & Rajagopal, J. (2009). Notch signaling promotes airway mucous metaplasia and inhibits alveolar development.

*Development*, 136(10), 1751–1759. <https://doi.org/10.1242/dev.029249>

- Haas, M., Gómez Vázquez, J. L., Sun, D. I., Tran, H. T., Brislinger, M., Tasca, A., Shomroni, O., Vleminckx, K., & Walentek, P. (2019).  $\Delta$ N-Tp63 Mediates Wnt/ $\beta$ -Catenin-Induced Inhibition of Differentiation in Basal Stem Cells of Mucociliary Epithelia. *Cell Reports*, 28(13), 3338–3352.e6. <https://doi.org/10.1016/j.celrep.2019.08.063>
- Hackett, N. R., Shaykhiev, R., Walters, M. S., Wang, R., Zwick, R. K., Ferris, B., Witover, B., Salit, J., & Crystal, R. G. (2011). The human airway epithelial basal cell transcriptome. *PLoS ONE*, 6(5). <https://doi.org/10.1371/journal.pone.0018378>
- Hackett, T. L., De Bruin, H. G., Shaheen, F., Van Den Berge, M., Van Oosterhout, A. J., Postma, D. S., & Heijink, I. H. (2013). Caveolin-1 controls airway epithelial barrier function implications for asthma. *American Journal of Respiratory Cell and Molecular Biology*, 49(4), 662–671. <https://doi.org/10.1165/rcmb.2013-0124OC>
- Hammad, H., & Lambrecht, B. N. (2021). The basic immunology of asthma. In *Cell* (Vol. 184, Issue 6, pp. 1469–1485). <https://doi.org/10.1016/j.cell.2021.02.016>
- Hancock, L. A., Hennessy, C. E., Solomon, G. M., Dobrinskikh, E., Estrella, A., Hara, N., Hill, D. B., Kissner, W. J., Markovetz, M. R., Grove Villalon, D. E., Voss, M. E., Tearney, G. J., Carroll, K. S., Shi, Y., Schwarz, M. I., Thelin, W. R., Rowe, S. M., Yang, I. V, Evans, C. M., & Schwartz, D. A. (2018). Muc5b overexpression causes mucociliary dysfunction and enhances lung fibrosis in mice. *Nature Communications*, 9(1). <https://doi.org/10.1038/s41467-018-07768-9>
- Hao, Y., Hao, S., Andersen-Nissen, E., Mauck, W. M., Zheng, S., Butler, A., Lee, M. J., Wilk, A. J., Darby, C., Zager, M., Hoffman, P., Stoeckius, M., Papalexi, E., Mimitou, E. P., Jain, J., Srivastava, A., Stuart, T., Fleming, L. M., Yeung, B., ... Satija, R. (2021). Integrated analysis of multimodal single-cell data. *Cell*, 184(13), 3573–3587.e29. <https://doi.org/10.1016/j.cell.2021.04.048>
- Hartl, D., Tirouvanziam, R., Laval, J., Greene, C. M., Habieli, D., Sharma, L., Yildirim, A. Ö., Dela Cruz, C. S., & Hogaboam, C. M. (2018). Innate Immunity of the Lung: From Basic Mechanisms to Translational Medicine. In *Journal of Innate Immunity* (Vol. 10, Issues 5–6, pp. 487–501). <https://doi.org/10.1159/000487057>
- He, P., Lim, K., Sun, D., Pett, J. P., Jeng, Q., Polanski, K., Dong, Z., Bolt, L., Richardson, L., Mamanova, L., Dabrowska, M., Wilbrey-Clark, A., Madisson, E., Tuong, Z. K., Dann, E., Suo, C., Kai'En, I. G., He, X., Barker, R. A., ... Rawlins, E. L. (2022). A human fetal lung cell atlas uncovers proximal-distal gradients of differentiation and key regulators of epithelial fates. *Cell*, 185(25), 4841–4860.e25. <https://doi.org/10.1016/j.cell.2022.11.005>
- Heaton, H., Talman, A. M., Knights, A., Imaz, M., Gaffney, D. J., Durbin, R., Hemberg, M., & Lawnczak, M. K. N. (2020). Souporecell: robust clustering of single-cell RNA-seq data by genotype without reference genotypes. *Nature Methods*, 17(6), 615–620. <https://doi.org/10.1038/S41592-020-0820-1>
- Herfs, M., Hubert, P., Poirrier, A.-L., Vandevenne, P., Renoux, V., Habraken, Y., Cataldo, D., Boniver, J., & Delvenne, P. (2012). Proinflammatory Cytokines Induce Bronchial Hyperplasia and Squamous Metaplasia in Smokers. *American Journal of Respiratory Cell and Molecular Biology*, 47(1), 67–79. <https://doi.org/10.1165/rcmb.2011-0353OC>
- Herriges, M., & Morrisey, E. E. (2014). Lung development: Orchestrating the generation and regeneration of a complex organ. In *Development (Cambridge)* (Vol. 141, Issue 3, pp. 502–513). The Company of Biologists. <https://doi.org/10.1242/dev.098186>
- Hewitt, R. J., & Lloyd, C. M. (2021). Regulation of immune responses by the airway epithelial cell

- landscape. *Nature Reviews Immunology*, 21(6), 347–362. <https://doi.org/10.1038/s41577-020-00477-9>
- Hill, D. B., Button, B., Rubinstein, M., & Boucher, R. C. (2022). Physiology and pathophysiology of human airway mucus. *Physiological Reviews*, 102(4), 1757–1836. <https://doi.org/10.1152/physrev.00004.2021>
- Hogan, B. L. M., Barkauskas, C. E., Chapman, H. A., Epstein, J. A., Jain, R., Hsia, C. C. W., Niklason, L., Calle, E., Le, A., Randell, S. H., Rock, J., Snitow, M., Krummel, M., Stripp, B. R., Vu, T., White, E. S., Whitsett, J. A., & Morrisey, E. E. (2014). Repair and Regeneration of the Respiratory System: Complexity, Plasticity, and Mechanisms of Lung Stem Cell Function. *Cell Stem Cell*, 15(2), 123–138. <https://doi.org/10.1016/j.stem.2014.07.012>
- Hong, K. U., Reynolds, S. D., Giangreco, A., Hurley, C. M., & Stripp, B. R. (2001). Clara Cell Secretory Protein–Expressing Cells of the Airway Neuroepithelial Body Microenvironment Include a Label-Retaining Subset and Are Critical for Epithelial Renewal after Progenitor Cell Depletion. *American Journal of Respiratory Cell and Molecular Biology*, 24(6), 671–681. <https://doi.org/10.1165/ajrcmb.24.6.4498>
- Huang, Y., McCarthy, D. J., & Stegle, O. (2019). Vireo: Bayesian demultiplexing of pooled single-cell RNA-seq data without genotype reference. *Genome Biology*, 20(1), 1–12. <https://doi.org/10.1186/S13059-019-1865-2/FIGURES/4>
- Huangfu, D., Liu, A., Rakeman, A. S., Murcia, N. S., Niswander, L., & Anderson, K. V. (2003). Hedgehog signalling in the mouse requires intraflagellar transport proteins. *Nature* 2003 426:6962, 426(6962), 83–87. <https://doi.org/10.1038/nature02061>
- Jackson, N. D., Everman, J. L., Chioccioli, M., Feriani, L., Goldfarbmuren, K. C., Sajuthi, S. P., Rios, C. L., Powell, R., Armstrong, M., Gomez, J., Michel, C., Eng, C., Oh, S. S., Rodriguez-Santana, J., Cicuta, P., Reisdorph, N., Burchard, E. G., & Seibold, M. A. (2020). Single-Cell and Population Transcriptomics Reveal Pan-epithelial Remodeling in Type 2-High Asthma. *Cell Reports*, 32(1). <https://doi.org/10.1016/j.celrep.2020.107872>
- Jain, R., Pan, J., Driscoll, J. A., Wisner, J. W., Huang, T., Gunsten, S. P., You, Y., & Brody, S. L. (2010). Temporal Relationship between Primary and Motile Ciliogenesis in Airway Epithelial Cells. *American Journal of Respiratory Cell and Molecular Biology*, 43(6), 731–739. <https://doi.org/10.1165/rcmb.2009-0328OC>
- Jakiela, B., Gielicz, A., Plutecka, H., Hubalewska-Mazgaj, M., Mastalerz, L., Bochenek, G., Soja, J., Januszek, R., Aab, A., Musial, J., Akdis, M., Akdis, C. A., & Sanak, M. (2014). Th2-type cytokine-induced mucus metaplasia decreases susceptibility of human bronchial epithelium to rhinovirus infection. *American Journal of Respiratory Cell and Molecular Biology*, 51(2), 229–241. <https://doi.org/10.1165/rcmb.2013-0395OC>
- Jakiela, B., Rebane, A., Soja, J., Bazan-Socha, S., Laanesoo, A., Plutecka, H., Surmiak, M., Sanak, M., Sladek, K., & Bochenek, G. (2021). Remodeling of bronchial epithelium caused by asthmatic inflammation affects its response to rhinovirus infection. *Scientific Reports*, 11(1), 12821. <https://doi.org/10.1038/s41598-021-92252-6>
- Jaramillo, A. M., Azzegagh, Z., Tuvim, M. J., & Dickey, B. F. (2018). Airway mucin secretion. *Annals of the American Thoracic Society*, 15, S164–S170. <https://doi.org/10.1513/AnnalsATS.201806-371AW>
- Jesenak, M., Durdik, P., Oppova, D., Franova, S., Diamant, Z., Golebski, K., Banovcin, P., Vojtkova, J., & Novakova, E. (2023). Dysfunctional mucociliary clearance in asthma and airway remodeling – New insights into an old topic. *Respiratory Medicine*, 107372. <https://doi.org/10.1016/j.rmed.2023.107372>

- Jones, K. G., Holland, J. F., Foureman, G. L., Bend, J. R., & Fouts, J. R. (1983). Xenobiotic metabolism in Clara cells and alveolar type II cells isolated from lungs of rats treated with  $\beta$ -naphthoflavone. *Journal of Pharmacology and Experimental Therapeutics*, *225*(2), 316–319.
- Junttila, I. S. (2018). Tuning the cytokine responses: An update on interleukin (IL)-4 and IL-13 receptor complexes. *Frontiers in Immunology*, *9*(JUN), 338745. <https://doi.org/10.3389/FIMMU.2018.00888/BIBTEX>
- Kaer, L. Van, Ashton-Rickardt, P. G., Ploegh, H. L., & Tonegawa, S. (1992). TAP1 mutant mice are deficient in antigen presentation, surface class I molecules, and CD4-8+ T cells. *Cell*, *71*(7), 1205–1214. [https://doi.org/10.1016/S0092-8674\(05\)80068-6](https://doi.org/10.1016/S0092-8674(05)80068-6)
- Kageyama, T., Ito, T., Tanaka, S., & Nakajima, H. (2024). Physiological and immunological barriers in the lung. *Seminars in Immunopathology*, *0123456789*. <https://doi.org/10.1007/s00281-024-01003-y>
- Kaya-Okur, H. S., Janssens, D. H., Henikoff, J. G., Ahmad, K., & Henikoff, S. (2020). Efficient low-cost chromatin profiling with CUT&Tag. *Nature Protocols*, *15*(10), 3264–3283. <https://doi.org/10.1038/s41596-020-0373-x>
- Kaya-Okur, H. S., Wu, S. J., Codomo, C. A., Pledger, E. S., Bryson, T. D., Henikoff, J. G., Ahmad, K., & Henikoff, S. (2019). CUT&Tag for efficient epigenomic profiling of small samples and single cells. *Nature Communications*, *10*(1). <https://doi.org/10.1038/S41467-019-09982-5>
- Keeling, J., Tsiokas, L., & Maskey, D. (2016). Cellular mechanisms of ciliary length control. *Cells*, *5*(1). <https://doi.org/10.3390/cells5010006>
- Kiyokawa, H., Yamaoka, A., Matsuoka, C., Tokuhara, T., Abe, T., & Morimoto, M. (2021). Airway basal stem cells reutilize the embryonic proliferation regulator, Tgf $\beta$ -Id2 axis, for tissue regeneration. *Developmental Cell*, *56*(13), 1917-1929.e9. <https://doi.org/10.1016/j.devcel.2021.05.016>
- Klein, H.-U. (2023). demuxmix: demultiplexing oligonucleotide-barcoded single-cell RNA sequencing data with regression mixture models. *Bioinformatics*, *39*(8). <https://doi.org/10.1093/bioinformatics/btad481>
- Koh, K. D., Bonser, L. R., Eckalbar, W. L., Yizhar-Barnea, O., Shen, J., Zeng, X., Hargett, K. L., Sun, D. I., Zlock, L. T., Finkbeiner, W. E., Ahituv, N., & Erle, D. J. (2023). Genomic characterization and therapeutic utilization of IL-13-responsive sequences in asthma. *Cell Genomics*, *3*(1), 100229. <https://doi.org/10.1016/j.xgen.2022.100229>
- Koh, K. D., Siddiqui, S., Cheng, D., Bonser, L. R., Sun, D. I., Zlock, L. T., Finkbeiner, W. E., Woodruff, P. G., & Erle, D. J. (2020). Efficient RNP-directed human gene targeting reveals SPDEF is required for IL-13-induced mucostasis. *American Journal of Respiratory Cell and Molecular Biology*, *62*(3), 373–381. [https://doi.org/10.1165/RCMB.2019-0266OC/SUPPL\\_FILE/DISCLOSURES.PDF](https://doi.org/10.1165/RCMB.2019-0266OC/SUPPL_FILE/DISCLOSURES.PDF)
- Konkimalla, A., Tata, A., & Tata, P. R. (2022). Lung Regeneration: Cells, Models, and Mechanisms. *Cold Spring Harbor Perspectives in Biology*, *14*(10), 1–24. <https://doi.org/10.1101/cshperspect.a040873>
- Kopf, M., Le Grost, G., Bachmann, M., Lamers, M. C., Bluethmann, H., & Köhler, G. (1993). Disruption of the murine IL-4 gene blocks Th2 cytokine responses. *Nature*, *362*(March), 245–248.
- Koppelman, G. H., Kersten, E. T. G., Pett, J. P., Malmström, K., Chun, Y., Jonker, M., Wilbrey-Clark, A., Worlock, K. B., Van den Berge, M., Vermeulen, R., Vonk, J., Sebire, N., Louhi, J., Timens, W., Teichmann, S., Bunyavanich, S., Nikolic, M., Nawijn, M. C., Mäkelä, M., & Meyer, K. (2024). Childhood-onset Asthma Is Characterized by Airway Epithelial Hillock-to-Squamous Differentiation in Early Life. *D101. UNCOVERING THE METABOLIC AND GENETIC UNSOLVED MYSTERIES IN ASTHMA*, A7286–A7286. <https://doi.org/10.1164/ajrccm->



conference.2024.209.1\_MeetingAbstracts.A7286

- Koretzky, G., Farrar, J. D., Asnagli, H., & Murphy, K. M. (2002). T helper subset development: roles of instruction, selection, and transcription. *The Journal of Clinical Investigation*, *109*(4), 431–435. <https://doi.org/10.1172/JCI15093>
- Kotton, D. N., & Morrisey, E. E. (2014). Lung regeneration: Mechanisms, applications and emerging stem cell populations. *Nature Medicine*, *20*(8), 822–832. <https://doi.org/10.1038/nm.3642>
- Kugler, M. C., Joyner, A. L., Loomis, C. A., & Munger, J. S. (2015). Sonic Hedgehog Signaling in the Lung. From Development to Disease. *American Journal of Respiratory Cell and Molecular Biology*, *52*(1), 1–13. <https://doi.org/10.1165/rcmb.2014-0132TR>
- Kuo, C., Lim, S., King, N. J. C., Bartlett, N. W., Walton, R. P., Zhu, J., Glanville, N., Aniscenko, J., Johnston, S. L., Burgess, J. K., Black, J. L., & Oliver, B. G. (2011). Rhinovirus infection induces expression of airway remodelling factors in vitro and in vivo. *Respirology*, *16*(2), 367–377. <https://doi.org/10.1111/J.1440-1843.2010.01918.X>
- Kuperman, D. A., Huang, X., Koth, L. L., Chang, G. H., Dolganov, G. M., Zhu, Z., Elias, J. A., Sheppard, D., & Erle, D. J. (2002). Direct effects of interleukin-13 on epithelial cells cause airway hyperreactivity and mucus overproduction in asthma. *Nature Medicine*, *8*(8), 885–889. <https://doi.org/10.1038/nm734>
- Kurche, J. S., Cool, C. D., Blumhagen, R. Z., Dobrinskikh, E., Heinz, D., Herrera, J. A., Yang, I. V., & Schwartz, D. A. (2024). MUC5B IPF Risk Variant Promotes a Muco-Secretory Phenotype and Loss of Small Airway Secretory Cells. <https://doi.org/10.1164/Rccm.202311-2111LE>
- Kyrousi, C., Arbi, M., Pilz, G.-A., Pefani, D.-E., Lalioti, M.-E., Ninkovic, J., Götz, M., Lygerou, Z., & Taraviras, S. (2015). Mcidas and GemC1/Lynkeas are key regulators for the generation of multiciliated ependymal cells in the adult neurogenic niche. *Development*. <https://doi.org/10.1242/dev.126342>
- La Manno, G., Soldatov, R., Zeisel, A., Braun, E., Hochgerner, H., Petukhov, V., Lidschreiber, K., Kastrioti, M. E., Lönnerberg, P., Furlan, A., Fan, J., Borm, L. E., Liu, Z., van Bruggen, D., Guo, J., He, X., Barker, R., Sundström, E., Castelo-Branco, G., ... Kharchenko, P. V. (2018). RNA velocity of single cells. *Nature*, *560*(7719), 494–498. <https://doi.org/10.1038/s41586-018-0414-6>
- Lafkas, D., Shelton, A., Chiu, C., De Leon Boenig, G., Chen, Y., Stawicki, S. S., Siltanen, C., Reichelt, M., Zhou, M., Wu, X., Eastham-Anderson, J., Moore, H., Roose-Girma, M., Chinn, Y., Hang, J. Q., Warming, S., Egen, J., Lee, W. P., Austin, C., ... Siebel, C. W. (2015). Therapeutic antibodies reveal Notch control of transdifferentiation in the adult lung. *Nature*, *528*(7580), 127–131. <https://doi.org/10.1038/nature15715>
- Lange, M., Bergen, V., Klein, M., Setty, M., Reuter, B., Bakhti, M., Lickert, H., Ansari, M., Schniering, J., Schiller, H. B., Pe'er, D., & Theis, F. J. (2022). CellRank for directed single-cell fate mapping. *Nature Methods* *2022* *19*:2, *19*(2), 159–170. <https://doi.org/10.1038/s41592-021-01346-6>
- Laoukili, J., Perret, E., Willems, T., Minty, A., Parthoens, E., Houcine, O., Coste, A., Jorissen, M., Marano, F., Caput, D., & Tournier, F. (2001). IL-13 alters mucociliary differentiation and ciliary beating of human respiratory epithelial cells. *Journal of Clinical Investigation*, *108*(12), 1817–1824. <https://doi.org/10.1172/JCI200113557>
- Lavoie, H., Gagnon, J., & Therrien, M. (2020). ERK signalling: a master regulator of cell behaviour, life and fate. *Nature Reviews Molecular Cell Biology*, *21*(10), 607–632. <https://doi.org/10.1038/s41580-020-0255-7>

- Leach, J. P., & Morrisey, E. E. (2018). Repairing the lungs one breath at a time: How dedicated or facultative are you? *Genes and Development*, 32(23–24), 1461–1471. <https://doi.org/10.1101/gad.319418.118>
- Lee, J., Lecher, J. C., Parigoris, E., Shinagawa, N., & Sentosa, J. (2024). Stably-Inverted Apical-Out Human Upper Airway Organoids for SARS-CoV-2 Infection and Therapeutic Testing. *BioRxiv*.
- Legaki, E., Arsenis, C., Taka, S., & Papadopoulos, N. G. (2022). DNA methylation biomarkers in asthma and rhinitis: Are we there yet? *Clinical and Translational Allergy*, 12(3), e12131. <https://doi.org/10.1002/CLT2.12131>
- Legendre, M., Zaragosi, L. E., & Mitchison, H. M. (2021). Motile cilia and airway disease. *Seminars in Cell and Developmental Biology*, 110(September), 19–33. <https://doi.org/10.1016/j.semcdb.2020.11.007>
- León, B. (2023). A model of Th2 differentiation based on polarizing cytokine repression. *Trends in Immunology*, 44(6), 399–407. <https://doi.org/10.1016/j.it.2023.04.004>
- Li, C., Li, A., Li, M., Xing, Y., Chen, H., Hu, L., Tiozzo, C., Anderson, S., Taketo, M. M., & Minoo, P. (2009). Stabilized  $\beta$ -catenin in lung epithelial cells changes cell fate and leads to tracheal and bronchial polyposis. *Developmental Biology*, 334(1), 97–108. <https://doi.org/10.1016/j.ydbio.2009.07.021>
- Li, M., Wetzel-Strong, S. E., Hua, X., Tilley, S. L., Oswald, E., Krummel, M. F., & Caron, K. M. (2014). Deficiency of RAMP1 Attenuates Antigen-Induced Airway Hyperresponsiveness in Mice. *PLOS ONE*, 9(7), e102356. <https://doi.org/10.1371/JOURNAL.PONE.0102356>
- Li, Y., Martin, L. D., Spizz, G., & Adler, K. B. (2001). MARCKS Protein Is a Key Molecule Regulating Mucin Secretion by Human Airway Epithelial Cells in Vitro. *Journal of Biological Chemistry*, 276(44), 40982–40990. <https://doi.org/10.1074/jbc.M105614200>
- Liang, Y., Meng, D., Zhu, B., & Pan, J. (2016). Mechanism of ciliary disassembly. *Cellular and Molecular Life Sciences*, 73(9), 1787–1802. <https://doi.org/10.1007/s00018-016-2148-7>
- Lim, K., Donovan, A. P. A., Tang, W., Sun, D., He, P., Pett, J. P., Teichmann, S. A., Marioni, J. C., Meyer, K. B., Brand, A. H., & Rawlins, E. L. (2023). Organoid modeling of human fetal lung alveolar development reveals mechanisms of cell fate patterning and neonatal respiratory disease. *Cell Stem Cell*, 30(1), 20–37.e9. <https://doi.org/10.1016/j.stem.2022.11.013>
- Lin, B., Shah, V. S., Chernoff, C., Sun, J., Shipkovenska, G. G., Vinarsky, V., Waghray, A., Xu, J., Leduc, A. D., Hintschich, C. A., Surve, M. V., Xu, Y., Capen, D. E., Villoria, J., Dou, Z., Hariri, L. P., & Rajagopal, J. (2024). Airway hillocks are injury-resistant reservoirs of unique plastic stem cells. *Nature*, 629(8013), 869–877. <https://doi.org/10.1038/s41586-024-07377-1>
- Lindhout, F. W., Cao, Y., Kevenaar, J. T., Bodzeta, A., Stucchi, R., Boumpoutsari, M. M., Katrukha, E. A., Altelaar, M., MacGillavry, H. D., & Hoogenraad, C. C. (2019). VAP-SCRN1 interaction regulates dynamic endoplasmic reticulum remodeling and presynaptic function. *The EMBO Journal*, 38(20). <https://doi.org/10.15252/emj.2018101345>
- Liu, J., Xiao, Q., Xiao, J., Niu, C., Li, Y., Zhang, X., Zhou, Z., Shu, G., & Yin, G. (2022). Wnt/ $\beta$ -catenin signalling: function, biological mechanisms, and therapeutic opportunities. *Signal Transduction and Targeted Therapy*, 7(1). <https://doi.org/10.1038/s41392-021-00762-6>
- Looi, K., Buckley, A. G., Rigby, P. J., Garratt, L. W., Iosifidis, T., Zosky, G. R., Larcombe, A. N., Lannigan, F. J., Ling, K. M., Martinovich, K. M., Kicic-Starcevic, E., Shaw, N. C., Sutanto, E. N., Knight, D. A., Kicic, A., & Stick, S. M. (2018). Effects of human rhinovirus on epithelial barrier integrity and function in children with asthma. *Clinical and Experimental Allergy*, 48(5), 513–524. <https://doi.org/10.1111/cea.13097>

- Lopez-Guisa, J. M., Powers, C., File, D., Cochrane, E., Jimenez, N., & Debley, J. S. (2012). Airway epithelial cells from asthmatic children differentially express proremodeling factors. *Journal of Allergy and Clinical Immunology*, *129*(4), 990-997.e6. <https://doi.org/10.1016/j.jaci.2011.11.035>
- Love, M. I., Huber, W., & Anders, S. (2014). Moderated estimation of fold change and dispersion for RNA-seq data with DESeq2. *Genome Biology*, *15*(12), 550. <https://doi.org/10.1186/s13059-014-0550-8>
- Luk, I. Y., Reehorst, C. M., & Mariadason, J. M. (2018). ELF3, ELF5, EHF and SPDEF transcription factors in tissue homeostasis and cancer. *Molecules*, *23*(9), 1–26. <https://doi.org/10.3390/molecules23092191>
- Lynch, T. J., Anderson, P. J., Rotti, P. G., Tyler, S. R., Crooke, A. K., Choi, S. H., Montoro, D. T., Silverman, C. L., Shahin, W., Zhao, R., Jensen-Cody, C. W., Adamcakova-Dodd, A., Evans, T. I. A., Xie, W., Zhang, Y., Mou, H., Herring, B. P., Thorne, P. S., Rajagopal, J., ... Engelhardt, J. F. (2018). Submucosal Gland Myoepithelial Cells Are Reserve Stem Cells That Can Regenerate Mouse Tracheal Epithelium. *Cell Stem Cell*, *22*(5), 653-667.e5. <https://doi.org/10.1016/j.stem.2018.03.017>
- Madisson, E., Oliver, A. J., Kleshchevnikov, V., Wilbrey-Clark, A., Polanski, K., Richoz, N., Ribeiro Orsi, A., Mamanova, L., Bolt, L., Elmentaite, R., Pett, J. P., Huang, N., Xu, C., He, P., Dabrowska, M., Pritchard, S., Tuck, L., Prigmore, E., Perera, S., ... Meyer, K. B. (2023). A spatially resolved atlas of the human lung characterizes a gland-associated immune niche. *Nature Genetics*, *55*(1), 66–77. <https://doi.org/10.1038/s41588-022-01243-4>
- Mahmoudi, T., Li, V. S. W., Ng, S. S., Taouatas, N., Vries, R. G. J., Mohammed, S., Heck, A. J., & Clevers, H. (2009). The kinase TNIK is an essential activator of Wnt target genes. *The EMBO Journal*, *28*(21), 3329–3340. <https://doi.org/10.1038/emboj.2009.285>
- Malleske, D. T., Hayes, D., Lallier, S. W., Hill, C. L., & Reynolds, S. D. (2018). Regulation of Human Airway Epithelial Tissue Stem Cell Differentiation by  $\beta$ -Catenin, P300, and CBP. *Stem Cells*, *36*(12), 1905–1916. <https://doi.org/10.1002/stem.2906>
- Mano, H., Nakatani, S., Kimira, Y., Mano, M., Sekiguchi, Y., Im, R. H., Shimizu, J., & Wada, M. (2015). Age-related decrease of IF5/BTG4 in oral and respiratory cavities in mice. *Bioscience, Biotechnology, and Biochemistry*, *79*(6), 960–968. <https://doi.org/10.1080/09168451.2015.1008976>
- Mao, S., Shah, A. S., Moninger, T. O., Ostedgaard, L. S., Lu, L., Tang, X. X., Thornell, I. M., Reznikov, L. R., Ernst, S. E., Karp, P. H., Tan, P., Keshavjee, S., Alaiwa, M. H. A., & Welsh, M. J. (2018). Motile cilia of human airway epithelia contain hedgehog signaling components that mediate noncanonical hedgehog signaling. *Proceedings of the National Academy of Sciences of the United States of America*, *115*(6), 1370–1375. [https://doi.org/10.1073/PNAS.1719177115/SUPPL\\_FILE/PNAS.1719177115.SM01.AVI](https://doi.org/10.1073/PNAS.1719177115/SUPPL_FILE/PNAS.1719177115.SM01.AVI)
- Marcet, B., Chevalier, B., Coraux, C., Kodjabachian, L., & Barbry, P. (2011). MicroRNA-based silencing of Delta/Notch signaling promotes multiple cilia formation. *Cell Cycle*, *10*(17), 2858–2864. <https://doi.org/10.4161/cc.10.17.17011>
- Marcet, B., Chevalier, B., Luxardi, G., Coraux, C., Zaragosi, L. E., Cibois, M., Robbe-Sermesant, K., Jolly, T., Cardinaud, B., Moreilhon, C., Giovannini-Chami, L., Nawrocki-Raby, B., Birembaut, P., Waldmann, R., Kodjabachian, L., & Barbry, P. (2011). Control of vertebrate multiciliogenesis by miR-449 through direct repression of the Delta/Notch pathway. *Nature Cell Biology*, *13*(6), 693–701. <https://doi.org/10.1038/ncb2241>
- Marshall, C. B., Mays, D. J., Beeler, J. S., Rosenbluth, J. M., Boyd, K. L., Santos Guasch, G. L., Shaver, T. M., Tang, L. J., Liu, Q., Shyr, Y., Venters, B. J., Magnuson, M. A., & Pietenpol, J. A. (2016). P73 Is

- Required for Multiciliogenesis and Regulates the Foxj1-Associated Gene Network. *Cell Reports*, 14(10), 2289–2300. <https://doi.org/10.1016/j.celrep.2016.02.035>
- McCauley, K. B., Kukreja, K., Tovar Walker, A. E., Jaffe, A. B., & Klein, A. M. (2024). A map of signaling responses in the human airway epithelium. *Cell Systems*, 15(4), 307-321.e10. <https://doi.org/10.1016/j.cels.2024.02.005>
- McConnell, A. M., Yao, C., Yeckes, A. R., Wang, Y., Selvaggio, A. S., Tang, J., Kirsch, D. G., & Stripp, B. R. (2016). p53 Regulates Progenitor Cell Quiescence and Differentiation in the Airway. *Cell Reports*, 17(9), 2173–2182. <https://doi.org/10.1016/j.celrep.2016.11.007>
- McCubrey, J. A., Steelman, L. S., Chappell, W. H., Abrams, S. L., Wong, E. W. T., Chang, F., Lehmann, B., Terrian, D. M., Milella, M., Tafuri, A., Stivala, F., Libra, M., Basecke, J., Evangelisti, C., Martelli, A. M., & Franklin, R. A. (2007). Roles of the Raf/MEK/ERK pathway in cell growth, malignant transformation and drug resistance. *Biochimica et Biophysica Acta (BBA) - Molecular Cell Research*, 1773(8), 1263–1284. <https://doi.org/10.1016/J.BBAMCR.2006.10.001>
- McMillan, S. J., & Lloyd, C. M. (2004). Prolonged allergen challenge in mice leads to persistent airway remodelling. *Clinical & Experimental Allergy*, 34(3), 497–507. <https://doi.org/10.1111/J.1365-2222.2004.01895.X>
- McShane, A., Bath, J., Jaramillo, A. M., Ridley, C., Walsh, A. A., Evans, C. M., Thornton, D. J., & Ribbeck, K. (2021). Mucus. *Current Biology*, 31(15), R938–R945. <https://doi.org/10.1016/j.cub.2021.06.093>
- Mercer, R. R., Russell, M. L., Roggli, V. L., & Crapo, J. D. (1994). Cell Number and Distribution in Human and Rat Airways. In *Cell Mol. Biol* (Vol. 10).
- Mercey, O., Al Jord, A., Rostaing, P., Mahuzier, A., Fortoul, A., Boudjema, A. R., Faucourt, M., Spassky, N., & Meunier, A. (2019). Dynamics of centriole amplification in centrosome-depleted brain multiciliated progenitors. *Scientific Reports*, 9(1). <https://doi.org/10.1038/s41598-019-49416-2>
- Mercey, O., Levine, M. S., LoMastro, G. M., Rostaing, P., Brotslaw, E., Gomez, V., Kumar, A., Spassky, N., Mitchell, B. J., Meunier, A., & Holland, A. J. (2019). Massive centriole production can occur in the absence of deuterosomes in multiciliated cells. *Nature Cell Biology*, 21(12), 1544–1552. <https://doi.org/10.1038/s41556-019-0427-x>
- Meyrick, B., Sturgess, J. M., & Reid, L. (1969). A reconstruction of the duct system and secretory tubules of the human bronchial submucosal gland. *Thorax*, 24(6), 729–736. <https://doi.org/10.1136/thx.24.6.729>
- Miller, A. J., Yu, Q., Czerwinski, M., Tsai, Y. H., Conway, R. F., Wu, A., Holloway, E. M., Walker, T., Glass, I. A., Treutlein, B., Camp, J. G., & Spence, J. R. (2020). In Vitro and In Vivo Development of the Human Airway at Single-Cell Resolution. *Developmental Cell*, 53(1), 117-128.e6. <https://doi.org/10.1016/j.devcel.2020.01.033>
- Miller, L.-A. D., Wert, S. E., Clark, J. C., Xu, Y., Perl, A.-K. T., & Whitsett, J. A. (2004). *Role of Sonic hedgehog in Patterning of Tracheal-Bronchial Cartilage and the Peripheral Lung*. <https://doi.org/10.1002/dvdy.20105>
- Mo, Y., Zhang, K., Feng, Y., Yi, L., Liang, Y., Wu, W., Zhao, J., Zhang, Z., Xu, Y., Hu, Q., He, J., & Zhen, G. (2019). Epithelial serpinb10, a novel marker of airway eosinophilia in asthma, contributes to allergic airway inflammation. *American Journal of Physiology - Lung Cellular and Molecular Physiology*, 316(1), L245–L254. <https://doi.org/10.1152/ajplung.00362.2017>
- Montoro, D. T., Haber, A. L., Biton, M., Vinarsky, V., Lin, B., Birket, S. E., Yuan, F., Chen, S., Leung, H. M., Villoria, J., Rogel, N., Burgin, G., Tsankov, A. M., Waghray, A., Slyper, M., Waldman, J., Nguyen, L.,

- Dionne, D., Rozenblatt-Rosen, O., ... Rajagopal, J. (2018). A revised airway epithelial hierarchy includes CFTR-expressing ionocytes. *Nature*, *560*(7718), 319–324. <https://doi.org/10.1038/s41586-018-0393-7>
- Morgenstern, M., Peikert, C. D., Lübbert, P., Suppanz, I., Klemm, C., Alka, O., Steiert, C., Naumenko, N., Schendzielorz, A., Melchionda, L., Mühlhäuser, W. W. D., Knapp, B., Busch, J. D., Stiller, S. B., Dannenmaier, S., Lindau, C., Licheva, M., Eickhorst, C., Galbusera, R., ... Warscheid, B. (2021). Quantitative high-confidence human mitochondrial proteome and its dynamics in cellular context. *Cell Metabolism*, *33*(12), 2464–2483.e18. <https://doi.org/10.1016/j.cmet.2021.11.001>
- Mori, M., Mahoney, J. E., Stupnikov, M. R., Paez-Cortez, J. R., Szymaniak, A. D., Varelas, X., Herrick, D. B., Schwob, J., Zhang, H., & Cardoso, W. V. (2015). Notch3-Jagged signaling controls the pool of undifferentiated airway progenitors. *Development (Cambridge, England)*, *142*(2), 258–267. <https://doi.org/10.1242/dev.116855>
- Morimoto, M., Liu, Z., Cheng, H. T., Winters, N., Bader, D., & Kopan, R. (2010). Canonical Notch signaling in the developing lung is required for determination of arterial smooth muscle cells and selection of Clara versus ciliated cell fate. *Journal of Cell Science*, *123*(2), 213–224. <https://doi.org/10.1242/jcs.058669>
- Morimoto, M., Nishinakamura, R., Saga, Y., & Kopan, R. (2012). Different assemblies of Notch receptors coordinate the distribution of the major bronchial Clara, ciliated and neuroendocrine cells. *Development (Cambridge)*, *139*(23), 4365–4373. <https://doi.org/10.1242/dev.083840>
- Morrissey, E. E., & Hogan, B. L. M. (2010). Preparing for the First Breath: Genetic and Cellular Mechanisms in Lung Development. *Developmental Cell*, *18*(1), 8–23. <https://doi.org/10.1016/j.devcel.2009.12.010>
- Mou, H., Vinarsky, V., Tata, P. R., Brazauskas, K., Choi, S. H., Crooke, A. K., Zhang, B., Solomon, G. M., Turner, B., Bihler, H., Harrington, J., Lapey, A., Channick, C., Keyes, C., Freund, A., Artandi, S., Mense, M., Rowe, S., Engelhardt, J. F., ... Rajagopal, J. (2016). Dual SMAD Signaling Inhibition Enables Long-Term Expansion of Diverse Epithelial Basal Cells. *Cell Stem Cell*, *19*(2), 217–231. <https://doi.org/10.1016/j.stem.2016.05.012>
- Mucenski, M. L., Nation, J. M., Thitoff, A. R., Besnard, V., Xu, Y., Wert, S. E., Harada, N., Taketo, M. M., Stahlman, M. T., & Whitsett, J. A. (2005).  $\beta$ -catenin regulates differentiation of respiratory epithelial cells in vivo. *American Journal of Physiology - Lung Cellular and Molecular Physiology*, *289*(6 33-6), 971–979. <https://doi.org/10.1152/ajplung.00172.2005>
- Naik, S., & Fuchs, E. (2022). Inflammatory memory and tissue adaptation in sickness and in health. In *Nature* (Vol. 607, Issue 7918, pp. 249–255). Springer US. <https://doi.org/10.1038/s41586-022-04919-3>
- Naik, S., Larsen, S. B., Gomez, N. C., Alaverdyan, K., Sandoel, A., Yuan, S., Polak, L., Kulukian, A., Chai, S., & Fuchs, E. (2017). Inflammatory Memory Sensitizes Skin Epithelial Stem Cells to Tissue Damage. *Nature*, *550*(7677), 475. <https://doi.org/10.1038/NATURE24271>
- Narita, K., Nagatomo, H., Kozuka-Hata, H., Oyama, M., & Takeda, S. (2020). Discovery of a Vertebrate-Specific Factor that Processes Flagellar Glycolytic Enolase during Motile Ciliogenesis. *iScience*, *23*(4), 100992. <https://doi.org/10.1016/j.isci.2020.100992>
- Nawroth, J. C., Roth, D., van Schadewijk, A., Ravi, A., Maulana, T. I., Senger, C. N., van Riet, S., Ninaber, D. K., de Waal, A. M., Kraft, D., Hiemstra, P. S., Ryan, A. L., & van der Does, A. M. (2023). Breathing on chip: Dynamic flow and stretch accelerate mucociliary maturation of airway epithelium in vitro. *Materials Today Bio*, *21*, 100713. <https://doi.org/10.1016/j.mtbio.2023.100713>

- Neavin, D., Senabouth, A., Arora, H., Lee, J. T. H., Ripoll-Cladellas, A., Franke, L., Prabhakar, S., Ye, C. J., McCarthy, D. J., Melé, M., Hemberg, M., & Powell, J. E. (2024). Demuxafy: improvement in droplet assignment by integrating multiple single-cell demultiplexing and doublet detection methods. *Genome Biology*, 25(1), 1–24. <https://doi.org/10.1186/S13059-024-03224-8/FIGURES/5>
- Nechipurenko, I. V. (2020). The Enigmatic Role of Lipids in Cilia Signaling. *Frontiers in Cell and Developmental Biology*, 8(August), 1–10. <https://doi.org/10.3389/fcell.2020.00777>
- Nemajerova, A., Kramer, D., Siller, S. S., Herr, C., Shomroni, O., Pena, T., Gallinas Suazo, C., Glaser, K., Wildung, M., Steffen, H., Sriraman, A., Oberle, F., Wienken, M., Hennion, M., Vidal, R., Royen, B., Alevra, M., Schild, D., Bals, R., ... Lizé, M. (2016). TAp73 is a central transcriptional regulator of airway multiciliogenesis. *Genes & Development*, 30(11), 1300–1312. <https://doi.org/10.1101/gad.279836.116>
- Netea, M. G., Domínguez-Andrés, J., Barreiro, L. B., Chavakis, T., Divangahi, M., Fuchs, E., Joosten, L. A. B., van der Meer, J. W. M., Mhlanga, M. M., Mulder, W. J. M., Riksen, N. P., Schlitzer, A., Schultze, J. L., Stabell Benn, C., Sun, J. C., Xavier, R. J., & Latz, E. (2020). Defining trained immunity and its role in health and disease. In *Nature Reviews Immunology* (Vol. 20, Issue 6, pp. 375–388). Nature Publishing Group. <https://doi.org/10.1038/s41577-020-0285-6>
- Nikolić, M. Z., Sun, D., & Rawlins, E. L. (2018). Human lung development: Recent progress and new challenges. In *Development (Cambridge)* (Vol. 145, Issue 16 Special Issue). <https://doi.org/10.1242/dev.163485>
- Okuda, K., Chen, G., Subramani, D. B., Wolf, M., Gilmore, R. C., Kato, T., Radicioni, G., Kesimer, M., Chua, M., Dang, H., Livraghi-Butrico, A., Ehre, C., Doerschuk, C. M., Randell, S. H., Matsui, H., Nagase, T., O’Neal, W. K., & Boucher, R. C. (2019). Localization of Secretory Mucins MUC5AC and MUC5B in Normal/Healthy Human Airways. *American Journal of Respiratory and Critical Care Medicine*, 199(6), 715–727. <https://doi.org/10.1164/rccm.201804-0734OC>
- Ordovas-Montanes, J., Beyaz, S., Rakoff-Nahoum, S., & Shalek, A. K. (2020). Distribution and storage of inflammatory memory in barrier tissues. *Nature Reviews Immunology*, 20(5), 308–320. <https://doi.org/10.1038/s41577-019-0263-z>
- Ordovas-Montanes, J., Dwyer, D. F., Nyquist, S. K., Buchheit, K. M., Vukovic, M., Deb, C., Wadsworth, M. H., Hughes, T. K., Kazer, S. W., Yoshimoto, E., Cahill, K. N., Bhattacharyya, N., Katz, H. R., Berger, B., Laidlaw, T. M., Boyce, J. A., Barrett, N. A., & Shalek, A. K. (2018). Allergic inflammatory memory in human respiratory epithelial progenitor cells. *Nature*, 560(7720), 649–654. <https://doi.org/10.1038/s41586-018-0449-8>
- Pachitariu, M., & Stringer, C. (2022). Cellpose 2.0: how to train your own model. *Nature Methods* 2022 19:12, 19(12), 1634–1641. <https://doi.org/10.1038/s41592-022-01663-4>
- Papi, A., Brightling, C., Pedersen, S. E., & Reddel, H. K. (2018). Asthma. *The Lancet*, 391(10122), 783–800. [https://doi.org/10.1016/S0140-6736\(17\)33311-1](https://doi.org/10.1016/S0140-6736(17)33311-1)
- Paranjapye, A., Mutolo, M. J., Ebron, J. S., Leir, S. H., & Harris, A. (2020). The FOXA1 transcriptional network coordinates key functions of primary human airway epithelial cells. *American Journal of Physiology - Lung Cellular and Molecular Physiology*, 319(1), L126–L136. <https://doi.org/10.1152/ajplung.00023.2020>
- Pardo-Saganta, A., Law, B. M., Gonzalez-Celeiro, M., Vinarsky, V., & Rajagopal, J. (2013). Ciliated cells of pseudostratified airway epithelium do not become mucous cells after ovalbumin challenge. *American Journal of Respiratory Cell and Molecular Biology*, 48(3), 364–373. <https://doi.org/10.1165/rcmb.2012-0146OC>

- Pardo-Saganta, A., Law, B. M., Tata, P. R., Villoria, J., Saez, B., Mou, H., Zhao, R., & Rajagopal, J. (2015). Injury induces direct lineage segregation of functionally distinct airway basal stem/progenitor cell subpopulations. *Cell Stem Cell*, *16*(2), 184–197. <https://doi.org/10.1016/j.stem.2015.01.002>
- Pardo-Saganta, A., Tata, P. R., Law, B. M., Saez, B., Chow, R. D.-W., Prabhu, M., Gridley, T., & Rajagopal, J. (2015). Parent stem cells can serve as niches for their daughter cells. *Nature*, *523*(7562), 597–601. <https://doi.org/10.1038/nature14553>
- Park, K. S., Korfhagen, T. R., Bruno, M. D., Kitzmiller, J. A., Wan, H., Wert, S. E., Khurana Hershey, G. K., Chen, G., & Whitsett, J. A. (2007). SPDEF regulates goblet cell hyperplasia in the airway epithelium. *The Journal of Clinical Investigation*, *117*(4), 978–988. <https://doi.org/10.1172/JCI29176>
- Park, S., Newton, J., Hidjir, T., & Young, E. W. K. (2023). Bidirectional airflow in lung airway-on-a-chip with matrix-derived membrane elicits epithelial glycocalyx formation. *The Royal Society of Chemistry*, *23*(16), 3671–3682. <https://doi.org/10.1039/D3LC00259D>
- Park, T. J., Mitchell, B. J., Abitua, P. B., Kintner, C., & Wallingford, J. B. (2008). Dishevelled controls apical docking and planar polarization of basal bodies in ciliated epithelial cells. *Nature Genetics*, *40*(7), 871–879. <https://doi.org/10.1038/ng.104>
- Parker, J. C., Thavagnanam, S., Skibinski, G., Lyons, J., Bell, J., Heaney, L. G., & Shields, M. D. (2013). Chronic IL9 and IL-13 Exposure Leads to an Altered Differentiation of Ciliated Cells in a Well-Differentiated Paediatric Bronchial Epithelial Cell Model. *PLoS ONE*, *8*(5), 61023. <https://doi.org/10.1371/journal.pone.0061023>
- Parker, J., Sarlang, S., Thavagnanam, S., Williamson, G., O'Donoghue, D., Villenave, R., Power, U., Shields, M., Heaney, L., & Skibinski, G. (2010). A 3-D well-differentiated model of pediatric bronchial epithelium demonstrates unstimulated morphological differences between asthmatic and nonasthmatic cells. *Pediatric Research*, *67*(1), 17–22. <https://doi.org/10.1203/PDR.0b013e3181c0b200>
- Pease, J. E., & Williams, T. J. (2001). Eotaxin and asthma. In *Current Opinion in Pharmacology* (Vol. 1, Issue 3, pp. 248–253). [https://doi.org/10.1016/S1471-4892\(01\)00044-3](https://doi.org/10.1016/S1471-4892(01)00044-3)
- Pepicelli, C. V., Lewis, P. M., & McMahon, A. P. (1998). Sonic hedgehog regulates branching morphogenesis in the mammalian lung. *Current Biology*, *8*(19), 1083–1086. [https://doi.org/10.1016/S0960-9822\(98\)70446-4](https://doi.org/10.1016/S0960-9822(98)70446-4)
- Perez-Moreno, M., Jamora, C., & Fuchs, E. (2003). Sticky business: Orchestrating cellular signals at adherens junctions. In *Cell* (Vol. 112, Issue 4, pp. 535–548). Elsevier. [https://doi.org/10.1016/S0092-8674\(03\)00108-9](https://doi.org/10.1016/S0092-8674(03)00108-9)
- Peters, M. C., Ringel, L., Dyjack, N., Herrin, R., Woodruff, P. G., Rios, C., O'Connor, B., Fahy, J. V., & Seibold, M. A. (2019). A transcriptomic method to determine airway immune dysfunction in T2-high and T2-low asthma. *American Journal of Respiratory and Critical Care Medicine*, *199*(4), 465–477. <https://doi.org/10.1164/rccm.201807-1291OC>
- Phipson, B., Sim, C. B., Porrello, E. R., Hewitt, A. W., Powell, J., & Oshlack, A. (2022). Propeller : testing for differences in cell type proportions in single cell data. *Bioinformatics*, *38*(20), 4720–4726. <https://doi.org/10.1093/bioinformatics/btac582>
- Piunti, A., & Shilatifard, A. (2021). The roles of Polycomb repressive complexes in mammalian development and cancer. *Nature Reviews Molecular Cell Biology* *2021* *22*:5, *22*(5), 326–345. <https://doi.org/10.1038/S41580-021-00341-1>
- Post, S., Heijink, I. H., Hesse, L., Koo, H. K., Shaheen, F., Fouadi, M., Kuchibhotla, V. N. S., Lambrecht, B.

- N., Van Oosterhout, A. J. M., Hackett, T. L., & Nawijn, M. C. (2018). Characterization of a lung epithelium specific E-cadherin knock-out model: Implications for obstructive lung pathology. *Scientific Reports*, 8(1). <https://doi.org/10.1038/s41598-018-31500-8>
- Prescott, R. A., Pankow, A. P., Vries, M. de, Crosse, K., Patel, R. S., Alu, M., Loomis, C., Torres, V., Korolov, S., Ivanova, E., Dittmann, M., & Rosenberg, B. R. (2023). A comparative study of in vitro air-liquid interface culture models of the human airway epithelium evaluating cellular heterogeneity and gene expression at single cell resolution. *BioRxiv*, 2023.02.27.530299. <https://www.biorxiv.org/content/10.1101/2023.02.27.530299v1%0Ahttps://www.biorxiv.org/content/10.1101/2023.02.27.530299v1.abstract>
- Quarmany, L. M. (2004). Cellular Deflagellation. *International Review of Cytology*, 233, 47–91. [https://doi.org/10.1016/S0074-7696\(04\)33002-0](https://doi.org/10.1016/S0074-7696(04)33002-0)
- Ramsey, K. A., Rushton, Z. L., & Ehre, C. (2016). Mucin Agarose Gel Electrophoresis: Western Blotting for High-molecular-weight Glycoproteins. *J. Vis. Exp*, 112, 54153. <https://doi.org/10.3791/54153>
- Rao Tata, P., Mou, H., Pardo-Saganta, A., Zhao, R., Prabhu, M., Law, B. M., Vinarsky, V., Cho, J. L., Breton, S., Sahay, A., Medoff, B. D., & Rajagopal, J. (2013). Dedifferentiation of committed epithelial cells into stem cells in vivo. *Nature*, 503. <https://doi.org/10.1038/nature12777>
- Rawlins, E. L., Clark, C. P., Xue, Y., & Hogan, B. L. M. (2009). The Id2+ distal tip lung epithelium contains individual multipotent embryonic progenitor cells. *Development*, 136(22), 3741–3745. <https://doi.org/10.1242/dev.037317>
- Rawlins, E. L., & Hogan, B. L. M. (2008). Ciliated epithelial cell lifespan in the mouse trachea and lung. *American Journal of Physiology - Lung Cellular and Molecular Physiology*, 295(1), 231–234. <https://doi.org/10.1152/ajplung.90209.2008>
- Rawlins, E. L., Okubo, T., Xue, Y., Brass, D. M., Auten, R. L., Hasegawa, H., Wang, F., & Hogan, B. L. M. (2009). The Role of Scgb1a1+ Clara Cells in the Long-Term Maintenance and Repair of Lung Airway, but Not Alveolar, Epithelium. *Cell Stem Cell*, 4(6), 525–534. <https://doi.org/10.1016/j.stem.2009.04.002>
- Redman, E., Fierville, M., Cavard, A., & Plaisant, M. (2024). Cell culture differentiation and proliferation conditions influence the in vitro regeneration of the human airway epithelium. *BioRxiv Cell Biology*. [https://www.biorxiv.org/content/10.1101/2024.03.16.584842v1?rss=1&utm\\_source=researcher\\_app&utm\\_medium=referral&utm\\_campaign=RESR\\_MRKT\\_Researcher\\_inbound](https://www.biorxiv.org/content/10.1101/2024.03.16.584842v1?rss=1&utm_source=researcher_app&utm_medium=referral&utm_campaign=RESR_MRKT_Researcher_inbound)
- Reehorst, C. M., Nightingale, R., Luk, I. Y., Jenkins, L., Koentgen, F., Williams, D. S., Darido, C., Tan, F., Anderton, H., Chopin, M., Schoffer, K., Eissmann, M. F., Buchert, M., Mouradov, D., Sieber, O. M., Ernst, M., Dhillon, A. S., & Mariadason, J. M. (2021). EHF is essential for epidermal and colonic epithelial homeostasis, and suppresses Apc-initiated colonic tumorigenesis. *Development (Cambridge)*, 148(12). <https://doi.org/10.1242/dev.199542>
- Reid, C. J., Gould, S., & Harris, A. (1997). Developmental Expression of Mucin Genes in the Human Respiratory Tract. *American Journal of Respiratory Cell and Molecular Biology*, 17(5), 592–598. <https://doi.org/10.1165/ajrcmb.17.5.2798>
- Revinski, D. R., Zaragosi, L.-E., Boutin, C., Ruiz-Garcia, S., Deprez, M., Thomé, V., Rosnet, O., Gay, A.-S., Mercey, O., Paquet, A., Pons, N., Ponzio, G., Marcet, B., Kodjabachian, L., & Barbry, P. (2018). CDC20B is required for deuterosome-mediated centriole production in multiciliated cells. *Nature Communications*, 9(1), 4668. <https://doi.org/10.1038/s41467-018-06768-z>
- Reynolds, S. D., Zemke, A. C., Giangreco, A., Brockway, B. L., Teisanu, R. M., Drake, J. A., Mariani, T., Di,



- P. Y. P., Taketo, M. M., & Stripp, B. R. (2008). Conditional Stabilization of  $\beta$ -Catenin Expands the Pool of Lung Stem Cells. *Stem Cells*, 26(5), 1337–1346. <https://doi.org/10.1634/stemcells.2008-0053>
- Rezaee, F., & Georas, S. N. (2014). Breaking barriers: New insights into airway epithelial barrier function in health and disease. *American Journal of Respiratory Cell and Molecular Biology*, 50(5), 857–869. <https://doi.org/10.1165/rcmb.2013-0541RT>
- Roberts, N., Al Mubarak, R., Francisco, D., Kraft, M., & Chu, H. W. (2018). Comparison of paired human nasal and bronchial airway epithelial cell responses to rhinovirus infection and IL-13 treatment. *Clinical and Translational Medicine* 2018 7:1, 7(1), 1–10. <https://doi.org/10.1186/S40169-018-0189-2>
- Robinson, D., Humbert, M., Buhl, R., Cruz, A. A., Inoue, H., Korom, S., Hanania, N. A., & Nair, P. (2017). Revisiting Type 2-high and Type 2-low airway inflammation in asthma: current knowledge and therapeutic implications. In *Clinical and Experimental Allergy* (Vol. 47, Issue 2, pp. 161–175). John Wiley & Sons, Ltd. <https://doi.org/10.1111/cea.12880>
- Rock, J. R., Gao, X., Xue, Y., Randell, S. H., Kong, Y. Y., & Hogan, B. L. M. (2011). Notch-dependent differentiation of adult airway basal stem cells. *Cell Stem Cell*, 8(6), 639–648. <https://doi.org/10.1016/j.stem.2011.04.003>
- Rock, J. R., & Hogan, B. L. M. (2011). Epithelial Progenitor Cells in Lung Development, Maintenance, Repair, and Disease. *Annual Review of Cell and Developmental Biology*, 27(1), 493–512. <https://doi.org/10.1146/annurev-cellbio-100109-104040>
- Rock, J. R., Onaitis, M. W., Rawlins, E. L., Lu, Y., Clark, C. P., Xue, Y., Randell, S. H., & Hogan, B. L. M. (2009). Basal cells as stem cells of the mouse trachea and human airway epithelium. *Proceedings of the National Academy of Sciences of the United States of America*, 106(31), 12771–12775. <https://doi.org/10.1073/pnas.0906850106>
- Rock, J. R., Randell, S. H., & Hogan, B. L. M. (2010). Airway basal stem cells: a perspective on their roles in epithelial homeostasis and remodeling. *Disease Models & Mechanisms*, 3(9–10), 545–556. <https://doi.org/10.1242/dmm.006031>
- Rogers, D. (1994). Airway goblet cells: responsive and adaptable front-line defenders. *European Respiratory Journal*, 7(9), 1690–1706. <https://doi.org/10.1183/09031936.94.07091690>
- Rollinger, J. M., & Schmidtke, M. (2011). The human rhinovirus: Human-pathological impact, mechanisms of antirhinoviral agents, and strategies for their discovery. In *Medicinal Research Reviews* (Vol. 31, Issue 1, pp. 42–92). John Wiley & Sons, Ltd. <https://doi.org/10.1002/med.20176>
- Rosenberg, A. B., Roco, C. M., Muscat, R. A., Kuchina, A., Sample, P., Yao, Z., Graybuck, L. T., Peeler, D. J., Mukherjee, S., Chen, W., Pun, S. H., Sellers, D. L., Tasic, B., & Seelig, G. (2018). Single-cell profiling of the developing mouse brain and spinal cord with split-pool barcoding. *Science*, 360(6385), 176–182. [https://doi.org/10.1126/SCIENCE.AAM8999/SUPPL\\_FILE/PAPV2.PDF](https://doi.org/10.1126/SCIENCE.AAM8999/SUPPL_FILE/PAPV2.PDF)
- Roth, D., Şahin, A. T., Ling, F., Senger, C. N., Quiroz, E. J., Calvert, B. A., van der Does, A. M., Güney, T. G., Tephro, N., Glasl, S., van Schadewijk, A., Laura, von S., Olmer, R., Kanso, E., Nawroth, J. C., & Ryan, A. L. (2024). Structure-function relationships of mucociliary clearance in human airways. *BioRxiv*. <https://doi.org/10.1101/2023.12.24.572054>
- Ruat, M., Roudaut, H., Ferent, J., & Traiffort, E. (2012). Hedgehog trafficking, cilia and brain functions. *Differentiation*, 83(2), S97–S104. <https://doi.org/10.1016/j.diff.2011.11.011>
- Ruiz García, S., Deprez, M., Lebrigand, K., Cavard, A., Paquet, A., Arguel, M.-J., Magnone, V., Truchi, M., Caballero, I., Leroy, S., Marquette, C.-H., Marcet, B., Barbry, P., & Zaragosi, L.-E. (2019). Novel

- dynamics of human mucociliary differentiation revealed by single-cell RNA sequencing of nasal epithelial cultures. *Development*, 146(20). <https://doi.org/10.1242/dev.177428>
- Russell, R. J., Chachi, L., FitzGerald, J. M., Backer, V., Olivenstein, R., Titlestad, I. L., Ulrik, C. S., Harrison, T., Singh, D., Chaudhuri, R., Leaker, B., McGarvey, L., Siddiqui, S., Wang, M., Braddock, M., Nordenmark, L. H., Cohen, D., Parikh, H., Colice, G., ... Howarth, P. (2018). Effect of tralokinumab, an interleukin-13 neutralising monoclonal antibody, on eosinophilic airway inflammation in uncontrolled moderate-to-severe asthma (MESOS): a multicentre, double-blind, randomised, placebo-controlled phase 2 trial. *The Lancet Respiratory Medicine*, 6(7), 499–510. [https://doi.org/10.1016/S2213-2600\(18\)30201-7](https://doi.org/10.1016/S2213-2600(18)30201-7)
- Saetta, M., Di Stefano, A., Rosina, C., Thiene, G., & Fabbri, L. M. (1991). Quantitative structural analysis of peripheral airways and arteries in sudden fatal asthma. *American Review of Respiratory Disease*, 143(1), 138–143. <https://doi.org/10.1164/ajrccm/143.1.138>
- Salter, M., Biggadike, K., Matthews, J. L., West, M. R., Haase, M. V., Farrow, S. N., Uings, I. J., & Gray, D. W. (2007). Pharmacological properties of the enhanced-affinity glucocorticoid fluticasone furoate in vitro and in an in vivo model of respiratory inflammatory disease. *American Journal of Physiology-Lung Cellular and Molecular Physiology*, 293(3), L660–L667. <https://doi.org/10.1152/ajplung.00108.2007>
- Sayers, I., John, C., Chen, J., & Hall, I. P. (2024). Genetics of chronic respiratory disease. *Nature Reviews Genetics*. <https://doi.org/10.1038/s41576-024-00695-0>
- Schiller, H. B., Montoro, D. T., Simon, L. M., Rawlins, E. L., Meyer, K. B., Strunz, M., Vieira Braga, F. A., Timens, W., Koppelman, G. H., Budinger, G. R. S., Burgess, J. K., Waghay, A., Van Den Berge, M., Theis, F. J., Regev, A., Kaminski, N., Rajagopal, J., Teichmann, S. A., Misharin, A. V., & Nawijn, M. C. (2019). The human lung cell atlas: A high-resolution reference map of the human lung in health and disease. *American Journal of Respiratory Cell and Molecular Biology*, 61(1), 31–41. <https://doi.org/10.1165/rcmb.2018-0416TR>
- Schindelin, J., Arganda-Carreras, I., Frise, E., Kaynig, V., Longair, M., Pietzsch, T., Preibisch, S., Rueden, C., Saalfeld, S., Schmid, B., Tinevez, J. Y., White, D. J., Hartenstein, V., Eliceiri, K., Tomancak, P., & Cardona, A. (2012). Fiji: an open-source platform for biological-image analysis. *Nature Methods* 2012 9:7, 9(7), 676–682. <https://doi.org/10.1038/nmeth.2019>
- Schlingmann, K. P., Waldegger, S., Konrad, M., Chubanov, V., & Gudermann, T. (2007). TRPM6 and TRPM7—Gatekeepers of human magnesium metabolism. *Biochimica et Biophysica Acta (BBA) - Molecular Basis of Disease*, 1772(8), 813–821. <https://doi.org/10.1016/j.bbadis.2007.03.009>
- Seibold, M. A., Wise, A. L., Speer, M. C., Steele, M. P., Brown, K. K., Loyd, J. E., Fingerlin, T. E., Zhang, W., Gudmundsson, G., Groshong, S. D., Evans, C. M., Garantziotis, S., Adler, K. B., Dickey, B. F., du Bois, R. M., Yang, I. V., Herron, A., Kervitsky, D., Talbert, J. L., ... Schwartz, D. A. (2011). A Common MUC5B Promoter Polymorphism and Pulmonary Fibrosis. *New England Journal of Medicine*, 364(16), 1503–1512. <https://doi.org/10.1056/nejmoa1013660>
- Setty, M., Kiseliovas, V., Levine, J., Gayoso, A., Mazutis, L., & Pe'er, D. (2019). Characterization of cell fate probabilities in single-cell data with Palantir. *Nature Biotechnology*, 37(4), 451–460. <https://doi.org/10.1038/s41587-019-0068-4>
- Shah, V. S., Meyerholz, D. K., Tang, X. X., Reznikov, L., Alaiwa, M. A., Ernst, S. E., Karp, P. H., Wohlford-Lenane, C. L., Heilmann, K. P., Leidinger, M. R., Allen, P. D., Zabner, J., McCray, P. B., Ostedgaard, L. S., Stoltz, D. A., Randak, C. O., & Welsh, M. J. (2016). Airway acidification initiates host defense abnormalities in cystic fibrosis mice. *Science (New York, N.Y.)*, 351(6272), 503. <https://doi.org/10.1126/SCIENCE.AAD5589>

- Shankar, A., McAlees, J. W., & Lewkowich, I. P. (2022). Modulation of IL-4/IL-13 cytokine signaling in the context of allergic disease. *Journal of Allergy and Clinical Immunology*, *150*(2), 266–276. <https://doi.org/10.1016/j.jaci.2022.06.012>
- Siddiqui, S., Johansson, K., Joo, A., Bonser, L. R., Koh, K. D., Le Tonqueze, O., Bolourchi, S., Bautista, R. A., Zlock, L., Roth, T. L., Marson, A., Bhakta, N. R., Mark Ansel, K., Finkbeiner, W. E., Erle, D. J., & Woodruff, P. G. (2021). Epithelial miR-141 regulates IL-13–induced airway mucus production. *JCI Insight*, *6*(5). <https://doi.org/10.1172/JCI.INSIGHT.139019>
- Silva, J. P., Lelianova, V. G., Ermolyuk, Y. S., Vysokov, N., Hitchen, P. G., Berninghausen, O., Rahman, M. A., Zangrandi, A., Fidalgo, S., Tonevitsky, A. G., Dell, A., Volynski, K. E., & Ushkaryov, Y. A. (2011). Latrophilin 1 and its endogenous ligand Lasso/teneurin-2 form a high-affinity transsynaptic receptor pair with signaling capabilities. *Proceedings of the National Academy of Sciences of the United States of America*, *108*(29), 12113–12118. [https://doi.org/10.1073/PNAS.1019434108/SUPPL\\_FILE/PNAS.201019434SI.PDF](https://doi.org/10.1073/PNAS.1019434108/SUPPL_FILE/PNAS.201019434SI.PDF)
- Skapenko, A., Leipe, J., Niesner, U., Devriendt, K., Beetz, R., Radbruch, A., Kalden, J. R., Lipsky, P. E., & Schulze-Koops, H. (2004). GATA-3 in Human T Cell Helper Type 2 Development. *Journal of Experimental Medicine*, *199*(3), 423–428. <https://doi.org/10.1084/JEM.20031323>
- Som, P. M., & Naidich, T. P. (2013). Illustrated review of the embryology and development of the facial region, part 1: Early face and lateral nasal cavities. In *American Journal of Neuroradiology* (Vol. 34, Issue 12, pp. 2233–2240). <https://doi.org/10.3174/ajnr.A3415>
- Song, H., Yao, E., Lin, C., Gacayan, R., Chen, M.-H., & Chuang, P.-T. (2012). Functional characterization of pulmonary neuroendocrine cells in lung development, injury, and tumorigenesis. *Proceedings of the National Academy of Sciences*, *109*(43), 17531–17536. <https://doi.org/10.1073/pnas.1207238109>
- Sorokin, S. P. (1968). Reconstructions of centriole formation and ciliogenesis in mammalian lungs. *Journal of Cell Science*, *3*(2), 207–230. <https://doi.org/10.1242/jcs.3.2.207>
- Spector, C., De Sanctis, C. M., Panettieri, R. A., & Koziol-White, C. J. (2023). Rhinovirus induces airway remodeling: what are the physiological consequences? *Respiratory Research*, *24*(1), 238. <https://doi.org/10.1186/s12931-023-02529-9>
- Spinelli, J. B., & Haigis, M. C. (2018). The multifaceted contributions of mitochondria to cellular metabolism. *Nature Cell Biology* *20*:7, *20*(7), 745–754. <https://doi.org/10.1038/S41556-018-0124-1>
- Spinozzi, S., Albin, S., Best, H., & Richard, I. (2021). Calpains for dummies: What you need to know about the calpain family. *Biochimica et Biophysica Acta (BBA) - Proteins and Proteomics*, *1869*(5), 140616. <https://doi.org/10.1016/J.BBAPAP.2021.140616>
- Stikker, B. S., Hendriks, R. W., & Stadhouders, R. (2023). Decoding the genetic and epigenetic basis of asthma. *Allergy: European Journal of Allergy and Clinical Immunology*, *January*, 940–956. <https://doi.org/10.1111/all.15666>
- Stoeckius, M., Zheng, S., Houck-Loomis, B., Hao, S., Yeung, B. Z., Mauck, W. M., Smibert, P., & Satija, R. (2018). Cell Hashing with barcoded antibodies enables multiplexing and doublet detection for single cell genomics. *Genome Biology*, *19*(1), 1–12. <https://doi.org/10.1186/s13059-018-1603-1>
- Stringer, C., Wang, T., Michaelos, M., & Pachitariu, M. (2020). Cellpose: a generalist algorithm for cellular segmentation. *Nature Methods* *2020* *18*:1, *18*(1), 100–106. <https://doi.org/10.1038/s41592-020-01018-x>
- Stubbs, J. L., Vladar, E. K., Axelrod, J. D., & Kintner, C. (2012). Multicilin promotes centriole assembly

- and ciliogenesis during multiciliate cell differentiation. *Nature Cell Biology*, 14(2), 140–147. <https://doi.org/10.1038/ncb2406>
- Suly Saray Villa Vasquez, John van Dam, G. W. (2021). *An updated SYSCILIA gold standard (SCGSv2) of known ciliary genes, revealing the vast progress that has been made in the cilia research field.*
- Sun, D., Llorca Batlle, O., van den Ameele, J., Thomas, J. C., He, P., Lim, K., Tang, W., Xu, C., Meyer, K. B., Teichmann, S. A., Marioni, J. C., Jackson, S. P., Brand, A. H., & Rawlins, E. L. (2022). SOX9 maintains human foetal lung tip progenitor state by enhancing WNT and RTK signalling. *The EMBO Journal*, 41(21), 1–17. <https://doi.org/10.15252/embj.2022111338>
- Sun, X., Perl, A.-K., Li, R., Bell, S. M., Sajti, E., Kalinichenko, V. V., Kalin, T. V., Misra, R. S., Deshmukh, H., Clair, G., Kyle, J., Crotty Alexander, L. E., Masso-Silva, J. A., Kitzmiller, J. A., Wikenheiser-Brokamp, K. A., Deutsch, G., Guo, M., Du, Y., Morley, M. P., ... Morrissey, E. E. (2022). A census of the lung: CellCards from LungMAP. *Developmental Cell*, 57(1), 112-145.e2. <https://doi.org/10.1016/j.devcel.2021.11.007>
- Tan, H. T. T., Hagner, S., Ruchti, F., Radzikowska, U., Tan, G., Altunbulakli, C., Eljaszewicz, A., Moniuszko, M., Akdis, M., Akdis, C. A., Garn, H., & Sokolowska, M. (2019). Tight junction, mucin, and inflammasome-related molecules are differentially expressed in eosinophilic, mixed, and neutrophilic experimental asthma in mice. *Allergy: European Journal of Allergy and Clinical Immunology*, 74(2), 294–307. <https://doi.org/10.1111/all.13619>
- Tata, A., Kobayashi, Y., Chow, R. D., Tran, J., Desai, A., Massri, A. J., McCord, T. J., Gunn, M. D., & Tata, P. R. (2018). Myoepithelial Cells of Submucosal Glands Can Function as Reserve Stem Cells to Regenerate Airways after Injury. *Cell Stem Cell*, 22(5), 668-683.e6. <https://doi.org/10.1016/j.stem.2018.03.018>
- Tata, P. R., & Rajagopal, J. (2017). Plasticity in the lung: making and breaking cell identity. *Development*, 144(5), 755–766. <https://doi.org/10.1242/dev.143784>
- Terré, B., Piergiovanni, G., Segura-Bayona, S., Gil-Gómez, G., Youssef, S. A., Attolini, C. S.-O., Wilsch-Bräuninger, M., Jung, C., Rojas, A. M., Marjanović, M., Knobel, P. A., Palenzuela, L., López-Rovira, T., Forrow, S., Huttner, W. B., Valverde, M. A., de Bruin, A., Costanzo, V., & Stracker, T. H. (2016). GEMC 1 is a critical regulator of multiciliated cell differentiation. *The EMBO Journal*, 35(9), 942–960. <https://doi.org/10.15252/embj.201592821>
- Thomas, B., Rutman, A., Hirst, R. A., Haldar, P., Wardlaw, A. J., Bankart, J., Brightling, C. E., & O’Callaghan, C. (2010). Ciliary dysfunction and ultrastructural abnormalities are features of severe asthma. *Journal of Allergy and Clinical Immunology*, 126(4), 722-729.e2. <https://doi.org/10.1016/j.jaci.2010.05.046>
- Thomas, J., Morlé, L., Soulavie, F., Laurençon, A., Sagnol, S., & Durand, B. (2010). Transcriptional control of genes involved in ciliogenesis: a first step in making cilia. *Biology of the Cell*, 102(9), 499–513. <https://doi.org/10.1042/bc20100035>
- Tian, E., Syed, Z. A., Edin, M. L., Zeldin, D. C., & Ten Hagen, K. G. (2023). Dynamic expression of mucins and the genes controlling mucin-type O-glycosylation within the mouse respiratory system. *Glycobiology*, 33, 476–489. <https://doi.org/10.1093/glycob/cwad031>
- Toczyłowska-Mamińska, R., & Dołowy, K. (2012). Ion transporting proteins of human bronchial epithelium. *Journal of Cellular Biochemistry*, 113(2), 426–432. <https://doi.org/10.1002/jcb.23393>
- Tsao, P. N., Vasconcelos, M., Izvolsky, K. I., Qian, J., Lu, J., & Cardoso, W. V. (2009). Notch signaling controls the balance of ciliated and secretory cell fates in developing airways. *Development*, 136(13), 2297–2307. <https://doi.org/10.1242/dev.034884>

- Tsiogka, A., Kyriazopoulou, M., Kontochristopoulos, G., Nicolaidou, E., Stratigos, A., Rigopoulos, D., & Gregoriou, S. (2022). The JAK/STAT Pathway and Its Selective Inhibition in the Treatment of Atopic Dermatitis: A Systematic Review. *Journal of Clinical Medicine* 2022, Vol. 11, Page 4431, 11(15), 4431. <https://doi.org/10.3390/JCM11154431>
- Tsukui, T., Sun, K. H., Wetter, J. B., Wilson-Kanamori, J. R., Hazelwood, L. A., Henderson, N. C., Adams, T. S., Schupp, J. C., Poli, S. D., Rosas, I. O., Kaminski, N., Matthay, M. A., Wolters, P. J., & Sheppard, D. (2020). Collagen-producing lung cell atlas identifies multiple subsets with distinct localization and relevance to fibrosis. *Nature Communications*, 11(1), 1–16. <https://doi.org/10.1038/s41467-020-15647-5>
- Tugores, A., Le, J., Sorokina, I., Snijders, A. J., Duyao, M., Reddy, P. S., Carlée, L., Ronshaugen, M., Mushegian, A., Watanaskul, T., Chu, S., Buckler, A., Emtage, S., & McCormick, M. K. (2001). The Epithelium-specific ETS Protein EHF/ESE-3 is a Context-dependent Transcriptional Repressor Downstream of MAPK Signaling Cascades. *Journal of Biological Chemistry*, 276(23), 20397–20406. <https://doi.org/10.1074/jbc.M010930200>
- Turner, J., Roger, J., Fitau, J., Combe, D., Giddings, J., Van Heeke, G., & Jones, C. E. (2011). Goblet cells are derived from a FOXJ1-expressing progenitor in a human airway epithelium. *American Journal of Respiratory Cell and Molecular Biology*, 44(3), 276–284. <https://doi.org/10.1165/rcmb.2009-0304OC>
- Tyner, J. W., Kim, E. Y., Ide, K., Pelletier, M. R., Roswit, W. T., Morton, J. D., Battaile, J. T., Patel, A. C., Patterson, G. A., Castro, M., Spoor, M. S., You, Y., Brody, S. L., & Holtzman, M. J. (2006). Blocking airway mucous cell metaplasia by inhibiting EGFR antiapoptosis and IL-13 transdifferentiation signals. *Journal of Clinical Investigation*, 116(2), 309–321. <https://doi.org/10.1172/JCI25167>
- Varricchi, G., Ferri, S., Pepys, J., Poto, R., Spadaro, G., Nappi, E., Paoletti, G., Virchow, J. C., Heffler, E., & Canonica, W. G. (2022). Biologics and airway remodeling in severe asthma. *Allergy: European Journal of Allergy and Clinical Immunology*, August. <https://doi.org/10.1111/all.15473>
- Verploegen, S., Ulfman, L., Van Deutekom, H. W. M., Van Aalst, C., Honing, H., Lammers, J. W. J., Koenderman, L., & Coffey, P. J. (2005). Characterization of the role of CaMKI-like kinase (CKLiK) in human granulocyte function. *Blood*, 106(3), 1076–1083. <https://doi.org/10.1182/BLOOD-2004-09-3755>
- Vieira Braga, F. A., Kar, G., Berg, M., Carpaaj, O. A., Polanski, K., Simon, L. M., Brouwer, S., Gomes, T., Hesse, L., Jiang, J., Fasouli, E. S., Efremova, M., Vento-Tormo, R., Talavera-López, C., Jonker, M. R., Affleck, K., Palit, S., Strzelecka, P. M., Firth, H. V., ... Teichmann, S. A. (2019). A cellular census of human lungs identifies novel cell states in health and in asthma. *Nature Medicine*, 25(7), 1153–1163. <https://doi.org/10.1038/s41591-019-0468-5>
- Virshup, I., Rybakov, S., Theis, F. J., Angerer, P., & Wolf, F. A. (2021). anndata: Annotated data. *BioRxiv*, 2021.12.16.473007. <https://doi.org/10.1101/2021.12.16.473007>
- Vladar, E. K., Antic, D., & Axelrod, J. D. (2009). Planar Cell Polarity Signaling: The Developing Cell's Compass. *Cold Spring Harbor Perspectives in Biology*, 1(3), a002964–a002964. <https://doi.org/10.1101/cshperspect.a002964>
- Waghray, A., Monga, I., Lin, B., Shah, V., Slyper, M., Giotti, B., Xu, J., Waldman, J., Dionne, D., Nguyen, L. T., Lou, W., Cai, P., Park, E., Muus, C., Sun, J., Surve, M. V., Yang, L. C. C., Rozenblatt-Rosen, O., Dolerey, T. M., ... Rajagopal, J. (2023). A deep lung cell atlas reveals cytokine-mediated lineage switching of a rare cell progenitor of the human airway epithelium. *BioRxiv : The Preprint Server for Biology*, 2023.11.28.569028. <https://doi.org/10.1101/2023.11.28.569028>
- Walentek, P. (2018). *Manipulating and Analyzing Cell Type Composition of the Xenopus Mucociliary*

- Epidermis* (K. Vleminckx (ed.); Vol. 1865, pp. 251–263). Springer New York. [https://doi.org/10.1007/978-1-4939-8784-9\\_18](https://doi.org/10.1007/978-1-4939-8784-9_18)
- Walentek, P., Beyer, T., Thumberger, T., Schweickert, A., & Blum, M. (2012). ATP4a Is Required for Wnt-Dependent Foxj1 Expression and Leftward Flow in *Xenopus* Left-Right Development. *Cell Reports*, 1(5), 516–527. <https://doi.org/10.1016/j.celrep.2012.03.005>
- Wallmeier, J., Nielsen, K. G., Kuehni, C. E., Lucas, J. S., Leigh, M. W., Zariwala, M. A., & Omran, H. (2020). Motile ciliopathies. *Nature Reviews Disease Primers* 2020 6:1, 6(1), 1–29. <https://doi.org/10.1038/S41572-020-0209-6>
- Walters, M. S., Gomi, K., Ashbridge, B., Moore, M. A. S., Arbelaez, V., Heldrich, J., Ding, B. Sen, Rafii, S., Staudt, M. R., & Crystal, R. G. (2013). Generation of a human airway epithelium derived basal cell line with multipotent differentiation capacity. *Respiratory Research*, 14(1), 1–18. <https://doi.org/10.1186/1465-9921-14-135/FIGURES/9>
- Wang, S.-Z., Rosenberger, C. L., Bao, Y.-X., Stark, J. M., & Harrod, K. S. (2003). Clara Cell Secretory Protein Modulates Lung Inflammatory and Immune Responses to Respiratory Syncytial Virus Infection. *The Journal of Immunology*, 171(2), 1051–1060. <https://doi.org/10.4049/JIMMUNOL.171.2.1051>
- Warner, S. M., Wiehler, S., Michi, A. N., & Proud, D. (2019). Rhinovirus replication and innate immunity in highly differentiated human airway epithelial cells. *Respiratory Research*, 20(1), 1–13. <https://doi.org/10.1186/s12931-019-1120-0>
- Watelet, J. B., & Van Cauwenberge, P. (1999). Applied anatomy and physiology of the nose and paranasal sinuses. *Allergy: European Journal of Allergy and Clinical Immunology, Supplement*, 54(57), 14–25.
- Watson, J. H. L., & Brinkman, G. L. (1964). ELECTRON MICROSCOPY OF THE EPITHELIAL CELLS OF NORMAL AND BRONCHITIC HUMAN BRONCHUS. *Clinical and Laboratory Studies of Tuberculosis and Respiratory Diseases*, 90(December), 851–866.
- Watson, J. K., Rulands, S., Wilkinson, A. C., Wuidart, A., Ousset, M., Van Keymeulen, A., Göttgens, B., Blanpain, C., Simons, B. D., & Rawlins, E. L. (2015). Clonal Dynamics Reveal Two Distinct Populations of Basal Cells in Slow-Turnover Airway Epithelium. *Cell Reports*, 12(1), 90–101. <https://doi.org/10.1016/j.celrep.2015.06.011>
- Weibel, E. R., & Gomez, D. M. (1962). Architecture of the human lung. *Science*, 137(3530), 577–585. <https://doi.org/10.1126/science.137.3530.577>
- Weiler, P., Lange, M., Klein, M., Pe’er, D., & Theis, F. (2024). CellRank 2: unified fate mapping in multiview single-cell data. *Nature Methods*, 21(7), 1196–1205. <https://doi.org/10.1038/s41592-024-02303-9>
- Werner, S., Pimenta-Marques, A., & Bettencourt-Dias, M. (2017). Maintaining centrosomes and cilia. *Journal of Cell Science*, 130(22), 3789–3800. <https://doi.org/10.1242/jcs.203505>
- Whitsett, J. A., & Alenghat, T. (2015). Respiratory epithelial cells orchestrate pulmonary innate immunity. *Nature Immunology*, 16(1), 27–35. <https://doi.org/10.1038/ni.3045>
- Widdicombe, J. H., & Wine, J. J. (2015). Airway Gland Structure and Function. *Physiological Reviews*, 95(4), 1241–1319. <https://doi.org/10.1152/physrev.00039.2014>
- Wills-Karp, M., Luyimbazi, J., Xu, X., Schofield, B., Neben, T. Y., Karp, C. L., & Donaldson, D. D. (1998). Interleukin-13: Central mediator of allergic asthma. *Science*, 282(5397), 2258–2261. <https://doi.org/10.1126/science.282.5397.2258>
- Wolf, F. A., Angerer, P., & Theis, F. J. (2018). SCANPY: Large-scale single-cell gene expression data

- analysis. *Genome Biology*, 19(1), 1–5. <https://doi.org/10.1186/S13059-017-1382-0/FIGURES/1>
- Wong, Y. L., Anzola, J. V., Davis, R. L., Yoon, M., Motamedi, A., Kroll, A., Seo, C. P., Hsia, J. E., Kim, S. K., Mitchell, J. W., Mitchell, B. J., Desai, A., Gahman, T. C., Shiau, A. K., & Oegema, K. (2015). Reversible centriole depletion with an inhibitor of Polo-like kinase 4. *Science*, 348(6239), 1155–1160. <https://doi.org/10.1126/science.aaa5111>
- Woo, L. N., Guo, W. Y., Wang, X., Young, A., Salehi, S., Hin, A., Zhang, Y., Scott, J. A., & Chow, C. W. (2018). A 4-Week Model of House Dust Mite (HDM) Induced Allergic Airways Inflammation with Airway Remodeling. *Scientific Reports*, 8(1), 1–11. <https://doi.org/10.1038/s41598-018-24574-x>
- Woodruff, P. G., Boushey, H. A., Dolganov, G. M., Barker, C. S., Yee, H. Y., Donnelly, S., Ellwanger, A., Sidhu, S. S., Dao-Pick, T. P., Pantoja, C., Erle, D. J., Yamamoto, K. R., & Fahy, J. V. (2007). Genome-wide profiling identifies epithelial cell genes associated with asthma and with treatment response to corticosteroids. *Proceedings of the National Academy of Sciences of the United States of America*, 104(40), 15858–15863. <https://doi.org/10.1073/pnas.0707413104>
- Woodruff, P. G., Dolganov, G. M., Ferrando, R. E., Donnelly, S., Hays, S. R., Solberg, O. D., Carter, R., Wong, H. H., Cadbury, P. S., & Fahy, J. V. (2004). Hyperplasia of smooth muscle in mild to moderate asthma without changes in cell size or gene expression. *American Journal of Respiratory and Critical Care Medicine*, 169(9), 1001–1006. <https://doi.org/10.1164/rccm.200311-1529oc>
- Woodruff, P. G., Modrek, B., Choy, D. F., Jia, G., Abbas, A. R., Ellwanger, A., Arron, J. R., Koth, L. L., & Fahy, J. V. (2009). T-helper type 2-driven inflammation defines major subphenotypes of asthma. *American Journal of Respiratory and Critical Care Medicine*, 180(5), 388–395. <https://doi.org/10.1164/rccm.200903-0392OC>
- Wu, B., & Guo, W. (2015). The exocyst at a glance. *Journal of Cell Science*, 128(15), 2957–2964. <https://doi.org/10.1242/JCS.156398/-/DC1>
- Xiao, C., Puddicombe, S. M., Field, S., Haywood, J., Broughton-Head, V., Puxeddu, I., Haitchi, H. M., Vernon-Wilson, E., Sammut, D., Bedke, N., Cremin, C., Sones, J., Djukanović, R., Howarth, P. H., Collins, J. E., Holgate, S. T., Monk, P., & Davies, D. E. (2011). Defective epithelial barrier function in asthma. *Journal of Allergy and Clinical Immunology*, 128(3). <https://doi.org/10.1016/j.jaci.2011.05.038>
- Ximena, M., Ostrowski, L. E., & Bennett, W. D. (2006). Cilia and Mucociliary Clearance. *Encyclopedia of Respiratory Medicine, Four-Volume Set*, 466–470. <https://doi.org/10.1016/B0-12-370879-6/00079-X>
- Xu, C., Lopez, R., Mehlman, E., Regier, J., Jordan, M. I., & Yosef, N. (2021). Probabilistic harmonization and annotation of single-cell transcriptomics data with deep generative models. *Molecular Systems Biology*, 17(1). <https://doi.org/10.15252/MSB.20209620>
- Yang, Y., Riccio, P., Schotsaert, M., Mori, M., Lu, J., Lee, D. K., García-Sastre, A., Xu, J., & Cardoso, W. V. (2018). Spatial-Temporal Lineage Restrictions of Embryonic p63+ Progenitors Establish Distinct Stem Cell Pools in Adult Airways. *Developmental Cell*, 44(6), 752–761.e4. <https://doi.org/10.1016/j.devcel.2018.03.001>
- You, Y., Huang, T., Richer, E. J., Schmidt, J. E. H., Zabner, J., Borok, Z., & Brody, S. L. (2004). Role of f-box factor foxj1 in differentiation of ciliated airway epithelial cells. *American Journal of Physiology - Lung Cellular and Molecular Physiology*, 286(4 30-4), 650–657. <https://doi.org/10.1152/ajplung.00170.2003>
- Yu, G., Wang, L.-G., & He, Q.-Y. (2015). ChIPseeker: an R/Bioconductor package for ChIP peak annotation, comparison and visualization. *Bioinformatics*, 31(14), 2382–2383.

<https://doi.org/10.1093/bioinformatics/btv145>

- Yu, H., Li, Q., Kolosov, V. P., Perelman, J. M., & Zhou, X. (2010). Interleukin-13 Induces Mucin 5AC Production Involving STAT6/SPDEF in Human Airway Epithelial Cells. *Cell Communication & Adhesion*, 17(4–6), 83–92. <https://doi.org/10.3109/15419061.2010.551682>
- Yu, X., Ng, C. P., Habacher, H., & Roy, S. (2008). Foxj1 transcription factors are master regulators of the motile ciliogenic program. *Nature Genetics*, 40(12), 1445–1453. <https://doi.org/10.1038/ng.263>
- Zaragosi, L.-E., Gouleau, A., Delin, M., Lebrigand, K., Arguel, M.-J., Girard-Riboulleau, C., Rios, G., Redman, E., Plaisant, M., Waldmann, R., Magnone, V., Marcet, B., Barbry, P., & Ponzio, G. (2024). Combination of CRISPR-Cas9-RNP and Single-Cell RNAseq to Identify Cell State-Specific FOXJ1 Functions in the Human Airway Epithelium. In *MiMB: Vol. Soumis* (pp. 1–25). [https://doi.org/10.1007/978-1-0716-3507-0\\_1](https://doi.org/10.1007/978-1-0716-3507-0_1)
- Zaragosi, L. E., Deprez, M., & Barbry, P. (2020). Using single-cell RNA sequencing to unravel cell lineage relationships in the respiratory tract. *Biochemical Society Transactions*, 48(1), 327–336. <https://doi.org/10.1042/BST20191010>
- Zemke, A. C., Teisanu, R. M., Giangreco, A., Drake, J. A., Brockway, B. L., Reynolds, S. D., & Stripp, B. R. (2009).  $\beta$ -Catenin is not necessary for maintenance or repair of the bronchiolar epithelium. *American Journal of Respiratory Cell and Molecular Biology*, 41(5), 535–543. <https://doi.org/10.1165/rcmb.2008-0407OC>
- Zhao, H., Zhu, L., Zhu, Y., Cao, J., Li, S., Huang, Q., Xu, T., Huang, X., Yan, X., & Zhu, X. (2013). The Cep63 paralogue Deup1 enables massive de novo centriole biogenesis for vertebrate multiciliogenesis. *Nature Cell Biology*, 15(12), 1434–1444. <https://doi.org/10.1038/ncb2880>
- Zhen, G., Park, S. W., Nguyenvu, L. T., Rodriguez, M. W., Barbeau, R., Paquet, A. C., & Erle, D. J. (2007). IL-13 and Epidermal Growth Factor Receptor Have Critical but Distinct Roles in Epithelial Cell Mucin Production. *American Journal of Respiratory Cell and Molecular Biology*, 36(2), 244–253. <https://doi.org/10.1165/rcmb.2006-0180OC>
- Zhou, F., Narasimhan, V., Shboul, M., Chong, Y. L., Reversade, B., & Roy, S. (2015). Gmnc Is a Master Regulator of the Multiciliated Cell Differentiation Program. *Current Biology*, 25(24), 3267–3273. <https://doi.org/10.1016/j.cub.2015.10.062>
- Zhou, X., Franklin, R. A., Adler, M., Carter, T. S., Condiff, E., Adams, T. S., Pope, S. D., Philip, N. H., Meizlish, M. L., Kaminski, N., & Medzhitov, R. (2022). Microenvironmental sensing by fibroblasts controls macrophage population size. *Proceedings of the National Academy of Sciences of the United States of America*, 119(32). <https://doi.org/10.1073/pnas.2205360119>
- Zhou, X., Franklin, R. A., Adler, M., Jacox, J. B., Bailis, W., Shyer, J. A., Flavell, R. A., Mayo, A., Alon, U., & Medzhitov, R. (2018). Circuit Design Features of a Stable Two-Cell System. *Cell*, 172(4), 744–757.e17. <https://doi.org/10.1016/j.cell.2018.01.015>
- Zhu, Y., Ehre, C., Abdullah, L. H., Sheehan, J. K., Roy, M., Evans, C. M., Dickey, B. F., & Davis, C. W. (2008). Munc13-2<sup>-/-</sup> baseline secretion defect reveals source of oligomeric mucins in mouse airways. *Journal of Physiology*, 586(7), 1977–1992. <https://doi.org/10.1113/jphysiol.2007.149310>